Title
Optimization and Characterization of a Layer-by-Layer, Fully Printed, Secondary Zn-MnO2 Battery with an Ionic Liquid Gel Polymer Electrolyte for Internet of Things Applications

Author
Kim, Bernard Jeongkyu

Publication Date
2019

Peer reviewed|Thesis/dissertation

Optimization and Characterization of a Layer-by-Layer, Fully Printed, Secondary Zn-MnO_2 Battery with an Ionic Liquid Gel Polymer Electrolyte for Internet of Things Applications

by

Bernard Kim

A dissertation submitted in partial satisfaction of the

requirements for the degree of

Doctor of Philosophy

in

Engineering - Mechanical Engineering

in the

Graduate Division

of the

University of California, Berkeley

Committee in charge:

Professor Paul K. Wright, Chair
Professor Tarek I. Zohdi
Professor James W. Evans

Fall 2019

Optimization and Characterization of a Layer-by-Layer, Fully Printed, Secondary Zn-MnO_2 Battery with an Ionic Liquid Gel Polymer Electrolyte for Internet of Things Applications

Abstract

Optimization and Characterization of a Layer-by-Layer, Fully Printed, Secondary Zn-MnO_2 Battery with an Ionic Liquid Gel Polymer Electrolyte for Internet of Things Applications

by

Bernard Kim

Doctor of Philosophy in Engineering - Mechanical Engineering

University of California, Berkeley

Professor Paul K. Wright, Chair

Advancements in manufacturing for printed electronics have brought with it a demand for printed, rechargeable batteries capable of powering these devices. This research aims to meet this demand by characterizing and optimizing components and performance of a printed, rechargeable Zn-MnO_2 cell with an ionic liquid gel polymer electrolyte.

The cathode and anode are comprised of manganese dioxide (MnO_2) and zinc (Zn) respectively. The ionic liquids 1-butyl-3-methylimidazolium trifluoromethanesulfonate ($[BMIM]^+[OTf]^-$) and 1-ethyl-3-methylimidazolium trifluoromethanesulfonate ($[EMIM]^+[OTf]^-$) with the dissolved salt zinc trifluoromethanesulfonate ($Zn(OTf)_2$) are used as the electrolyte. These nonaqueous electrolytes have been shown to enable rechargeable zinc chemistries as well as compatibility with solution-cast polymer membranes to form gel polymer electrolytes (GPEs). When combined with poly(vinylidene fluoride-co-hexafluoropropylene) (PVDF-HFP) that is dissolved in n-methyl-2-pyrrolidone, a printable separator membrane capable of ionic conductance is produced. This separator membrane can then be incorporated into a layer-by-layer additive manufacturing process to produce a fully printed battery.

To produce consistent fully printed cells and to prevent catastrophic cell degradation and failure, additional variables must be considered and optimized. The printed electrode composition must be optimized for surface profile, rheology, and electric conductivity in order to enable uniform and dense separator layers. The ionic liquid electrolyte composition and gel polymer electrolyte morphology must be controlled in order to optimize mass transport and reaction kinetics. Furthermore, the mass transport and kinetic properties of Zn deposition and dissolution in ionic liquid electrolytes and gel polymer electrolytes must be characterized and understood. To characterize these aspects, battery components were produced via stencil casting, doctor blade coating, and solution casting. Electrochemical properties were characterized by cyclic voltammetry, chronoamperometry, and electrochemical impedance spectroscopy. Physical and electric properties were characterized by rheometry, profilometry, four point probe resistivity, and scanning electron microscopy. Cell performance was

characterized by galvanostatic and potentiostatic cycle life testing and pulsed current discharging, and differential capacity analysis was performed for further insights.

Ball milling and mechanical sieving was found to be an effective method to improve printed electrode surface profile, reducing waviness and roughness each by a factor of 4 compared to unoptimized electrodes while retaining similar conductivity.

Zn deposition and dissolution were found to be kinetically (rather than mass transport) limited and therefore quasireversible in both ionic liquids. Zn^{2+} diffusivity ranged from 1.42-3.38e-9 cm^2/s in $[BMIM]^+[OTf]^-$ electrolytes and from 1.64-4.87e-9 cm^2/s in $[EMIM]^+[OTf]^-$ electrolytes, decreasing with higher concentrations of $Zn(Otf)_2$ salt. $[EMIM]^+[OTf]^-$ electrolytes were found to provide higher Zn diffusivity, ionic conductivity, and redox kinetics, but were also more prone to forming electrical shorts through the GPE and offered lower discharge capacities than $[BMIM]^+[OTf]^-$ electrolytes. The polymer structure in the GPE was found to be highly dependent on processing temperature and pressure.

Fully printed cells were produced that prevented catastrophic cell failure from delamination of the cathode, resulting in at least a 20x improvement in cycle life compared to mechanically assembled cells. Average discharge capacities for fully printed cells ranged from 1.8-3.6 mAh/cm^3, and cells were cycled at least 200 times without catastrophic failure. Critical cell failure mechanisms including phase transformations of MnO_2 and deposition of Zn within poor GPE microstructures were identified. Finally, printed cells were discharged under a pulsed current discharge regime typical of those found in Internet of Things devices for 650 cycles without signs of degradation.

This research has successfully produced and characterized fully printed, rechargeable, Zn-MnO_2 cells with an ionic liquid gel polymer electrolyte for printed electronics and the Internet of Things. The results presented herein seek to further understanding of Zn interactions with ionic liquid gel polymer electrolytes and additive manufacturing methods for printed energy storage devices.

To my family and friends, for their love and support.

Contents

Contents **ii**

List of Figures **iv**

List of Tables **xiii**

1 Introduction **1**
1.1 Scope of Dissertation 2
1.2 Goals of Dissertation 4

2 Background **5**
2.1 Battery Fundamentals 5
2.2 Zinc-Based Batteries 8
2.3 Ionic Liquids and Zinc Redox Kinetics 9
2.4 Gel Polymer Electrolytes 10
2.5 Printing for Energy Storage 13

3 Nickel Current Collector and Ball Milling **14**
3.1 Motivation 14
3.2 Background 15
3.3 Experimental Methods 22
3.4 Results and Discussion 27
3.5 Conclusions 36

4 Optimization of Electrode Composition **38**
4.1 Motivation 38
4.2 Background 39
4.3 Experimental Methods 46
4.4 Results and Discussion 56
4.5 Conclusions 82

5 Ionic Liquids and Electrochemical Analysis **84**
5.1 Motivation 85

5.2 Background . . . 85
5.3 Electrochemical Methods . . . 87
5.4 Experimental Methods . . . 95
5.5 Results and Discussion . . . 100
5.6 Conclusions . . . 139

6 Development of Gel Polymer Electrolyte 141
6.1 Motivation . . . 142
6.2 Background . . . 142
6.3 Experimental Methods . . . 146
6.4 Results and Discussion . . . 156
6.5 Conclusions . . . 196

7 Full Cell Manufacturing and Cycling 199
7.1 Motivation . . . 199
7.2 Background . . . 200
7.3 Experimental Methods . . . 202
7.4 Results and Discussion . . . 206
7.5 Conclusions . . . 230

8 Battery Cycling for IoT Devices 232
8.1 Motivation . . . 232
8.2 Background . . . 233
8.3 Experimental Methods . . . 237
8.4 Results and Discussion . . . 242
8.5 Conclusion . . . 248

9 Conclusions and Future Work 249
9.1 Conclusions . . . 249
9.2 Future Work . . . 251

A Python Code 253

Bibliography 268

List of Figures

2.1 Schematic of an electrochemical cell during discharge. 6
2.2 Voltage and current during one cycle of charge discharge for Zn-MnO_2 cell. The cell was first charged to 1.8V, allowed to rest, and then discharged to 1.0V. . . . 7
2.3 Theoretical maximum capacity densities and specific capacities of Li, Na, Mg, Ca, and Zn metals. 8
2.4 1-ethyl-3-methylimidazolium ($[EMIM]^+$) and 1-butyl-3-methylimidazolium ($[BMIM]^+$) cations and trifluoromethanesulfonate ($[OTf]^-$) anion. 10
2.5 Ionic conductivities and diffusivities of $[EMIM]^+[OTf]^-$ and $[BMIM]^+[OTf]^-$ neat ionic liquids from available literature data [30]. 11
2.6 SEM micrographs of PVDF-HFP membranes cast from different solvents. *A*: THF+water; *B*: NMP+acetone; *C*: NMP+acetone+water; *D*: THF+ethanol [69]. 12

3.1 Dependence of conductivity on conductive particle loading as described by percolation theory. V_c indicates the volume loading corresponding to the percolation threshold of the composite. 17
3.2 Planetary ball mill used for this work, Across International PQ-N04. The four planet gears revolve around the sun gear while rotating in the opposite direction. Two sample holders are shown mounted and clamped on the left and right poles. 20
3.3 Geometry for resistance measurements for 3-dimensional and planar samples. . . 21
3.4 Probe setup for inline four-point probe. The outer pins apply a current, and the resulting potential is measured by the inner pins 22
3.5 *Left*: Drawing of ball milling jar. All dimensions are in mm; *Right*: picture of ball milling jar and lid with gasket (orange). 23
3.6 Sample preparation for conductivity measurements. *Left*: Printing samples with doctor blade and Kapton stencil. The direction of the doctor blade introduces a possible axis along which particles in the slurry may be aligned. *Middle*: Electrodes cast on Kapton substrate. *Right*: Top, four point probe measurement perpendicular to the direction of casting; Bottom, four point probe measurement parallel to the direction of casting. 27
3.7 *Left*: Picture of stencil-cast nickel current collector printed by hand; *Middle*: SEM image of unmilled nickel powder; *Right*: Conductivity of unmilled nickel powder ink. 28

3.8 SEM images for ball milling at 15 Hz 29
3.9 SEM images for ball milling at 20 Hz 30
3.10 SEM images for ball milling at 30 Hz 31
3.11 Average conductivity measurements for ball milling at 15 Hz. Error bars represent standard deviation for each batch of samples. 33
3.12 Average conductivity measurements for ball milling at 20 Hz. Error bars represent standard deviation for each batch of samples. 34
3.13 Average conductivity measurements for ball milling at 30 Hz. Error bars represent standard deviation for each batch of samples. 34

4.1 Electrode development diagram 39
4.2 Shear stress responses of Newtonian and non-Newtonian fluids 42
4.3 Effective shear rates for blade coater and doctor blade. 43
4.4 Graphical example of Fourier transform. The original signal is decomposed into the sum of its two constituent sinusoids, and their respective frequency and amplitude contributions are plotted. 45
4.5 Comparison of number of computations between DFT and FFT 46
4.6 Visualization of moving window algorithm to isolate region of interest in profile. *1*: raw profile scan, *2*: application of moving window algorithm where both size and position of window are varied to find the best linear fit within each window, *3*: applying best linear fits for overhanging substrate (green), sample edge (red), and center of sample (blue) to determine sample region (green and red intersection) and center of sample region (red and blue intersection), *4*: isolated profile for further analysis 53
4.7 Visualization of extended primary profile and extraction of roughness and waviness. 55
4.8 SEM image of unmilled MnO_2 powder (Sigma-Aldrich). 57
4.9 Resistivity of cathode as a function of acetylene black content. The number of samples tested per recipe are displayed above each point. 58
4.10 Resistivity of anode as a function of acetylene black content. The number of samples tested per recipe are displayed above each point. 58
4.11 Initial average viscosity results of cathode (left) and anode (right) inks compared to commercial ink. Error bars represent one standard deviation. 60
4.12 Initial average shear stress results of cathode (left) and anode (right) inks compared to commercial ink. Error bars represent one standard deviation. 60
4.13 Initial results of viscosities and yield stresses at 120 1/s for cathode and anode inks. 61
4.14 Viscosity and shear stress results of 40, 45, 50, and 60wt% solid phase cathode inks. 62
4.15 Rheology of cathode inks with no ball milling and varying solid phases. 63
4.16 Profilometry scans of 40, 45, 50 and 60wt% cathode ink. Doctor blade height: 50μm; casting speed: 10 mm/s 65

4.17 MnO_2 powder after ball milling. *A*: 30Hz, 3mm balls, 8 hours; *B*: 30Hz, 5mm balls, 8 hours; *C*: 30Hz, 5mm balls, 24 hours; *D*: 30Hz, 10mm balls, 8 hours; *E*: 30Hz, 15mm balls, 8 hours; *F*: 30Hz, 15mm balls, 24 hours 67
4.18 Profilometry scans of 40wt% cathode inks with ball milling. Doctor blade height: $100\mu m$; casting speed: 10mm/s 68
4.19 Profilometry scans of 45wt% cathode inks with ball milling. Doctor blade height: $100\mu m$; casting speed: 10mm/s 69
4.20 Rheology for 40 and 45wt% cathode inks with ball milling. 70
4.21 MnO_2 powder after ball milling at 30Hz, 10mm balls, 8 hours and sieving. *A*: no sieving; *B*: $250\mu m$ mesh; *C*: $150\mu m$ mesh; *D*: $45\mu m$ mesh 73
4.22 Profilometry scans of 45wt% cathode inks with ball milling and sieving. Doctor blade height: $100\mu m$; casting speed: 50mm/s 74
4.23 Profilometry scans of 47wt% cathode inks with ball milling and sieving. Doctor blade height: $100\mu m$; casting speed: 50mm/s 75
4.24 Rheology for 45wt% and 47wt% cathode inks with ball milling and sieving. All ball milling was performed at 30Hz, 10mm, 8 hours. 77
4.25 Optimized resistivity for cathode inks. Resistivities are labeled by ink composition by weight percent of MnO_2/AB/PVDF-HFP. 78
4.26 Profilometry scans of cathode inks with ball milling and sieving, optimized for conductivity. 79
4.27 Rheology for cathode inks optimized for conductivity. 80
4.28 SEM image of Zn powder (Alfa Aesar) 80
4.29 Profilometry scan of anode ink, optimized for conductivity and printing. 81
4.30 Rheology for anode ink. Metrics are labeled by weight percent of Zn/AB/PVDF-HFP. 81

5.1 Schematic representation of three electrode cell. 87
5.2 *Left*: Potential applied during CV; *Right*: Example cyclic voltammogram. . . . 89
5.3 *Top*: Potential applied during CA; *Bottom*: Chronoamperometric current response. 91
5.4 Applied AC potential and AC current response. 92
5.5 *Left*: Lissajous plot from AC potential and current; *Right*: Lissajous analysis . . 93
5.6 Example Nyquist plot for mixed kinetic and charge transfer control. 94
5.7 Equivalent circuit model for mixed kinetic and charge transfer control. 94
5.8 Deviation from ideality or Pt working electrode area 96
5.9 *Left*: Three-electrode electrochemical cell used for this work with working, counter, and reference electrodes; *Right*: Close-up of electrodes in contact with electrolyte. 97
5.10 Cyclic voltammograms of neat $[BMIM]^+[OTf]^-$ and $[EMIM]^+[OTf]^-$. 101
5.11 Cyclic voltammograms of 0.1, 0.2, 0.3, and $0.4m$ $Zn(OTf)_2$ in $[BMIM]^+[OTf]$. . 103
5.12 Nucleation potential, E_N, and crossover potential, E_{co} by cycle number for tested $[BMIM]^+[Otf]^-$ electrolytes. 104

5.13 Example cyclic voltammogram with points explaining redox reactions.
A-*E*: Potential not yet negative enough for Zn deposition.
B: Nucleation of Zn deposition begins (nucleation potential).
B-*C*: More Zn nuclei and nuclei grow (more area for further Zn deposition).
C: Diffusion of Zn^{2+} from nearby electrolyte starts to limit deposition.
C-*D*: Further depletion of Zn^{2+} from near electrode region, causing current to diminish.
D: Negative sweep of current switches to a positive (anodic) sweep.
D-*E*: Zn deposition continues at a diminishing rate because of Zn depletion from electrolyte near the electrode.
E: Electrode potential switches from deposition (cathodic reaction) to dissolution (anodic reaction) of Zn (crossover potential).
F: Electrolyte near electrode becomes saturated with Zn^{2+}, and diffusion of Zn^{2+} away from the electrode starts to limit reaction.
A: Positive sweep of current switches to a negative (cathodic) sweep. 105
5.14 Peak separation (ΔE), peak current ratio (i_a/i_c), and coulombic efficiency (Q_{ox}/Q_{red}) by cycle number for $[BMIM]^+[OTf]^-$ electrolytes. 106
5.15 Example CV and visual representation of integration of current with respect to time in order to calculate coulombic efficiency (amount of oxidation charge/amount of reduction charge). 107
5.16 Cyclic voltammograms of 0.1, 0.2, and $0.3m$ $Zn(OTf)_2$ in $[EMIM]^+[OTf]$. 107
5.17 Nucleation potential, E_N, and crossover potential, E_{co} by cycle number for tested $[EMIM]^+[Otf]^-$ electrolytes. 108
5.18 Peak separation (ΔE), peak current ratio (i_a/i_c), and coulombic efficiency (Q_{ox}/Q_{red}) by cycle number for $[EMIM]^+[OTf]^-$ electrolytes. 109
5.19 CVs of $[BMIM]^+[OTf]^-$ at $0.3m$ concentration and $[EMIM]^+[OTf]^-$ at $0.1m$ concentration. Dual peaks observed during oxidation are indicated. 110
5.20 Coulombic efficiency, difference in reduction charge and oxidation charge, and Zn^{2+} during cycling of $0.2m$ $[BMIM]^+[OTf]^-$. Original mass of electrolyte used was 1g. 114
5.21 Application of Randles-Sevcik equation to CV data for $[BMIM]^+[OTf]^-$ electrolytes. 115
5.22 Application of Randles-Sevcik equation to CV data for $[EMIM]^+[OTf]^-$ electrolytes. 116
5.23 Long cycle cyclic voltammograms with $\nu = 100$ mV/s for 0.1, 0.2, and $0.3m$ $Zn(OTf)_2$ in $[BMIM]^+[OTf]$. 118
5.24 Long cycle cyclic voltammograms with $\nu = 100$ mV/s for 0,1, 0.2, and $0.3m$ $Zn(OTf)_2$ in $[EMIM]^+[OTf]$. 119
5.25 Cyclic voltammograms, charge per cycle, and coulombic efficiency with $\nu = 20$ mV/s for 0.2 and $0.3m$ $Zn(OTf)_2$ in $[BMIM]^+[OTf]$. 122
5.26 Cyclic voltammograms, charge per cycle, and coulombic efficiency with $\nu = 20$ mV/s for 0.2 and $0.3m$ $Zn(OTf)_2$ in $[EMIM]^+[OTf]$. 122
5.27 Current (left) and Cottrell (right) plots of $0.1m$ $Zn(OTf)_2$ in $[BMIM]^+[OTf]$ with varying oxidation and reduction step potentials. 125

5.28 Current (left) and Cottrell (right) plots of $0.2m$ $Zn(OTf)_2$ in $[BMIM]^+[OTf]$ with varying oxidation and reduction step potentials. 125
5.29 Current (left) and Cottrell (right) plots of $0.3m$ $Zn(OTf)_2$ in $[BMIM]^+[OTf]$ with varying oxidation and reduction step potentials. 126
5.30 Current (left) and Cottrell (right) plots of $0.1m$ $Zn(OTf)_2$ in $[EMIM]^+[OTf]$ with varying oxidation and reduction step potentials. 126
5.31 Current (left) and Cottrell (right) plots of $0.2m$ $Zn(OTf)_2$ in $[EMIM]^+[OTf]$ with varying oxidation and reduction step potentials. 127
5.32 Current (left) and Cottrell (right) plots of $0.3m$ $Zn(OTf)_2$ in $[EMIM]^+[OTf]$ with varying oxidation and reduction step potentials. 127
5.33 Diffusivity of Zn^{2+} in $[BMIM]^+[OTf]^-$ electrolytes calculated from chronoamperometric reduction and oxidation. 131
5.34 Diffusivity of Zn^{2+} in $[EMIM]^+[OTf]^-$ electrolytes calculated from chronoamperometric reduction and oxidation. 131
5.35 Diffusion layers of $[BMIM]^+[OTf]^-$ and $[EMIM]^+[OTf]^-$ electrolytes. 132
5.36 *Left*: Current responses of chronoamperometric oxidation; *Right*: Optical micrographs of Pt electrode after interrupted chronoamperometry during oxidation with $0.3m$ $Zn(OTf)_2$ in $[BMIM]^+[OTf]$ electrolyte. *A*: 0s; *B*: 6s; *C*: 12s; *D*: 30s. 133
5.37 *Left*: Current responses of chronoamperometric oxidation; *Right*: Optical micrographs of Pt electrode after interrupted chronoamperometry during oxidation with $0.3m$ $Zn(OTf)_2$ in $[EMIM]^+[OTf]$ electrolyte. *A*: 0s; *B*: 6s; *C*: 12s; *D*: 30s. 133
5.38 Bode and Nyquist plots of 0.1, 0.2, and $0.3m$ $Zn(OTf)_2$ in $[BMIM]^+[OTf]$ before and after 200 cycles of CV break-in. 135
5.39 Bode and Nyquist plots of 0.1, 0.2, and $0.3m$ $Zn(OTf)_2$ in $[EMIM]^+[OTf]$ before and after 200 cycles of CV break-in. 136
5.40 Solution resistance (R_{sol}) and charge transfer resistance (R_{ct}) for $[BMIM]^+[OTf]$ electrolytes before and after 200 cycles of CV break-in. 137
5.41 Solution resistance (R_{sol}) and charge transfer resistance (R_{ct}) for $[EMIM]^+[OTf]$ electrolytes before and after 200 cycles of CV break-in. 137

6.1 Cyclic voltammograms of circuit elements. *left*: capacitor; *middle*: resistor; *right*: resistor and capacitor in parallel. 143
6.2 Example plot of dQ/dV vs. V. 145
6.3 Calculated and measured dQ/dV of $LiMn_2O_4$/graphite cell. [86] 145
6.4 Order of components inside coin cells for half cells, mechanically assembled full cells, and fully printed cells. 151
6.5 Scanning electron micrographs of 1:3 by mass PVDF-HFP:NMP (no electrolyte). 158
6.6 Scanning electron micrographs of 1:5 by mass PVDF-HFP:NMP (no electrolyte). 159
6.7 Scanning electron micrographs of GPE, 3:1:4 electrolyte:PVDF-HFP:NMP. . . . 161
6.8 GPE sweating from GPEs both cast in coin cells *left* and cast via doctor blade *right*. 162
6.9 Median of thickness vs. mass of cast 3:1:4 GPE for $n = 20$ samples. 163

6.10 CV of half cell with 0.5M $[BMIM]^+[OTf]^-$ GPE, scan rates of 20 mV/s and 100 mV/s, cured under ambient, vacuum, and argon. 165
6.11 Cathodic and anodic crossover potentials and cycle efficiency of $[BMIM]^+[OTf]^-$ GPEs. 165
6.12 CV of half cell 0.5M $[EMIM]^+[OTf]^-$ GPE, scan rates of 20 mV/s and 100 mV/s, cured under ambient, vacuum, and argon. 166
6.13 Cathodic and anodic crossover potentials and cycle efficiency of $[EMIM]^+[OTf]^-$ GPEs. 166
6.14 SEM images of half cell with GPE dried in ambient after cycling at 10mV/s. *left*: GPE surface showing Zn crystallization into the GPE; *right*: Zn foil surface showing various morphologies of Zn plating and ZnO mesocrystals. 169
6.15 CV of mechanically assembled full cell with $[BMIM]^+[OTf]^-$ GPEs. Cycling was interrupted every 10 cycles to perform EIS. 171
6.16 CV of mechanically assembled full cell with $[EMIM]^+[OTf]^-$ GPEs. Cycling was interrupted every 10 cycles to perform EIS. 171
6.17 Cathodic and anodic crossover potentials and cycle efficiency for CV of mechanically assembled full cells with $[BMIM]^+[OTf]^-$ GPEs. 172
6.18 Cathodic and anodic crossover potentials and cycle efficiency for CV of mechanically assembled full cells with $[EMIM]^+[OTf]^-$ GPEs. 173
6.19 Nyquist plots of mechanically assembled full cells with $[BMIM]^+[OTf]^-$ GPEs. EIS was performed between every 10 cycles of CV. 176
6.20 Solution resistance, R_{sol}, and charge transfer resistance, R_{ct}, of mechanically assembled full cells with $[BMIM]^+[OTf]^-$ GPEs. 176
6.21 Nyquist plots of mechanically assembled full cells with $[EMIM]^+[OTf]^-$ GPEs. EIS was performed between every 10 cycles of CV. 177
6.22 Solution resistance, R_{sol}, and charge transfer resistance, R_{ct}, of mechanically assembled full cells with $[EMIM]^+[OTf]^-$ GPEs. 177
6.23 Discharge capacity, coulombic efficiency, and DC internal resistance per cycle for mechanically assembled full cells with $[BMIM]^+[OTf]^-$ GPEs dried in ambient and under vacuum. 180
6.24 Discharge capacity, coulombic efficiency, and DC internal resistance per cycle for mechanically assembled full cells with $[EMIM]^+[OTf]^-$ GPEs dried in ambient and under vacuum. 181
6.25 Differential capacity and voltage profiles of cells with lowest and highest internal resistance for mechanically assembled full cells with $[BMIM]^+[OTf]^-$ GPEs dried in ambient. 183
6.26 Differential capacity and voltage profiles of cells with lowest and highest internal resistance for mechanically assembled full cells with $[BMIM]^+[OTf]^-$ GPEs dried under vacuum. 183
6.27 Differential capacity and voltage profiles of cells with lowest and highest internal resistance for mechanically assembled full cells with $[EMIM]^+[OTf]^-$ GPEs dried in ambient. 184

6.28 Differential capacity and voltage profiles of cells with lowest and highest internal resistance for mechanically assembled full cells with $[EMIM]^+[OTf]^-$ GPEs dried under vacuum. 184
6.29 SEM image of fully printed cell with $[EMIM]^+[OTf]^-$ GPE dried under vacuum. Anode-GPE interface has been drawn in blue, and cathode-GPE interface has been drawn in red. 186
6.30 Nyquist plots of fully printed cells with $0.5M$ $[BMIM]^+[OTf]^-$ GPE, dried under ambient. 188
6.31 Solution resistance and charge transfer resistance of fully printed cells with $0.5M$ $[BMIM]^+[OTf]^-$ GPE, dried under ambient. 188
6.32 Nyquist plots of fully printed cells with $0.5M$ $[EMIM]^+[OTf]^-$ GPE, dried under ambient. 189
6.33 Solution resistance and charge transfer resistance of fully printed cells with $0.5M$ $[EMIM]^+[OTf]^-$ GPE, dried under ambient. 189
6.34 Discharge capacity, coulombic efficiency, and DC internal resistance per cycle for fully printed cells with $[BMIM]^+[OTf]^-$ GPEs dried in ambient and under vacuum. 190
6.35 Discharge capacity, coulombic efficiency, and DC internal resistance per cycle for fully printed cells with $[EMIM]^+[OTf]^-$ GPEs dried in ambient and under vacuum. 191
6.36 Differential capacity and charge/discharge voltages of most and least stable cells for fully printed cells with $[BMIM]^+[OTf]^-$ GPEs dried in ambient. 194
6.37 Differential capacity and charge/discharge voltages of most and least stable cells for fully printed cells with $[BMIM]^+[OTf]^-$ GPEs dried under vacuum. 194
6.38 Differential capacity and charge/discharge voltages of most and least stable cells for fully printed cells with $[EMIM]^+[OTf]^-$ GPEs dried in ambient. 195
6.39 Differential capacity and charge/discharge voltages of most and least stable cells for fully printed cells with $[EMIM]^+[OTf]^-$ GPEs dried under vacuum. 195

7.1 Pyrolusite (a) and ramsdellite (b) structures and resulting γ-MnO_2 structure (c) [7]. 201
7.2 Types of cells manufactured. 202
7.3 Discharge capacity, coulombic efficiency, and internal resistance of initial mechanically assembled cells. 208
7.4 Differential capacity and voltage profile for stable and unstable initial mechanically assembled cells. Note different scales and ranges for differential capacity. . 208
7.5 *Left*: SEM of printed MnO_2 cathode surface after cycling; *right*: SEM of Zn foil anode surface after cycling 209
7.6 Delamination of printed cathode and printed anode after cycling in mechanically assembled cell. 209
7.7 Discharge capacity, coulombic efficiency, and internal resistance of initial half printed cells. 212
7.8 Differential capacity and voltage profile for stable and unstable initial half printed cells. 212

7.9 *Left*: half printed cell with printed MnO_2 cathode and GPE; *right*: SEM cross section of printed MnO_2 cathode and GPE. Tweezers are gripping excess overhanging GPE. 213
7.10 *Left*: SEM of GPE surface over cathode surface after cycling; *right*: SEM of Zn foil anode surface after cycling 213
7.11 Discharge capacity, coulombic efficiency, and internal resistance of initial fully printed cells with 5 layers of GPE. 215
7.12 Differential capacity and voltage profile for stable and unstable initial fully printed cells with 5 layers of GPE. Note different scales and ranges for differential capacity. 215
7.13 Discharge capacity, coulombic efficiency, and internal resistance of initial fully printed cells with 3 layers of GPE. 216
7.14 Differential capacity and voltage profile for stable and unstable initial fully printed cells with 3 layers of GPE. 216
7.15 Front (*left*) and side (*right*) views of fully printed cell. From front to back, layers of the fully printed cell are MnO_2 cathode, GPE, Zn anode. Tweezers are holding the GPE. 217
7.16 SEMs of initial fully printed cells with 5 layers (*left*) and 3 layers (*right*) of GPE. 217
7.17 Discharge capacity, coulombic efficiency, and DC internal resistance per cycle for half printed cells with $0.2m$ $[BMIM]^+[OTf]^-$ GPEs, dried in ambient. 220
7.18 Discharge capacity, coulombic efficiency, and DC internal resistance per cycle for half printed cells with $0.3m$ $[EMIM]^+[OTf]^-$ GPEs, dried in ambient. 220
7.19 Discharge capacity, coulombic efficiency, and DC internal resistance per cycle for fully printed cells with $0.3m$ $[BMIM]^+[OTf]^-$ GPEs with 2 layers, dried in ambient. 222
7.20 Differential capacity and charge/discharge voltages of most and least stable cells for fully printed cells with $0.3m$ $[BMIM]^+[OTf]^-$ GPEs with 2 layers, dried in ambient. 222
7.21 SEM cross section of fully printed cell with 2 layers of $0.3m$ $[BMIM]^+[OTf]^-$ GPE. 223
7.22 Discharge capacity, coulombic efficiency, and DC internal resistance per cycle for fully printed cells with $0.2m$ $[BMIM]^+[OTf]^-$ GPEs with 3 layers, dried in ambient. 224
7.23 Differential capacity and charge/discharge voltages of most and least stable cells for fully printed cells with $0.2m$ $[BMIM]^+[OTf]^-$ GPEs with 3 layers, dried in ambient. 224
7.24 Discharge capacity, coulombic efficiency, and DC internal resistance per cycle for fully printed cells with 0.2 m $[BMIM]^+[OTf]^-$ GPEs with 4 layers, dried in ambient. 225
7.25 Differential capacity and charge/discharge voltages of most and least stable cells for fully printed cells with $0.2m$ $[BMIM]^+[OTf]^-$ GPEs with 4 layers, dried in ambient. 225
7.26 Discharge capacity, coulombic efficiency, and DC internal resistance per cycle for fully printed cells with $0.3m$ $[BMIM]^+[OTf]^-$ GPEs with 4 layers, dried in ambient. 226
7.27 Differential capacity and charge/discharge voltages of most and least stable cells for fully printed cells with $0.3m$ $[BMIM]^+[OTf]^-$ GPEs with 4 layers, dried in ambient. 226

7.28 Discharge capacity, coulombic efficiency, and DC internal resistance per cycle for fully printed cells with $0.3m$ $[EMIM]^+[OTf]^-$ GPEs with 4 layers, dried in ambient. 227
7.29 Differential capacity and charge/discharge voltages of most and least stable cells for fully printed cells with $0.3m$ $[EMIM]^+[OTf]^-$ GPEs with 4 layers, dried in ambient. 227
7.30 SEM cross sections of fully printed cell with 3 and 4 layers of GPE. *A*: $0.2m$ $[BMIM]^+[OTf]^-$, 3 layers; *B*: $0.2m$ $[BMIM]^+[OTf]^-$, 4 layers; *C*: $0.3m$ $[BMIM]^+[OTf]^-$, 4 layers; *D*: $0.3m$ $[EMIM]^+[OTf]^-$, 4 layers. 228

8.1 Pulse load demand profile of Nordic Semiconductor nrf51822 [19]. 235
8.2 Discharge limit with constant current discharge vs. pulsed current discharge. . . 236
8.3 Pulsed discharge profile for fully printed Zn-MnO_2 cells. *Left*: example pulsed discharge profile for fully printed cells (with normalized time); *Right*: inset of pulsed discharging profile highlighting individual current pulses. 238
8.4 Pulsed discharge of $0.5M$ $[BMIM]^+[OTf]^-$ cell with GPE dried in vacuum, 5 layers. *Left*: internal resistance; *right*: average ending discharge voltage for each set of pulses. 242
8.5 Cyclic voltammetry of Panasonic ML-2020 cell at 100mV/s scan rate. *Left*: CV for selected cycles; *right*: Crossover potentials, cumulative charge, and cycle efficiency per cycle. 244
8.6 Voltage profiles of Panasonic ML-2020 cells during constant current discharge. Cells were discharged until 40mAh of capacity was discharged. 245
8.7 Discharge capacity during constant current (CC) cycling of Panasonic ML-2020 cells. 245
8.8 Cell voltage during 10mA pulsed current discharging with 1mA baseline discharge of Panasonic ML-2020 cell. *Inset*: voltage during pulsed current discharge. . . . 247
8.9 Megacycle testing by pulsed discharge of Panasonic ML-2020 cells with 10mA pulse and varying duty cycles. *Inset*: voltage of cell with 0.132s pulse width. . . 247

List of Tables

3.1 Electrophysical properties of candidate metals for a printed current collector [66] 15
3.2 Characteristics of different types of ball and rod mills [25] 19
3.3 Nickel Current Collector Composition 25

4.1 Printing thicknesses and viscosities of various printing methods [46] 41
4.2 Electrode Material Components 47
4.3 Ball milling parameters tested 48
4.4 Printing speeds and doctor blade heights for stencil casting with automatic film applicator. 50
4.5 Brookfield DV3T-HB Viscosity Test Method 51
4.6 Profile statistics for 40wt%, 45wt%, 50wt%, and 60wt% solid phase cathode ink with unmilled MnO_2. 66
4.7 Profile statistics for 40wt% solid phase cathode ink with ball milled MnO_2. . . . 70
4.8 Profile statistics for 45wt% solid phase cathode ink with ball milled MnO_2. . . . 71
4.9 Profile statistics for 45wt% solid phase cathode ink with ball milled and sieved MnO_2. 76
4.10 Profile statistics for 47wt% solid phase cathode ink with ball milled and sieved MnO_2. 76
4.11 Cathode inks developed for conductivity re-optimization. 77
4.12 Profile statistics for cathode ink with ball milled and sieved MnO_2 optimized for conductivity. 78
4.13 Anode inks composition. 81
4.14 Profile statistics for anode ink. 82

5.1 Electrolyte salt concentrations 95
5.2 Test parameters for cyclic voltammetry (CV) experiments 98
5.3 Test parameters for chronoamperometry (CA) experiments. 99
5.4 Test parameters for electrochemical impedance spectroscopy (EIS) experiments. 100
5.5 Electrolyte Conductivities 138

6.1 Neat polymer compositions 146
6.2 Gel polymer electrolyte compositions 147

6.3 Drying temperatures and environments. 148
6.4 Cathode and Anode Ink Compositions 149
6.5 Fully printed cell printing procedure 150
6.6 Coin cell components 151
6.7 Gamry Reference 600 Potentiostat test parameters for cyclic voltammetry (CV) experiments. 153
6.8 Bio-Logic test parameters for cyclic voltammetry (CV) experiments 154
6.9 Gamry Reference 600 Potentiostat test parameters for electrochemical impedance spectroscopy (EIS) experiments. 154
6.10 Bio-Logic test parameters for electrochemical impedance spectroscopy (EIS) experiments. 155
6.11 Bio-Logic test parameters for galvanostatic cycling. 156
6.12 Mean GPE Ionic Conductivity and Charge Transfer Resistance 178

7.1 Coin cell components 203
7.2 Fully printed cell printing procedure 203
7.3 Initial cell ink compositions 204
7.4 Fully printed cell printing procedure, final cells 204
7.5 Final ink compositions 205
7.6 Neware test parameters for CCCV charge and CC discharge cycling. 206
7.7 Bio-Logic test parameters for combined galvanostatic and potentiostatic cycling. 207
7.8 Final printed GPE thickness 229

8.1 Transmission frequency, transmit and receive currents and powers, and voltage ranges for commercially available radios for wireless sensor applications (reproduced with permission from Bala Thoravi-Kumarel). 234
8.2 Cycling parameters for pulsed discharging of printed Zn-MnO_2 cells. 239
8.3 Cycling parameters for pulsed discharging of commercial li-ion cells. 241
8.4 Capacity and depth of discharge of pulsed current discharge. 246

Acknowledgments

My time at UC Berkeley and in the AME Lab has brought me immense growth. I am grateful for all of the opportunities I have been afforded and for all of the brilliant and wonderful people I have had the privilege to meet along the way. Without the support and guidance from these people and from family and friends, this work would not have been possible.

First, I would like to thank my parents, Allen and Elizabeth Kim, and my sister and brother-in-law, Erin Kim and Vyasa Murthy, for their unwavering love and support and for always believing in me.

I would like to thank my advisors, Prof. Paul K. Wright and Prof. James W. Evans, for their mentorship and for allowing me to pursue the research directions I wished. Their guidance kept me focused on the bigger picture and kept me on the right track.

I would like to thank Prof. Ana C. Arias for accepting me into her lab and providing infrastructural support when lab space was lost.

I would like to thank Dan Chapman for providing perspective and for always helping with administrative issues in the AME Lab.

I would like to thank Dr. Rich Winslow for his invaluable mentorship and guidance. His work set an example for me to follow, and his advice provided a guiding light in times when I felt uncertain about what direction to take. I would also like to thank Dr. Zuoqian Wang for bringing me into the AME Lab as an undergraduate so many years ago and introducing me to the world of research and printed energy storage. This beginning led me to pursue a graduate degree and bought me to where I am today.

I would like to thank Qian Zhang, Ian Lin, Karthik Gururangan, Isabel Yang, Brian Xiao, Vanessa Fernandez Morales, Allison Green, Angela Hou, Felicia Trinh, Daniel Ringness, and Nicholas Bachand for all of their help in carrying out experimental work. Without their contributions, much of this work would not have been possible to accomplish. I would also like to thank Dr. Alic Chen, Dr. Peter Minor, Sean Wihera, Dr. Pit Pillatsch, and Dr. Balthazar Lechene.

Finally, I would like to thank my peers and the former members of the AME Lab for their camaraderie and for making grad school a fulfilling and enriching chapter in my life: Dr. Martin Cowell, Dr. Christine Gregg, Zachary Gima, Zhiwei Wu, Dominic Cincione, Payton Goodrich, Bala Thoravi-Kumarel, Dr. Max Micali, Miguel Rodriguez, and everyone in the Arias Group.

Chapter 1

Introduction

As advancements in manufacturing have enabled the production of printed electronics for the Internet of Things, a demand for compatible energy storage has grown [75]. In order to power these printed devices, printed energy storage that can be manufactured in line with these devices is necessary. While several types of printed batteries have been developed and reported, there still exists a whitespace to optimize the performance and manufacture of printed batteries in order to best adapt to this new manufacturing paradigm. While printing allows for scalable, additive manufacturing, it brings its own device requirements and manufacturing limitations that preclude traditional battery manufacturing methods.

Zinc has long been considered for cheap, safe, and abundant energy storage [103]. As developments with lithium-ion chemistries approach the material limits of what the chemistry is capable of provding, there has been renewed interest in exploring other cell chemistries. Of the class of multivalent ion intercalation chemistries, Zn has emerged as an attractive option for printed energy storage due to its stability in ambient environments compared to Group I metals (Li, Na, Ca) as well as its low cost and abundance.

Ionic liquids have become the subject of investigation as electrolyte materials due to their low volatility and high potential stability windows, offering greater safety over conventional organic solvents [30, 28]. Recent research has proven the compatibility with zinc-based chemistries, with favorable deposition morphologies and cells that can be cycled over 100 times without failure [45, 39]. In tandem with cheap and abundant zinc, this may enable cheap and safe energy storage that may serve as an alternative to lithium-ion chemistries. However, mass transport and kinetic values for Zn deposition and dissolution in ionic liquids have not been well characterized, leaving room for further understanding and optimization of this system.

Ionic liquids have also been shown to be compatible with polymer membranes to form gel polymer electrolytes (GPEs) [95, 105, 111]. These gel polymer films serve as both mechanical separators and ionic conductors and can be incorporated with printed or conventionally manufactured electrodes as a replacement for traditional separator materials. The interplay between the ionic liquid electrolyte and the gel polymer structure is crucial to successful cell

performance and cycling. Furthermore, gel polymer electrolytes are typically solution cast, enabling novel manufacturing methods for batteries via printed electrolytes.

Printing has emerged as an attractive option in recent years as a scalable method for manufacturing flexible electronics and energy storage devices. This is particularly suited for energy storage devices where large print areas and throughput are beneficial to increase device capacity. Traditional batteries are unable to be fully printed due to their separator membranes, but solution-cast gel polymer electrolytes provide a printable solution.

However, cells printed directly onboard a flexible substrate with other flexible devices may be incompatible with traditional battery manufacturing processes involving particle compaction. This places additional importance on electrode-electrolyte interfaces, specifically regarding electrode surface morphology. This morphology is affected by a number of factors, including the particle size, solids loading, and slurry rheology, all of which must be characterized and controlled in order to produce uniform electrodes amenable to solution cast separators.

Finally, many of the applications for these devices are for the Internet of Things, which often requires bespoke devices with specific power demands. The performance of printed batteries must therefore be characterized not only through traditional cycle life testing but also via pulsed current discharging methods typical for wireless sensors with intermittent duty cycles.

1.1 Scope of Dissertation

While previous work has demonstrated the feasibility of dispenser printed secondary Zn-MnO_2 cells with an ionic liquid gel polymer electrolyte [39] and improved cell yield via separate manufacturing of the gel polymer electrolyte [102], there exists much room to optimize individual components and to gain a deeper understanding of the underlying electrochemistry. Specifically, previous work improved cell yield compared to dispenser printing by printing thick cathode films, separate solution casting of GPEs, and using Zn foil anodes, combining all components together manually. This work sought to further develop the manufacturing process to enable layer-by-layer fully printed cells via doctor blade coating and to more deeply investigate the effect of compositional and manufacturing parameters on cell performance and degradation.

This work investigates optimization of printed electrodes and printed gel polymer electrolytes for use in a fully printed secondary Zn-MnO_2 battery for Internet of Things applications. The ionic liquids investigated in this work are 1-butyl-3-methylimidazolium trifluoromethanesulfonate ($[BMIM]^+[OTf]^-$) and 1-ethyl-3-methylimidazolium trifluoromethanesulfonate ($[EMIM]^+[OTf]^-$). The salt zinc trifluoromethanesulfonate ($Zn(OTf)_2$) dissolved in these ionic liquids to form the electrolyte. The polymer investigated for the gel polymer electrolyte and used in both electrodes is poly(vinylidene fluoride-co-hexafluoropropylene) (PVDF-HFP), which is dissolved in n-methyl-2-pyrrolidone (NMP). The combination of the ionic liquid electrolyte and the polymer forms the solution from which the gel polymer elec-

trolyte is cast. Electrode slurries are composed of manganese dioxide (MnO_2) or zinc (Zn), PVDF-HFP, and acetylene black (AB). NMP is again used to dissolve PVDF-HFP and as the liquid component of the slurries. Zinc and manganese dioxide were chosen for electrode materials based on their low cost, abundance, and stability in ambient and because previous work had demonstrated reversible cycling in $[BMIM]^+[OTf]^-$. PVDF-HFP was chosen as the polymer binder for its compatibility with this chemistry and ability to be solution cast with ionic liquids to form stable GPEs. $[EMIM]^+[OTf]^-$ was investigated alongside $[BMIM]^+[OTf]^-$ because of its high ionic conductivity and similarity in cation structure.

Individual components are optimized and characterized separately and combined in an effort to improve overall cell performance, as quantified by capacity, internal resistance, and coulombic efficiency from cycle life testing. Electrode slurries and printed electrodes are characterized by profilometry, rheology, four point probe resistance, and scanning electron microscopy. Ionic liquid electrolytes are characterized by cyclic voltammetry, chronoamperometry, and electrochemical impedance spectroscopy. Gel polymer electrolytes are characterized by scanning electron microscopy, cyclic voltammetry, and electrochemical impedance spectroscopy. Cell performance is primarily characterized by galvanostatic cycle life testing, with differential capacity analysis providing further insight into degradation mechanisms. Cell performance is also characterized by pulsed current discharging to simulate intermittent loads as expected from Internet of Things devices.

Chapter 2 presents relevant background for the work presented in this dissertation, focusing on whitespaces in the literature and opportunities for further understanding of the investigated cell chemistry. Chapter 3 presents findings from ball milling of nickel powder for a printed nickel current collector, the results of which inform electrode slurry optimization. Chapter 4 presents the results of optimization of electrode slurries, which were optimized for surface profile, rheology, and electrical conductivity while maintaining a high active material fraction. Chapter 5 presents electrochemical analysis and characterization of Zn deposition and dissoluton in the ionic liquid electrolytes and quantifies Zn^{2+} diffusivity, solution resistance, and charge transfer resistance. Chapter 6 presents the effects of manufacturing processing parameters on gel polymer electrolyte structure and electrochemical performance in half cells and full cells. Chapter 7 presents cell cycling results with mechanically assembled cells, half printed cells, and fully printed cells and seeks to identify failure and degradation mechanisms within cells. Chapter 8 presents cycling results of fully printed cells under pulsed current discharge and results of megacycle testing of commercial lithium-ion cells under pulsed current discharge. Finally, Chapter 9 summarizes all key findings and discusses directions for future investigation.

1.2 Goals of Dissertation

The goals of this research are

1. to optimize cathode and anode slurries for profilometry, rheology, and electrical conductivity while maximizing active material fraction,
2. to determine the diffusivity of Zn^{2+} in and the ionic conductivity of $[BMIM]^+[OTf]^-$ and $[EMIM]^+[OTf]^-$ ionic liquid electrolytes with various concentrations of $Zn(OTf)_2$ salt,
3. to characterize Zn deposition and dissolution in ionic liquid electrolytes,
4. to investigate the effects of processing temperature and environment on gel polymer electrolyte and structure,
5. to develop layer-by-layer fully prined Zn-MnO_2 cells with an ionic liquid gel polymer electrolyte and identify degradation mechanisms, and
6. to characterize cell performance under constant current and pulsed current discharge as would be observed with load demands of Internet of Things devices.

Chapter 2

Background

This chapter discusses the principles of battery operation and performance metrics used to quantify cell performance. An overview of zinc-based batteries and some of the challenges with developing rechargeable zinc cells is presented. Ionic liquids and their use as electrolytes and the development and structure of gel polymer electrolyte is then discussed. The need for printed energy storage devices and an optimal manufacturing process is then discussed. Finally, the scope and goals of this work is presented.

2.1 Battery Fundamentals

A battery is an electrochemical energy storage device that stores and delivers electrical energy via charge transfer (faradaic) reactions. A battery is composed of three primary components - the cathode, the anode, and the electrolyte. While strict electrochemical definitions define the name of each electrodes by the redox reactions occuring (*e.g.* the anode is the electrode at which oxidation occurs), battery terminology fixes the names of the electrodes by their function during discharge. During discharge, reduction occurs at the cathode, and oxidation occurs at the anode. The electrolyte is responsible for separation of the two electrodes to prevent electrical shorts as well as to serve as a medium for ionic conduction between the two electrodes. The electrodes are then connected through an external circuit through which current flows.

During cell discharge, reduction (cathodic) and oxidation (anodic) half reactions occur at the cathode and anode respectively. Depending on the cell chemistry, cations may migrate across the electrolyte from the anode to the cathode, or anions may migrate from the cathode to the anode. In ideal operation, the total magnitudes of each half reaction are equal and opposite. The difference in reduction potentials of both half reactions determines the cell's potential, and the rate at which the reactions occur determine the current provided by the cell. Primary cells are cells whose set of half reactions is irreversible and therefore cannot be recharged while secondary cells are cells whose set of half reactions are reversible and therefore can be recharged. During charge of secondary cells, the polarity of the cell is

reversed, and redox reactions occur at opposite electrodes compared to discharge (reduction at the anode and oxidation at the cathode). The half reactions occuring at the anode and cathode respectively may be defined as in Equations 2.1 and 2.2, where n is the number of electrons involved in each overall half reaction. Figure 2.1 presents a visual representation of a cell during discharge.

$$A \leftrightarrows A^{n+} + ne^- \tag{2.1}$$

$$B^{n+} + ne^- \leftrightarrows B \tag{2.2}$$

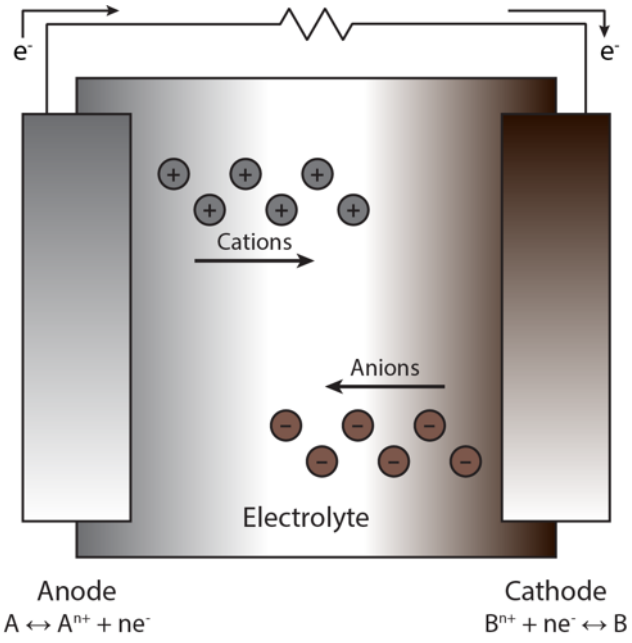

Figure 2.1: Schematic of an electrochemical cell during discharge.

Figure 2.2 presents example voltage and current with respect to time as observed during cell cycling. During electrochemical cycling, the only cell states that may be directly measured are the cell potential (V, [V]), current (I, [I]), and temperature (T, [°C]) with respect to time (t [s]). Metrics that are traditionally used to measure battery performance are the capacity (Q, [mAh]), energy capacity (W, [mWh]), coulombic efficiency, energy efficiency, and internal resistance ([Ω]). During cycling of cells, capacity is determined by integrating current with respect to time. Thus, the total amount of capacity for both charge and discharge can be determined by Eq. 2.3 and as seen in Figure 2.2.

$$Q = \int I(t)dt \tag{2.3}$$

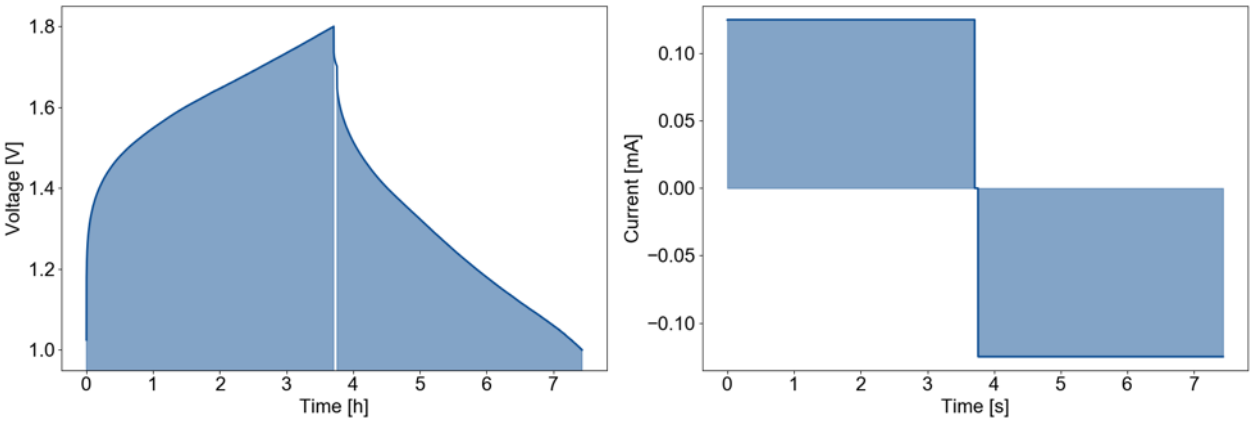

Figure 2.2: Voltage and current during one cycle of charge discharge for Zn-MnO_2 cell. The cell was first charged to 1.8V, allowed to rest, and then discharged to 1.0V.

Similarly, energy capacity is determined by integrating the product of voltage and current with respect to time, as defined by Eq 2.4 and seen in Figure 2.2.

$$W = \int V(t)I(t)dt \tag{2.4}$$

The coulombic efficiency is therefore calculated as the ratio between the discharge capacity and the charge capacity (Eq. 2.5), and the energy efficiency is calculated as the ratio between the discharge energy and the charge energy (Eq. 2.6).

$$\text{Coulombic Efficiency} = \frac{Q_{discharge}}{Q_{charge}} \tag{2.5}$$

$$\text{Energy Efficiency} = \frac{W_{discharge}}{W_{charge}} \tag{2.6}$$

The internal resistance may be calculated by a number of methods but is typically calculated from cycling data by taking the numerical derivative of the voltage with respect to current (Eq. 2.7). This is typically performed at points where an ohmic drop is observed, as seen just prior at the beginning of the rest period in Figure 2.2.

$$\text{Internal Resistance} = \frac{dV}{dI} = \frac{V_i - V_{i-1}}{I_i - I_{i-1}} \tag{2.7}$$

Electroneutrality must be maintained at all times within the cell. If parasitic side reactions occur that consume material involved redox reactions necessary for cell operation, overall cell perfomance may decrease. The presence and continuation of side reactions may therefore result in decreased capacity and increased internal resistance depending on the nature of the side reactions present. The identity and rate of these side reactions depends

on each individual cell chemistry and is also depending on cell geometry, current densities, and variations in local concentration and overpotential, among other factors.

2.2 Zinc-Based Batteries

Multivalent ion batteries have garnered interest as potential solutions to meet the demands of next-generation energy storage needs that exceed the theoretical limit of lithium-ion batteries [58, 15, 31, 84, 80]. While lithium-ion currently dominates the battery market, advancements on the material level are approaching a fundamental limit, thus spurring investigation into alternate chemistries. Multivalent ions are of particular interest due to their intrinsically higher volumetric energy density by use of a metallic anode, compared to lithium-ion. Of the multivalent ion metals of common interests, Zn offers the highest theoretical volumetric energy density (but the lowest specific energy density), as shown in Figure 2.3. This makes Zn a promising material for stationary energy storage applications, such as grid storage, where weight is not a critical performance metric.

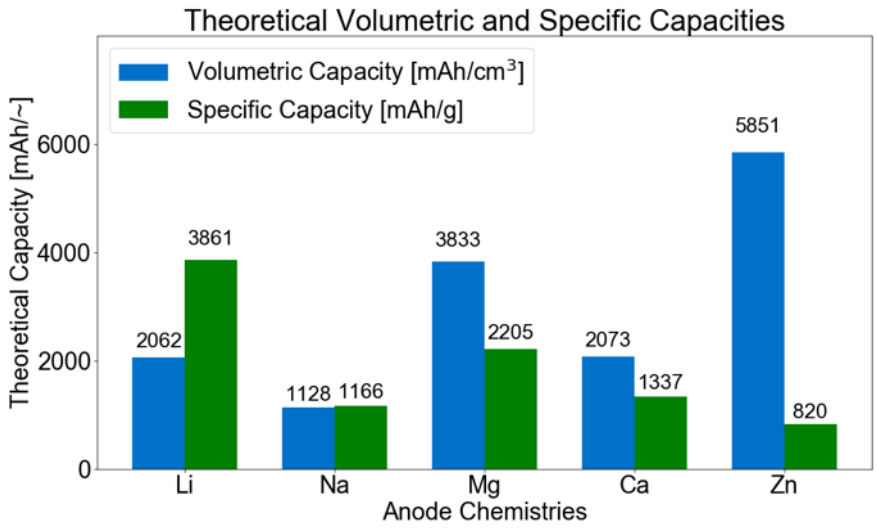

Figure 2.3: Theoretical maximum capacity densities and specific capacities of Li, Na, Mg, Ca, and Zn metals.

Zinc has long garnered interest for energy storage due to its low cost, high safety, and abundance. Commercially successful alkaline Zn-MnO_2 batteries were first introduced in 1952 and have since become a ubiquitous power source for many electronic devices [103, 38] due to their low cost, high capacity, and high ionic conductivity. These cells utilize MnO_2 as the cathode material, Zn as the anode material, and KOH as an alkaline (and aqueous) electrolyte. This alkaline cell chemistry has traditionally been regarded as a primary cell chemistry and is there unable to be recharged.

However, a number of studies have investigated secondary aqueous Zn-MnO_2 cells relying on intercalation mechanisms of Zn^{2+} rather than protonation as in primary cells [103, 70, 50, 9, 72, 64]. Intercalation mechanisms utilize charge transfer via reversible insertion and de-insertion of the intercalant ion into spaces in the crystal structure of a host material. Multiple factors contribute to rapid degradation of these aqueous Zn-MnO_2 systmems, including irreversible phase transformations within the MnO_2 cathode [38, 70] and irreversible Zn dissolution and deposition [36, 37]. In particular, deposition of Zn in aqueous environments typically forms dendritic structures which may lead to electrical shorts between the anode and cathode [63, 21, 99]. Furthermore, charging and discharging potentials for aqueous Zn-MnO_2 cells must be tightly controlled to prevent electrolysis of water, the formation of inert zinc oxides and hetaerolite ($ZnMn_2O_4$), and irreversible destruction of the MnO_2 crystal lattice leading to capacity loss [24, 38].

While issues related to MnO_2 crystal lattice degradation are intrinsic to any ion-intercalating system, Zn dendrite formation has been shown to be inhibited by the use of non-aqueous electrolytes, improving cycle life of secondary Zn-MnO_2 systems [62, 100, 85, 63, 45]. Of particular interest are systems based on ionic liquid electrolytes have shown significant promise and compatibility with printed energy storage systems.

2.3 Ionic Liquids and Zinc Redox Kinetics

Ionic liquids, also known as room temperature ionic liquids or RTILs, are salts characterized by low melting points below room temperature [30, 28, 41]. They consist of large, asymmetrical ions whose differing sizes prevent effective coordination at room temperature. Compared to classical electrolytes which are composed of a salt dissolved in an uncharged solvent, ionic liquids are composed purely of charged species. This results in a number of properties that makes these materials attractive for electrochemical applications, including high thermal stability, high electrical stability, low vapor pressure, and the ability to dissolve a wide range of inorganic and organic compounds [28].

A wide range of possible cations and anions exist, resulting in hundreds of possible ionic liquid combinations. Cations are typically large and bulky organic species with low symmetry based on cyclic amines, including imidazolium, pyridinium, pyrrolidinium, piperidinium, and ammonium [28, 30]. These cations may also have complexes branching off the central amine, affecting ionic liquid properties. Anions are typically smaller organic or inorganic species, including tetrafluoroborate, hexafluorophosphate, trifluoromethanesulfonate, bis(trifluoromethanesulfonyl)imide, and acetate. Varying the anion generally has a more significant effect on ionic liquid properties than variations in the cation [28].

Due to their immense number, there exists room for characterization of many ionic liquid properties, particularly those relevant for electrochemical applications. The ionic liquids investigated in this work are 1-butyl-3-methylimidazolium trifluoromethanesulfonate ($[BMIM]^+[OTf]^-$) and 1-ethyl-3-methylimidazolium trifluoromethanesulfonate ($[EMIM]^+[OTf]^-$) and are presented in Figure 2.4. These two ionic liquids share the same

anion, and the ionic liquids differ in their cation by the length of the alkyl chain off of the central imidazolium complex.

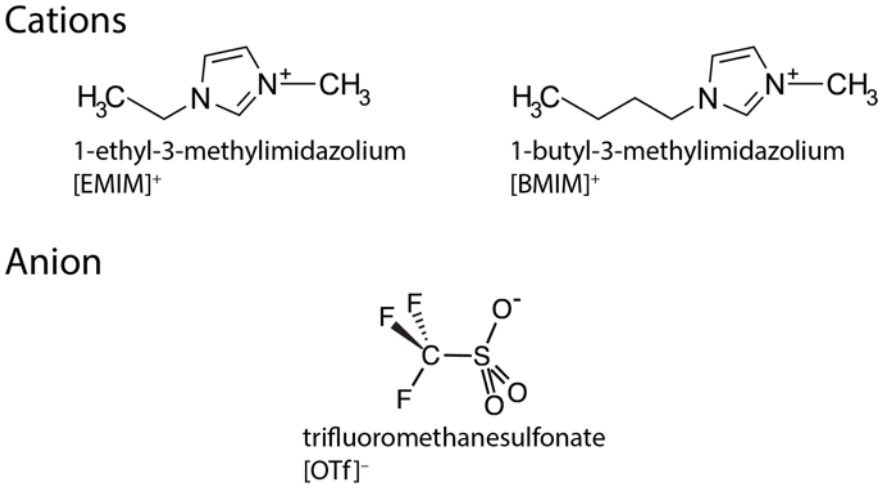

Figure 2.4: 1-ethyl-3-methylimidazolium ($[EMIM]^+$) and 1-butyl-3-methylimidazolium ($[BMIM]^+$) cations and trifluoromethanesulfonate ($[OTf]^-$) anion.

Most ionic liquids are known to be hygroscopic and absorb ambient moisture, likely leading to unwanted side reactions [17, 110]. The amount of water absorbed was affected by the length of the alkyl chain off the cation with longer chains decreasing the solubility of water. However, the effect of water on the electrochemical performance of ionic liquids has not been quantified.

Reversible Zn dissolution and deposition with suppressed dendrite formation has been reported in these and other ionic liquid electrolytes [63, 45, 39, 95, 61, 60]. Some electrochemical and transport properties of the neat ionic liquids have been characterized, specifically their conductivity and the diffusivities of the cation and anion in $[EMIM]^+[OTf]^-$, as seen in Figure 2.5 [30]. In addition, the diffusivity of Zn^{2+} from $Zn(OTf)_2$ has been characterized in various other nonaqueous solvents [37], but no studies on the diffusivity of Zn^{2+} in $[BMIM]^+[OTf]^-$ and $[EMIM]^+[OTF]^-$ as well as the resulting conductivity were found. Furthermore, no studies characterizing the kinetics of Zn deposition and dissolution in ionic liquids were found.

2.4 Gel Polymer Electrolytes

Traditional batteries utilize a membrane-like separator layer to prevent electrical contact between electrodes, which is then soaked with the electrolyte to be used. Conventional separator materials used in commercial lithium-ion batteries are polyolefins such as polyethylene and polypropylene [89]. In addition to the ionic conductivity of the electrolyte itself, separator membrane properties such as porosity, pore-size distribution, tortuosity, morphology,

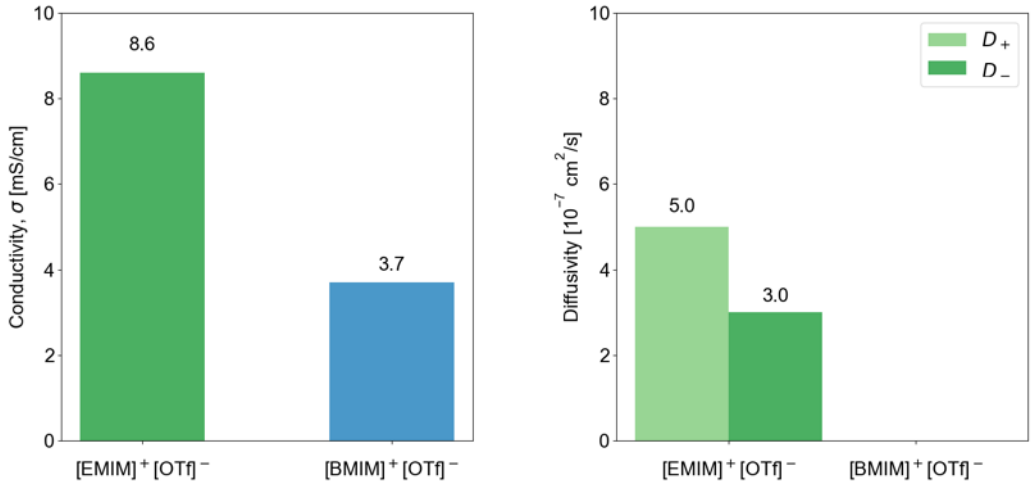

Figure 2.5: Ionic conductivities and diffusivities of $[EMIM]^+[OTf]^-$ and $[BMIM]^+[OTf]^-$ neat ionic liquids from available literature data [30].

thickness, and wettability also significantly affect observed ionic conductivity [1]. Furthermore, conventional lithium-ion battery manufacturing involves laminating a cathode layer, separator layer, and anode layer which then require additional sealing and packaging in order to form a free-standing cell.

The use of a microporous plasticized polymer membrane allows for the formation of a gel separator from solution that is able to serve as both a mechanical separator as well as an ionic conductor. This polymer membrane is able to be formed as a separate process and can be used as a replacement for traditional membrane separators. The use of gel polymer electrolytes offers significant benefits, including suppression of dendrite growth, higher tolerance to electrode volume changes during cycling, and more robust mechanical properties [88]. Of particular interest are poly(vinylidene fluoride)-based polymers due to its chemical stability and mechanical properties [107, 16, 69].

The polymer separator is typically solution cast, but various processing methods on final separator formation have been reported, the most notable being the Bellcore method [89, 34]. In this method, the polymer is dissolved in a solvent with a plasticizer and solution cast. The solvent is then driven off, leaving the polymer and plasticizer together. A second solvent is then used to dissolve and remove the plasticizer while leaving the empty polymer structure behind. Finally, the second solvent is removed and the empty polymer structure is then filled with electrolyte. The plasticizer is used to control the microstructure of the polymer in order to improve ionic conductivity and tune desired parameters. This creates a gel polymer electrolyte which contains both solid and liquid domains and whose charge transport properties resemble those of liquid electrolytes [65, 88]. Thus, the polymer structure provides

mechanical separation and structure while allowing for a liquid electrolyte of choice to be used.

Many factors can affect the polymer structure, including choice of solvent, processing method, and processing enviroments, and the resulting structures can exhibit a range of morphologies. Figure 2.6 presents some possible structures with PVDF-HFP. The resulting structure plays a significant impact on the overall ionic conductivity of the separator based on porosity and pathways [69].

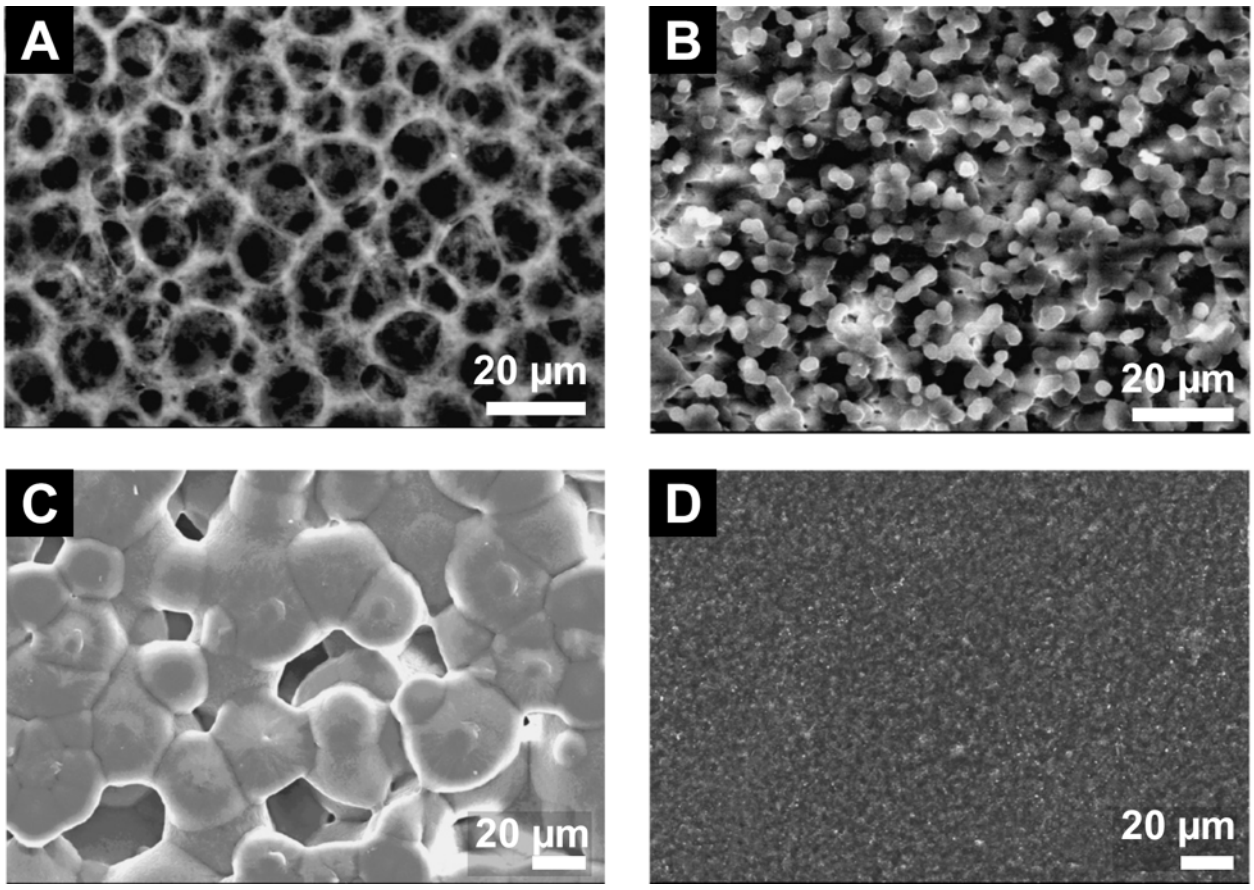

Figure 2.6: SEM micrographs of PVDF-HFP membranes cast from different solvents. *A*: THF+water; *B*: NMP+acetone; *C*: NMP+acetone+water; *D*: THF+ethanol [69].

Ionic liquid electrolytes are particularly compatible with plasticized gel polymer electrolytes due to their low vapor pressures. The ionic liquid itself may function as a plasticizer during the solution casting process, eliminating the need for multiple dissolution and drying steps. The use of ionic liquids with gel polymer electrolytes has been investigated, with ions successully transported through them [95, 105, 111]. Gel polymer electrolytes with zinc trifluoromethanesulfonate salt have also been investigated with evidence of Zn^{2+} transport [52, 51, 43].

2.5 Printing for Energy Storage

The development of printed electronics has brought with it a demand for printed energy storage devices in order to enable fully printed devices [75]. Printing itself is an attractive manufacturing method for electronic devices due to its cost-effectiveness, high throughput, reduced material wastage, and simple patterning techniques [46]. Furthermore, printing allows for manufacturing on flexible substrates, which enables the manufacturing of flexible electronics and their myriad applications.

A number of printed primary and secondary batteries devices have been reported which use screen printing and gravure printing [98, 10, 64]. In addition, previous work has manufactured secondary Zn-MnO_2 cells via dispenser printing, flexographic printing, stencil casting, and doctor blade coating [39, 100, 47, 48]. While dispenser printing allows for control of fine feature geometries through dropwise ink deposition, it is unsuited for scaled up manufacturing due to its low throughput and high variability between samples. Flexographic, gravure, and screen printing are easily scalable printing methods but require stricter ink rheologies in order to be compatible with the demands of rollers and screen meshes. While doctor blade coating offers the lowest amount of feature control, its tolerance to a wide range of ink rheologies and high throughput make it an attractive option for printed batteries where deposition of large print areas is necessary.

An ideal printing process would minimize the number of layers and steps involved to reduce possibilities for contamination or errors in the printing process. Individual inks should therefore be optimized not only for device performance but also for manufacturing. For inks for printed batteries in particular, optimization of ink rheology and surface profile is necessary, in addition to performance metrics such as electrical conductivity and electrochemical performance.

Use of the solution cast ionic liquid gel polymer electrolyte is critical to enabling printed cells. Because the low vapor pressure of the ionic liquid enables its use as a plasticizer in the formation of the polymer membrane structure, it can be easily integrated into the printing process, removing the need for separate processing and flushing as required other processing methods.

Chapter 3

Nickel Current Collector and Ball Milling

This chapter presents findings from ball milling on commercially available nickel powder and the results of adjusting ball milling parameters on particle size and morphology. The goals of this work are

1. to qualitatively identify the effect of each parameter has on the resulting particle size and morphology,
2. to use these findings to develop a printable nickel current collector, and
3. to translate these findings on a metal powder to powders of other compositions

Specifically, these results are used to inform process parameters in optimizing electrode compositions, as seen in Chapter 4.

Section 3.1 presents the motivation and the reasoning behind the material selection of nickel for this work. Section 3.2 discusses the theory behind the conductivity of polymer composites, principles of planetary ball milling, and methods of sheet resistance for printed films. Section 3.3 discusses the experimental methods and procedures used for this work. Section 3.4 presents the findings from ball milling nickel powder and conductivity measurements of the printed current collectors made from the ball milled powder. Section 3.5 summarizes these findings and suggests future work.

3.1 Motivation

The goal of this work is to characterize the relationship between various ball milling parameters on the resulting particle morphology as a result of ball milling. This is in order to develop a printable nickel current collector as well as to apply the findings to powders of other materials, ultimately to aid in the optimization of the printed MnO_2 cathode.

Nickel powder was investigated as an initial target for ball milling for number of reasons. Being a metal powder, nickel is able to plastically deform prior to fracture and thus allows for significant and observable changes in morphology as a result of ball milling. Compared to stainless steel, nickel has a lower yield stress as well as lower resistivity. While zinc and copper have even lower resistivities, their yield stresses are lower, resulting in excessive deformation and mechanical alloying of the powder to the grinding balls [14]. Similarly, silver and gold offer the same benefits with the same low yield stress disadvantage, but with the added disadvantage of high cost. Aluminum powder was investigated as a possible alternative due to its low resistivity and low cost, but it was removed from consideration due to the fact that aluminum powder is extremely pyrophoric in ambient environments. Table 3.1 summarizes the differences in material properties of these metals.

Table 3.1: Electrophysical properties of candidate metals for a printed current collector [66]

Metal	**Electrical Resistivity [Ω-cm]**	**Yield Stress [MPa]**	**Ultimate Tensile Stress [MPa]**
Nickel	6.4e-6	59	317
1199 Aluminum	2.7e-6	10.0	45.0
316 Stainless Steel	7.4e-5	240	550
Zinc	5.92e-6	–	37.0
Copper	1.7e-6	33.3	210
Silver	1.55e-6	–	140
Gold	2.20e-6	–	120

One requirement for current collectors for electrochemical cells is that they be nonreactive with the materials in the electrodes and electrolyte in order to remove the presense of any parasitic side reactions that may degrade the cell [73]. While it has not been investigated whether nickel is a suitable choice for the ionic liquid system studied in this work, its electrophysical properties make it an excellent candidate to investigate changes in particle morphology via ball milling.

3.2 Background

This section discusses percolation theory and contact resistance as pertains to the conductivity of polymer composite. The operational principles of planetary ball milling and the factors that affect it as well as sheet resistance measurements via a four point probe are also discussed.

3.2.1 Conductivity of Metal-Polymer Composites

Colloidal and particle-based coatings and slurries can be described as polymer composites in which the properties of the bulk coating are determined by the properties of a dispersed material within a dispersion medium [78]. These composites are typically cured at temperatures significantly lower than those required for ceramic or metal sintering and thus exhibit different properties and phenomena. A number of models to describe such composites have been proposed since their inception, but such systems are most often characterized as disordered systems in which there is no regular or ordered structure to the dispersant in the medium. The framework of percolation theory thus emerged to describe the electrophysical properties of disordered systems [78].

Accompanying percolation theory itself is typically a discussion of fractal geometry, which emerged when it was observed that individual particles would self-assemble into similar agglomerates, which then was adopted as the long-range unit structure of study [68]. Fractal geometry provides a framework to quantitatively describe the disordered structure of the aggregate particles by their fractal parameters [94, 27]. An in-depth discussion of fractal geometry is beyond the scope of this work, but the geometry of the aggregates affects the long-range percolation behavior of the composite [78].

Percolation theory provides a framework to describe the change of a composite material from an insulator to a conductor as the amount of conductive material loaded into an insulating matrix is increased. As the volume fraction of conductive material increases, more percolated linkages form, and the probability of a conductive pathway being formed increases accordingly [81]. This is shown in Figure 3.1. Once a critical number of linkages allowing for a conductive pathway is formed, the conductivity of the composite increases significantly and continues to increase as the volume fraction of conductive particles increases. The volume fraction at which this occurs is called the percolation threshold, V_c [67].

Bueche [12] proposed a model that simplifies the composite to a mixture of two phases, where the overall resistivity is a weighted sum proportional to the amount of each phase, and accounting for the fact that not all conductive particles present may be in contact and contributing to the conductive pathway. This is given by Equation 3.1, where ρ is the resistivity of the composite, ρ_m is the resistivity of the nonconductive matrix, ρ_p is the resistivity of the conductive particles, V_p is the volume fraction of the conductive particles, and w_g is the fraction of contributing conductive particles.

$$\frac{1}{\rho} = \frac{1 - V_p}{\rho_m} + \frac{V_p w_g}{\rho_p} \tag{3.1}$$

Further refinements to this model were made by Springett [90], which provide more realistic behavior at the percolation threshold and, though spherical particles are assumed, include a lattice packing fraction term which helps further account for the disordered positions of the conductive particles. This average model of conductance is given by Equation 3.2, where σ_α is the insulator conductivity, σ_m is the metallic conductivity, v_m is the volume fraction of metal, and f is the lattice packing fraction.

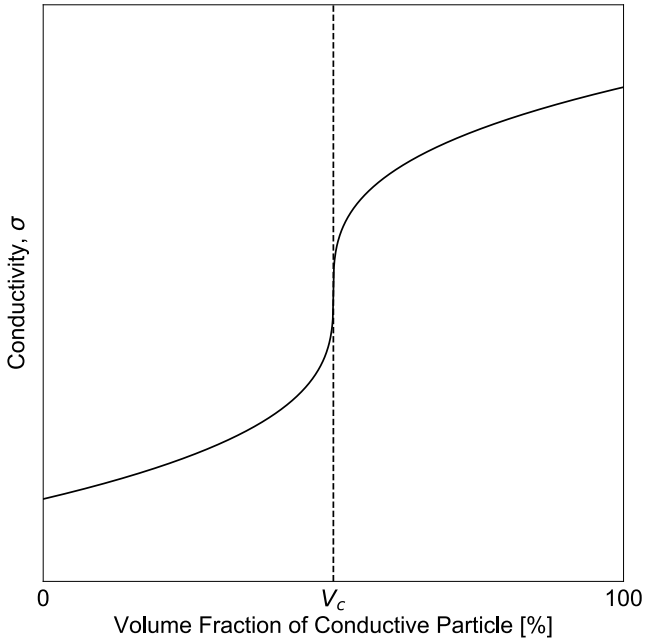

Figure 3.1: Dependence of conductivity on conductive particle loading as described by percolation theory. V_c indicates the volume loading corresponding to the percolation threshold of the composite.

$$4\sigma = \sigma'_m\sigma'_\alpha + \left[(\sigma\_m + \sigma'_\alpha)^2 + 8\sigma_m\sigma_\alpha\right]^{1/2} \tag{3.2}$$
$$\sigma'_m = \left(\frac{3v_m}{f} - 1\right)\sigma_m$$
$$\sigma'_\alpha = \left(2 - \frac{3v_m}{f}\right)\sigma_\alpha$$

However, despite the formation of a continuous conductive pathway, it is more accurate to consider the pathway as a series of resistors made up of each percolated linkage, with the resistance of each linkage and the interfacial contact resistance between linkages contributing to the overall resistance of the entire pathway [81]. The contact resistance, R_c, can be further broken down as the sum of the constriction resistance, R_{cr}, and tunneling resistance, R_t (Equation 3.3) [67].

$$R_c = R_{cr} + R_t \tag{3.3}$$

Constriction resistance results from a constriction of electron flow from each particle to the contact area between two particles. This resistance has been derived and shown to be inversely proportional to the diameter of the contact spot by Equation 3.4, where ρ_i is the resistivity of the particle material and d is the diameter of the contact spot. [81]. The denominator of this relationship has been defined as the diameter of the contact spot rather than the contact spot area because the ratio of the particle diameter, D, and the the contact spot diameter determines the upper limit of validity of this relationship (when $D/d > \sim 10$).

$$R_{cr} = \frac{\rho_i}{d} \tag{3.4}$$

Tunneling resistance derives from resistances associated with any insulating film or layer that may be coating each particle [81]. In the case of metals in a polymer matrix, these layers can be oxide layers formed on each metal particle or even the polymer itself. Depending on the manufacturing and processing methods performed on the particles, there may be residual organic films remaining as well. Based on the physics of quantum-mechanical tunneling, an electron may "tunnel through" instead of overcome a potential barrier based on a probability proportional to the conductor's work function, the film thickness, and the film's relative dielectric permittivity. The resistivity of the film is absent from this proportionality, so for primarily organic and polymer films, the thickness of the film becomes the primary differentiating factor. This tunneling resistance is inversely proportional to the contact spot area, as in Equation 3.5, where ρ_i is the resistivity associated with tunneling and a is the contact spot area.

$$R_t = \frac{\rho_t}{a} \tag{3.5}$$

The degree of contact resistance is also dependent on any internal stresses that may be present in the composite. These stresses may result from differences in thermal expansion during the curing process, capillary action from solvent evaporation in the slurry, and shrinkage from polymer crosslinking during the curing process [67]. The degree to which these play a role depends on the compositions of the polymer, conductive particles, and slurry, but the resulting internal stresses impart elastic and plastic deformation on the conductive particles, which assists in maintaining good contact.

In general, the magnitude of the tunneling resistance outweighs the magnitude of the constriction resistance and is impacted by the thickness of any insulating layers between conductive particles and the contact area, which are both consequently a result of internal stresses between particles, particle morphology, and packing fractions. Depending on the relationship between these factors, the overall resistivity of the composite may vary wildly [81].

3.2.2 Planetary Ball Milling

Adjustment of the particle morphology through mechanical deformation of the conductive powder is one method to affect contact resistance and therefore improve the conductivity of composite matrices. Milling processes via ball or rod milling has emerged as a method for producing high quality powders and for powder milling and refining [25]. Within ball mills, there exist a number of different types, including drum ball mills, jet ball mills, bead mills, roller ball mills, vibration ball mills, and planetary ball mills. The difference in rotation speeds each type is capable of providing separates them into low- or high-energy ball mills. Table 3.2.2 provides a comparison of speeds and energies different types of mills are capable of providing.

Table 3.2: Characteristics of different types of ball and rod mills [25]

	Vibratory Ball Mill	**Planetary Ball Mill**	**Roller Mill**
Ball velocity [m/s]	$\leq$3.9	0.24-11.24	≤ 5
Kinetic Energy [10^{-3} J/hit]	120	0.4-884	0-190
Shock Frequency [Hz]	15-2000	4.5-100	0-2.4
Power [W/g/ball or rod]	0.005-0.24	0-1.604	0-0.1

For this work, the use of a planetary ball mill was explored as a method for inducing particle deformation. A planetary ball mill is characterized by a motor-driven larger central gear (the sun gear) which drives a set of smaller gears that revolve around its circumference (planet gears). The gear ratio between the two enables faster rotation of the planets than is directly provided by the motor to the sun, and the rotational speeds of the smaller allow for significant forces to be imparted on materials placed inside appropriate grinding vessels. Figure 3.2 shows the planetary ball mill used for this work with the sun gear and four planet gears visible.

The factors that affect the result of the milling process include the shape of milling jars, composition of the milling media, milling time, milling speed, milling atmosphere and temperature, milling environment (wet or dry), and powder to milling media weight ratio. When the jars come up to speed, the balls inside are given enough kinetic energy to rise up the sides of the jars and fall back into the center, impacting the material inside against the sides and floor of the jars along the way. For a given combination of jar geometry and ball size and composition, there is a window of milling speeds that will yield good results as speed that are too low will not allow the balls to rise up the sides of the jar while speeds that are too high will trap the balls along the sides of the jar via centrifugal force [71].

Figure 3.2: Planetary ball mill used for this work, Across International PQ-N04. The four planet gears revolve around the sun gear while rotating in the opposite direction. Two sample holders are shown mounted and clamped on the left and right poles.

In order for deformation to occur, the specific impact energy of the balls must impart a stress that exceeds the yield stress for a given particle geometry. This specific impact energy, E_W with units [J/(g·s)], can be calculated by Equation 3.6, where v_j is the relative impact velocity between two colliding balls or a ball colliding against the wall of a jar, m is the mass of the grinding media, n is the number of collisions per second of a ball, and W is the weight of the powder sample charged into the milling jar [71].

$$E_W = \sum_{j=1}^{n} \frac{1}{2W} m v_j^2 \tag{3.6}$$

The final result of powder processing via ball milling depends on myriad parameters. Metal powders are more able to withstand significant strains from deformation before fracture compared to ceramic powders, so their use in experimental work enables more facile observation of the effects of changing various ball milling parameters.

3.2.3 Sheet Resistance

Two-dimensional films, such as those produced by printing, evaporation, or any thin-film deposition method, are typically characterized by their sheet resistance. Sheet resistance is a specialized case of resistance measurements that is more applicable in cases where the current runs along the plane of a sheet instead of through it, as in the case of a wire.

In a traditional 3-dimensional sample, the resistance can be written as

$$R = \rho \frac{L}{A}, \tag{3.7}$$

where ρ is the material resistivity, A is the cross-sectional area, and L is the length. For planar samples, the cross-sectional area can be broken down to the width, W, and thickness, t. The terms can then be rearranged to define the sheet resistance, R_s, with units of $\Omega \cdot \square$ (Equation 3.8). This geometry is shown in Figure 3.3.

$$R = \rho \frac{L}{Wt} = \rho \frac{1}{t} \frac{L}{W} = R_s \frac{L}{W} \tag{3.8}$$

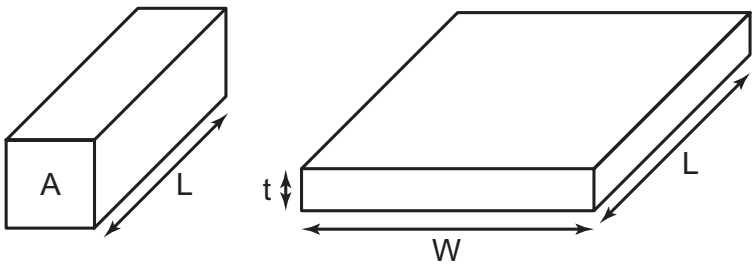

Figure 3.3: Geometry for resistance measurements for 3-dimensional and planar samples.

The relationship between sheet resistance and bulk resistivity can therefore be correlated by the sample thickness.

$$\rho = R_s \cdot t \tag{3.9}$$

It can be seen from Equation 3.8 that the measured resistance, R, is proportional the sample's aspect ratio, $\frac{L}{W}$. Because both planar dimensions are taken into account, the resistance measured via sheet resistance is invariant to the sample size. In the case of a square sample, the sample resistance is equal to the material sheet resistance, provided that the ratio of length to width is maintained and the thickness is constant.

The unit $\Omega \cdot \square$ derives from the length units cancelling out when dividing the resistivity (units $\Omega \cdot m$) by the thickness (units m). The square is unitless but denotes a sheet resistance measurement to avoid confusion with a traditional resistance measurement (units Ω), which would otherwise have identical units.

In order to take sheet resistance measurements, a four-point probe is typically used in order to mitigate contact resistances that may dominate the measurememt. The Van der Pauw method utilizes a square probe configuration and offers a robust method for capturing any anisotropic behavior in the sample [18], but can be difficult to uniformly repeat and set up due to the precision required in placing contacts and in sample shape. Another common configuration is inline, in which the four probes are placed in a straight line and are placed in the center of the sample. For an inline probe, the two outer pins apply a fixed current, which is measured as a potential difference by the two inner pins (Figure 3.4). This is used to obtain a direct sheet resistance measurement.

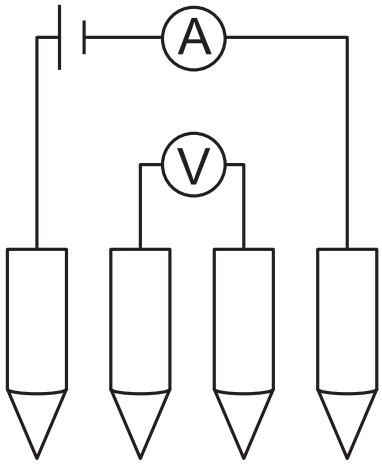

Figure 3.4: Probe setup for inline four-point probe. The outer pins apply a current, and the resulting potential is measured by the inner pins

3.3 Experimental Methods

This section provides an account of the experimental methods followed. First, the nickel powder was ball milled according to the specified ball milling parameters. Next, scanning electron microscopy pictures were taken of the milled powder. Inks were made with the milled powder and printed via stencil casting by hand. The samples' sheet resistances and thicknesses were then measured and used to determine the bulk conductivity of each ink.

3.3.1 Ball Milling

The ball milling jars and lids were custom machined out of stainless steel. The dimensions of the jar and the jar and lid are presented in Figure . The lids featured a rubber gasket and were able to be tightened to the jar with machine screws, creating a sealed enclosure inside. Stainless steel grinding balls (Retsch) of 3mm, 5mm, 10mm, and 15mm diameter were used as the grinding media. The milling frequency was varied from 15Hz, 20Hz, and 30Hz, and the milling time was varied from 1 hour, 2 hours, and 8 hours.

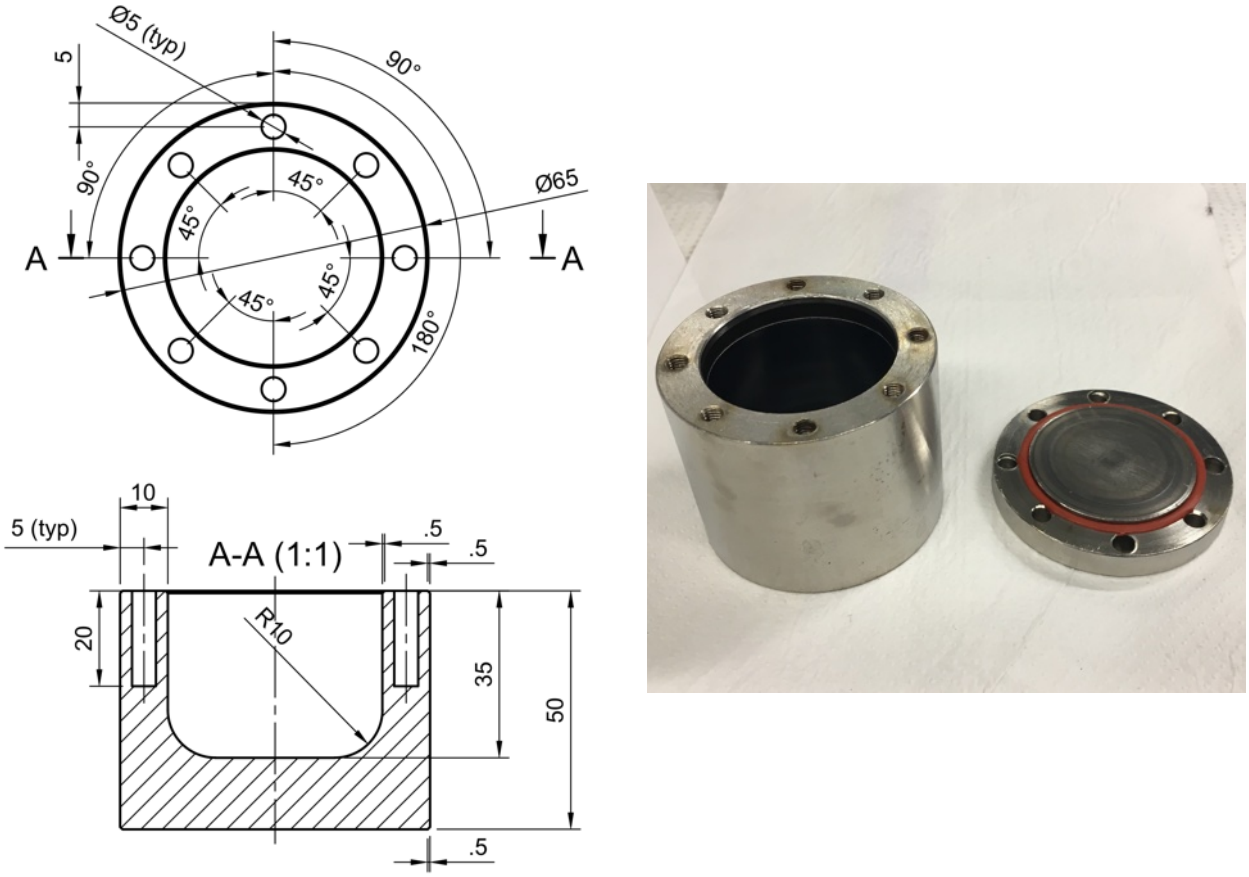

Figure 3.5: *Left*: Drawing of ball milling jar. All dimensions are in mm; *Right*: picture of ball milling jar and lid with gasket (orange).

Prior to adding the powder, the jars, lids, gaskets, and balls were all thoroughly cleaned. The jars, lids, and gaskets were first wiped down with water and a Texwipe to remove any residual Ni present. They were then wiped down with acetone and a Texwipe until there was no visible residue on the Texwipe, then placed into an ultrasonic water bath for one hour. Once sonication was completed, the parts were placed in an oven at 50°C to dry, then wiped down one last time with acetone to remove any residue left behind by the water.

To clean the balls, as much residual Ni as possible was first removed with water and a Texwipe. The balls were then added to a plastic jar, which was filled partially with water and dish soap. The jar was closed and shaken vigorously, and the waste water was poured into a waste beaker through a funnel and sieve to avoid losing the grinding balls. This process was repeated with water and dish soap for a total of three times, then once more with acetone. The balls were then also placed in an ultrasonic water bath for 1 hour, then removed and dried in an oven at 50°. Finally, they were rinsed once more with acetone and dried one more time.

The nickel powder and grinding balls were added to the jar in a mass ratio of 1:10 of powder to balls. Approximately 8g of powder was milled per jar per run. The powder was first added to the jars, and the balls were then carefully added on top, making sure not to cause the underlying powder to spill out. Isopropyl alcohol was then added to cover the powder and partially cover the balls in order to form a wet grinding environment inside the jars. The jars were then sealed and tightened with machine screws to form a closed environment. The sealed jars were placed in a planetary ball mill (Across International, PQ-N04). The direction of rotation was reversed every 15 minutes to ensure even milling of all the material inside.

Once ball milling was complete, the jars were removed from the ball mill and the lids removed. With the balls still inside the jars, both the jars and lids were placed inside an oven at 50°C until all of the isopropyl alchol was driven off. The powder and balls were then poured into a mesh sieve (30 mesh, or 0.5mm opening) in order to separate the balls from the powder. The powder was then poured into a vial for further use.

3.3.2 Scanning Electron Microscopy

A tabletop scanning electron microscope (Hitachi TM-1000) was used for all scanning electron microscope images. First, aluminum SEM stages (Ted Pella) were covered with double-sided adhesive carbon tape to create a substrate upon which to secure the samples. For the nickel powder, a roughly $1cm^2$ wide strip of carbon tape was firmly adhered to the SEM stage. A small amount of nickel powder was then spread onto the carbon tape and lightly pressed into the tape with the end of a wooden applicator (Puritan). The stage was then tapped a few times against the edge of a workbench to remove any excess unadhered nickel powder.

The chamber atmosphere was pumped down to vacuum prior to engaging the electron beam. Where possible, the software's automatic focus and brightness/contrast settings were used when capturing images, but manual adjustment was necessary for some samples.

3.3.3 Ink Compositions

In order to investigate the effect of changing particle morphologies and sizes on printed sample conductivity, a slurry was made with each ball milled nickel powder. The composition was kept constant in order to isolate the effect of changing particle size on slurry conductivity.

The composition used was 80 wt% nickel powder (Alfa Aesar, 3-7ÂţmÂţm median size) and 20 wt% poly(vinylidene fluoride)-hexafluoropropylene (PVDF-HFP, Kynar Flex 2801) with n-methyl-2-pyrrolidone (NMP) added as a solvent in a 4:1 mass ratio to the mass of PVDF-HFP. For each ink, 4g of nickel powder was used to yield 9g total of each ink. This composition is summarized in Table 3.3.

Table 3.3: Nickel Current Collector Composition

	Weight Percent [wt%]	**Mass [g]**
Nickel Powder	44.44	4
PVDF-HFP	11.11	1
NMP	44.44	4

To make each ink, 1g of PVDF-HFP was first dissolved into 4g of NMP in a 20mL glass vial. Dissolution was aided by a combination of agitation on a vortex mixer and an ultrasonic water bath. After the polymer was fully dissolved, 4g of ball-milled nickel powder was added to the vial. The vial was then mixed for 5 minutes on the vortex mixer and then placed into the ball mill for 2 hours at 45Hz, changing directions every 15 minutes, in order to ensure more homogeneous particle dispersion. However, noticeable settling of the nickel powder occurred over time due to its density, so each ink was mixed for 10 minutes on the vortex mixer immediately prior to use for printing.

3.3.4 Stencil Casting

Nickel inks were printed by hand using a combination of stencil casting and doctor blade. Inks were printed on a 75ÂţmÂţm Kapton (polyimide) substrate (American Durafilm). A stencil was cut out of the same Kapton material to form a 2×4 array of 1cm^2 squares.

Printing was done on a 1/4 inch thick 6×6 inch MIC6 aluminum plate (McMaster-Carr) with a nominal flatness tolerance of 0.015 inches, which served as a heat-resistant and acceptably flat surface. The Kapton substrate was cut to size with scissors, and both the surface of the aluminum plate and both sides of the substrate were cleaned with a Kimwipe and acetone to remove any dust and debris that could be trapped between the subtrate and the plate. Prior to laying down the Kapton, a small amount of acetone was added to the aluminum plate upon which the Kapton was laid. As the Kapton was laid down, the capillary forces from the acetone pulled down the Kapton to the plate, which created smooth contact and eliminated the possibility for any trapped air bubbles as the acetone evaporated. Excess acetone from under the sides of the substrate was wiped away with a Kimwipe, and the top surface of the Kapton was again wiped to remove dust and debris. Both the top and bottom ends of the substrate were then secured to the aluminum plate with masking tape.

The Kapton stencil was then aligned in the center of the substrate and cleaned and affixed using the same method as the substrate to the plate with acetone and masking tape. The acetone under the stencil was allowed to evaporate fully, especially along the edges of each $1cm^2$ square, in order to allow for clean edges after printing.

A wooden applicator (Puritan) was used to place a small amount (0.1-0.2 mL) of ink ahead of each square. The doctor blade was then cleaned with a Kimwipe and acetone and drawn by hand towards the user from the top of the stencil to the bottom. The doctor blade was held at roughly a 60° angle from the plate towards the direction of casting to ensure only one edge of the blade was in contact with the stencil. Care was taken to ensure both sides of the doctor blade were drawn forward at the same speed and to apply enough pressure to maintain constant contact with the stencil but not so much that ink would be squeezed out between the stencil and the substrate. After printing, the stencil was removed and the plate and substrate placed in an oven at 80°C for at least 1 hour to drive off all solvent. The stencil and doctor blade were then cleaned for future use.

For all inks, 2 batches of 8 samples were printed for a total sample size of 16 per combination of ball milling parameters.

3.3.5 Sheet Resistance Measurements

An inline four point probe was used for all conductivity characterization. The direct measurement being taken was sheet resistance, which was then converted to bulk resistivity and bulk conductivity by measuring the average thickness of each printed electrode.

Sample were printed on 75μm Kapton to as an insulating substrate. The printing method used introduced the possibility for some particle alignment along the printing direction, so resistance measurements were taken in two directions, one parallel and one perpendicular to the direction of casting. This is visualized in Figure 3.6.

Thickness measurements were taken with a handheld ratcheting screw micrometer (Mitutoyo). The micrometer was first zeroed to the thickness of the substrate. The sheet of samples was positioned such that the rotating side of the micrometer was in contact with the back of the substrate to avoid measurement errors that could be caused by shearing the sample, and the ratcheting function of the micrometer was utilized to minimize measurement error via compression of the sample.

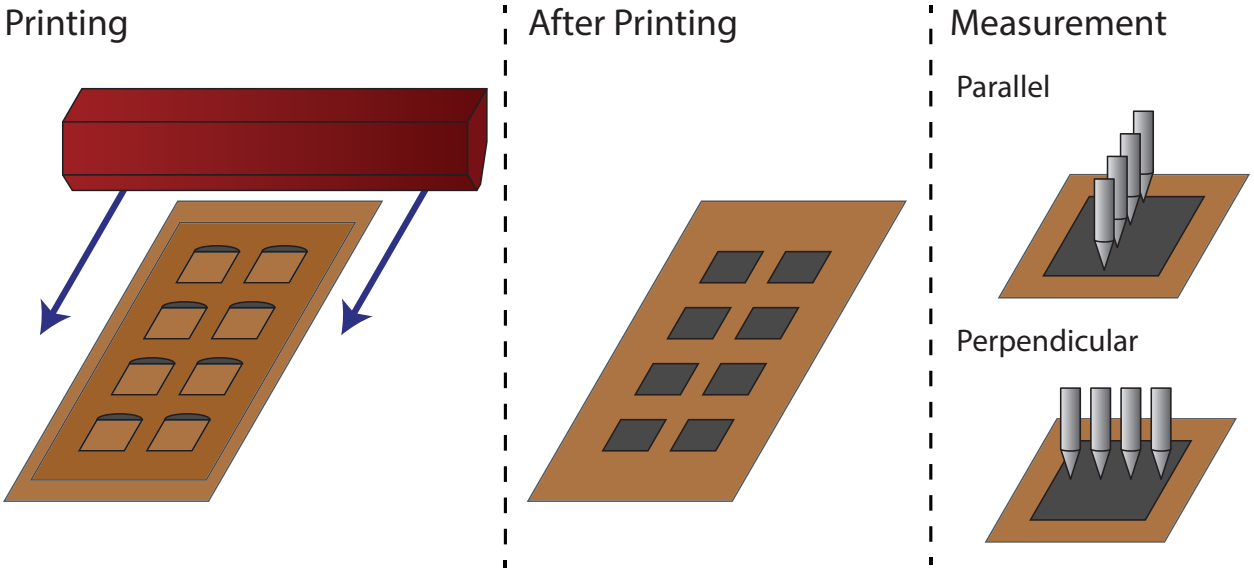

Figure 3.6: Sample preparation for conductivity measurements. *Left*: Printing samples with doctor blade and Kapton stencil. The direction of the doctor blade introduces a possible axis along which particles in the slurry may be aligned. *Middle*: Electrodes cast on Kapton substrate. *Right*: Top, four point probe measurement perpendicular to the direction of casting; Bottom, four point probe measurement parallel to the direction of casting.

3.4 Results and Discussion

The goal of this section is to obtain data correlating a qualitative analysis of ball-milled nickel powder to quantitative determination of the effect of ball milling on ink conductivity, with the primary intention of optimizing conductivity.

3.4.1 Scanning Electron Microscopy of Unmilled Nickel Powder

As a control, a current collector ink was made and printed using the unmilled nickel powder. Figure 3.7 presents a picture of the resulting print, an SEM image of the unmilled powder, and the conductivity of the ink that was made.

The observed particle size ranges from roughly 3-7μm, as stated by the manufacturer, and the morphology of each particle is roughly spherical, though the surface of each particle itself is jagged and dendritic in appearance.

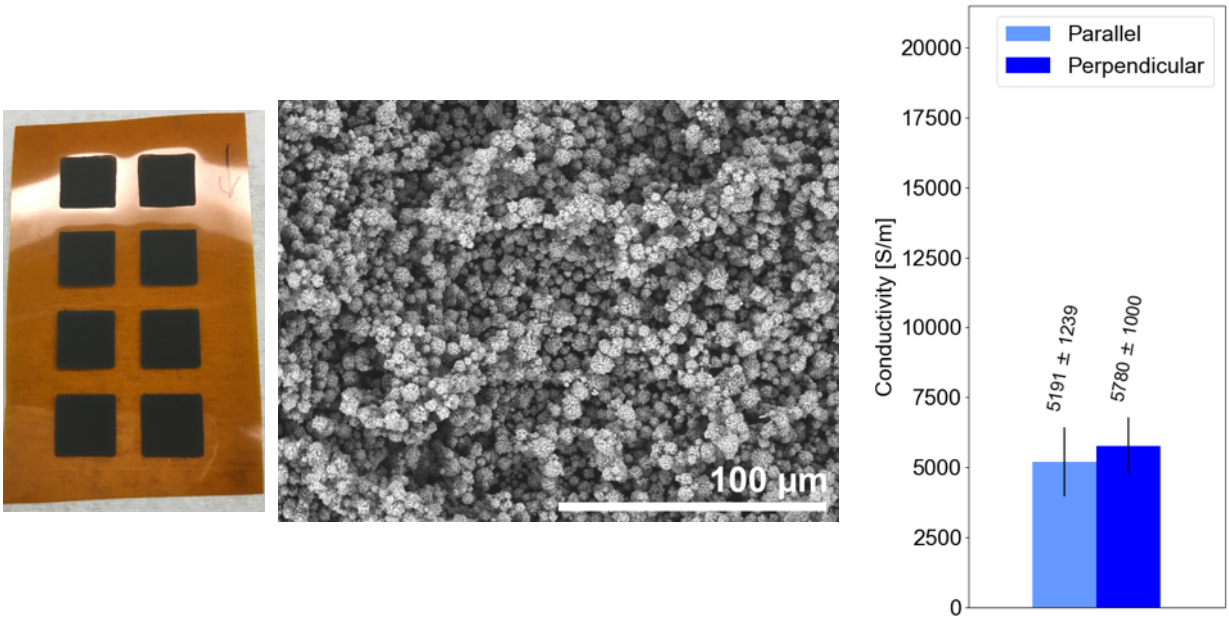

Figure 3.7: *Left*: Picture of stencil-cast nickel current collector printed by hand; *Middle*: SEM image of unmilled nickel powder; *Right*: Conductivity of unmilled nickel powder ink.

3.4.2 Scanning Electron Microscopy of Milled Nickel Powder

Figures 3.8, 3.9, and 3.10 present SEM images of ball-milled nickel powder at 15 Hz, 20 Hz, and 30 Hz respectively.

The effect of ball milling on the powder was such that the initial powders were flattened and in some cases deformed into each other. The resulting shapes can be roughly described as raw (unmilled), pebbles (see 30Hz, 3mm, 3 hours), and flakes (30Hz, 15mm, 8 hours), where the pebbles are an intermediate stage of being flattened between the raw powder and flakes. Between the three parameters of milling frequency, ball size, and milling time, the ball size had a more significant impact on the shape of the deformed particles while the milling frequency and time affected the amount of powder that was deformed.

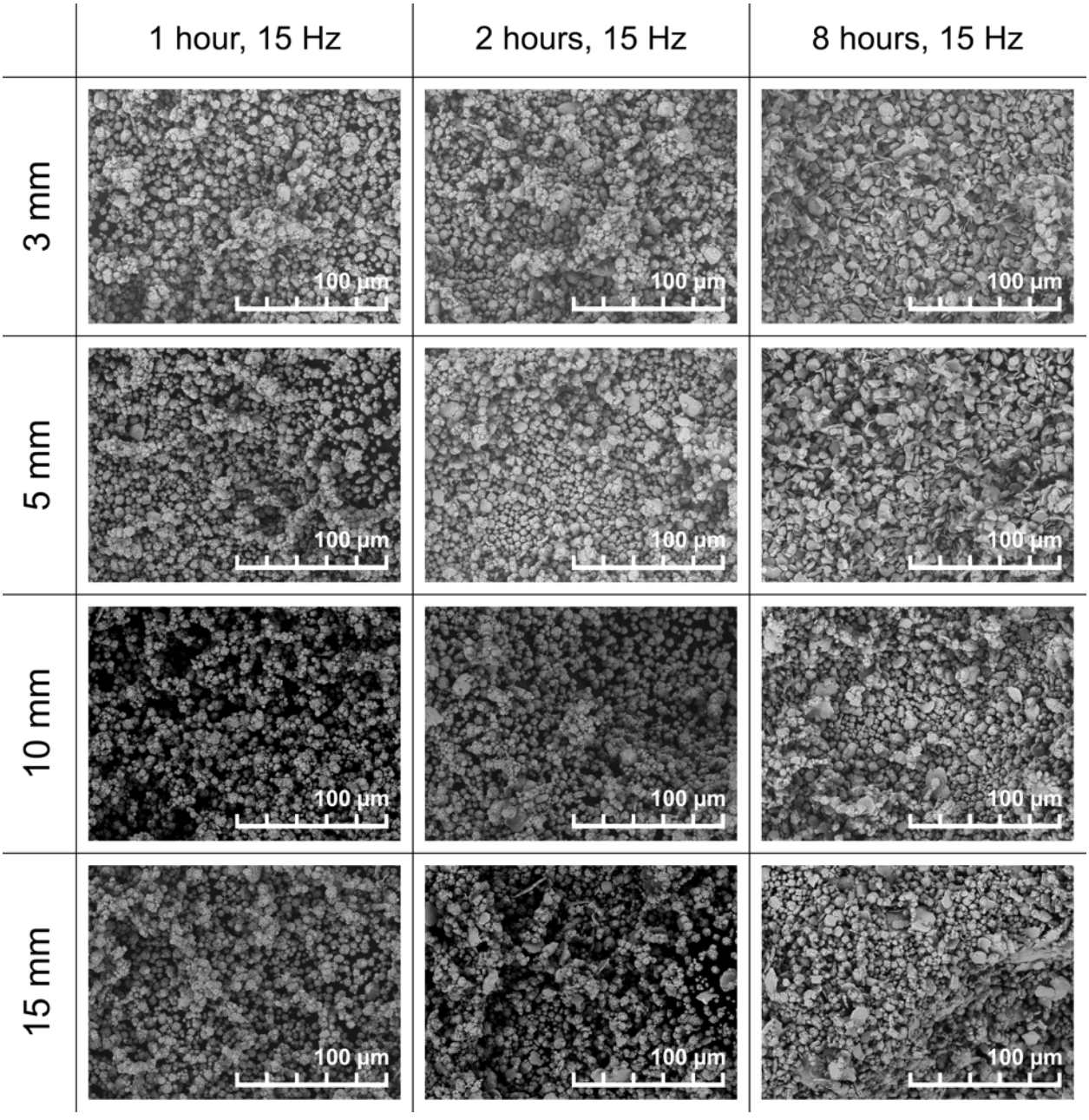

Figure 3.8: SEM images for ball milling at 15 Hz

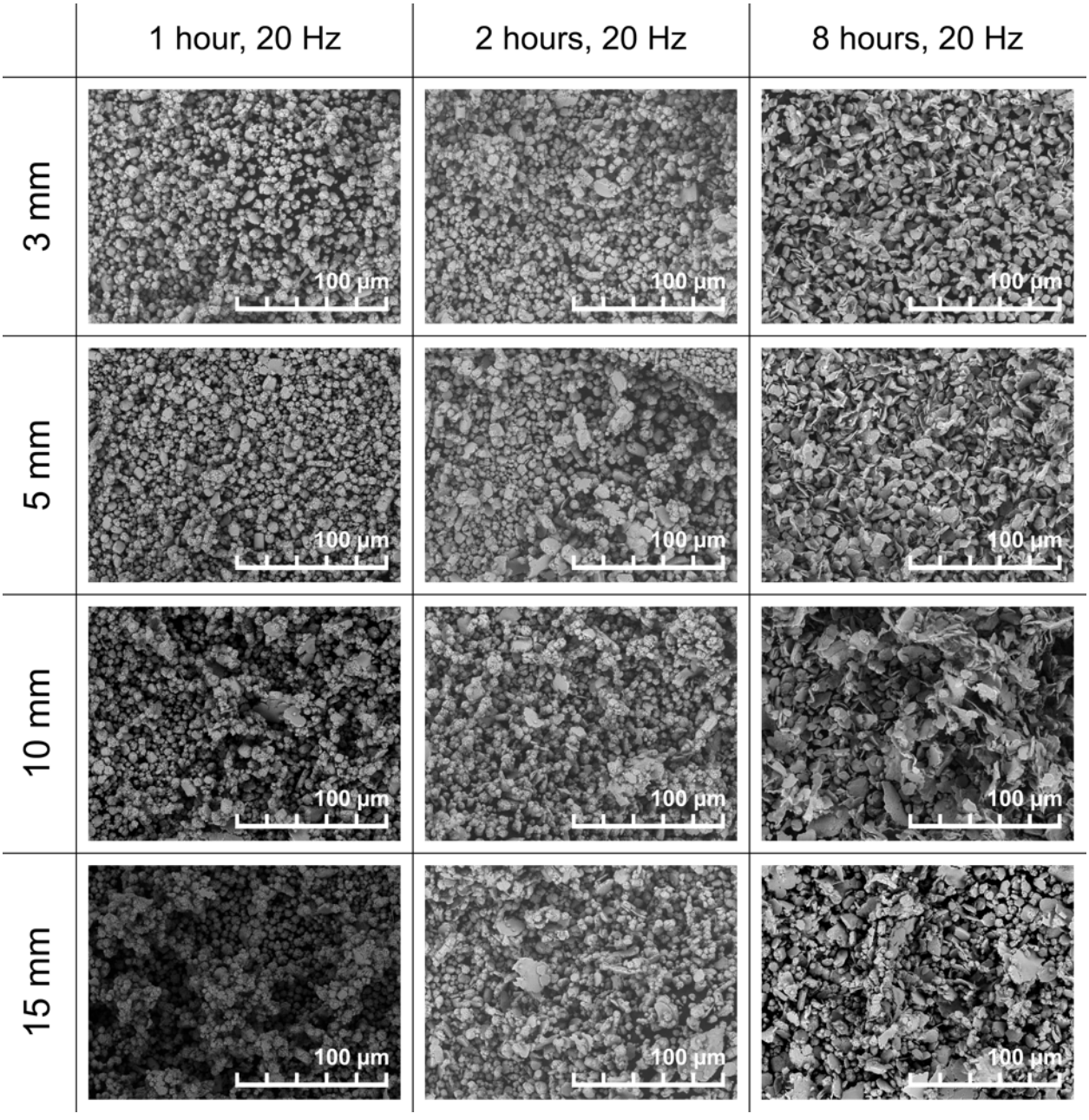

Figure 3.9: SEM images for ball milling at 20 Hz

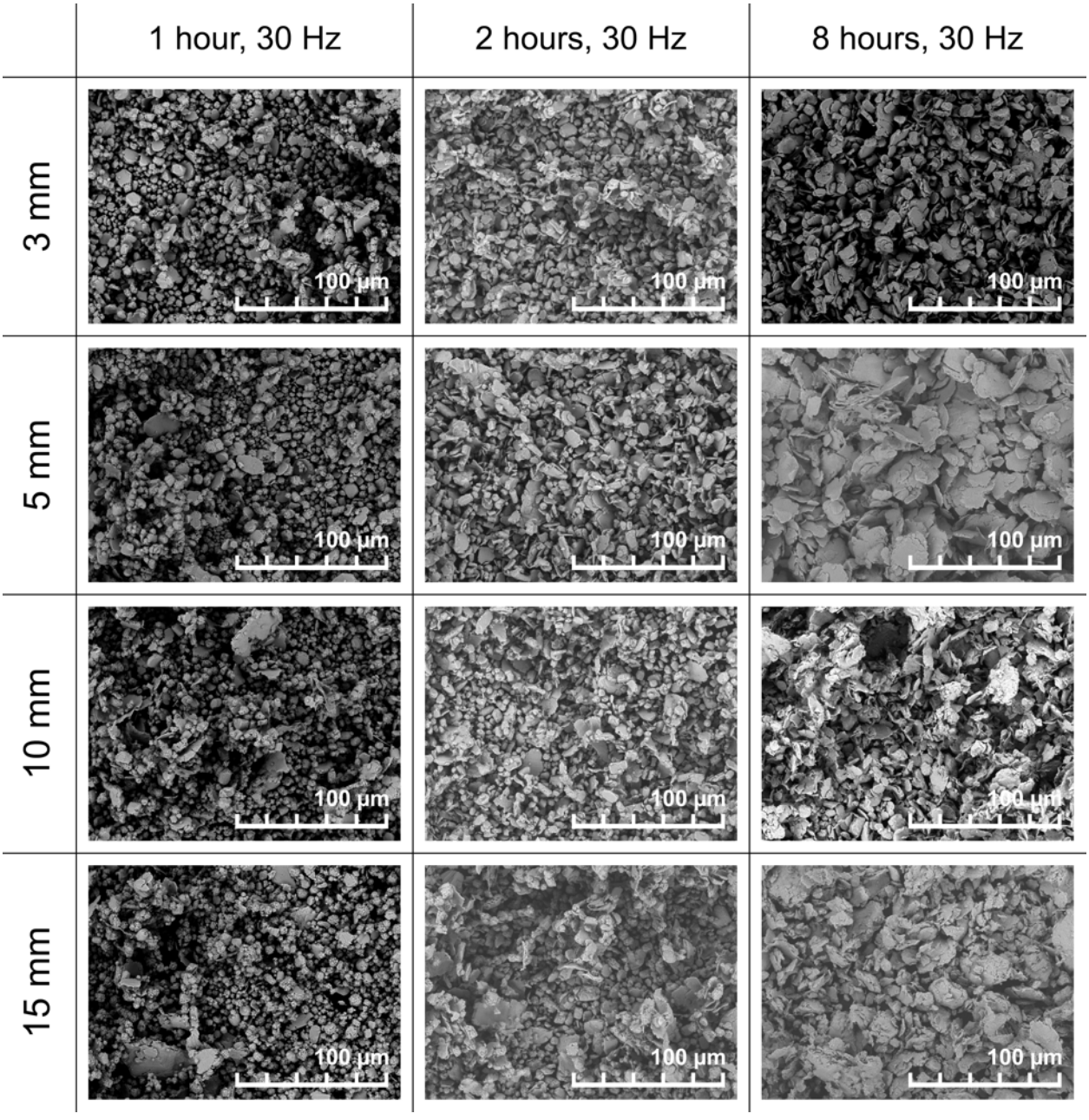

Figure 3.10: SEM images for ball milling at 30 Hz

As expected, the higher milling times and frequencies resulted in a larger percentage of the the powder being more significantly deformed. The effect of increasing milling frequency is subdued, especially for the smaller ball sizes (3mm and 5mm), but becomes more dramatic as both the ball size and the milling time increases. Similarly, the effect of increasing milling time becomes more pronounced at higher frequencies and ball diameters. This is due to the balls requiring a threshold amount of momentum in order to overcome the yield stress of the nickel powder. The higher frequencies impart more kinetic energy to the balls and therefore increase the probability that a given collision between a ball and a particle against the jar or against another ball will cause deformation. As the milling time increases once the frequency is above a threshold amount (for the combination of the mass ratio of powder to balls and jar geometry), the balls are given more opportunity to deform a larger percentage of the powder. Based on the findings, the most dramatic deformations for all ball sizes occurred at milling frequency of 30 Hz and a milling time of 8 hours.

The grinding ball size dictated the final deformed morphology of each particle. This is most likely due to the increasing contact area between each ball and the wall of the grinding jar or between colliding balls, as well as the increasing impact force as the ball diameter increased, assuming a constant volume deformation for each particle with no fractures occurring. The 3mm balls were most apparent in producing pebbles, which are characterized by having a flattened diameter just slightly wider than the unmilled powder with a thickness of roughly half that of the diameter of the unmilled powder. With 5mm balls, the formation of flakes, characterized by flattened diameters of at least 2-3 times (10-20μm) that of the unmilled powder, became significantly more apparent, especially at 20 Hz and 30 Hz. Some combining of particles became apparent with separate flakes visibly fusing to each other, but flakes generally retained edge integrity and did not show signs of flakes breaking apart.

At 10mm and 15mm ball diameter, the flakes did begin to show signs of fracture and began to take on a more "shredded" texture. Agglomerates of different particles began to appear, and the effective diameters of flakes present ranged from 5-20Âţm. Agglomerates were most likely formed by multiple flakes being caught in a single collision, and smaller flakes were most likely formed by an already deformed particle being impacted again, causing fracture. At the most energetic parameter combination (30 Hz, 15 mm, 8 hours), The size of the agglomerates began to increase beyond the diameter of the unmilled powder, ranging from 20-50 Âţm.

The effect of these resulting particle morphologies and the proportion of unmilled to milled powder on slurry conductivity will be discussed in the following section.

3.4.3 Conductivity

Figures 3.11 to 3.13 present the average conductivity of each current collector ink made with ball-milled nickel powder.

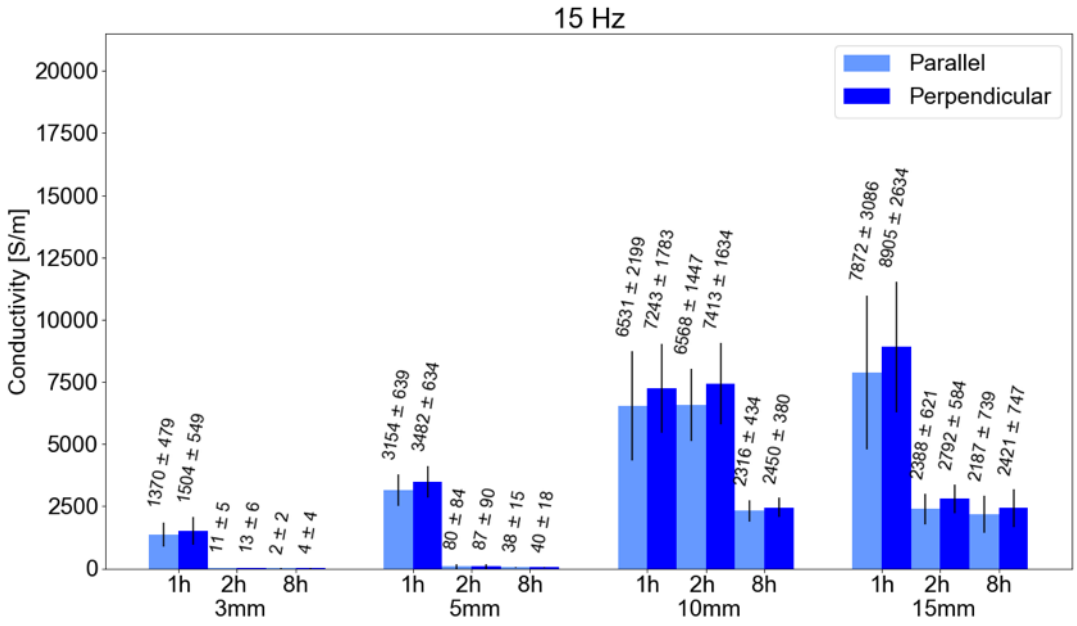

Figure 3.11: Average conductivity measurements for ball milling at 15 Hz. Error bars represent standard deviation for each batch of samples.

The total amount of energy applied to the system in each jar (the balls and the charged powder) can be determined by multiplying Equation 3.6 by the total milling time and the total mass of the balls. By doing so, all three ball milling parameters that were tested are accounted for, with the milling frequency being related to the impact velocity and mass of the balls and the ball size being directly related to the mass of the balls. Considering this relationship, each set of ball milling parameters can be thought of as imparting a set amount of energy to the system. Therefore, changing different ball milling parameters is a proxy for changing the total amount of energy applied to the system.

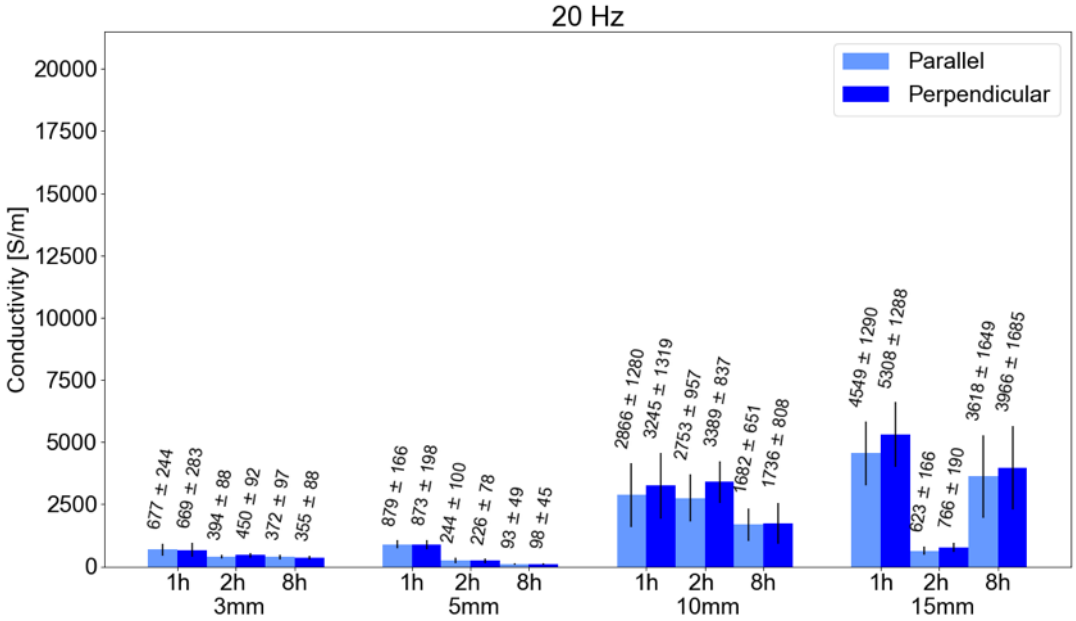

Figure 3.12: Average conductivity measurements for ball milling at 20 Hz. Error bars represent standard deviation for each batch of samples.

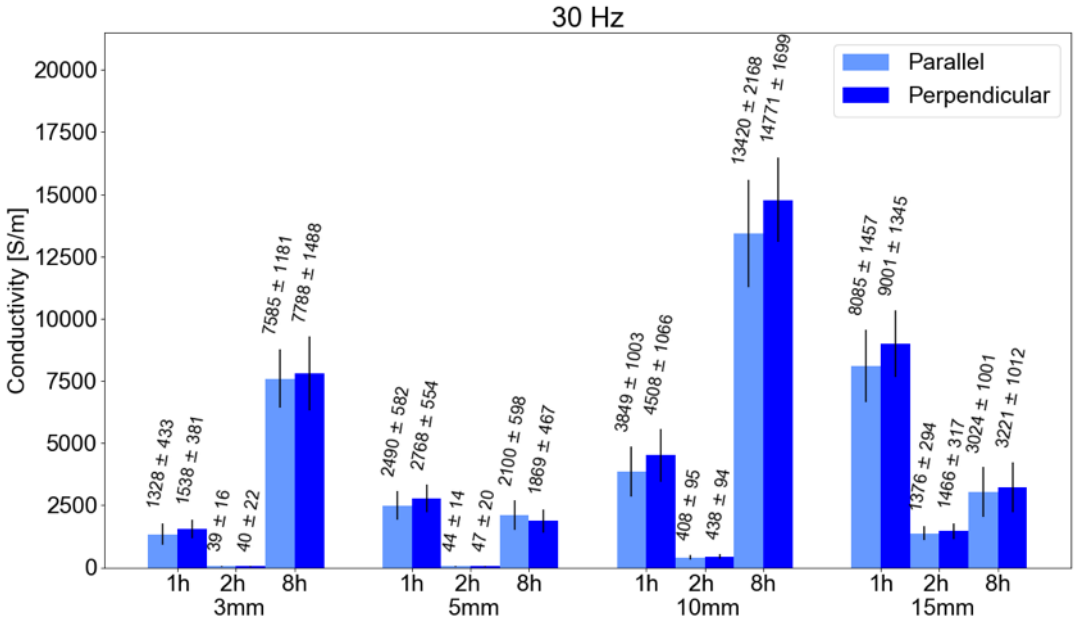

Figure 3.13: Average conductivity measurements for ball milling at 30 Hz. Error bars represent standard deviation for each batch of samples.

For almost all combinations of parameters, the resulting current collector inks exhibited significantly lower conductivity than the unmilled ink (Figure 3.7). Particularly for the 3mm and 5mm balls at 15Hz and 20Hz, the measured conductivity was up to three orders of magnitude lower than the unmilled ink. Examination of the SEM images reveals an inverse correlation between the conductivity and the formation of pebbles whose diameters are roughly equal to that of the unmilled powder. This drop in conductivity may be attributable to a decrease in packing factor. Given that the packing density of random close-packed uniform spheres is roughly 64% [83], it can be posited that the packing density of the pebbles is less than that, resulting in fewer parallel conductive pathways. Furthermore, in the case of edge to plane contact between two pebbles, both the diameter and area of the contact spot would be lower than the contact spot between two spheres, increasing both terms of the contact resistance. It is also possible that the increased surface area of each particle results in a significantly higher tunneling resistance contribution to the contact resistance as the thickness of the insulating polymer layer on the flat side of each pebble might be increased.

For the combinations of parameters that yielded higher conductivity values, the resulting particle morphology tended more towards larger flakes that were formed from agglomerating multiple particles. The set of parameters that yielded the highest conductivity (30Hz, 10mm, 8 hours) resulted in flakes of various sizes ranging from 5-20ÂţmÂţm in diameter with some powder being unmilled and or milled into pebbles, though the flakes did begin to take on a slightly shredded texture as well. In the more extreme case of flake formation (30Hz, 5mm, 8 hours), all particles were deformed into flakes, but the resulting conductivity was an order of magnitude lower than the best case, possibly for similar reasons as with the case of forming entirely pebbles. In the most extreme case of flake formation (30Hz, 15mm, 8 hours), the flakes were almost entirely shredded which resulted in a lower conductivity compared to the unmilled powder. However, in the case where only a small fraction of flakes were formed without the formation of any pebbles at all (30Hz, 15mm, 1 hour), the conductivity was increased beyond that of the unmilled powder. Similar behavior can be observed for 15Hz, 10mm/15mm, 1 hour, though the effect is more subtle.

Comparing conductivity values across all combinations of parameters while considering approximately how much energy each combination imparts, a trend emerges where a threshold level of energy is required in order to obtain a favorable particle morphology. This is most apparent with respect to time at 30Hz, 10mm. At 1 hour, some large flakes are noticeable, but much of the powder remains in its spherical, unmilled shape, resulting in a conductivity about half that of the unmilled powder. At 2 hours, flake formation is very apparent, but there exists a wide range of particle morphologies from spherical to pebbles to flakes, corresponding to an order of magnitude drop in conductivity. At 8 hours, the proportion of flakes increases with most particles being deformed to large flakes with some smaller pieces present, resulting in an increase in conductivity almost three times that of the original powder.

Considering the optimal case of 30Hz, 10mm, 8 hours, it can be seen that enough energy to induce wide-scale flake formation simultaneously with a varied particle size and morphology distribution provides the best conductivity. In the case of 30Hz, 15mm, 8 hours, the average

flake size is larger than at 30Hz, 10mm, 8 hours, suggesting that there is an upper limit to the particle size before the packing factor again becomes an issue.

Finally, for almost all combinations of parameters, the perpendicular measurement yielded higher values of conductivity by about 5-15% than the parallel measurement. This indicates that the stencil casting process aligned the particles to some degree. The absolute difference between the parallel and perpendicular measurements is larger for parameter combinations that caused more particle deformation, which is consistent with the intuitive assumption that uniform spheres would behave more isotropically.

3.5 Conclusions

This chapter investigated the effect of ball milling nickel powder on the resulting conductivity of a printed current collector with the intent of translating these results to optimization of the cathode. Nickel powder was ball milled in a planetary ball mill with varying milling speed, milling time, and ball size, and the resulting powder was examined with scanning electron microscopy. Inks were made with the powder and printed by hand via stencil casting, and the conductivity of each ink was determined via sheet resistance measurements of the printed ink using a four point probe and thickness measurements. The variation in particle size and morphology as a result of different ball-milling parameters was correlated with the conductivity of each powder in the printed ink.

In general, the new behavior of each powder depends significantly on the morphology produced by ball milling. The packing factor of the particles is very sensitive even at low amounts of deformation, and the morphology of the deformed particles impacts whether the results of deformation are favorable or not, with larger flakes being preferred to smaller pebbles. Considering each combination of ball-milling parameters as imparting a set amount of energy to the powder, there is an optimal amount of energy that results in the optimal morphology for the best conductivity.

The resulting morphology itself depends on the size of the milling balls used, with larger diameter balls being more conducive to forming large flakes. However, the number of factors affecting the ball milling process are myriad and interconnected, with the ball size also affecting the impact velocity of each ball as well as the number of collisions per second each ball is capable of due to both the volume and mass of each ball increasing with ball diameter.

The combination of parameters that yielded the highest conductivity was 30Hz, 10mm, 8 hours. Visually, the most dramatic amounts of deformation occurred for all ball sizes at 30Hz, 8 hours, which corresponds to the highest milling frequency tested for the longest amount of time. It is this subset of parameters that will be used for further cathode optimization.

Other factors that affect particle morphology that were not varied in this work were the jar geometry, the mass ratio of balls to powder, the grinding environment and atmosphere, the composition of the grinding balls, and the amount that each jar was filled with powder and jars. An in-depth study of all factors would be very laborious and time-consuming, so future work may consider simulation or modeling of the system in order to predict how much energy each set of parameters would impart as well as the resulting particle morphology.

Chapter 4

Optimization of Electrode Composition

This chapter discusses the work done in optimizing the cathode and anode slurries for printing and cell performance as characterized by slurry rheology, printed film conductivity, profilometry. The goals of this optimization are

1. to produce a slurry that can be easily and uniformly printed,
2. to maximize the amount of active material in the printed film while maintaining a threshold level of conductivity needed to keep ohmic losses reasonable, and
3. to produce a printed film with a uniformly smooth surface profile to minimize the thickness of gel polymer electrolyte needed to prevent shorts in the full cell.

The fractions of active material, conductive additive, polymer binder, and solvent and the particle morphology of the active material (in the case of the cathode) were adjusted in order to improve performance of these three properties with the intention of improving performance in the full cell. Characterization was peformed on the ink (rheology) and printed film (conductivity, profilometry) as appropriate. This process is summarized in Figure 4.1.

Section 4.1 overviews the motivation behind electrode ink optimization and the contributions of the overall cell performance. Section 4.2 discusses the role of each component in the electrode composition as well as electrode ink and printed electrode characterization methods. Section 4.3 discusses the experimental methods used to develop and characterize the electrode inks. Section 4.4 presents results obtained to develop and improve the conductivity, profilometry, and rheology of the electrode inks. Finally, Section 4.5 summarizes conclusions and discusses future improvements to be made.

4.1 Motivation

The goal of this work is to improve the electrode inks with respect to printed surface profile without sacrificing active material loading or conductivity. The quality of the surface profile

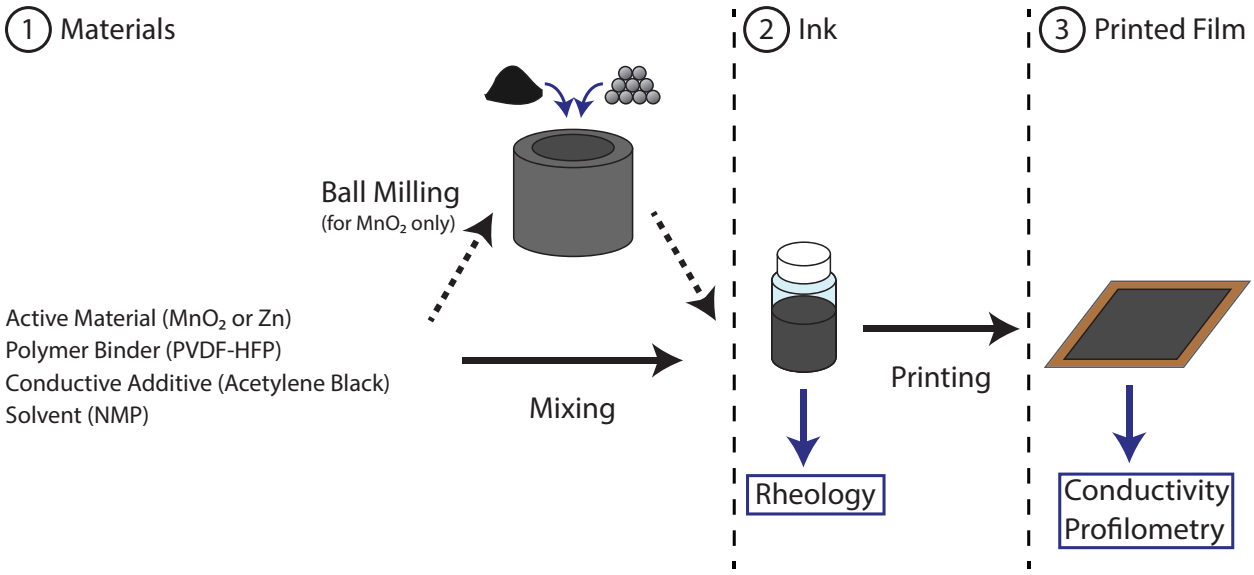

Figure 4.1: Electrode development diagram

is prioritized in order to enable a thinner gel polymer electrolyte layer with the intent of decreasing the diffusion distance between the cathode and anode in order to improve rate capabilities while also reducing the amount of material needed to be used.

In order to adjust the surface profile, the particle size of the active material is targeted as a parameter to be adjusted via ball milling. However, changing the particle size also affects the ink's conductivity and rheology, so other factors in the ink composition must be adjusted accordingly in order to ensure good overall performance.

4.2 Background

This section overviews the composition and development of the cathode and anode. The materials used in both electrodes as well as development and characterization methods of the slurry and printed films are discussed, with the goal of producing a uniform electrode layer that optimizes film printability and electrical conductivity while maximizing active material fraction.

4.2.1 Electrode Composition and Conductivity

The primary functions of the cathode and anode in the cell are to provide active material that can participate in charge transfer reactions and to provide electrically conductive pathways for current to be carried from the reaction interfaces to the external load. In a theoretically ideal case, both electrodes would be composed entirely of active material that would all participate in electrochemical reactions. However, the practical needs of electrical

conductivity and manufacturability require other components be present in the slurry and printed film.

The cathode and anode are formed by printing slurries composed of active material, polymer binder, conductive additive, and solvent. The role of the solvent is to dissolve the polymer binder. The mechanical, electrical, and electrochemical properties of each slurry and printed layer are determined by the ratio of each of these four components, and adjusting the amount of any one component with the intention to improve one property can inadvertently affect other properties.

The particle size of the active material, particularly for the cathode, has a significant affect on the electromechanical properties of the slurry, the printed film, and the overall cell performance. For the slurry, the particle size affects the slurry rheology as smaller particle size increases particle surface area, increasing interaction with the solvent for the same mass of powder, thus increasing the viscosity. For the printed film, the smaller particle size will result in a smaller average feature size, which will improve surface profiles, as well as affect electrical conductivity of the bulk electrode due, again due to the increased volume fraction. Finally, within the overall cell, smaller particle sizes should help improve intercalation of Zn^{2+} ions into the MnO_2 crystal structure and allow for higher utilization of MnO_2 due to the increased surface area to volume ratio.

Work done by Liu, *et. al.* [57, 56] investigated the effect of varying ratios between of AB:PVDF-HFP and AB/PVDF-HFP:active material loadings on long-range electrode conductivity. With regards to the ratio of AB:PVDF-HFP, it was found that there exists an optimum ratio between conductive additive and polymer binder that ensures longevity of long-range conductive pathways even under repeated cycling. If the loading of conductive additive is too high, the overall electrode conductivity will unintuitively decrease after cycling due to breakage of the AB linkages as the active material swells and contracts. However, at the right ratio of AB to PVDF-HFP, the polymer is able to accomodate the mechanical strain instead of the AB, and the linkages remain intact after numerous cycles. Though their work investigated this phenomenon for lithium-ion intercalation cathodes, a similar effect can be seen in the materials used in this work from the thermal expansion and contraction from the printing process.

4.2.2 Rheology and Printing Methods

In recent years, printing has emerged as an attractive option for printed electronics and energy storage devices. Different printing methods require the printing medium to fall within a specific viscosity window due to differing mechanisms of ink application and have their own benefits and drawbacks. Table 4.1 summarizes ink viscosity ranges for six common printing methods.

Table 4.1: Printing thicknesses and viscosities of various printing methods [46]

Printing Method	**Print Thickness [μm]**	**Viscosity Range [cP]**
Gravure	0.02-12	10-1100
Offset	0.6-2	2000-5000
Flexographic	0.17-8	10-500
Slotdie	0.15-60	2-5000
Screen	3-30	500-5000
Inkjet	0.01-0.5	1-1000

Rheology is the study of the viscoelastic and flow properties of fluids and is an important characteristic in working with printed slurries. Rheological factors that dictate ink printing compatibility include the ink's dynamic viscosity, shear response, and yield stress.

Typical fluids (*e.g.* water) are classified as Newtonian fluids, in which the fluid begins to flow immediately when a stress is applied and dynamic viscosity remains constant with changing stress. Therefore, for Newtonian fluids, the shear stress changes linearly when the applied shear rate is changed as well. This relationship is given by Newton's law of viscosity (Eq. 4.1) , in which the viscosity, μ, is a constant of proportionality between the shear stress, τ, and the shear rate, $\dot{\gamma}$.

$$\tau = \mu\dot{\gamma} \tag{4.1}$$

In contrast, many particle-laden fluids, such as inks used in this work, do not follow Newton's law of viscosity and are thus labeled non-Newtonian fluids. Specifically, these are characterized by viscosity that can either increase or decrease when a stress is applied, called shear thickening and shear thinning fluids respectively. In addition, some non-Newtonian fluids require a threshold level of applied stress before they will begin to flow, called the yield stress, and are called Bingham plastics. The difference between all of these fluids is visualized on a plot of shear stress vs. shear rate in Figure 4.2.

For printing and other applications where fluid deposition is the desired outcome, the yield stress and viscosity play significant roles in determining the viability of a fluid. For printing specifically, the desired outcome is for the ink to flow during printing but not to flow afterward in order to retain ink in the exact quantity and shape as was dictated by the printing process. This calls for a shear-thinning ink with some requisite value of yield stress

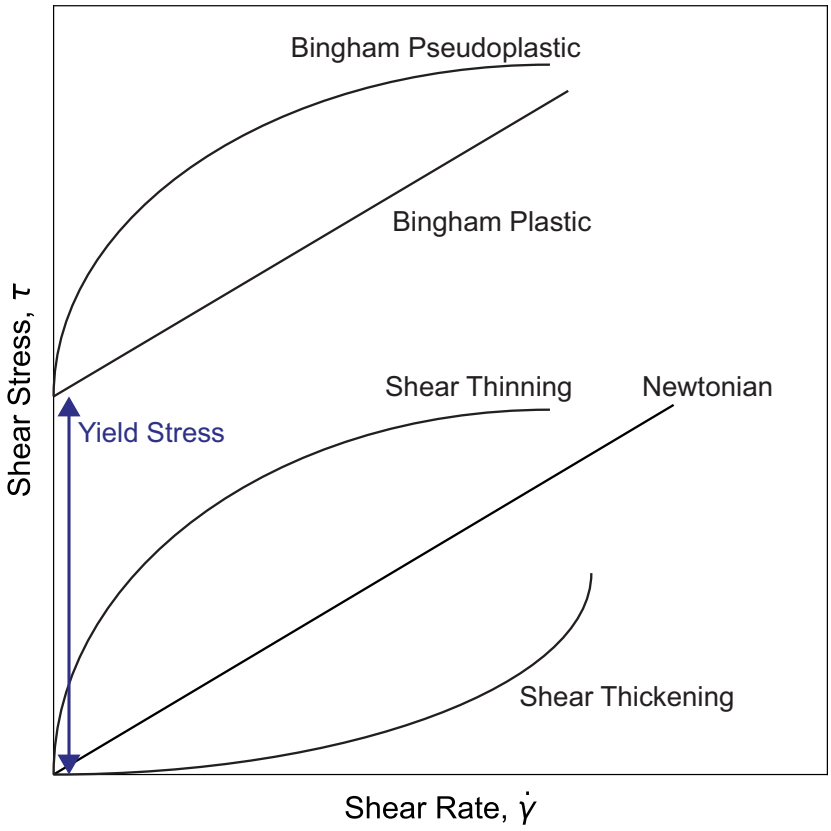

Figure 4.2: Shear stress responses of Newtonian and non-Newtonian fluids

to act as a threshold before flow occurs. The exact values for the viscosity during printing and the yield stress vary depending on the printing method.

For particle-laden inks such as the ones developed for this work, compositional factors that affect the rheology are the volume fraction of solvent relative to solid particles (active material and conductive additive) and the effective viscosity of the polymer binder and solvent mixture. Thus, the amount of solvent present effectively decides the rheology of the final ink. Conveniently, the solvent is driven off during the electrode drying process, so this provides a method to independently tune the ink viscosity for printing without significantly affecting the bulk electrode properties after drying.

For stencil printing with a doctor blade as done in this work, te printing process can be modeled as Couette flow in which a viscous fluid flows between two parallel plates, one moving (the doctor blade) and one stationary (the stencil). Couette flow can be described

by Equation 4.2, where $\dot{\gamma}$ is the shear rate, v is the velocity of the moving plate, and h is the separation distance between the two plates.

$$\dot{\gamma} = \frac{v}{h} \tag{4.2}$$

The effective shear rate applied to the ink can therefore be determined with knowledge of the doctor blade spacing and velocity. In conjunction with empirical rheological characterization, the shear stress applied to the ink during printing can then be determined for any printing speed and doctor blade spacing for all effective shear rates within testing limits. This relationship between shear rate and velocity for various doctor blade spacings is presented in Figure 4.3.

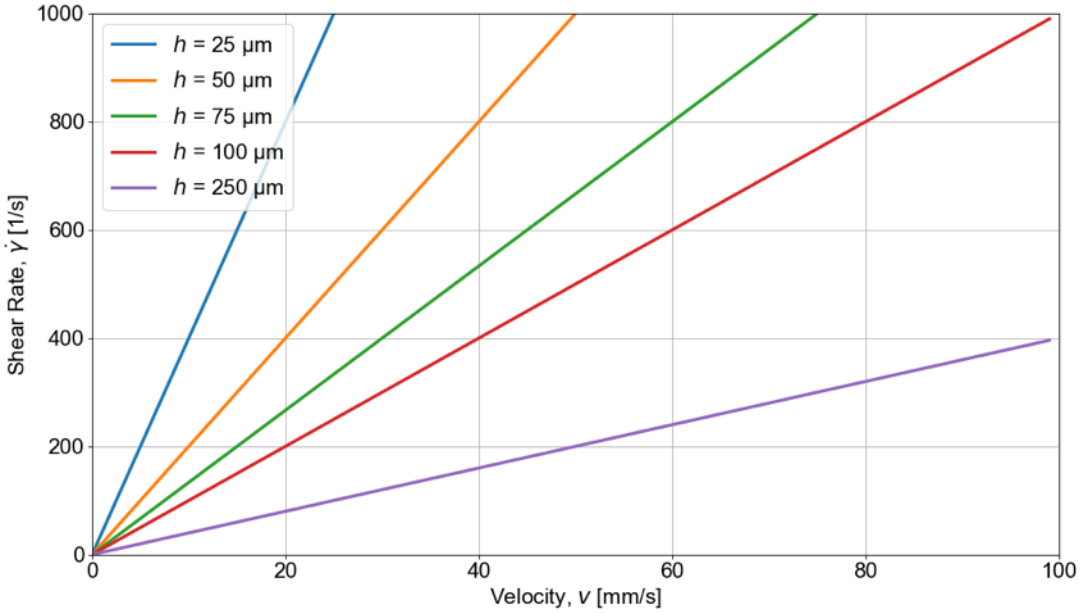

Figure 4.3: Effective shear rates for blade coater and doctor blade.

4.2.3 Profilometry

The morphology of the electrode at the electrode-electrolyte interface affects the minimum thickness of the gel polymer electrolyte that must be printed. Because there is a range of particle sizes present in the electrode slurries, the resulting surface morphology is uneven and made up of peaks and valleys. This uneven surface dictates the minimum thickness of gel polymer electrolyte that must be printed in order to provide sufficient insulation against electronic conduction between the cathode and anode based on the relative heights

and depths of the peaks and valleys respectively. Since a thicker separator layer increases diffusion distances as well as ohmic losses (as well as requires the use of more ionic liquid), it is preferred to minimize the amount of gel polymer electrolyte needed, which means a smoother surface morphology is desired.

Traditional roll-to-roll battery manufacturing processes introduce a calendaring step after slurry deposition, the goal of which is to decrease electrode porosity and flatten the surface to enable thinner overall layers prior to winding. For printed and flexible electronics applications, this may not be possible, particularly for cells that must be printed directly on substrates where other components are already present. Therefore, alternate methods for obtaining uniformly smooth electrode surfaces are desireable.

The approach taken in this work is to control the particle sizes and distributions of the solid particles in the electrode slurries themselves in order to minimize the variation in surface morphology. A Fourier transform was used to decompose a one-dimensional profile scan of the electrode surface into roughness and waviness values in order to quantify the morphology of each slurry composition.

4.2.4 Fourier Transforms

The Fourier transform is a method that decomposes a signal in the time or spatial domain to its constituent sinusoids and respective amplitudes in the frequency domain. No information about the original signal is lost in this transformation, and the new representation of the function or signal allows for analysis of waveforms in the transfer domain. Figure 4.4 shows this decomposition of a sinusoidal signal into its constituent parts and their respective frequencies and amplitudes in the frequency domain.

The time (or spatial) domain is transformed into the frequency domain by the Fourier integral (Eq 4.3), where $h(t)$ is the function in the time domain, $H(f)$ is the resulting frequency domain function, f is the frequency, t is time, and $j = \sqrt{-1}$ [11].

$$H(f) = \int_{-\infty}^{\infty} h(t) e^{-j2\pi ft} dt \tag{4.3}$$

The function can then be transformed from the frequency domain back to the time domain by the inverse Fourier transform (Eq 4.4). The functions $h(t)$ and $H(f)$ are defined as a Fourier pair and can be used to transform a function back and forth between the two domains.

$$h(t) = \int_{-\infty}^{\infty} H(f) e^{j2\pi ft} df \tag{4.4}$$

Both Equations 4.3 and 4.4 deal with infinite continuous signals. However, in order to apply Fourier transforms for numerical integration with real data, an appropriate modification must be made for use with sampled and non-continuous signals. This modification yields the

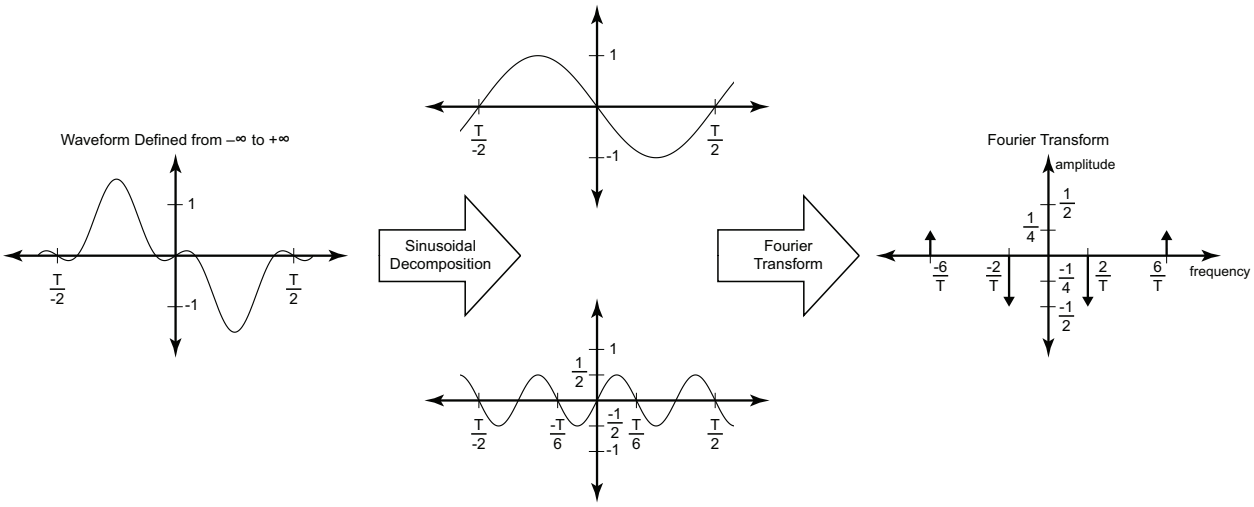

Figure 4.4: Graphical example of Fourier transform. The original signal is decomposed into the sum of its two constituent sinusoids, and their respective frequency and amplitude contributions are plotted.

discrete Fourier transform, or DFT, (Equation 4.5) and is the result of time-domain sampling, truncation, and frequency-domain sampling of the initial continuous Fourier transform pair [11].

$$G\left(\frac{n}{NT}\right) = \sum_{k=0}^{N-1} g(kT)e^{-j2\pi nk/N} \qquad n = 0, 1, ..., N-1 \tag{4.5}$$

The complementary inverse discrete Fourier transform is given by Equation 4.6.

$$g(kT) = \frac{1}{N}\sum_{n=0}^{N-1} G\left(\frac{n}{NT}\right) e^{j2\pi nk/N} \qquad k = 0, 1, ..., N-1 \tag{4.6}$$

Examination of Equations 4.5 and 4.6 show that for a signal of N samples, N^2 computations will be necessary. For practical amounts of data, direct application of the DFT will result in untenable computation times. Therefore, an algorithm to reduce the number of calcuations required is needed.

The fast Fourier Transform (FFT) offers a significant reduction in the number of calculations needed and therefore the total computation time by factorizing the DFT matrix and introducing zeros into the factored matrix. This process is paramount to enabling widespread adoption of the Fourier transform for myriad applications as it reduces an otherwise bulky and computationally expensive process to one that is much more easily adopted. The FFT

algorithm itself is omitted but can be found in [11]. Application of the FFT reduces the number of computations required from $O(N^2)$ to $O(NlogN)$. This comparison is visualized in Figure 4.5.

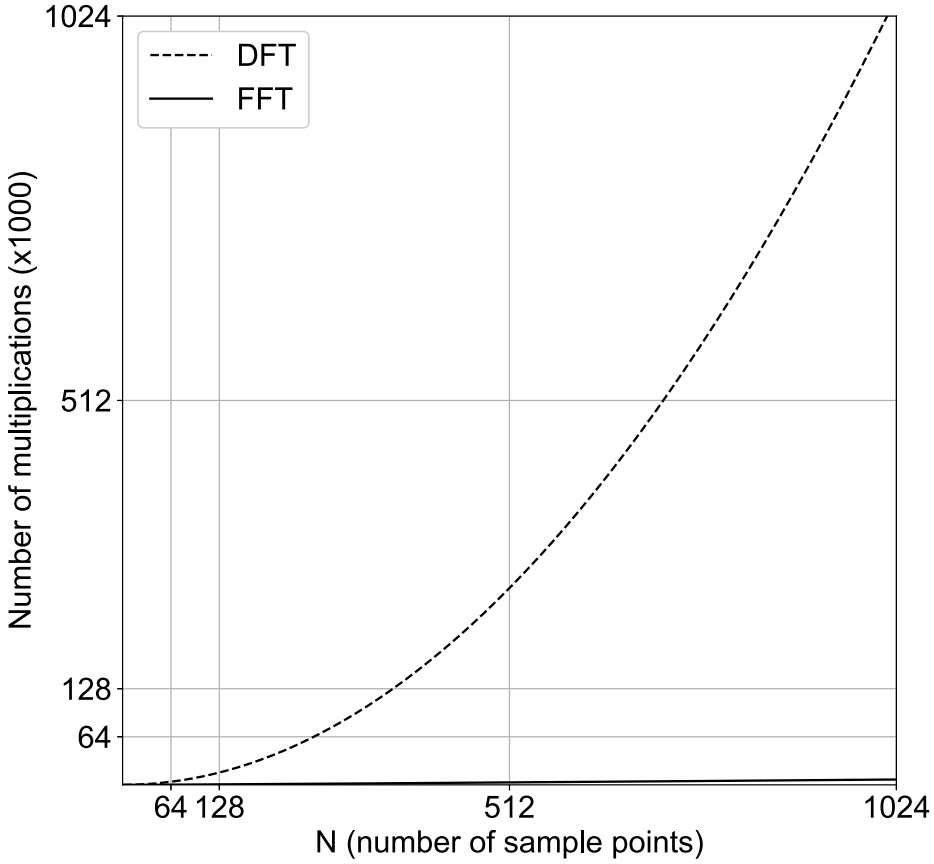

Figure 4.5: Comparison of number of computations between DFT and FFT

4.3 Experimental Methods

This section discusses the experimental methods and procedures used to print and characterize the electrode slurry and printed film performance, including modification of the particle size via ball milling and sieving and characterization by line profilometry, viscosity characterization, and four point probe conductivity measurements.

4.3.1 Electrode Ink Production

The active material in the cathode is MnO_2 (Sigma-Aldrich). The active material in the anode is Zn (Alfa Aesar). For both electrodes, the conductive additive is acetylene black (AB) (Alfa Aesar), the polymer binder is polyvinyldifluoride-hexafluoropropylene (PVDF-HFP) (Kynar Flex 2801), and the solvent is n-methyl-pyrrolidone (NMP) (Sigma-Aldrich). This general composition is summarized in Table 4.2. The solvent is driven off after printing, so the final dried electrodes are composed only of active material, conductive additive, and polymer binder, but the amount of solvent present in the slurry affects the rheology and profilometry of the printed film.

Table 4.2: Electrode Material Components

Material	**Cathode**	**Anode**
Active Material	MnO_2	Zn
Conductive Additive	AB	AB
Polymer Binder	PVDF-HFP	PVDF-HFP
Solvent	NMP	NMP

Both the cathode and anode inks made for this work followed the same mixing procedure. First, PVDF-HFP was dissolved in NMP in a 20mL glass vial to form a gel. The NMP was added to the PVDF-HFP in order to more quickly dissolve the polyer. The vial was slowly mixed on a vortex mixer (Fisher Scientific), starting from 1000 RPM up to 3000 RPM, while taking care not to spray the powder onto the sides of the vial. Once all of the polymer was wetted by solvent, the vial was heated on a hot plate at 50°C until the gel was completely transparent.

The gel was allowed to cool, and the active material (MnO_2 for the cathode, Zn for the anode) and acetylene black were added to the vial. The powders were added such that they did not stick to the sides of the vial to ensure the actual compositions of each ink were as accurate as possible. Additional NMP was added to the vial and in such a way to wash off any powder stuck to the sides of the vial into the bulk of the material. The slurry was again mixed on the vortex mixer, incrementally increasing the speed such that none of the powders sprayed onto the sides of the vial. Once the ink was fully incorporated and all powder was wetted, the vial was placed in a planetary ball mill for mixing (Across International, PQ-N04).

In a planetary ball mill, the rotation of the planet gears is driven by a larger sun gear. The planet gears are positioned along the outer circumference of the sun gear, and the gear ratio between the two enables faster rotation of the planets than is directly provided by the motor to the sun. The ball mill is used primarily for grinding material to adjust particle size, but the centrifugal forces imparted onto vials of ink are also effective at particle dispersion and mixing. Because the vials are rotated at high speeds (but not fast enough to separate particles from suspension), the radial shear forces imparted onto the ink are able to break up

agglomerates of powder and can effectively homogenize the ink mixture. For ink mixing, the ball mill was run at 45Hz for 2 hours, reversing the direction of rotation every 15 minutes to ensure good mixing.

After mixing on the ball mill, the inks were removed and set aside until ready for use. Immediately prior to use, the inks were sonicated for 10 minutes and mixed at high speed on the vortex mixer (3000 RPM) for 2 minutes.

4.3.2 Ball Milling and Sieving

For some cathode ink compositions, the MnO_2 in the cathode was ball milled in order to reduce the particle size prior to mixing into an ink. The zinc powder used in the anode inks was not ball milled because the powder's high malleability resulted in mechanical alloying of the powder to both the stainless steel milling balls as well as to the sides of the milling jars. Furthermore, a significant portion of the milled powder was deformed into flakes whose diameters were too large to make homogenous inks.

The same ball milling jars, lids and grinding balls as described in Chapter 3 were used. The same cleaning and preparation steps were followed.

The MnO_2 powder and grinding balls were added to the jar in a mass ratio of 1:10 of powder to balls. Approximately 8g of powder was milled per jar per run. The powder was first added to the jars, and the balls were then carefully added on top, making sure not to cause the underlying powder to spill out. Isopropyl alcohol was then added to cover the powder and partially cover the balls in order to form a wet grinding environment inside the jars. The jars were then sealed and tightened with machine screws to form a closed environment.

The sealed jars were placed in a planetary ball mill (Across International, PQ-N04). The ball mill was run at 30Hz for 8 hours or 24 hours, with the direction of rotation reversing every 15 minutes to ensure even milling of all the material inside. Grinding ball sizes of 3, 5, 10, and 15mm were used.

Table 4.3 summarizes all of the ball milling parameters that were tested. These parameters were chosen based on the SEM micrographs presented in Chapter 3 in order to maximize MnO_2 deformation and most dramatically alter the particle size.

Table 4.3: Ball milling parameters tested

	Milling Frequency	30Hz	
	Milling Time	8h	24h
Ball Size	3mm	○	×
	5mm	○	○
	10mm	○	×
	15mm	○	○

Once ball milling was complete, the jars were removed from the ball mill and the lids removed. With the balls still inside the jars, both the jars and lids were placed inside an oven at 50°C until all of the isopropyl alchol was driven off. The powder and balls were then poured into a mesh sieve (Number 30 mesh, or 0.5mm opening) in order to separate the balls from the powder. The powder was then poured into a vial to be used to make inks or for further processing.

In the case of further processing, the powder was then manually sieved through a series of three fine stainless steel mesh sieves (Endecotts USA) of opening size 250, 150, and 45μm (Number 60, 100, and 325 mesh sizes respectively). In the case of the finer mesh sieves, the powder was first sent through the larger sizes prior to finer sieving (*e.g.* the powder was sieved through the 250μm sieve, then the 150μm sieve, then the 45μm sieve). Disposable plastic spatulas were used to help push the powder through, particularly for the 45μm mesh.

4.3.3 Doctor Blade and Stencil Printing

The electrodes were created via stencil casting with a doctor blade. This method was chosen for its efficient use of ink, high tolerance window for ink rheology, and ability to quickly deposit thick layers of ink. Initial work was done with the same method as described in Chapter 3. All other printing was performed as described below.

The stencils were produced by a laser cutter (Universal Laser Systems) out of 75μm polyimide (Kapton) film (American Durafilm) to cut an array of 1cm^2 squares. The squares were spaced in a 4×2 array (4 rows, 2 columns) with 7mm between rows and 5mm between the columns to ensure good separation between the electrodes to prevent capillary forces from the solvent from bridging beneath the stencil while also ensuring they were close enough to reduce the amount of gel polymer electrolyte needed. The printing substrate used was either 25μm aluminum foil or 75μm polyimide. Aluminum foil was used for profilometry measurements, and polyimide was used for sheet resistance measurements where a non-conductive substrate was required.

An automatic film applicator (Zehntner PVA 2000) with a separate doctor blade (Zehntner) was used for the printing process. The automatic film applicator allowed for controllable and consistent drawing speeds from 1mm/s to 99mm/s in increments of 1mm/s and also featured a vacuum hold down plate for consistent and repeatable substrate positioning. The separation distance between the leading edge of the doctor blade and the substrate was controlled by two dial micrometers on either side of the doctor blade. The pressure applied by the doctor blade to the ink was simply controlled by the weight of the doctor blade itself. Previous work required both the sample positioning as well as printing to be done manually, which exposed the process to a large amount of variability between batches. In this new setup, the flatness of the substrate, the speed at which the doctor blade was moved, and the downward pressure applied by the doctor blade onto the ink were all able to be controlled and repeated from test to test.

Two printing parameters were varied via profilometry to determine the optimal parameters for printing, tested via profilometry. The printing speed was set from 10, 20, and

50 mm/s. The effective printing height was set from $25\mu m$ and $75\mu m$. Accounting for the thickness of the substrate, this meant that the actual micrometer markings on the dial equaled the sum of the desired spacing and the thickness of the substrate (*e.g.* for the $25\mu m$ thick aluminum foil, a desired printing height of $25\mu m$ would require a micrometer setting of $50\mu m$). These parameters are summarized in Table 4.4.

Table 4.4: Printing speeds and doctor blade heights for stencil casting with automatic film applicator.

		Printing Speeds [mm/s]		
		10	20	50
Doctor Blade Height [μm]	50	○	○	○
	100	○	○	○

To set up the film applicator for printing, the substrate was first cut out to roughly a 7cm × 12cm rectangle. This was centered roughly in the bottom half of the vacuum hold down plate. The stencil was cut out of a large sheet of polyimide whose width was wide enough to cover the width of the vacuum plate. Both the substrate and the stencil were wiped down with acetone and a Texwipe to remove any dust or debris before being placed on the vacuum plate. A spare sheet of polyimide was used to cover the vacuum holes in the upper half of the plate that were not being used to ensure pressures were low enough in the working area to hold down the substrate. The front and end stops of the film applicator dictating the range of motion of the doctor blade were set, and the printing bar was reset at the front stop. The position of the front stop was set such that the doctor blade would have ample distance to be pushed parallel to the print bar before reaching the holes in the stencil. The vacuum was applied, and the stencil and subtrate were wiped down once more to remove dust and debris. A wooden applicator stick (Puritan) was used to apply roughly 0.2ml of ink ahead of each square in the stencil. The doctor blade was placed at the front stop, and the film applicator was turned on.

After the run was completed, the doctor blade was removed from the printing surface and the print bar reset. With the vacuum still on, the stencil was peeled back in one motion to avoid disturbing the samples on the substrate, and the substrate was moved to a drying oven or hot plate at 80°C to dry. The stencil and doctor blade were then thoroughly cleaned with acetone.

4.3.4 Rheology

A Brookfield DV3T-HB rheometer was used for all rheology measurements. A small sample adapter with either a size CP-52 or CP-40 cone spindle was used in order to minimize the amount of ink needed per test. The CP-52 spindle was used for most tests due to its tolerance for higher shear stresses, but the CP-40 was used in cases where a more sensitive

measurement was needed for low viscosity inks. The rheometer was capable of applying a maximum rotational speed of 250 RPM, which translates to a maximum shear rate of 500 1/s for the CP-52 spindle and 1750 1/s for the CP-40 spindle. The sample cup was maintained at 25°C for all tests via hoses attached to a Brookfield TC-550 water bath.

Prior to each sample run, the cone and sample cup were thoroughly cleaned with acetone and dried with a texwipe to remove any trace contaminants or debris. Before adding any ink, the distance between the cone and sample cup was calibrated according to the manufacturing instructions. Approximately 0.5ml of ink was deposited in the center of the sample cup using a wooden applicator or a plastic spatula. The amount of ink deposited was enough to completely fill the gap between the cone and the sample cup with some excess. Before initiating the test, the sample cup with ink was allowed to rest for 5 minutes to ensure the ink was at a temperature of 25°C.

At the beginning of the test, the ink was first subjected to a spindle rotation speed of 100 RPM (200 1/s) for 2 minutes to ensure full dispersion of the ink and wetting of the cone and sample cup. The speed was then dropped to 12.5 RPM and increased every minute in increments of 12.5 RPM until a maximum of 250 RPM was reached. The measured torque of the final 10 seconds of each 1 minute interval was averaged, and the single averaged point was recorded as the torque value for each applied speed. The corresponding values of viscosity and shear stress were automatically converted by the rheometer based on the spindle geometry. The testing steps are summarized in Table 4.5.

Table 4.5: Brookfield DV3T-HB Viscosity Test Method

Step Number	**Speed [RPM]**	**Time [m:ss]**	**Data Collected**
1	100	2:00	No
2-21	12.5, 25, 37.5, 50 62.5, 75, 87.5, 100, 112.5, 125, 137.5, 150, 162.5, 175, 187.5, 200, 212.5, 225, 237.5, 250	1:00	Yes

For initial work, the maximum tested shear rate was 120 1/s, approached in 10 steps of 12 1/s each. The inks were also subjected to an initial shear rate of 60 1/s, again in order to ensure full ink dispersion and wetting of the cone and sample cup.

4.3.5 Profilometry

A Dektak profilometer was used for all surface profile scans. Electrodes were printed on $25\mu m$ aluminum foil. Excess foil was trimmed, and each batch of electrodes was mounted onto a prepared glass slide with a gel pack layer to adhere the electrodes to a flat, rigid

surface. To ensure even contact and remove air bubbles that may disrupt measurement, the electrodes were covered with a Texwipe and gently rolled over with a foam roller to press out any air bubbles from between the foil and gel pack. Care was taken not to press down too hard to avoid damaging any of the surface structures.

Each electrode was scanned twice, once parallel and once perpendicular to the direction of casting. Each scan length was set to a total distance of 15mm with 45000 total points taken (resolution of $0.33\mu m$) and a scan speed of 6mm/minute. A scan distance of 15mm was chosen to ensure full capture of the entire sample (10mm on a side) with enough overlap of the bare substrate on either side for robust data analysis. The stylus tip used had a radius of $12.5\mu m$ and applied a force equivalent to 3mg of mass on the sample surface.

After the raw scan was collected, an onboard leveling function was used to remove any bias from possible unevenness of the sample stage. This leveling function required manual inpute of a start and endpoint within the raw sample data and set those points as zero, adjusting all other points to those points. Typically, a known flat region of the sample was selected (*e.g.* part of the substrate that was clean and without any sample printed on it) and the collected data adjusted to that. The data was then exported to a comma separated value (CSV) file for analysis.

A custom library was written in Python to first isolate the region of interest of each scanned profile via a series of linear fits and intersections and then to analyze and quantify the performance of each profile via an FFT.

Each profile can be separated into a higher central plateau with a rough and uneven surface (corresponding to the printed sample) and two lower and smoother ends (corresponding to the overhanging substrate). To identify the index points of this central plateau, first the beginning and ending 30% of the scan were isolated. A moving window algorithm with varying window size was developed and used to find the steepest slopes of each end of the scan (positive slope for the beginning of the sample, negative slope for the end of the sample) as well as the flattest regions (slope closest to zero).

In this algorithm, a series of m windows with sizes smaller than the working region are moved across the region in n positions. For each combination of window and position, a linear fit is taken of the points in that combination, and the line with the best fit of all $m \times n$ combinations (as determined by lowest residual score) is saved.

Once the steepest and flattest slopes of each end were identified, the intersection of these points was taken in order to roughly identify the endpoints of the central plateau, including the edges from the bare substrate. The central 80% of this region was then taken and a rough linear fit applied. Finally, the intersection points of this central linear fit and the best linear fits of both steepest slopes of the front and back of the scan were identified. These endpoints are then finalized as the index points of the central plateau, upon which analysis was performed. This central region prior was called the primary profile. Figure 4.6 visualizes this region-isolating algorithm.

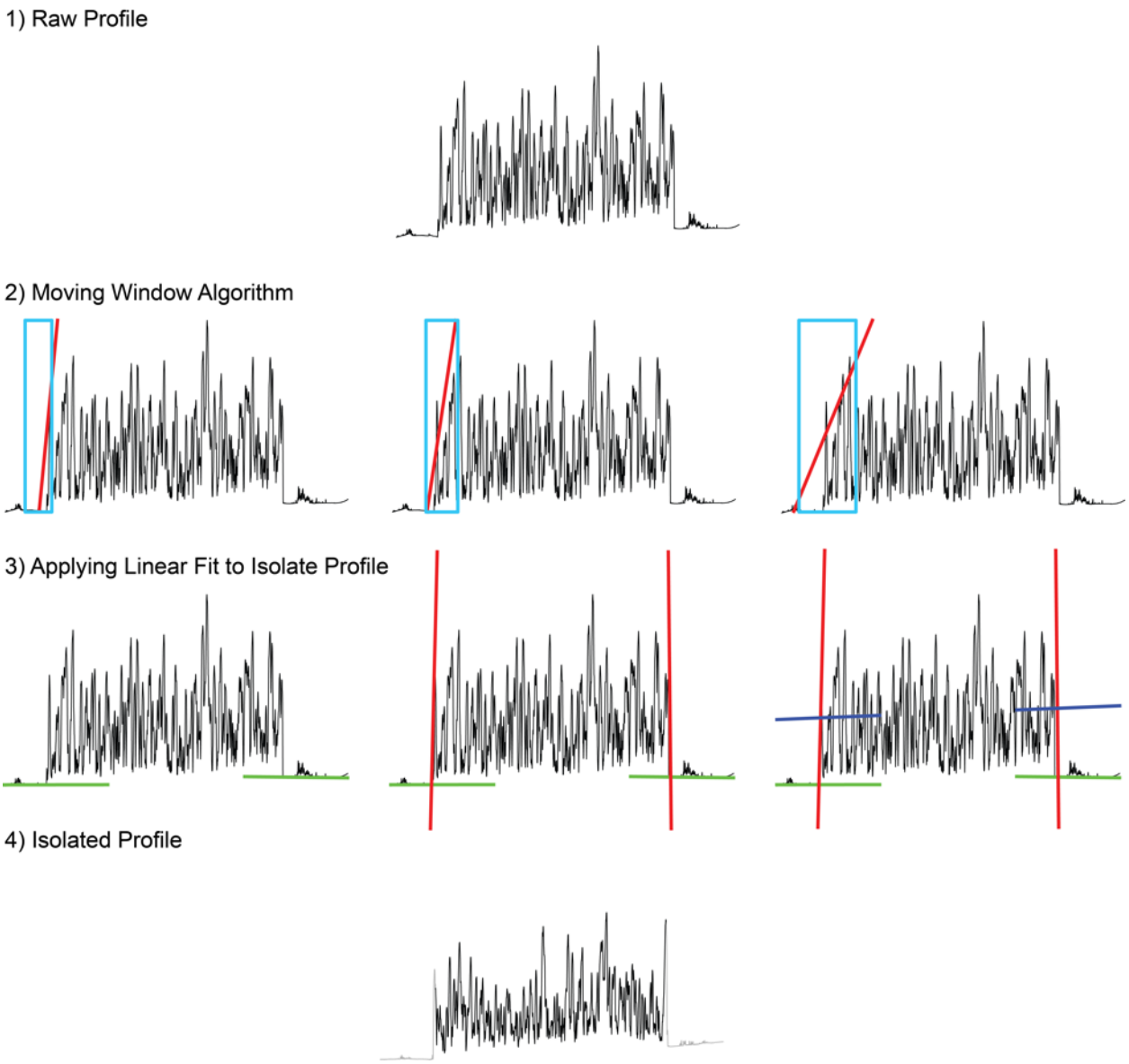

Figure 4.6: Visualization of moving window algorithm to isolate region of interest in profile. *1*: raw profile scan, *2*: application of moving window algorithm where both size and position of window are varied to find the best linear fit within each window, *3*: applying best linear fits for overhanging substrate (green), sample edge (red), and center of sample (blue) to determine sample region (green and red intersection) and center of sample region (red and blue intersection), *4*: isolated profile for further analysis

In order to ensure the isolated region did not include any of the overhanging substrate or include the sharp vertical dropoffs from the edge of the sample, parameters within the algorithm were adjusted to bias the isolated region inwards from the true edge of the sample, even at the expense of some of the scanned profile. Because of the scale of the phenomena being investigated, it was decided that losing a fraction of the scan at the edges would not impact further analysis.

Once the primary profile was isolated, an FFT was applied to characterize each scan. This transformed the height data in the spatial domain into a sum of sinusoids that can be represented in the frequency domain as a spectrum of frequencies and amplitudes. For spatial signals as found in electrode surface morphology, this allows for separation of a profile scan into frequencies that correspond to short- and long-range phenomena, which can be attributed to the roughness and waviness respectively.

An $80\mu m$m cutoff wavelength was applied to the FFT data using a low-pass filter in order to remove all frequencies with a wavelength higher than $80\mu m$, following the standard from the American Society of Mechanical Engineers (Standard B46.1-2009). This was done simply by setting the corresponding amplitudes to zero in the frequency-domain transformed data. An inverse FFT was then applied to return the data back to the spatial domain.

However, direct application of the FFT and IFFT on the primary profile resulted in two issues: first, the returned magnitudes of the height data in the spatial domain were cut in half, and second, the new profile had a value of zero at the origin. The first issue was due to the FFT producing a symmetric map of frequencies and amplitudes corresponding to the real and complex parts of the frequency spectrum and the IFFT only using the real parts to transform the data back to the spatial domain. Because the contributions of the real parts were equal to the complex parts, the magnitudes of the returned height data were simply doubled. The second issue was due to the returned profile being reconstructed from sine waves but not actually being an infinite, continuous function. To mitigate this issue, the primary profile was extended prior to application of the FFT.

The extended primary profile was created by mirroring the primary profile and book-ending the primary profile with its mirror image. This placed the primary profile at the center of an extended profile, which provided a buffer against the zero origin issue while ensuring continuity at the edges. The FFT, low-pass filter, and IFFT were then applied to this extended profile, and the position and height values of the center corresponding to the primary profile were extracted as the correct profile.

Because application of the low-pass filter removed the contributions of the higher frequency sinusoids, the output of the IFFT corresponded to the waviness of the profile, or the long-range characteristics. In order to determine the roughness of the profile, or the short-range characteristics, the waviness profile was subtracted from the primary profile. The process of extending the primary profile, applying the Fourier transforms and low-pass filter, and extracting the roughness and waviness is visualized in Figure 4.7.

Finally, to quantify the profile characteristics, the root mean square (RMS) of the roughness and waviness (R_q, W_q) and the arithmetic mean of the height in the primary profile (P_a) were calculated.

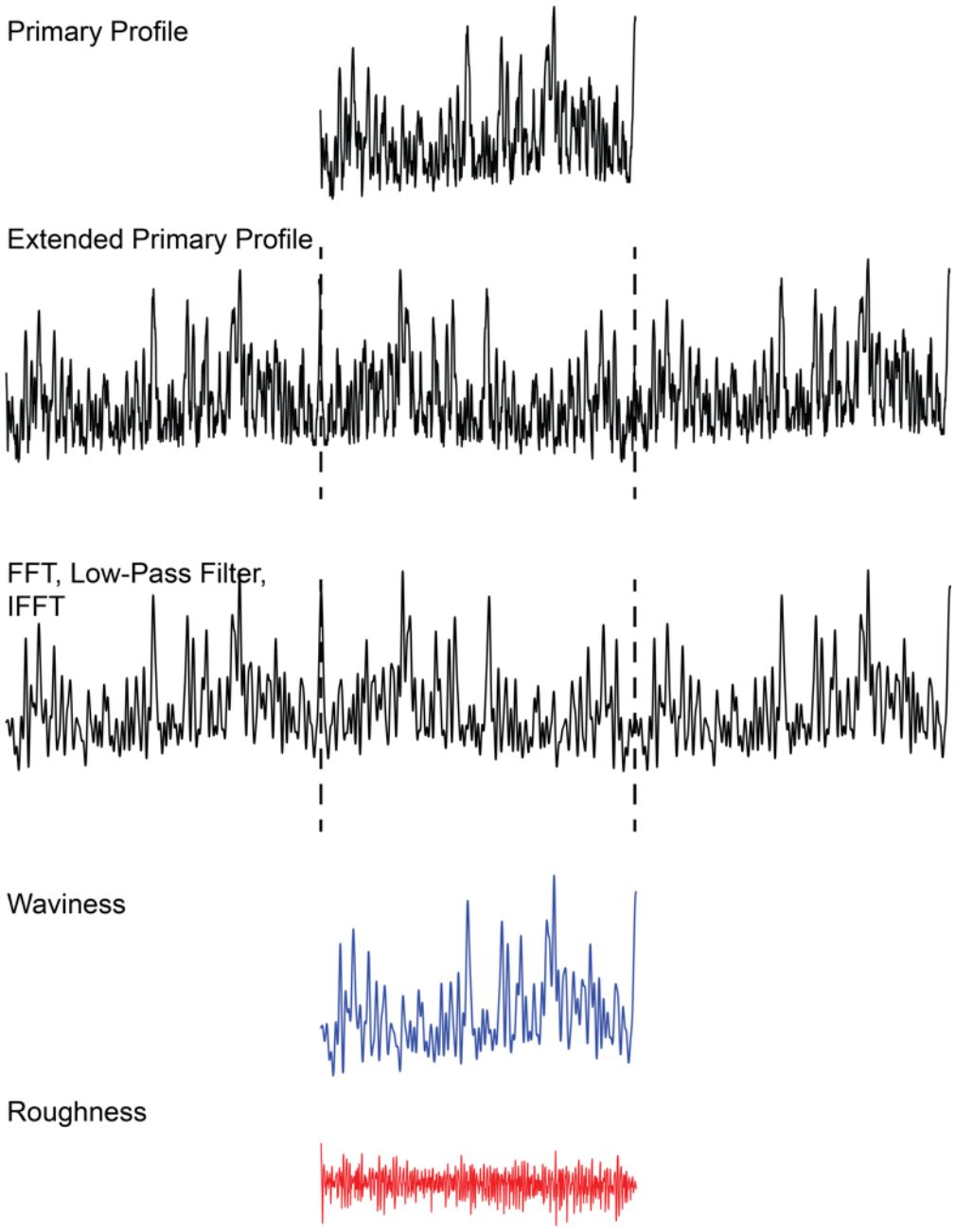

Figure 4.7: Visualization of extended primary profile and extraction of roughness and waviness.

One shortcoming of one dimensional profilometry as shown in this work is its inability to accurately capture all details of a three-dimensional surface. Specifically, features that are small relative to the surface's edge dimensions may not be accurately portrayed in the scan if they do not fall directly in the path of the needle. To remedy this, multiple samples were scanned and average profile statistics calculated for each type of sample investigated.

4.3.6 Conductivity

An inline four point probe was used for all conductivity characterization. The direct measurement being taken was sheet resistance, which was then converted to bulk resistivity and bulk conductivity by measuring the average thickness of each printed electrode.

Sample were printed on $75\mu m$ Kapton as an insulating substrate. The printing method used (doctor blade and stencil) introduced the possibility for some particle alignment along the printing direction, so resistance measurements were taken in two directions, one parallel and one perpendicular to the direction of casting. Resistance measurements were taken as described in Section 3.

Thickness measurements were taken either by micrometer or by profilometry. In the case of micrometer measurements, the electrode was sandwiched between two glass slides and a handheld screw micrometer (Mitutoyo) was used to measure the apparent thickness of the stack. The thicknesses of the glass slides and the substrate were then measured and subtracted from the initial measurement. In the case of profilometer measurements, the average height of the perpendicular scan was used. The parallel scan was not used for thickness values because in most cases, the average height value differed significantly from the actual thickness of the electrode.

4.4 Results and Discussion

This section presents results obtained during electrode ink optimization. The first section presents initial work considering only the cathode and anode conductivity. The second section presents work done to improve the surface profile of the cathode ink by adjusting active material particle morphology. The third section presents re-optimization of the cathode for conductivity after surface profile development. The fourth section presents profilometry and rheology characterization of the anode ink.

4.4.1 Initial Results

This section presents initial work done on optimizing the cathode and anode inks for conductivity and rheology separately. The purpose of presenting this data is to demonstrate the validity of each of these approaches individually prior to a more holistic approach of electrode optimization.

4.4.1.1 Scanning Electron Microscopy

Figure 4.8 presents an SEM image of the unmilled MnO_2 powder.

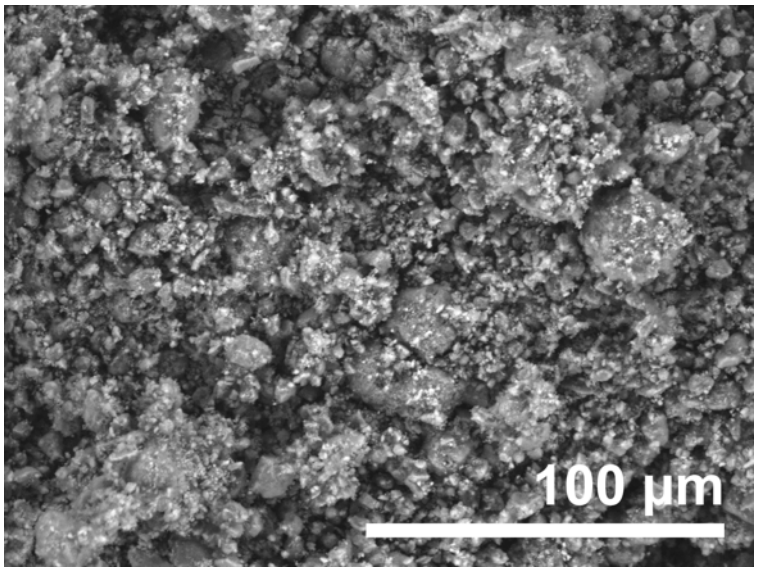

Figure 4.8: SEM image of unmilled MnO_2 powder (Sigma-Aldrich).

Examination of the SEM reveals agglomerates ranging from 10-30μm in diameter, each comprised of much smaller particles roughly 1-3μm in diameter.

4.4.1.2 Conductivity

Figures 4.9 and 4.10 present the initial results of electrode conductivity optimization for the cathode and anode respectively. The active material loading was maintained at 91 wt% for both electrodes, with the remaining 9 wt% divided between the conductive additive and polymer binder. An active material loading of 91 wt% was chosen in order to maintain a reasonably high fraction of active material to not compromise capacity in fully assembled cells. The amount of polymer binder was not lowered beyond 4-4.5 wt% because the dried printed films became too fragile beyond that point.

Similar to the work performed by Liu, *et. al.* [57], there exists a minimum in electrode resistivity at 2.57 wt% of solids loading (corresponding to a ratio of acetylene black to PVDF-HFP of 0.4:1) for both the cathode and the anode. The existence of this minimum is otherwise unexpected as otherwise the resistivity intuitively drops as more conductive additive is added to the ink composition and is a promising result as it indicates that other ink optimization strategies that exist for Li-ion chemistries may be applicable as well for this Zn-MnO_2 chemistry.

However, these initial results, performed with a manual and less repeatable printing process, are valid only for this given particle size of active material, and do not account for

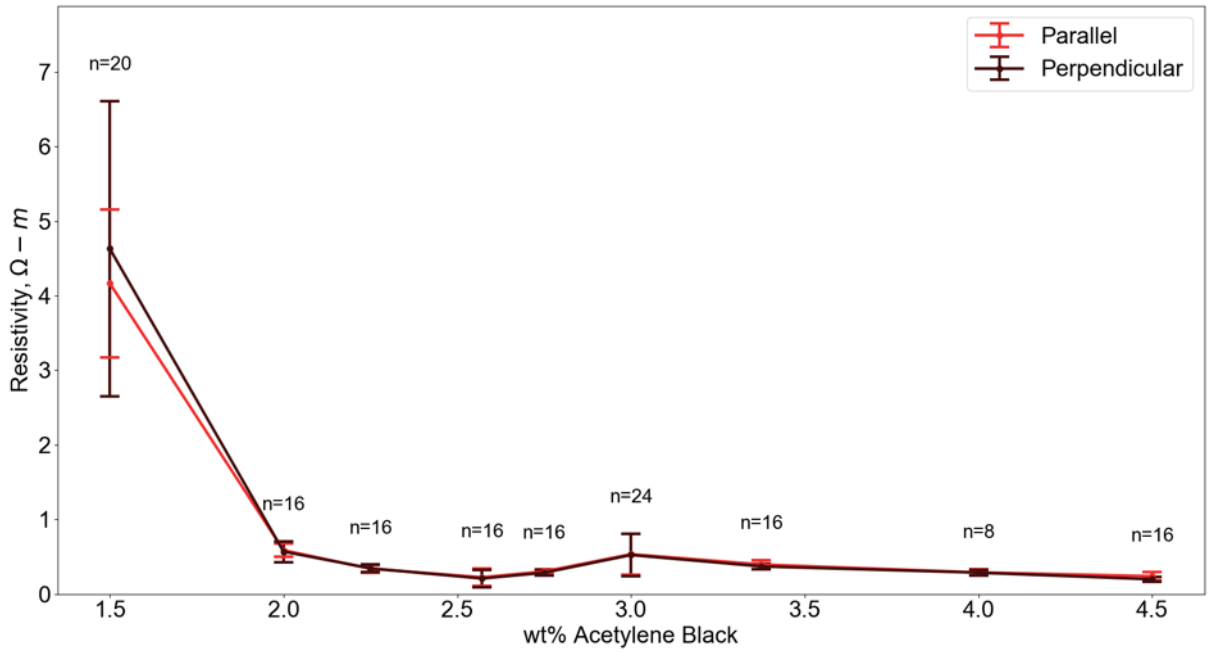

Figure 4.9: Resistivity of cathode as a function of acetylene black content. The number of samples tested per recipe are displayed above each point.

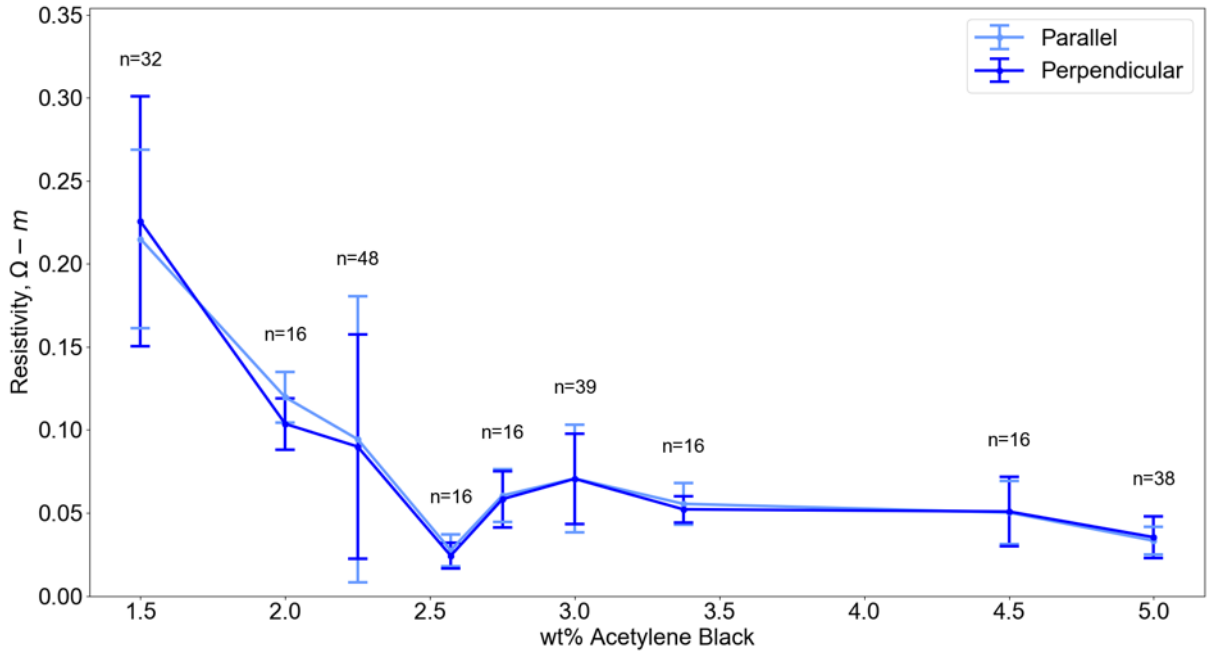

Figure 4.10: Resistivity of anode as a function of acetylene black content. The number of samples tested per recipe are displayed above each point.

the surface profile or rheology of the inks. As the particle size changes, the volume fractions of polymer binder and conductive additive must be adjusted as well due to differences in contact surface area of the active material.

4.4.1.3 Rheology

Figures 4.11 and 4.12 present the initial viscosity and shear stress results respectively of rheology optimization for the cathode and anode compared to a commercial ink for printed electronics applications (DuPont 5025). For both electrodes, the solid composition of the inks was kept constant, and only the solid phase (adjusted via the amount of solvent used) was changed. For initial testing, only shear rates up to 120 1/s were tested, though future results were obtained at a maximum shear rate of 500 1/s. The intent of these initial results was to verify if the solvent content could be used as a tuning parameter independent from the solids loading to adjust the desired viscosity and yield stress of the electrode inks.

Figure 4.13 presents a comparison of observed viscosities and yield stresses at the maximum tested shear rate (120 1/s), again compared to the same commercially available ink.

As shown by Figure 4.11, the viscosities of the inks are able to be adjusted simply by adjusting the amount of solid phase in the inks. Furthermore, as the applied shear rate increases, the ink viscosities decrease to a steady-state value, indicating that these inks are shear thinning, which is further supported by the shear stress curves in Figure 4.12. However, the viscosity response of the commercial DuPont ink is much faster and steadier than the cathode and anode inks, indicating a more uniform particle distribution and a more homogenous ink.

From Figure 4.13, the viscosity and yield stress of the inks can be controlled simply by adjusting the solvent content within the inks, and the rheology of the ink can be adjusted to match the characteristics seen in a commercial ink. While these initial results were unable to match the viscosity and the yield stress of the DuPont ink simultaneously, the importance of the exact values of these properties will depend on the exact printing method used and the demands of the manufacturing process during handling and drying of the inks. Of primary importance is the printability of the inks themselves and the homogeneity of the printed and dried electrode films.

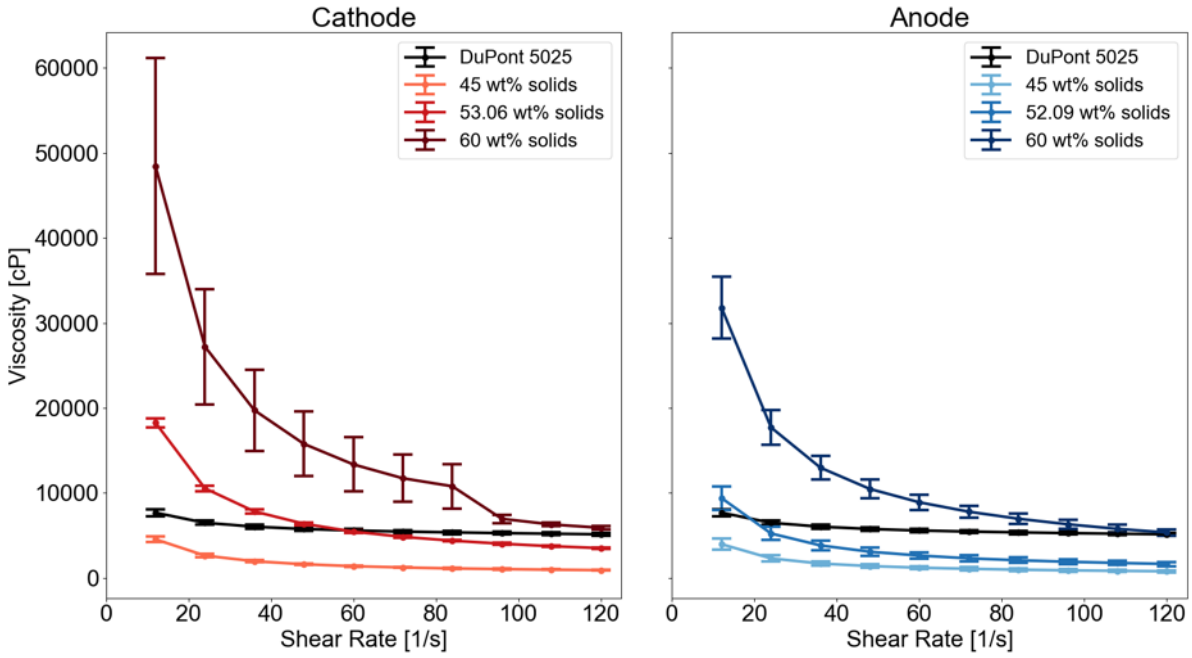

Figure 4.11: Initial average viscosity results of cathode (left) and anode (right) inks compared to commercial ink. Error bars represent one standard deviation.

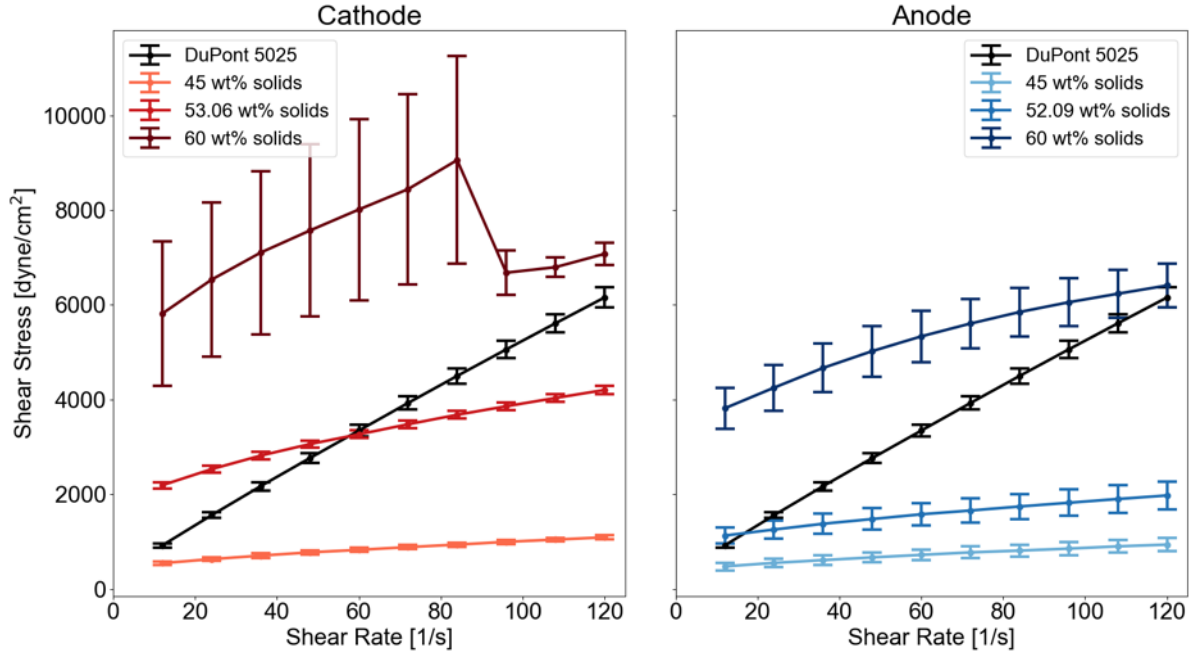

Figure 4.12: Initial average shear stress results of cathode (left) and anode (right) inks compared to commercial ink. Error bars represent one standard deviation.

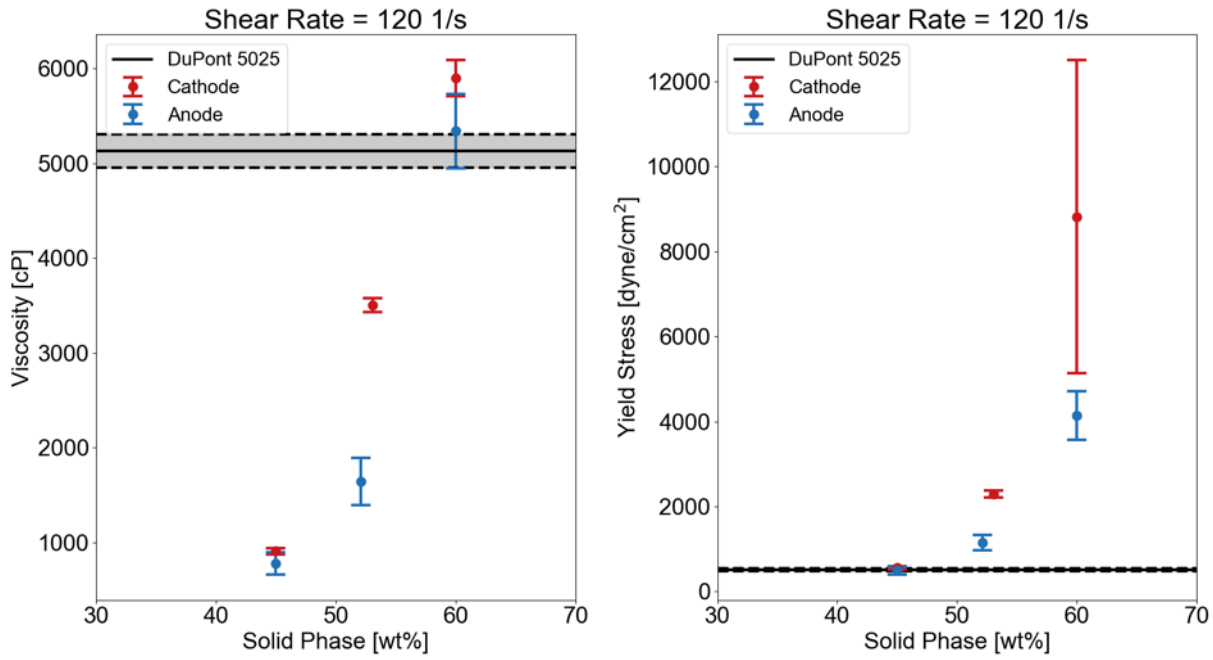

Figure 4.13: Initial results of viscosities and yield stresses at 120 1/s for cathode and anode inks.

4.4.2 Initial Ink Optimization for Profilometry

This section details the progress and results obtained when prioritizing profilometry for the cathode optimization and is divided into parts following cathode ink development. The first section presents improvements made by adjusting only the solid phase content. The second section presents results when the active material powder was ball-milled prior to mixing the ink. The third section presents further improvements when the ball-milled powder was sieved prior to mixing inks. Finally, the fourth section presents re-optimization of the newly developed cathode inks for electrical conductivity as well as characterization performed on the anode.

The profilometry figures in this section present representative samples of each ink composition for brevity.

4.4.2.1 Effect of Solid Phase

Figure 4.14 presents viscosity and shear stress results for cathode inks with 40, 45, 50, and 60wt% solid phases. Figure 4.15 presents the viscosity at a shear rate of 500 1/s (the maximum testable shear rate for most inks by the rheometer used) and the yield stress for each cathode ink. The solid loadings of all inks were identical with the only difference being the weight percent of solid phase in the ink (*e.g.* for 40wt% solid phase, 60wt% of the wet ink is the solvent). No ball milling was performed on the active material.

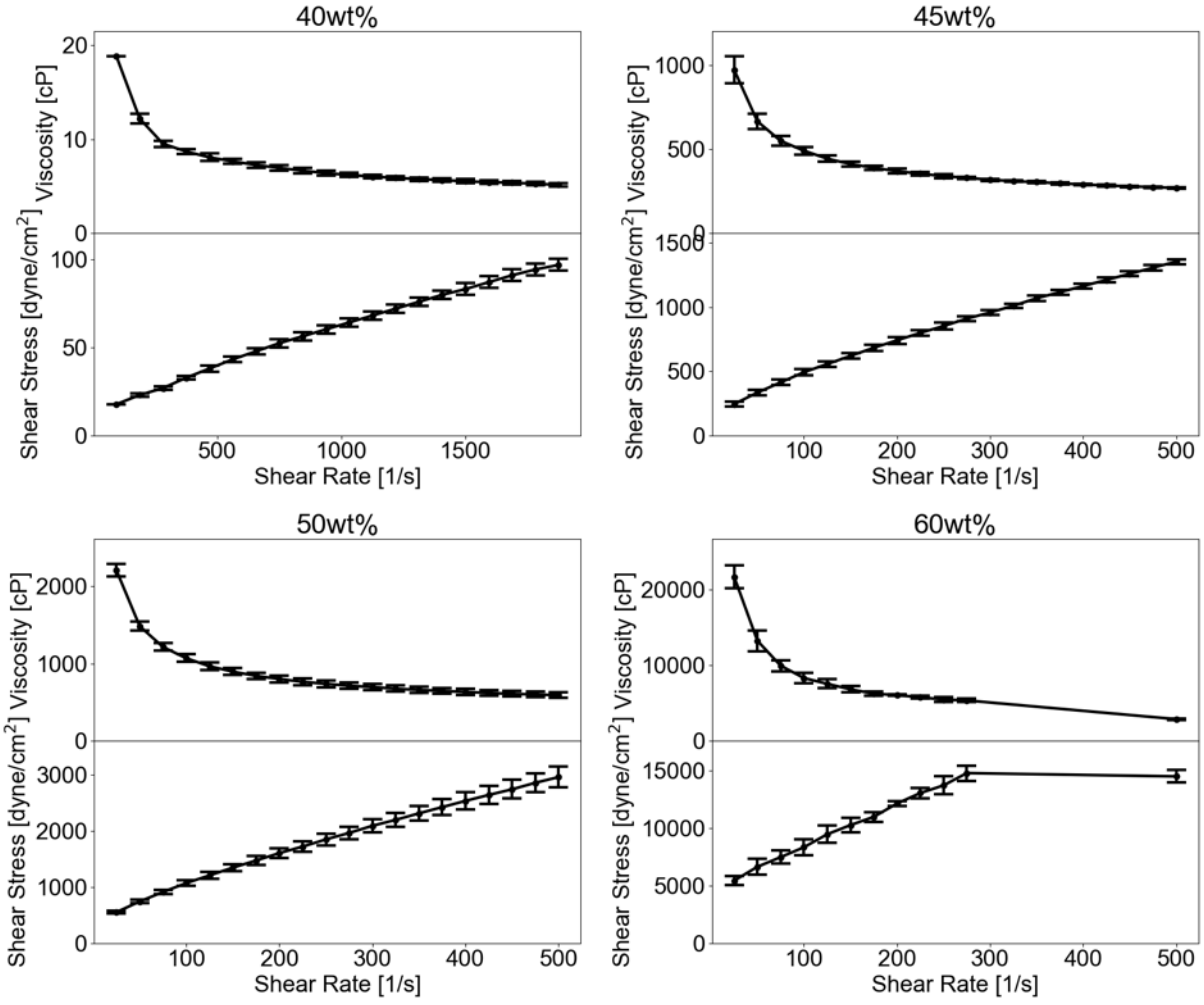

Figure 4.14: Viscosity and shear stress results of 40, 45, 50, and 60wt% solid phase cathode inks.

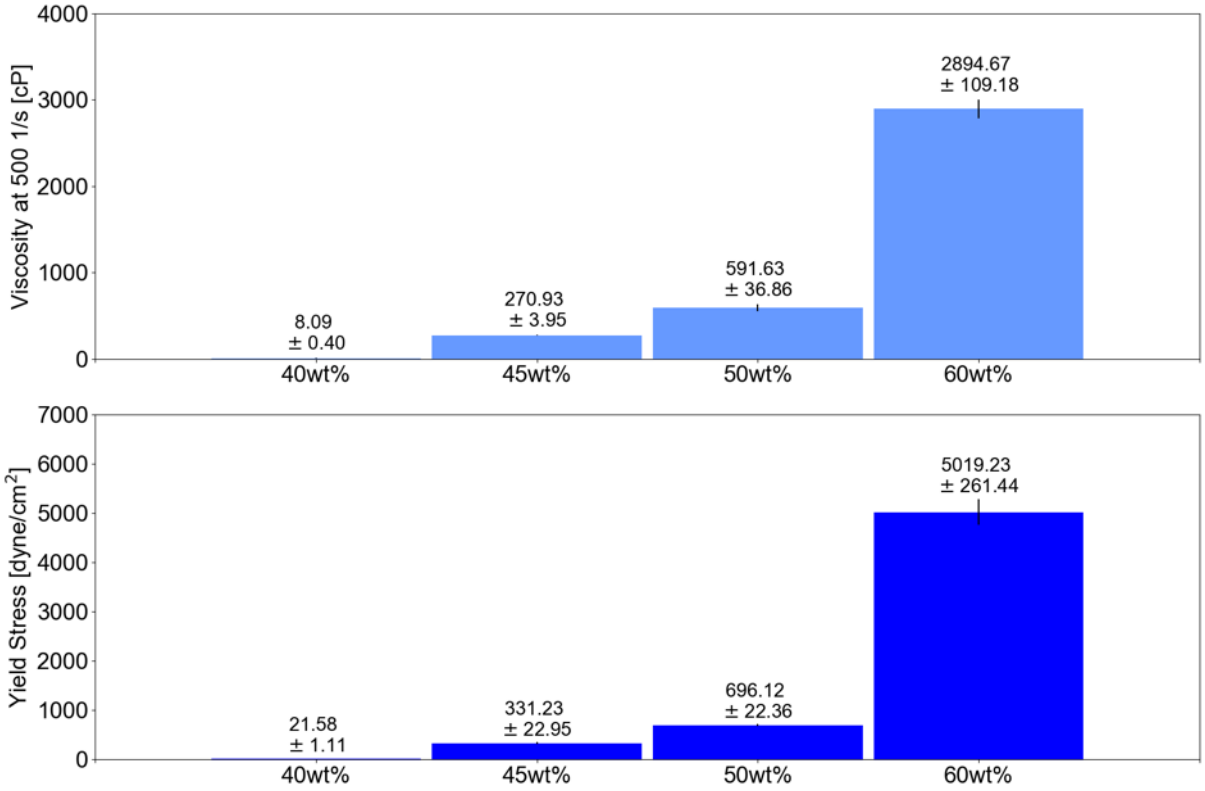

Figure 4.15: Rheology of cathode inks with no ball milling and varying solid phases.

The 40wt% ink exhibited a significantly lower viscosity than the other three inks, so the CP-40 spindle was used which allowed for testing shear rates up to 1875 1/s. At higher shear rates (about 300 1/s and above), the rheometer was unable to consistently collect data for the 60wt% ink due to the shear stress exceeding the maximum detectable limit of the rheometer until 500 1/s. The inconsistency in measureable shear stress may be due to particle agglomerates impeding the rotation of the spindle until the spindle rotation is able to shear apart the agglomerates during the measurement process.

Within the range of 40-60wt% solid phase, there is a range of three orders of magnitude for observed viscosity and shear stress. Outside of this window, the ink viscosity becomes unprintable due to being too thin or too thick. Furthermore, there is a significant increase in viscosity from 40wt% to 45wt% solid phase as well as from 50wt% to 60wt% solid phase. Both 45wt% and 50 wt%solids displayed very similar rheologies. The observed yield stress increases linearly with increasing solid phase from 40-50wt% but increases significantly by 60wt%. The effect of ink rheology on printability is further observed in the results of profilometry.

Figure 4.16 presents profilometry for 40, 45, 50, and 60wt% inks. The lighter trace represents the raw scan data after leveling, and the darker trace represents the isolated profile as detected by the algorithm described in Section 4.3.5. Two profilometry scans were performed per sample, one parallel to the direction of casting, and one perpendicular to the direction of casting. For both directions, the scan was performed from left to right on the plot.

For all samples with these inks, as well as for future samples, the parallel scan exhibited a higher "shelf" at the end of the scan. This is most likely due to a build-up of solid particles caused by the step height difference caused by the edge of the stencil on the substrate. As the volume of deposited ink is pushed along the printing path, the solid particles may compress against the edge of the stencil, leading to a higher fraction of solid particles to build up. Furthermore, prior to drying, there was a visible difference in light reflection between the last quarter of the sample compared to the first three quarters, indicating a difference in ink composition between these two regions. Although this phenomenon results in nonuniform scans in the parallel direction, it is a product of the specific printing method and geometry used for this work, and the use of a roll-to-roll process or increasing the sample geometry size will mitigate this effect. Profile statistics for this work will therefore be applied only on the perpendicular scan where this "shelf" is not an issue.

The main statistic to minimize is the geometrically averaged waviness, W_q, as it reflects the large peaks and valleys present in the electrode surface. Examination of the perpendicular profile scans suggests that the waviness is caused primarily by agglomerates of powder that contribute to the formation of sharp peaks and valleys across the electrode surface. The formation of these agglomerates may be a result of a combination of capillary forces during the drying process, the individual particle size and morphology, and ink composition (including the solid phase and solid loading). Across the four different solid phases tested, there was no clear trend in the waviness value by varying the solvent content alone.

The geometrically averaged roughness, R_q, reflects the shorter-range oscillations in the profile. This is likely driven by the individual particle size of the active material on the surface of the printed electrode. The roughness may improve overall cell performance by increasing the contact surface area between the electrode and electrolyte but is also a metric to minimize in order to further reduce variation in the electrode surface profile.

Table 4.6 presents profile statistics for the perpendicular scan for these inks for all tested printing parameters. Fewer tests were performed for 40 and 60 wt% inks because they were chronologically developed after tests were performed for the 45 and 50wt% inks, as explained further below.

Chronologically, all combinations of doctor blade height and casting speed were tested first for the 45 and 50wt% inks. From these results, it was observed that better results were seen printing at 10mm/s for both doctor blade heights, considering both the average waviness and the sample yield of each ink. After initial results were collected for the 40wt% and 60wt% inks, further testing was foregone after seeing no improvements in the waviness or sample yield.

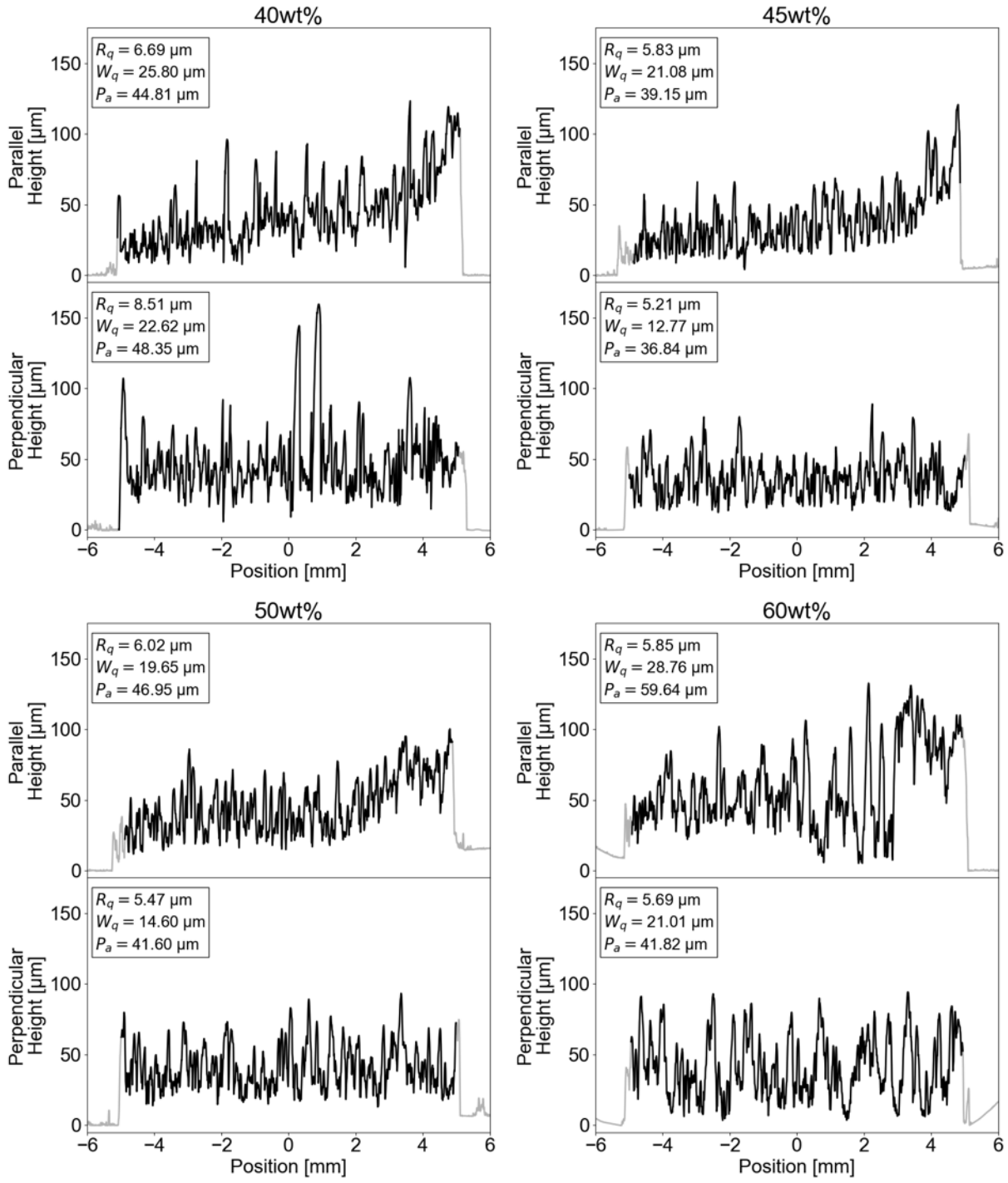

Figure 4.16: Profilometry scans of 40, 45, 50 and 60wt% cathode ink. Doctor blade height: 50μm; casting speed: 10 mm/s

Table 4.6: Profile statistics for 40wt%, 45wt%, 50wt%, and 60wt% solid phase cathode ink with unmilled MnO_2.

Doctor Blade Height [μm]	**Casting Speed [mm/s]**	**Roughness, R_q [μm]**	**Waviness, W_q [μm]**	**Thickness, P_a [μm]**	**Sample Size**
		40wt% solid phase			
50	10	6.933	20.631	47.175	8
		45wt% solid phase			
50	10	5.592	13.718	33.140	8
	20	6.080	18.187	34.532	8
	50	6.012	16.815	29.613	8
100	10	5.490	15.887	51.794	8
	20	6.221	19.785	52.498	8
	50	6.130	20.195	47.531	8
		50wt% solid phase			
50	10	5.603	16.511	43.597	7
	20	5.624	18.699	41.055	8
	50	5.299	14.837	34.401	8
100	10	6.278	20.349	67.041	6
	20	6.091	24.650	68.659	4
	50	6.143	24.818	67.220	6
		60wt% solid phase			
50	10	6.091	25.369	65.316	2
100	10	6.167	28.778	67.722	2

As the solid phase content increased, the yield per batch of electrodes printed decreased from maximum with the 60wt% ink yielding only 2 out of 8 samples. It was observed during printing that the ink's viscosity was too high to freely flow with the path of the doctor blade. Conversely, the 40wt% ink produced a maximum sample yield by displayed very high values for waviness and roughness.

A dried electrode thickness of at least $50\mu m$ was desired to ensure adequate MnO_2 based on previously calculated Zn utilization, so printing for future inks was performed only at a doctor blade height of $100\mu m$.

From these results, it was determined that the ideal solid phase content for this solid loading and for unmilled powder lies around 45-50wt% and that no further improvements could be made to the cathode surface profile by modification of the solid phase content alone.

4.4.2.2 Ball Milling

Ball milling was investigated as a method of altering the MnO_2 particle size to improve the surface profile. Figure 4.17 presents SEMs of the MnO_2 powder after ball milling.

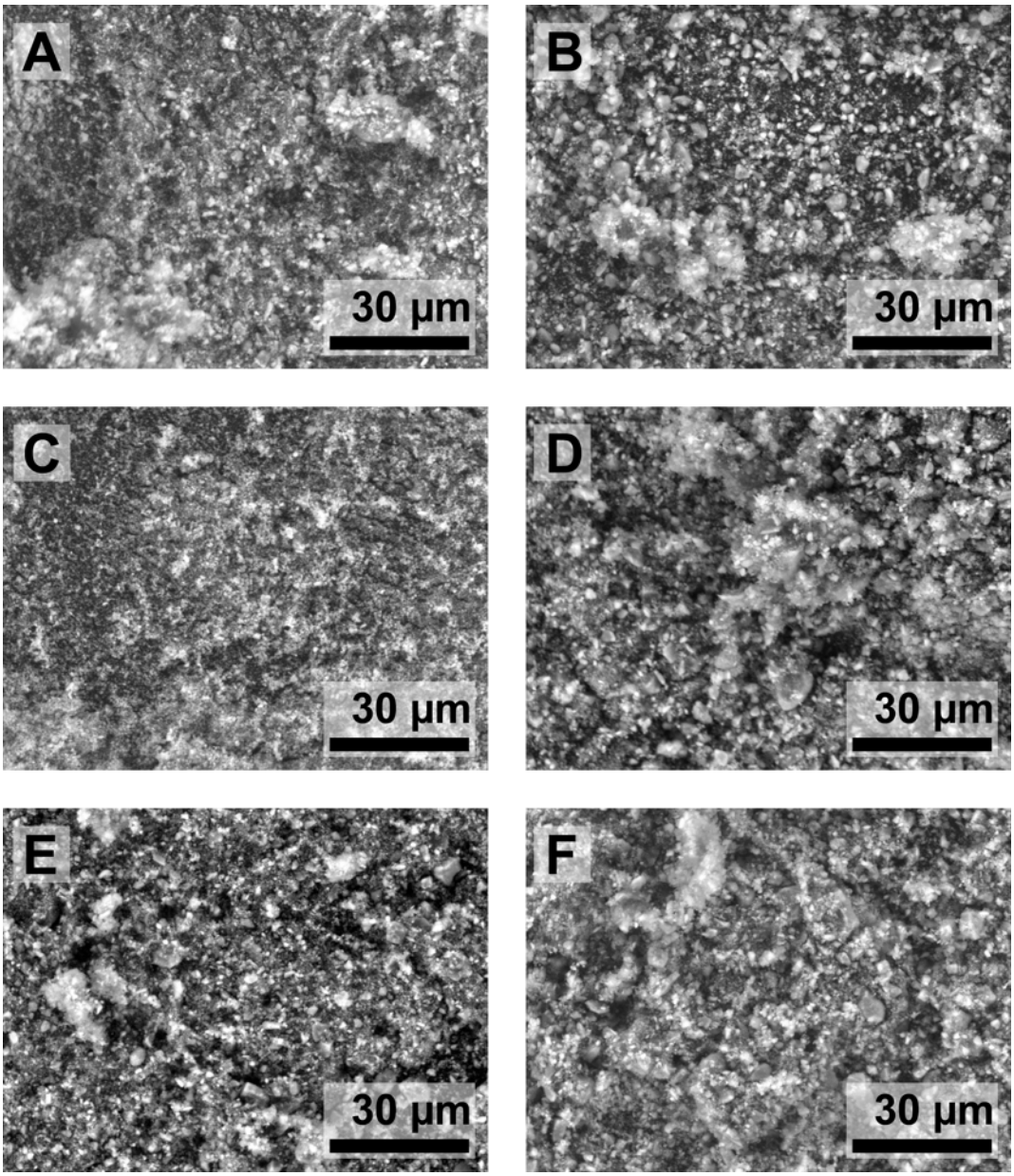

Figure 4.17: MnO_2 powder after ball milling. *A*: 30Hz, 3mm balls, 8 hours; *B*: 30Hz, 5mm balls, 8 hours; *C*: 30Hz, 5mm balls, 24 hours; *D*: 30Hz, 10mm balls, 8 hours; *E*: 30Hz, 15mm balls, 8 hours; *F*: 30Hz, 15mm balls, 24 hours

Compared to the unmilled powder (Fig. 4.8), a clear difference in particle size and morphology can be seen. The agglomerates have been broken up, bringing the average particle size much closer to the individual particles comprising the agglomerates. For most combinations of parameters, the individual particle size has not been changed. However, ball milling at both 30Hz, 3mm, 8 hours and 30HZ, 5mm, 24 hours results in a much finer particle size with average individual diameters of around $1\mu m$. There is no visibly significant difference in particle size between 30Hz, 15mm, 8 hours and 30Hz, 15mm, 24 hours, possibly due to the larger diameter balls being unable to efficiently impact the powder.

Considering increasing ball diameter at 8 hours of milling time (A, B, D, E in Figure 4.17), the degree to which agglomerates were broken and individual particle size reduced generally decreases with increasing ball size. This may be due to the smaller sized balls having increased impact surface area compared to an equal mass of larger sized balls as well as a higher frequency of collision due to smaller sized balls being more numerous.

Figures 4.18 and 4.19 present profilometry scans of 40wt% and 45wt% solid phase cathode inks with ball milled powder. Tables 4.7 and 4.8 present profile statistics for these inks. Figure 4.20 presents the viscosity at a shear rate of 500 1/s and the yield stress for all inks.

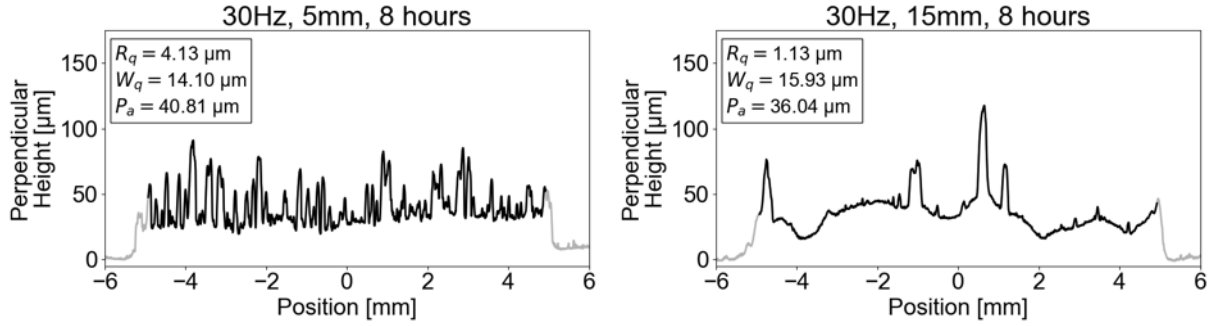

Figure 4.18: Profilometry scans of 40wt% cathode inks with ball milling. Doctor blade height: $100\mu m$; casting speed: 10mm/s

Ball milling was first performed at 30Hz, 5mm, 8 hours and 30Hz, 15mm, 8 hours. For both 40wt% and 45wt% inks, no significant improvements were seen with powder milled with 5mm balls aside from a small reduction in roughness. Inks made with powder milled with 15mm balls yielded a significant reduction in roughness, clearly exposing the waviness. However, the large peaks and valleys still persisted, indicating inhomogeneities in the final printed electrode. Of particular importance to target are the large isolated peaks that can add an additional 50-100μm to the maximum height of the profile. While initial results did not show a significant difference between 40wt% and 45wt% and even showed a higher yield with 40wt% inks, the difference in average thickness drove the decision to continue only with 45wt% solid phase cathodes. In addition, no conclusive advantages could be determined from casting at 20mm/s, so future inks were only cast at 10 and 50mm/s.

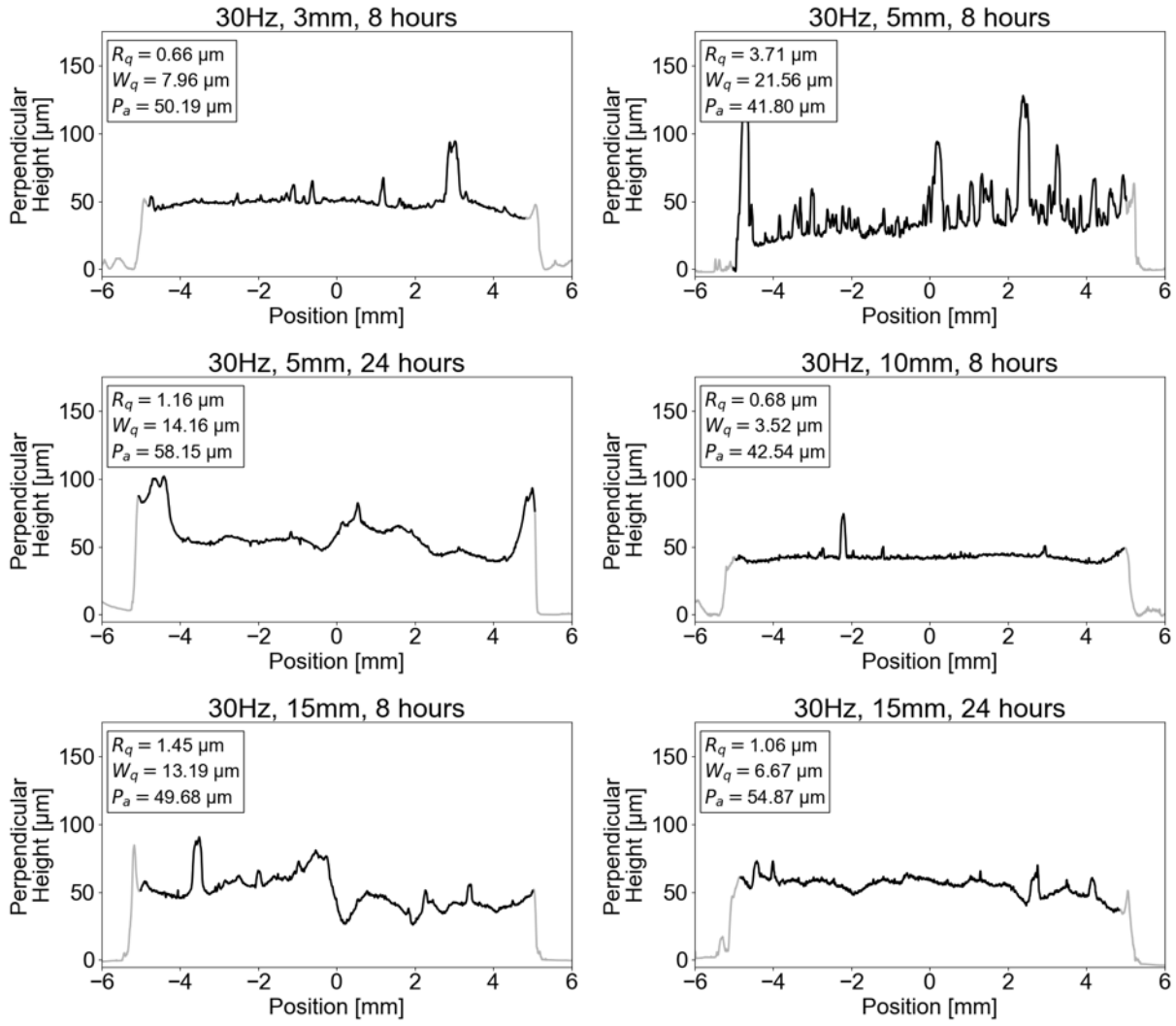

Figure 4.19: Profilometry scans of 45wt% cathode inks with ball milling. Doctor blade height: 100μm; casting speed: 10mm/s

Ball milling was then performed at 30Hz, 3mm, 8 hours, 30Hz, 5mm, 24 hours, 30Hz, 10mm, 8 hours, and 30Hz, 15mm, 24 hours. While the waviness and roughness both improved for all ball milling parameters compared to the unmilled powder, the combination of 30Hz, 10mm, 8h also showed the best sample yield for all inks at 45wt%. From Figure 4.20, this may be due to the low yield stress for those ball milling parameters. Furthermore, those parameters also produced the lowest waviness and roughness statistics for both casting speeds. Visually, the surfaces of the these electrodes were significantly freer from large agglomerates, but some peaks in the profile indicate their persistence.

Table 4.7: Profile statistics for 40wt% solid phase cathode ink with ball milled MnO_2.

Doctor Blade Height [μm]	**Casting Speed [mm/s]**	**Roughness, R_q [μm]**	**Waviness, W_q [μm]**	**Thickness, P_a [μm]**	**Sample Size**
		40wt% solid phase ball milling: 30Hz, 5mm, 8h			
100	10	3.567	14.723	34.900	8
	20	3.578	13.782	33.742	5
	50	3.212	12.459	34.514	7
		40wt% solid phase ball milling: 30Hz, 15mm, 8h			
100	10	1.062	14.732	42.406	4
	20	1.538	16.211	38.965	4
	50	0.989	9.262	34.351	4

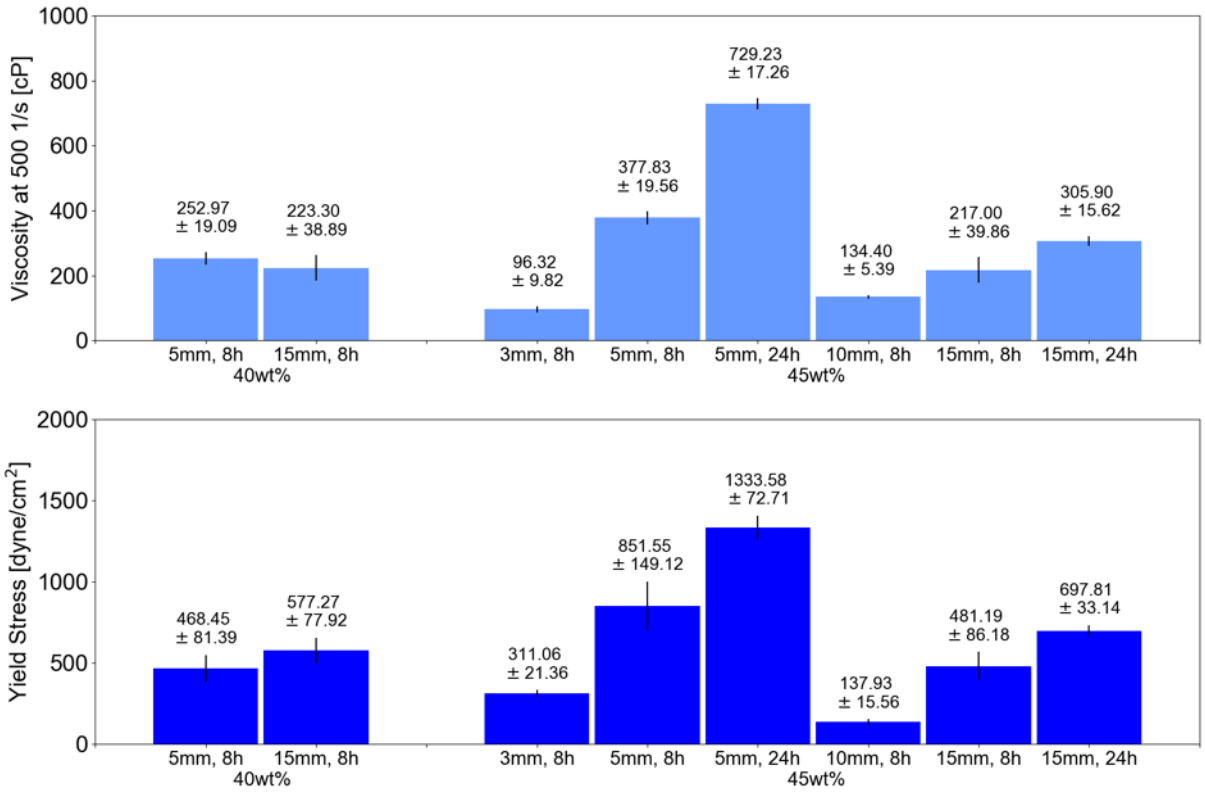

Figure 4.20: Rheology for 40 and 45wt% cathode inks with ball milling.

Table 4.8: Profile statistics for 45wt% solid phase cathode ink with ball milled MnO_2.

Doctor Blade Height [μm]	**Casting Speed [mm/s]**	**Roughness, R_q [μm]**	**Waviness, W_q [μm]**	**Thickness, P_a [μm]**	**Sample Size**
		45wt% solid phase ball milling: 30Hz, 3mm, 8h			
100	10	0.917	7.454	50.745	4
	50	1.018	14.129	47.316	2
		45wt% solid phase ball milling: 30Hz, 5mm, 8h			
100	10	3.254	18.275	42.313	3
	20	2.957	10.840	44.643	3
	50	2.934	15.314	42.520	4
		45wt% solid phase ball milling: 30Hz, 5mm, 24h			
100	10	1.028	11.756	51.975	2
	50	0.724	10.346	54.340	1
		45wt% solid phase ball milling: 30Hz, 10mm, 8h			
100	10	0.680	4.604	43.584	7
	50	0.770	4.491	41.167	7
		45wt% solid phase ball milling: 30Hz, 15mm, 8h			
100	10	1.088	12.642	50.665	4
	20	0.959	11.238	52.489	4
	50	0.979	10.284	40.463	2
		45wt% solid phase ball milling: 30Hz, 15mm, 24h			
100	10	0.871	8.345	54.737	2
	50	2.268	17.364	62.229	1

When increasing the milling time from 8 hours to 24 hours for the 5mm and 15mm balls, both the roughness and waviness improved but at the expense of sample yield. Because the solid phase was maintained constant, the overall ink viscosity increased due to the increased surface area caused by breaking up particle agglomerates. This effect was most pronounced with the 5mm balls as the viscosity at 500 1/s roughly doubled after increased milling time. However, the improved profile metrics still were inferior to those from the powder milled with 10mm balls. This rheology change is also observed with 15mm balls, though to a lower degree.

Considering these profilometry results from ball milling, the decision was made to move forward only with powder milled at 30Hz, 10mm, 8 hours. This powder also yielded the second lowest viscosity (134 cP at 500 1/s) and the lowest yield stress (138 dyne/cm^2) of all inks tested. These rheology values are lower than those for the commercial ink tested (about 5000 cP and 500 dyne/cm^2), but no significantly adverse behavior during printing was observed. While the improvements afforded by longer milling times were promising, the longer powder processing time as well as significant rheological changes prevented further investigation. Furthermore, while this powder showed a significant improvement over unmilled powder, the continued appearance of large agglomerates necessitated further processing.

4.4.2.3 Sieving and Conductivity Optimization

The final processing step investigated in the cathode ink development was sieving. The intent behind introducing this step was to mechanically break apart any large agglomerates that remained after ball milling or that were introduced as the powder was handled during solvent evaporation after ball milling, as some agglomeration may have been exacerbated as a result of capillary forces as the wet grinding agent used (isopropyl alcohol) was driven off.

Figure 4.21 presents SEM micrographs of the ball-milled and sieved powder. The powder was sieved through successively finer mesh sizes to facilitate processing.

While no significant difference can be observed between the unsieved powder and the powder sieved through the $250\mu m$ mesh, the size of agglomerates decreases slightly by the $150\mu m$ mesh and decrease even further, though not entirely absent, with the $45\mu m$ mesh. The largest visibile agglomerate in the micrograph is roughly $7\mu m$ in diameter (in the bottom left), and otherwise the individual particles are separated from each other.

Figures 4.22 and 4.23 present representative perpendicular profilometry scans for cathode inks with ball-milled and sieved powder at 45wt% and 47wt% respectively. Tables 4.9 and 4.10 present profile statistics for the tested inks. Figure 4.24 presents viscosity at a shear rate of 500 1/s and yield stresses for all tested inks. For all inks, the MnO_2 powder was ball milled at 30Hz, 10mm, 8 hours.

When characterizing ink with sieved powder, it was observed that casting at 50mm/s yielded better results with higher yield than casting at 10mm/s. This may be due to a more pronounced shear thinning effect resulting in a lower viscosity at higher casting speeds. Thus, all profilometry scans reflect samples cast at 50mm/s.

The sieved powder was first used to make 45wt% solid phase cathode inks. No significant difference in profilometry was observed between the unsieved and sieved powder until the finest mesh ($45\mu m$ opening) was used. Furthermore, the resulting profile metrics after only one sieving step with the coarsest mesh ($250\mu m$) produced worse results than not sieving at all. This may be due to agglomerates reforming as the powder was mechanically agitated and pushed through the sieve due to the mesh opening being much wider than the average particle or agglomerate diameter.

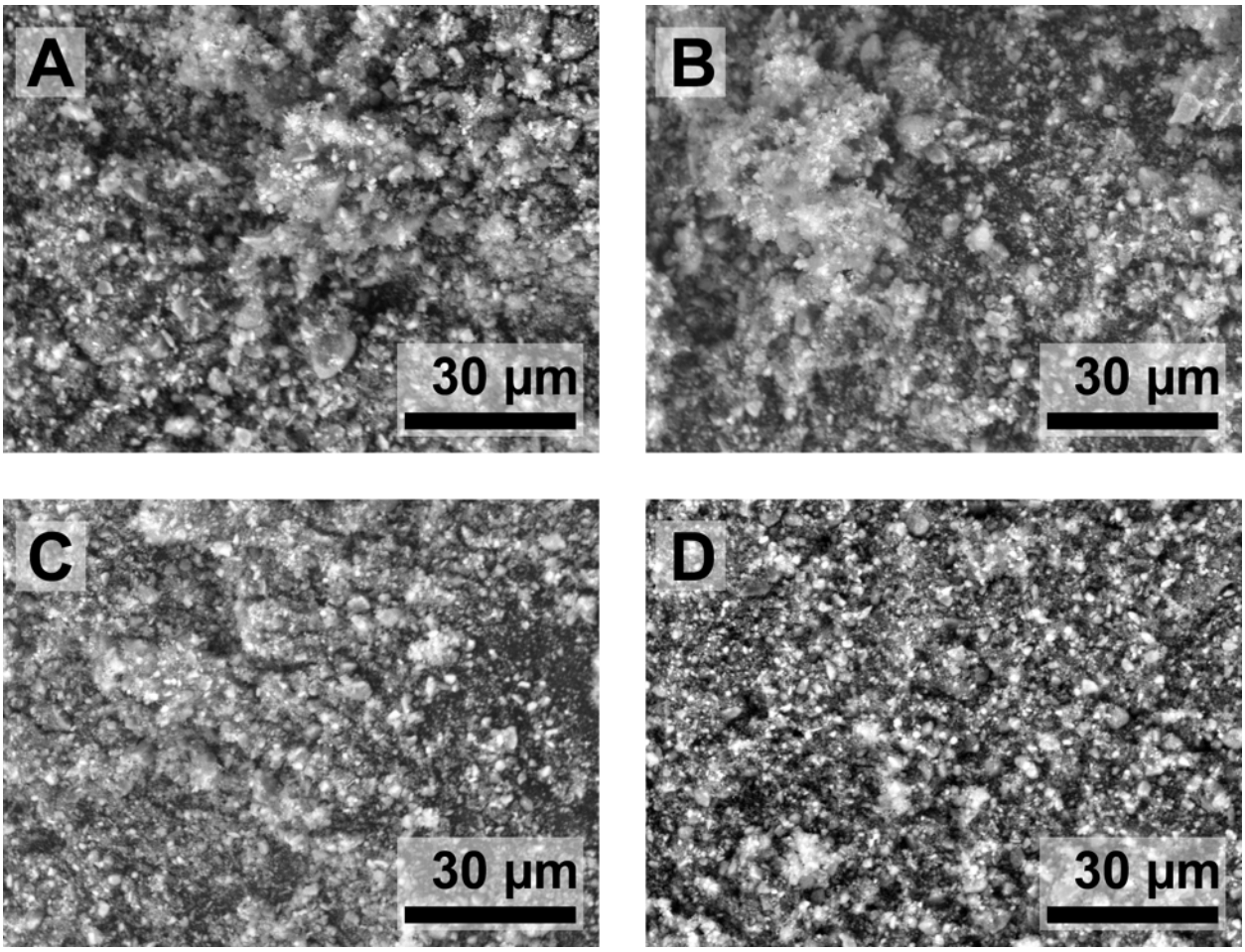

Figure 4.21: MnO_2 powder after ball milling at 30Hz, 10mm balls, 8 hours and sieving. *A*: no sieving; *B*: 250μm mesh; *C*: 150μm mesh; *D*: 45μm mesh

For cathodes printed with the 45μm mesh sieved powder, the large peaks characteristic of the unmilled and unsieved powders were completely absent across all samples. This is reflected in a lower average waviness by almost half when compared to the unmilled powder with the same ball milling parameters.

However, sieving the powder with a 45μm mesh also increased the viscosity and yield stress of the cathode inks. With this powder, the viscosity of the 45wt% cathode ink increased by about a factor of 3, and the yield stress increased by about a factor of 5. Similar to ball milling for 24 hours, this is likely due to the increased surface area from the separated particles.

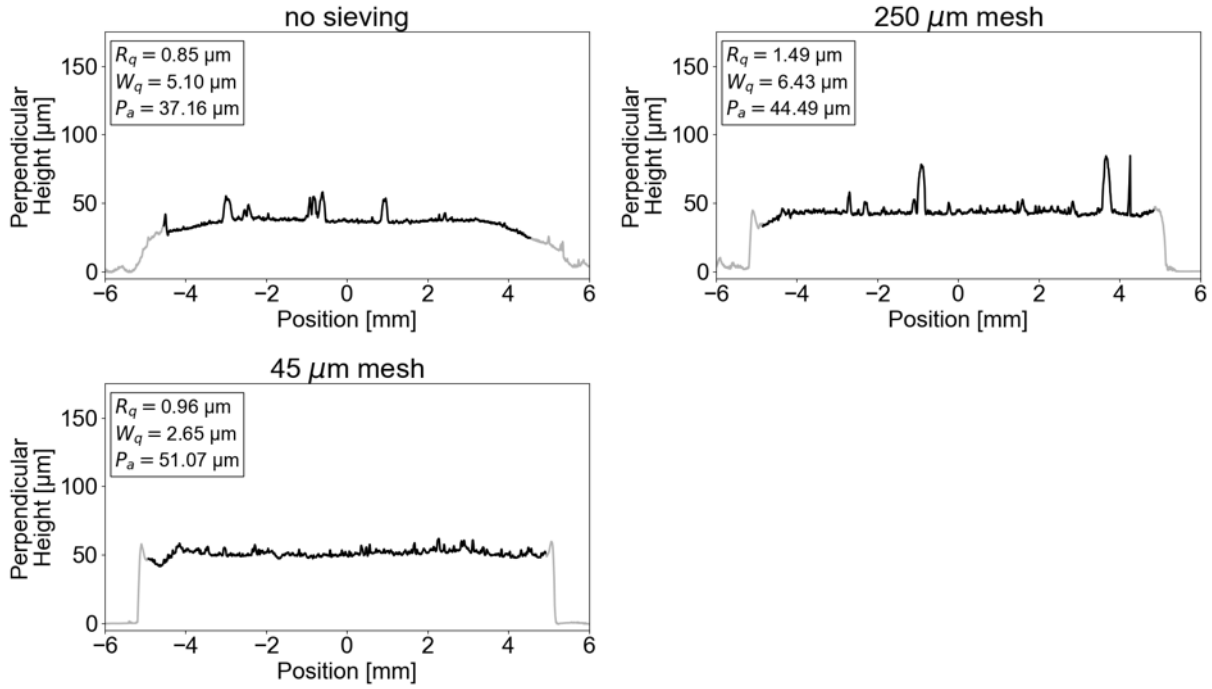

Figure 4.22: Profilometry scans of 45wt% cathode inks with ball milling and sieving. Doctor blade height: 100μm; casting speed: 50mm/s

A cathode ink with 47wt% solid phase was created with the same ball-milled and sieved powder. This was in order to slightly increase the viscosity in order to ensure edge fidelity at the edges of the sample. One observed issue with the 45wt% ink was that excess solvent would run out and blur the edges of the each electrode as defined by the stencil during the casting process. This is most apparent in the profile scans of the 45wt% ink with unsieved or 250μm mesh sieved powder. With the 47wt% ink, this issue was improved significantly, and the viscosity of the ink with 45μm mesh sieved powder was not significantly increased compared to the 45wt% ink. Although this change also slightly lowered the average waviness, the average roughness increased as well. Inks and samples were made at 47wt% with all stages sieved and ball-milled powder in order to verify that 45μm mesh sieving remained necessary.

The profile results from this step of processing were deemed adequate, and no further processing was performed on the MnO_2 powder with the intent of improving the surface profile.

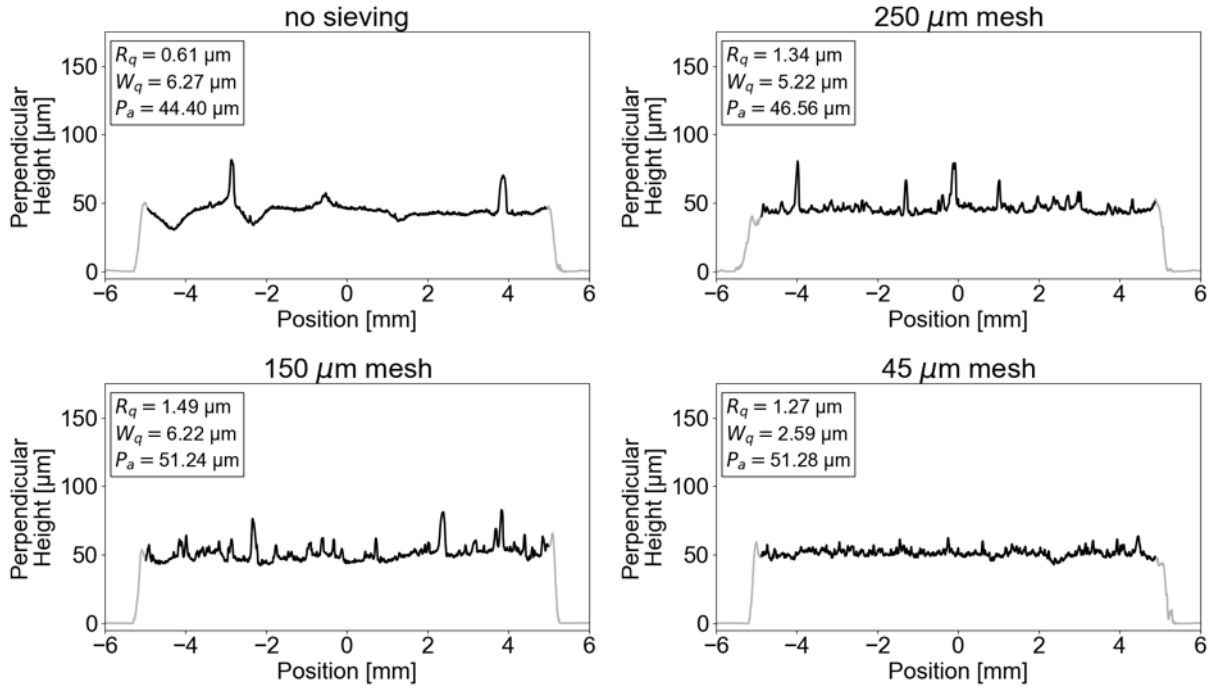

Figure 4.23: Profilometry scans of 47wt% cathode inks with ball milling and sieving. Doctor blade height: 100μm; casting speed: 50mm/s

4.4.3 Conductivity Re-Optimization

As a consequence of changing the active material particle morphology, the conductivity of the cathode was decreased significantly. Although the fractions of each component remained the same by weight, the dispersion of the active material throughout the cathode was increased significantly, impeding the formation of conductive pathways by the conductive additive. The weight fractions of active material, conductive additive, and polymer binder thus needed to be adjusted to bring the electrode resistivity back to acceptable levels as ohmic losses were too high for cycleable cells.

The cathode ink was adjusted three times with increasing amounts of conductive additive before an acceptable level of resistivity was reached. The active material content was maintained above 80wt% of the solids loading. The ink compositions developed are summarized in Table 4.11.

Figure 4.25 presents the resistivity data collected for these ink compositions. Figure 4.26 presents the perpendicular profilometry scans, and Table 4.12 presents the profile statistics. Finally, Figure 4.27 presents the rheology data for the re-optimized cathode inks. These figures tables are labeled by ink composition by weight percent (*e.g.* 87/5/8 refers to 87wt% MnO_2, 5wt% AB, 8wt% PVDF-HFP).

Table 4.9: Profile statistics for 45wt% solid phase cathode ink with ball milled and sieved MnO_2.

Doctor Blade Height [μm]	**Casting Speed [mm/s]**	**Roughness, R_q [μm]**	**Waviness, W_q [μm]**	**Thickness, P_a [μm]**	**Sample Size**
		45wt% solid phase ball milling: 30Hz, 10mm, 8h; sieve: none			
100	10	0.656	3.090	39.056	7
	50	0.878	5.136	41.146	8
		45wt% solid phase ball milling: 30Hz, 10mm, 8h; sieve: 250μm			
100	10	2.041	13.669	44.989	8
	50	1.290	6.162	40.043	8
		45wt% solid phase ball milling: 30Hz, 10mm, 8h; sieve: 45μm			
100	10	1.300	6.551	61.219	4
	50	1.013	2.651	49.324	6

Table 4.10: Profile statistics for 47wt% solid phase cathode ink with ball milled and sieved MnO_2.

Doctor Blade Height [μm]	**Casting Speed [mm/s]**	**Roughness, R_q [μm]**	**Waviness, W_q [μm]**	**Thickness, P_a [μm]**	**Sample Size**
		47wt% solid phase ball milling: 30Hz, 10mm, 8h; sieve: none			
100	10	0.730	6.338	61.335	4
	50	0.646	6.263	49.821	4
		47wt% solid phase ball milling: 30Hz, 10mm, 8h; sieve: 250μm			
100	10	1.367	7.724	59.064	4
	50	1.443	7.550	47.315	6
		47wt% solid phase ball milling: 30Hz, 10mm, 8h; sieve: 150μm			
100	10	1.488	8.051	65.581	2
	50	1.472	6.191	53.492	5
		47wt% solid phase ball milling: 30Hz, 10mm, 8h; sieve: 45μm			
100	10	1.234	5.234	62.051	3
	50	1.202	2.436	52.192	4

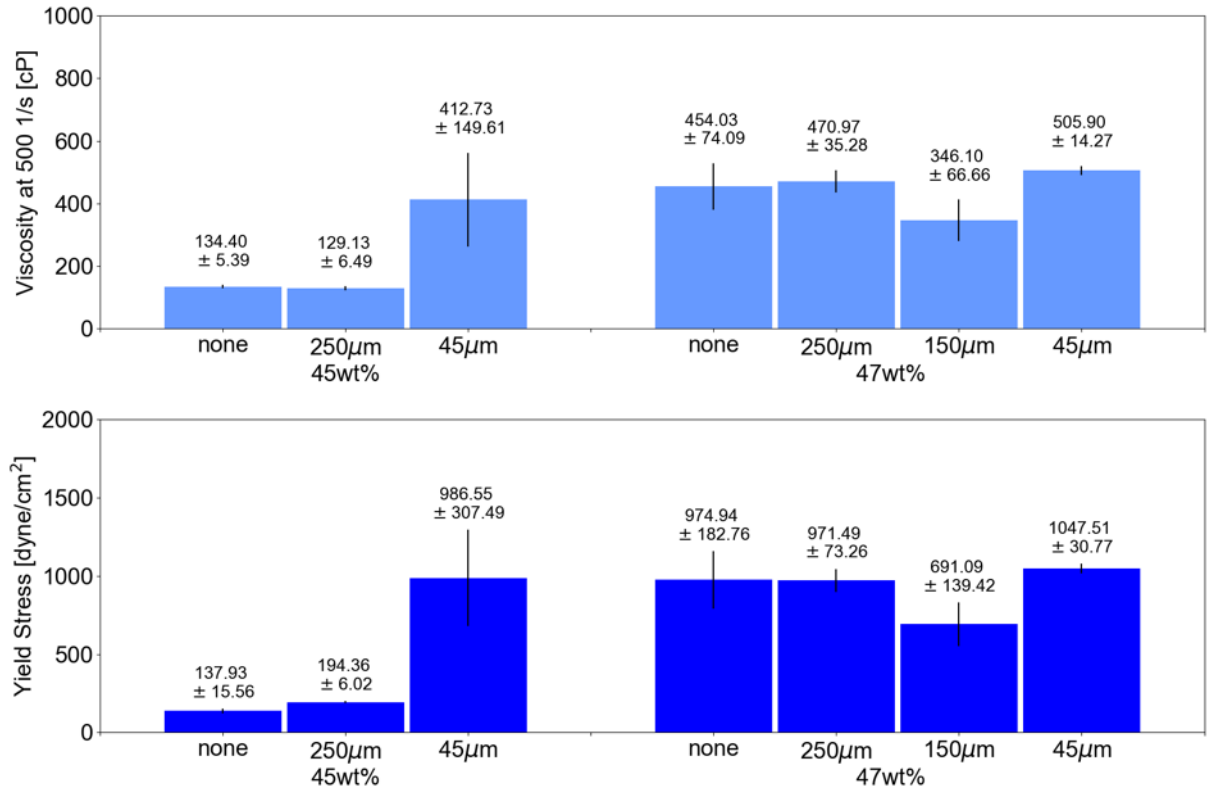

Figure 4.24: Rheology for 45wt% and 47wt% cathode inks with ball milling and sieving. All ball milling was performed at 30Hz, 10mm, 8 hours.

Table 4.11: Cathode inks developed for conductivity re-optimization.

Material	Composition 1	Composition 2	Composition 3
MnO_2	87wt%	83wt%	81wt%
AB	5wt%	10wt%	12wt%
PVDF-HFP	8wt%	7wt%	7wt%
Solid Phase	47wt%	47wt%	38wt%

The first composition tested roughly doubled the amount of conductive additive present by weight, but the resistivity remained roughly an order of magnitude above the best result obtained during the initial conductivity optimization. The second composition again doubled the amount of conductive additive and this brought the resistivity to about the same level as the initial optimization (about 0.3 Ω-m). However, the addition of so much more acetylene black also significantly increased the viscosity and also negatively affected the profilometry. The third composition both increased the amount of conductive additive

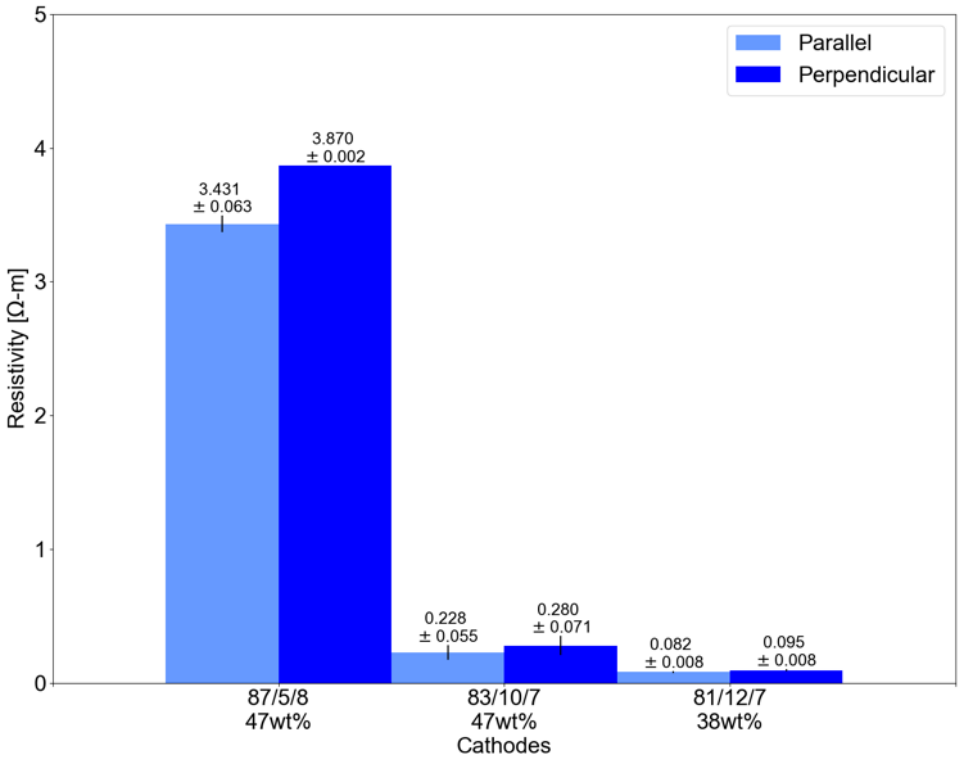

Figure 4.25: Optimized resistivity for cathode inks. Resistivities are labeled by ink composition by weight percent of MnO_2/AB/PVDF-HFP.

Table 4.12: Profile statistics for cathode ink with ball milled and sieved MnO_2 optimized for conductivity.

Doctor Blade Height [μm]	**Casting Speed [mm/s]**	**Roughness, R_q [μm]**	**Waviness, W_q [μm]**	**Thickness, P_a [μm]**	**Sample Size**
		87/5/8, 47wt% solid phase ball milling: 30Hz, 10mm, 8h; sieve: 45μm			
100	50	2.349	6.930	39.375	2
		83/10/7, 47wt% solid phase ball milling: 30Hz, 10mm, 8h; sieve: 45μm			
100	50	2.202	9.490	46.499	7
		81/12/7, 38wt% solid phase ball milling: 30Hz, 10mm, 8h; sieve: 45μm			
100	50	1.841	5.749	37.023	6

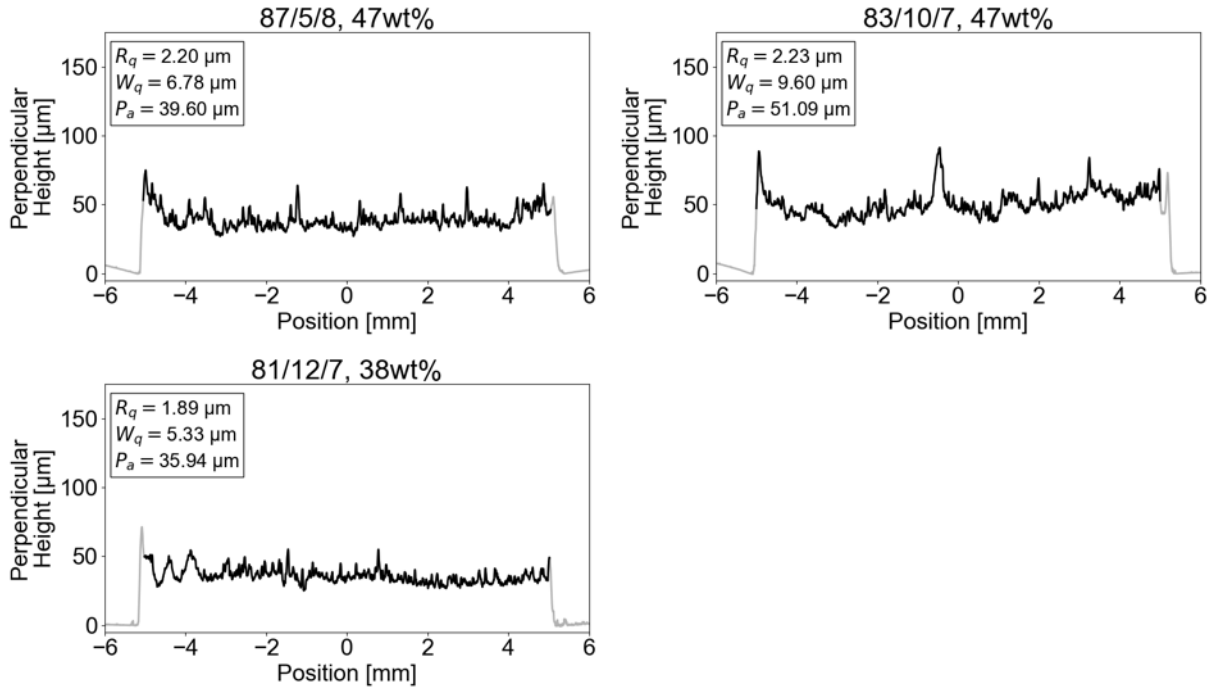

Figure 4.26: Profilometry scans of cathode inks with ball milling and sieving, optimized for conductivity.

again as well as lowered the solid phase content of the ink to compensate for the increased volume fraction of solid particles due to the additional conductive additive. This change improved the profilometry results as well as the ink viscosity, though the same improvements in waviness from the profilometry optimization were not obtained. However, the combined profilometry and conductivity improvements of this final ink result in an improved overall cathode ink compared to the ink prior to surface profile optimization.

4.4.4 Anode

The zinc powder comprising the active material in the anode was unable to be ball milled due to the excessive deformation of each particle, so the particle morphology was unable to be changed. Figure 4.28 presents an SEM of the Zn powder.

The average particle diameter ranges from about 3-15μm with some large particles being visible. However, due to the spherical geometry of each particle, regardless of diameter, no large agglomerates similar to those seen in the unmilled MnO_2 powder are observed.

The composition of the anode ink is presented in Table 4.13. No further adjustments were made since the initial conductivity optimization work done.

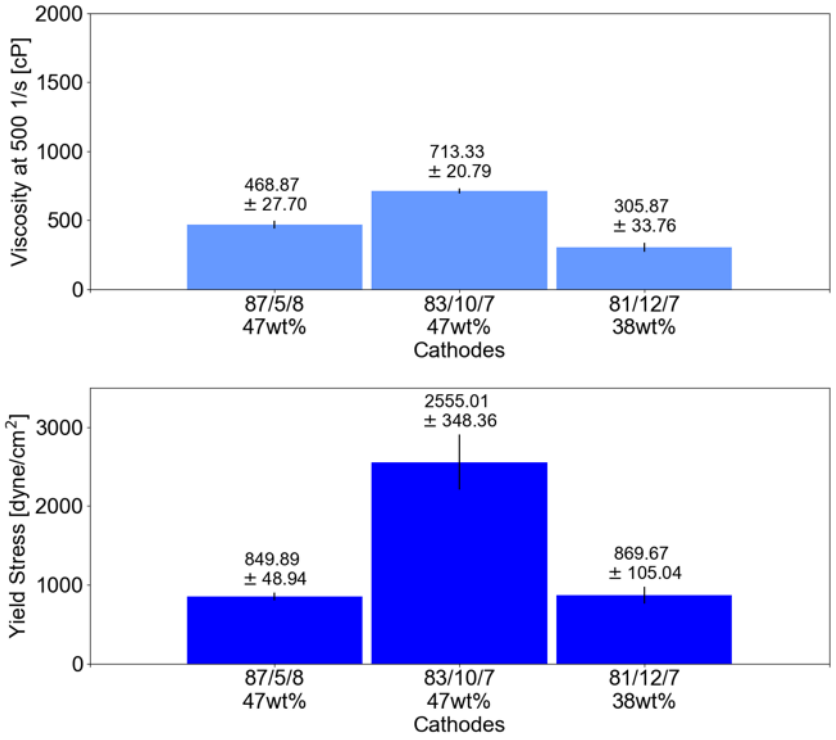

Figure 4.27: Rheology for cathode inks optimized for conductivity.

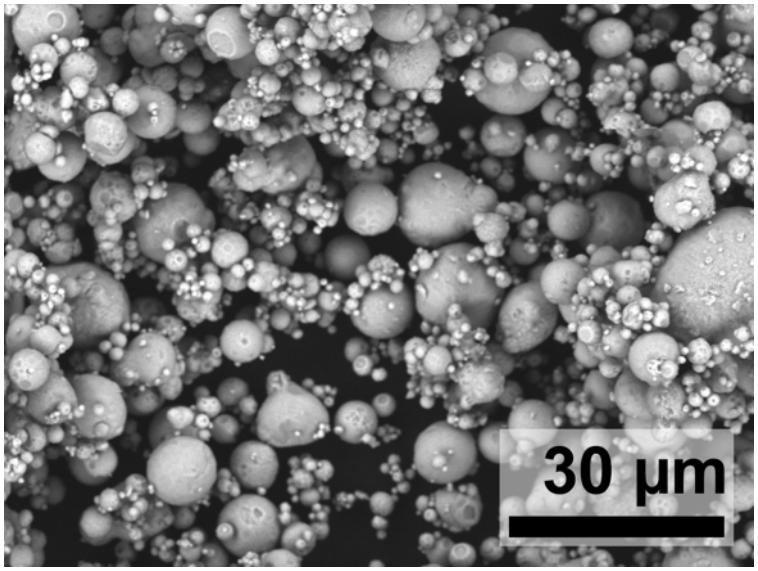

Figure 4.28: SEM image of Zn powder (Alfa Aesar)

Table 4.13: Anode inks composition.

Material	Composition
Zn	91wt%
AB	2.57wt%
PVDF-HFP	6.43wt
Solid Phase	70wt%

Initial profilometry was performed on the conductivity-optimized anode ink to determine profile metrics. Figure 4.29 presents the profilometry scan of the anode ink, and Table 4.14 presents profile statistics. Figure 4.30 presents rheology data for the anode ink.

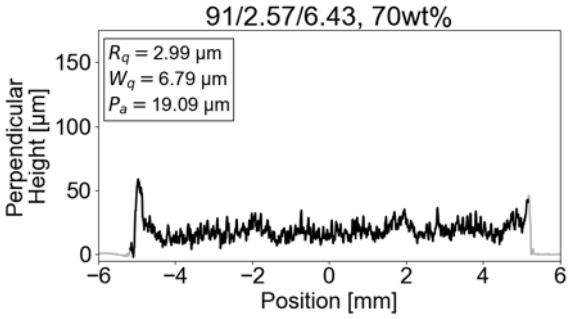

Figure 4.29: Profilometry scan of anode ink, optimized for conductivity and printing.

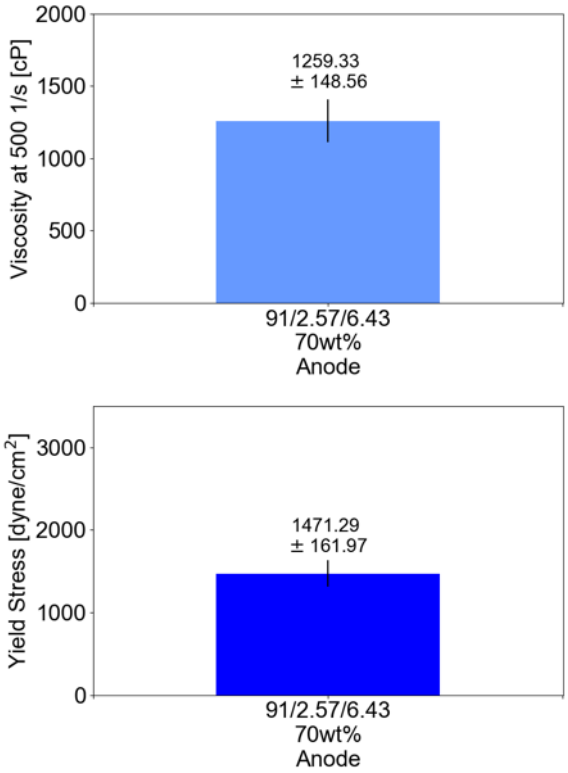

Figure 4.30: Rheology for anode ink. Metrics are labeled by weight percent of Zn/AB/PVDF-HFP.

Table 4.14: Profile statistics for anode ink.

Doctor Blade Height [μm]	**Casting Speed [mm/s]**	**Roughness, R_q [μm]**	**Waviness, W_q [μm]**	**Thickness, P_a [μm]**	**Sample Size**
		Anode			
100	50	2.968	6.837	23.301	6

While the profile waviness and roughness are worse than the surface profile of the optimized cathode ink (Fig. 4.29), the metrics are better than the unoptimized cathode ink. The ink rheology and print yield (Fig. 4.30) also sit in an accetable range. Because modification of the particle size is not possible, the ink composition is the only factor that can be changed. Since the ink resistivity is already known to be optimized, the decision was made to accept the current anode ink and not develop it further.

4.5 Conclusions

This chapter investigated optimizaton of the cathode and anode inks with respect to conductivity, surface profile, and rheology. All three of these metrics are affected by the ink composition, which includes the solid loadings of the active material, conductive additive, and polymer binder, as well as the active material particle morphology and the solid phase of each ink. Optimizing for only one metric without considering the others can lead to detrimental performance in other metrics.

Initial work found a resistivity minimum corresponding to an acetylene black to PVDF-HFP ratio of 0.4:1. Subsequent work sought to improve the surface profile of the electrodes, focusing primarily on the cathode, using ball milling and sieving as a method to change the active material particle size prior to mixing the ink. It was found that ball milling at 30Hz with 10mm diameter balls for 8 hours with a powder to ball mass ratio of 1:10 produced the best particle size and morphology. Results were further improved by sieving the ball-milled powder with a $45\mu m$ mesh opening. This was due to breaking up agglomerates of particles that were present in the raw powder or were exacerbated by mechanical agitation during powder processing. The profile was characterized by the average waviness and roughness per batch of samples for each ink. Compared to the ink prior to surface profile optimization, the waviness and roughness were reduced by about factor of 10 and 5 respectively.

Throughout the surface profile optimization, the ink's viscosity and yield stress were considered in order to maintain acceptable printing yield per batch of samples. As the particle morphology changed and the volume fraction of active material increased, the ink's viscosity also increased, requiring a change in solid phase to maintain desireable ink rheology.

Surface profile optimization came at the expense of conductivity, so the cathode composition was re-optimized for conductivity in order to reduce the resistivity. This was due to the active material powder consuming a larger volume fraction of the ink after ball milling

and sieving, which inhibited the formation of conductive pathways. The final cathode ink showed waviness and roughness improvements by factors of about 4 each compared to the unoptimized ink.

The particle size of the active material in the anode was unable to be modified due to the excessive deformation and mechanical alloying experienced by the Zn powder during ball milling. However, characterization of the surface profile revealed that the profile of the anode was within an acceptable range without further optimization.

In order to improve this process, alternate methods for breaking up agglomerates should be investigated as sieving was a very manually intense process. Increasing the ball milling time, particularly for the 3mm and 10mm balls, could be one method for achieving similar results with a more manually passive process. The use of other equipment such as a three roll mill or a sonic horn could also prove effective at breaking up particles.

The profilometry characterization method used was not ideal for three-dimensional surfaces as only a one-dimensional scan was able to be taken. This method, while facilitating speedy data acquistion, was unable to truly capture the frequency and density of surface agglomerates as such agglomerates needed to fall directly in the path of the scan in order to be captured. Other surface characterization methods such as laser confocal microscopy may be able to capture a more holistic representation of the surface, though likely at the expense of characterization speed.

Additional optimization could be performed with respect to conductivity and rheology. The final conductivity optimization steps did not consider the ratio of acetylene black to PVDF-HFP in favor of dramatically reducing the resistivity while maintaining an active material fraction of at least 80wt%. Further work should investigate the composition space to minimize the amount of conductive additive and polymer binder used in order to further maximize active material fraction. The solid phase could also be further optimized in order to better tune the final printed layer thickness as well as the yield stress in order to improve sample yield.

Chapter 5

Ionic Liquids and Electrochemical Analysis

This chapter presents findings from electrochemical analysis of ionic liquid electrolytes for use with a Zn-based electrochemical cell. The goals of this work are

1. to empirically determine the diffusivity and ionic conductivity of Zn^{2+} in $[BMIM]^+[OTf]^-$ and $[EMIM]^+[OTf]^-$ for various concentrations of $Zn(OTf)_2$,
2. to characterize the reaction kinetics and reversibility of the Zn/Zn^{2+} redox reaction in an ionic liquid environment, and
3. to gain insight into the stability of repeated Zn deposition and stripping within these ionic liquids.

The electrochemical analytical methods used are cyclic voltammetry (CV), chronoamperometry (CA), and electrochemical impedance spectroscopy (EIS). Some optical microscope images were also taken to observe the evolution of Zn dissolution. CV was used primarily to characterize Zn/Zn^{2+} redox kinetics. CA was also used to characterize Zn/Zn^{2+} redox kinetics as well as to empirically calculate the diffusivity of Zn^{2+}. EIS was used to calculate the ionic conductivity of Zn^{2+} as well as to further characterize redox reactions.

Section 5.1 presents the motivation for the following analysis and material choice. Section 5.2 discusses common degradation products mechanisms of imidazolium-based ionic liquid such as those found this work as well as an overview on mass transport and related properties in an electrolyte. Section 5.3 discusses the theory and application of the electrochemical analytical methods used (CV, CA, EIS). Section 5.4 discusses the experimental methods and procedures used for this work. Section 5.5 presents the findings from electrochemical analysis and optical microscopy. Section 5.6 summarizes these findings and suggests directions for future work.

5.1 Motivation

The goal of this work is to characterize Zn^{2+} transport properties and reaction kinetics within two ionic liquid electrolytes. This is in order to select a stable and high-performing ionic liquid electrolyte for fully printed Zn-MnO_2 electrochemical cells.

The ionic liquids investigated are $[BMIM]^+[OTf]^-$ and $[EMIM]^+[OTf]^-$, and the supporting salt added is $Zn(OTf)_2$. These two ionic liquids were specifically chosen for their inherent high ionic conductivities as well as their prior proven compatibility with Zn/Zn^{2+}. A range of concentrations of $Zn(OTf)_2$ was tested in order to investigate any relationships between additional salt concentration and redox behavior.

In addition to empirically determining values for Zn^{2+} diffusivity and ionic conductivity, the behavior of repeated Zn deposition and dissolution was also investigated to gain insight into repeated cycling of a full electrochemical cell.

The presence of additional charged species from the ionic liquid itself creates an uninvestigated environment for Zn/Zn^{2+} redox reactions. Previous work has demonstrated that favorable Zn deposition occurs within ionic liquid electrolytes [39, 45], but reaction kinetics have not been characterized. Furthermore, deposition and dissolution with repeated cycling as would be expected in a full cell has also not been characterized.

5.2 Background

This section discusses known degration mechanisms of imidazolium-based ionic liquids and mass transport of charged species in an electrolyte. Examination of the mass transport equation provides insight into the significance of characterizing the diffusivity and ionic conductivity of Zn^{2+} in these electrolytes.

5.2.1 Imidazolium Ionic Liquid Degradation

Ionic liquids have been reported to have high electrochemical stability windows, but the degradation mechanisms and products have not been well studied be electrochemical means for individual ionic liquids. For imidazolium-based cations, it has been reported that the length of the N-1 *n*-alkyl substituent (alkyl chains branching off the N-1 position of the imidazolium ring) correlates directly with degradability, with longer alkyl chains correlating with more stable species [92]. Longer alkyl substituents also correlate with the number of possible degradation products, which can include substitution of two hydroxyl groups in the imidazolium ring as well as the substitution of carboxyl, carbonyl, and hydroxyl groups for the methyl groups in the alkyl chain [20]. It has also been reported that 1-butyl-3-methylimidazolium species in particular can be fully degraded via electrochemical means in aqueous solutions [93]. While these studies were performed on ionic liquids in aqueous solutions (which is not the case for the ionic liquids and salts of the present investigation) using advanced oxidation processes or biodegradation mechanisms, there is agreement between

reaction products despite the different methods used, which may give insight to degradation via electrochemical means as well.

5.2.2 Mass Transport

As electrons flow to and from an electrochemical cell, an equal flux of charged species must also flow across the electrolyte in order to preserve electroneutrality across the entire system. The current density in solution is therefore equal to the net flux of charged species i (Eq. 5.1), where $\mathbf{N}_i$ is the flux of ionic species i and z_i is the charge per ion [74].

$$\mathbf{i} = \sum_i z_i F \mathbf{N}_i \tag{5.1}$$

Movement of ions in an electrolyte can be effected by migration (in response to an electric field, Eq. 5.2), diffusion (concentration gradients, Eq. 5.3), and convection (bulk fluid motion, Eq. 5.4). u_i is the mobility of species i, F is Faraday's constant, c_i is the concentration of species i, D_i is the diffusivity of species i, Φ is the potential, and $\mathbf{v}$ is the fluid velocity.

$$\mathbf{N}_{i,migration} = -z_i u_i F c_i \nabla \Phi \tag{5.2}$$

$$\mathbf{N}_{i,diffusion} = -D_i \nabla c_i \tag{5.3}$$

$$\mathbf{N}_{i,convection} = c_i \mathbf{v} \tag{5.4}$$

These three contributions can be summed to describe all mass flux within the electrolyte (Eq. 5.5).

$$\mathbf{N}_i = -z_i u_i F c_i \nabla \Phi - D_i \nabla c_i + c_i \mathbf{v} \tag{5.5}$$

Rearranging terms yields an expression for the current in the electrochemical cell as a result of mass transport (Eq. 5.6).

$$\mathbf{i} = -F^2 \nabla \Phi \sum_i z_i^2 u_i c_i - F \sum_i z_i D_i \nabla c_i + F \mathbf{v} \sum_i z_i c_i \tag{5.6}$$

However, in most small electrochemical cells without appreciable amounts of liquid, convection can be omitted, leaving migration and diffusion as the two drivers of mass transport (Eq. 5.7).

$$\mathbf{i} = -F^2 \nabla \Phi \sum_i z_i^2 u_i c_i - F \sum_i z_i D_i \nabla c_i \tag{5.7}$$

Examining the two groups of terms on the right side of Eq. 5.7, it can be observed that migration is dependent on the mobility of species i (u_i) and that diffusion is dependent on

the diffusivity of species i (D_i). The diffusivity is apparent in Eq. 5.7, and terms within the migration term can be gathered to define the ionic conductivity κ (Eq. 5.20) [74].

$$\kappa = F^2 \sum_i z_i^2 u_i c_i \tag{5.8}$$

Therefore, characterizing both the diffusivity and ionic conductivity of a species i in a solution is paramount to characterizing its performance within an electrochemical cell.

5.3 Electrochemical Methods

This section discusses the theory and application of the electrochemical methods used in this work. The electrochemical analytical methods used to characterize the two ionic liquid electrolytes are cyclic voltammetry (CV), chronoamperometry (CA), and electrochemical impedance spectroscopy (EIS).

5.3.1 Three Electrode Cell

For many electrochemistry experiments, a three electrode cell is the standard setup in order to properly isolate the reaction mechanism of interest. A three electrode cell is comprised of a working electrode, a counter electrode, a reference electrode, and an electrolyte. All three electrodes are in contact with the electrolyte, and the working electrode should be placed close to the reference electrode. For potential-controlled experiments, a potential (which may vary with time) is applied between the working and reference electrodes, and the current response of the working electrode is measured. An equal and opposite current is produced at the counter electrode to complete the circuit. The compositions of the working and counter electrodes should be inert with the system in order to avoid noise from side reactions, so Pt or graphite electrodes are typically used. This setup is schematically represented in Figure 5.1.

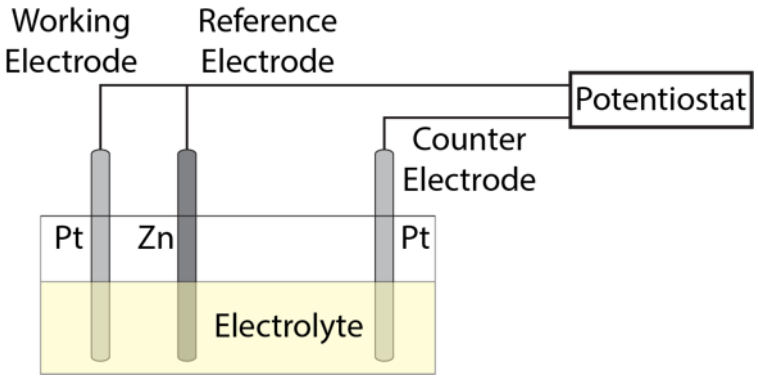

Figure 5.1: Schematic representation of three electrode cell.

The redox reactions of interest take place at the working electrode, so its area should be defined and well controlled. The counter electrode completes the electrical circuit and exists to provide a site for opposite redox reactions to occur. Because both forward and reverse reactions can occur at the working electrode, the surface area of the counter electrode is typically much larger than that of the working electrode in order to minimize any adverse effects of the reverse reaction during the experiment.

For traditional systems, the reference electrode is a well defined redox couple with very fast electrode kinetics and a known reduction potential. However, the majority of commercially available reference electrodes are meant for use in aqueous or traditional non-aqueous electrolytes, and their behavior in ionic liquids is not well understood. In lieu of these options, a pseudo-reference electrode may be used instead, which typically consists of a piece of metal wire or foil with the same composition as the metal whose deposition and dissolution is under investigation.

5.3.2 Cyclic Voltammetry

Cyclic voltammetry (CV) is a standard electrochemical analytical technique in which the potential applied to the working electrode is swept between two potential limits at a constant scan rate. The main advantage of this technique is its ability to easily visualize and provide a wealth of qualitative information about the redox reactions that are occurring.

Figure 5.2 presents an example input voltage and the resulting cyclic voltammogram. The primary parameters that dictate CV are the initial potential (E_0, point A), switching potential (E_λ, point B), and the scan rate (ν). The initial potential is the potential that is first applied between the working and reference electrodes at the beginning of the scan. The scan rate has units of mV/s and is the rate at which the potential is changed. The applied potential is changed at this constant rate until the switching potential is reached. The direction of the scan is then reversed, and the applied potential is changed at the same magnitude of scan rate until the initial potential is reached once more. This process can then be repeated for multiple cycles. The current response at the working electrode is measured throughout this process and current vs. potential plotted on a cyclic voltammogram.

For a three electrode cell, the initial potential is typically the positive limit of the potential window to be scanned. As the potential is scanned towards negative potentials, no redox reactions take place until the reduction potential of the analyte is reached, at which point a cathodic peak characteristic of analyte reduction appears. As the reduction peak grows, analyte immediately near the electrode surface is depleted, and a diffusion layer develops next to the electrode surface which replenishes analyte concentration from the bulk. At the point of maximum current, the rate of analyte consumption is equal to the rate of mass transfer to the electrode. As the potential is scanned further negatively, the measured current decreases as the system becomes mass transfer limited. When the switching potential is reached, the scan direction reverses and the same process occurs at the electrode for the reverse oxidation reaction. Typically, as the scan rate increases, the magnitudes of current for both redox

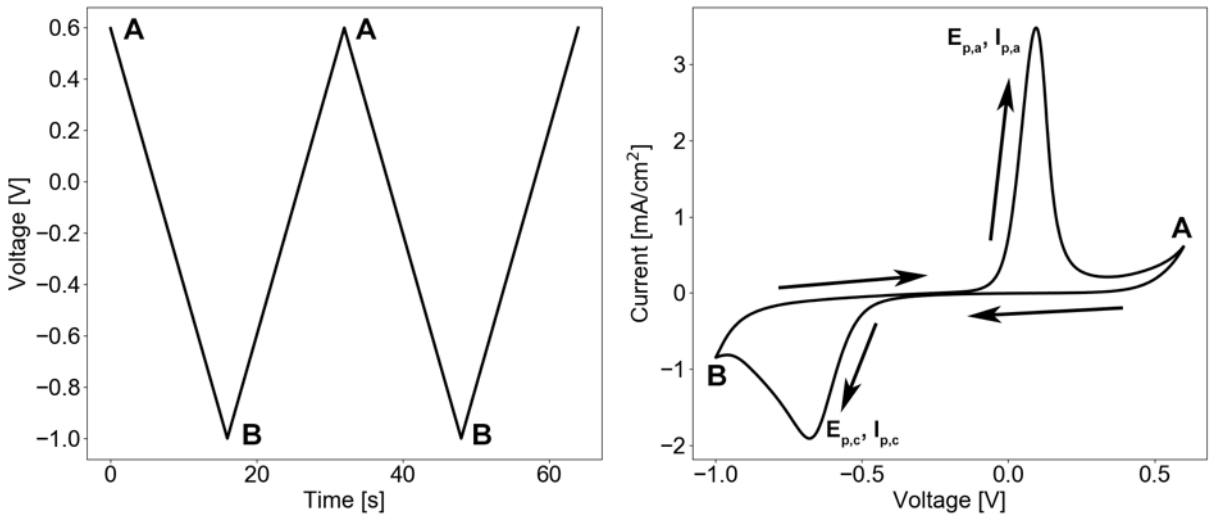

Figure 5.2: *Left*: Potential applied during CV; *Right*: Example cyclic voltammogram.

peaks increase due to less depletion of the diffusion layer at the electrode at higher scan rates.

Key parameters of interest from the cyclic voltammogram are the potential and current values of the cathodic (reduction) and anodic (oxidation) peaks ($E_{p,c}$, $I_{p,c}$ and $E_{p,a}$, $I_{p,a}$ respectively. The separation of the peak potentials, the relative values of the peak currents, and the relationship between the peak potentials and currents with scan rate can provide insight into the reversibility and kinetic values of the redox reaction.

A Nernstian redox couple is defined as a redox couple that exhibits reversible behavior and fast electrode kinetics and therefore follows the Nernst equation (Equation 5.9). U is the cell potential at open circuit, U^{Θ} is the standard reduction potential of the reaction, R is the universal gas constant, T is the temperature, n is the number of electrons involved in reaction, F is Faraday's constant, m_i is the molality of species i, and s_i is the stoichiometric coefficient of species i. The Nernst equation relates the equilibrium potential to the concentrations of reactants and produts. The potential difference between the reduction peak (negative) and oxidation peak (positive), ΔE_p, should be equal to $59/n$ mV at 25° [8] for Nernstian couples. The reactions occuring at the electrodes can be said to diffusion controlled as the rate at which reaction occurs depends solely on the rate of mass transport of the reduced or oxidized species to the electrode surface.

$$U = U^{\Theta} - \frac{RT}{nF} \ln \left(\prod_i m_i^{s_i} \right)_{\text{right}} + \frac{RT}{nF} \ln \left(\prod_i m_i^{s_i} \right)_{\text{left}} \tag{5.9}$$

While the strength of CV lies in its ability to quickly and easily gather qualitative data about a set of redox reactions, some quantitative information can be gathered as well, as-

suming a Nernstian couple. By varying the scan rate and relating it to the resulting peak currents, the diffusivity of the analyte may be calculated. This relationship is described by the Randles-Sevcik Equation (Eq. 5.10), where F is Faraday's constant, R is the universal gas constant, T is temperature, n is the number of electrons involved in the reaction, A is the reaction area, D_O is the analyte diffusivity, C_O is the bulk analyte concentration, and ν is the scan rate. At 25°C, this relationship reduces to Eq. 5.11.

$$i_p = 0.4463 \left(\frac{F^3}{RT}\right)^{1/2} n^{3/2} A D_O^{1/2} C_O^* \nu^{1/2} \tag{5.10}$$

$$i_p = \left(2.69 \times 10^5\right) n^{3/2} A D_O^{1/2} C_O^* \nu^{1/2} \tag{5.11}$$

The key assumptions that provide validity to this relationship are fast electrode kinetics, constant area, and constant bulk concentration. Assuming a Nernstian couple, this therefore requires a robust experimental setup to ensure these criteria are satisfied. Plotting the peak current (i_p) against the square root of the scan rate ($\nu^{1/2}$) results in a straight line whose slope is proportional to the diffusivity of the analyte.

5.3.3 Chronoamperometry

Chronoamperometry (CA) is another potential-controlled electrochemical analytical technique. Instead of gradually changing the applied potential as in CV, a sustained potential step is applied to the electrode and the resulting current response over time is measured. While the current response is still dependent on reaction kinetics, CA allows for the transient response to be investigated and analyzed. An example chronoamperogram is presented in Figure 5.3.

The potential steps chosen for chronoamperometry are typically first identified using a potential sweep method such as CV in order to locate the redox potentials for the system. As seen in the example, multiple potential steps may be performed in succession, corresponding to potentials of separate reduction or oxidation processes. In this instance, a cathodic potential is first applied (Point A), and the current quickly increases to its maximum cathodic current and decays following an inverse square root law to a steady state value. As the current decreases to steady state, the concentration of analyte at the electrode surface is depleted until the reaction rate is completely mass transfer controlled and dictated by the diffusion of species to the electrode surface. Once sufficient time has been allowed for steady state behavior, a second, anodic potential is applied (Point B), and the reverse reaction occurs. Deviations from the inverse square root decay indicate non-Nernstian behavior and can provide insight into reaction kinetics.

Chronoamperometry provides a more quantitative approach to characterizing kinetic parameters. The Cottrell equation (Eq. 5.12) provides another method for calculating the diffusivity of an analyte via the transient current response. On a Cottrell plot, the current

response ($i(t)$) is plotted against the inverse square root of time ($t^{-1/2}$). Again, for a Nernstian process, this results in a straight line whose slope is proportional to the diffusivity of the analyte.

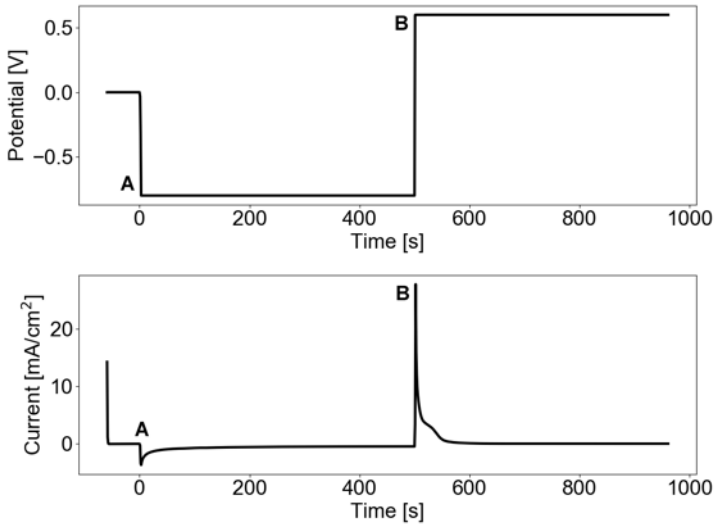

Figure 5.3: *Top*: Potential applied during CA; *Bottom*: Chronoamperometric current response.

$$i(t) = i_d(t) = \frac{nFAD_O^{1/2}C_O^*}{\pi^{1/2}t^{1/2}} \tag{5.12}$$

5.3.4 Electrochemical Impedance Spectroscopy

Electrochemical impedance spectroscopy (EIS) is an AC analytical method in which a low amplitude alternating potential input is applied to an electric component or an electrochemical cell and its current response measured. The resulting current response can be analyzed and correlated to various circuit elements to represent the electrochemical cell as an equivalent circuit whose components represent various physical phenomena. For electrochemical systems, EIS provides a non-destructive characterization method that offers insights that other electrochemical analytical methods may not be able to provide.

The applied AC potential can be represented as a sine wave as in Eq. 5.13, where E_t is the potential at time t, E_0 is the amplitude of the signal, and ω is the radial frequency described by $\omega = 2\pi f$ with f being the frequency of the applied potential.

$$E_t = E_0 \sin(\omega t) \tag{5.13}$$

The potential amplitude is typically small (around 10mV) in order to produce a pseudolinear response whose frequency is equal to the input but shifted in phase. This current response can therefore be described by Eq. 5.14, where I_t is the current response at time t, I_0 is the current amplitude, and ϕ is the phase shift. Figure 5.4 presents an example AC potential input and the resulting phased shifted AC current response plotted against time.

$$I_t = I_0 \sin(\omega t + \phi) \tag{5.14}$$

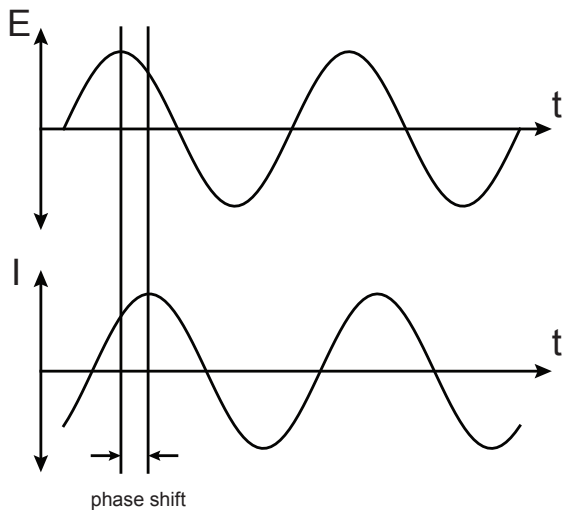

Figure 5.4: Applied AC potential and AC current response.

The impedance of the system can then be calculated by Ohm's Law for impedance, where Z_0 is the impedance magnitude (Eq. 5.15) [40].

$$Z = \frac{E_t}{I_t} = \frac{E_0 \sin(\omega t)}{I_0 \sin(\omega t + \phi)} = Z_0 \frac{\sin(\omega t)}{\sin(\omega t + \phi)} \tag{5.15}$$

Using Euler's relationship (Eq. 5.16), the impedance can be expressed as complex function (Eq. 5.17).

$$e^{j\phi} = \cos(\phi) + j \sin(\phi) \tag{5.16}$$

$$Z(\omega) = \frac{E}{I} = Z_0 e^{j\phi} = Z_0(\cos(\phi) + j \sin(\phi)) \tag{5.17}$$

Finally, Z_0 and ϕ can be calculated via geometric analysis from the Lissajous plot (Figure 5.5) by Eq. 5.18 and Eq. 5.19 respectively.

$$|Z_0| = \frac{\Delta E}{\Delta I} = \frac{OA}{OB} = \frac{\Delta Y}{\Delta X} \tag{5.18}$$

$$\phi = \sin^{-1}\left(-\frac{OD}{OA}\right) \tag{5.19}$$

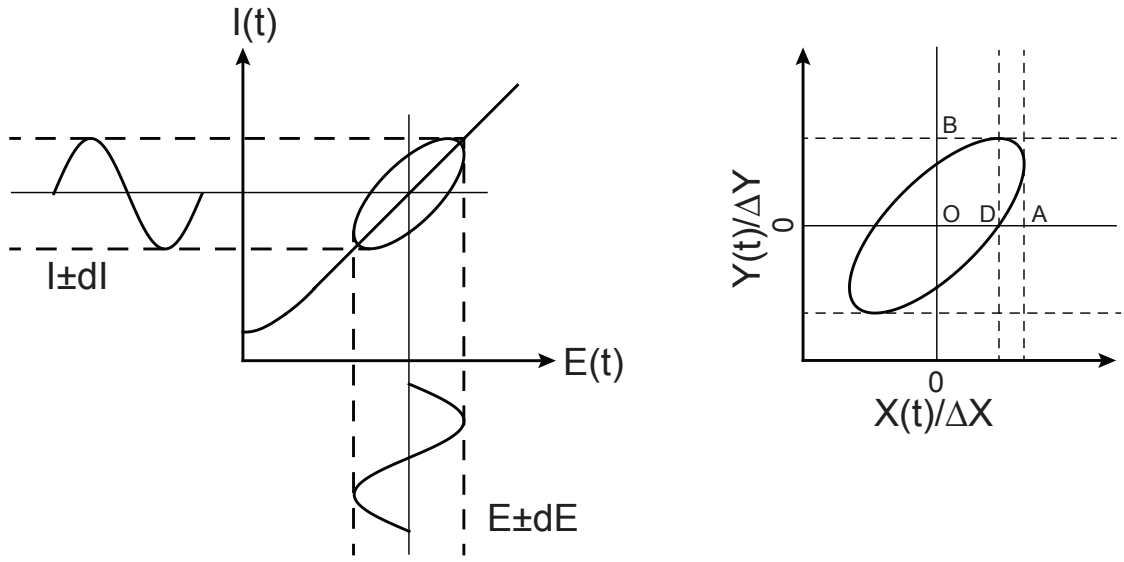

Figure 5.5: *Left*: Lissajous plot from AC potential and current; *Right*: Lissajous analysis

EIS is commonly used to find an appropriate equivalent circuit model with which to model an electrochemical cell. The equivalent circuit model is typically composed of common circuit elements whose values correspond to physical parameters that may be present in the cell. While discretion must be used with higher order models in order to ensure physical meaning is preserved, simpler models can still reveal useful information about the electrochemical system. Behavior captured by higher frequencies on the Nyquist plot of the real and complex parts of the impedance are typically easier to represent with simpler models. Specifically, the solution resistance (R_{sol}) can be determined by the zero intercept with the real axis at high frequencies, and the charge transfer resistance (R_{ct}) can be determined the real axis intercept of a semicircular fit at lower frequencies. Figure 5.6 presents an example Nyquist representation of impedance for an electrochemical cell with mixed kinetic and mass transfer control, modeled by the circuit in Figure 5.7. The included circuit elements are a series resistor representing the solution resistance (R_{sol}), a parallel capacitor representing the double layer capacitance (C_{dl}), and a parallel resistor and Warburg element in series which represent the charge transfer resistance (R_{ct}) and diffusion elements (W) respectively.

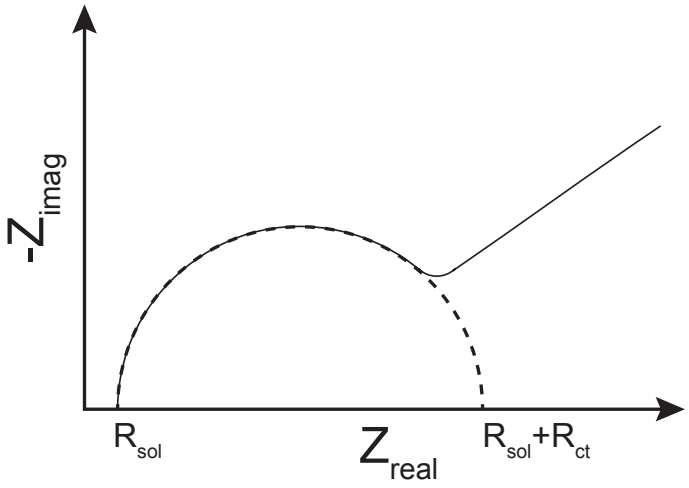

Figure 5.6: Example Nyquist plot for mixed kinetic and charge transfer control.

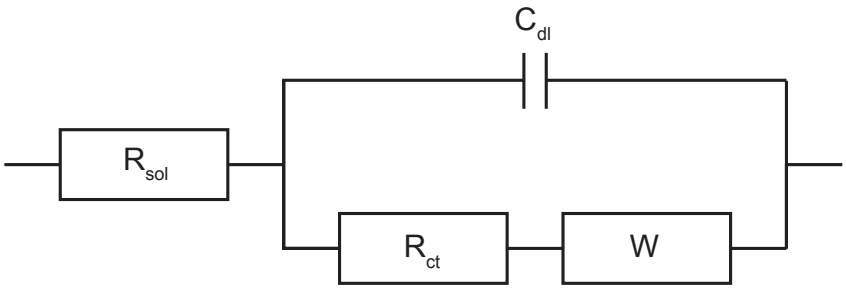

Figure 5.7: Equivalent circuit model for mixed kinetic and charge transfer control.

With an empirically determined solution resistance, the ionic conductivity, σ, can therefore be calculated via Eq. 5.20, where t is the separation between the two electrodes and A is the electrode surface area. This equation is valid for an electrolyte volume of uniform cross-section with parallel electrodes on each end, so some assumptions must be made for application with a three electrode cell, as discussed later.

$$\sigma = \frac{t}{R_{sol} A} \tag{5.20}$$

5.4 Experimental Methods

This section discusses the experimental procedures and setups used in this work.

5.4.1 Electrolyte Preparation

The ionic liquids investigated for this work were 1-butyl-3-imidazolium trifluoromethanesulfonate ($[BMIM]^+[OTf]^-$, Iolitec) and 1-ethyl-3-imidazolium trifluoromethanesulfonate ($[EMIM]^+[OTf]^-$, Iolitec). The zinc salt used was zinc trifluoromethanesulfonate ($Zn(OTf)_2$, Sigma-Aldrich). All materials were reported as having 99.9% purity. The zinc salt concentration was varied between $0.1m$, $0.2m$, $0.3m$, and $0.4m$, depending on the tests being run. Concentrations of $0.4m$ were only tested for $[BMIM]^+[OTf]^-$ because the concentration of salt exceeded the solubility limit for $[EMIM]^+[OTf]^-$. Table 5.1 summarizes all of these concentrations and relates the concentrations in molality to the molarity for each ionic liquid and to the mass ratios between the salt and ionic liquid.

Table 5.1: Electrolyte salt concentrations

Molality [mol/kg]	**Molarity, BMIM [mol/L]**	**Molarity, EMIM [mol/L]**	**Mass Ratio of Salt to Ionic Liquid**
0.1	0.1292	0.1387	1:27.510
0.2	0.2584	0.2774	1:13.754
0.3	0.3876	0.4161	1:9.170
0.4	0.5168	–	1:6.877

All material was prepared in an argon glove box (VAC Systems) in order to minimize the presence of oxygen or water. The zinc salt was first measured out by mass and added to a 20mL glass vial. The ionic liquid was then pipetted into the vial, and the mixture was heated at 80° until all of the salt dissolved, typically 24 hours. Once the entirety of the salt was dissolved, the solution was removed from the heat and allowed to cool back to room temperature before being added to the electrochemical cell via pipette.

5.4.2 Electrode Preparation

The working and counter electrodes were made from a length of platinum wire. In order to control the surface area of the working electrode, a potting procedure using chemically inert epoxy was followed.

For the working electrode, A 5cm piece of 500Âţm diameter platinum wire (Alfa Aesar) was cut with snips, and 2-3cm of one end was coated with Loctite 1C Epoxi-Patch Hysol epoxy adhesive. This specific epoxy was chosen for its chemical inertness and established use in electrochemical applications [22]. The epoxy was allowed to cure for three days to ensure full curing. The coated end was then sanded by hand first on 800 grit polishing paper

and then on 4000 grit polishing paper to obtain a mirror-smooth finish. Care was taken to polish only in one direction per grit to ensure an even surface. The electrode was then rinsed with acetone and sonicated for 1 minute in deionized water to remove any debris left from the polishing process. Following this procedure yielded a repeatable method to prepare a Pt microelectrode with a nominal surface area of $0.00196 cm^2$.

One possible source of unreliability with the hand polishing method used can come from the angle of the electrode relative to the polishing surface. However, Figure 5.8 presents the percent area deviation from perfectly perpendicular as a function of electrode angle. This area was found by calculating the area of the resulting cross-sectional ellipse as the angle of the slice through the cylindrical wire was changed. It was found that angles of greater than 5% were obvious during the process, so the average deviation from ideality was less than 0.5%.

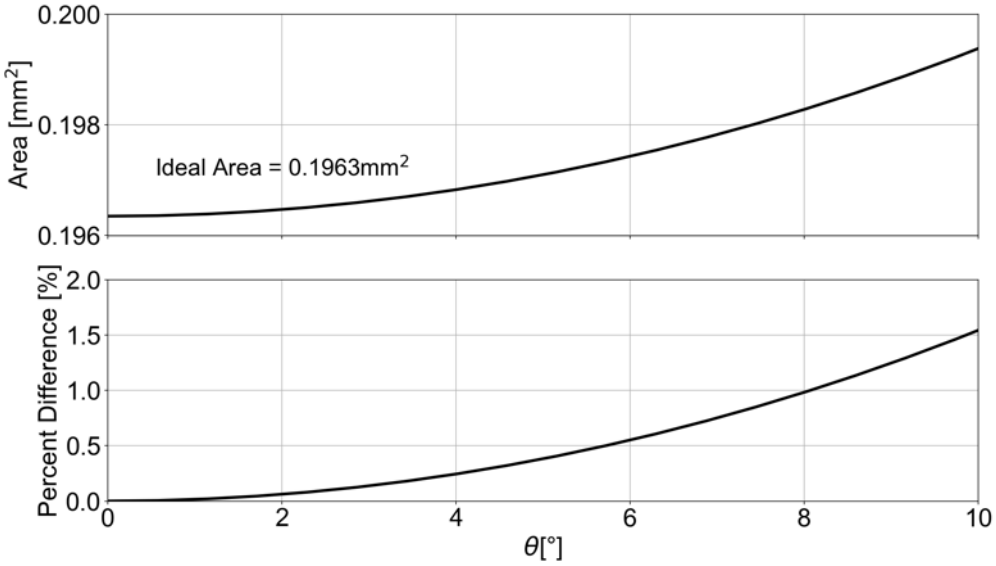

Figure 5.8: Deviation from ideality or Pt working electrode area

For the counter electrode, a similiar 5cm piece of the same Pt wire was cut, but the epoxy coating procedure was not followed. This was to ensure that the surface area of the counter electrode present in the electrolyte during testing was greater than that of the working electrode.

For the reference electrode, a piece of Zn 500Âţm diameter zinc wire (Alfa Aesar) was used as a pseudo-reference electrode. No coating procedure was followed for the zinc wire, again to ensure that ample surface area was in contact with the electrolyte solution.

The electrodes were reused for all tests, with the exception of the Zn reference electrode. To clean the working electrode, the prepared end was rinsed with acetone, polished with

the same grits of polishing paper as previously described, and again sonicated for 1 minute in deionized water. To clean the counter electrode, the exposed end in contact with the electrolyte was rinsed with acetone, polished with a strip of 4000 grit polishing paper, and also sonicated for 1 minute in deionized water. For the reference electrode, the exposed end was cut off with a pair of snips, and the new end was polished with a strip of 4000 grit polishing paper and rinsed with acetone to remove any oxide layer that may have formed. The reference electrode was replenished with a new piece of wire as necessary.

5.4.3 Three-Electrode Cell

A three-electrode cell (Gamry Instruments) was used for all electrochemical measurements. The three-electrode cell used was specifically designed for assembly inside a glove box and subsequent removal for testing in an ambient atmosphere. The cell was also chosen because it allowed for the use of minimal electrolyte material (1mL per test). The working, counter, and reference electrodes were positioned as shown in Figure 5.9. Care was taken during positioning to ensure that the reference electrode was close to the working electrode and that the electrode positions were similar every time the cell was reassembled.

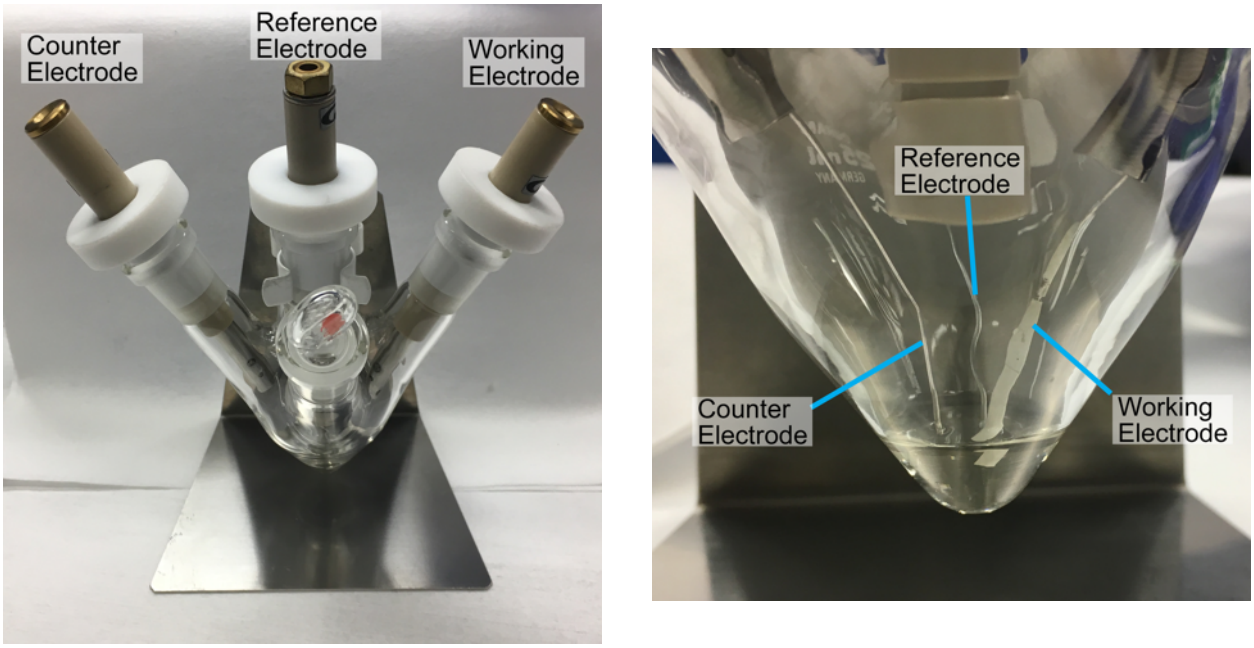

Figure 5.9: *Left*: Three-electrode electrochemical cell used for this work with working, counter, and reference electrodes; *Right*: Close-up of electrodes in contact with electrolyte.

Prior to transferring the cell into the glove box, the cell was first cleaned outside of the glove box. After any material inside was removed via pipette the inside of the cell was rinsed thoroughly with acetone, and a cotton swab was used to clean off any residue on the inside of the cell. The cell was then rinsed once more with acetone and once with isopropyl alcohol.

The inside of the cell was then dried with house compressed air to dry off any residual isopropyl alcohol. The cleaned electrodes were then attached to their holders, and the cell was transferred inside the glove box with the glass stopper removed. The transfer chamber was pumped down to -30PSI vacuum and flushed with argon back to atmospheric pressure three times to remove any adsorbed water and oxygen. The oxygen content of the glove box was maintained at 0.20 PPM of oxygen or lower, and the dew point was maintained at -80°C.

5.4.4 Reference Potentiostat Setup

All electrochemical testing for cyclic voltammetry, chronoamperometery, and electrochemical impedance spectroscopy was performed on a Gamry Reference 600 Potentiostat. The three-electrode cell was placed inside an environmental chamber that maintained an atmosphere of 25° and 0%RH for the duration of testing. The cell was allowed to rest in this environment for 30 minute prior to the start of testing to allow the electrodes and electrolyte to equilibrate with the chamber temperature.

5.4.4.1 Cyclic Voltammetry

Table 5.2 presents typical testing parameters used for cyclic voltammetry experiments. The initial potential (Initial E), final potential (Final E) and second scan limit (Scan Limit 2) were always set equal to each other. The values for the scan limits (Scan Limit 1 and Scan Limit 2) were adjusted depending on whether a neat ionic liquid or a salt and ionic liquid electrolyte was tested. The scan rate and cycle number were adjusted depending on the intended goal of the experiment (short vs. long cycle numbers, effect of scan rate). The step size was chosen based on the file size limits of the data acquisition software.

Table 5.2: Test parameters for cyclic voltammetry (CV) experiments

Setting	Value	Setting	Value
Electrode Area [cm^2]	0.00196	IRComp	None
Initial E [V]	0.6 vs E_{ref}	PF Corr. [ohm]	50
Scan Limit 1 [V]	-1 vs E_{ref}	Equil. Time [s]	5
Scan Limit 2 [V]	0.6 vs E_{ref}	Init. Delay	On
Final E [V]	0.6 vs E_{ref}	Init. Delay Time [s]	60
Scan Rate [mV/s]	100	Init. Delay Stab. [mV/s]	0
Step Size [mV]	5	Sampling Mode	Noise Reject
Cycles [#]	200	Advanced Pstat Setup	On
I/E Range Mode	Auto	Electrode Setup	On
Max Current [mA]	0.5		

5.4.4.2 Chronoamperometry

Table 5.3 presents the typical testing parameters used for chronoamperometry experiments. The pre-step voltage was set with respect to the open circuit potential rather than the reference potential to allow time for the system to come to rest with no redox reactions occurring prior to applying a measured potential step. The values for the first and second potential steps (Step 1 Voltage and Step 2 Voltage) were varied depending on experimental needs. The first potential step corresponds with reduction and the second potential step with oxidation, so the first potential step was set more negatively than the second. The time for which the first potential was applied (Step 1 Time) was also shorter than the time for the second potential (Step 2 Time) to provide more time for oxidation to take place and strip the working electrode of any plated zinc.

Table 5.3: Test parameters for chronoamperometry (CA) experiments.

Setting	**Value**	**Setting**	**Value**
Electrode Area [cm^2]	0.00196	IRComp	None
Pre-step Voltage [V]	0 vs E_{OC}	PF Corr. [ohm]	50
Pre-step Delay Time [s]	60	Equil. Time [s]	5
Step 1 Voltage [V]	-0.8 vs E_{ref}	Init. Delay	On
Step 1 Time [s]	500	Init. Delay Time [s]	100
Step 2 Voltage [V]	0.4 vs E_{ref}	Init. Delay Stab. [mV/s]	0.1
Step 2 Time [s]	600	Sampling Mode	Noise Reject
Sample Period [s]	1	Advanced Pstat Setup	On
Decimate	On	Electrode Setup	On
I/E Range Mode	Auto		
Max Current [mA]	100		
Limit I [mA/cm^2]	100		

5.4.4.3 Electrochemical Impedance Spectroscopy

Table 5.4 presents the typical testing parameters used for EIS experiments. The frequency limits tested (Initial Freq. and Final Freq.) were chosen based on the testing limits of the reference potentiostat.

Table 5.4: Test parameters for electrochemical impedance spectroscopy (EIS) experiments.

Setting	Value	Setting	Value
Initial Freq. [Hz]	1e6	Conditioning	Off
Final Freq. [Hz]	1e-1	Init. Delay	On
Points/decade	10	Init. Delay Time [s]	100
AC Voltage [mV rms]	10	Init. Delay Stab. [mV/s]	0
DC Voltage [V]	0 vs E_{OC}	Estimated Z [ohms]	100
Area [cm^2]	0.00196	Optimize for	Normal

5.4.5 Optical Microscopy

Optical microscope images were taken of the working electrode surface in some cases to investigate zinc dissolution during chronoamperometry. The working electrode was carefully rinsed with acetone to remove any electrolyte clinging to the electrode, being careful not to damage the surface microstructure. The Pt wire was bent to roughly a 135° angle in order to minimize stress to the metal. The bent wire was then mounted on a glass slide at approximately at 45° on a glass slide using putty as a mount.

Images were captured using a Nikon Intensilight C-HGFI microscope camera. Since the high level of optical magnification made it difficult to align the electrode surface perfectly parallel with the magnification lens, a series of images was captured with each image focusing on one band of the electrode surface at a time. These images were then digitally combined to form a composite image with the entirety of the electrode surface in focus.

5.5 Results and Discussion

This section discusses the empirical results gathered from electrochemical analysis and their findings. Aside from initial CV performed on the neat ionic liquids, the salt concentrations for each respective experiment follow the concentrations specified in Table 5.1.

5.5.1 Neat Ionic Liquid

Figure 5.10 presents cyclic voltammograms of neat $[BMIM]^+[OTf]^-$ and $[EMIM]^+[OTf]^-$ taken at 10mV/s with a potential window of -1.0V to 1.0V. These scans were first taken to determine the potential stability window of both neat ionic liquids with no supporting electrolyte present.

Both ionic liquids exhibited small but current peaks on both the forward and reverse scans. These current peaks are small (except for the first cycle, less than 0.1 mA/cm^2) when compared to the peaks observed with the addition of the zinc triflate salt, and may be due to reduction and oxidation of impurities in the ionic liquid. The smaller peaks observed with $[EMIM]^+[OTf]^-$ suggests it may contain fewer impurities than in $[BMIM]^+[OTf]^-$.

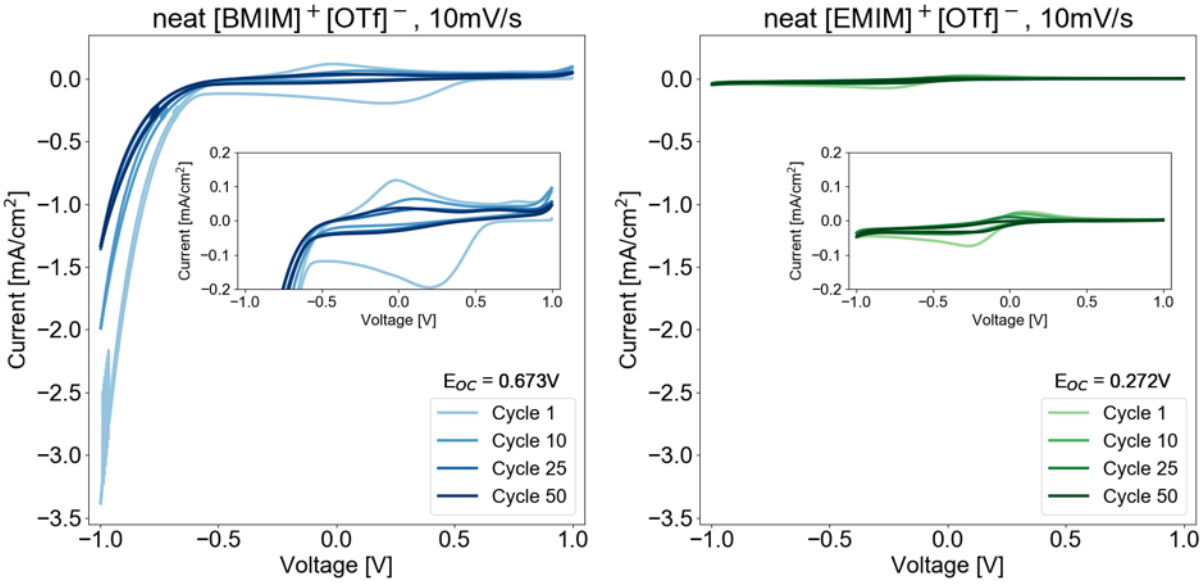

Figure 5.10: Cyclic voltammograms of neat $[BMIM]^+[OTf]^-$ and $[EMIM]^+[OTf]^-$.

$[BMIM]^+[OTf]^-$ exhibited a high negative current tail at negative potentials beginning around -0.6V, and the magnitude of this tail decreased with increasing cycle number. This indicates some initial breakdown of the charged species that compose the ionic liquid, the concentration of which depletes with continued cycling. The presence of this tail on the reduction scan suggests some breakdown of the $[BMIM]^+$ cation or reduction of impurities.

Work by Stepnowski, *et. al.* reports a general positive correlation between N-1 n alkyl chain length and ion stability (ions with longer alkyl chains are more stable) [92]. While the absence of a similar tail with $[EMIM]^+[OTf]^-$ contradicts this correlation, there may be other factors that affect relative stabilities of each ionic liquid.

5.5.2 Cyclic Voltammetry

Figure 5.11 presents cyclic voltammograms of $[BMIM]^+[OTf]^-$ with $Zn(OTf)_2$ with 0.1, 0.2, 0.3, and $0.4m$ concentrations. Scan rates of 10, 20, 50, and 100mV/s were tested with a potential window of -1.0 to 0.6V over 50 cycles.

Additional processing was performed on the voltammograms to calculate other metrics. Figure 5.12 presents the nucleation potential (E_N), crossover potential (E_{co}), and nucleation overpotential (η) by cycle for $[BMIM]^+[OTf]^-$ electrolytes. The nucleation potential was determined by taking the zero current intercept of the best fitting line of the rapid increase of cathodic (negative) current during the cathodic scan while scanning towards more negative potentials. This was performed by a custom window-gradient algorithm written in Python. The crossover potential was determined by taking the potential at which the sign of the

current switched from negative to positive on the anodic scan. The nucleation overpotential was determined by taking the difference between the crossover potential and the nucleation potential. Figure 5.13 presents one cycle of CV with the redox behavior marked. The criteria for these potentials were chosen based on the practices found in literature [45, 113].

Figures 5.14 presents the peak separation (ΔE_p), anodic to cathodic current ratio (i_a/i_c), and coulombic efficiency (Q_{ox}/Q_{red}) for $[BMIM]^+[OTF]^-$ electrolytes. The reduction and oxidation charges were calculated by numerical integration of the current responses over their respective time durations. An example of this is presented in Figure 5.15.

Figure 5.16 presents cyclic voltammograms of $[EMIM]^+[OTf]^-$ electrolytes. Figure 5.17 presents the nucleation potential (E_N), crossover potential (E_{co}), and nucleation overpotential (η) by cycle for $[EMIM]^+[OTf]^-$ electrolytes. Figure 5.18 presents the peak separation (ΔE_p), anodic to cathodic current ratio (i_a/i_c), and coulombic efficiency (Q_{ox}/Q_{red}) for $[EMIM]^+[OTF]^-$ electrolytes. $[EMIM]^+[OTf]^-$ electrolytes had $Zn(OTf)_2$ concentrations of 0.1, 0.2, and $0.3m$. Concentrations of $0.4m$ were not tested for $[EMIM]^+[Otf]^-$ due to the solubility limit of the zinc salt being exceeded.

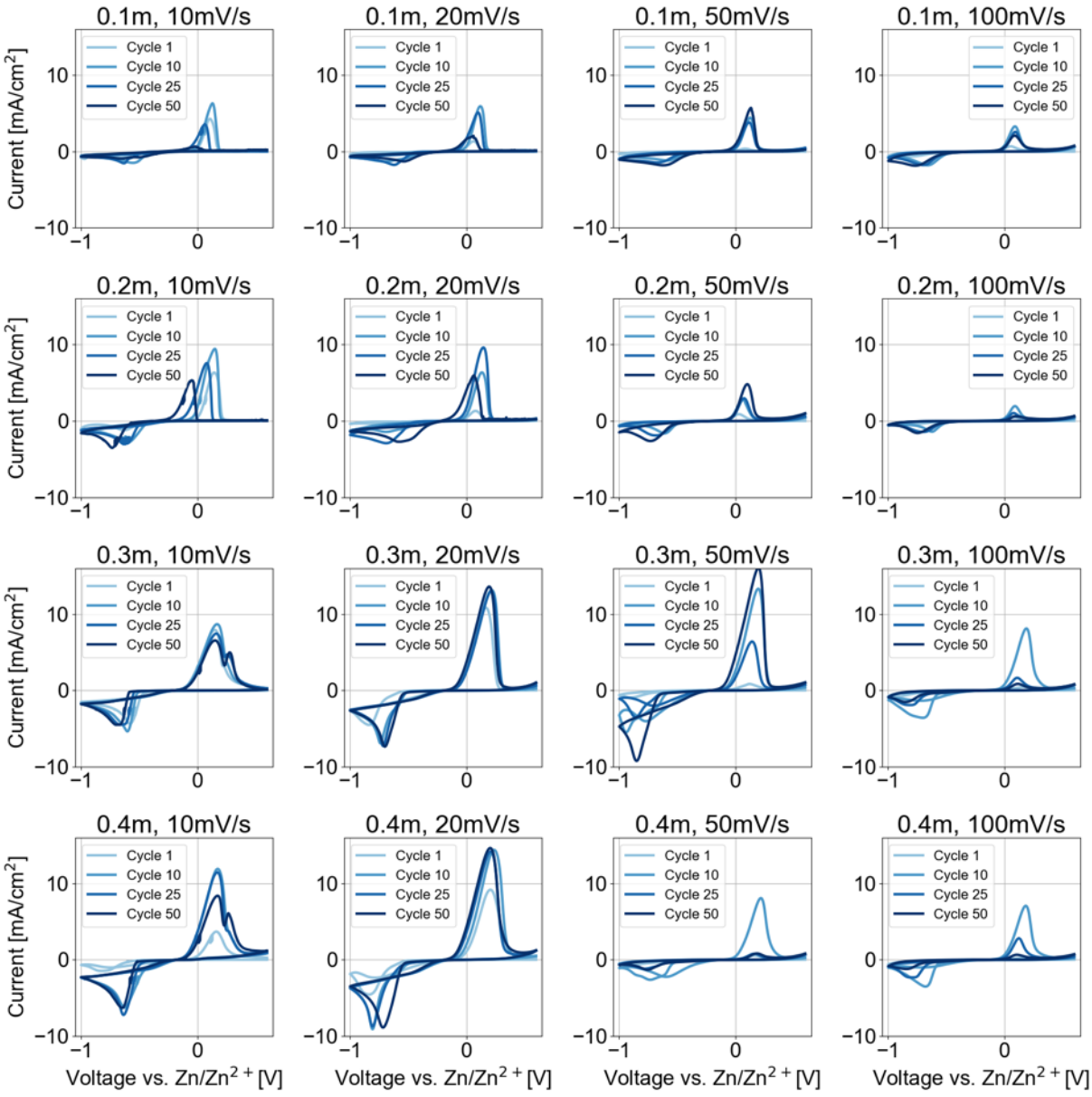

Figure 5.11: Cyclic voltammograms of 0.1, 0.2, 0.3, and 0.4m $Zn(OTf)_2$ in $[BMIM]^+[OTf]$.

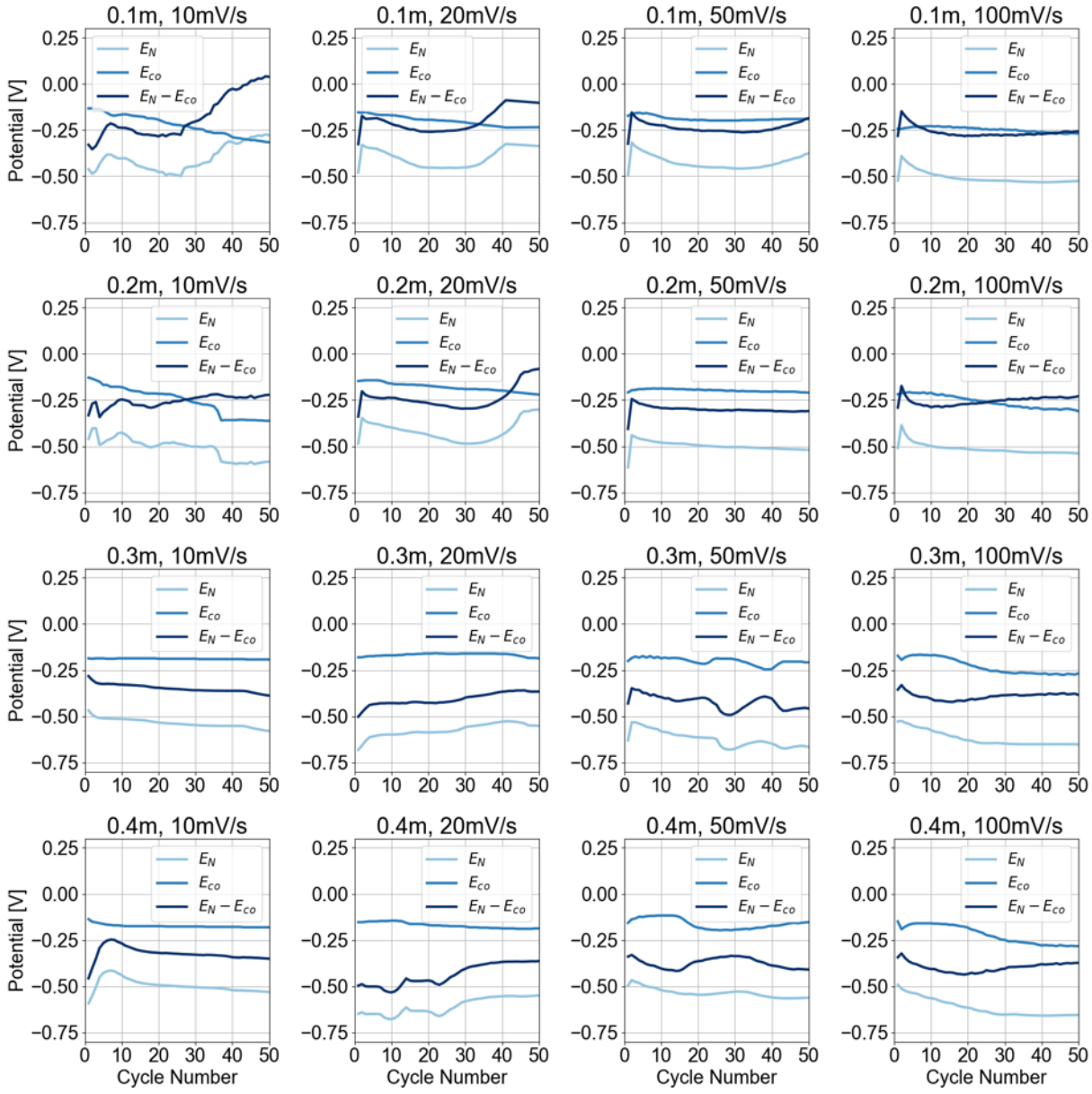

Figure 5.12: Nucleation potential, E_N, and crossover potential, E_{co} by cycle number for tested $[BMIM]^+[Otf]^-$ electrolytes.

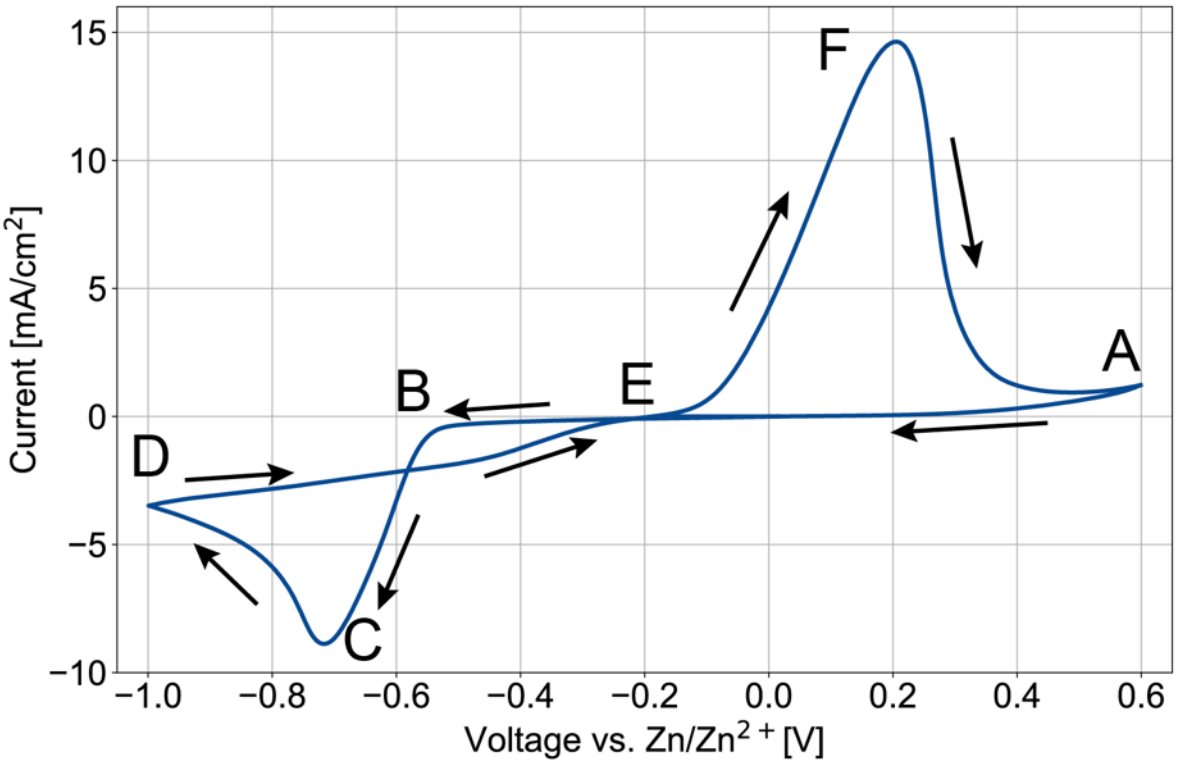

Figure 5.13: Example cyclic voltammogram with points explaining redox reactions.
A-*E*: Potential not yet negative enough for Zn deposition.
B: Nucleation of Zn deposition begins (nucleation potential).
B-*C*: More Zn nuclei and nuclei grow (more area for further Zn deposition).
C: Diffusion of Zn^{2+} from nearby electrolyte starts to limit deposition.
C-*D*: Further depletion of Zn^{2+} from near electrode region, causing current to diminish.
D: Negative sweep of current switches to a positive (anodic) sweep.
D-*E*: Zn deposition continues at a diminishing rate because of Zn depletion from electrolyte near the electrode.
E: Electrode potential switches from deposition (cathodic reaction) to dissolution (anodic reaction) of Zn (crossover potential).
F: Electrolyte near electrode becomes saturated with Zn^{2+}, and diffusion of Zn^{2+} away from the electrode starts to limit reaction.
A: Positive sweep of current switches to a negative (cathodic) sweep.

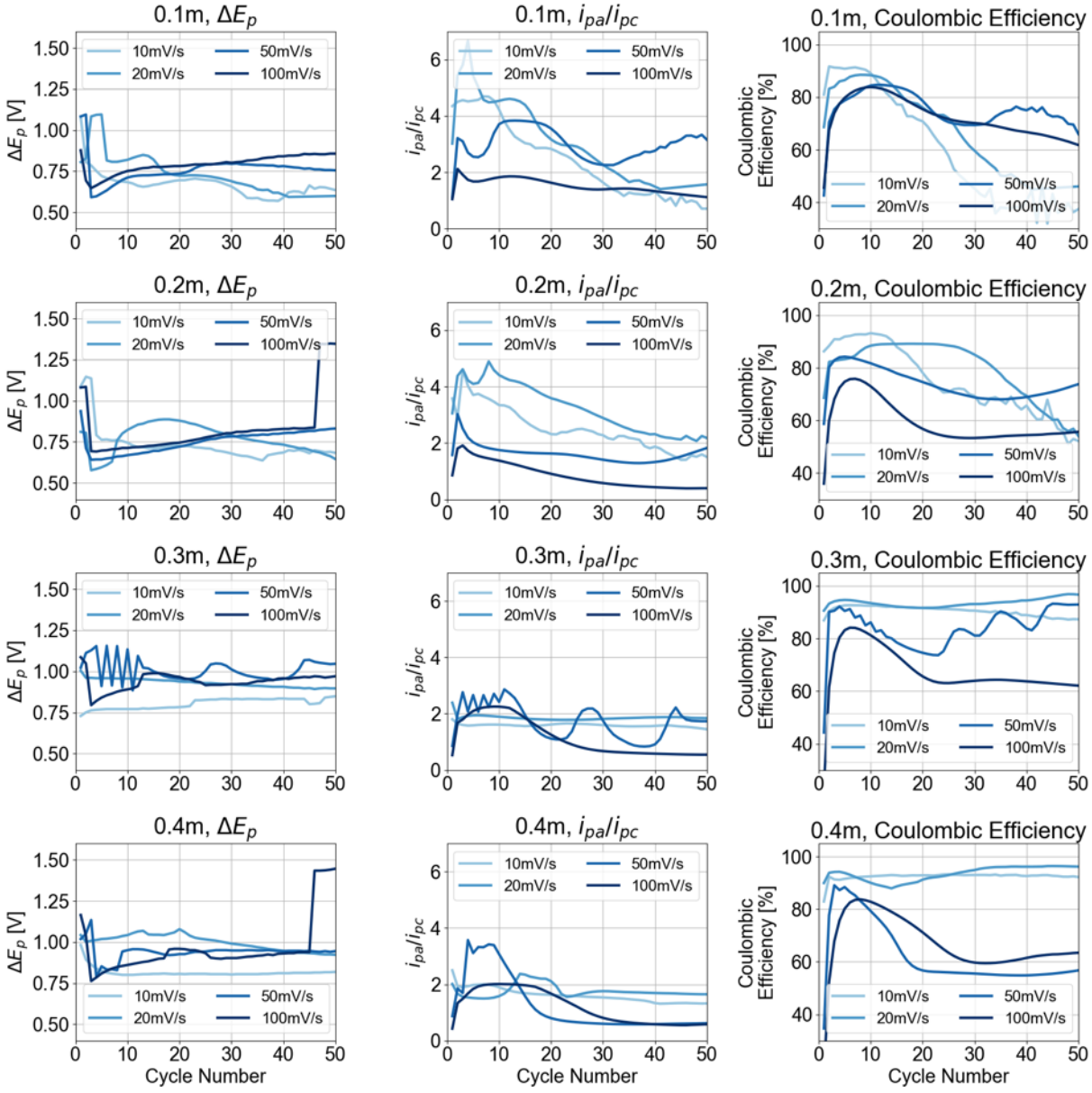

Figure 5.14: Peak separation (ΔE), peak current ratio (i_a/i_c), and coulombic efficiency (Q_{ox}/Q_{red}) by cycle number for $[BMIM]^+[OTf]^-$ electrolytes.

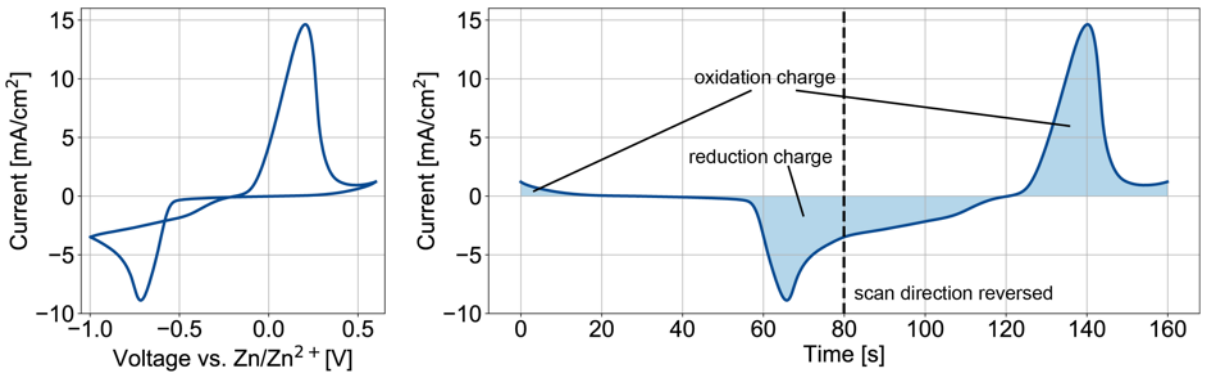

Figure 5.15: Example CV and visual representation of integration of current with respect to time in order to calculate coulombic efficiency (amount of oxidation charge/amount of reduction charge).

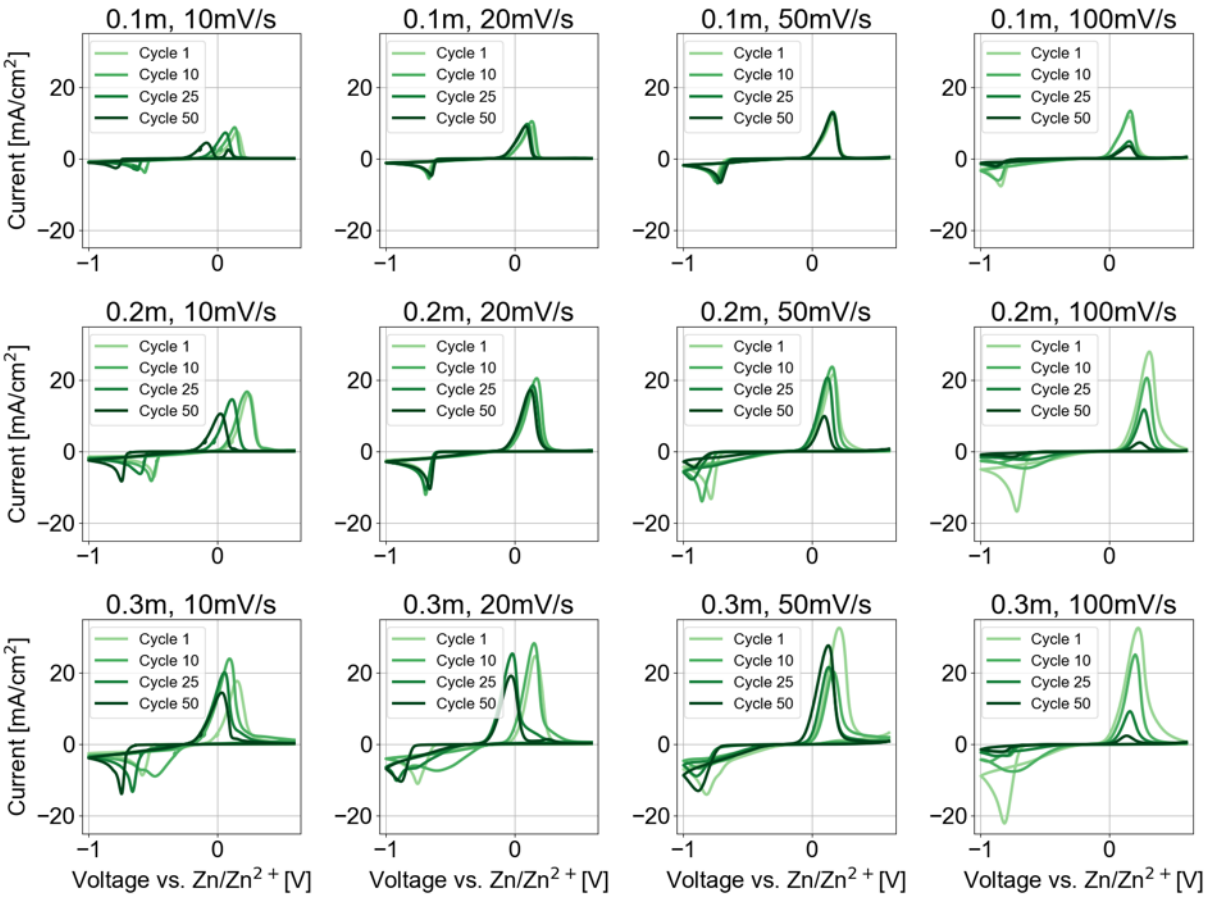

Figure 5.16: Cyclic voltammograms of 0.1, 0.2, and 0.3m $Zn(OTf)_2$ in $[EMIM]^+[OTf]$.

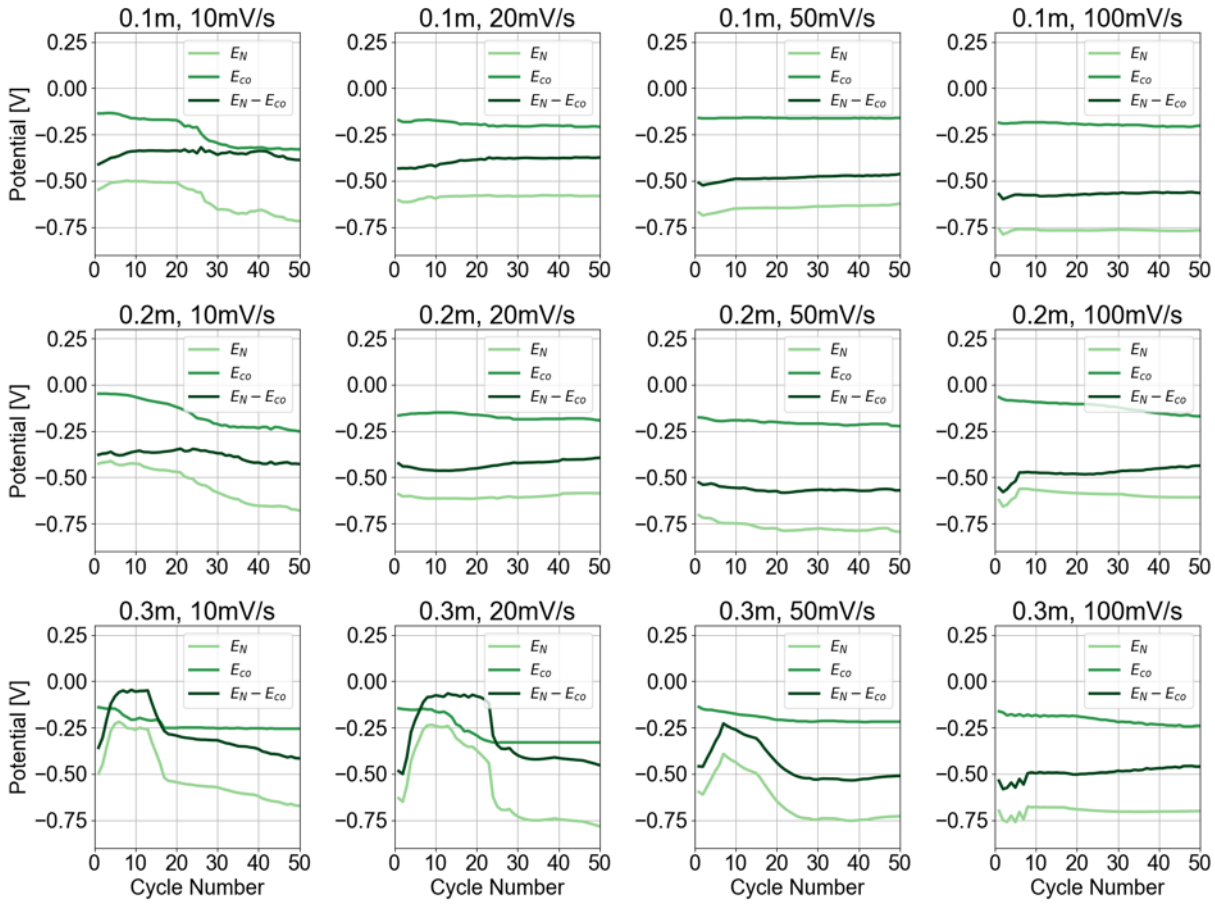

Figure 5.17: Nucleation potential, E_N, and crossover potential, E_{co} by cycle number for tested $[EMIM]^+[Otf]^-$ electrolytes.

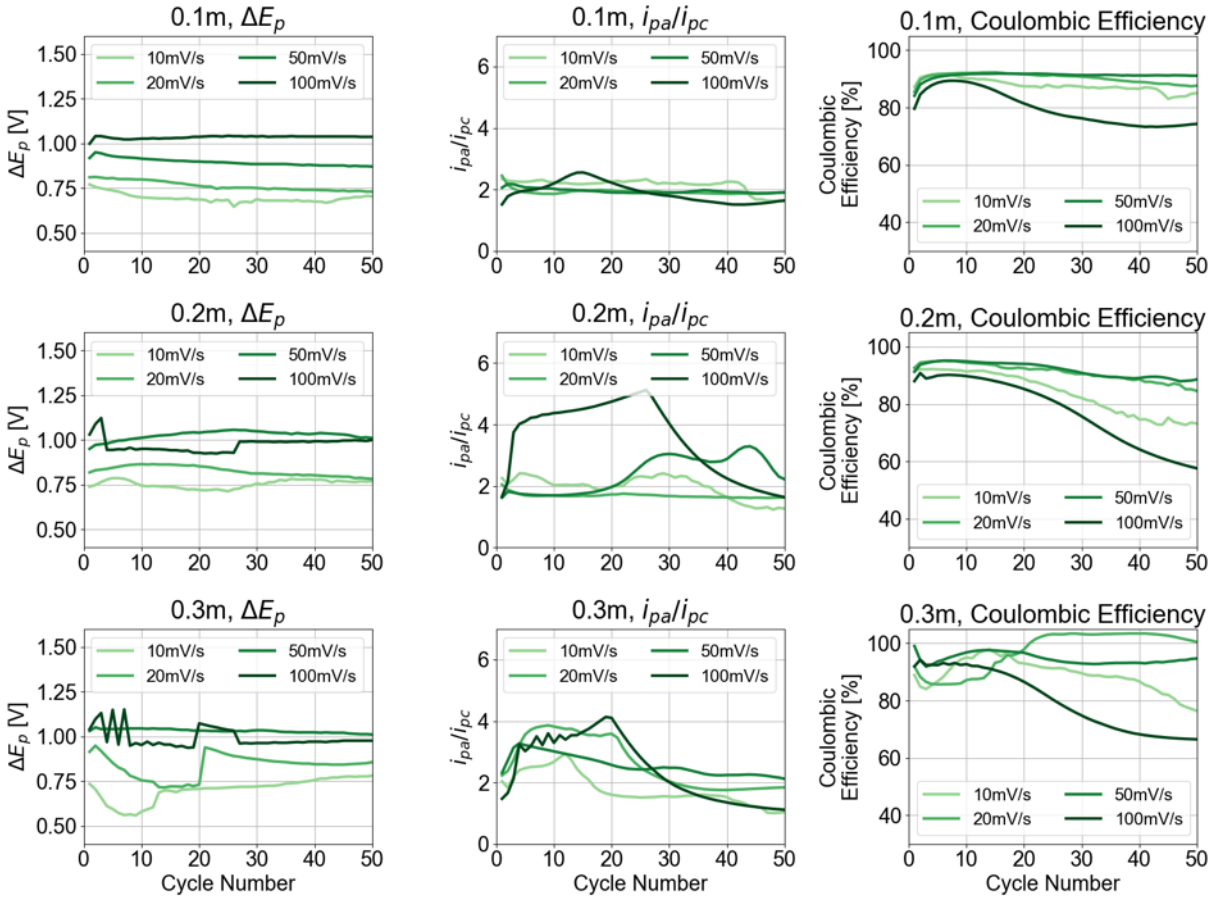

Figure 5.18: Peak separation (ΔE), peak current ratio (i_a/i_c), and coulombic efficiency (Q_{ox}/Q_{red}) by cycle number for $[EMIM]^+[OTf]^-$ electrolytes.

5.5.2.1 Reaction Reversibility and Kinetics

For both ionic liquids and for all concentrations and scan rates, the peak separation varies from 0.6-1.1V. The peak separation is far greater than the potential difference expected for a two-electron Nernstian process (29.5mV), indicating that the redox reactions of Zn/Zn^{2+} taking place within these ionic liquids are not fully reversible. Furthermore, ΔE_p varies with scan rate for both ionic liquids, indicating a quasi-reversible process.

The relative shapes of the reduction and oxidation peaks are not equal, with the oxidation peak being taller than the reduction peak. This higher oxidation peak indicates that dissolution of Zn is a faster process than deposition of Zn^{2+}. Furthermore, for both ionic liquids and for all scan rates, the peak current ratio i_a/i_c equals roughly 2 by 50 cycles. Since this ratio should equal unity for a Nernstian process, this result further indicates the presence of a quasi-reversible process.

Because the Zn^{2+} ion is a divalent ion, it would be expected to observe two peaks in a single scan direction, given the right combination of testing parameters. These dual peaks are only observed with $[BMIM]^+[OTf]^-$ at $0.3m$ and $0.4m$ concentration and with $[EMIM]^+[OTf]^-$ at $0.1m$ concentration at a scan rate of 10mV/s during the oxidation process. CVs of $[BMIM]^+[OTf]^-$ at $0.3m$ concentration and $[EMIM]^+[OTf]^-$ at $0.1m$ concentration are reproduced with the dual peaks directly indicated in Figure 5.19.

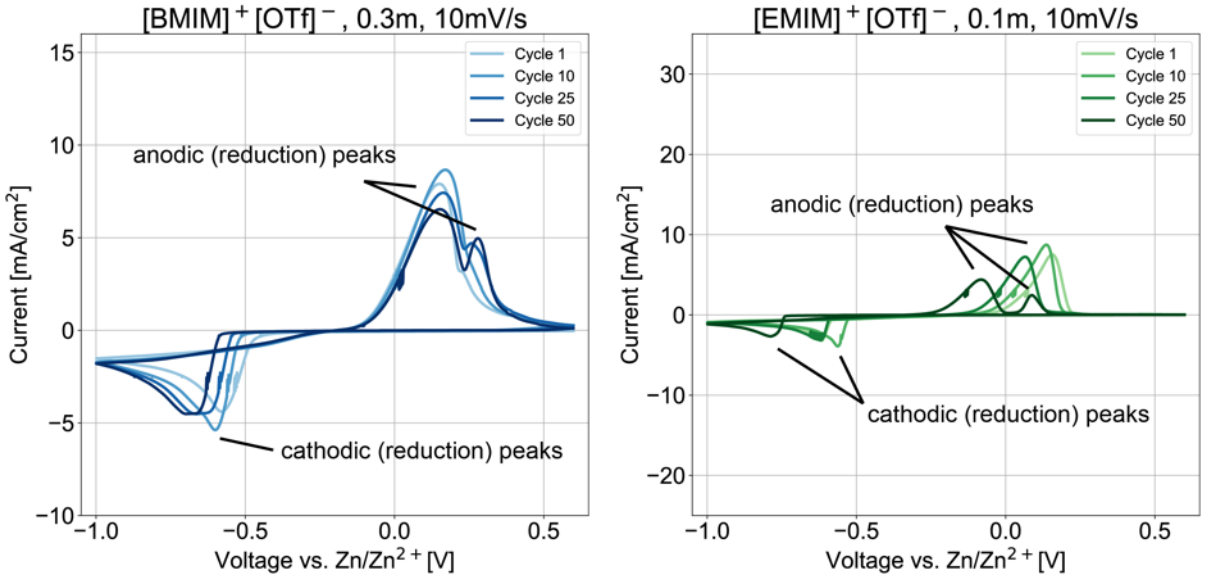

Figure 5.19: CVs of $[BMIM]^+[OTf]^-$ at $0.3m$ concentration and $[EMIM]^+[OTf]^-$ at $0.1m$ concentration. Dual peaks observed during oxidation are indicated.

The mechanism for the reduction of Zn^{2+} can be described as a two step electron transfer process in which a Zn^{2+} ion is first adsorbed onto a surface and then is further reduced to metallic Zn (Equations 5.21 and 5.22). The order of this electron transfer is reversed for Zn oxidation.

$$Zn^{2+}(sol) + e^- \leftrightarrow Zn^{1+}(ads) \tag{5.21}$$
$$Zn^{1+}(ads) + e^- \leftrightarrow Zn(s) \tag{5.22}$$

This reaction mechanism is common for divalent metal ions in which R^{2+} is more highly solvated and stabilized than R^+ [8]. The Zn^{2+} adsorption/desorption step (Equation 5.21) is the rate determining step with this proposed mechanism as supported by the two peak shape of the oxidation scan. Because Zn dissolution occurs in the reverse order as Zn deposition (Eq. 5.22 first, then Eq. 5.21), the first, higher peak corresponds to a faster rate of Zn oxidation from Zn to Zn^{1+} than the subsequent oxidation from Zn^{1+} to Zn^{2+}.

Considering these results, the Zn/Zn^{2+} redox couple exhibits signs of quasi-reversibility due to being kinetically limited rather than being diffusion controlled.

5.5.2.2 Zinc Electrodeposition and Dissolution

From the cyclic voltammograms, the cathodic current corresponds to reduction of Zn^{2+} on the Pt electrode surface while the anodic current corresponds to oxidation of Zn back to Zn^{2+}. A nucleation loop is observed on the reduction scan for all electrolytes, particularly for initial cycles. This phenomenon is well described in literature in which a large initial overpotential is required for initial nucleation and deposition on the electrode surface [113, 45].

For both ionic liquids, the crossover potential generally remained constant or decreased by 50-100mV for the duration of cycling (oxidation was occurring at more negative potentials). The crossover potential was consistent across all concentrations for both ionic liquids at around -200mV.

For $[BMIM]^+[OTf]^-$ electrolytes, there was no clear pattern for the nucleation potential across all tested concentrations and scan rates. A sharp increase from the 1st to 2nd cycle is observed in some cases due to the first cycle involving deposition of Zn onto Pt and subsequent cycles involving deposition of Zn onto further residual Zn. Generally, the nucleation overpotential increased with salt concentration, remaining at around -250mV for $0.1m$ concentrations and at around -350mV for $0.4m$ concentrations.

For $[EMIM]^+[OTf]^-$ electrolytes, the nucleation potential generally either decreased or remained constant throughout cycling, although a temporary high plateau was observed for $0.3m$ concentrations from Cycle 5 to about Cycle 20. The nucleation overpotential was generally more negative than for $[BMIM]^+[OTf]^-$ but seemed to become more negative with increasing scan rate rather than with salt concentration. The nucleation overpotential was around -300mV at 10mV/s and -500mV at 100mV/s.

The large negative nucleation overpotential for both ionic liquids is likely due to a lack of available nucleation sites due to the ionic liquid cation blocking their availability for Zn^{2+} adsorption [77, 112]. Nucleation overpotentials may be more negative for $[EMIM]^+[OTf]^-$ electrolytes due to their smaller ionic liquid cation as a result of the shorter alkyl chain, but this may be inconsistent with nucleation kinetics as discussed later with chronoamperometry results.

5.5.2.3 Effect of Ionic Liquid, Salt Concentration and Scan Rate

Between the two ionic liquids, peak heights were significantly higher with $[EMIM]^+[OTf]^-$ electrolytes than with $[BMIM]^+[OTf]^-$ electrolytes. This is likely due to the increased Zn^{2+} mobility in $[EMIM]^+[OTf]^-$ due to the shorter alkane chain off the imidazolium complex, which decreases ion-ion interactions due to the smaller size of the ionic liquid cation.

The peak heights also generally increased with increasing salt concentration for both ionic liquids. This is likely due to the increased concentration of charge carriers afforded by the addition of the supporting electrolyte. However, the peak heights decreased or remained constant at $0.4m$ concentration with $[BMIM]^+[OTf]^-$ when compared to $0.3m$ concentration. This may indicate some upper limit of salt concentration that, when exceeded, begins to hinder rather than improve Zn^{2+} transport. Compared to aqueous or more traditional non-aqueous solvents, this low concentration limit may be a result of the significantly larger number of ion-ion interactions due to the charged species that make up the ionic liquid solvent itself.

The difference in trends of initial peak heights between the two ionic liquids is again likely due to the smaller size of the cation due to the size difference between the ethyl and butyl groups off the imidazolium cation. However, the decrease in peak height with cycle number at 100mV/s may be due to the sluggishness of reaction kinetics dominating the effect of decreased diffusion layer thickenss as a result of higher scan rate. Effectively, the adsorption/desorption of Zn^{2+} may be too sluggish to keep up with the rate of Zn^{2+} diffusion dictated by the higher scan rate, pushing the process much closer towards being kinetically-controlled rather than mass transport-controlled in this regime. This would lead to a buildup of species within or near the diffusion layer at the working electrode.

At intermediate salt concentrations and intermediate scan rates (specifically $0.3m$ $[BMIM]^+[OTf]^-$ and $0.2m$ $[EMIM]^+[OTf]^-$ at 20mV/s), some reversible cycling behavior was observed as indicated by near identical hysteresis loops. The presence of this repeatable behavior at low scan rates but not at higher ones is again indicative of a quasi-reversible electron transfer process.

At higher scan rates and salt concentrations, the current at the positive limit during the oxidation scan increases with positive potential, possibly due to some degradation of species in the ionic liquid. Because of the inherent stability of the triflate anion due to its highly delocalized negative charge [23], oxidation of the triflate anion is unlikely. The increase in the magnitude of this positive tail with cycle number suggests that it may be due to oxidation of degradation products of the imidazolium cation that are formed during the reduction scan.

This degradation during the reductive scan may also contribute to low observed coulombic efficiencies, as discussed later.

The applied scan rate affected the observed peak height and location with increasing cycle number. For 10, 20, and 50 mV/s scan rates, the peak heights increased with increasing scan rate as expected due to greater amounts of cation remaining in the diffusion layer at higher scan rates.

However, a number of unexpected results are observed for 100mV/s scan rates for both ionic liquids. For $[BMIM]^+[OTf]^-$, the peak heights for all concentrations are lower than those observed at 50mV/s and all decrease with increasing cycle number. For $[EMIM]^+[OTf]^-$ electrolytes, the initial peak heights follow the expected trend of increasing with increasing scan rate, but subsequent peaks also decrease with increasing cycle number.

For all concentrations and scan rates, the coulombic efficiency (amount of oxidation/amount of reduction) was less than unity and decreased with increasing scan rate. The highest efficiencies (about 90%) were observed for low scan rates (10 and 20mV/s) for 0.3 and $0.4m$ $[BMIM]^+[OTf]^-$ electrolytes and for all concentrations of $[EMIM]^+[OTf]^-$ electrolytes. This behavior is likely due to a build up of plated Zn on the working electrode surface with each cycle and again points to a quasi-reversible process, as reversible behavior is seen at lower scan rates but not at higher ones.

The coulombic efficiency also generally decreased with increasing cycle number, and a scan rate of 100mV/s generally resulted in the lowest coulombic efficiencies. As mentioned above, part of this may be due to degradation of the imidazolium cation of ionic liquid during the reduction scan. This may also be due to loss of electrical contact with deposited Zn due to irregular dissolution. The steady decrease in coulombic efficiency with cycle number indicates a decrease in Zn dissolution compared to Zn^{2+} plating for each cycle. In addition to slow Zn dissolution kinetics, the difference in charge for oxidation versus reduction may be exacerbated by increasing surface area on the working electrode due to persistence of plated Zn. The resulting surface microstructure is very likely irregular, and local differences in surface energy would lead to preferred deposition on lower energy sites, resulting in the formation of rough and non-planar structures [45].

Figure 5.20 presents the coulombic efficiency, difference between reduction charge and oxidation charge, and the change in Zn^{2+} concentration during cycling as a percentage of the initial concentration or $0.2m$ $[BMIM]^+[OTf]^-$. This electrolyte was chosen based on the range of coulombic efficiencies observed. The change in concentration was calculated by measuring the difference in charge, converting to moles of Zn^{2+}, and determining the new concentration at the end of each cycle. More Zn remains undissolved after cycling with slower scan rates, but the total shift in concentration does not exceed 5% of the initial concentration, corresponding to a drop in molality from $0.2m$ to about $0.19m$.

Zinc deposition microstructure in aqueous solutions and ionic liquids has been investigated and for ionic liquids has been shown to be dominated by boulder and layer-like structures, with dendritic growth being largely suppressed with the potentiostatic deposition conditions used. [106, 44, 59, 99]. However, the effect of potential on deposition rate in ionic liquids has not been investigated, and work in aqueous solutions has determined

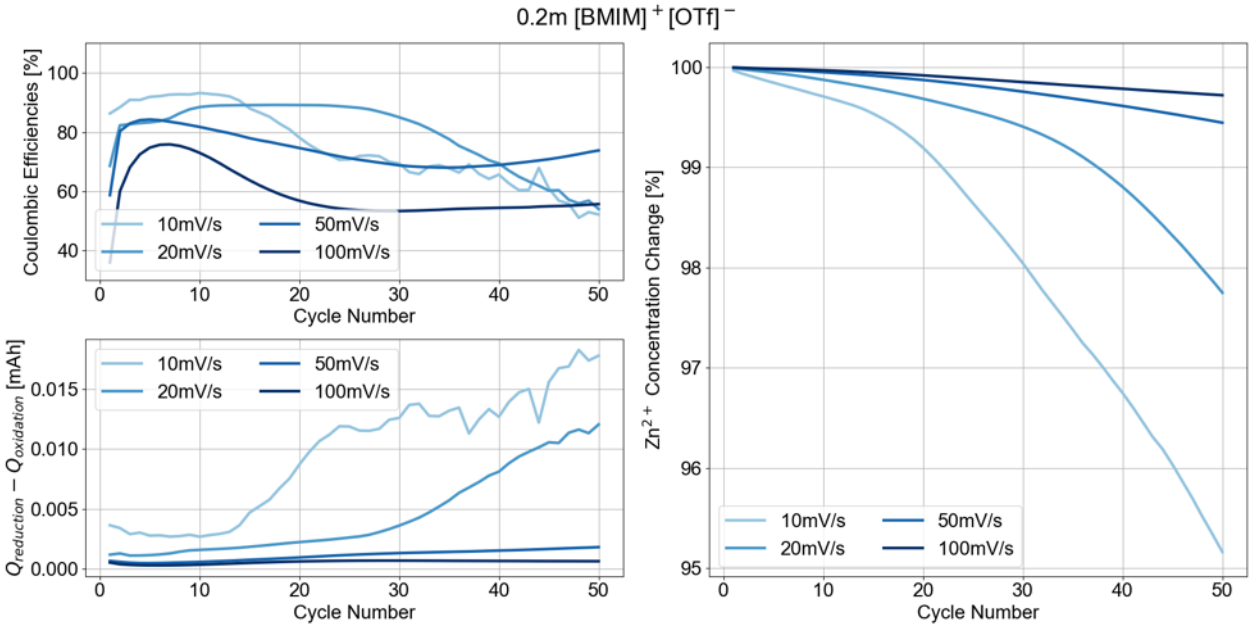

Figure 5.20: Coulombic efficiency, difference in reduction charge and oxidation charge, and Zn^{2+} during cycling of $0.2m$ $[BMIM]^+[OTf]^-$. Original mass of electrolyte used was 1g.

no universal overpotential responsible for dendritic growth alone past a threshold potential required for nucleation [99]. Therefore, while dendritic growth is unlikely, the lowered coulombic efficiencies observed at higher scan rates in this work may be consistent with the preferred formation of higher surface area microstructures.

Finally, other side reactions such as electrolysis of impurities such as water or breakdown of the epoxy coating on the working electrode may be occurring due to the presence of trace contaminants within the cell.

5.5.2.4 Diffusion Coefficient via the Randles-Sevcik Equation

Figures 5.21 and 5.22 present application of the Randles-Sevcik equation to the obtained CV data for $[BMIM]^+$ and $[EMIM]^+$ electrolytes respectively. The purpose of this analysis was to determine the diffusion coefficient of Zn^{2+} in both ionic liquids at various salt concentrations. Because of the unexpected behavior in peak heights at $\nu = 100$mV/s, data collected at that scan rate was not used in finding a linear fit.

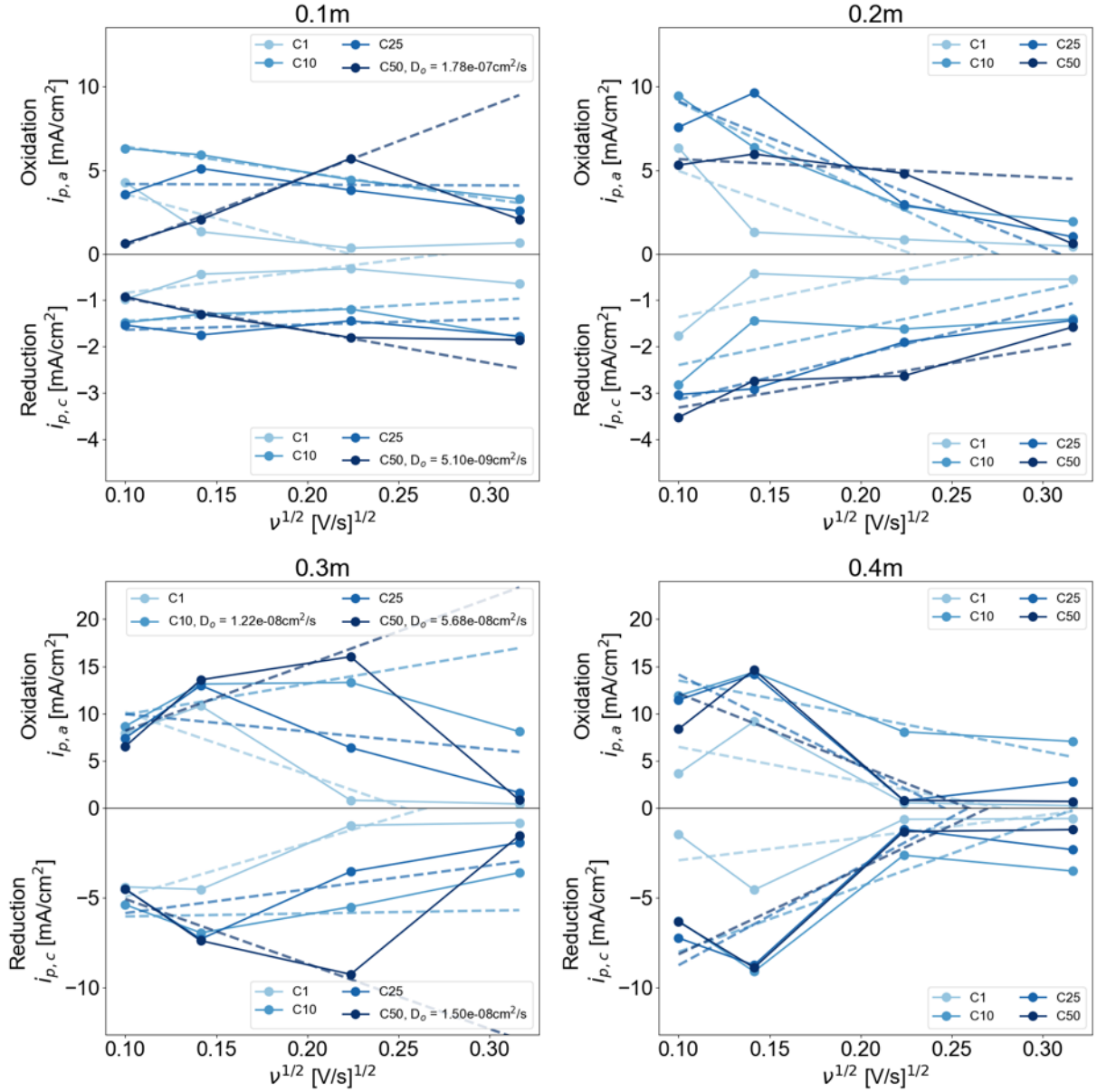

Figure 5.21: Application of Randles-Sevcik equation to CV data for $[BMIM]^+[OTf]^-$ electrolytes.

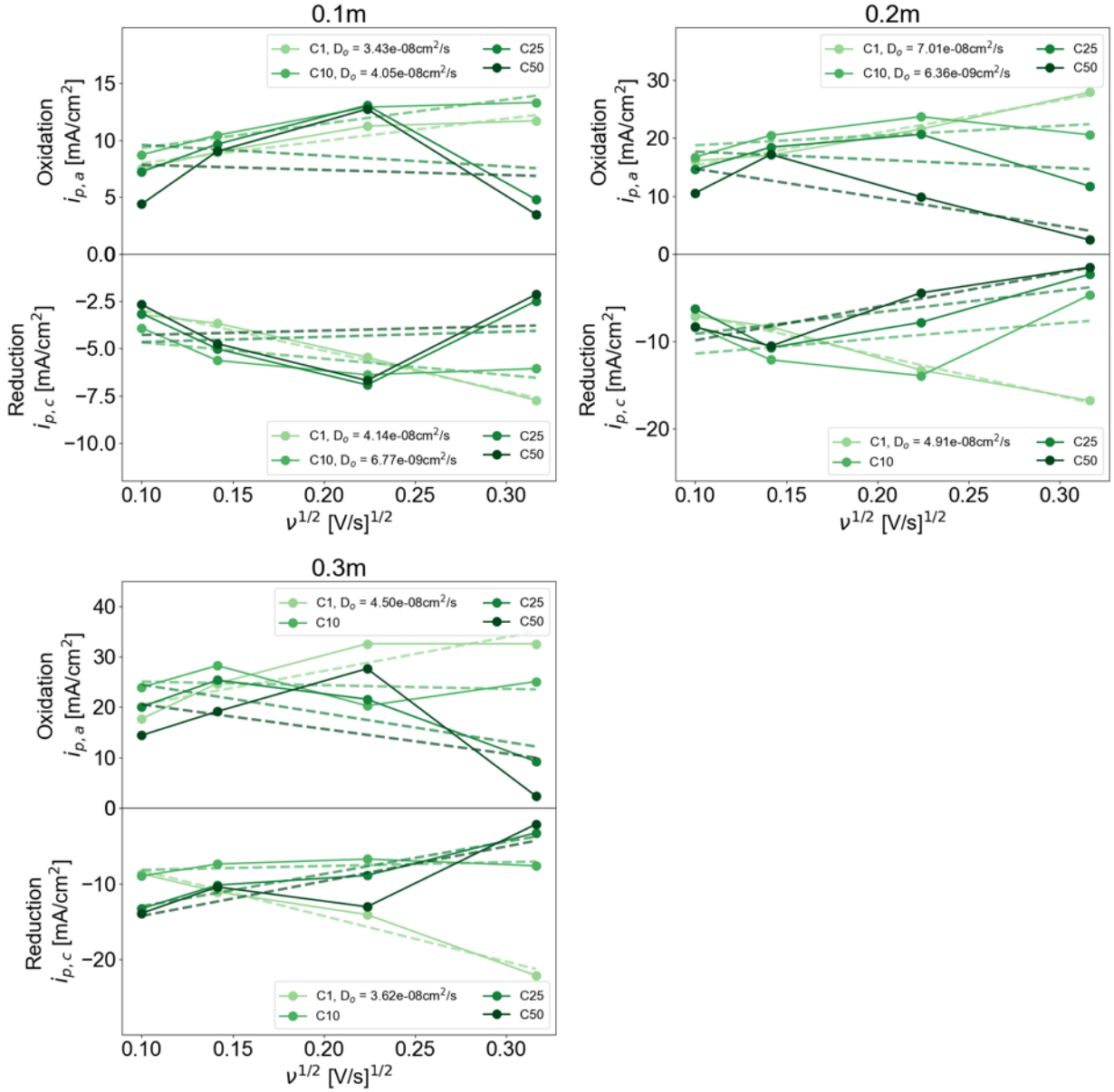

Figure 5.22: Application of Randles-Sevcik equation to CV data for $[EMIM]^+[OTf]^-$ electrolytes.

As observed from Figures 5.21 and 5.22, there is generally a very poor fit from the plots of i_p vs. $\nu^{1/2}$, likely due to quasi-reversible nature of the electron process. Further complicating the validity of this method is the superposition of the sluggish and fast electron transfer processes in the observed peak current. While higher scan rates may result in peaks that better reflect the combined contributions of both electron transfer processes, the resulting shift from diffusion-control to charge transfer-control at these scan rates invalidates any application of the Randles Sevcik equation as the equation assumes a Nernstian redox couple. Furthermore, the Randles-Sevcik equation assumes a constant area at the working electrode, which is likely not the case as suggested by the drop in peak magnitude with increasing cycle number as discussed in Section 5.5.2.3.

Therefore, a different electrochemical analytical technique must be used in order to determine the diffusion coefficient of Zn^{2+} for various salt concentrations. Section 5.5.4 discusses the use of chronoamperometry to determine this diffusion coefficient.

5.5.3 Long Cycle Cyclic Voltammetry

Cyclic voltammetry was also performed for both ionic liquids at concentrations of 0.1, 0.2, and 0.3m for a large number of cycles in order to investigate the long-term stability and performance of these electrolytes. Cycling was performed in increments of 400 cycles per test due to data acquisition limitations. In order to preserve testing conditions as much as possible, the electrolyte was not stirred or mixed between runs, and subsequent steps were started as soon as possible after a previous run had finished. Scan rates of 20 mV/s and 100 mV/s were tested in order to capture behavior in reversible and non-reversible regimes.

5.5.3.1 $\nu = 100$ mV/s

Figure 5.23 presents long cycle cyclic voltammograms, charge per cycle, and coulombic efficiency per cycle for $[BMIM]^+[OTf]^-$ with 0.1, 0.2, and 0.3m salt concentrations and a scan rate of 100mV/s for 1200 cycles. Figure 5.24 presents equivalent data for $[EMIM]^+[OTf]^-$ electrolytes.

For both $[BMIM]^+[OTf]^-$ and $[EMIM]^+[OTf]^-$ electrolytes, the 100mV/s cycling exhibited an initial break-in period within roughly the first 200 cycles. The observed peak heights increased with increasing $Zn(OTf)_2$ concentration as previously observed. Coulombic efficiencies initially started at around 80%, dropped within the first 50 cycles, and then slowly recovered by around cycle 200 before gradually declining through the end of cycling. However, starting by cycle 600 for $[BMIM]^+[OTf]^-$ and cycle 400 for $[EMIM]^+[OTf]^-$, the measured charge per cycle on both the reduction and oxidation scans started to become increasingly erratic, causing an erratic calculation of the coulombic effiency as well with some cycles returning over 100% coulombic efficiency.

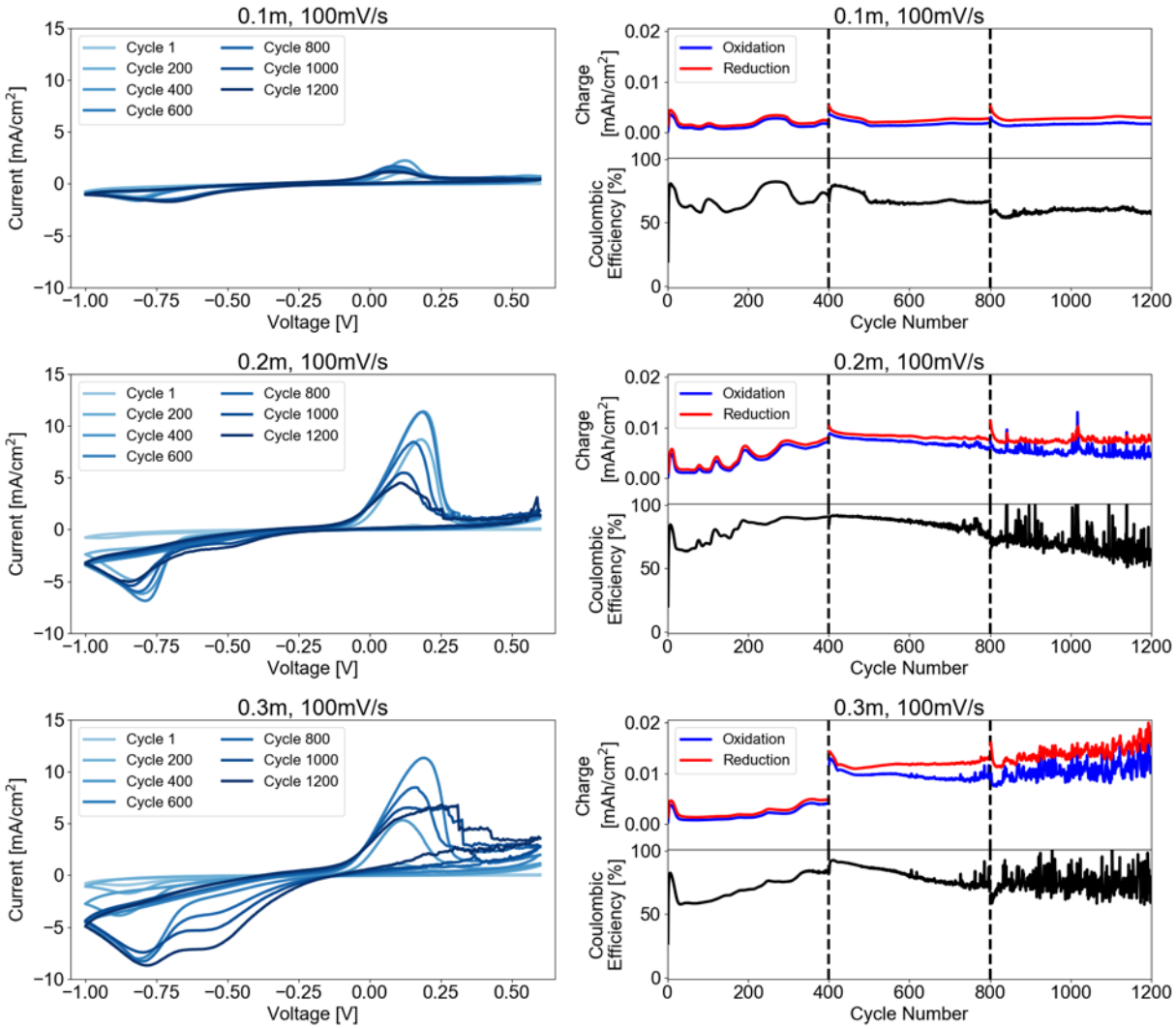

Figure 5.23: Long cycle cyclic voltammograms with $\nu = 100$ mV/s for 0.1, 0.2, and 0.3m $Zn(OTf)_2$ in $[BMIM]^+[OTf]$.

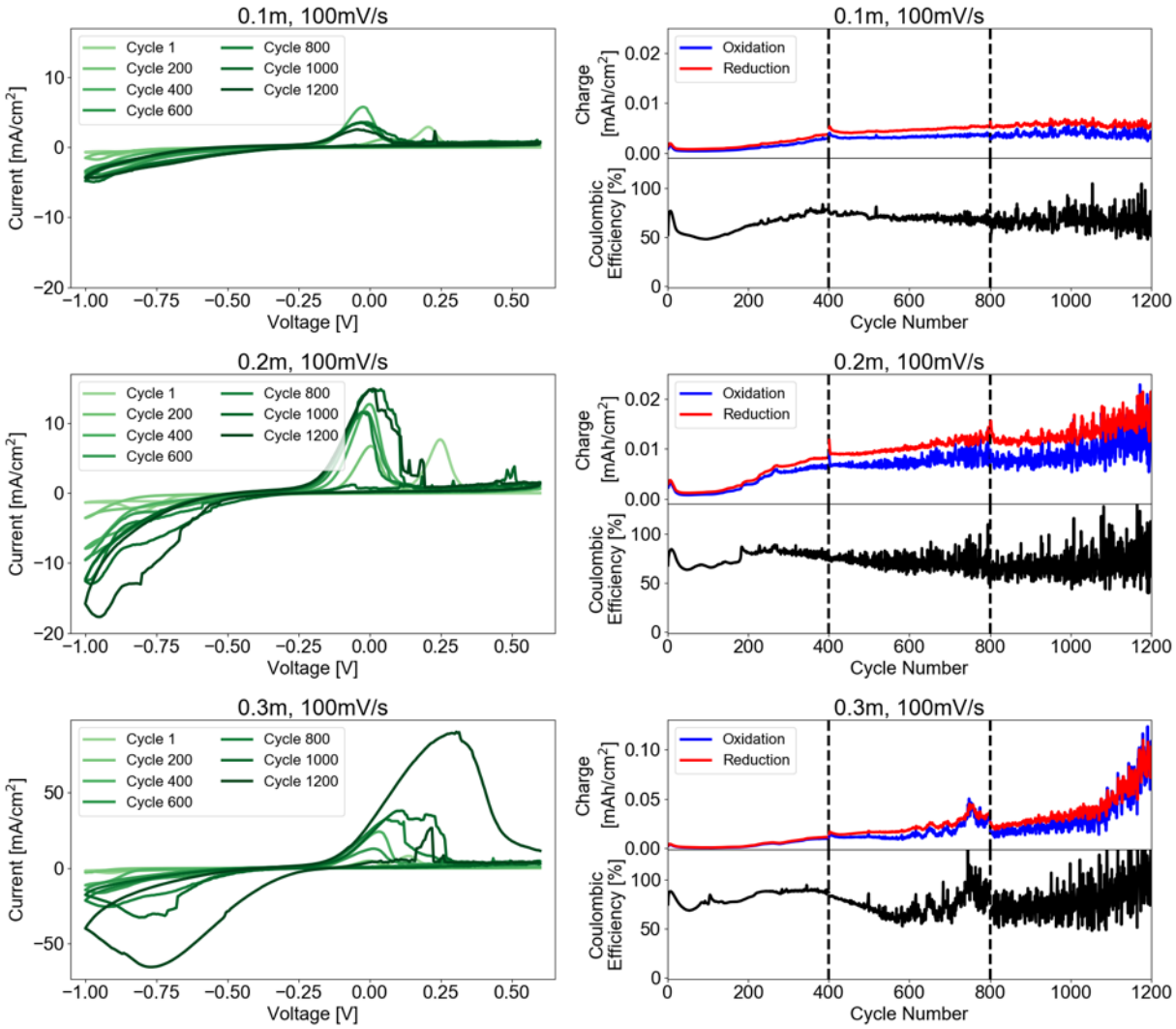

Figure 5.24: Long cycle cyclic voltammograms with $\nu = 100$ mV/s for 0,1, 0.2, and 0.3m $Zn(OTf)_2$ in $[EMIM]^+[OTf]$.

This initial break-in period may be due to the Pt working electrode surface requiring priming of nucleation sites during initial cycling. The observed coulombic efficiency within the first 400 cycles never exceeded 100%, again implying the persistence of plated Zn that was not fully oxidized during the oxidation scans. This remaining Zn would then provide already existing nucleation sites for further Zn^{2+} reduction, allowing for more reduction and consequently more oxidation, increasing the amounts of charge measured. This may be a direct consequence of using Pt as the working electrode and therefore a difference in the ease with which nucleation sites can be established on Pt vs. Zn. The "noisy" coulombic efficiency at later cycles may therefore be a result of changing surface morphologies and consequent irregular dissolution of Zn. Positive spikes but no negative drops in coulombic efficiency can be observed, further supporting the hypothesis that excess plated Zn is sometimes oxidized.

Differences in the cyclic voltammograms can be seen between the two ionic liquids over the length of the cycling investigated. For $[BMIM]^+[OTf]^-$ electrolytes, a two peak shape emerges at later cycles on the reduction scan while the nucleation loop present at initial cycle disappears as cycling continues. The two peak shape is particularly evident at 0.3m concentrations with peaks at roughly -0.55V and -0.75V at cycle 1200. The magnitude of the cathodic scan also increased with cycle number while the magnitude of the oxidation scan increased the first 600 cycles and then steadily decreased. Accompanying the drop in anodic peak is a noisier and more irregular current response, especially for the final 400 cycles. This irregular current response is also reflected in the total charge per cycle and coulombic efficiency per cycle, as the plots for both metrics become less smooth with increasing cycle number.

The emergence of the two peak shape as well as the increase in magnitude on the reduction scan is likely a consequence of the repeated incomplete dissolution of zinc at prior cycles, which would provide an increasing number of nucleation site for future reduction. The peak broadening that precedes the appearance of the two peak shape suggests that an increasingly lower overpotential is required to induce nucleation and Zn^{2+} adsorption, resulting in reduction of Zn^{2+} occurring at less negative potentials. While the two peak shape itself on the reduction scan did not appear at lower scan rates for fewer cycles, its appearance at higher cycle number even at $\nu = 100$mV/s may be due to the increased electrode surface area providing enough nucleation sites to overcome the sluggish reaction kinetics of the initial Zn^{2+} adsorption step. Higher Zn^{2+} concentration likely improved the distinction of the two peaks due to the higher availability of Zn^{2+} for reduction.

For $[EMIM]^+[OTf]^-$ electrolytes, the cyclic voltammogram exhibited different shapes and behaviors. Except for the final cycles at 0.3m concentration, a reduction peak was not resolved with the same distinctness as compared to $[BMIM]^+[OTf]^-$ electrolytes. However, the nucleation loop persisted through cycle 600, particularly for 0.2m and 0.3m concentrations, and the potential at which this loop appeared is pushed to more negative potentials until it no longer appeared. The shape of the voltammograms, particularly for later cycles at 0.1m and 0.2m concentrations, adopted a long negative "tail" that increased in current magnitude with increasing cycling. Similar to $[BMIM]^+[OTf]^-$ electrolytes, later cycles showed noisy current responses, but these appeared at earlier cycle numbers.

One noteworthy behavior was shifting of the potential of the oxidation peak from the first cycle to later cycles. For all electrolyte concentrations, the oxidation peak at the first cycle appeared at 0.15-0.2V but shifted to -0.1-0V within the first 200 cycles. Examination of the data for each cycle reveals that this peak shift correlates closely with the drop and consequent recovery of the coulombic efficiency with cycle number.

The lack of appearance of a distinct cathodic peak as well as the long persistence of the nucleation loop suggests that higher overpotentials are required to induce nucleation within $[EMIM]^+[OTf]^-$ electrolytes at fast scan rates. This more negative overpotential therefore limits the amount of Zn^{2+} that can be reduced per cycle, even after the surface is primed with nucleation sites, resulting in lower charge per cycle for both reduction and oxidation when compared to $[BMIM]^+[OTf]^-$ electrolytes.

The higher overpotential required may be a result of the smaller cation size of $[EMIM]^+$ compared to $[BMIM]^+$. As the ionic liquid electrolyte also contributes charged species to the overall solution, a double layer whose cations are comprised of both imidazolium-based species and Zn^{2+} likely forms when a negative potential is applied. The smaller size of the ethyl group compared to the butyl group would allow for more dense packing of $[EMIM]^+$, thus inhibiting the ability of Zn^{2+} to adsorb onto the electrode surface. This would be particularly significant when small negative potentials are first applied during each cycle, as a diffusion layer of Zn^{2+} may not have enough time to adequately develop compared to the immediately available $[EMIM]^+$ present in solution at the electrode surface. As the electrode surface breaks in and Zn^{2+} nucleation sites persist after repeated cycling, more reduction is able to occur as evidenced by the disappearance of the nucleation loop around cycle 600-800 and the higher measured amounts of charge. However, this is conflated with the dissolution of excess Zn per cycle as seen by the appearance of irregular coulombic efficiency as early as cycle 300 in the case of 0.2m concentration. These observations in $[EMIM]^+[OTf]^-$ electrolytes therefore indicate possible competition between $[EMIM]^+$ and Zn^{2+} for adsorption onto the electrode surface.

Finally, a significant increase in current magnitude was observed between 0.2m and 0.3m concentrations for $[EMIM]^+[OTf]^-$ electrolytes with peak oxidation currents exhibiting a higher magnitude current by a factor of 4-5. A similar increase was not seen with $[BMIM]^+[OTf]^-$ electrolytes at the same concentrations and is likely due to increased Zn^{2+} mobility in $[EMIM]^+[OTf]^-$. Furthermore, the shape of the voltammograms at later cycles at 0.3m $[EMIM]^+[OTf]^-$ reveals the presence of a significant reduction peak at about -0.8V, possibly again indicating a fully nucleated electrode surface with increased surface area that outweighs any kinetic limitations at this scan rate.

5.5.3.2 $\nu = 20$ mV/s

Figure 5.25 presents cyclic voltammograms, charge per cycle, and coulombic efficiency per cycle for $[BMIM]^+[OTf]^-$ for 0.2 and 0.3m salt concentrations and a scan rate of 20mV/s for 1200 and 800 cycles respectively. Figure 5.26 presents equivalent data for $[EMIM]^+[OTf]^-$ but for 800 cycles.

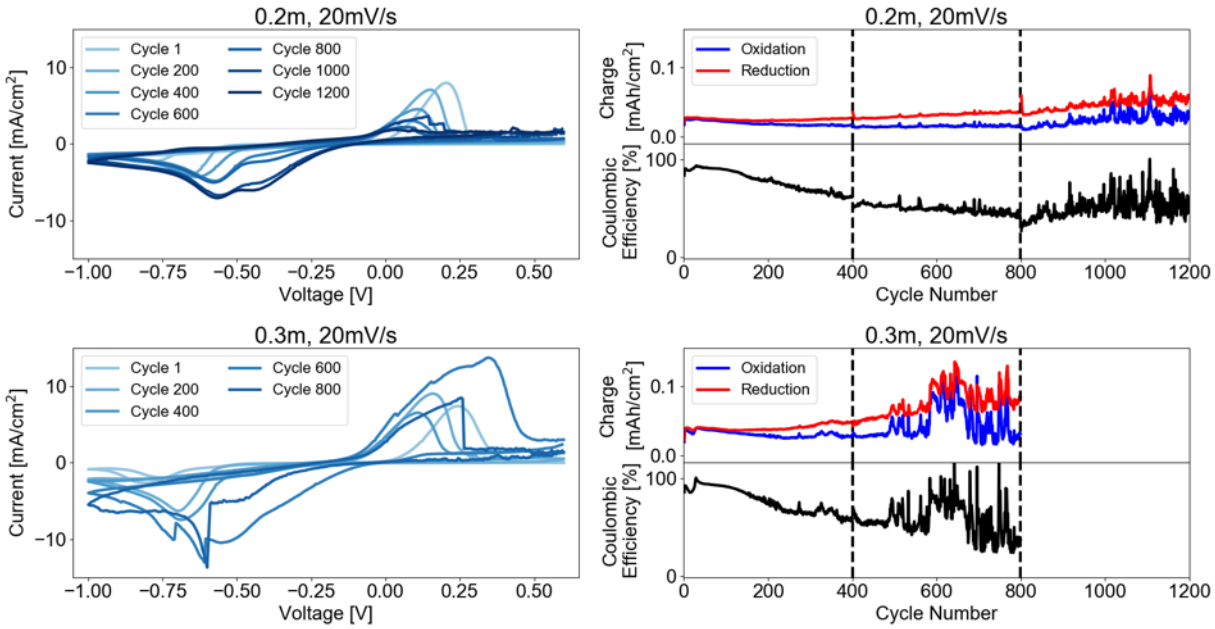

Figure 5.25: Cyclic voltammograms, charge per cycle, and coulombic efficiency with $\nu = 20$ mV/s for 0.2 and 0.3m $Zn(OTf)_2$ in $[BMIM]^+[OTf]$.

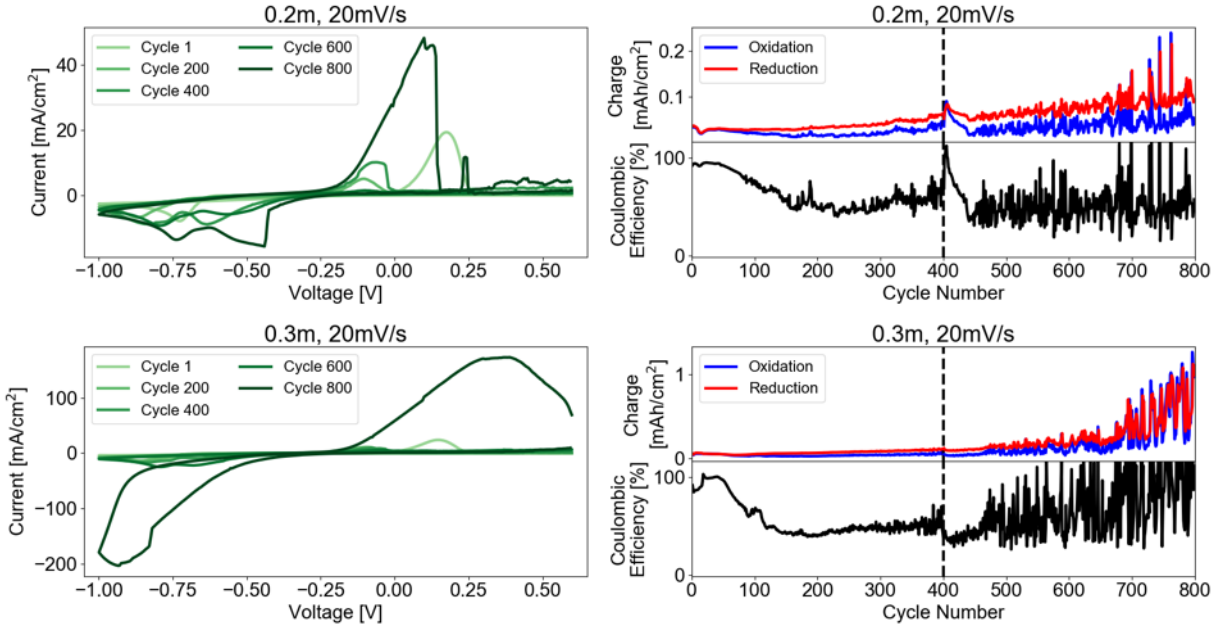

Figure 5.26: Cyclic voltammograms, charge per cycle, and coulombic efficiency with $\nu = 20$ mV/s for 0.2 and 0.3m $Zn(OTf)_2$ in $[EMIM]^+[OTf]$.

Similar to testing for fewer cycles, the voltammograms reveal more reversible behavior at this lower scan rate. For both ionic liquids at 0.2m concentration, the two peak shape can be observed in the reduction scan. For both ionic liquids and all concentrations, a similar shift in the oxidation peak can be observed from 0.15-0.25V on the initial cycle to -0.1-0V for $[BMIM]^+[OTf]^-$ electrolytes and -0.1-0V for $[EMIM]^+[OTf]^-$ electrolytes. Peak heights and the charge measured per cycle also increased with increasing salt concentration, but the effective increase was significantly more dramatic at $\nu = 20$mV/s compared to $\nu = 100$ mV/s. Peak heights also generally increased with increasing cycle number for both reduction and oxidation except for 0.2m $[BMIM]^+[OTf]^-$. The amount of charge per cycle for both reduction and oxidation was higher by roughly one order of magnitude compared to cycling at 100 mV/s.

The reappearance of the two peak shape on the reduction scan is likely due to the same mechanism as discussed previously at $\nu = 100$mV/s, in which the electrode surface becomes primed with nucleation sites which provide ample preferred reaction sites for Zn^{2+} adsorption. At this lower scan rate, all electrolytes tested exhibited the two peak shape to some degree, likely aided by the slower scan rate providing time for reactions to exhibit more reversible behavior.

A similar break-in effect can be observed for all electrolytes at this slower scan rate, but the initial drop and recovery in charge and coulombic efficiency takes place within the first 30 cycles, as revealed by their respective plots. Furthermore, the coulombic efficiency begins to steadily decline for all electrolytes until about 50-60% for $[BMIM]^+[OTf]^-$ electrolytes and 40-50% for $[EMIM]^+[OTf]^-$ electrolytes. After this point, the coulombic efficiency remains relatively constant or increases with significant irregularity observed in both the reduction and oxidation charges and the coulombic efficiency.

Based on when irregularities in the reduction and oxidation charges and coulombic efficiencies appear, the actual electrode surface area likely deviates from the assumed surface area much sooner than at the higher scan rate. This is consistent with a slower scan rate providing more time for redox reactions to occur as well as the higher measured charges.

The reason for the lower steady coulombic efficiency at roughly 50% is unclear. While the amount of oxidation tracks the amount of reduction per cycle, the amount of charge during oxidation still remains relatively constant throughout the entirety of cycles investigated while the amount of charge during reduction steadily increases. This may again be attributed to the differences in rates of the two charge transfer steps as Zn^{2+} reduction effectively occurs faster than Zn oxidation.

It is unexpected that the coulombic efficiency is lower at the slower scan rate as the redox reactions would be expected to be more reversible. One possible explanation is that the electrode surface area increases to such a degree that significantly more nucleation sites exist, exceeding any kinetic limitations during reduction. However, it would then be expected that a high surface area would also exist for oxidation, therefore also increasing the amount of oxidation charge measured by a similar proportion.

For 0.3m $[EMIM]^+][OTf]^-$, the average coulombic efficiency begins to increase steadily from roughly cycle 600 and onwards. A dramatic shift in voltammogram shape and magni-

tude is also observed at cycle 800 with current densities exceeding 100 mA/cm^2 observed. The presence of coulombic efficiencies exceeding 100% indicates some cycles where the amount of oxidation exceeds the amount of reduction, likely due to inconsistent surface geometries being formed that allow for more oxidation.

5.5.4 Chronoamperometry

Figures 5.27, 5.28, and 5.29 present chronoamperometry data for 0.1m, 0.2m, and 0.3m $[BMIM]^+[OTf]^-$ respectively. Figures 5.30, 5.31, and 5.32 present chronoamperometry data for 0.1m, 0.2m, and 0.3m $[EMIM]^+[OTf]^-$ respectively. For these experiments, the oxidation step was performed immediately following the reduction step. For the Cottrell plots, time was normalized for both reduction and oxidation in order to maintain a range of $t^{-0.5}$ of $1s^{-0.5}$ to $0s^{-0.5}$.

For experiments where reduction was investigated, the first negative potential step was immediately followed by a positive potential step at 0.6V for 1000 seconds. For experiments where oxidation was investigated, a negative potential step at -0.8V was first applied for 500 seconds, after which the second potential step was applied as specified. The current response is presented both against the normal time scale as well as against the inverse square root of time in order to facilitate application of the Cottrell equation.

5.5.4.1 Characterization of Reduction Phenomena

First examining reduction of $[BMIM]^+[OTf]^-$ electrolytes at -0.6V and -0.8V, the shape of the current transients follow the expected shape for a mass transport-limited system with fast electrode kinetics, especially at later times. The expected current response begins at the maximum current followed by a monotonically decaying current response as the concentration of reduced species near the electrode is depleted and diffusion limitations take over. Good agreement can be observed between the current responses for potential steps of -0.6V and -0.8V, particularly at later times. Similarities between these current responses are expected as the peak currents from cyclic voltammetry typically lie near these two potentials. Looking at times beyond t = 50s ($t^{-0.5} = 0.2$), the current responses at both of these two potential steps are roughly equal and linear on the Cottrell plot, allowing for application of the Cottrell equation to calculate Zn^{2+} diffusivity as discussed later. As expected, the observed maximum current increases with increasing salt concentration.

The shapes of the initial current transients, particularly for $0.2m$ and $0.3m$, are consistent with progressive nucleation of metal on a foreign metal surface [82]. These transients are characterized by an initial double-layer charging current decay in magnitude, followed by an increasing current magnitude caused by nucleation and growth of Zn [76]. As nucleation sites coalesce, diffusion limitations dominate over adsorption kinetics, and the magnitude of the current response again begins to decay. Similar to results from CV, there is some initial nucleation necessary before faster reduction kinetics are able to take place.

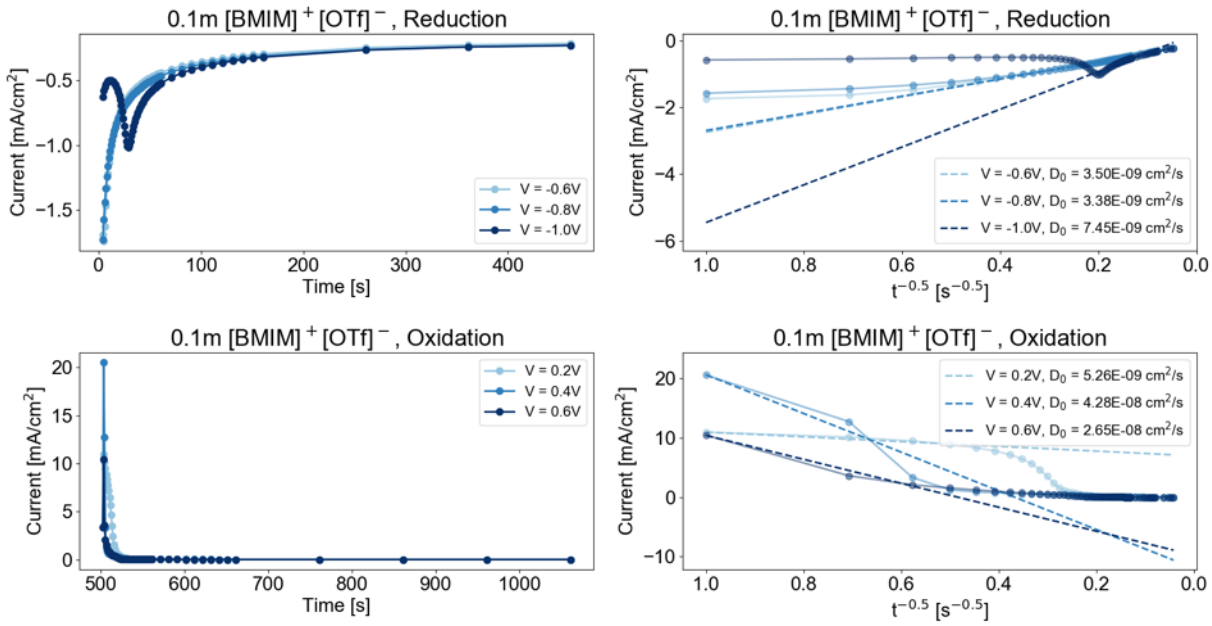

Figure 5.27: Current (left) and Cottrell (right) plots of $0.1m$ $Zn(OTf)_2$ in $[BMIM]^+[OTf]$ with varying oxidation and reduction step potentials.

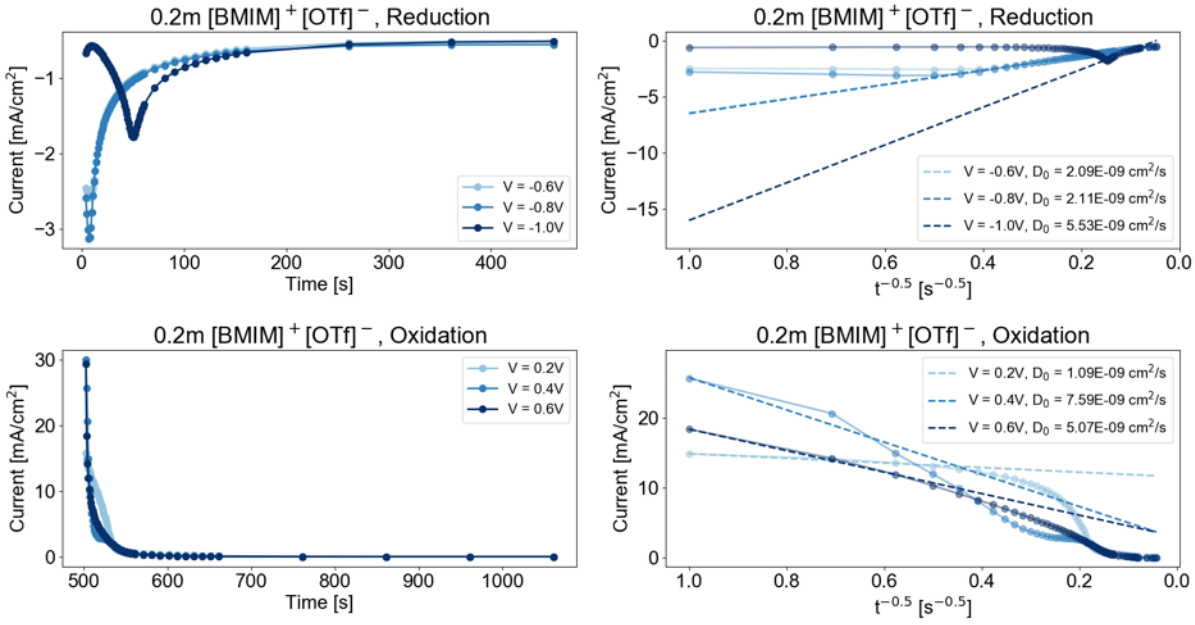

Figure 5.28: Current (left) and Cottrell (right) plots of $0.2m$ $Zn(OTf)_2$ in $[BMIM]^+[OTf]$ with varying oxidation and reduction step potentials.

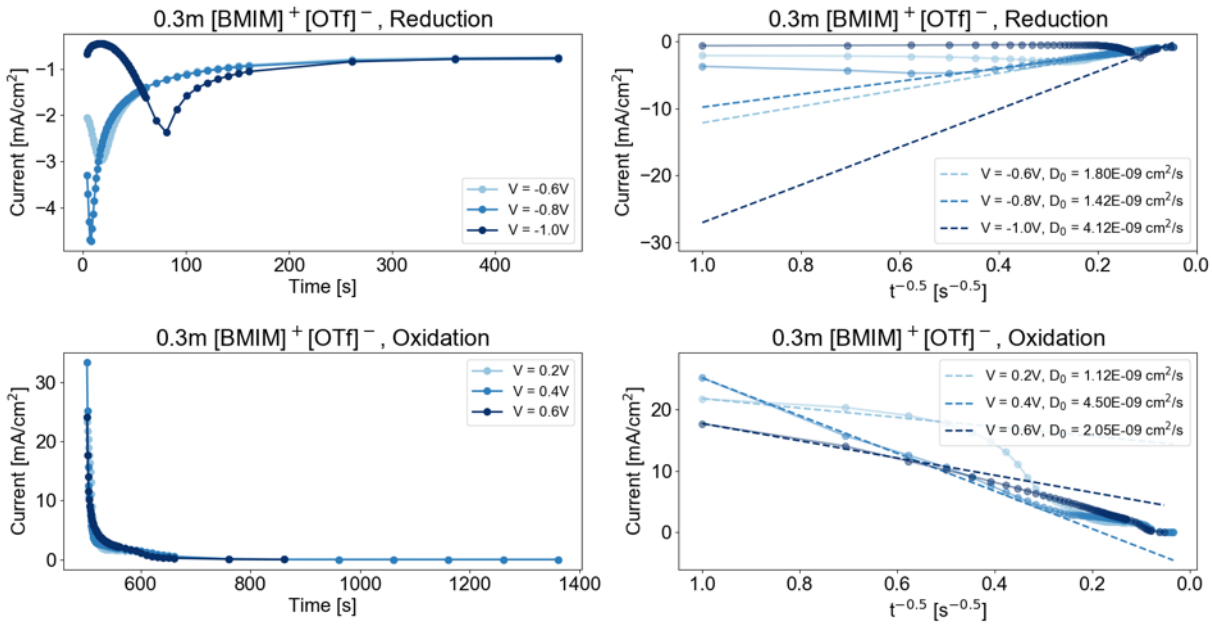

Figure 5.29: Current (left) and Cottrell (right) plots of 0.3m $Zn(OTf)_2$ in $[BMIM]^+[OTf]$ with varying oxidation and reduction step potentials.

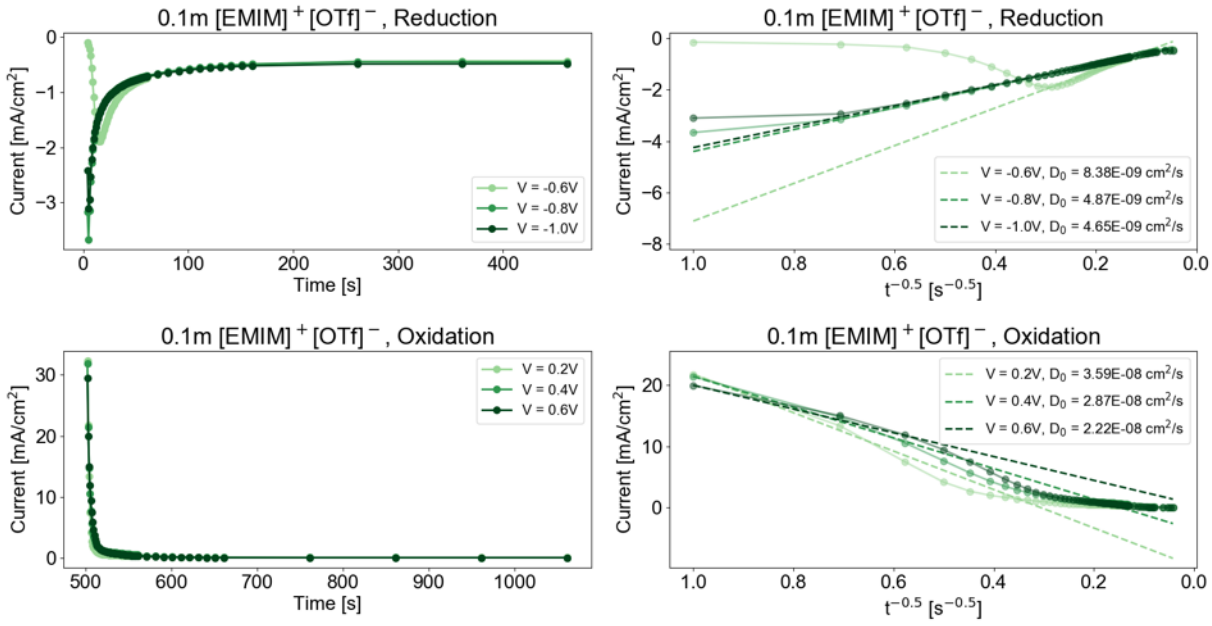

Figure 5.30: Current (left) and Cottrell (right) plots of 0.1m $Zn(OTf)_2$ in $[EMIM]^+[OTf]$ with varying oxidation and reduction step potentials.

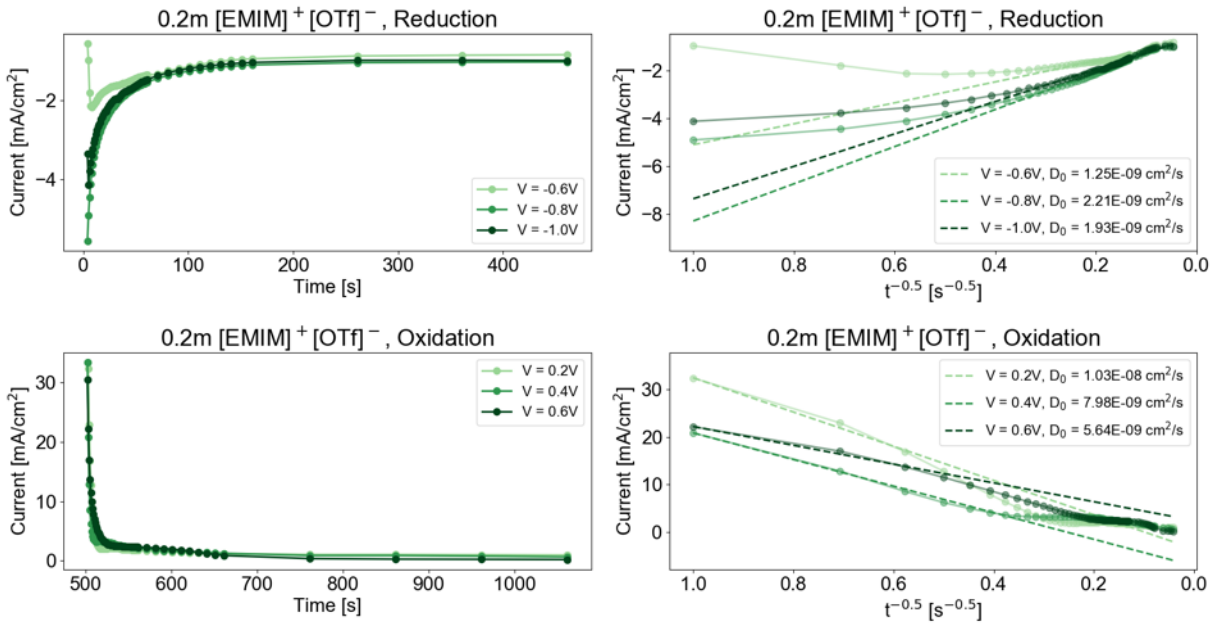

Figure 5.31: Current (left) and Cottrell (right) plots of $0.2m$ $Zn(OTf)_2$ in $[EMIM]^+[OTf]$ with varying oxidation and reduction step potentials.

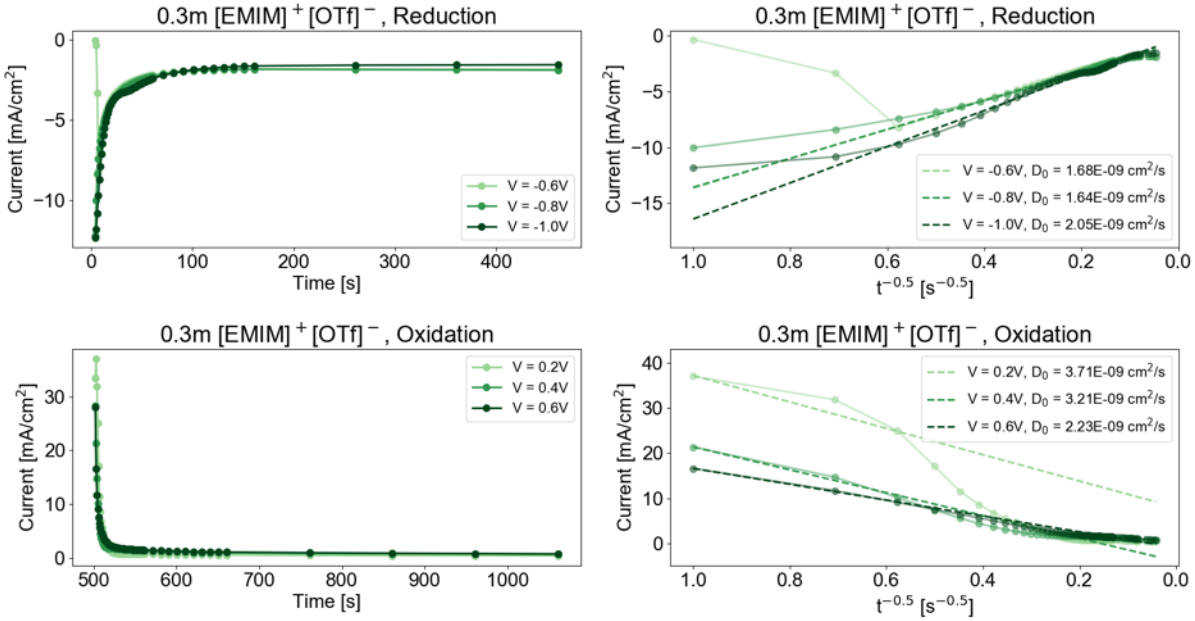

Figure 5.32: Current (left) and Cottrell (right) plots of $0.3m$ $Zn(OTf)_2$ in $[EMIM]^+[OTf]$ with varying oxidation and reduction step potentials.

The maximum current is observed earlier and is higher for -0.8V than for -0.6V. This is due to a higher overpotential applied by the more negative applied potential and is consistent with the requisite nucleation overpotential determined by CV.

For all potential steps, the time at which the maximum current magnitude is observed increases with increasing salt concentration. There may be some contribution of higher salt concentrations slowing Zn^{2+} diffusion rates due to increased ion-ion interactions, consequently slowing Zn^{2+} delivery for nucleation. There may also be contributions from surface interactions related specifically with the $[BMIM]^+$ cations that impede Zn^{2+} reduction.

The effect of initial nucleation is more pronounced for potential steps of -1.0V for all salt concentrations with the current increase being more drawn out and also preceded by a drop in current magnitude. The origin for this behavior is less clear as the initial decrease in current is not observed at any other applied potential. It is unclear why nucleation takes significantly longer to reach its maximum current as well as why the maximum current magnitude is lower than at -0.8V. The local minimum of current indicates a significantly slower rate of reduction compared to the other potentials which is contrary to what should be a higher overpotential providing a higher current density and increased Zn^{2+} migration to the electrode surface.

The absence of the same phenomenon for $[EMIM]^+[OTf]^-$ electrolytes suggests that this is a consequence of electrochemical degradation of the $[BMIM]^+$ cation and that the $[BMIM]^+$ cation may be preferentially reduced before Zn^{2+} at sufficiently negative potentials. This again contradicts findings by [92] that $[BMIM]^+$ cations should be more stable than $[EMIM]^+$ cations due to their longer alkyl chain.

With $[EMIM]^+[OTf]^-$ electrolytes, similar phenomena as with $[BMIM]^+[OTf]^-$ electrolytes are observed but for different concentrations and potentials. The effect of progressive nucleation is primarily only observed for 0.1m concentration at -0.6V, but double-layer charging effects are also observed for 0.2m and 0.3m concentrations at -0.6V. Current responses for -0.8V and -1.0V as well as -0.6V after any initial current increases agree closely with each other for all concentrations. Good agreement between current responses for -0.8V and -1.0V for $[EMIM]^+[OTf]^-$ electrolytes is not unexpected as higher nucleation overpotentials were also observed compared to $[BMIM]^+[OTf]^-$ from the CV. The maximum current observed again increases with increasing salt concentration, and the maximum current magnitudes are notably higher than those observed for $[BMIM]^+[OTf]^-$ electrolytes. In general, all current responses exhibit behavior closer to Nernstian systems than $[BMIM]^+[OTf]^-$ electrolytes and show linear responses on the Cottrell plot, again allowing for the use of the Cottrell equation to calculate Zn^{2+} diffusivity.

The absence of transients indicative of progressive nucleation for potentials other than -0.6V may indicate faster electrode kinetics as well as possibly faster Zn^{2+} diffusion. Furthermore, the effect of progressive nucleation is mitigated with increasing salt concentration, converging with the other potential steps within 3 seconds at 0.3m concentration. This is contrary to the trend observed with $[BMIM]^+[OTf]^-$ where initial nucleation contributions persist as salt concentration increases.

The presence of this opposite trend suggests differences in electrode kinetics depending on the ionic liquid cation. The different alkyl chain lengths may be significant enough to differently affect their respective cation interactions with the electrode and thus Zn^{2+} reduction kinetics.

However, the faster kinetics observed with $[EMIM]^+[OTf]^-$ may be inconsistent with electrode nucleation sites being blocked by the ionic liquid cation [112], as it would be expected that the smaller alkyl chain would allow for denser packing of the imidazolium cation. Further investigation into the complexes formed by these ionic liquids and their surface interactions are therefore necessary to determine the exact mechanism of nucleation.

5.5.4.2 Characterization of Oxidation Phenomena

For both ionic liquids, the chronoamperometric oxidation is as not quantitatively useful due to the kinetic limitations of Zn^{2+} oxidation. For reduction, the slow electron transfer step associated with Zn^{2+} adsorption and nucleation takes place first, followed by the fast step involving reduction of Zn^{1+} to Zn. Therefore, once a threshold amount of Zn^{2+} has been reduced, the overall reaction becomes dominated by the faster electron transfer step and exhibits more Nernstian behavior. For Zn oxidation, the order of the electron transfer steps is reversed, therefore causing the process to be dominated by the slower step at later times. Therefore, a Nernstian region is only realized at the beginning of oxidation, limiting the amount of useful data for quantitative analysis.

For $[BMIM]^+[OTf]^-$ electrolytes, similar current responses are observed for each potential step for all concentrations. In general, the current responses for 0.2V and 0.4V show a significantly sharper "knee" when plotted against linear time. For 0.2V potential steps, the current initially remains high and does not begin to rapidly decay until about 5 seconds, resulting in a large plateau on the Cottrell plot. Similar behavior is observed for 0.4V potential steps as well, although the current decay begins much sooner, after about 2-3 seconds. For 0.6V potential steps, the current response most closely resembles that of a fast electron transfer process, exhibiting both a soft "knee" when plotted against linear time and a mostly straight line on the Cottrell plot. All current responses showed a region of downward concavity followed by a region of upward concavity. The initial current for all potential steps increases with increasing salt concentration, but the relative increase is not as dramatic as compared to reduction.

The different shapes of the oxidation current responses are likely due to differences in overpotential for each potential step. The persistence of the initial high current plateau at 0.2V followed by the steepest current decay is likely a result of the fast electron transfer process being favored initially, followed by charge transfer being dominated by stripping of adsorbed Zn^{1+}. Consequently, faster current decays are observed for 0.4V and 0.6V potential steps, which likely are due to a combination of both the fast and slow electron transfer steps occurring at more equal rates.

Similar current responses can also be seen for $[EMIM]^+[OTf]^-$ electrolytes, with the most notable difference being the absence of the plateau at 0.2V except at 0.3m concentration. In

general, the current responses at all potentials for each salt concentration were much more similar than for $[BMIM]^+[OTf]^-$ electrolytes, similar to the reduction current responses. While a transition to upwards concavity can be observed on the Cottrell plot for all current responses, the decays are not as steep as compared to $[BMIM]^+[OTf]^-$ with the overall plot being more linear. Similar to the reduction phenomena, this is may be due to faster electrode kinetics in $[EMIM]^+[OTf]^-$ than in $[BMIM]^+[OTf]^-$ due to the smaller cation.

5.5.4.3 Determination of Zn^{2+} Diffusivity

As discussed previously, the current response for reduction converges to a linear response on the Cottrell plot after a sufficient amount of time for most concentrations and potential steps. This is likely due to both steps in the overall Zn^{2+} reduction mechanism occurring at more equal rates once a sufficient amount of nucleation has taken place to enable rapid Zn^{2+} adsorption. Therefore, a linear fit can be applied to the Cottrell plot and the slope used to calculate the diffusivity of Zn^{2+} for each combination of concentration and potential step for both ionic liquids. A custom window-gradient algorithm was written in Python and used to find the best linear fit as better fit was yielded compared to a weighted linear fit based on time. The current data was truncated to only include points after the onset of diffusion limitations.

Although the chronoamperometric oxidation responses are not as quantitatively useful, a linear fit was still applied and the resulting diffusivity calculated. For the oxidation plots, the linear fit was weighted based on the inverse square root of time to a power of 3.5 as this was found to give the most accurate fit. Figures 5.33 and 5.34 present the calculated diffusivities using the Cottrell Equation (Eq. 5.12) for $[BMIM]^+[OTf]^-$ and $[EMIM]^+[OTf]^-$ electrolytes respectively.

Values of Zn^{2+} diffusivity are similar between potential steps where good agreement was observed for each electrolyte (between -0.6V and -0.8V for $[BMIM]^+[OTf]^-$ and between -0.8V and -1.0V for $[EMIM]^+[OTf]^-$). Because of the unexpected behavior at -1.0V for $[BMIM]^+[OTf]^-$ electrolytes, less data was available for linear fitting, lowering the accuracy of the calculated diffusivity. Similarly, calculated diffusivities for -0.6V for $[EMIM]^+[OTf]^-$ electrolytes were also less accurate due to the nonideal behavior present at that potential for all salt concentrations.

Considering both the linear current response and the Cottrell plot, the potential step providing the most accurate diffusivity was -0.8V for all salt concentrations and both electrolytes. This was due to the absence of any current increases, no matter how brief, as well as the most linearity on the Cottrell plot. Determination of the diffusivity allows for calculation of the diffusion layer ($\sqrt{Dt}$), the region away from the electrode in which the electrolyte concentration differs from the bulk concentration. The calculated diffusion layer for all electrolytes for 500 seconds is presented in Figure 5.35 and ranges from 8-13μm for $[BMIM]^+[OTf]^-$ electrolytes and from 9-16μm for $[EMIM]^+[OTf]^-$ electrolytes.

Comparing these calculated diffusivity values across salt concentrations, the diffusivity decreases as salt concentration increases. It has been reported that the addition of lithium

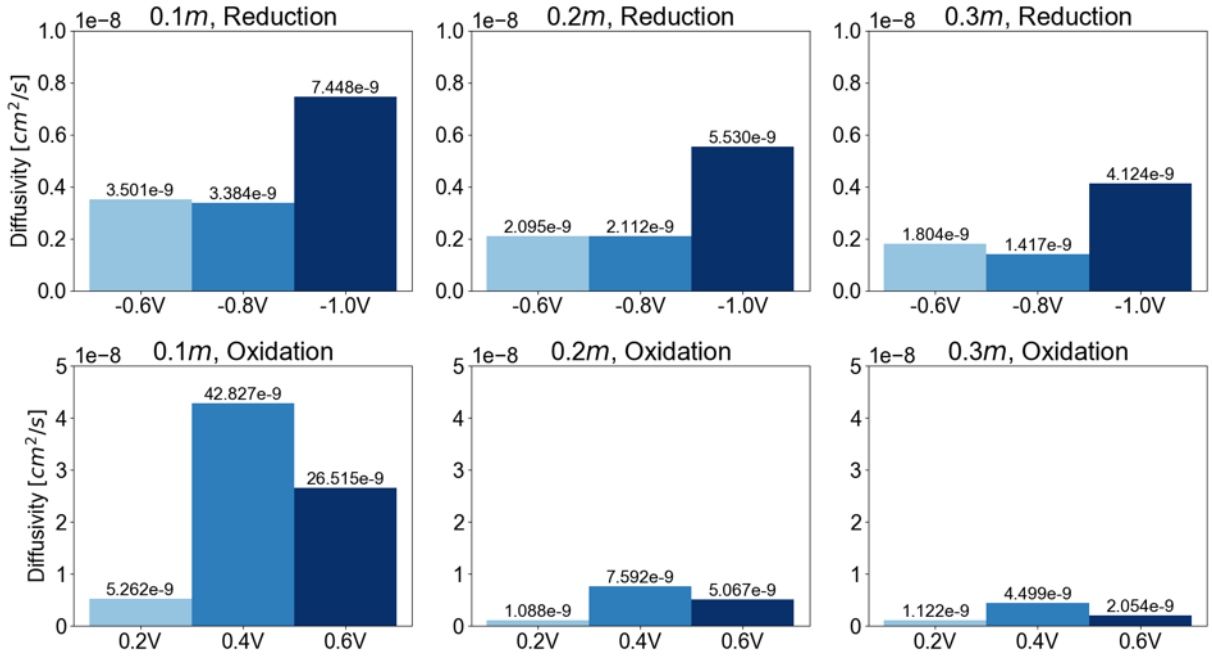

Figure 5.33: Diffusivity of Zn^{2+} in $[BMIM]^{+}[OTf]^{-}$ electrolytes calculated from chronoamperometric reduction and oxidation.

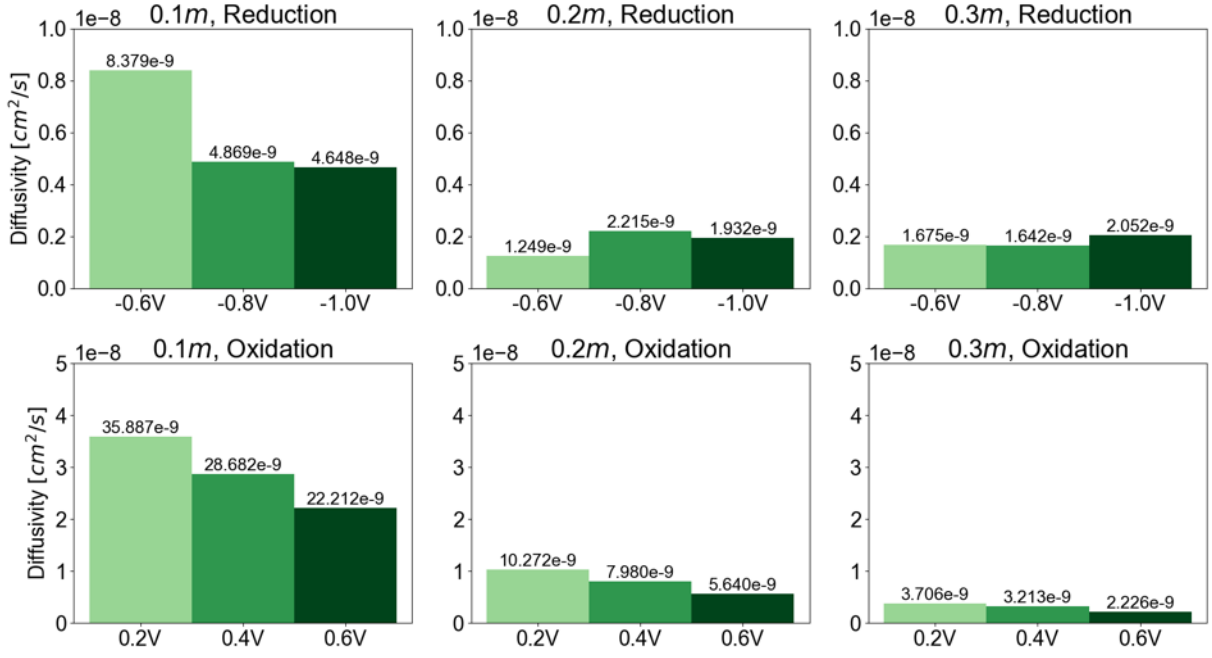

Figure 5.34: Diffusivity of Zn^{2+} in $[EMIM]^{+}[OTf]^{-}$ electrolytes calculated from chronoamperometric reduction and oxidation.

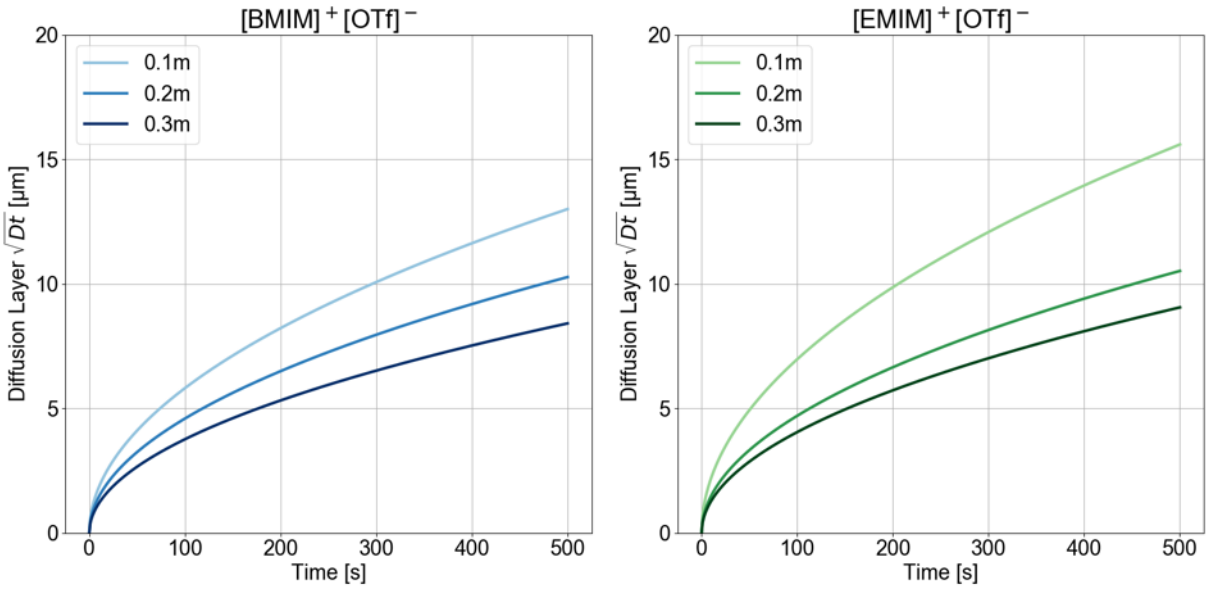

Figure 5.35: Diffusion layers of $[BMIM]^+[OTf]^-$ and $[EMIM]^+[OTf]^-$ electrolytes.

salts to ionic liquids increases the viscosity and consequently decreases the diffusivity of lithium ions within them [5]. It is therefore reasonable to assume a similar effect occurs within systems with zinc ions.

For the oxidation data, a similar trend of decreasing diffusivity with increasing salt concentration was observed, but less agreement between the same potential steps was observed for each ionic liquid. Furthermore, compared to the values calculated from the reduction data, values calculated from oxidation differed by up to an order of magnitude. Again, the efficacy of these calculations on oxidation data is suspect based on the rate and order of electron transfer steps during oxidation and the resulting lack of accurate data points to which a linear fit may be applied.

5.5.4.4 *ex situ* Optical Microscopy of Pt Electrode Surface during Oxidation

In order to further investigate the non-ideal behavior during oxidation, optical micrographs were taken of the electrode surface at different times during oxidation. Figures 5.36 and 5.37 present optical micrographs of the Pt electrode in 0.3m $[BMIM]^+[OTf]^-$ and 0.3m $[EMIM]^+[OTf]^-$. A reduction potential of -0.8V was first applied for 500 seconds, and then an oxidation step of 0.4V was applied for 0s, 6s, 12s, and 30s in order to observe the evolution of the plated Zn surface.

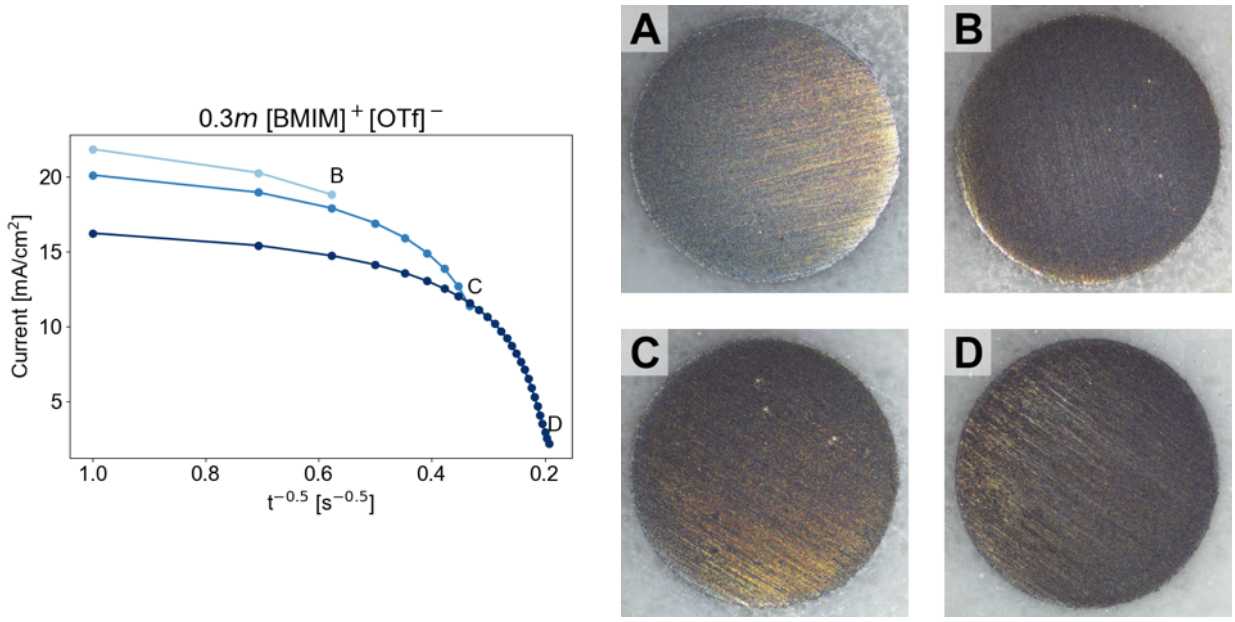

Figure 5.36: *Left*: Current responses of chronoamperometric oxidation; *Right*: Optical micrographs of Pt electrode after interrupted chronoamperometry during oxidation with 0.3m $Zn(OTf)_2$ in $[BMIM]^+[OTf]$ electrolyte. *A*: 0s; *B*: 6s; *C*: 12s; *D*: 30s.

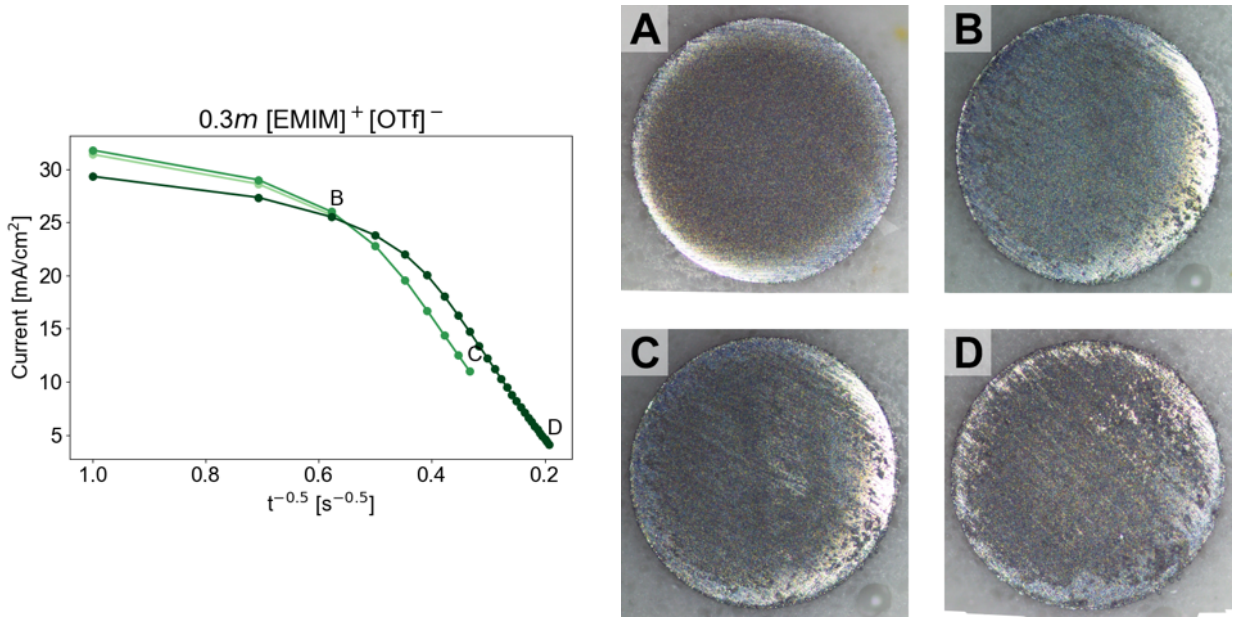

Figure 5.37: *Left*: Current responses of chronoamperometric oxidation; *Right*: Optical micrographs of Pt electrode after interrupted chronoamperometry during oxidation with 0.3m $Zn(OTf)_2$ in $[EMIM]^+[OTf]$ electrolyte. *A*: 0s; *B*: 6s; *C*: 12s; *D*: 30s.

Deposition and stripping of Zn occurs more uniformly in $[BMIM]^+[OTf]^-$ than in $[EMIM]^+[OTf]^-$. However for both ionic liquids, the electrode surface is irregular and has ill-defined area by 6 seconds of oxidation. This uneven area is another contributor to the chronoamperometric data being less quantitatively useful.

By 30 seconds of oxidation, the electrode surface exhibits a range of Zn deposition from bare Pt to almost completely unoxidized Zn. This points to the persistence of both electron transfer steps occuring simultaneously during oxidation, again as a result of the Zn adsorption/desorption limiting the rate of the overall reaction.

Finally, more oxidation occurs in $[EMIM]^+[OTf]^-$ than in $[BMIM]^+[OTf]^-$, as evidenced by the higher initial currents measured as well as examination of the electrode surfaces. This again points to faster reaction kinetics in $[EMIM]^+[OTf]^-$.

5.5.5 Electrochemical Impedance Spectroscopy

Electrochemical impedance spectroscopy (EIS) was also performed on the electrolyte solutions in order to characterize their solution resistances and charge transfer resistances. EIS was performed twice on each sample of material, once on fresh material and once again after a break-in period of 20 cycles of CV at 100 mV/s.

The solution resistance was calculated by taking the value of the high frequency intercept on the real axis of the Nyquist plot. To calculate the charge transfer resistance, a custom Python module was written in order to find the best fitting semicircle to the high frequency portion of the Nyquist plot and determining the real axis intercept of the right side of the semicircle.

Figures 5.38 and 5.39 present the Bode and Nyquist representations of the EIS data on $[BMIM]^+[OTf]^-$ and $[EMIM]^+[OTf]^-$ electrolytes respectively. The Nyquist plots show the semicircle fit used in calculating the charge transfer resistance as well as an inset of the high frequency region used to determine the solution resistance.

Figures 5.40 and 5.41 present the calculated solution resistances and charge transfer resistances before and after breaking in via CV for $[BMIM]^+[OTf]^-$ and $[EMIM]^+[OTf]^-$ electrolytes respectively.

The shapes of the Nyquist plots are all consistent with those found for electrochemical cells with mixed kinetic and diffusion control [40]. The two distinctive characteristics across the Nyquist plots for both ionic liquids is the presence of a short positive tail at high frequencies and the general initial double semicircle shape. The positive tail corresponds with a slight drop in phase on the Bode plot at high frequencies and may be due to formation of an electric double layer by the ionic liquid at rates exceeding the kinetics of the Zn/Zn^{2+} redox reaction. However, further investigation is required to isolate the cause of this phenomenon.

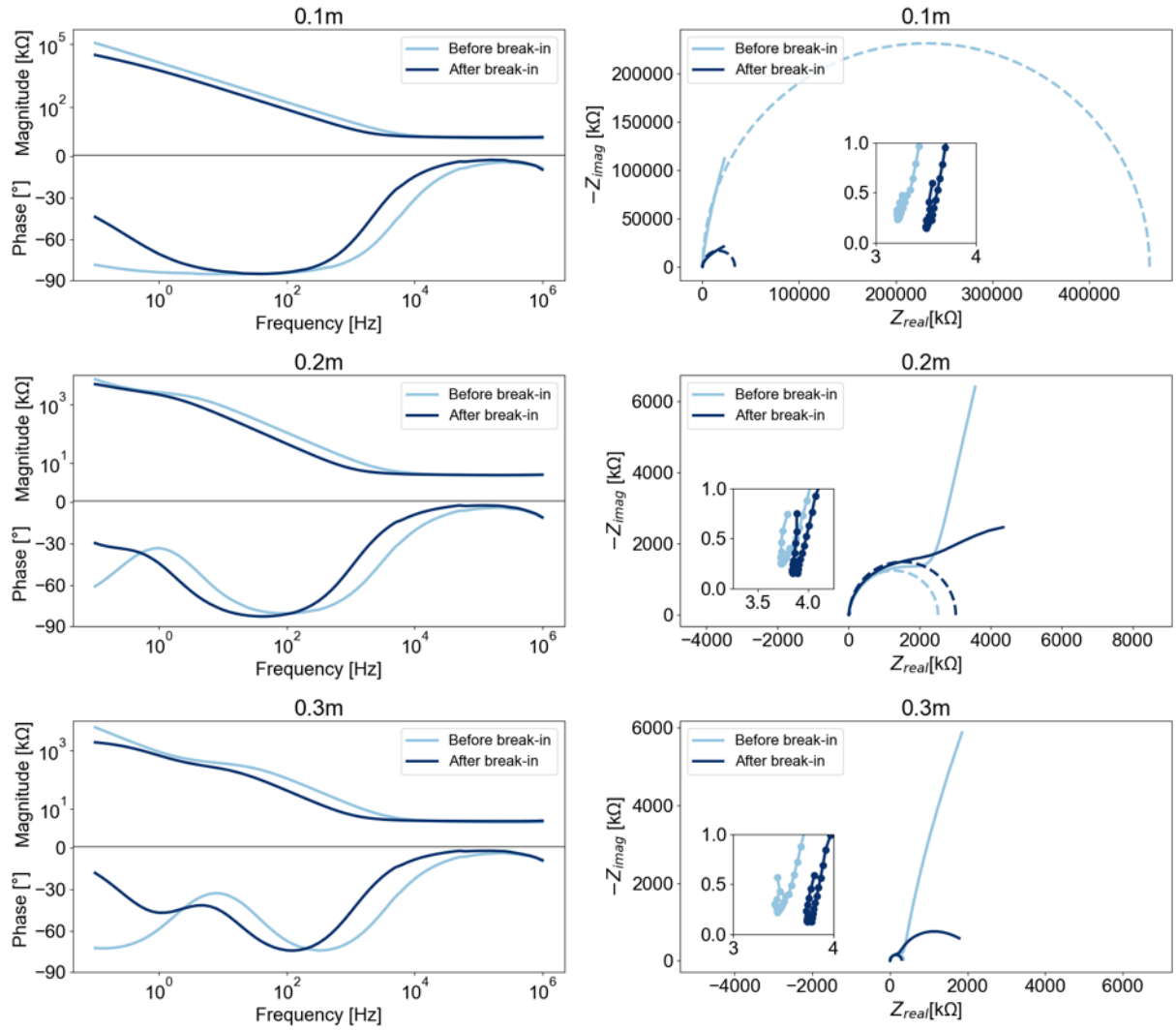

Figure 5.38: Bode and Nyquist plots of 0.1, 0.2, and 0.3m $Zn(OTf)_2$ in $[BMIM]^+[OTf]$ before and after 200 cycles of CV break-in.

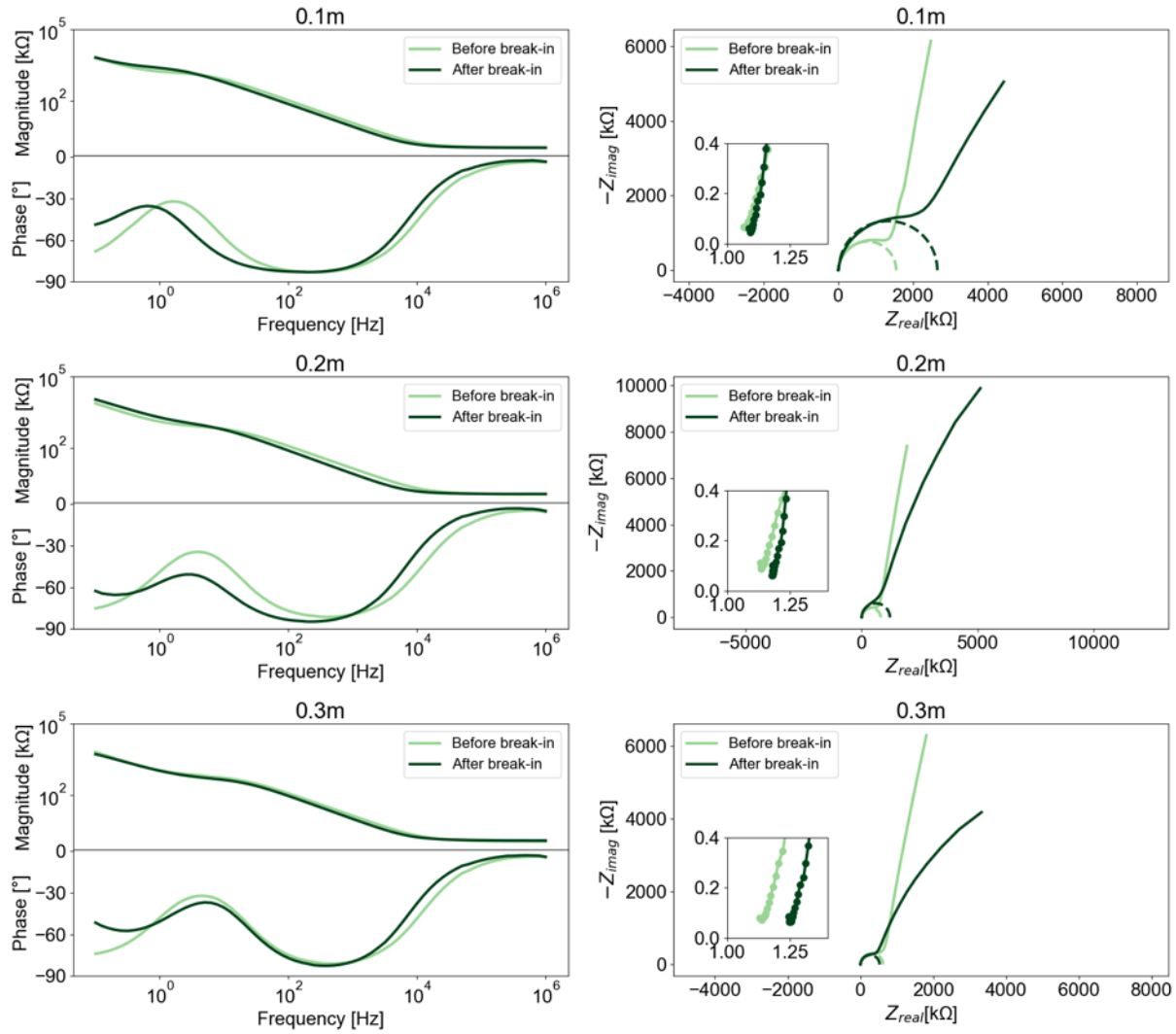

Figure 5.39: Bode and Nyquist plots of 0.1, 0.2, and 0.3m $Zn(OTf)_2$ in $[EMIM]^+[OTf]$ before and after 200 cycles of CV break-in.

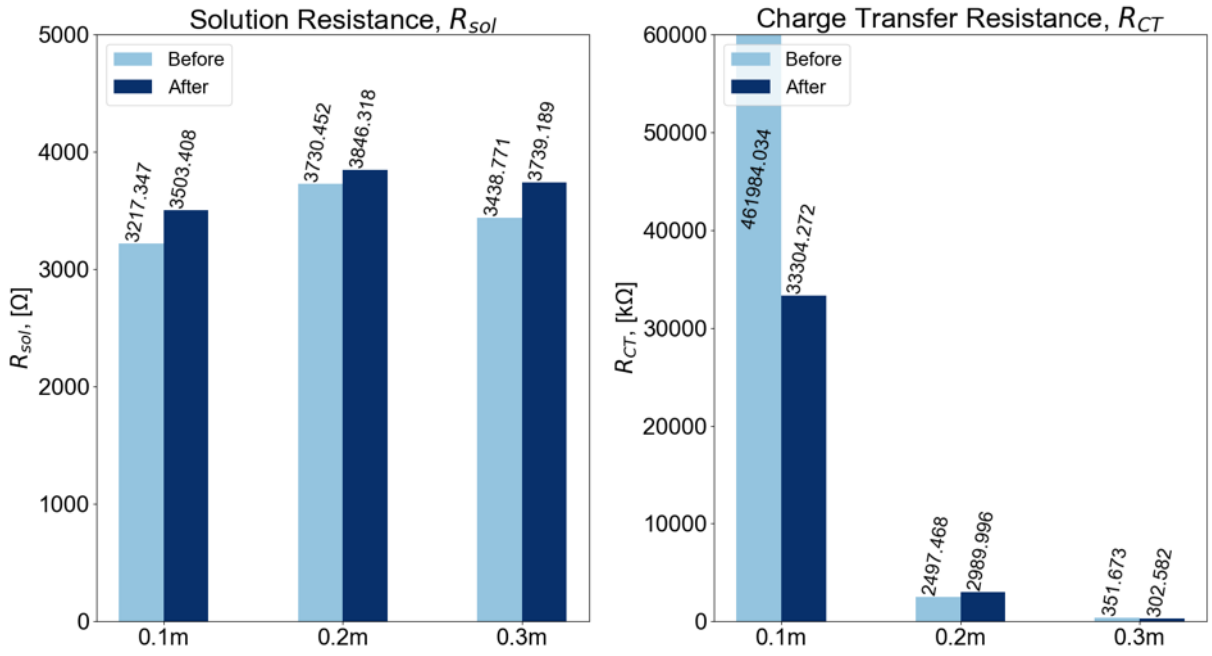

Figure 5.40: Solution resistance (R_{sol}) and charge transfer resistance (R_{ct}) for [BMIM]$^+$[OTf] electrolytes before and after 200 cycles of CV break-in.

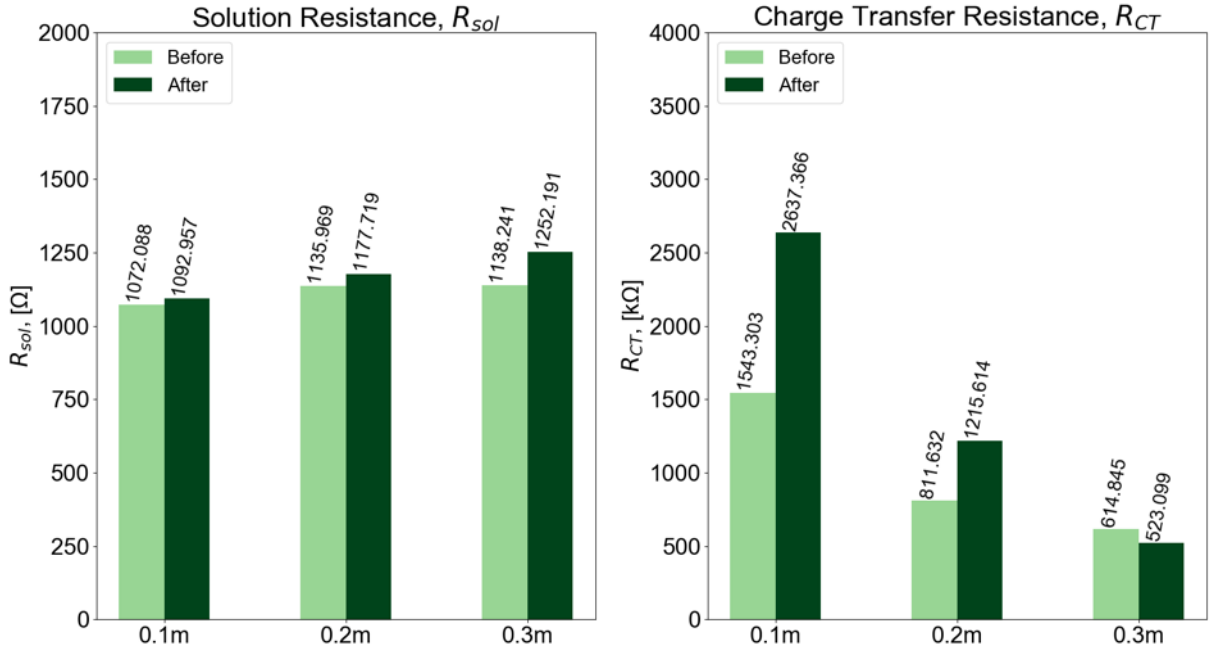

Figure 5.41: Solution resistance (R_{sol}) and charge transfer resistance (R_{ct}) for [EMIM]$^+$[OTf] electrolytes before and after 200 cycles of CV break-in.

The semicircle shape leading into a second semicircle or region with positive slope corresponds to well-known spectra delineating the regions of kinetic control and mass transfer control [8]. The smaller semicircle on the Nyquist plot at lower magnitudes corresponds to regions of kinetic control, while the second larger semicircle corresponds to charge transfer control. Therefore, the size of the smaller semicircle provides insight into kinetic limitations of the system.

The solution resistance remained relatively constant across all salt concentrations for each ionic liquid, though it did increase in all cases after CV. Solution resistances were about 3 times higher within $[BMIM]^+[OTf]^-$ than $[EMIM]^+[OTf]^-$. The increase in solution resistance after CV may be due to a decrease in available Zn^{2+} for transport as coulombic efficiencies were observed to be less than unity during CV.

For both ionic liquids, the charge transfer resistance decreased with increasing salt concentration. This drop indicates a transition from kinetic control to charge transfer control at lower frequencies and therefore faster kinetics. Particularly for the case before performing CV, this may be due to more available nucleation sites being utilitized due to higher availability of Zn^{2+}. Overall, charge transfer resistances were lower for $[EMIM]^+[OTf]^-$ than for $[BMIM]^+[OTf]^-$ which is consistent with results observed from chronoamperometry. In particular, the charge transfer resistance was significantly larger for $0.1m$ prior to CV compared to any other case, likely due to the combination of low Zn^{2+} concentration and inherently slower kinetics.

In some cases, the charge transfer resistance increased after running CV, which is contrary to what is expected from electrochemical methods as the electrode surface should be adequately primed with nucleation sites after CV. The reason for this is unclear, and further investigation is recommended.

In order to determine the ionic conductivity, the calculated solution resistances were applied to Eq. 5.20. The separation between the working and counter electrodes was roughly 5mm, and the area of the counter electrode was 0.00196 cm^2. The resulting electrolyte conductivities are presented in Table 5.5.

Table 5.5: Electrolyte Conductivities

Ionic Liquid	**Concentration**	κ, before [mS/cm]	κ, after [mS/cm]
$[BMIM]^+[OTf]^-$	0.1m	79.189	72.723
	0.2m	68.297	66.239
	0.3m	74.090	68.137
$[EMIM]^+[OTf]^-$	0.1m	237.646	233.108
	0.2m	224.282	216.331
	0.3m	223.834	203.465

The conductivity values are lower compared to traditional aqueous electrolytes [30] as expected. However, the addition of $Zn(OTf)_2$ does significantly increase ionic conductivity compared to the respective neat ionic liquids. The relatively consistent conductivity across all tested salt concentrations suggests that an upper limit of conductivity improvement has already been exceeded, even with the lowest tested concentration of salt. This is unexpected, as the calculated diffusivities from chronoamperometric testing were dependent on salt concentration. Future work should test lower concentrations of salt to further investigate this relationship between salt concentration and ionic conductivity and diffusivity.

5.6 Conclusions

This chapter characterized $0.1m$, $0.2m$, and $0.3m$ concentrations of $Zn(OTf)_2$ in $[BMIM]^+[OTf]^-$ and $[EMIM]^+[OTf]^-$ ionic liquids via cyclic voltammetry, chronoamperometry, and electrochemical impedance spectroscopy. All electrochemical experiments were performed in a three electrode cell with Pt working and counter electrodes and a Zn pseudo-reference electrode. All material preparation and cell assembly was performed in an inert argon environment.

Zn^{2+} reduction in both ionic liquids was found to follow a two step mechanism, first requiring adsorption of Zn^{2+} at available nucleation sites on the Pt electrode followed by further reduction of Zn^{2+} to Zn^{1+}. The initial adsorption step is the rate determining step and is likely impeded by the presence of the imidazolium cation from the ionic liquid itself. Oxidation takes place in the reverse direction with the rate limiting step occuring second. Redox kinetics were observed to be faster in $[EMIM]^+[OTf]^-$ than in $[BMIM]^+[OTf]^-$. Overall, the redox couple is determined to be non-Nernstian.

From CV, Zn/Zn^{2+} reduction and oxidation was found to be quasireversible due to large peak separation, asymmetric peak shapes, and peak current ratios not equal to unity. Furthermore, coulombic efficiencies were found to be higher and more reversible behavior was observed at slower scan rates, further indicative of a kinetically limited system. This may limit rate performance in order to preserve system health in full cells. The nucleation overpotential was more negative in $[EMIM]^+[OTf]^-$ (300-500mV) than in $[BMIM]^+[OTf]^-$ (250-350mV), likely due to the smaller $[EMIM]^+$ cation blocking more nucleation sites than $[BMIM]^+$.

When cycling for large numbers of cycles via CV, more noisy coulombic efficiencies were observed for $[EMIM]^+[OTf]^-$ electrolytes than $[BMIM]^+[OTf]^-$ electrolytes. This was accompanied by growing hysteresis loops on voltammograms and is likely due to more non-uniform surface morphologies. Overall capacities were not significantly higher with $[EMIM]^+[OTf]^-$ than $[BMIM]^+[OTf]^-$.

Due to kinetic limitations, CV was unable to provide accurate data to calculate the diffusivity of Zn^{2+}. Instead, chronoamperometry was performed and Zn^{2+} calculated from the Cottrell equation applied to Zn^{2+} reduction. Diffusivity was found to decrease with increasing salt concentration and ranged from 1.42-3.38e-9 cm^2/s for $[BMIM]^+[OTf]^-$ and 1.64-4.87e-9 cm^2/s for $[EMIM]^+[OTf]^-$ when sufficient overpotentials were applied. Exami-

nation of the electrode surface during oxidation revealed uneven stripping of the Zn, leading to changing active electrode area.

EIS was used to determine the ionic conductivity which ranged from 68.3-79.2 mS/cm for $[BMIM]^+[OTf]^-$ and 223.8-237.6 mS/cm for $[EMIM]^+[OTf]^-$ with fresh electrolyte. The ionic conductivity did not vary significantly with salt concentration or after cycling with CV. The charge transfer resistance decreased with increasing salt concentration for both ionic liquids and was lower for $[BMIM]^+[OTf]^-$, consistent with higher nucleation overpotentials required for $[EMIM]^+[OTf]^-$.

In general, higher peak currents and coulombic efficiences were observed with $[EMIM]^+[OTf]^-$, but the higher overpotentials and overall faster kinetics led to more irregular area and unstable deposition and dissolution compared to $[BMIM]^+[OTf]^-$.

Higher salt concentrations are also preferred due to higher observed currents and no observed correlation between Zn^{2+} and ionic conductivity. Diffusivity was higher at lower salt concentrations, likely due to fewer interactions wthin the ionic liquid, but the negative effect of concentration on diffusivity decreased as concentration increased.

Between the two ionic liquids, $[EMIM]^+[OTf]^-$ offers faster mass transport, evidenced by higher diffusivity of Zn^{2+} and higher ionic conductivity, and faster Zn redox kinetics, evidenced by generally lower charge transfer resistance, compared to $[BMIM]^+[OTf]^-$. This may result in higher rate capabilities with $[EMIM]^+[OTf]^-$ than $[BMIM]^+[OTf]^-$ when used in full cells. However, inconsistent deposition and dissolution, potentially leading to shorter cycle life, was also observed with $[EMIM]^+[OTf]^-$, so $[BMIM]^+[OTf]^-$ may a better choice for long cycle life and low power applications.

Future work should seek to improve the limitations of the three electrode cell. Although a small electrode area was used, low coulombic efficiencies mean that the electrode area changes with each successive cycle of deposition and dissolution, casting uncertainty on the validity of the calculated values. Future work should seek to develop a setup where electrode area can be maintained constant or at a known value throughout. Future work should also seek to test more granular concentrations of salt in both ionic liquids to determine if there is a lower limit at which ionic conductivity decreases.

Chapter 6

Development of Gel Polymer Electrolyte

This chapter presents findings from development and characterization of a PVDF-HFP-based gel polymer electrolyte for use with a MnO_2/Zn cell chemistry. The goals of this work are

1. to investigate the effect of drying temperature and drying environment on polymer microstructure and gel polymer electrolyte performance,
2. to characterize the performance of solution-cast gel polymer electrolytes in half cells, mechanically assembled full cells, and fully printed cells,
3. and to determine the best performing candidate of ionic liquid and manufacturing environment for fully printed cells.

The electrochemical analytical methods used are cyclic voltammetry (CV) and electrochemical impedance spectroscopy (EIS). CV was used to characterize GPE performance within half cells and mechanically assembled full cells, and EIS was used to determine ionic conductivities and charge transfer resistances. Mechanically assembled full cells and fully printed cells were galvanostatically cycled in order to characterize cycle life performance, and differential capacity analysis was performed in order to further investigate degradation mechanisms.

Section 6.1 presents the motivation for the analysis and work in this chapter. Section 6.2 presents relevant background on PVDF-HFP gel polymer electrolytes, CV responses of simple circuit elements found in equivalent circuit models of electrochemical cells, and differential capacity analysis. Section 6.3 presents the experimental methods and procedures used for this work. Section 6.4 presents the findings from scanning electron microscopy, electrochemical analysis, and galvanostatic cycling. Section 6.5 summarizes these findings and suggests directions for future work.

6.1 Motivation

The goal of this work is to investigate the effect of manufacturing parameters on gel polymer electrolyte microstructure and performance in full electrochemical cells. The final aim is to optimize performance of a fully printed cell, and work presented in this chapter investigates GPE performance in half cells, mechanically assembled full cells, and finally fully printed cells.

The ionic liquids investigated are $[BMIM]^+[OTf]^-$ and $[EMIM]^+[OTf]^-$ with dissolved $Zn(OTf)_2$. As the ionic liquids and salt have already been investigated in Chapter 5, this chapter focuses on application of the ionic liquids with the polymer separator layer.

Good performance and characterization of the gel polymer electrolyte is crucial for development of fully printed cells. The GPE is not only responsible for mechanical separation between the electrodes but also serves to bind both printed electrodes together and enable a free-standing and monolithic cell. Therefore, it is necessary to understand the effect of manufacturing parameters and processes on GPE performance within full cells.

6.2 Background

This section presents background on PVDF-HFP-based gel polymer electrolytes as well as analytical methods relevant for half cells and full cells with gel electrolytes. Cyclic voltammetry responses of common circuit elements are presented, and differential capacity analysis for full cells is introduced.

6.2.1 PVDF-HFP Gel Polymer Electrolytes

The polymer used in development and optimization of a gel polymer electrolyte for this work is poly(vinylidene) fluoride-co-hexafluoropropylene (PVDF-HFP). PVDF and its copolymers have been have been of interest for use in battery gel polymer electrolytes because of its high solubility, lower crystallinity, and lower glass transition temperature when compared to PVDF [69]. However, hybrid polymer matrix separators based on PVDF homopolymers traditionally suffered from poor mechanical properties that required significant additional processing, despite high ionic conductivities [88].

PVDF-HFP is a block co-polymer based on PVDF whose copolymer allows for both semicrystalline and amorphous regions to be established. These amorphous domains are capable of large amounts of electrolyte uptake, and crystalline domains provide sufficient mechanical integrity to form free-standing films [97, 88, 16]. The process developed by Gozdz, *et. al.* [33, 34] results in a two step procedure in which a microporous polymer membrane is first solution cast with a salt-free plasticizer which is then flushed and substituted by the liquid electrolyte during the final stage of processing. Conventional casting methods are also able to be used to form free-standing films [49].

The use of this plasticizer allows for the development of a favorable pore structure within the PVDF-HFP copolymer which is able to be refilled by an electrolyte of choice. The advantages of this method, known as a phase inversion method, is that initial steps may be performed without stringent moisture control until the final step due to moisture-sensitive species such as lithium salts not being required until the end [88]. Furthermore, use of the block co-polymer and its separation into crystalline and amorphous domains is critical for good performance of the eletrolyte, and the resulting microstructure can be readily influenced by drying temperatures and choice of solvent and plasticizer [69].

Compatibilty between ionic liquids and PVDF-HFP for gel polymer electrolytes for lithium-ion batteries has been proven [109]. The structure of PVDF-HFP and ionic liquid GPEs has also been shown to be affected by pressure during the drying process [111]. Finally, compatibility of these GPEs with zinc-based systems and evidence of Zn^{2+} ion transport has been shown [43].

As this work seeks to investigate compatibility of these GPEs for fully printed systems, the phase inversion method is not investigated due to the inability of the free-standing film to be mechanically adhered to the printed electrodes without external pressure. Thus, conventional casting methods are used instead.

6.2.2 CV Responses of Common Circuit Elements

As discussed in Section 5.3.4, electrochemical cells can be modeled by fundamental circuit elements as equivalent circuit models. Understanding the current response of these circuit elements can also provide insight into phenomena observed from cyclic voltammetry.

Figure 6.1 presents voltammograms of a, capacitor, resistor and a resistor and capacitor in parallel.

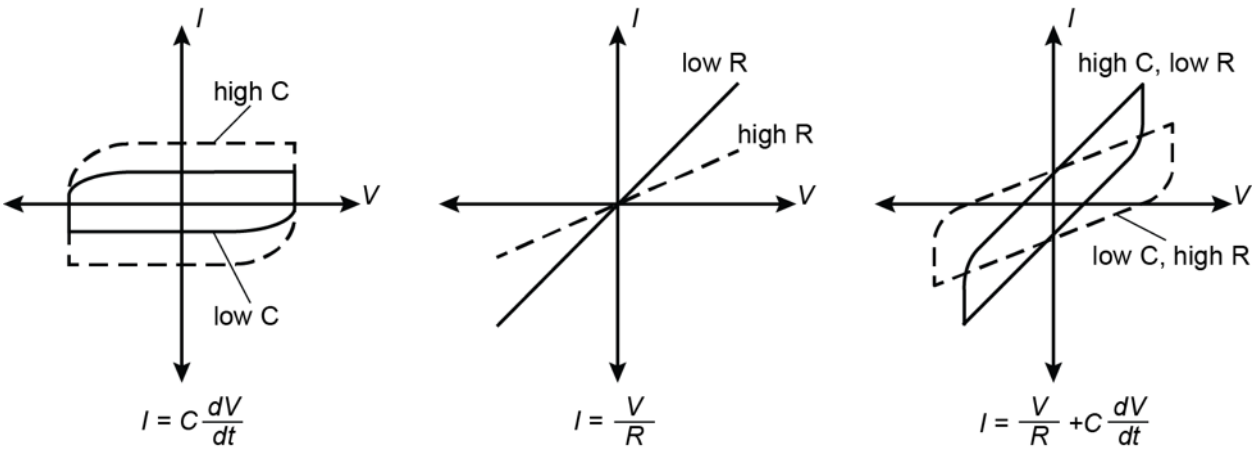

Figure 6.1: Cyclic voltammograms of circuit elements. *left*: capacitor; *middle*: resistor; *right*: resistor and capacitor in parallel.

The voltammogram for a real capacitor is a rectangle with two opposite rounded corners with constant positive and negative currents equal to the product of the capacitance and scan rate. This relationship is derived from the relationship between the rate of change of potential, $\frac{dV}{dt}$ or ν, and the capacitance, C (Eq. 6.1). While an ideal capacitor would not feature rounded corners according to Eq. 6.1, they are present in real capacitors due to the time required for charge separation in the dielectric.

$$I = C\frac{dV}{dt} = C \cdot \nu \tag{6.1}$$

The voltammogram for a resistor is a straight line interecting the origin as there the current response of a resistor is directly proportional to the applied potential following Ohm's Law (Eq. 6.2).

$$I = V\frac{1}{R} \tag{6.2}$$

Placing a resistor in parallel with a capacitor results in a parallelogram with two opposite rounded corners where the slopes of regions of increasing and decreasing current is proportional to the resistance. The current response is determined by summing the currents of the individual capacitor and resistor (Eq. 6.3).

$$I = V\frac{1}{R} + C\frac{dV}{dt} \tag{6.3}$$

6.2.3 Differential Capacity Analysis

Differential capacity analysis is analytical technique that offers insight into reactions that may be occuring at specific potentials within a cell. With this technique, the derivative of capacity is taken with respect to potential and is then plotted against potential for each cycle (*e.g.* dQ/dV vs. V). The presence and location of specific peaks revealed by differential capacity can then be matched to reactions that occur at known potentials based on individual cell chemistries [4, 13]. An example of dQ/dV vs. V is presented in Figure 6.2, and calculated and measured analysis of a $LiMn_2O_4$/graphite cell is presented in Figure 6.3, as presented by Smith, *et. al.* [86]. Cycling occurs clockwise with positive peaks reflecting reactions occuring during charge and negative peaks reflecting reactions occuring during discharge. Differential capacity analysis is particularly useful with cell cycling data under galvanostatic conditions where the rate of potential change is not directly controlled.

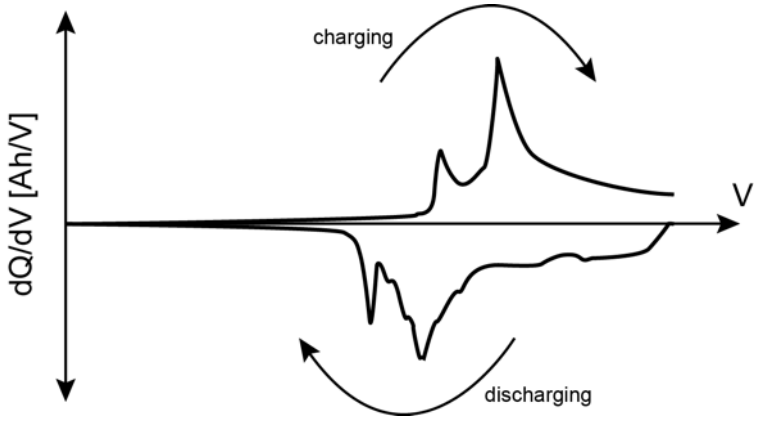

Figure 6.2: Example plot of dQ/dV vs. V.

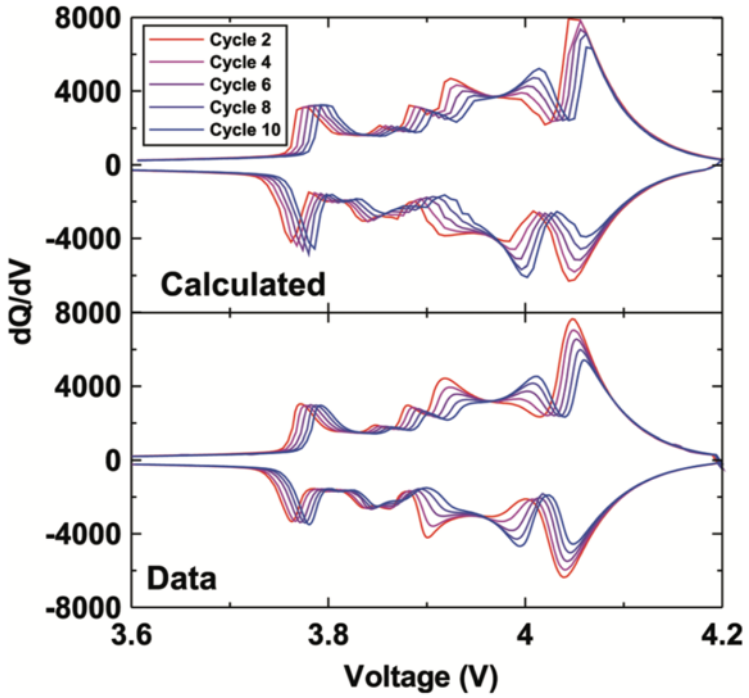

Figure 6.3: Calculated and measured dQ/dV of $LiMn_2O_4$/graphite cell. [86]

The strength of differential capacity analysis lies its ability to extract more meaningful data and track more sensitive processes from simple time-series data of current and voltage. Plateaus in potential when plotted against charge (vertical lines when plotting voltage against charge) appear as clearly identifiable peaks in dQ/dV and can probe cell degradation over a cycle life test [87]. These peaks can therefore reflect changes in phase at an electrode or unwanted side reactions that may only be present at the beginning of a cell's lifetime. In addition, the magnitude of the response correlates to the amount of redox reactions occuring at a given potential, with a flat and low magnitude response indicating a uniform and low level of reaction occurring.

6.3 Experimental Methods

This section discusses all experimental methods used in printing and testing gel polymer electrolytes (GPE) in half cells, mechanically assembled (MA) full cells, and fully printed (FP) cells. GPE manufacturing and cell assembly are first presented, followed by the electrochemical techniques used as well as other observation methods.

6.3.1 Gel Polymer Electrolyte Manufacturing

This section presents all manufacturing and processing as pertains only to the gel polymer electrolyte.

6.3.1.1 GPE Solution Preparation

The gel polymer electrolyte solution was prepared in two parts. First, a measured amount of PVDF-HFP (Kynar Flex 2801) was dissolved in n-methyl-2-pyrrolidone (NMP, Sigma-Aldrich) in a 20ml glass vial until completely homogenous. In order to shorten dissolution times, the vial was heated to 50°C on a hot plate until the polymer was fully dissolved. For experiments involving only the neat polymer, preparation took place in ambient. The polymer solution was then allowed to cool fully to room temperature before proceeding. Investigation of the neat polymer proceeded with only this solution. Table 6.1 presents the two compositions of neat polymer investigated.

Table 6.1: Neat polymer compositions

	1:3 ratio	**1:5 ratio**
PVDF-HFP [g]	1	1
NMP [g]	3	5

The ionic liquid and salt were prepared as described in Chapter 6. All material preparation took place in an argon glove box (VAC Systems) whose oxygen content was maintained at 0.20 PPM or lower and a dew point of -80°C. This solution was then transferred out of the of the glove box when necessary in order to minimize exposure to air.

The ionic liquid and salt solution was then added to the polymer solution via pipette, and the resulting gel polymer electrolyte solution was mixed using a vortex mixer until fully combined. Use of the vortex mixer introduced bubbles into the the gel polymer electrolyte solution, so the solution was allowed to rest for 30 minutes to provide time for the bubbles to rise to the surface. Table 6.2 presents masses and mass ratios for the investigated GPE compositions. Note that salt concentrations were measured in molarity instead of molality as used in Chapter 6.

Table 6.2: Gel polymer electrolyte compositions

	$[BMIM]^+[OTf]^-$	**$[EMIM]^+[OTf]^-$**
Density, ρ [g/mL]	1.292	1.387
Molarity [mol/L]	0.5	0.5
Molality [mol/kg]	0.387	0.361
IL+salt [g]	3	
PVDF-HFP [g]	1	
NMP [g]	4	

6.3.1.2 Gel Polymer Electrolyte Solution Casting

For investigation of the neat polymer and for use with half cells and mechanically assembled full cells, the GPE was solution cast into a disc. A stainless steel 2032 coin cell can (20mm diameter, 3.2mm thickness) was used as a mold. A measured amount of neat polymer solution or GPE by mass was added to the coin cell can and dried in order to drive off all NMP and cure the polymer.

For the neat polymer, drying temperatures of 60°C, 80°C, 100°C, and 120°C under ambient, vacuum, and argon environments were tested. These temperatures were chosen to remain under the stated melting temperature of 140°C [3]. For the GPE, drying temperature was maintained at 80°C, but the same three environments were tested. A combination vacuum and argon oven with PID temperature control (Jeiotech Co, OV-11) was used to dry all neat polymer samples and GPE samples under ambient and vacuum. GPE samples dried under argon were dried on a hot plate inside an argon glove box (VAC Systems). All samples were dried for 24 hours. Ambient moisture ranged from 20-50% RH, and the dew point inside the glove box was maintained at -80°C. The vacuum oven was able to maintain a gauge pressure of -0.8MPa.

These three drying environments were chosen in order to investigate the effects of pressure and humidity on polymer microstructure. Drying under ambient provided conditions with atmospheric pressure and humidity. Drying under vacuum provided low pressure and humidity, and drying under argon resulted in atmospheric pressure but low humidity. Table 6.3 presents all possible combinations of temperatures and environments that were investigated.

Table 6.3: Drying temperatures and environments.

	Environment		
Temperature	Ambient	Vacuum	Argon
60°C	○	○	○
80°C	○	○	○
100°C	○	○	○
120°C	○	○	○

Once the polymer or GPE had fully cured, the discs were allowed to cool back to room temperature. A 5/8 inch steel punch was then used to cut out the center of each disc which was used for further testing. Care was taken to center the punch as best as possible in order to avoid the cast polymer or GPE at the perimeter of the coin cell can where thickness increased due to surface tension during drying. These discs were then used for further testing.

6.3.2 Cell Manufacturing

This section presents the manufacturing process and assembly method for half cells, mechanically assembled full cells, and fully printed cells. The compositions of the cathode and anode inks are also presented. All cells were assembled in coin cells for more uniform manufacturing, but the makeup of each type of cell differs. Half cells consist of two symmetric electrodes that represent one set of the redox reactions that comprise the full cell chemistry, typically reactions associated with a metallic anode material.

6.3.2.1 Cathode and Anode Ink Compositions

Table 6.4 presents the cathode and anode ink compositions used for this chapter. Inks were made as discussed in Chapter 4.

Table 6.4: Cathode and Anode Ink Compositions

Cathode		**Anode**	
Material	**Composition**	**Material**	**Composition**
MnO_2	91wt%	Zn	91wt%
AB	2.57wt%	AB	2.57wt%
PVDF-HFP	6.43wt%	PVDF-HFP	6.43wt
Solid Phase	55wt%	Solid Phase	70wt%

6.3.2.2 Half Cells and Mechanically Assembled Full Cells

Half cells and mechanically assembled full cells were assembled for electrochemical testing and cycling. For half cells, both electrodes were 250μm Zn foil (Goodfellow) that was cut into 1cm^2 squares. For mechanically assembled full cells, 1cm^2 MnO_2 cathodes were printed on stainless steel foil (as described in Chapter 4) and cut out with scissors, leaving a roughly 0.5mm border of stainless steel foil around the printed electrode. The same Zn foil as used in half cells was used as the anode. These cells were assembled in coin cells and immediately sealed after assembly. Coin cell assembly is discussed in detail in Section 6.3.2.4.

6.3.2.3 Fully Printed Cells

For fully printed cells, a doctor blade was used to cast the GPE solution directly on top of the printed cathode layer. Work described in this chapter was performed by a manually controlled offset doctor blade with the same aluminum plate setup as described in Chapter 3.

For each batch of cells, 8 cathodes were printed on a 0.001 inch thick stainless steel foil substrate with the same size Kapton stencil as described in Chapter 3. The cathode was fully dried in air at 80°C before the first layer of electrolyte was printed. A wooden applicator (Puritan) was used to place enough electrolyte to cover all electrodes at the top of all cathodes, and the doctor blade was manually pulled forward to cover all electrodes. Multiple passes with increasing doctor blade offset height were required in order to ensure full coverage of the cathode layer. In order to ensure cohesion between printed GPE layers, drying times were controlled to ensure good mixing between previous and currently printed layers.

Once the final layer of GPE was fully dried, a similar Kapton stencil was placed directly on top of the electrolyte, and the anode slurry was printed. No additional tape or adhesive was used to affix this final stencil as the adhesion between the Kapton and the electrolyte was adequate to prevent stencil movement. The doctor blade was separated from its offset holder such that the blade was in direct contact with the stencil, again similar to the methods described in Chapter 3. Care was taken to align the anode stencil directly above the cathode below the printed electrolyte layers. Separate stencils were used in order to avoid

contamination between the cathode and anode inks. Table 6.5 presents doctor blade heights and drying times for both electrode layers and all GPE layers. All drying was performed at 80°C.

Table 6.5: Fully printed cell printing procedure

Component	Layer Number	Doctor Blade Height	Drying Time [m]
Cathode	–	stencil	20
GPE	1	200μm	15
	2	250μm	15
	3	300μm	30
	4	300μm	30
	5	300μm	180
Anode	–	stencil	60

Once the anode layer was fully dried, the cells were allowed to cool back to room temperature. The multiple cast layers of GPE resulted in a mechanically sound layer that allowed for a free standing cell without the need for external pressure to maintain contact between the electrode and electrolyte layers. A razor blade was used to carefully cut out each cell from the surrounding excess polymer, leaving a roughly 1mm excess border of GPE around the electrode stack. The cell was then peeled off the foil substrate, being careful to minimize any bending stresses to the cell, and sealed in a coin cell.

6.3.2.4 Cell Assembly

All cells were assembled and sealed in 2032 coin cells (MTI Corp.) for electrochemical testing and cell cycling. The use of a reuseable two-electrode Swagelok cell was initially investigated, but the resulting electrode contact and pressure were found to be too inconsistent for reliable use compared to sealing in coin cells.

Cell assembly varied slightly based on the type of cell and GPE casting method. For half cells and mechanically assembled full cells, cells were assembled directly within the coin cell, building the cell as part of the coin cell assembly process. For fully printed cells, the entire cell was mechanically free standing after printing and removal from the stainless steel foil substrate, so coin cell assembly was much simpler and consisted only of additional spacers and springs.

For half cells, one Zn foil electrode was first placed down, followed by the solution cast disc of GPE, followed by the second Zn foil electrode. For mechanically assembled half cells, the printed MnO_2 cathode was first placed, followed by the solution cast disc of GPE, followed by a Zn foil electrode.

Additional spacers and springs were used within coin cells in order to properly match cell thickness to the required coin cell can and lid thicknesses for proper crimping and sealing. A second spacer was used for half cells and fully printed cells prior to any electrode placement

in order to ensure good electrical contact between the positive electrode and the coin cell housing. This spacer was not used for mechanically assembled cells because the additional thickness of the stainless steel foil resulting in poor crimping during the sealing process. Care was taken to ensure all components were properly centered and aligned within the cell stack in order to avoid electrical shorts that could arise from contacting spacers, overhanging electrodes, or misaligned GPE layers.

Table 6.6 presents the order of components for half cells, mechanically assembled (MA) full cells, and fully printed (FP) cells. Figure 6.4 visually shows the order of cell assembly by type. All spacers and springs were made from stainless steel.

Table 6.6: Coin cell components

	Half Cell	**MA Cell**	**FP Cell**
Top	coin cell lid spring 0.5mm spacer	coin cell lid spring 0.5mm spacer	coin cell lid spring 0.5mm spacer
	$1cm^2$ zinc foil GPE $1cm^2$ zinc foil	$1cm^2$ zinc foil GPE printed MnO_2 cathode	fully printed cell
Bottom	0.5mm spacer coin cell can	coin cell can	0.5mm spacer coin cell can

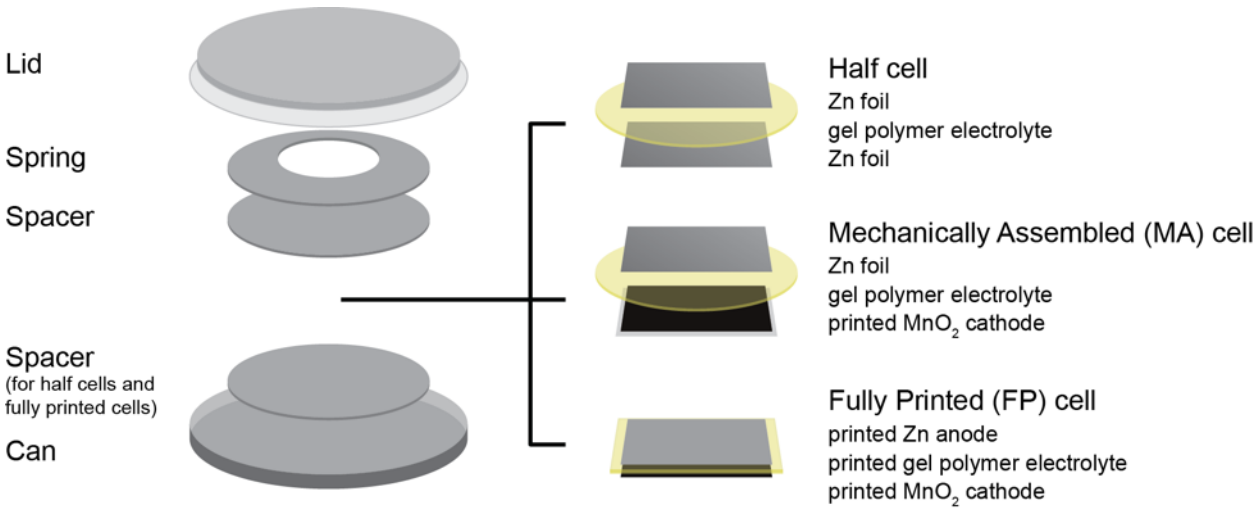

Figure 6.4: Order of components inside coin cells for half cells, mechanically assembled full cells, and fully printed cells.

After cells were fully assembled, a multimeter was used to test series resistance for half cells and open circuit potential for mechanically assembled full cells and fully printed cells in order to ensure cycleability. The coin cells were then sealed with a hand powered coin cell press which crimped the outer lip of the coin cell can around the plastic ring on the lid, sealing the components inside and preventing further movement. The cells were then allowed to rest for 24 hours before beginning testing.

6.3.3 Scanning Electron Microscopy

Scanning electron microscopy was used to investigate the microstructure of the cast polymer and GPE from varying drying temperatures and environments. A tabletop scanning electron microscope (Hitachi TM-1000) was used to take all SEM images. After punching out the polymer or GPE discs, a razor blade was used to cut out a sample towards the center of each disc. These samples were then mounted on aluminum SEM stages (Ted Pella) with double-sided adhesive carbon tape.

The chamber atmosphere was pumped down to vacuum prior to engaging the electron beam. Because of the low conductivity of the polymer, the automatic focus and brightness/-contrast settings could not be reliably used. Furthermore, it was observed that the electron beam itself degraded the polymer if focused on one area for too long, so speed was required in order to capture images that accurately represented the polymer and GPE microstructure.

6.3.4 Reference Potentiostat and Battery Cycler Setup

This section discusses the parameters for the electrochemical testing methods used to characterize half cells and full cells. Cyclic voltammetry (CV) and electrochemical impedance spectroscopy (EIS) were used to characterize the effects of drying environments on GPE performance as well as GPE casting method. Full cells were cycled galvanostatically (constant current) to test full cell performance.

CV and EIS were performd on a Gamry Reference 600 Potentiostat for half cells. For full cells, CV and EIS were performed on a Bio-Logic BCS-805 or BCS-810. Full cells were galvanostatically cycled on a Bio-Logic BCS-805 or BCS-810.

Unlike testing performed on the ionic liquid and salt only, investigation of the gel polymer electrolyte prevented the use of a three electrode setup as a reference electrode could not be easily and repeatably placed inside the system. Therefore, all testing used a two electrode cell setup where the reference electrode and counter electrode terminals of the potentiostat were connected.

6.3.4.1 Cyclic Voltammetry

For half cells, cyclic voltammetry was performed on a Gamry Reference 600 Potentiostat. Table 6.7 presents the testing parameters used. The initial potential was set at 0V, and the potential window ranged from -2V to 2V. The initial potential was set due to the two electrode limitation imposed by the cell setup causing the counter electrode to also serve as the reference electrode, effectively polarizing the reference electrode during cycling. The wider potential window compared to testing performed with the three electrode cell in Chapter 5 was to investigate the stability of the polymer in addition to the ionic liquid itself. Scan rates of 10mV/s and 100mV/s were tested for 6 and 20 cycles respectively.

Table 6.7: Gamry Reference 600 Potentiostat test parameters for cyclic voltammetry (CV) experiments.

Setting	**Value**	**Setting**	**Value**
Electrode Area [cm^2]	1	IRComp	None
Initial E [V]	0 vs E_{ref}	PF Corr. [ohm]	50
Scan Limit 1 [V]	2 vs E_{ref}	Equil. Time [s]	5
Scan Limit 2 [V]	-2 vs E_{ref}	Init. Delay	On
Final E [V]	0 vs E_{ref}	Init. Delay Time [s]	60
Scan Rate [mV/s]	100	Init. Delay Stab. [mV/s]	0
Step Size [mV]	5	Sampling Mode	Noise Reject
Cycles [#]	200	Advanced Pstat Setup	On
I/E Range Mode	Auto	Electrode Setup	On
Max Current [mA]	0.5		

For full cells, CV was performed on a Bio-Logic BCS-805. Table 6.8 presents the testing parameters used. The open circuit voltage was first measured and used as the starting potential for CV. The potential limits were set to 1.0V and 1.8V based on the cycling limits for full cells as well as the the limitations of the battery cycler, which was unable to apply negative potentials. From the starting potential, the potential was first swept to the more positive limit (1.8V) and then reversed to the less positive limit (1.0V) before returning to the open circuit voltage in order to mimic a potentiostatic cycling protocol. Each run of CV was cycled 10 times.

6.3.4.2 Electrochemical Impedance Spectroscopy

Table 6.9 presents the testing parameters used for EIS experiments on the Gamry Reference 600 Potentiostat. The frequency limits tested (Initial Freq. and Final Freq.) were chosen based on the testing limits of the reference potentiostat.

Table 6.8: Bio-Logic test parameters for cyclic voltammetry (CV) experiments

Setting	Value
E_i	0 [V] vs. E_{oc}
dE/dt	10 or 100 [mV/s]
E_1	1.8 [V] vs. Ref
E_2	1.0 [V] vs. Ref
n_c	10
Measure <I> over the last	100 [%] of the step duration
Record <I> averaged over N	10 voltage steps
E Range	0V; 9V
I Range	Auto
Bandwidth	4 - fast
E_f	0 [V] vs. E_{oc}
dE*N	1.5 [mV]
points per cycle	1067

Table 6.9: Gamry Reference 600 Potentiostat test parameters for electrochemical impedance spectroscopy (EIS) experiments.

Setting	Value	Setting	Value
Initial Freq. [Hz]	1e6	Conditioning	Off
Final Freq. [Hz]	1e-1	Init. Delay	On
Points/decade	10	Init. Delay Time [s]	100
AC Voltage [mV rms]	10	Init. Delay Stab. [mV/s]	0
DC Voltage [V]	0 vs E_{OC}	Estimated Z [ohms]	100
Area [cm^2]	0.00196	Optimize for	Normal

Table 6.10 presents the testing parameters used for EIS experiments on the Bio-Logic testers. Both the high and low frequency limits of the Bio-Logic tester were one order of magnitude lower than those of the Gamry potentiostat.

Table 6.10: Bio-Logic test parameters for electrochemical impedance spectroscopy (EIS) experiments.

Setting	**Value**
E	0 [V] vs E_{oc}
f_i	10.000 [kHz]
f_f	0.010 [Hz]
N_d	10 points per decade in Logarithmic spacing
V_a	10 [mV]
N_a	1 measure(s) per frequency
drift correction	Off
E Range	0V; 9V
I Range	Auto
Bandwidth	4 - fast

6.3.4.3 Galvanostatic Cycling

Table 6.11 presents the galvanostatic testing parameters used on Bio-Logic testers. Cells were first allowed to rest for 3 minutes before cycling in order to measure OCV. Cells were then cycled from 1.0-1.8V at a constant charge and discharge current of $\pm 125 \mu$m. Cells were allowed 24h to reach the target potentials at constant current, after which the test procedure proceeded to the next step if unable. Cells were allowed to rest for 3 minutes after being charged.

Table 6.11: Bio-Logic test parameters for galvanostatic cycling.

Setting	**Value**		
	Sequence 0	**Sequence 1**	**Sequence 2**
Step 1			
Set I to I_s (vs. None) =	0mA	-125μA	125μA
for at most t_1 =	0h 0mn 0s	24h	24h
Limit $E_{cell} > E_M$ =	0V	1V	1.8V
Record every dE_1 =	0mV	0mV	0V
or dt_1 =	0s	5s	5s
Hold E_M for t_M =	0h 0mn 0s	0h 0mn 0s	0h 0mn 0s
Limit |I| < I_m =	0mA	0mA	0mA
or |dI/dt| < dI/dt_f =	0mA/s	0mA/s	0mA/s
Record every dQ =	0A.h	1A.h	1A.h
or dt_q =	0s	120s	120s
Limit |ΔQ| > ΔQ_M =	0mA.h	0mA.h	0mA.h
<=> Δx_M =	0	0	0
Step 2			
Rest for t_R =	0h 3mn 0s	0h 0mn 0s	0h 3mn 0s
Limit |dE_{cell}/dt| < dE_R/dt =	0mV/h	0.1mV/h	0.1mV/h
Record every dE_R =	0mV	0mV	0mV
or dt_R =	5s	5s	5s
Step 3			
If $E_{cell} < E_L$ =	pass	pass	pass
Step 4			
Go back to seq. N'_s =	0	0	1
for n_c =	0	0	200

6.4 Results and Discussion

This section presents results from scanning electron microscopy and electrochemical testing for testing the influence of environmental manufacturing conditions on GPE performance. GPEs were assembled into half cells, mechanically assembled full cells, and fully printed cells for testing.

6.4.1 Gel Polymer Morphology

This section presents SEM images of neat polymer and gel polymer electrolyte. Polymers and GPEs were solution cast and dried at 60, 80, 100, and 120°C and under ambient, vacuum, and argon environments.

6.4.1.1 Neat Polymer

Figures 6.5 and 6.6 present SEM images of the neat polymer cast from 1:3 and 1:5 mass ratios of PVDF-HFP:NMP. The two mass ratios of polymer to solvent were investigated to characterize the role solvent content plays in polymer microstructure, and a range of temperatures were tested to investigate the effect of rates of polymer curing on microstructure. The three drying environments were tested in order to isolate any effect pressure and humidity may have on the polymer alone in the absence of ionic liquid and salt.

For both mass ratios of polymer to solvent, spherulites were observed for all combinations of temperature and drying environment. The formation of these spherulites is due to the self-assembly of the block co-polymer. Where spherulites impinge on each other, deformation and adhesion are visible, resulting in the formation of a large network of polymer throughout the entire cast sample. This cohesive network is likely responsible for the mechanical strength and integrity observed for the GPE. All samples were mechanically free-standing and able to be handled without issue.

Between 1:3 and 1:5 mass ratios of polymer to solvent, no significant differences in microstructure were observed for all combinations of temperature and drying environment. This indicates that the amount of solvent present has little effect on the resulting polymer microstructure and suggests that the polymer structure is not dependent upon the amount of polymer deposited at a given time. Therefore, the polymer structure is likely independent upon casting method.

In general, higher temperatures resulted in smaller spherulites with diameters averaging 20-40μm at 60°C to 5-10μm at 120°C. The smaller microstructure from higher temperatures is likely due to faster solvent evaporation which provides less time for micelles to coalesce. Furthermore, higher drying temperatures caused higher thermal expansion of the polymer during the drying process, which resulted in more contraction of the polymer as it cooled to room temperature and thus a more densely packed microstructure. In contrast, lower temperatures generally resulted in larger spherulites that were less densely packed, resulting in more voids within the polymer. Drying temperatures of 80°C resulted in a microstructure with the largest spherulites, averaging 30-50μm, but also clear regions of voids between them.

Notably, microstructures were more similar between ambient and argon environments than vacuum, indicating that pressure plays a larger role in determining polymer microstructure than humidity. For samples dried under vacuum, there was a large drop in spherulite size from about 30μm at 80°C to about 5μm at 100°C, compared to a more gradual decrease for samples dried in ambient and argon. The reason for this jump in spherulite size is unclear but may be due to the combination of higher temperature and low pressure causing a significant increase in solvent evaporation rate that is absent for the other two drying environments.

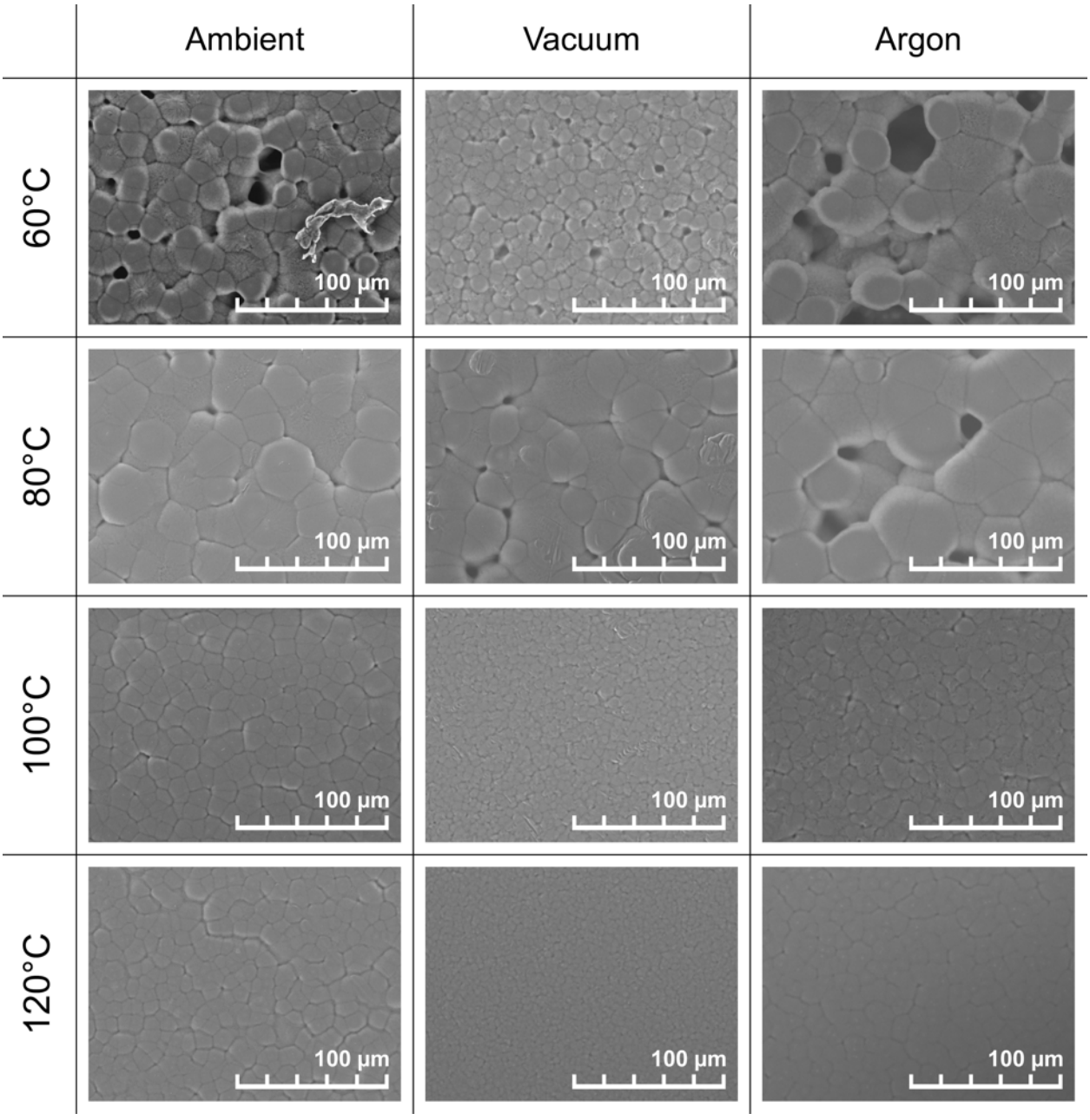

Figure 6.5: Scanning electron micrographs of 1:3 by mass PVDF-HFP:NMP (no electrolyte).

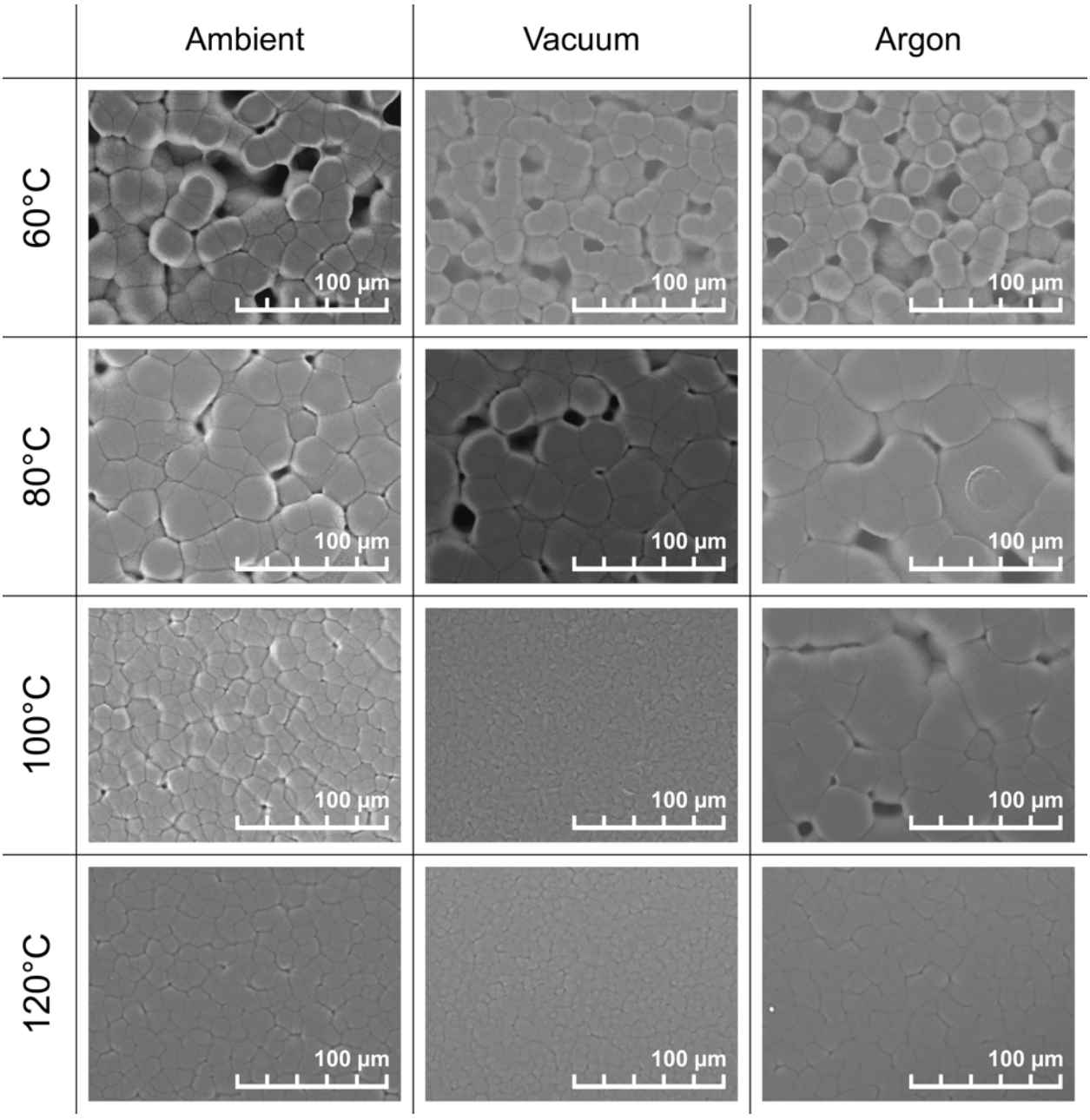

Figure 6.6: Scanning electron micrographs of 1:5 by mass PVDF-HFP:NMP (no electrolyte).

6.4.1.2 Gel Polymer Electrolyte Morphology

Figure 6.7 presents SEM images of a 3:1:4 $[BMIM]^+[OTf]^-$ GPE (by weight, 3 parts $0.5M$ $Zn(OTf)_2$ in $[BMIM]^+[OTf]^-$, 1 part PVDF-HFP, 4 parts NMP) cast at the same temperatures and under the same environments. These samples were examined in order to investigate the resulting microstructure of the GPE with the inclusion of ionic liquid and salt. Gel polymer electrolytes with $[EMIM]^+[OTf]^-$ were not tested because it was assumed that both ionic liquids would produce similar mechanical and structural effects on the gel polymer microstructure.

The inclusion of the ionic liquid and salt significantly affected the gel polymer microstructure by behaving like a plasticizer during the drying process. The high vapor pressure of the ionic liquid resulted in a liquid phase persisting as the polymer cured, interfering with spherulite formation and cohesion. This is most apparent with 100°C and 120°C samples dried under vacuum and in argon, where individual spherulites are distinguishable from each other with cohesion between spherulites being absent. However, samples dried at 60°C and 80°C for all drying environments did display cohesion between spherulites. Unfortunately, image contrast was poor for samples dried in ambient and under vacuum at 60°C and under vacuuum at 80°. However, GPEs dried under vacuum and in argon at 80°C otherwise appear similar.

While all GPEs dried at 60°C and 80°C were able to be handled as 5/8 inch diameter discs without issue, samples dried at 100°C and 120°C were fragile and prone to fracturing and crumbling. These higher temperature disc samples were unable to be picked up by a pair of tweezers without fracturing near the tweezer tips.

Spherulite diameter generally remained constant across drying environments, ranging from 5-10μm at 60°C to 40-80μm at 120°C. In addition, spherulite diameter increased with increasing temperature, opposite the trend observed in the absence of the ionic liquid. Because of the persistence of a liquid phase throughout the entirety of the drying process, the higher temperature likely allowed nucleated spherulites to grow and coalesce into larger micelles. This would in turn result in increased phase separation between the polymer and the ionic liquid solution, leading to individual spherulites separated by a boundary of ionic liquid instead a more homegenous phase distribution. This separation of spherulites would thus prevent adhesion between them and result in lower mechanical strength upon cooling.

Samples dried at 80°C and higher under an ambient environment resulted in larger spherulites compared to the other drying environments. This phenomenon was absent with the neat polymer and may be due to the polymer and ionic liquid and salt solution absorbing water into the spherulite structure itself. For samples dried at 100°C and 120°C, the spherulites no longer retained a spherical shape upon examination but rather showed evidence of deformation and fracture. The absorbed water likely caused each spherulite to expand upon each other and then contract and fracture upon cooling back to room temperature. This would again contribute to lower mechanical integrity for each cast sample.

A significant amount of "sweating" of the ionic liquid was observed as the cast samples cooled back to room temperature. Evidence of this sweating from GPEs both cast in coin

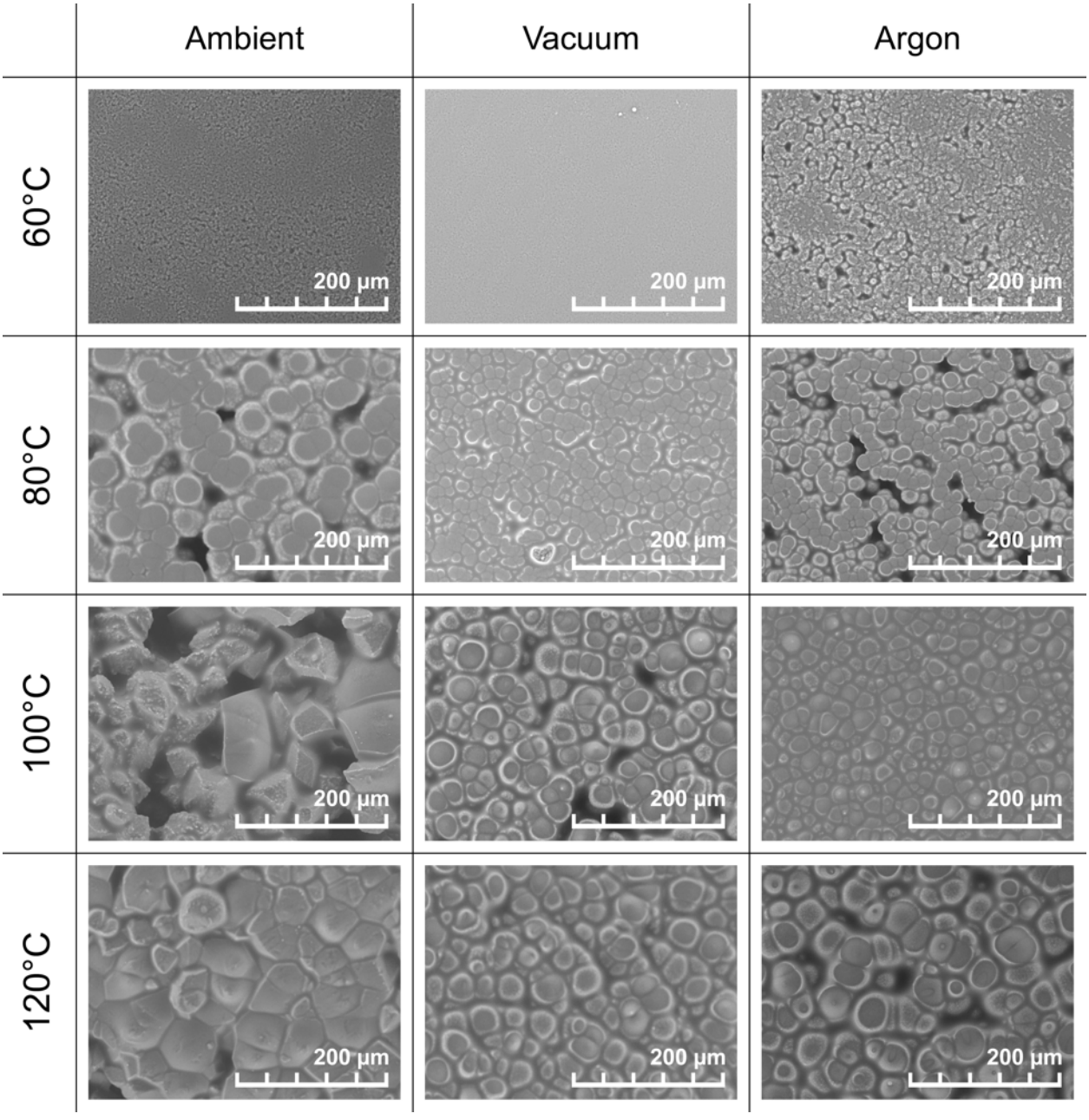

Figure 6.7: Scanning electron micrographs of GPE, 3:1:4 electrolyte:PVDF-HFP:NMP.

cells and via doctor blade is presented in Figure 6.8. This has been reported previously and was evidenced by the appearance of droplets of the ionic liquid and salt solution on the surface of the cast GPEs once the samples cooled due to the polymer structure contracting and squeezing out excess ionic liquid. The ratio of electrolyte to polymer was chosen to take advantage of this phenomenon in order to ensure adequate wetting between electrode-GPE interfaces for half cells and full cells.

GPEs for further testing were dried only at 80°C. Samples dried at 100°C and 120°C did not exhibit the mechanical stability required for assembly of half cells and full cells. Since no significant differences were observed when handling GPEs dried at 60°C or 80°C, the higher temperature was chosen in order to ultimately facilitate faster drying times for fully printed cells.

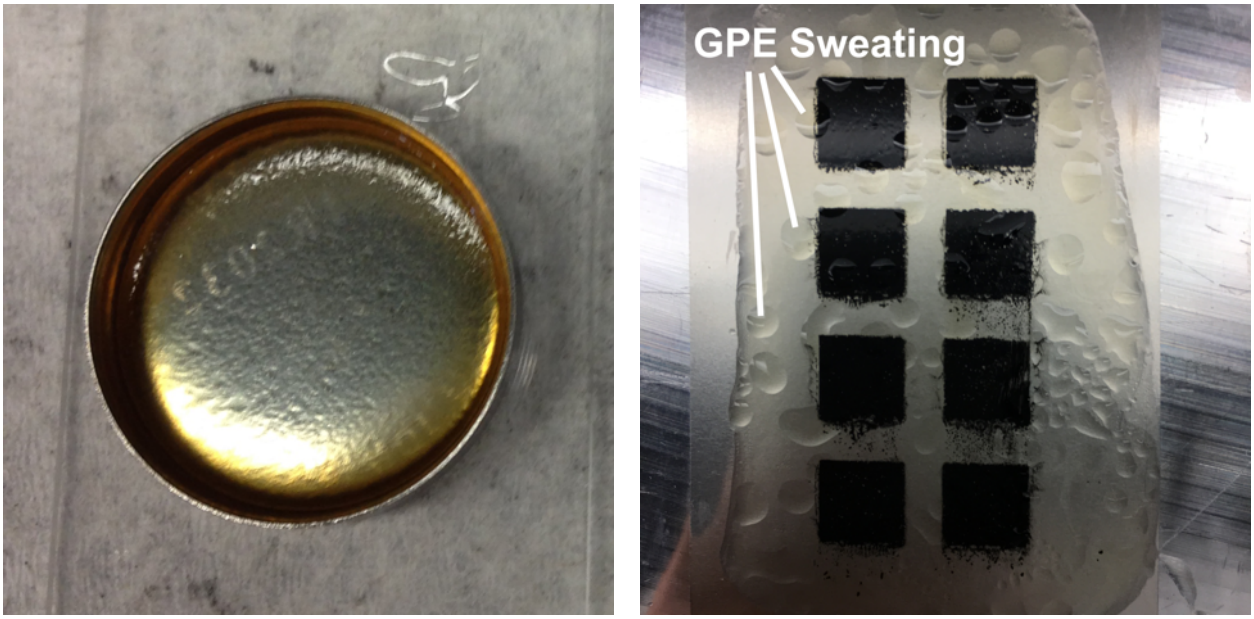

Figure 6.8: GPE sweating from GPEs both cast in coin cells *left* and cast via doctor blade *right*.

6.4.2 GPE Thickness

Figure 6.9 presents thickness vs. mass data of 20 samples of 3:1:4 $[BMIM]^+[OTf]^-$ GPE. Samples were dried at 80°C under ambient. For each sample, an ideal mass of 0.4g was targeted, but the actual mass of GPE deposited was recorded. Sample thickness was measured by sandwiching each GPE between two glass slides, measuring the entire stack's thickness via a handheld screw micrometer (Mitutoyo), and then subtracting the thickness of the slides.

Despite only small variations in deposited GPE mass (0.3965-0.4085g), a large range of sample thicknesses were observed (0.326-0.408mm). However, no clear trend was observed

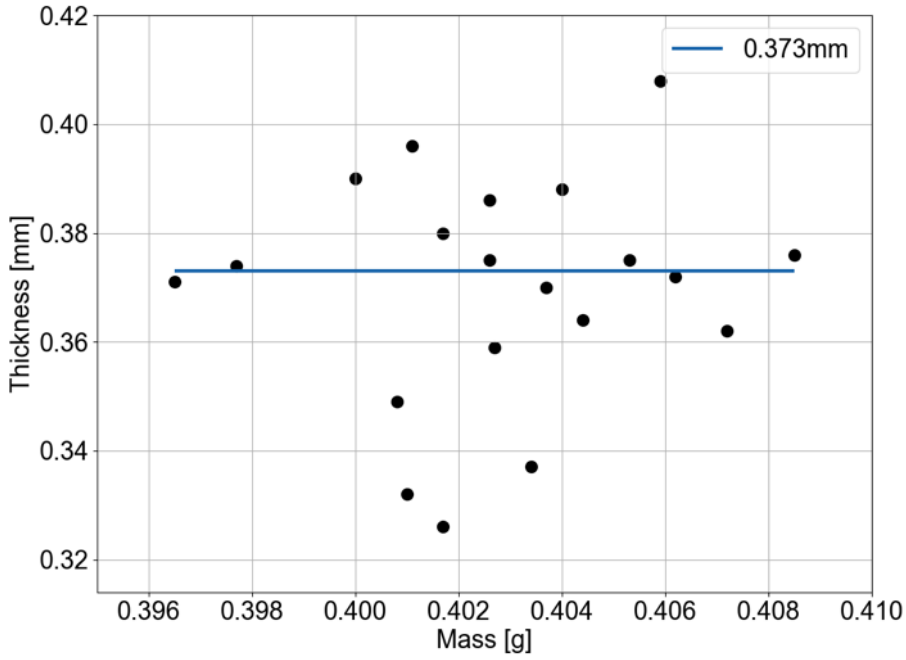

Figure 6.9: Median of thickness vs. mass of cast 3:1:4 GPE for $n = 20$ samples.

for outlier samples, and the majority of samples fell within a range of 0.36-0.40mm thickness with an overall median value of 0.373mm.

Because of the method of sealing GPE samples within coin cells for testing with half cells and mechanically assembled full cells, non-destructive disassembly of the cell stack was not possible, and thus individual GPE thicknesses could not be measured after testing. GPE thickness measurement prior to coin cell assembly was also undesirable as sandwiching the GPE between glass slides inevitably led to not insigificant loss of absorbed ionic liquid due to the applied pressure and contact area.

Since all coin cell cast GPEs were cast with an ideal mass of 0.4g, this median thickness value was used for all future calculations where the GPE thickness was required (primarily for ionic conductivity measurements with EIS data).

6.4.3 Half Cells

This section presents results from electrochemical testing of half cells. Cyclic voltammetry was used to characterize half cell performance. Cells were disassembled and scanning electron microscopy used to examine post-cycling microstructures.

6.4.3.1 Cyclic Voltammetry

Figures 6.10 and 6.11 present cyclic voltammetry results and the cathodic and anodic crossover potentials and cyclic efficiency for half cells with cast GPEs with $[BMIM]^+[OTf]^-$. Figures 6.12 and 6.13 present the same results for $[EMIM]^+[OTf]^-$ GPEs. Samples were cured under ambient, vacuum, and argon at 80°C for 24 hours. Half cells were cycled at 20mV/s for 6 cycles or 100mV/s for 20 cycles. Cycle efficiencies for the first cycle were not plotted as a smaller anodic voltage window was scanned for that cycle only, leading to misleading calculated efficiencies.

6.4.3.2 Effect of Drying Environment

For both ionic liquids, the cyclic voltammograms produced current responses that were generally rotationally symmetric, as expected from the two electrode setup used. Current responses for GPEs cast in argon were an order of magnitude lower compared to the stable current responses for samples dried in ambient or under vacuum. In addition, peak currents for samples dried in argon steadily increased with cycle number for the range of cycles tested, compared to responses of GPEs dried in ambient or under vacuum that either decreased over the range of cycles tested or showed evidence of electrical shorts developing, as discussed later. This difference in current responses indicates that water introduced during processing plays a significant role in the electrochemical performance of these GPEs.

GPEs dried under vacuum showed the highest peak currents for both ionic liquids. Based on the differences in current magnitude between the three tested environments, the inclusion of absorbed water likely plays a role in increasing Zn^{2+} diffusivity within the GPE. However, the fact that peak currents were not higher with GPEs dried in ambient suggests there is an optimal amount of water that is beneficial but also does not impede Zn^{2+} redox reaction rates or potentials. This is consistent with findings from previously reported work in which GPEs with about 14% water resulted in the highest current densities for the tests performed [102].

Zinc is known to oxidize readily in the presence of water to form zinc hydroxide and zinc oxide (Eq. 6.4 and 6.5) [104]. These oxidation reactions are known to occur in alkaline zinc cells with aqueous electrolytes and may be present in the tested GPEs.

$$Zn + 2OH^- \rightarrow Zn(OH)_2 + 2e^- \tag{6.4}$$

$$Zn(OH)_2 \rightarrow ZnO + H_2O \tag{6.5}$$

The presence of these side reactions likely contributes to the higher Zn^{2+} deposition and dissolution overpotentials observed with GPEs dried in ambient and under vacuum. Furthermore, the persistence of zinc oxide and zinc hydroxide removes cycleable zinc from the system and may also increase GPE internal resistance, respectively causing a drop in peak current with increasing cycle number and pushing the peak locations to higher potentials.

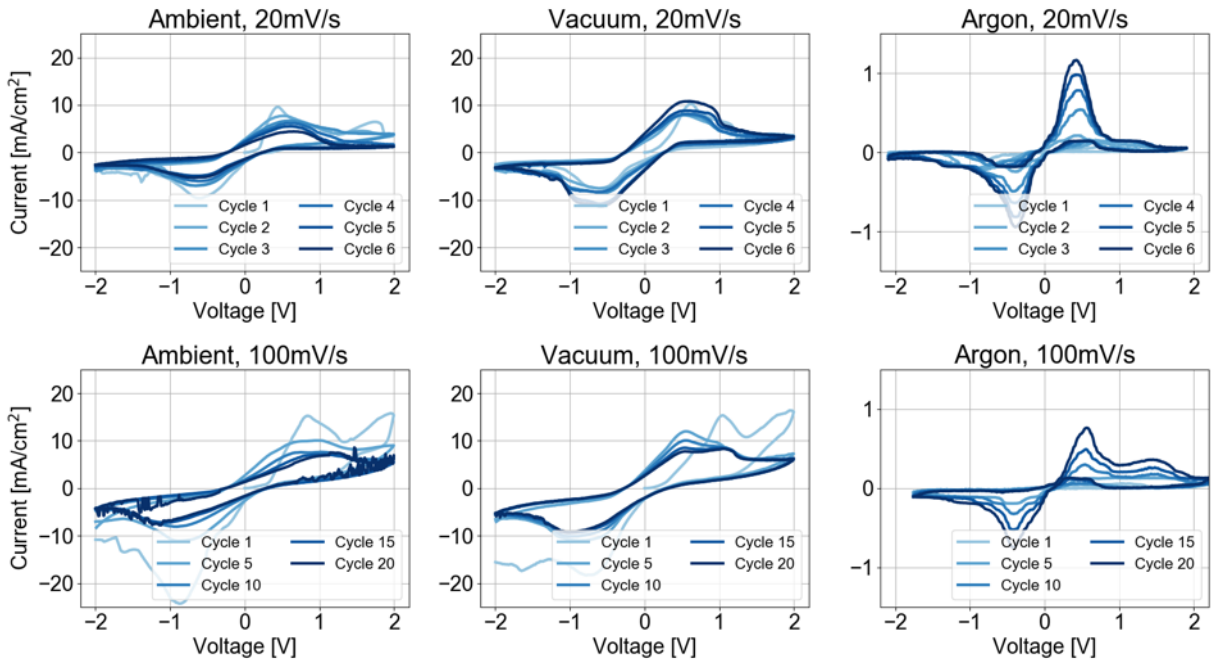

Figure 6.10: CV of half cell with $0.5M$ $[BMIM]^+[OTf]^-$ GPE, scan rates of 20 mV/s and 100 mV/s, cured under ambient, vacuum, and argon.

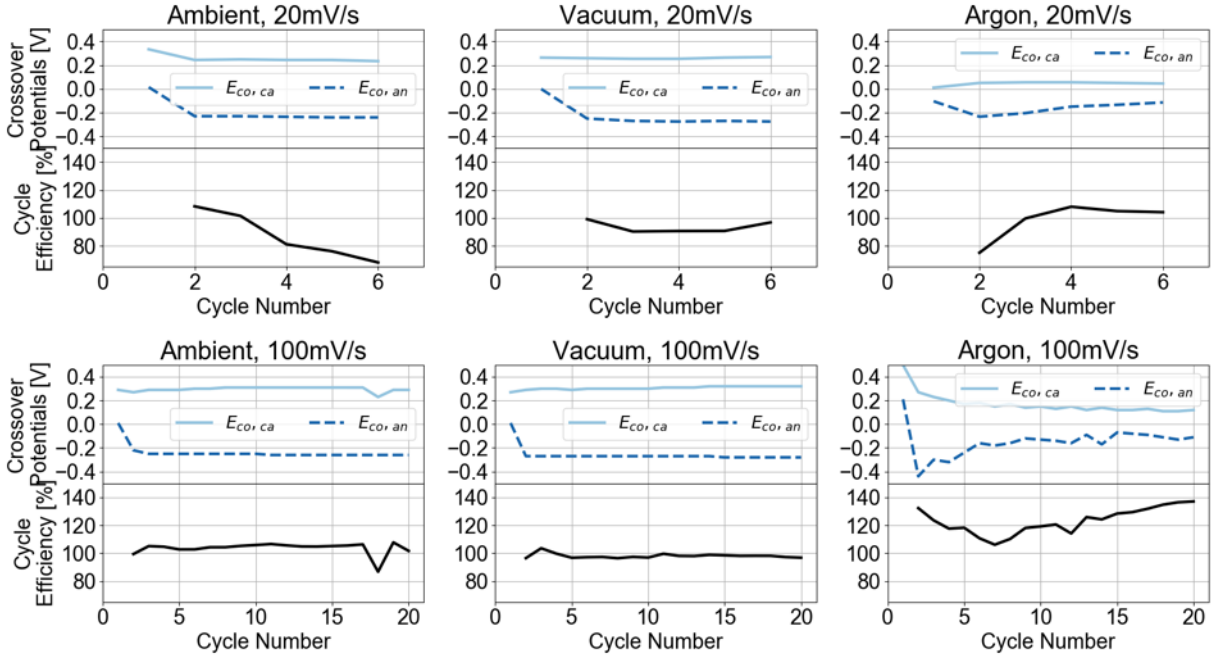

Figure 6.11: Cathodic and anodic crossover potentials and cycle efficiency of $[BMIM]^+[OTf]^-$ GPEs.

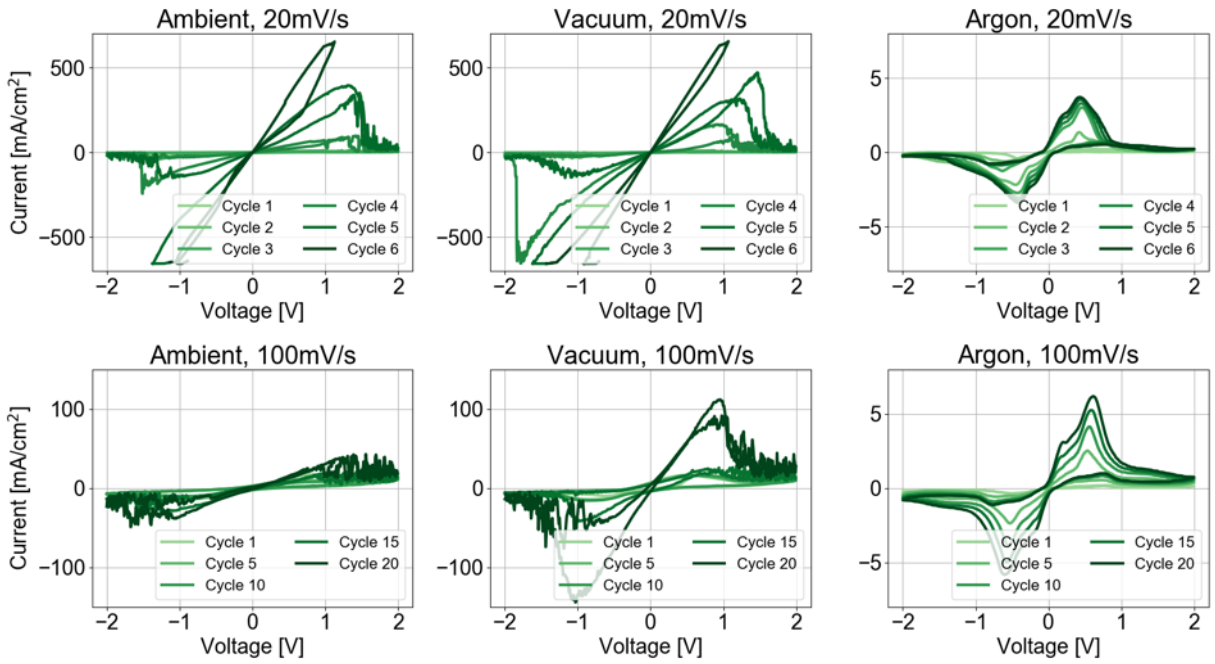

Figure 6.12: CV of half cell 0.5M $[EMIM]^+[OTf]^-$ GPE, scan rates of 20 mV/s and 100 mV/s, cured under ambient, vacuum, and argon.

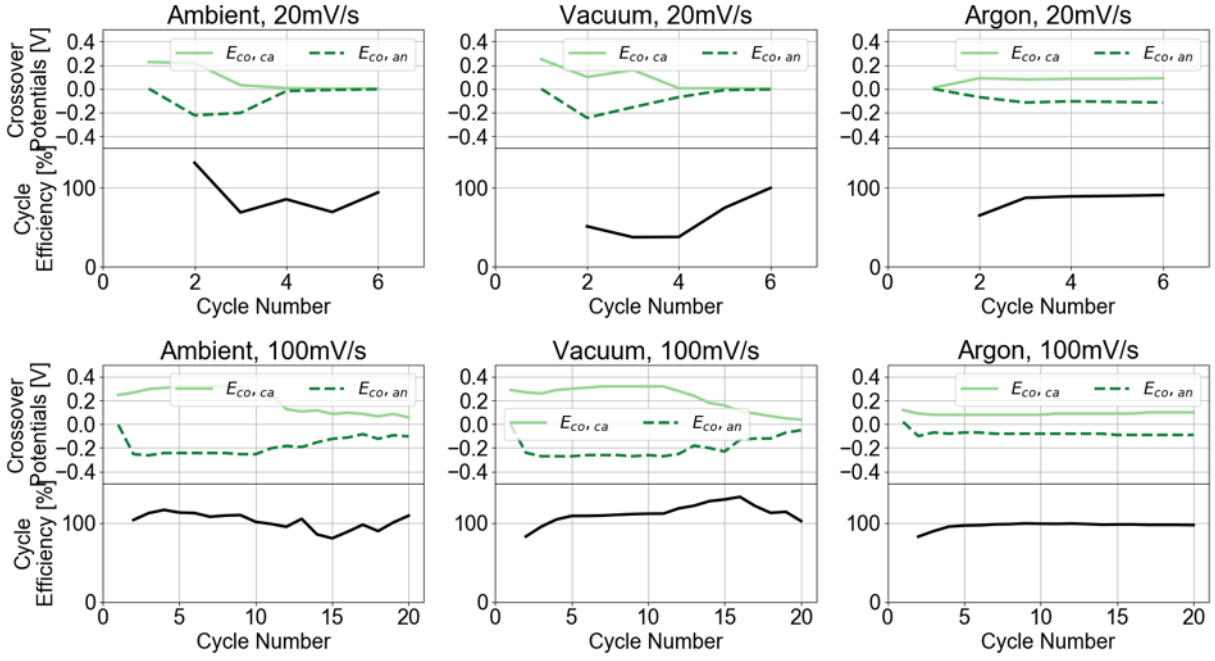

Figure 6.13: Cathodic and anodic crossover potentials and cycle efficiency of $[EMIM]^+[OTf]^-$ GPEs.

Crossover potentials also varied by drying environment. For GPEs dried in ambient and under vacuum, both cathodic and anodic crossover potentials remained relatively constant at around ±0.25-0.3V. For GPEs dried in argon, crossover potentials were lower at about 0.05-0.1V for cathodic crossover potentials and -0.1V for anodic crossover potentials. While crossover potentials were expected to be at 0V due to cells being symmetric, connection of the reference electrode and counter electrode terminals to accomodate the two electrode setup likely influenced the measurement.

With the exception of GPEs dried in ambient and scanned at 20mV/s, cycle efficiencies remained relatively constant throughout cycling and ranged from 90-105%. Cycle effieciencies were defined as the amount of oxidation charge divided by the amount of reduction charge, as presented in Chapter 5. In general, the slower scan rate resulted in cycle efficiencies less than unity (more reduction), while the faster scan rate resulted in cycle efficiencies greater than unity (more oxidation), though these trends were not followed for argon GPEs with $[BMIM]^+[OTf]^-$ or with much less effect for argon GPEs with $[EMIM]^+[OTf]^-$. This difference in cycle efficiency may be due to absorbed water present within GPEs exposed to ambient and the rate of side reactions involving water. In general, lower

As seen with investigation into ionic liquid solutions in Chapter 5, cycle efficiencies remained less than unity primarily due to more time being allowed for reduction than oxidation based on the order of the reaction mechanism. At slow scan rates with GPEs, the longer times afforded for reaction may allow the deposition and dissolution of Zn^{2+} to dominate the overall measured charge and discharge capacities. However, at faster scan rates with water present, the contribution of side reactions involving water may be large enough to significantly add to the overall current response, leading to efficiencies greater than unity as some oxidized zinc is consumed by unwanted side reactions. Observed cycle efficiencies for $[EMIM]^+[OTf]^-$ GPEs dried in argon are near but slightly less than unity, but the behavior seen for $[BMIM]^+[OTf]^-$ GPEs dried under argon requires further explanation.

Finally, GPEs dried under argon displayed secondary opposite redox peaks on each scan (*i.e.* a small oxidation peak during the cathodic scan and a small reduction peak during the anodic scan), particularly at 20mV/s scan rates. These secondary peaks were located at potentials slightly greater in magnitude than the primary peaks, about ±0.7V, with currents of 0.5-1mA/cm^2. The origin of these secondary peaks is unclear as an increase when the scan direction is reversed is typically not seen before the crossover potential.

6.4.3.3 Effect of Ionic Liquid

For GPEs with $[BMIM]^+[OTf]^-$, some two peak shapes were favored upon oxidation of the working electrode, particularly for GPEs cast under vacuum and in argon. Contrary to expected behavior with CV as observed in Chapter 5 in the absence of polymer, peak heights were not significantly higher with faster scan rates and were even lower at 100mV/s than 20mV/s for GPEs dried in argon. The similar peak heights observed with investigation of GPEs may be due to a combination of larger electrode surface areas (1cm^2 vs. 0.00196cm^2) and no initial nucleation on a foreign metal surface required due to zinc foil electrodes used

(vs. Pt electrodes). Further discussion of GPE resistance and ionic conductivity is presented in Section 6.4.4.2.

Peak currents were observed at ±0.5-0.6V for all $[BMIM]^+[OTf]^-$ GPEs scanned at 20mV/s and the GPE dried in argon and scanned at 100mV/s. For GPEs dried in ambient and under vacuum and scanned at 100mV/s, peaks were much broader and more difficult to identify but were present around ±1V.

For $[EMIM]^+[OTf]^-$ GPEs, the emergence of some two peak shapes were visible for both GPEs dried in argon, as well as similarly inceasing peak heights. Furthermore, peak currents were about five times higher for $[EMIM]^+[OTf]^-$ GPEs than for $[BMIM]^+[OTf]^-$ GPEs.

GPEs with $[EMIM]^+[OTf]^-$ dried in ambient and under vacuum showed clear signs of electrical shorts developing and growing throughout the duration of cycling. These shorts manifest a transition from a typical electrochemical current response to that of a resistor. The shorts are due to plated Zn pathways through the GPE that bridge the two Zn foil electrodes. The effective resistance drops as cycling continues, leading to lines with steeper slopes as more parallel pathways are developed.

For samples scanned at 20mV/s, evidence of shorts is observed as early as cycle 4. For samples scanned at 100mV/s, shorts are not observed until at least cycle 10, but they emerge by cycle 15. Notably, no shorts are observed for samples dried under argon.

As seen previously with cyclic voltammetry performed with only the ionic liquid and salt, use of $[EMIM]^+[OTf]^-$ offers higher current densities than $[BMIM]^+[OTf]^-$. However, these higher current densities in the presence of water also likely lead to more irregular Zn deposition morphologies that lead to the formation of electrical shorts. The formation of shorts at both slow and fast scan rates suggests that exposing $[EMIM]^+[OTf]^-$ GPEs to ambient conditions during processing leads to catastrophic results during cycling. Though $[BMIM]^+[OTf]^-$ GPEs provided lower currents, they remained free from shorts throughout the duration of cycling.

6.4.3.4 Scanning Electron Microscopy

Figure 6.14 presents SEM images of a half cell with GPE dried in ambient after cycling at 10mV/s. The coin cell was opened and the Zn foil electrode rinsed with acetone and air dried in order to avoid damaging the microstructure.

The SEM images show evidence of Zn transport through the GPE. Crystallized Zn is visible within the pores of the GPE structure on the side directly adjacent to the Zn foil. This confirms compatibility of Zn transport through the GPE as well as deposition and dissolution.

A number of microstructures are visible on the Zn foil after repeated cycling. The most common structure that was observed was Zn plating in hexagonal crystals with planes whose directions ranged from close to parallel to the foil surface to almost perpendicular. However, some crystals were also observed with much smaller disorganized platelets only perpendicular to the electrode surface, in addition to zinc oxide mesocrystals. The presence of these

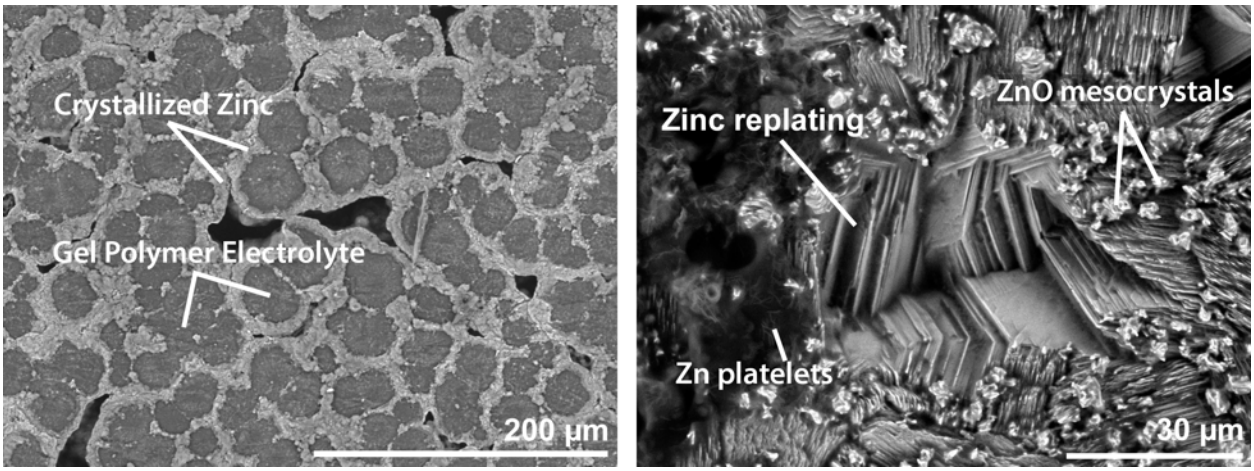

Figure 6.14: SEM images of half cell with GPE dried in ambient after cycling at 10mV/s. *left*: GPE surface showing Zn crystallization into the GPE; *right*: Zn foil surface showing various morphologies of Zn plating and ZnO mesocrystals.

microstructures and oxide products are the result of varying levels of water present in the system which influences surface morphologies [59].

6.4.4 Mechanically Assembled Full Cells

This section presents cyclic voltammetry, electrochemical impedance spectroscopy, and galvanostatic cycling data for mechanically assembled full cells. GPEs were cured under ambient, vacuum, and argon at 80°C for 24 hours. All cells used the same printed MnO_2 cathode and a zinc foil anode.

For CV and EIS, 4 samples were tested for each combination of environment and scan rate. Representative samples were chosen for presentation for CV and EIS results, but all cycleable cells are included when presenting solution resistances and charge transfer resistances. For CV, cells were cycled at 10mV/s or 100mV/s from 1.0-1.8V for 50 cycles total. This potential window was chosen to match the potential limits for galvanostatic cycling as presented in Chapter 7. EIS was performed prior to cycling with CV and then every 10 cycles after. For galvanostatic cycling, 8 cells were made per batch, but only cycleable cells are presented.

6.4.4.1 Cyclic Voltammetry

Figures 6.15 and 6.16 present cyclic voltammograms of representative samples for mechanically assembled full cells with cast GPEs with $[BMIM]^+[OTf]^-$ and $[EMIM]^+[OTf]^-$ respectively. Figures 6.17 and 6.18 present, cathodic and anodic crossover potentials, cumulative oxidation and reduction charges, and cycle efficiencies for the same cells. Cycle efficiencies for the first cycle were not plotted in order to avoid misleading calculated efficiencies due

to the first cycle of CV beginning the scan at open circuit voltage instead of at the lower potential limit, resulting in an incomplete potential range being scanned.

For both ionic liquids, cells with GPEs dried in ambient or under vacuum exhibited current responses up to two orders of magnitude greater than cells with GPEs dried under argon. However, these cells also did not show any notable peaks and instead resulted in voltammograms more consistent with electrochemical double layer capacitors [53] but with not insignificant parallel resistance. Cells with GPEs dried in argon with $[EMIM]^+[OTf]^-$ showed cathodic peaks at around 1.1-1.3V and anodic peaks at around 1.55V. Cells with argon GPEs with $[BMIM]^+[OTf]^-$ did not show any peaks except for a small and broad cathodic peak centered at 1.2V when scanned at 10mV/s while a similar response but lower in magnitude was observed when scanned at 100mV/s.

OCVs for cells with $[BMIM]^+[OTf]^-$ GPEs ranged significantly from about 1.4V for GPEs dried in ambient, 1.5V for GPEs dried under vacuum, and 0.86-1.29V for GPEs dried in argon. OCVs for cells with $[EMIM]^+[OTf]^-$ GPEs were more consistent but still varied by drying environment from 1.48V for ambient, 1.46-1.47V for vacuum, and 1.36-1.4V for argon. Lower OCVs for argon GPEs were consistent across both ionic liquids. The variation for samples within each environment and ionic liquid combination are indicative of variability during the manufacturing process, likely originating from the GPE and the printed MnO_2 cathode. The presence of water from the manufacturing process results in a higher OCV, and lower OCVs as observed with GPEs dried in argon with $[BMIM]^+[OTf]^-$ are indicative of poor cycling performance.

Generally, scanning at higher scan rates resulted in responses with lower resistance and lower capacitance, as evidenced by steeper slopes and smaller hysteresis envelopes. This is likely due to a thinner diffusion layer afforded by the faster scan rate. Scanning at higher scan rates also resulted in larger magnitude maximum currents, though the cause of this is likely due more to higher internal resistance than from faradaic processes as no maximum peaks were visible.

With the exception of $[BMIM]^+[OTf]^-$ GPEs scanned at 100mV/s, GPEs dried under vacuum displayed wider envelopes and steeper slopes, again suggesting higher capacitance and lower resistance. Again, water absorbed from ambient during processing is likely to play a role in GPE performance. The lower water content of GPEs dried under vacuum may result in more available sites for Zn^{2+} adsorption on the electrode surfaces not blocked by water itself as well as less zinc oxide and zinc hydroxide formation that would reduce the amount of electroactive Zn^{2+}.

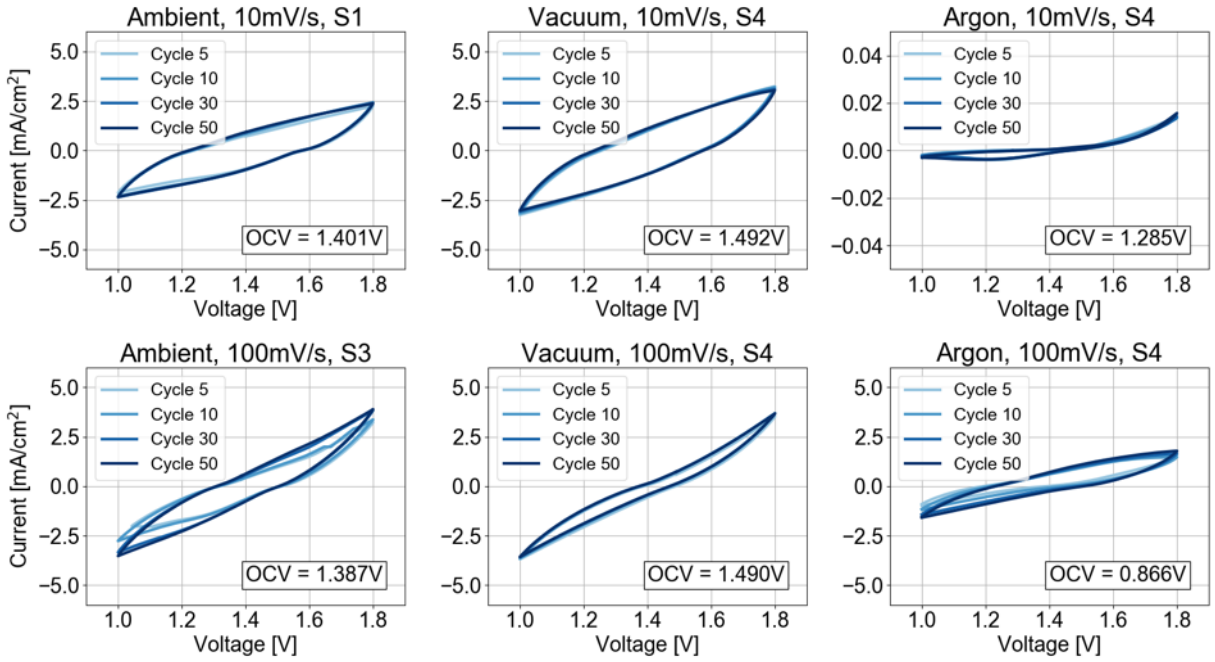

Figure 6.15: CV of mechanically assembled full cell with $[BMIM]^+[OTf]^-$ GPEs. Cycling was interrupted every 10 cycles to perform EIS.

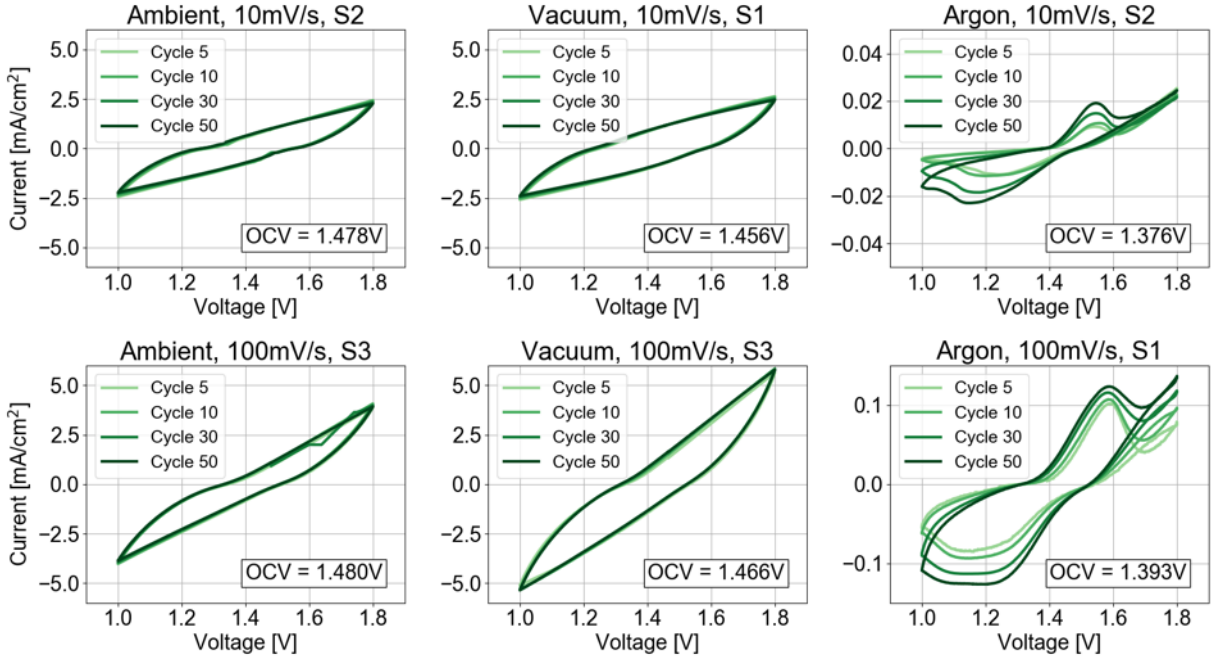

Figure 6.16: CV of mechanically assembled full cell with $[EMIM]^+[OTf]^-$ GPEs. Cycling was interrupted every 10 cycles to perform EIS.

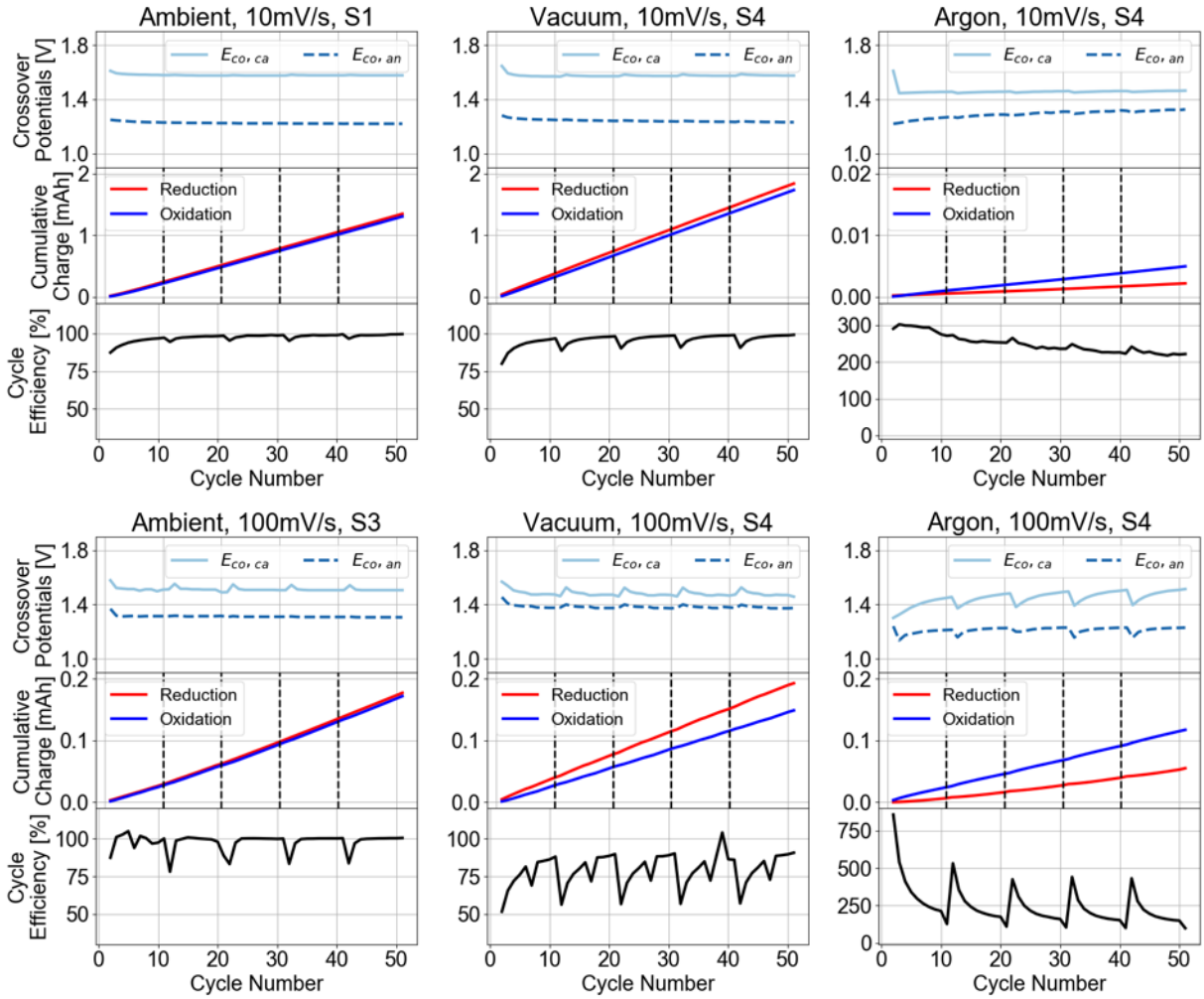

Figure 6.17: Cathodic and anodic crossover potentials and cycle efficiency for CV of mechanically assembled full cells with $[BMIM]^+[OTf]^-$ GPEs.

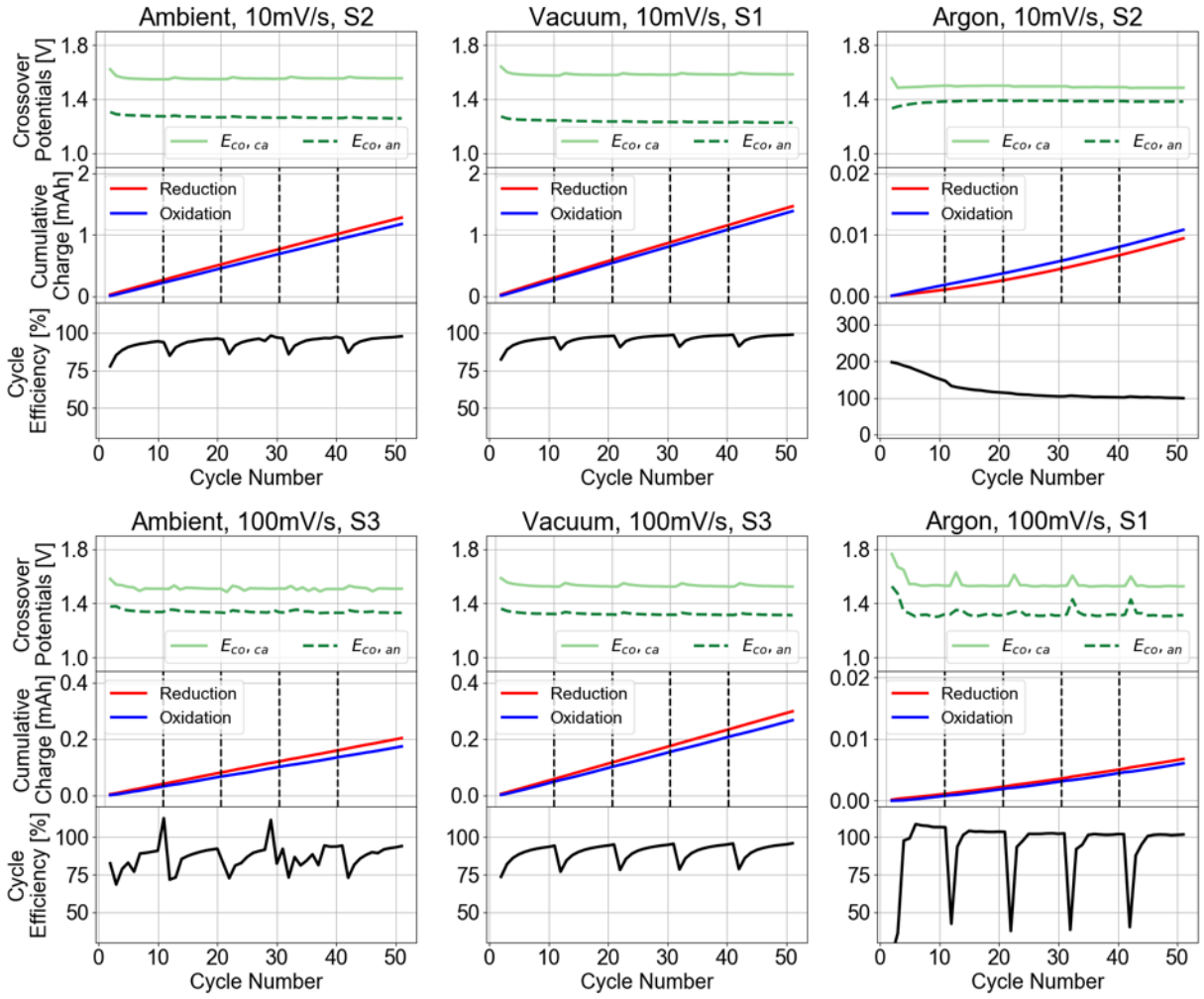

Figure 6.18: Cathodic and anodic crossover potentials and cycle efficiency for CV of mechanically assembled full cells with $[EMIM]^+[OTf]^-$ GPEs.

$[BMIM]^+[OTf]^-$ GPEs showed wider envelopes than $[EMIM]^+[OTf]^-$ GPEs at 10mV/s while the opposite was observed at 100mV/s. This indicates that capacitive contributions are higher with $[BMIM]^+[OTf]^-$ at slower scan rates and higher with $[EMIM]^+[OTf]^-$ at faster scan rates, possibly due to the greater ionic liquid cation mobility afforded by the shorter alkyl chain on $[EMIM]^+$. These electric double layer capacitive effects have been observed with ionic liquid supercapacitors and may thus be occurring on a limited scale in this system as well [19]. The slightly higher molality for $[BMIM]^+[OTf]^-$ $(0.387m)$ vs. $[EMIM]^+[OTf]^-$ $(0.361m)$ for the same molarity may also play a role as slightly more salt was able to be dissolved, further increasing the amount of charge separation possible due to a higher concentration of mobile Zn^2 ions.

While half cells had previously exhibited higher currents for $[EMIM]^+[OTf]^-$ GPEs than $[BMIM]^+[OTf]^-$ GPEs, no such trend is observed for mechanically assembled full cells. Maximum currents are roughly equal between ionic liquids for GPEs dried in ambient and under vacuum, again except for [BMIM]$^+$[OTf-] dried under vacuum and scanned at 100mV/s. This suggests that the introduction of the printed MnO_2 cathode significantly affects cell internal resistance, dominating the contributions of the GPE itself. Furthermore, maximum currents observed with full cells are 2-4 times lower than the peaks observed with half cell CV, indicating the MnO_2 cathode contributes significant kinetic limitations as well.

While no obvious peaks are observed, some deviations from purely capacitive behavior are observed at 1.5V on the cathodic scan and 1.3V on the anodic scan. These are likely the contributions of Zn/Zn^{2+} redox reactions as the locations of these deviations correspond roughly with the peaks observed from GPEs dried in argon.

Both cathodic and anodic crossover potentials for GPEs dried in ambient and under vacuum remained constant throughout cycling. For both ionic liquids, the cathodic crossover potential ranged from 1.5-1.6V, and the anodic crossover potential ranged from 1.25-1.4V. Cathodic crossover potentials were more positive and anodic crossover potentials more negative when scanned at slower scan rates. For GPEs dried in ambient, GPEs with $[BMIM]^+[OTf]^-$ showed a larger potential window between crossover potentials than GPEs with $[EMIM]^+[OTf]^-$. For GPEs dried under vacuum and at 10mV/s, no significant difference in crossover potentials was observed between ionic liquids.

The smaller window between crossover potentials observed at higher scan rates may again be due to less time provided for double layer charge separation. The larger windows observed for GPEs with $[BMIM]^+[OTf]^-$ indicates less sensitivity to water than GPEs with $[EMIM]^+[OTf]^-$.

For GPEs dried in argon, the window between crossover potentials was generally much smaller. For all samples except $[BMIM]^+[OTf]^-$ scanned at 100mV/s, cathodic crossover potentials ranged from 1.45-1.55V and anodic crossover potentials from 1.35-1.4V. The differences observed in voltammogram shape and crossover potentials between GPEs dried in argon vs. ambient and vacuum again clearly show the presence of side reactions likely involving absorbed water. The crossover potentials determined for $[BMIM]^+[OTf]^-$ GPEs scanned at 100mV/s shows different values and behavior compared to all other GPEs and is due to almost entirely capacitive behavior.

For GPEs dried in ambient and under vacuum, cumulative charges are lower for higher scan rates. This is because current responses did not increase proportionally with the scan rate, resulting in a lower cumulative total charge due to the current response persisting for a shorter time. For GPEs dried in argon, cumulative charges remained low, though a less significant difference is observed between both scan rates for $[EMIM]^+[OTf]^-$ GPEs. This suggests some beneficial contribution from water that improves performance with the printed MnO_2 cathode at slow scan rates. In addition, $[BMIM]^+[OTf]^-$ GPEs provide higher cumulative charges at slower scan rates while $[EMIM]^+[OTf]^-$ GPEs provide higher charges at faster scan rates. However, this difference is smaller than comparing scan rates and is thus more likely a consequence of more facile mass transport when in $[EMIM]^+[OTf]^-$.

Finally, cycle efficiencies for almost all cells scanned at 10mV/s with ambient and vacuum GPEs remained close to 100% throughout the tested cycles. Cells scanned at 100mV/s showed steady cycle efficiencies of 90-95% except for ambient GPEs with $[BMIM]^+[OTf]^-$. Dips in cycle efficiency are observed every 10 cycles which coincides with EIS that was performed every 10 cycles. For cells scanned at 10mV/s, 2-5 cycles were required before the cycle efficiency recovered while cells scanned at 100mV/s required 9-10 cycles or never reached a steady cycle efficiency before cycling was interrupted for the next EIS test. Furthermore, more drastic drops in cycle efficiency were observed for cells scanned at 100mV/s. This difference in cycle efficiency by scan rate may again be attributed to the time provided for ion separation of the ions comprising the ionic liquid and salt. In general, cells with $[BMIM]^+[OTf]^-$ GPEs showed higher steady cycle efficiencies than cells with $[EMIM]^+[OTf]^-$ GPEs.

For cells with argon GPEs, GPEs with $[EMIM]^+[OTf]^-$ showed similar steady cycle efficiencies close to 100%. GPEs with $[BMIM]^+[OTf]^-$ showed steady cycle efficiencies starting at 300% and decreasing to about 210% by the end of cycling. As no distinct peaks or evidence of charge transfer reactions were observed, these efficiencies likely represent degradation of the GPE via oxidation.

6.4.4.2 Electrochemical Impedance Spectroscopy

Figures 6.19 and 6.20 present Nyquist plots and the calculated solution resistance, R_{sol}, and charge transfer resistance, R_{ct}, of mechanically assembled full cells with GPEs with $[BMIM]^+[OTf]^-$. Figures 6.21 and 6.22 present the same data for GPEs with $[EMIM]^+[OTf]^-$. An explanation of how solution resistance and charge transfer resistance are calculced from EIS data is discussed in Chapter 5. The same representative samples are presented for Nyquist plots, but all cycleable samples are presented in the plots of solution resistance and charge transfer resistance. Table 6.12 presents calculated mean ionic conductivities and charge transfer resistances for all GPEs at Cycles 0 and 50.

For all cells, charge transfer resistance was highest prior to cycling with CV (Cycle 0) and decreased with further cycling. Nyquist plots visually present the reduction of the first semicircle whose diameter corresponds to the charge transfer resistance. Ionic conductivities for all cells remained constant for all tested cycles per cell.

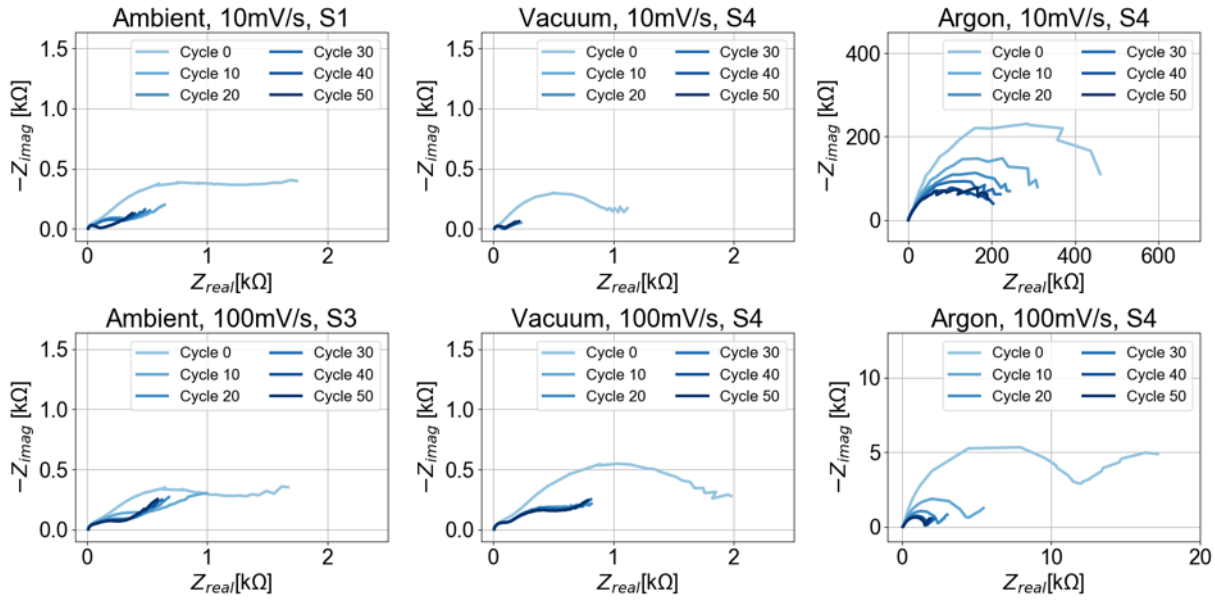

Figure 6.19: Nyquist plots of mechanically assembled full cells with $[BMIM]^+[OTf]^-$ GPEs. EIS was performed between every 10 cycles of CV.

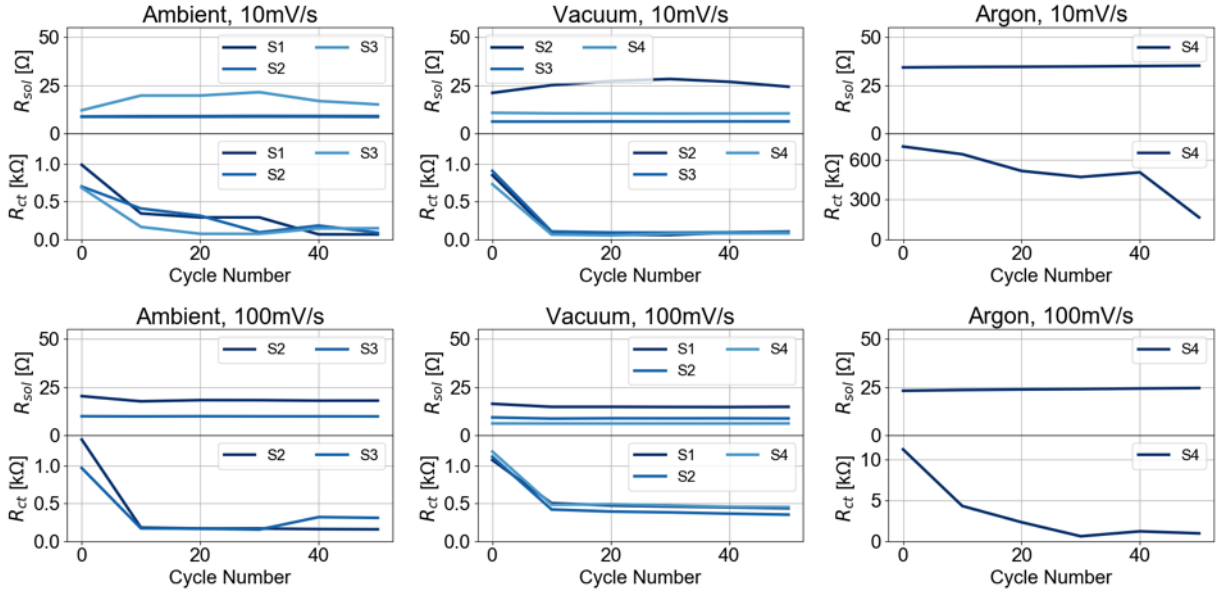

Figure 6.20: Solution resistance, R_{sol}, and charge transfer resistance, R_{ct}, of mechanically assembled full cells with $[BMIM]^+[OTf]^-$ GPEs.

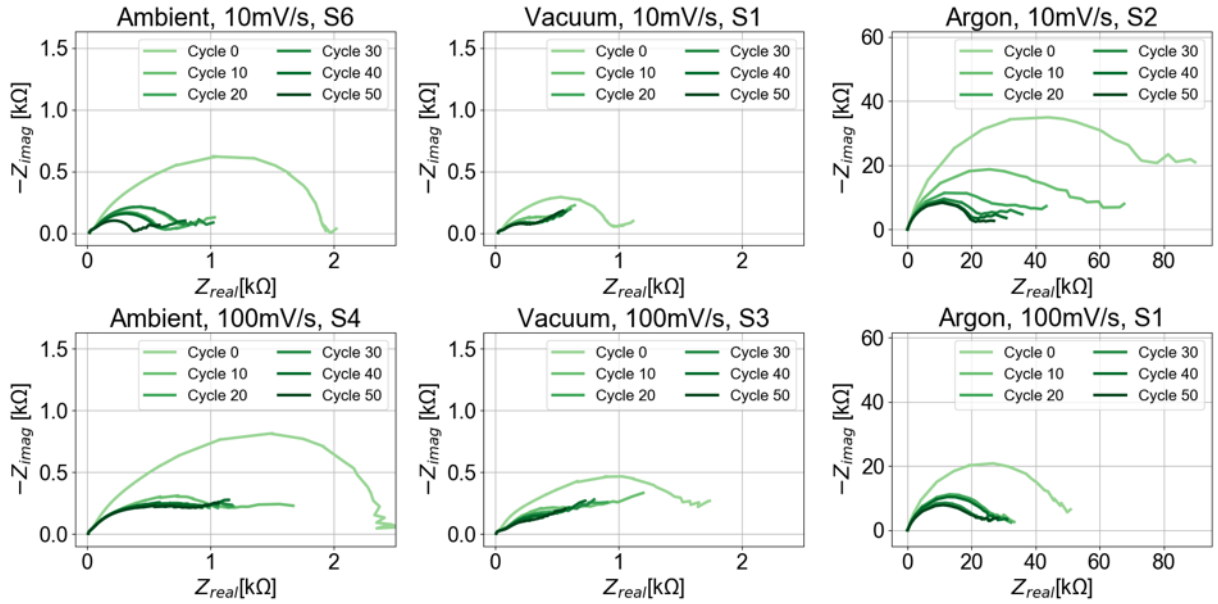

Figure 6.21: Nyquist plots of mechanically assembled full cells with $[EMIM]^+[OTf]^-$ GPEs. EIS was performed between every 10 cycles of CV.

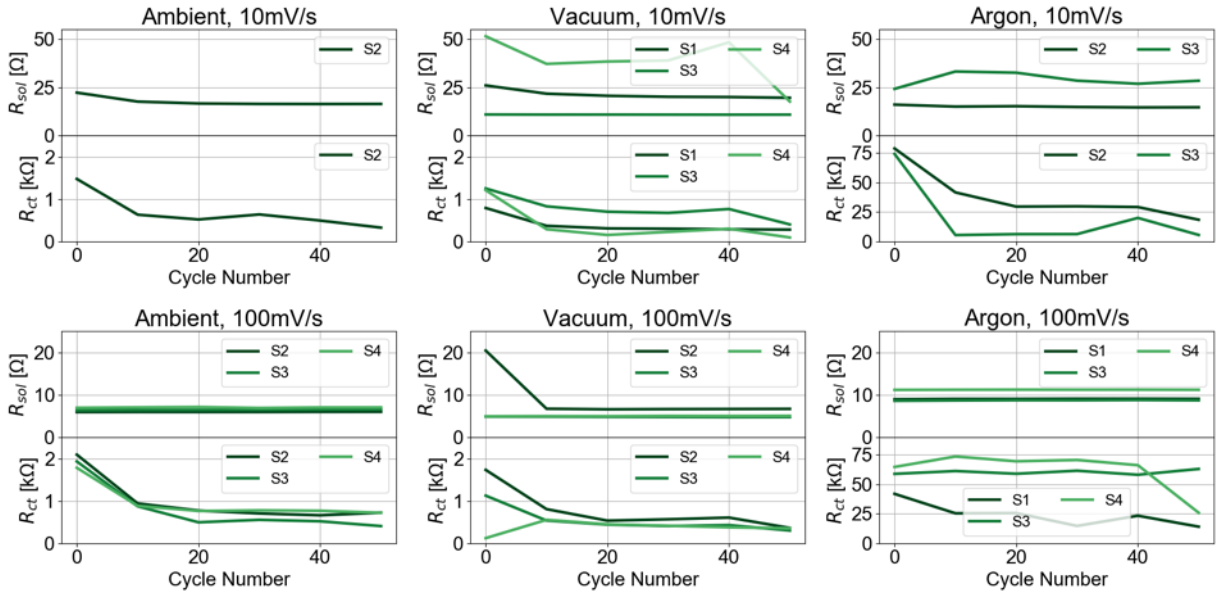

Figure 6.22: Solution resistance, R_{sol}, and charge transfer resistance, R_{ct}, of mechanically assembled full cells with $[EMIM]^+[OTf]^-$ GPEs.

Table 6.12: Mean GPE Ionic Conductivity and Charge Transfer Resistance

Scan Rate, ν [mV/s]	**Environment**	**n**	κ [mS/cm] Cycle 0	κ [mS/cm] Cycle 50	R_{ct} [kΩ] Cycle 0	R_{ct} [kΩ] Cycle 50
$[BMIM]^+[OTf]^-$						
10	Ambient	3	3.797	3.412	0.7889	0.101
	Vacuum	3	2.945	2.732	0.827	0.094
	Argon	1	1.088	1.060	701.263	166.118
100	Ambient	2	2.472	2.683	1.156	0.233
	Vacuum	3	3.525	3.771	1.124	0.413
	Argon	1	1.614	1.522	11.264	0.963
$[EMIM]^+[OTf]^-$						
10	Ambient	1	1.677	2.277	1.474	0.325
	Vacuum	3	1.266	2.333	1.082	0.257
	Argon	2	1.854	1.732	76.630	11.947
100	Ambient	3	5.804	5.701	1.933	0.614
	Vacuum	3	3.696	6.774	0.991	0.338
	Argon	3	3.890	3.860	55.211	34.329

Cells with GPEs dried in argon displayed both lower ionic conductivities and higher charge transfer resistances than cells with GPEs dried in ambient and under vacuum. For cells with GPEs dried in ambient and under vacuum, GPEs dried under vacuum generally showed lower charge transfer resistance and higher ionic conductivity.

For both ionic liquids, initial charge transfer resistances at Cycle 0 were relatively consistent for samples dried in the same environment, as to be expected. Charge transfer resistances decreased significantly from Cycle 0 to Cycle 10, after which resistances continued to slowly decrease. Charge transfer resistances are likely also influenced by high resistance contributed by the MnO_2 cathode.

The lower ionic conductivity with GPEs dried in argon compared to those dried in ambient or vacuum is not as significant as the difference in charge transfer resistance, but the difference for $[BMIM]^+[OTf]^-$ is obfuscated by the low sample yield. The presence of water therefore may not play a significant role in affecting ionic conductivity within the GPE. In addition, the consistency of the ionic conductivity wth cycling indicates the bulk electrolyte composition is not significantly affected as a result of cycling.

However, the significantly higher charge transfer resistance observed with argon GPEs indicates absorbed water likely affects Zn^{2+} intercalation or deposition. Furthermore, the higher charge transfer resistances at Cycle 0 observed with higher scan rates followed by their continued decline suggests some dependence on the amount of charge passed. This could be due to changing surface microstructures on the Zn foil providing more kinetically

favorable nucleation sites or changes to the MnO_2 crystal structure as a result of repeated Zn^{2+} intercalation.

In general, the presence of some amount of water improves reaction kinetics but does not affect the bulk electrolyte composition or ionic conductivity.

6.4.4.3 Galvanostatic Cycling

Figures 6.23 and 6.24 present discharge capacity, coulombic efficiency, and DC internal resistance per cycle for mechanically assembled full cells with $[BMIM]^+[OTf]^-$ and $[EMIM]^+[OTf]^-$ GPEs respectively, dried in ambient and under vacuum. Based on the poor performance observed from CV and EIS, cells with GPEs dried in argon were not made. Cells were cycled for up to 200 cycles or until cell failure, though some cell measurements were interrupted due to equipment failure.

Eight cells were made per batch of cells for each combination of drying environment and ionic liquid, and all cycleable cells were presented. Cycleable cells are defined as cells that were able to maintain potentials between 1.0-1.8V when a galvanostatic current was applied and also demonstrated evidence of charging and discharging.

For both drying environments, $[BMIM]^+[OTf]^-$ cells exhibited higher discharge capacities than $[EMIM]^+[OTf]^-$. All cells showed an initial steep decline in discharge capacity from cycles 1-20, after which discharge capacity slowly and steadily decreased throughout the remaining tested cycles. After the initial 20 cycles, discharge capacities for $[BMIM]^+[OTf]^-$ cells generally ranged from 0.35-0.2mAh/cm^2 for GPEs dried in ambient and from 0.4-0.25mAh/cm^2 for GPEs dried under vacuum. For cells with $[EMIM]^+[OTf]^-$ GPEs, discharge capacities generally ranged from 0.2-0.1mAh/cm^2 for GPEs dried in ambient and from 0.3-0.2mAh/cm^2 for GPEs dried under vacuum.

For all cells, coulombic efficiency per cycle remained close to 100%, though the value per cycle oscillated between 97-103%.

Similar to discharge capacity, DC internal resistance also experienced a shift during the first 20 cycles and then remained more steady throughout, though resistance increased rather than decreased. DC internal resistances between drying environments were similar for both ionic liquids, though resistances were lower for cells with $[BMIM]^+[OTf]^-$. After the initial 20 cycles, internal resistances for $[BMIM]^+[OTf]^-$ generally ranged from 500-650Ω for GPEs dried in ambient and from 200-350Ω for GPEs dried under vacuum. For cells with $[EMIM]^+[OTf]^-$ GPEs, much more variability was observed, but the common internal resistances remained relatively constant at 600Ω for GPEs dried in ambient and ranged from 250-300Ω for GPEs dried under vacuum.

For both ionic liquids, discharge capacities were higher and internal resistances lower for cells with GPEs dried in vacuum than those dried in ambient. This is again consistent with the results obtained from CV and EIS where charge transfer and long-term performance is likely improved by the presence of some but limited absorbed water.

newpage

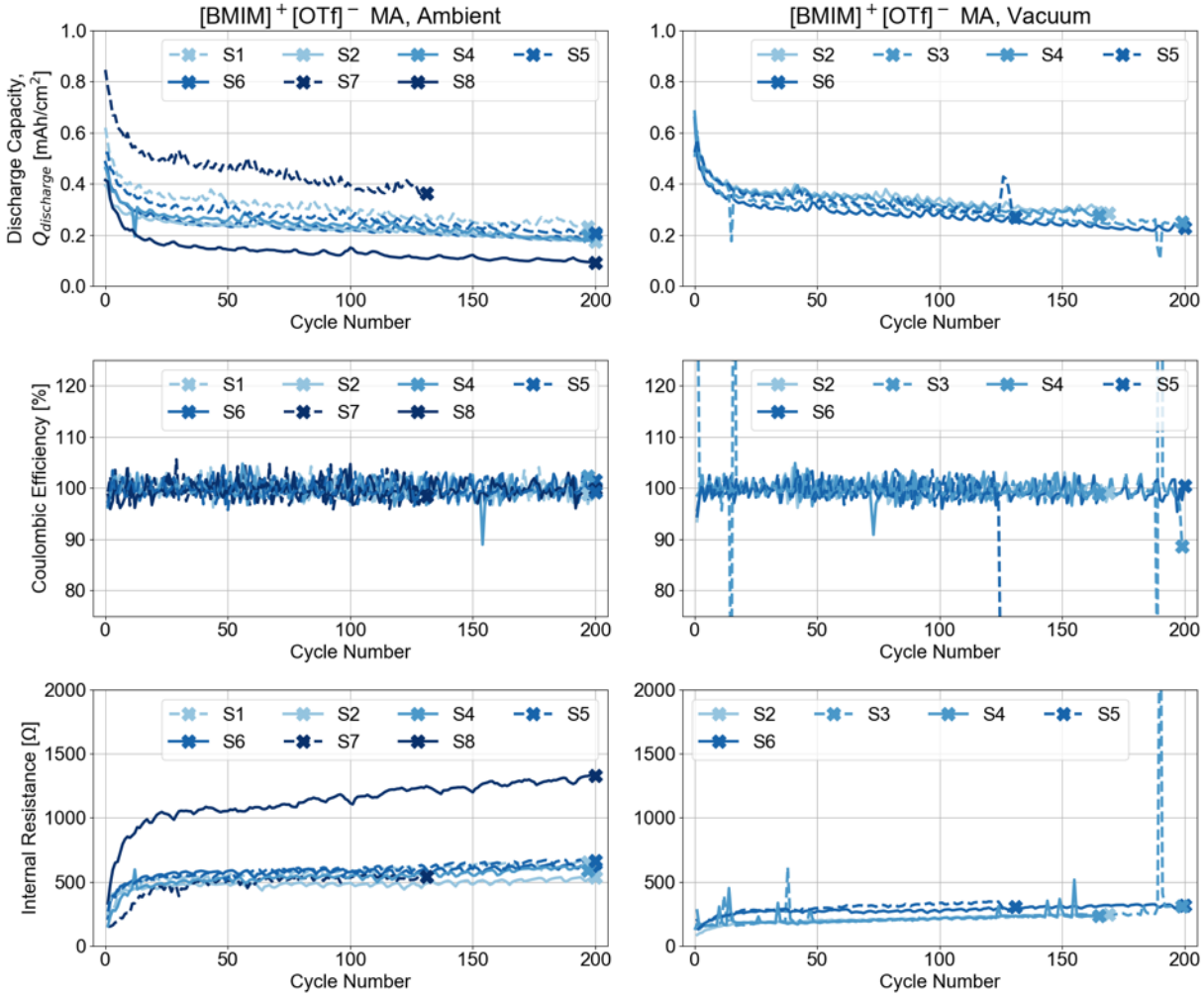

Figure 6.23: Discharge capacity, coulombic efficiency, and DC internal resistance per cycle for mechanically assembled full cells with $[BMIM]^+[OTf]^-$ GPEs dried in ambient and under vacuum.

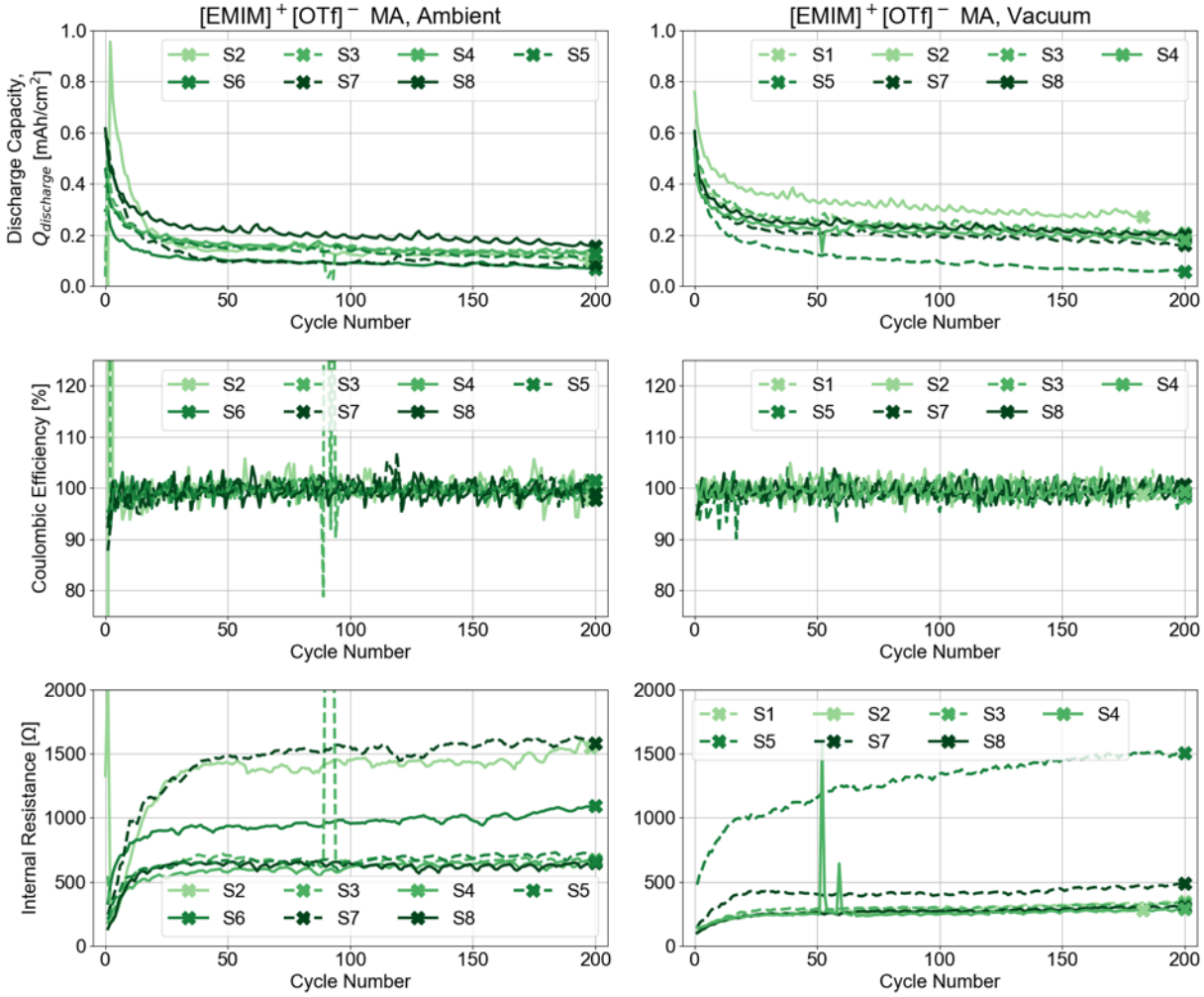

Figure 6.24: Discharge capacity, coulombic efficiency, and DC internal resistance per cycle for mechanically assembled full cells with $[EMIM]^+[OTf]^-$ GPEs dried in ambient and under vacuum.

A relationship can be observed between internal resistance and discharge capacity where internal resistance inversely correlates with discharge capacity. The internal resistance, as determined by uncontrolled or undetermined differences in cell manufacturing for samples within the same batch, drives the observed capacity and reflects per-sample differences in electrode and electrolyte composition, electrode alignment, and coin cell pressure.

Both discharge capacity and internal resistances for most cells started at similar values at the first cycle, but their development throughout the first 20 cycles determines each cell's long term performance. The observed increase in internal resistance that drives the decrease in discharge capacity for the first 20 cycles likely reflects initial side reactions and changes in persisting redox reactions. Further insight into these reactions themselves can be provided by differential capacity analysis.

6.4.4.4 Differential Capacity Analysis

Figures 6.25 and 6.26 present differential capacity and voltage profiles of cells which showed the most variation in performance throughout cycle life testing for mechanically assembled full cells with $[BMIM]^+[OTf]^-$ dried in ambient and vacuum respectively. Figures 6.27 and 6.28 present the same data for mechanically assembled full cells with $[EMIM]^+[OTf]^-$ GPEs. The cells were chosen based on the lowest and highest internal resistance (which is inversely proportional to discharge capacity) observed per batch of cells. A custom smoothing algorithm was applied to the differential capacity in order to reduce noise arising from numerical differentiation with a small step size. The cycles plotted for each cell were chosen to capture the change in reactions taking place over the lifetime of each cell.

For all examined cells, distinct peaks at specific potentials are unable to be identified. While there is likely some contribution from phase changes in the material and reactions taking place, the more likely cause is noise introduced from numerical differentiation with such a short step. However, observations about cell stability and aging can still be made.

In general, plots of differential capacity show much more variation by ionic liquid type and environment. This is expected due to the differences in interaction between water and each ionic liquid specifically. Of note is that the IR difference between the low IR and high IR cells for $[BMIM]^+[OTf]^-$ dried in vacuum is much smaller than the difference for all other combinations of ionic liquid and drying environment. This suggests more robustness to manufacturing parameters for these cells and thus results in similar plots of differential capacity.

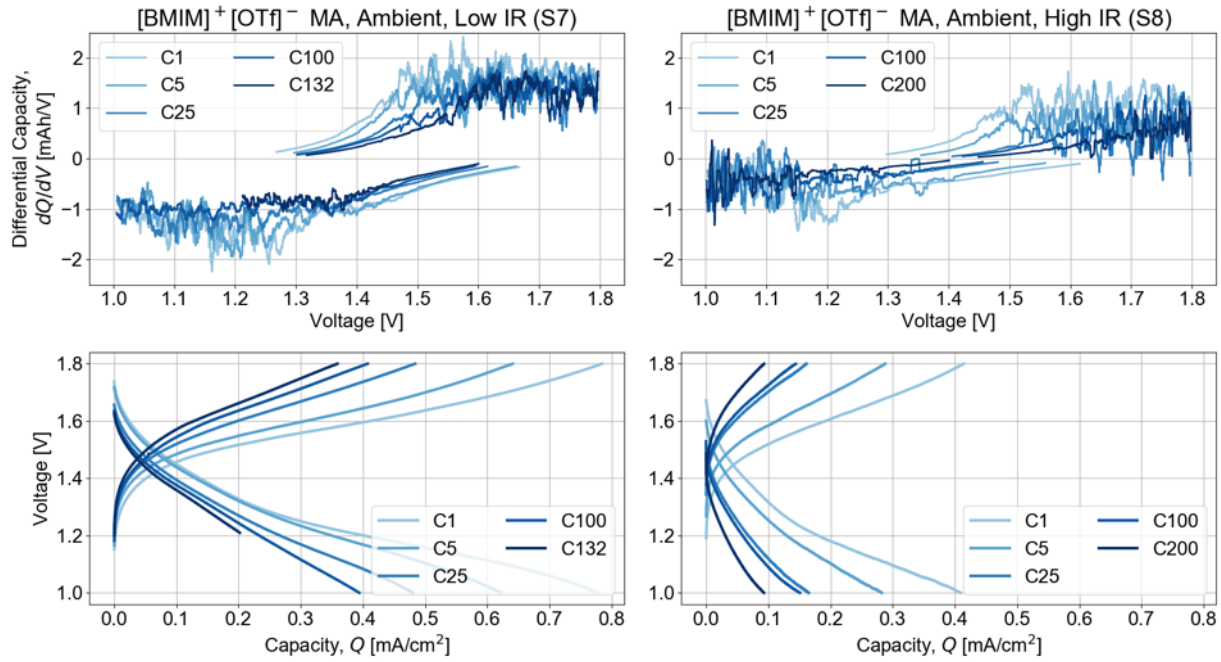

Figure 6.25: Differential capacity and voltage profiles of cells with lowest and highest internal resistance for mechanically assembled full cells with $[BMIM]^+[OTf]^-$ GPEs dried in ambient.

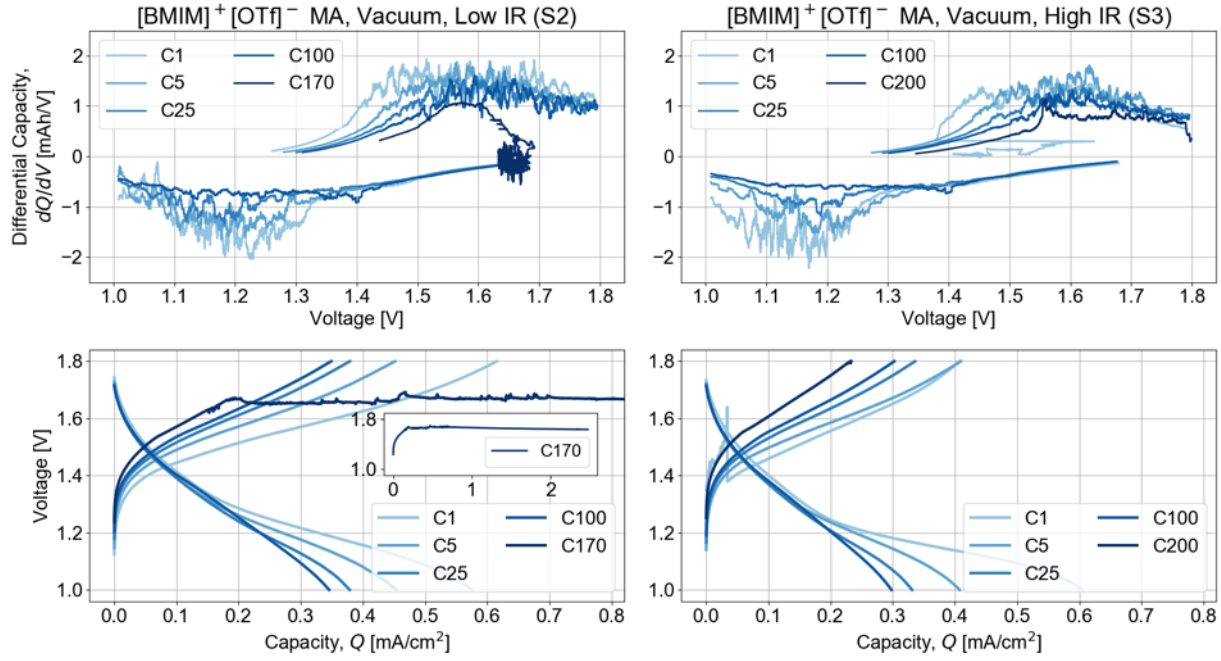

Figure 6.26: Differential capacity and voltage profiles of cells with lowest and highest internal resistance for mechanically assembled full cells with $[BMIM]^+[OTf]^-$ GPEs dried under vacuum.

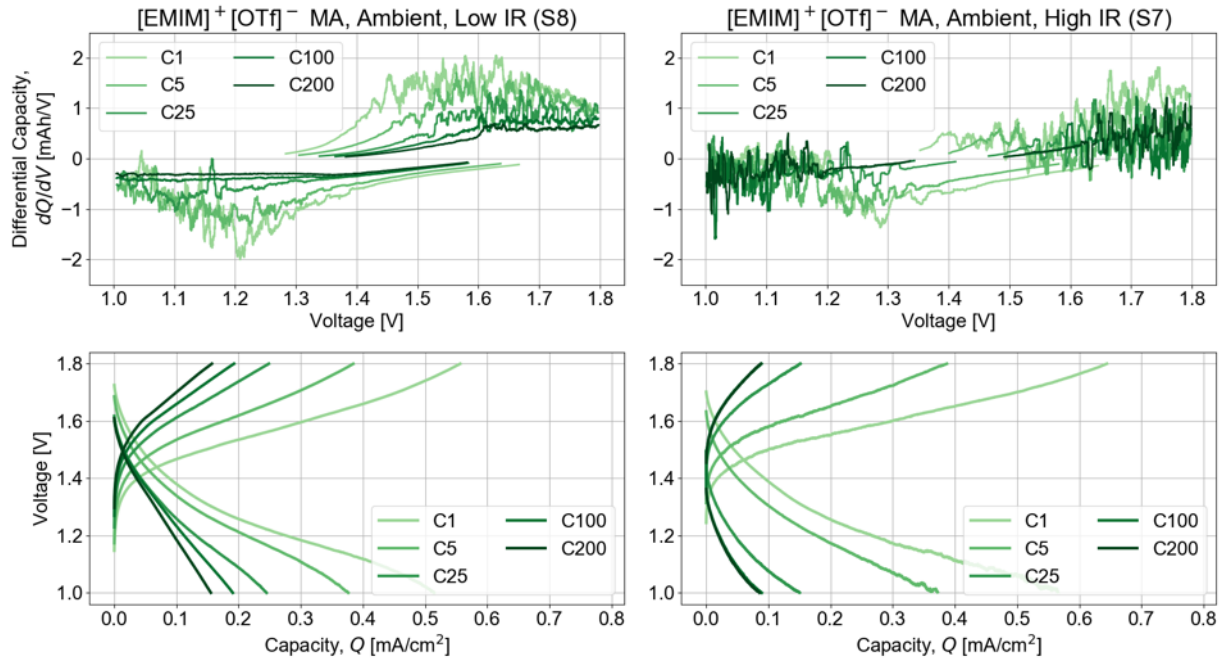

Figure 6.27: Differential capacity and voltage profiles of cells with lowest and highest internal resistance for mechanically assembled full cells with $[EMIM]^+[OTf]^-$ GPEs dried in ambient.

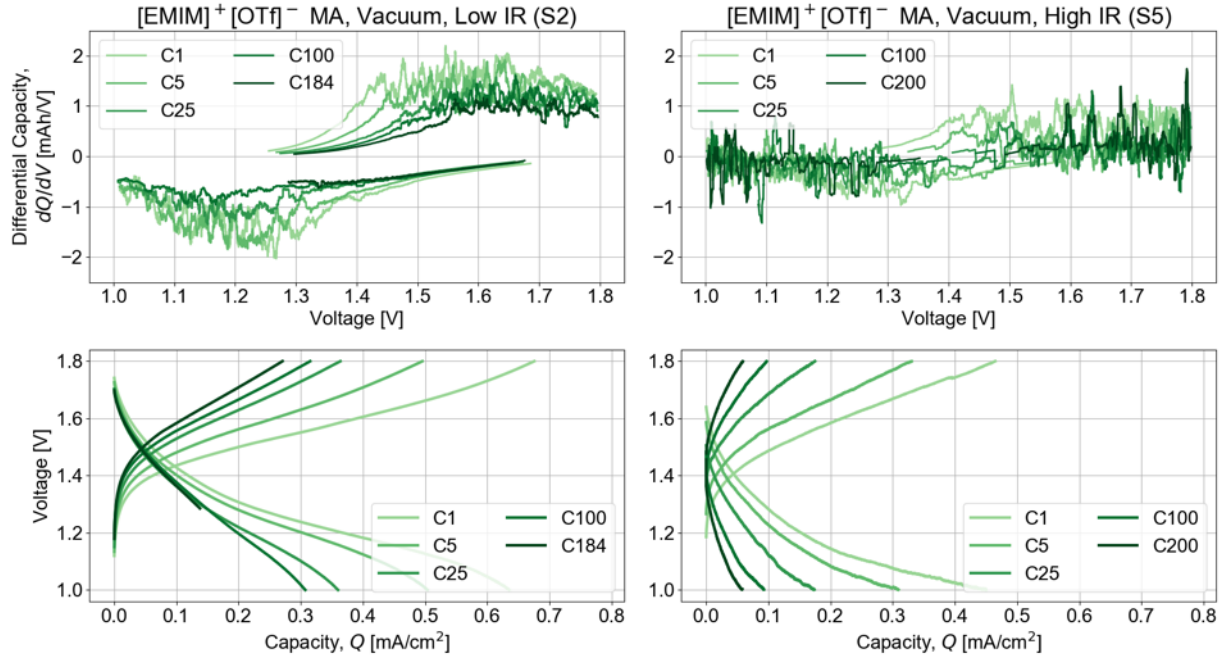

Figure 6.28: Differential capacity and voltage profiles of cells with lowest and highest internal resistance for mechanically assembled full cells with $[EMIM]^+[OTf]^-$ GPEs dried under vacuum.

For both ionic liquids and both environments, low IR cells showed higher peaks closer to 1.4V on both charge and discharge for the first cycle. As cycling of low IR cells continues, the potentials of these peaks shift more positively upon charge and more negatively upon discharge and also decrease in magnitude. At the end of cycling, individual peaks are significantly decreased and the differential capacity response forms a plateau. This plateau is maintained at the limits of the potential window, spanning 1.55-1.8V for charging and 1.4-1.0V for discharging. The potential shift is likely due to increasing internal resistance as the cell is cycled. The peaks themselves suggest phase changes or side reactions that are occuring, and their decrease with further cycling implies a drop in those same reactions, likely due to consumption or depletion of reactants. At the center of these plots, differential capacities show a mostly linear response with voltage until the plateau region is reached.

For high IR cells, these plateaus are not preserved, and differential capacities are mostly linear proportional to potential or are close to zero as the the cell ages. The individual potential windows for charging and discharging decrease again due to intrinsically higher internal resistances causing a high potential jump upon applying a positive or negative current. In addition, more noise is observed at the outer limits of the potential windows as the cell ages, a phenomenon which is absent from low IR cells. While responses at Cycle 1 resemble those observed from low IR cells, the initial peaks are lower in magnitude.

For low IR cells with $[BMIM]^+[OTf]^-$ GPEs, cells dried in ambient showed a higher magnitude plateau and more noise than cells dried under vacuum. In contrast, for low IR cells with $[EMIM]^+[OTf]^-$ GPEs, cells dried in ambient showed lower magnitude and less noise than cells dried under vacuum. Between the two ionic liquids, responses for cells with GPEs dried under vacuum were similar. For cells with GPEs dried in ambient, cells with $[BMIM]^+[OTf]^-$ GPEs showed higher magnitude peaks and more noise than cells with $[EMIM]^+[OTf]^-$ GPEs.

Of selected cells whose differential capacity was investigated, the low IR cell for $[BMIM]^+[OTf]^-$ cells dried under vacuum was the only cell to fail. During its final charge cycle, the cell failed to reach a potential of 1.8V and only reached a maximum of 1.65V, after which potential slowly declined as observed on the voltage profile. Suspected causes of cell failure are discussed further in Chapter 7, but a likely cause for this failure method is loss of electrical contact with the cathode and subsequent loss of active material due to volumetric expansion of the MnO_2 upon accepting intercalated Zn^{2+} ions. This is due to the absence of significant changes in discharge capacity and internal resistance that would otherwise indicate other causes.

Since higher magnitude peaks and more noise indicate more phase changes or side reactions occuring, the trends observed across ionic liquids and drying environments implies $[BMIM]^+[OTf]^-$ GPEs are more sensitive to water. In addition, the greater amount of noise present during charging and discharging even at later cycles for GPEs dried in ambient suggests continued degradation of the Zn foil anode and the MnO_2 cathode respectively due to interactions with the ionic liquid and water. While $[BMIM]^+[OTf]^+$ GPEs dried under vacuum displayed the best cycling performance, the distinction between its differential capacity

response and that of other combinations of ionic liquid and environment is not specifically clear.

6.4.5 Fully Printed Cells

This section presents electrochemical impedance spectroscopy and galvanostatic cycling data for fully printed cells. GPEs were cured under ambient and vacuum at 80°C. All cells used the same printed MnO_2 cathode and printed Zn anode.

For both EIS and galvanostatic cycling, 8 cells were made per batch. All cells are presented for EIS, but only cycleable cells are presented for galvanostatic cycling results.

6.4.5.1 Scanning Electron Microscopy

Because fully printed cells resulted in a monolithic cell that was impossible to separate, the GPE layer thickness could not be determined by physical measurement. Thus, scanning electron microscopy was used to take cross sectional images of fully printed cells in order to determine GPE thickness for use in ionic conductivity calculations.

Figure 6.29 presents a cross section of a fully printed cell with $[EMIM]^+[OTf]^-$ GPE dried under vacuum. The electrode-electrolyte interfaces have been added to make each layer visually distinct.

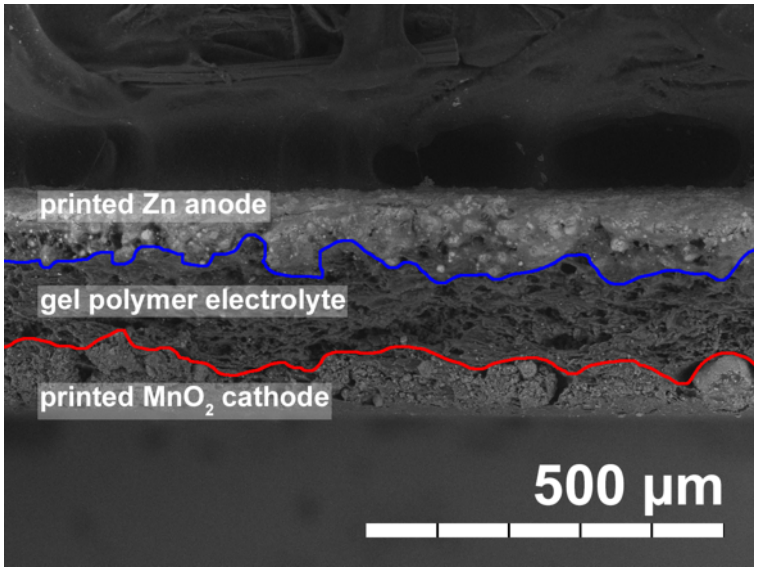

Figure 6.29: SEM image of fully printed cell with $[EMIM]^+[OTf]^-$ GPE dried under vacuum. Anode-GPE interface has been drawn in blue, and cathode-GPE interface has been drawn in red.

From the SEM, GPE thickness ranges from 100-150μm depending on each electrode's morphology. Thus, an average thickness of 125μm was used for calculations where thickness was required.

The total cell thickness is about 300μm with each electrode ranging from 75-125μ in thickness. Profilometry-optimized inks were not used for these cells, so a significant amount of variation in surface profile can be observed. However, use of the printed GPE results in good adhesion between layers and likely more even utilization of electrode material close to the electrode-electrolyte interface by providing even contact at all points. Furthermore, the GPE layer itself appears homogeneous and shows no obvious signs of successive GPE layers being unable to mix with each other during the casting process.

6.4.5.2 Electrochemical Impedance Spectroscopy

Figures 6.30 and 6.31 present Nyquist plots from EIS and the calculated solution resistances and charge transfer resistances of fully printed cells with $[BMIM]^+[OTf]^-$ GPEs dried in air. Figures 6.32 and 6.33 present the same data for fully printed cells with $[EMIM]^+[OTf]^-$ GPEs. The median values for solution resistance and charge transfer resistance are included on each bar plot. EIS was performed on new cells with no prior cycling.

For both ionic liquids, at least 2 of 8 samples show significant deviation from the rest of the samples for both ionic conductivity and charge transfer resistance. Outlier samples are not identical between ionic conductivity and charge transfer resistance, indicating separate differences in manufacturing that lead to variations in both resistances. Median values for ionic conductivity and charge transfer resistance are respectively higher and lower (better performance in both cases) for cells with $[BMIM]^+[OTf]^-$.

For cells with $[EMIM]^+[OTf]^-$ GPEs, ionic conductivity is similar to mechanically assembled full cells, but fully printed cells with $[BMIM]^+[OTf]^-$ showed lower ionic conductivities compared to their mechanically assembled counterparts. This may in part be due to the low sample size available for mechanically assembled full cells, but increased sensitivity of $[BMIM]^+[OTf]^-$ to absorbed water may also play a role. The additive printing process involves building up the GPE one layer at a time which allows many opportunities for ambient water to be absorbed by internal layers of the GPE during the manufacturing process.

For cells with both ionic liquids, charge transfer resistances were lower for uncycled fully printed cells compared to uncycled mechanically assembled full cells dried in ambient. This is likely due to improved interfacial contact at the electrode-electrolyte interfaces due to direct printing of the GPE on the cathode and of the anode on the GPE. Because the GPE and anode are deposited as a solution and slurry respectively, both layers would be able to fill all available voids within their respective underlying layers, increasing interfacial surface area compared to relying on mechanical pressure as in the case of mechanically assembled cells.

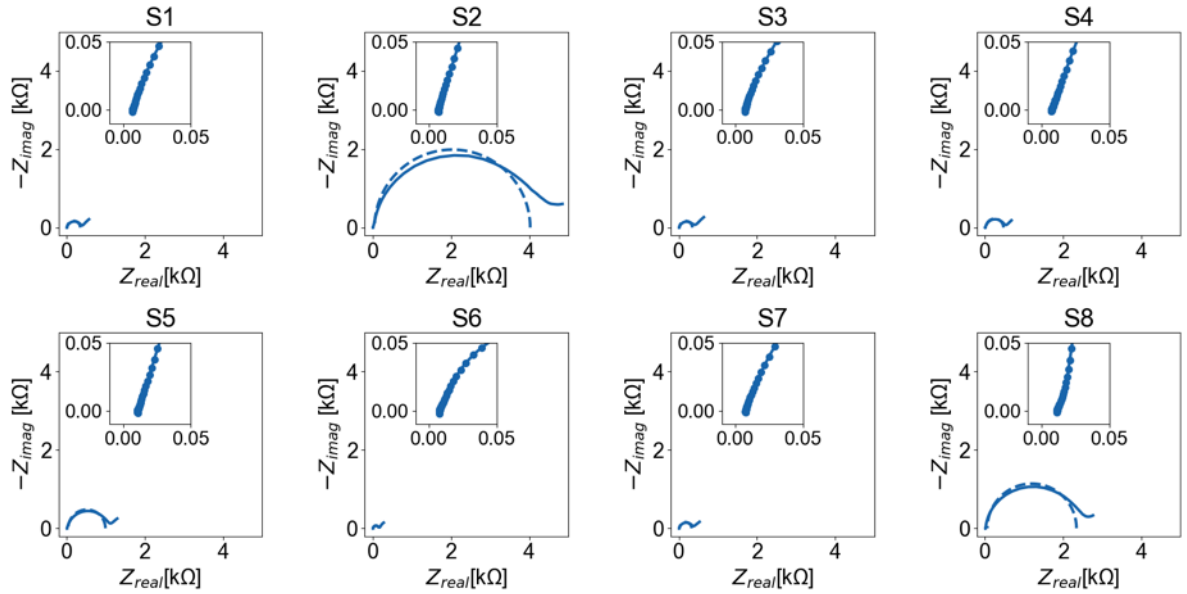

Figure 6.30: Nyquist plots of fully printed cells with $0.5M$ $[BMIM]^+[OTf]^-$ GPE, dried under ambient.

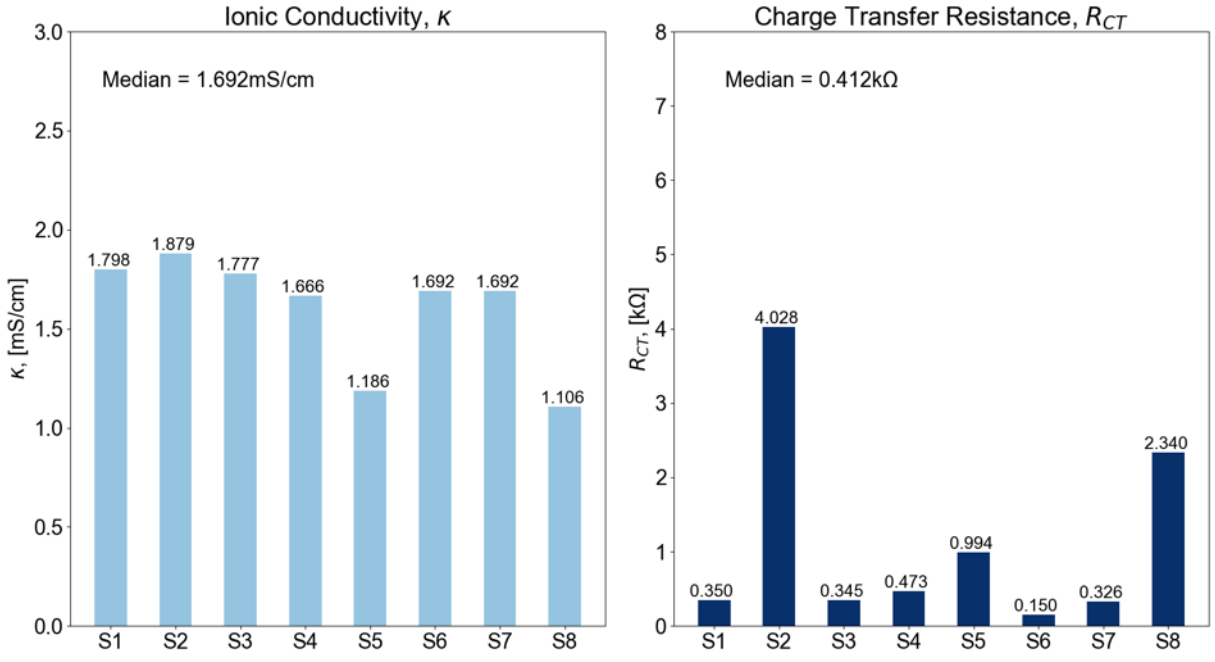

Figure 6.31: Solution resistance and charge transfer resistance of fully printed cells with $0.5M$ $[BMIM]^+[OTf]^-$ GPE, dried under ambient.

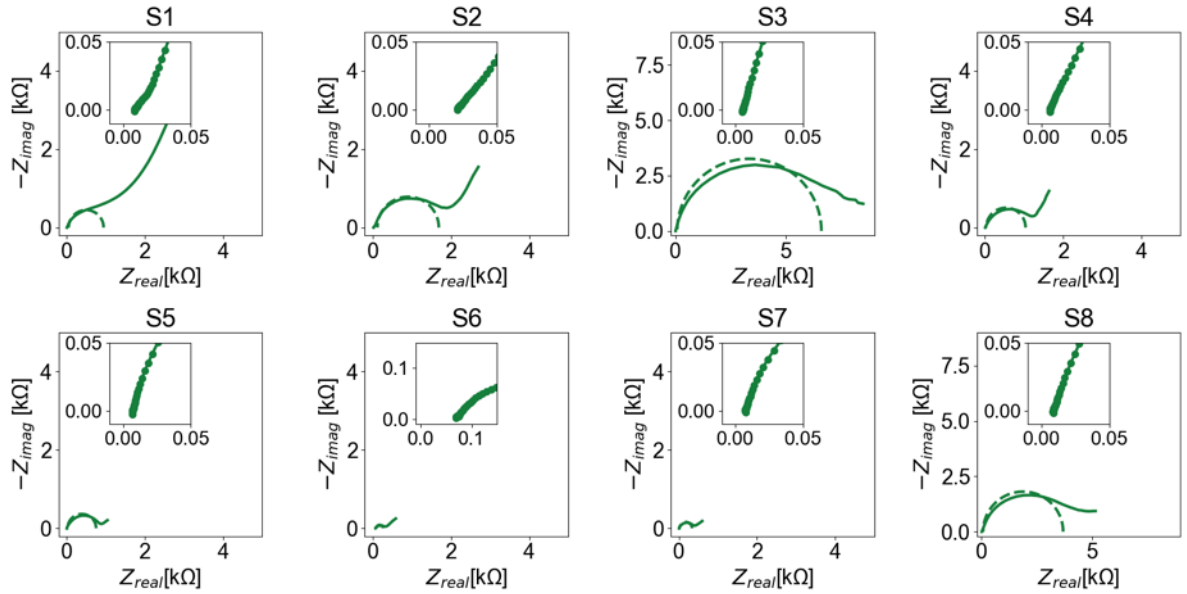

Figure 6.32: Nyquist plots of fully printed cells with $0.5M$ $[EMIM]^+[OTf]^-$ GPE, dried under ambient.

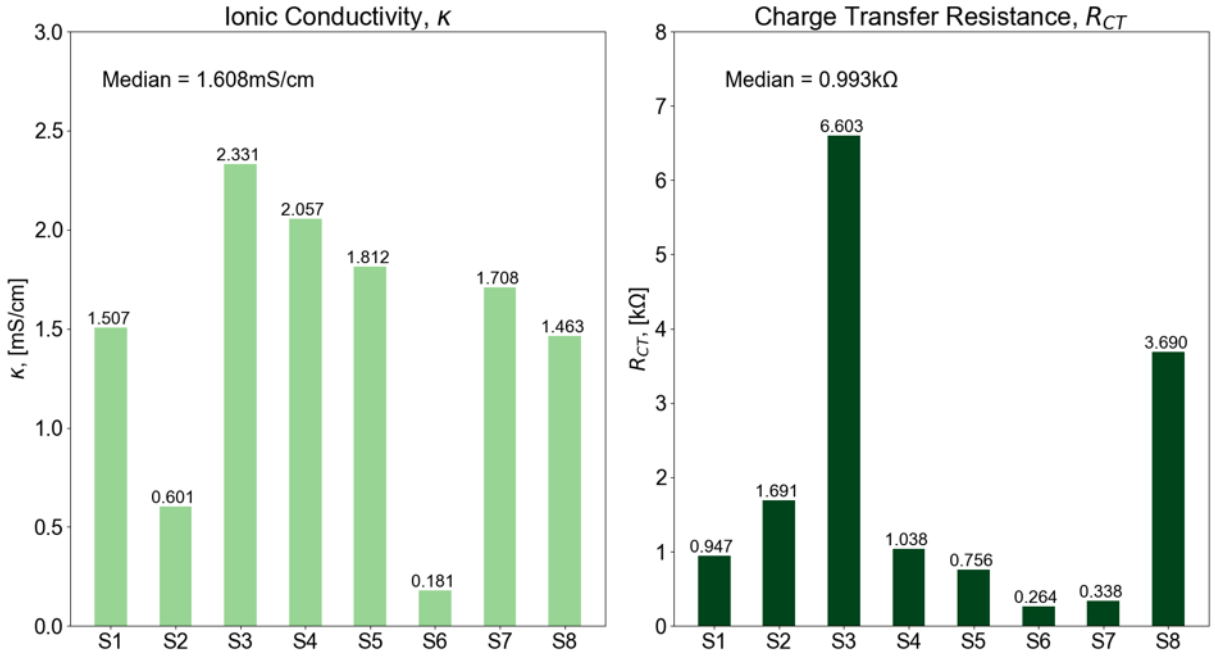

Figure 6.33: Solution resistance and charge transfer resistance of fully printed cells with $0.5M$ $[EMIM]^+[OTf]^-$ GPE, dried under ambient.

6.4.5.3 Galvanostatic Cycling

Figures 6.34 and 6.35 present discharge capacity, coulombic efficiency, and DC internal resistance per cycle for fully printed cells with $[BMIM]^+[OTf]^-$ and $[EMIM]^+[OTf]^-$ GPEs respectively, dried in ambient and under vacuum. Again, cells with GPEs dried in argon were not tested. Cells were cycled for up to 200 cycles or until cell failure.

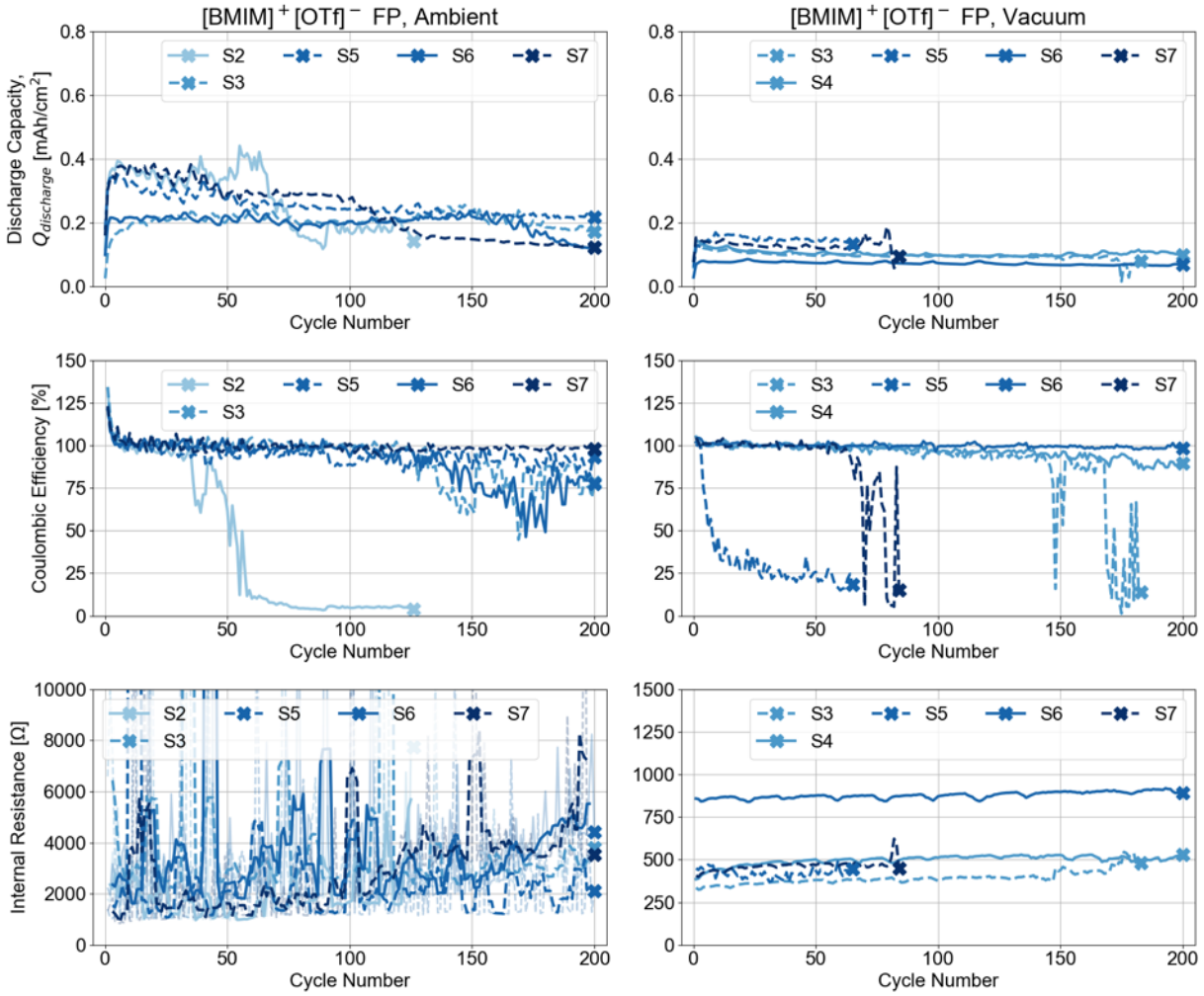

Figure 6.34: Discharge capacity, coulombic efficiency, and DC internal resistance per cycle for fully printed cells with $[BMIM]^+[OTf]^-$ GPEs dried in ambient and under vacuum.

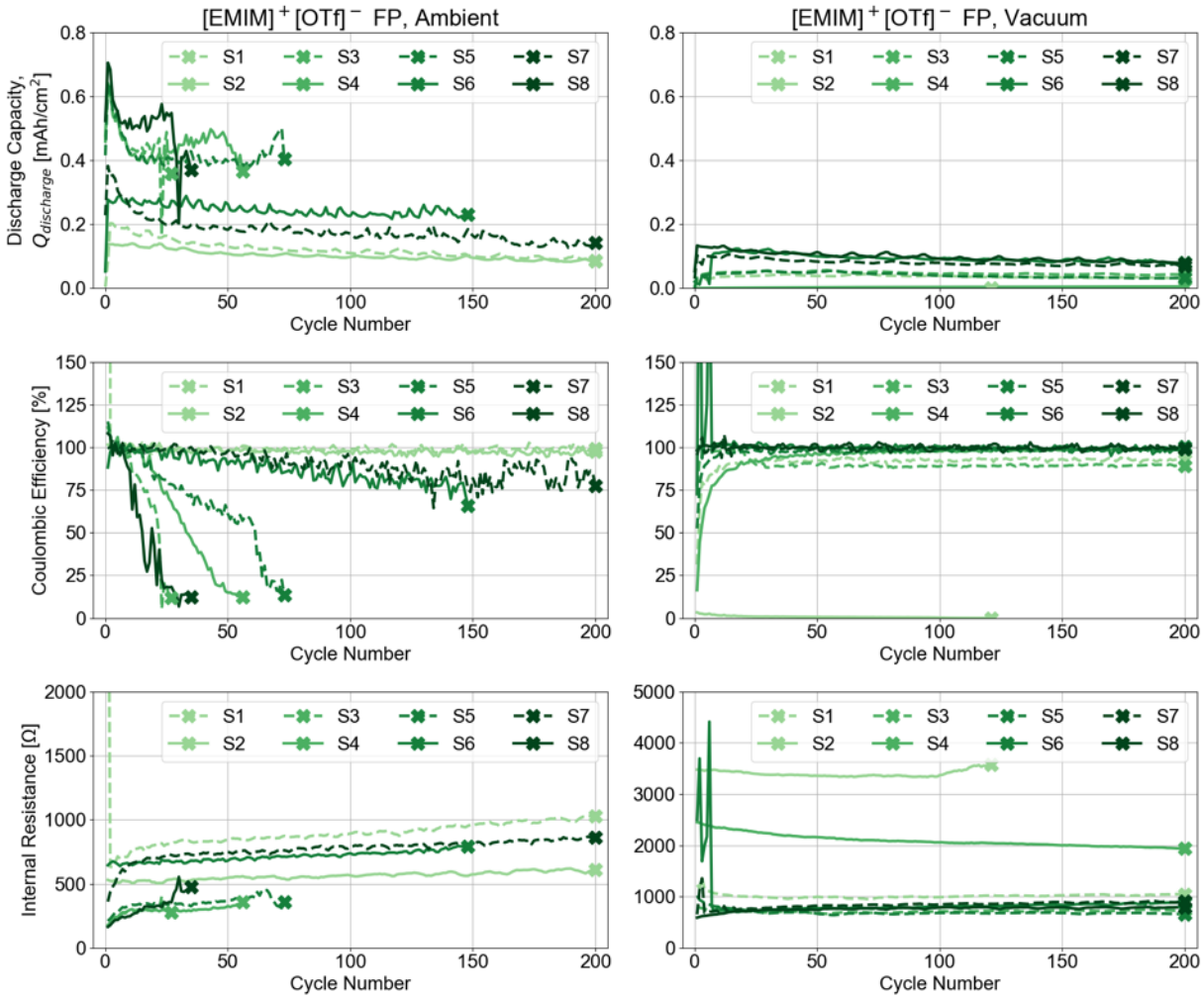

Figure 6.35: Discharge capacity, coulombic efficiency, and DC internal resistance per cycle for fully printed cells with $[EMIM]^+[OTf]^-$ GPEs dried in ambient and under vacuum.

Fully printed cells showed more variation per batch than mechancially assembled full cells. Again, cells with $[BMIM]^+[OTf]^-$ GPEs showed higher median discharge capacities than cells with $[EMIM]^+[OTf]^-$. However, the same decline over the first 20 cycles as observed with mechanically assembled full cells was not observed for most cells. Cells consistently showed an immediately sharp increase in discharge capacity following initial discharge. This initial discharge (at Cycle "0") is a result of the cycling protocol that was programmed and reflects the amount of charge available for use when the cell is discharged after assembly and before any other charging steps.

For cells with $[BMIM]^+[OTf]^-$ GPEs, cells showed discharge capacities of 0.4-0.1mAh/cm^2 for cells dried in ambient and 0.15-0.06mAh/cm^2 for cells dried under vacuum. Variation between cells was much higher for cells with $[EMIM]^+[OTf]^-$ GPEs, and cells showed steady discharge capacities of 0.5-0.08mAh/cm^2 for cells dried in ambient and 0.13-0.001mAh/cm^2 for cells dried under vacuum.

In general, cycling behavior was more unstable compared to mechanically assembled cells. Except in the case of $[EMIM]^+[OTf]^-$ cells dried under vacuum, fewer cells were able to cycle to 200 cycles before failing or showing signs of significant degradation. Sharply declining or erratic coulombic efficiency is indicative of cell failure and breakdown as cells were unable to reach the target potential of 1.8V even after sustained current.

Internal resistances were particularly unstable for cells with $[BMIM]^+[OTf]^-$ GPE dried in ambient and ranged from 1000Ω to over 10000Ω. Even with coulombic efficiencies close to unity, internal resistance was not steady and showed significant differences from cycle to cycle. For all other cells, internal resistnace was more stable throughout cycling. Cells with $[BMIM]^+[OTf]^-$ GPEs dried in vacuum generally ranged from 300-500Ω. For cells with $[EMIM]^+[OTf]^-$ GPEs, internal resistances ranged from 250-1000Ω for cells dried in ambient and from 600-3500Ω for cells dried under vacuum. Thus, cells with $[BMIM]^+[OTf]^-$ showed the lowest internal resistance.

For all ionic liquids and environments, internal resistance was higher than corresponding mechanically assembled full cells. This is likely due to the use of the printed Zn anode rather than the Zn foil which would offer lower resistivity. This increased resistance likely also contributes to the lower overall discharge capacities observed.

The reason for lower cycle life with fully printed cells is not fully understood. One issue that was resolved by fully printed cells was delamination and loss of mechanical integrity of the MnO_2 cathode from repeated cycling. However, the form of cell failure observed shows similar signs as failure of initial mechanically assembled cells. Differential capacity analysis may provide additional insight.

While the highest individual discharge capacities of 0.4-0.55mAh/cm^2 were observed with $[EMIM]^+[OTf]^-$ cells dried in air, these cells all failed by 75 cycles and showed rapidly declining coulombic efficiencies by cycle 15. This suggests that these higher earlier discharge capacities may be at the expense of cell health. Again, further insight may be gained from differential capacity analysis.

6.4.5.4 Differential Capacity Analysis

Figures 6.36 and 6.37 present differential capacity and charge/discharge voltages of cells with the most and least stable cycling behavior for fully printed cells with $[BMIM]^+[OTf]^-$ dried in ambient and vacuum respectively. Figures 6.27 and 6.28 present the same data for fully printed cells with $[EMIM]^+[OTf]^-$ GPEs. Because cell discharge capacity and cycle life was significantly more varied than with mechanically assembled full cells, stable and unstable cycling behavior was determined by consistency in coulombic efficiency for the cycle life of each cell, where the most stable cells showed high coulombic efficiency for the largest number

of cycles. Again, a custom smoothing algorithm was applied to the differential capacity in order to reduce noise arising from numerical differentiation with a small step size. The cycles plotted for each cell were chosen to capture the change in reactions taking place over the lifetime of each cell. Stable and unstable cells were chosen based on cycle life and change in coulombic efficiency with cycling as rapid decline in both indicate cell degradation.

Differential capacity responses for fully printed cells follow similar trends to those observed for mechanically assembled full cells, but most individual cell responses are more similar to high IR mechanically assembled full cells. Of all stable cells, only the $[EMIM]^+[OTf]^-$ cell dried in ambient showed peaks and plateaus similar to mechanically assembled full cells. All other cells showed mostly linear responses with significantly lower plateau magnitudes. Cells with $[BMIM]^+[OTf]^-$ dried in ambient showed noisier peaks at discharging potential limit (1.0V) for the first 5 cycles but then settled to a flat response. Both stable cells dried under vacuum showed almost no peaks throughout except for at 1.8V at the last cycle for $[BMIM]^+[OTf]^-$ and the first cycle for $[EMIM]^+[OTf]^-$.

Examining the behavior of stable cells, all cells except for $[EMIM]^+[OTf]^-$ dried in ambient showed minimal or no peaks, as mentioned above. The discharge curve for that cell resembles those observed with mechanically assembled cells with an initial decline over the first 20 cycles followed by a more steady drop in discharge capacity.

Both unstable cells with $[BMIM]^+[OTf]^-$ initially showed promising discharge capacities but quickly declined and failed within 100 cycles. While their differential capacity responses initially showed similar peaks and plateaus to well-performing mechanically assembled cells, the responses quickly decayed to more linear ones with increasing noise at the potential limits with further cycling. In the case of the cell dried in ambient, the charging response remained similar until the end of cycling, but the discharging response showed signs of increasing noise sooner (within 25 cycles). Conversely, the cell dried under vacuum showed no peaks on its discharging response even at its initial cycles. The cell with $[EMIM]^+[OTf]^-$ dried under vacuum showed no peaks throughout cycling except at the charging potential limit (1.8V) for the first two cycles. The cell dried in ambient showed promising behavior for the first 5 cycles, but peaks drastically declined by cycle 25 following a significant loss in discharge capacity.

Notably for all unstable cells, a more significant decline in differential capacity response was observed only upon charging. This is consistent with cell failure occuring upon charge and the cell taking longer or eventually being unable to reach a potential of 1.8V. This inability to reach 1.8V suggests insufficient reactant at one of the electrodes, thus being unable to reach the target potential. Discharge capacities for early cycles were high for cells that failed earlier while discharge capacities remained low throughout cycling for cells that did not fail.

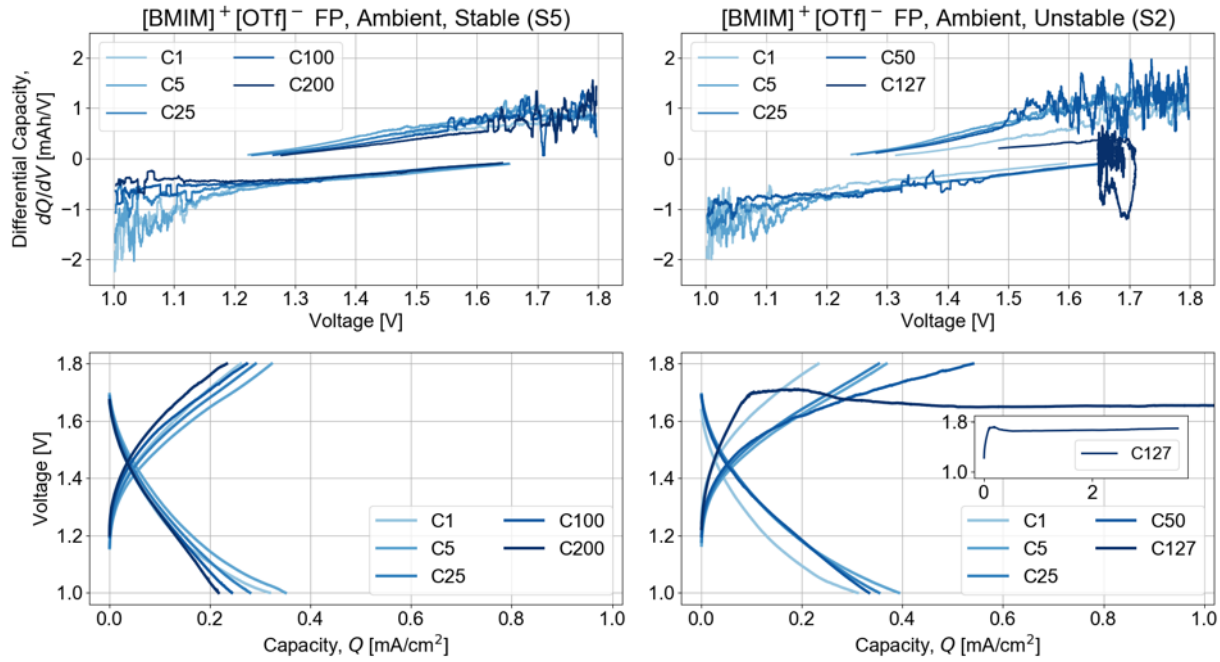

Figure 6.36: Differential capacity and charge/discharge voltages of most and least stable cells for fully printed cells with $[BMIM]^+[OTf]^-$ GPEs dried in ambient.

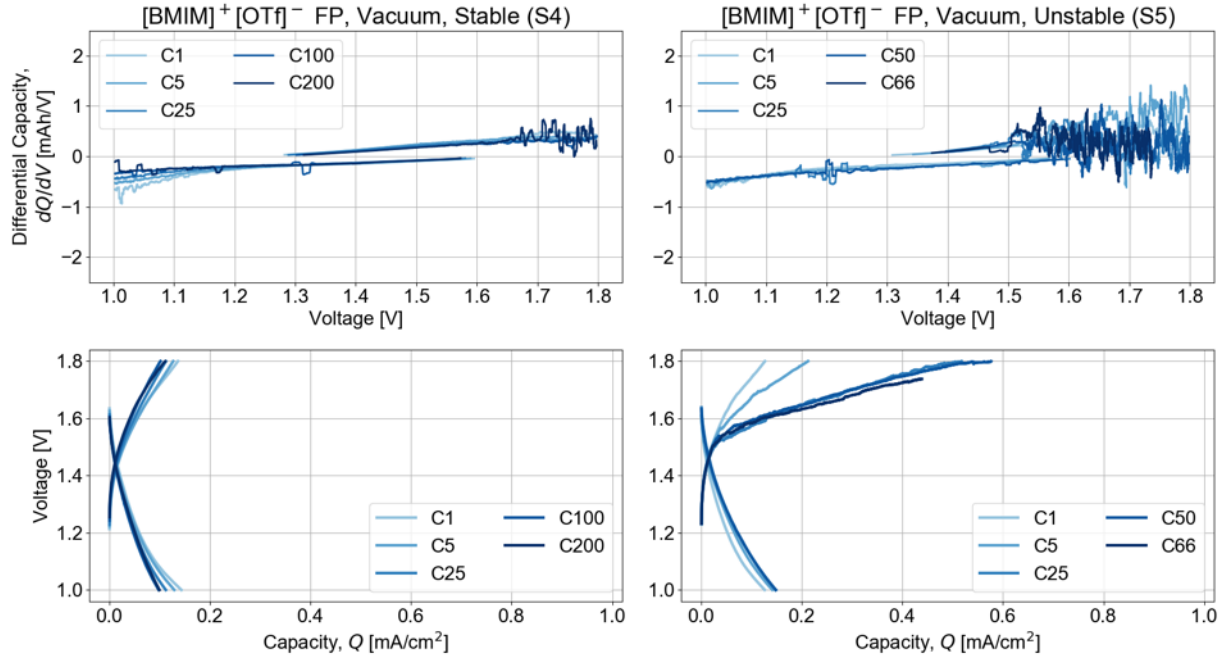

Figure 6.37: Differential capacity and charge/discharge voltages of most and least stable cells for fully printed cells with $[BMIM]^+[OTf]^-$ GPEs dried under vacuum.

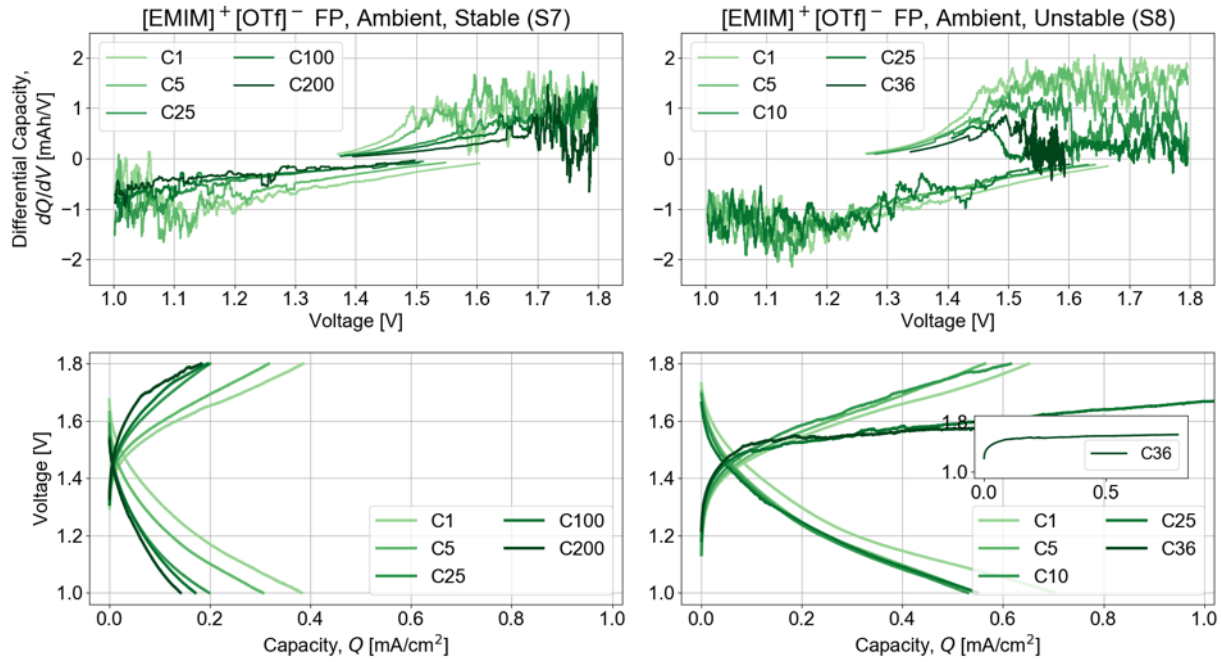

Figure 6.38: Differential capacity and charge/discharge voltages of most and least stable cells for fully printed cells with $[EMIM]^+[OTf]^-$ GPEs dried in ambient.

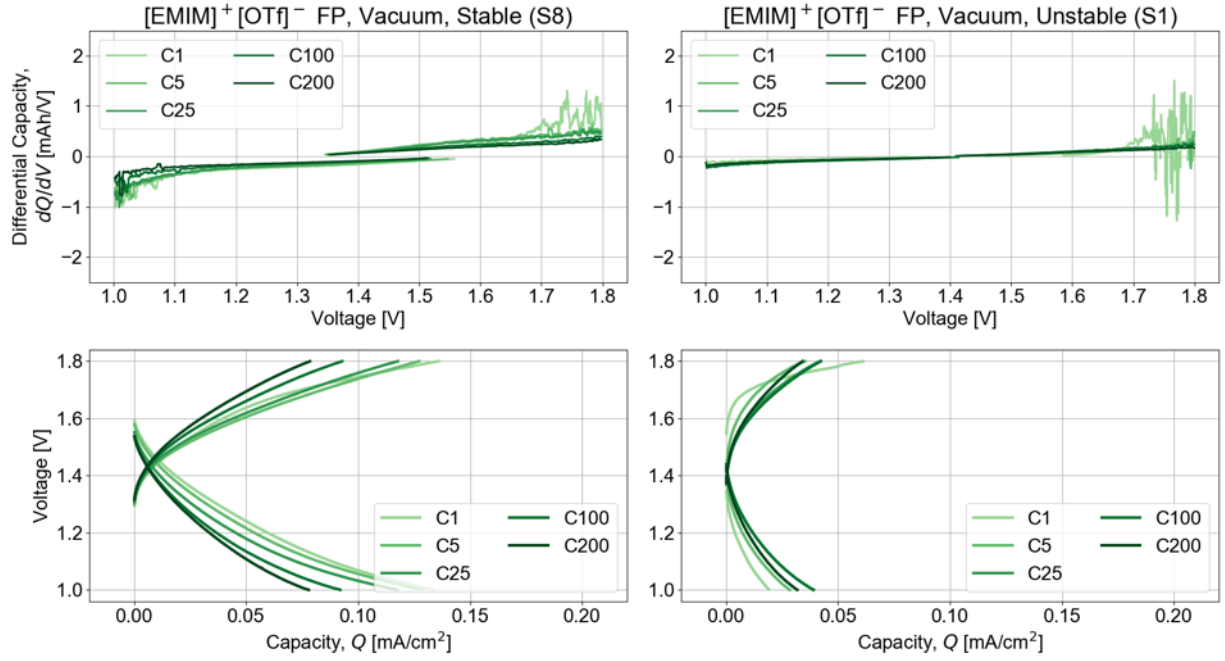

Figure 6.39: Differential capacity and charge/discharge voltages of most and least stable cells for fully printed cells with $[EMIM]^+[OTf]^-$ GPEs dried under vacuum.

The differences in differential capacity response and discharge capacity between stable and unstable cells suggest different general mechanisms of charge transfer between mechanically assembled and fully printed cells. The lack of peaks observed on the differential capacity responses of most fully printed cells combined with their lower discharge capacity suggests a shallower method of ion intercalation that does not involve significant phase changes but also prevents higher capacity densities. For overall cell performance, this effectively limits the depth of discharge capable by the cell without initiating catastrophic degradation. This suggests that the phase changes and reactions that take place for high depths of discharge are ultimately detrimental to cycle life while lower discharge capacities that result in lower and smoother differential capacity responses allow for longer cycle life.

6.5 Conclusions

This chapter characterized gel polymer electrolytes made from PVDF-HFP with $0.5M$ concentrations of $Zn(OTf)_2$ in $[BMIM]^+[OTf]^-$ and $[EMIM]^+[OTf]^-$ dried in ambient, vacuum, and argon. GPEs were solution cast as free standing films and their morphologies investigated via SEM or assembled into cells. Free standing films were assembled into half cells and mechanically assembled full cells, and GPEs were also directly cast onto printed electrodes to manufacture fully printed cells. Cells were characterized by cyclic voltammetry, electrochemical impedance spectroscopy, and galvanostatic cycling. All ionic liquid and salt solutions were prepared in an argon environment, but casting with the polymer took place both in ambient and in argon.

PVDF-HFP microstructure was found to be dependent more on drying temperature than drying environment. When dried at temperatures of 100°C and 120°C, GPE films were not mechanically stable and were unable to be handled without crumbling. The polymer formed spherulites with both crystalline and amorphous domains, where the crystalline structure provided mechanical integrity and the amorphous domains absorbed the ionic liquid electrolyte. GPEs were observed to "sweat" as they cooled to room temperatures, squeezing out excess electrolyte which was then utilized to ensure wet interfaces during cell assembly.

Half cells were made with GPEs dried in ambient, under vacuum, and in argon. GPEs dried in argon showed the lowest performance across both ionic liquids with CV peak currents one order of magnitude lower than GPEs dried in ambient and under vacuum. GPEs with $[BMIM]^+[OTf]^-$ showed more stable cycling behavior than GPEs with $[EMIM]^+[OTf]^-$, which showed a tendency to quickly form electrical shorts through the GPE within a few cycles, likely due to faster mass transport. While the presence of water in GPEs manufactured even partially in ambient improves cycling performance, it also leads to the formation of undesired oxides and microstructures.

Mechanically assembled full cells showed no notable peaks during CV, likely due to significantly higher internal resistances due to the printed MnO_2 cathode. CV responses more closely resembled those of a parallel resistor and capacitor, likely due to the increased surface area afforded by the printed cathode allowing for greater electric double layer capacitance by

ionic liquid. Calculated mean ionic conductivities were higher for $[EMIM]^+[OTf]^-$ GPEs at faster scan rates but higher for $[BMIM]^+[OTf]^-$ at slower scan rates. Calculated mean charge transfer resistances were generally lower for $[BMIM]^+[OTf]^-$ GPEs across all environments and scan rates. Ionic conductivities were generally higher for GPEs dried under vacuum than under ambient, and the performance for GPEs dried in argon was poor across both ionic liquids and scan rates. Charge transfer resistances decreased significantly from new cells to after cycling with CV for 10 cycles, but ionic conductivity did not, suggesting a changes in electrode structure or morphology and not in bulk electrolyte concentration.

For mechanically assembled full cells, cells with $[BMIM]^+[OTf]^-$ GPEs showed the highest stable discharge capacities upon galvanostatic cycling. Most cells were able to be cycled for 200 cycles. Across both ionic liquids, cells with GPEs dried in vacuum showed higher median discharge capacities and lower internal resistances than cells with GPEs dried in ambient. Differential capacity analysis revealed that low IR cells exhibited phase change or side reactions at the beginning of cycling, which then decreased and plateaued as cycling continued. However, high IR or poorly performing cells continued to show evidence of unwanted reactions even as cycling continued, particularly at the limits of the cycled potential window (1.0V and 1.8V). Cells with GPE dried in ambient showed a larger discrepancy in differential capacity response as cycling continued than cells with GPEs dried in vacuum, indicating that water is involved in these side reactions. $[BMIM]^+[OTf]^-$ may be more sensitive to water as higher magnitude peaks are observed with those GPEs.

Fully printed cells were printed as free-standing, monolithic structures. From EIS, ionic conductivities were lower with fully printed cells dried in ambient than their mechanically assembled counterparts, but initial charge transfer resistances were also lower. The lower charge transfer resistance is likely due to the use of the printed anode rather than Zn foil as well as the excellent interfacial contact at both electrode-electrolyte interfaces.

However, fully printed cells showed significant variation within each batch upon galvanostatic cycling, and cells in general showed poorer performance than mechanically assembled full cells. The highest discharge capacities were observed for cells with $[BMIM]^+[OTF]^-$ GPEs dried in ambient, and cells dried in ambient showed higher discharge capacities than cells dried under vacuum for both ionic liquids. Internal resistance was higher with fully printed cells, likely due to the printed anode over the Zn foil anode. Differential capacity responses were different for fully printed cells than for mechanically assembled full cells with fully printed cells showing significantly fewer peaks. Furthermore, more significant reduction in differential capacity response was observed on the discharge side, suggesting more rapid degradation and variations in Zn^{2+} intercalation mechanism with fully printed cells than with mechanically assembled cells. However, fully printed cells were shown to be cycled with some cells reaching 200 cycles without failure.

From these results, $[BMIM]^+[OTf]^-$ GPEs dried in ambient offer the best performance for fully printed cells. While $[EMIM]^+[OTf]^-$ does offer higher rate capabilities, its long term stability is hindered by higher formation of electrical shorts and lower overall discharge capacities. Future work should seek to further develop the manufacturing process for fully printed cells to determine the underlying causes of manufacturing variability. In addition, further investigation should seek to elucidate the degradation mechanisms leading to capacity loss and inability to reach 1.8V upon charge for fully printed cells.

Chapter 7

Full Cell Manufacturing and Cycling

This chapter presents results from cycle life testing of printed Zn-MnO_2 cells with an ionic liquid-based gel polymer electrolyte.

The goals of this work are

1. to characterize and test Zn-MnO_2 cells with varying degrees of printed components,
2. to investigate mechanisms of cell failure and degradation, and
3. to incorporate development and optimization of individual cell components into final fully printed cells.

Section 7.1 presents the motivation for the analysis and work performed in this chapter. Section7.2 discusses reported changes in MnO_2 phases as a result of reduction via electrochemical cycling. Section 7.3 presents the experimental methods used to manufacture, test, and analyze full cells. Section 7.4 presents the findings from cycle life testing and scanning electron microscopy on cell performance and degradation. Section 7.5 discusses conclusions and future work.

7.1 Motivation

The goal of this work is to incorporate development and optimization work performed on individual cell components in order to improve overall cell performance through cycle life testing. Cell performance is determined by discharge capacity, coulombic efficiency, and internal resistance over cycles tested. The cathode, anode, and gel polymer electrolyte were optimized in previous chapters, and work presented in this chapter seeks to combine all findings to improve cell performance.

Initial cells sought to determine the validity and establish a proof-of-concept that fully printed cells are cycleable and offer benefits to conventional mechanically assembled cells. Final cells sought to improve performance metrics established by initial fully printed cells.

Traditional cells are made in a sandwich structure with electrodes and the electrolyte requiring additional encapsulation to maintain contact and structural integrity, so their application with small and flexible electronics is limited due to their inherent rigidity. In addition, the manufacturing steps involved prevent their incorporation into flexible electronics where components are additively manufactured and delicate enough to be unable to withstand typical battery cell manufacturing processes. Thus, the development of a fully printed cell with a printable electrolyte takes a step towards enabling printed and flexible energy storage.

7.2 Background

This section presents findings from literature about MnO_2 polymorphs and phase changes induced by Mn^{4+} reduction and ion insertion.

7.2.1 MnO_2 Polymorphs and Zn-Ion Intercalation-Induced Phase Changes

MnO_2 has attracted attention as a candidate for multivalent cathode materials for energy storage systems. A number of polymorphs exist for MnO_2, the fundamental unit of which is an octahedral MnO_6 unit in which one Mn^{4+} ion is surrounded by six oxygen neighbors. These units are then linked via edges and corners to form a variety of polymorphs [2].

Specific polymorphs of MnO_2 have been investigated for use with multivalent intercalating ions, including α-MnO_2 (Hollandite), δ-MnO_2 (layered birnessite), and γ-MnO_2 (electrolytic manganese dioxide, EMD). These phases have been investigated specifically for their crystal structures which provide sites for ion insertion and range from 1x1 and 2x2 unit cell tunnel structures for γ-MnO_2 and α-MnO_2 respectively to layered structures for δ-MnO_2 [2, 54, 55, 38, 36]. It was initially posited that intercalation required phases with larger tunnel structures or layers, limiting phases to α-MnO_2 and δ-MnO_2, but work by Alfaruqi, *et. al.* showed that intercalation was possible with the narrower tunnel structures of γ-MnO_2 as well [2].

γ-MnO_2 is of particular interest due to its ubiquity and use in commercial primary alkaline Zn-MnO_2 cells. The structure of this polymorph can be described by alternating 1x1 and 1x2 tunnel structures, corresponding to pyrolusite and ramsdellite domains respectively. These structures and the resulting γ-MnO_2 structure are presented in Figure 7.1. Within aqueous systems, the presence of multiple structural domains results in multiple discharge processes for the reduction of Mn^{4+}, each of which occur at different potentials [7].

Insertion into γ-MnO_2 in aqueous environments results in the reduction of Mn^{4+} to lower oxidation states, specifically to Mn^{3+} and Mn^{2+} and intermediary γ-Zn_xMnO_2 and L-Zn_yMnO_2 respectively [2]. The formation of $ZnMn_2O_4$ is particularly detrimental due to its inertness, leading to loss of active material and capacity fade [38]. Furthermore, it has been reported that electrochemical cycling results in the irreversible loss of surface area

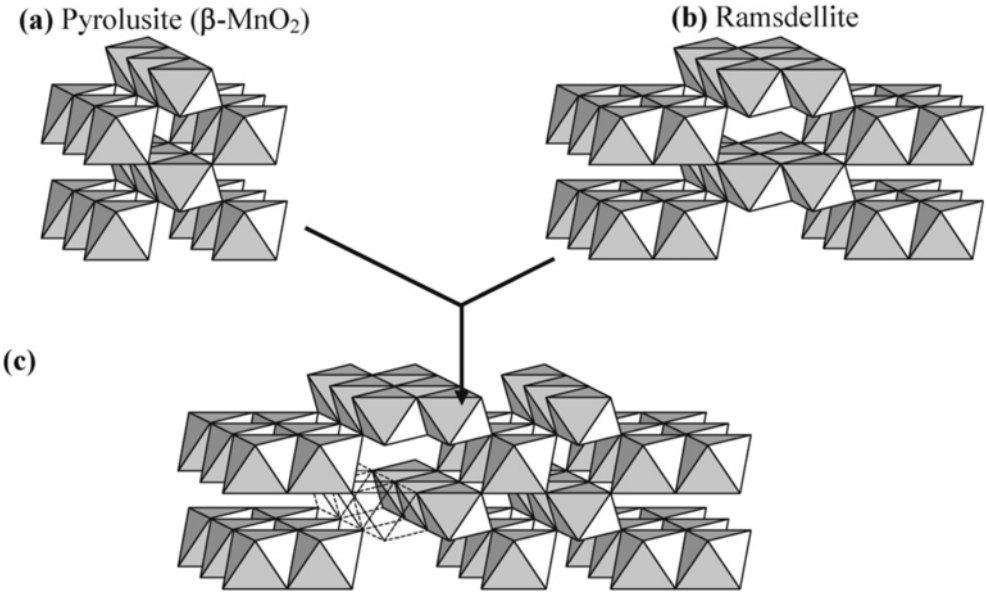

Figure 7.1: Pyrolusite (a) and ramsdellite (b) structures and resulting γ-MnO_2 structure (c) [7].

and expansion of the γ-MnO_2 lattice due to localized buckling of the oxygen framework [7]. Detrimental structural changes due to large stresses from these phase transitions have also been reported with α-MnO_2, also leading to capacity loss [55].

While the majority of work characterizing structural changes to MnO_2 during electrochemical cycling involves aqueous systems, work has also been reported on intercalation of divalent metal ions in non-aqueous systems, specifically with ionic liquid electrolytes. Tafur, *et. al.* posit an intercalation mechanism of Zn into MnO_2 within $[BMIM]^+[OTf]^-$ with supporting $Zn(OTf)_2$ in which Zn^{2+} intercalates while expelling reduced Mn^{2+} [96]. Intercalation of Zn^{2+} would then induce reduction of Mn^{4+} to Mn^{3+} and Mn^{2+} by a general mechanism (Equations 7.1-7.2).

$$2MnO_2 + Zn^{2+} + 2e^- \rightarrow \left[2MnO_2 - Zn^{2+}\right] \tag{7.1}$$

$$\left[2MnO_2 - Zn^{2+}\right] + Zn^{2+} + 2e^- \rightarrow \left[2MnO_2^{2-} - 2Zn^{2+}\right] \tag{7.2}$$

However, this process is likely not entirely reversible with some Zn^{2+} persisting while stabilized by accompanying OTf^-. Han, *et. al.* report reversible insertion of Zn^{2+} into δ-MnO_2 but state that capacity fade and increasing impedance are due to diminished electrolyte performance and undesired side reactions [36]. No published work was found that reported phase changes induced in γ-MnO_2 in ionic liquid electrolytes.

7.3 Experimental Methods

This section discusses all experimental methods used in printing, cycling, and characaterizing full cells. The printing processes for initial and final cells are discussed, and the cell cycling protocol using combined galvanostatic and potentiostatic charging is presented. Preparation of samples for scanning electron microscopy is also discussed. The phase of all MnO_2 used in cathode inks was γ-MnO_2.

7.3.1 Cell Manufacturing

Figure 7.2 presents all types of cells made for this work. Cells ranged in level of printing from mechanically assembled (MA) cells, half printed (HP) cells, and fully printed (FP) cells. The printing process differed between initial cells and final cells, but coin cell assembly remained consistent. Half printed cells differ from mechanically assembled cells and fully printed cells in that they utilize a GPE directly cast on the printed cathode similar to fully printed cells but use a Zn foil anode. All drying steps were performed at 80°C in ambient. All cells were assembled in coin cells as described in Chapter 6. Table 7.1 presents the order of coin cell components used for each type of cell.

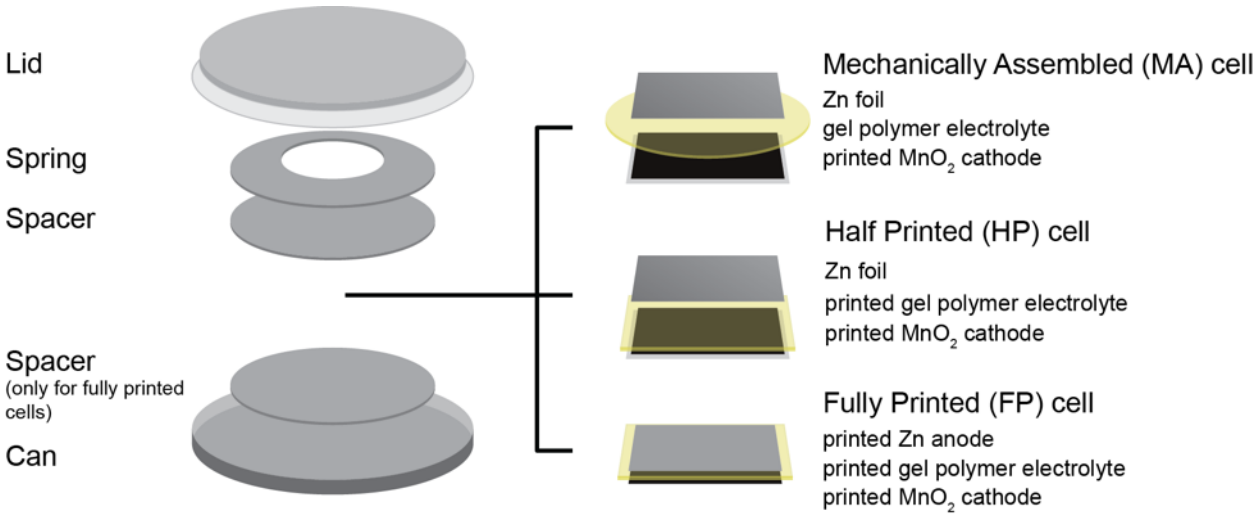

Figure 7.2: Types of cells manufactured.

Table 7.1: Coin cell components

	MA Cell	HP Cell	FP Cell
Top	coin cell lid spring 0.5mm spacer	coin cell lid spring 0.5mm spacer	coin cell lid spring 0.5mm spacer
	$1cm^2$ zinc foil GPE printed MnO_2 cathode	$1cm^2$ zinc foil printed MnO_2 cathode and GPE	fully printed cell
Bottom	coin cell can	coin cell can	0.5mm spacer coin cell can

7.3.1.1 Initial Cells

Initial cells used printed MnO_2 cathodes that were printed following methods described in Chapter 3. All initial cells were printed and assembled following methods described in Chapter 6. Half printed cells followed the same doctor blade offset heights as fully printed cells (reproduced in Table 7.2), but used a Zn foil anode instead of a printed Zn anode. Compositions for inks used for initial cells are presented in Table 7.3.

Table 7.2: Fully printed cell printing procedure

Component	Layer Number	Doctor Blade Height	Drying Time [m]
Cathode	–	stencil	20
GPE	1	200μm	15
	2	250μm	15
	3	300μm	30/180
	4	300μm	30
	5	300μm	180
Anode	–	stencil	60

7.3.1.2 Final Cells

Final cells used printed MnO_2 cathodes following methods described in Chapter 4. The same automatic film applicator and doctor blade (Zehntner) were used to cast the GPE. GPE heights are presented in Table 7.4. For fully printed cells, the anode was printed with a similar but separate $75\mu m$ Kapton stencil as used for the cathode, but using the methods described in Chapter 6 for fully printed cells to place the stencil. Heights for GPEs ranged from 2-4 layers following the doctor blade heights specified in Table 7.4. Layers 2 and 3 were dried for 20 minutes each if they were not the final layer, otherwise they were dried for 60 minutes.

Table 7.3: Initial cell ink compositions

Cathode

	Mass Fraction	Volume Fraction
MnO_2	86.25 wt%	69.75 vol%
AB	5.75 wt%	11.98 vol%
PVDF-HFP	8.00 wt%	18.27 vol%
Solid Phase	53.06 wt%	–

Anode

	Mass Fraction	Volume Fraction
Zn	84.27 wt%	58.10 vol%
AB	6.64 wt%	16.76 vol%
PVDF-HFP	9.09 wt%	25.14 vol%
Solid Phase	52.09 wt%	–

Gel Polymer Electrolyte

$[BMIM]^+[OTf]^-$:$Zn(OTf)_2$	1:6.5 by mass ($0.423m$)
electrolyte	2 parts by mass
PVDF-HFP	1 part by mass
NMP	5 (MA cells) parts by mass
	or 3 (HP and FP cells) parts by mass

Table 7.4: Fully printed cell printing procedure, final cells

Component	Layer Number	Doctor Blade Height	Drying Time [m]
Cathode	stencil	100μm	20
GPE	1	250μm	10
	2	325μm	20/60
	3	325μm	20/60
	4	350μm	60
Anode	stencil	325/350μm	30

Compositions for inks used for final cells are presented in Table 7.5. These inks account for optimizations in conductivity, profilometry, rheology, electrolyte concentration, and GPE processing performed in Chapters 4, 5, and 6.

7.3.2 Combined Galvanostatic and Potentiostatic Cycling

Combined galvanostatic (constant current) and potentiostatic (constant voltage) cycling was used for cycle life testing of initial and final cells. Cycling was performed on a Neware Battery Testing System (Model T1403-064242) for initial cells and on a Bio-Logic BCS-805 or BCS-

Table 7.5: Final ink compositions

Cathode

	Mass Fraction	Volume Fraction
MnO_2, ball-milled and sieved	81 wt%	61.51 vol%
AB	12 wt%	23.49 vol%
PVDF-HFP	7 wt%	15.00 vol%
Solid Phase	36.80 wt%	–

Anode

	Mass Fraction	Volume Fraction
Zn	91 wt%	72.11 vol%
AB	2.57 wt%	7.46 vol%
PVDF-HFP	6.43 wt%	20.44 vol%
Solid Phase	70 wt%	–

Gel Polymer Electrolyte

$Zn(OTf)_2$ in $[BMIM]^+[OTf]^-$	$0.2m$
	or $0.3m$
$Zn(OTf)_2$ in $[EMIM]^+[OTf]^-$	or $0.3m$
electrolyte	3 parts by mass
PVDF-HFP	1 part by mass
NMP	4 parts by mass

810 for final cells. Table 7.6 presents test parameters used for cycling on Neware testers, and Table 7.7 presents test parameters used for cycling Bio-Logic testers.

Cells were discharged at a constant current of 125μA (initial cells) or 100μA (final cells) until a potential of 1.0V was reached. Cells were then first charged at the same current as discharge until 1.8V was reached, after which a constant voltage of 1.8V was applied and the current allowed to exponentially decay until a target cut off current was reached (20μA for initial cells, 25μA for final cells). Cells were then allowed to rest for 3 minutes (initial cells) or 1 minute (final cells) before returning to discharge. A narrower current range was used for final cells in order to minimize side reactions and cell degradation that was observed with earlier testing.

7.3.3 Scanning Electron Microscopy

Scanning electron microscopy was used to examine cross sections of cells after cycling. Cells were removed from coin cells by breaking the plastic seal around the lid and prying back the crimped edge of the can. In order to reveal the cross section of cells, a clean razor blade was used to manually cut through the center of each cell. The angle of the blade was kept constant at about 30°, and care was taken to ensure only parallel movement of the blade to the cell in order to minimize downward compression on the cell.

Table 7.6: Neware test parameters for CCCV charge and CC discharge cycling.

Step Number	**Step Name**	**Time (min)**	**Voltage (V)**	**Current (mA)**	**Jump**	**Cycles**	**CurrStop (mA)**
1	CC_CV_ Charge	–	1.8	0.125	–	–	0.020
2	C_Curr Discharge	–	1.0	0.125	–	–	–
3	Rest	3	–	–	–	–	–
4	Cycle	–	–	–	1	200	–
5	End	–	–	–	–	–	–

Record Condition			Protect Param		
Time	On	60 sec	Hi Voltage	On	2.0 V
Current	Off	0 mA	Low Voltage	On	0.8 V
Voltage	On	10 mV	Current Range	Off	0 mA

The exposed edge of each cell was mounted on a 90° alumimum stub (Ted Pella) using a piece of conductive carbon tape. The same tabletop SEM as described in Chapter 3 (Hitachi T-1000) was used for all SEM images.

7.4 Results and Discussion

This section presents cycle life results obtained from initial cells and final cells. Initial cells were investigated at the beginning of this work prior to any development performed on individual components. Final cells were investigated at the end of this work to incorporate all development performed individually.

7.4.1 Initial Cells

This section presents results from cycle life testing and scanning electron microscopy of cycled cells.

7.4.1.1 Mechanically Assembled Cells

Figure 7.3 presents discharge capacity, coulombic efficiency, and internal resistance from cycle life testing of initial mechanically assembled cells, and Figure 7.4 presents differential capacity and voltage profiles for a stable and unstable cell from this batch. Cells were allowed to cycle for up to 100 cycles, but all cells failed earlier in cycling. Figure 7.5 presents SEM images of a disassembled printed cathode and Zn foil anode after cycling. Figure 7.6 presents a mechanically assembled cell with a printed cathode and anode highlighting delamination

Table 7.7: Bio-Logic test parameters for combined galvanostatic and potentiostatic cycling.

Setting	**Value**		
	Sequence 0	**Sequence 1**	**Sequence 2**
Step 1			
Set I to I_s (vs. None) =	0mA	-100μA	100μA
for at most t_1 =	0h 0mn 0s	24h	24h
Limit $E_{cell} > E_M$ =	0V	1V	1.8V
Record every dE_1 =	0mV	0mV	0V
or dt_1 =	0s	5s	5s
Hold E_M for t_M =	0h 0mn 0s	0h 0mn 0s	24h 0mn 0s
Limit |I| < I_m =	0mA	0mA	25μA
or |dI/dt| < dI/dt_f =	0mA/s	0mA/s	0mA/s
Record every dQ =	0A.h	1A.h	0A.h
or dt_q =	0s	120s	5s
Limit |ΔQ| > ΔQ_M =	0mA.h	0mA.h	0mA.h
<=> Δx_M =	0	0	0
Step 2			
Rest for t_R =	0h 3mn 0s	0h 0mn 0s	0h 1mn 0s
Limit |dE_{cell}/dt| < dE_R/dt =	0mV/h	0.1mV/h	0.1mV/h
Record every dE_R =	0mV	0mV	0mV
or dt_R =	5s	5s	5s
Step 3			
If $E_{cell} < E_L$ =	pass	pass	pass
Step 4			
Go back to seq. N'_s =	0	0	1
for n_c =	0	0	200

observed with printed electrodes in mechanically assembled cells, though the data presented reflects cells with Zn foil anodes.

As observed from SEMs of half printed and fully printed cells presented below, MnO_2 thickness was about 50μm. The median GPE thickness was 373μm and the 1cm^2 Zn foil anode used was 50μm (as presented in Chapter 6), resulting in a total volume of Zn of 0.0050cm^3. This results in a nominal cell thickness of 473μm. Assuming full insertion of every Zn^{2+} ion into the cathode, this results in a theoretical maximum capacity of 29.26mAh (Equation 7.3).

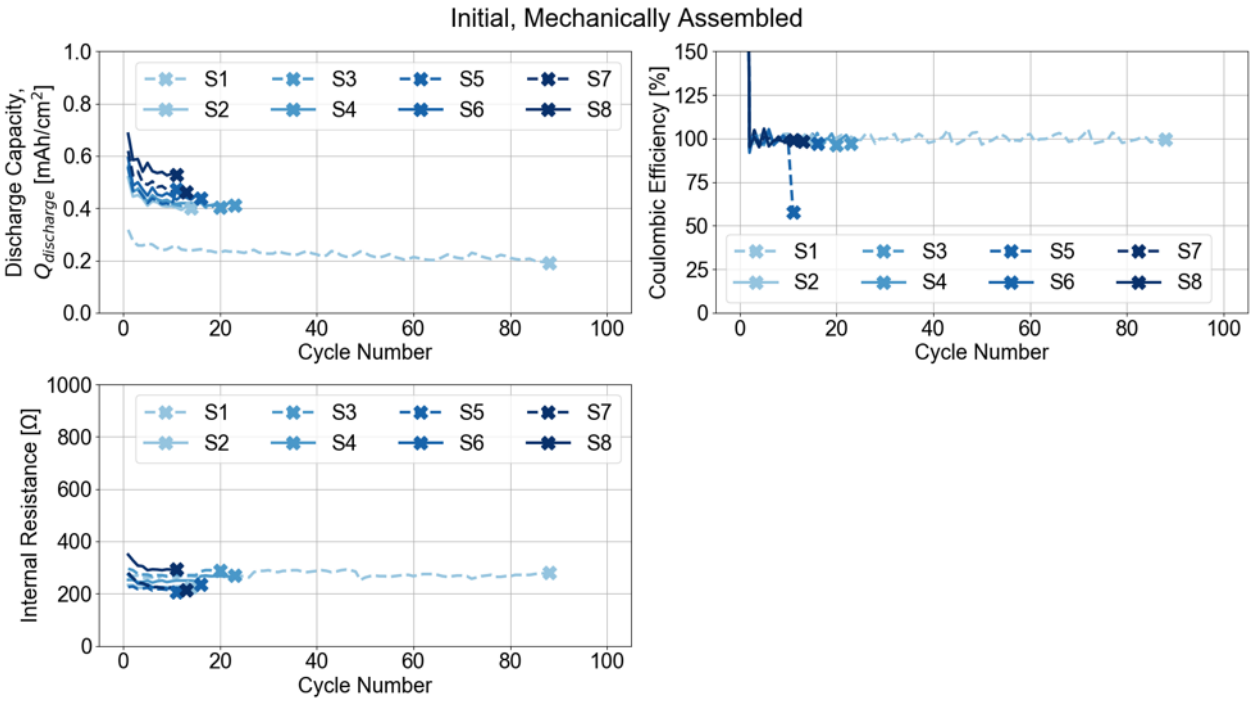

Figure 7.3: Discharge capacity, coulombic efficiency, and internal resistance of initial mechanically assembled cells.

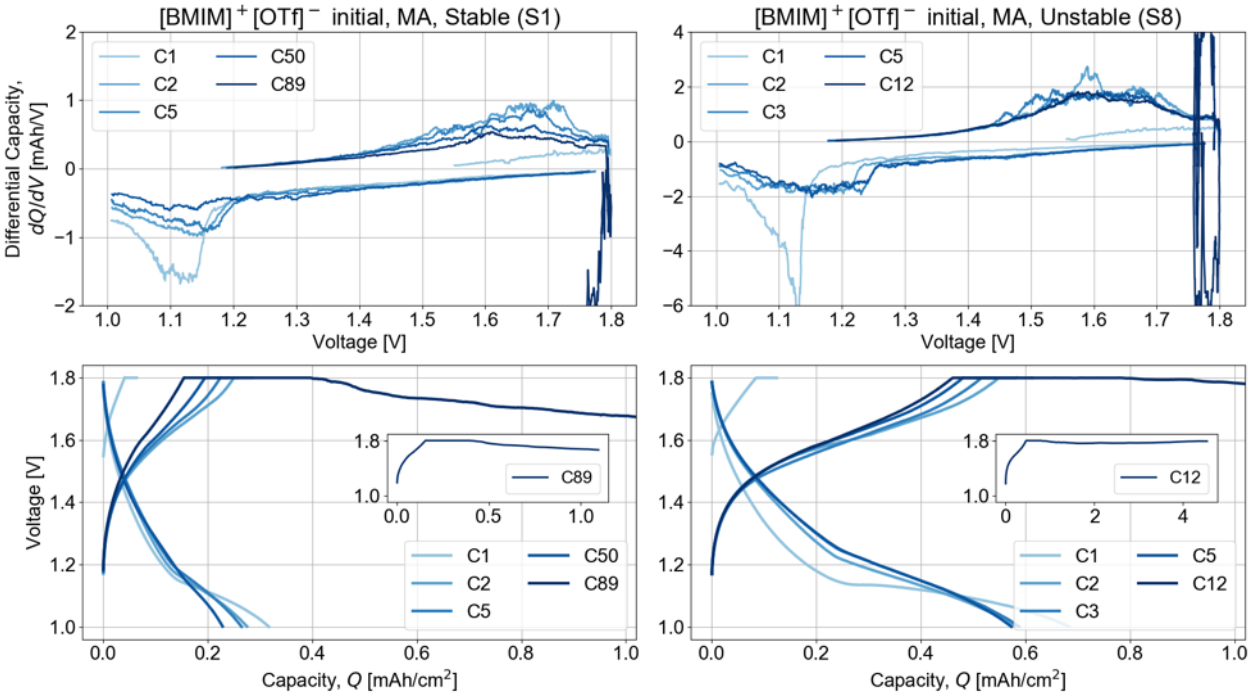

Figure 7.4: Differential capacity and voltage profile for stable and unstable initial mechanically assembled cells. Note different scales and ranges for differential capacity.

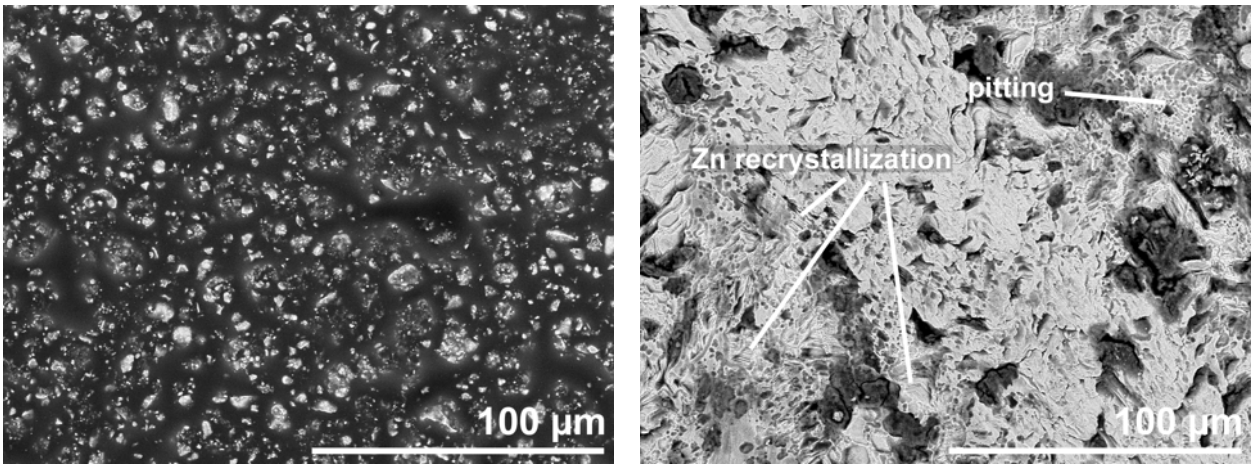

Figure 7.5: *Left*: SEM of printed MnO_2 cathode surface after cycling; *right*: SEM of Zn foil anode surface after cycling

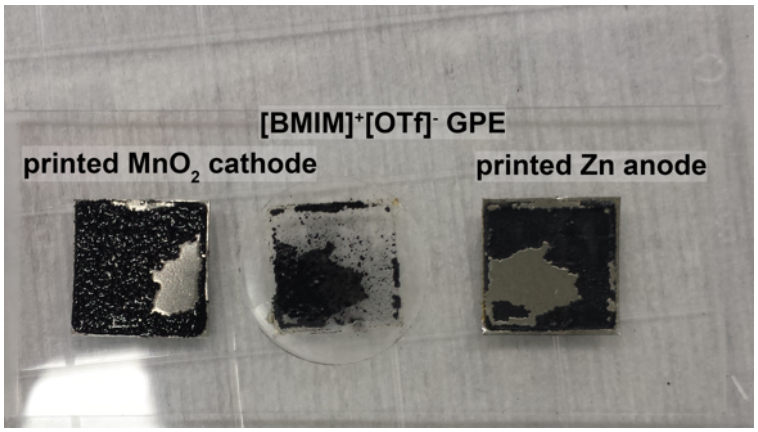

Figure 7.6: Delamination of printed cathode and printed anode after cycling in mechanically assembled cell.

$$\begin{aligned} Q_{max} &= \frac{m_{Zn}}{MW_{Zn}} nF \\ &= \frac{V \times \rho_{Zn}}{MW_{Zn}} nF \\ &= \frac{0.0050 cm^3 \times 7.14 g/cm^3}{65.38 g/mol} \cdot \left(2 \times 96485 \frac{C}{mol} \right) \cdot \frac{1 mAh}{3.6 C} \\ Q_{max} &= 29.27 mAh \end{aligned} \tag{7.3}$$

Most initial mechanically assembled cells were unable to cycle beyond 15 cycles, though one cell did cycle for almost 90 cycles. Initial discharge capacities were high at around 0.5mAh/cm^2 (10.8mAh/cm^3), but further progression was stymied by cell failure. This discharge capacity corresponds to 1.9% of the theoretical maximum, indicating significant limitations to discharge capacity. Even for the short duration of cycling, capacity loss is evident for all cells. For the duration of cycling, coulombic efficiency remained close to but below unity. Internal resistance initially decreased and ended at about 275Ω for most cells by the time of failure.

Differential capacity responses are presented in Figure 7.4, which highlight cells with the highest and lowest discharge capacities. For the cell with the highest discharge capacity (S8), clear plateaus with high differential capacities (±2mAh/V) are observed upon charge from 1.55-1.7V and upon discharge from 1.24-1.1V. The location and magnitude of these plateaus remain consistent from Cycle 2 until failure, suggesting the onset of repeatable faradaic reactions up until catastrophic failure. For the cell with the lowest discharge capacity (S1), differential capacity response decreased in magnitude and shifted outward with continued cycling, indicating a continued decline in redox reactions and resulting in capacity loss with continued cycling. However, this cell cycled for longer than any other tested cell, suggesting an inverse relationship between depth of discharge and cycle life.

Both cells showed a large peak upon the first cycle of discharge at 1.1-1.13V. This peak significantly decreased by the second cycle and may correspond to initial phase changes of the MnO_2 cathode. Conversely, the response upon the first cycle of charge remained flat but showed a prominent increase upon the second cycle. This discharge response is more expected as no Zn would have been dissolved prior to the first discharge step, which occured after the first charging step.

Both cells also showed similar behavior upon failure, as observed from their differential capacity responses. The primary mode of failure was the cells' inability to reach the cutoff charging potential of 1.8V. Examination of failed cells revealed delamination of the printed electrodes from their stainless steel foil substrates, as observed in Figure 7.6. Because a combined constant current and constant voltage charging method was used, a flat horizontal line is to be expected at 1.8V on the voltage profile of each cell as potential was held constant while current decayed and charging capacity increases. However, as seen from both voltage profiles, the cell was unable to maintain a potential of 1.8V even though such a potential was applied externally, resulting in negative values for dQ/dV during charge. One likely cause of this for the cathode is repeated expansion and contraction of the MnO_2 crystal structure upon intercalation of Zn^{2+}. On a microscale, this would lead to loss of electrical connection from the network of conductive additive present within the electrode matrix as well as possibly separation from the polymer binder, ultimately leading to loss of cycleable Zn^{2+}. The formation of electrically conductive pathways through the GPE may also be a contributing factor.

From the SEM images, no Zn is obviously apparent on the MnO_2 cathode. Due to the low conductivity of the MnO_2, the image contrast was increased significantly in order to resolve features. However, examination of the Zn foil anode shows evidence of both oxidation and

reduction in the form of pitting on the electrode surface and hexagonal Zn crystal structures respectively.

Two separate phenomena are posited that result in cell failure, both of which result in loss of cycleable Zn. The first is repeated expansion and contraction of crystals in the MnO_2 cathode as discussed above, which may ultimately cause catastrophic failure via electrode delamination and loss of electrically accessible MnO_2. The second is deposition of Zn within the GPE and its subsequent loss of electrical connection. As observed with cyclic voltammetry of half cells, Zn has been observed to deposit in voids within semi-crystalline domains of the GPE. If the tortuosity of pathways through the polymer are too high, Zn may become trapped within the polymer and be unable to participate in future faradaic reactions, leading to loss of cycleable Zn. This could also contribute to dropping cell potentials and an inability to reach the desired upper potential of 1.8V as there is inadequate Zn^{2+} to be reduced on the anode during charge. Evidence suggesting this is observed in cells presented later.

While issues with phase changes or expansion in crystal structure are unable to be solved by processing alone, one primary motivation for moving towards fully printed cells was mitigation of cell failure by electrode delamination. Thus, half printed and fully printed cells were manufactured and tested.

7.4.1.2 Half Printed Cells

Figure 7.7 presents discharge capacity, coulombic efficiency, and internal resistance from cycle life testing of initial half printed cells, and Figure 7.8 presents differential capacity and voltage profiles for a stable and unstable cell from this batch. While cells were initially intended to cycle for 100 cycles, testing was interrupted for all cells prior to failure except for cell S4. Figure 7.9 presents a half printed cathode with GPE and the cross section of the cathode and GPE taken by SEM. Figure 7.10 presents SEM images of the GPE surface and Zn foil anode surface of a disassembled half cell after cycling.

Directly casting the GPE on the cathode resulted in a mechanically free-standing film that combined the cathode and the GPE. Separation of the two layers was impossible without destroying the film. Examination of the cross section via SEM reveals good interfacial contact between the cathode and GPE as the the GPE followed the profile of the cathode surface to even out peaks and valleys. GPE thickness was about 275μm, resulting in a total cell thickness of 375μm.

Examination of the GPE surface after cycling reveals Zn crystal deposits. This surface was in direct contact with the anode, and presence of Zn crystals within the voids of the GPE suggest that Zn crystals may continue to extend further into the GPE. The Zn foil surface again shows evidence of Zn dissolution and deposition, but oxides are also visible.

Discharge capacities with half printed cells were higher than for mechanically assembled cells, averaging 0.6-0.7mA/cm^2 (16-18.7mAh/cm^3) and corresponding to 2.28-2.66% of the maximum theoretical capacity. In addition cycle life before failure was also improved by at least 3-4 times with all cells cycling for at least 60 cycles. Coulombic efficiencies before the

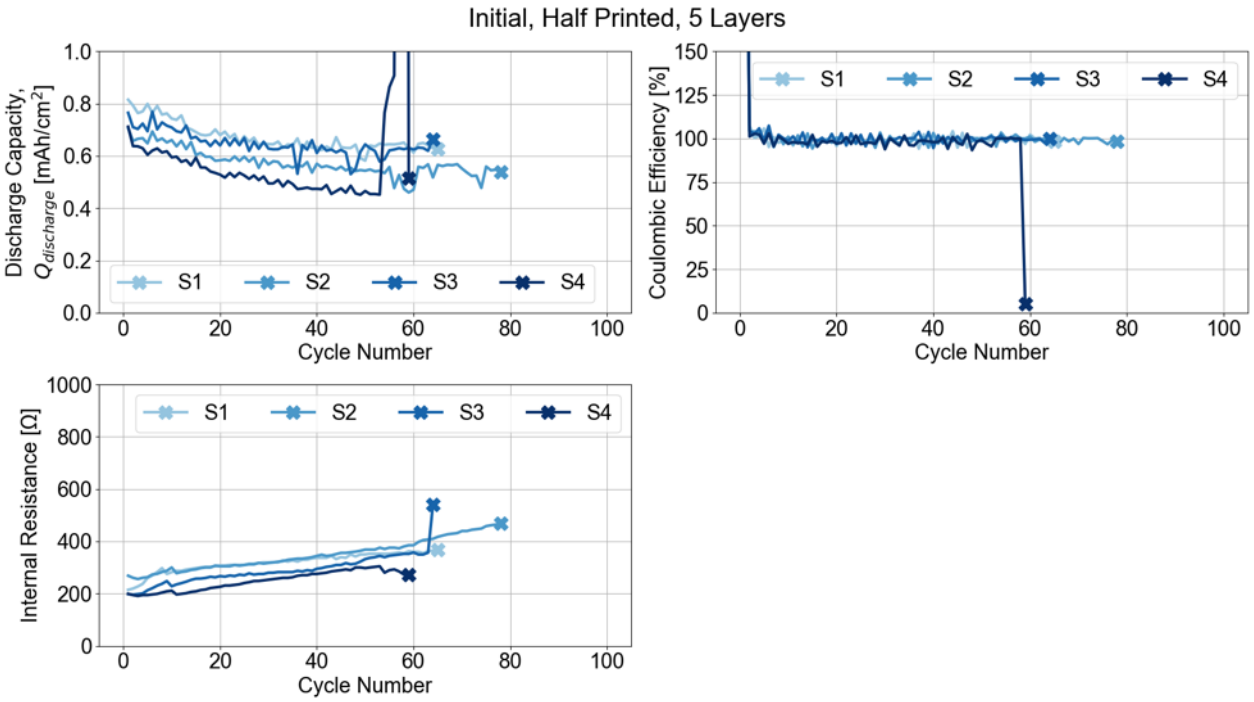

Figure 7.7: Discharge capacity, coulombic efficiency, and internal resistance of initial half printed cells.

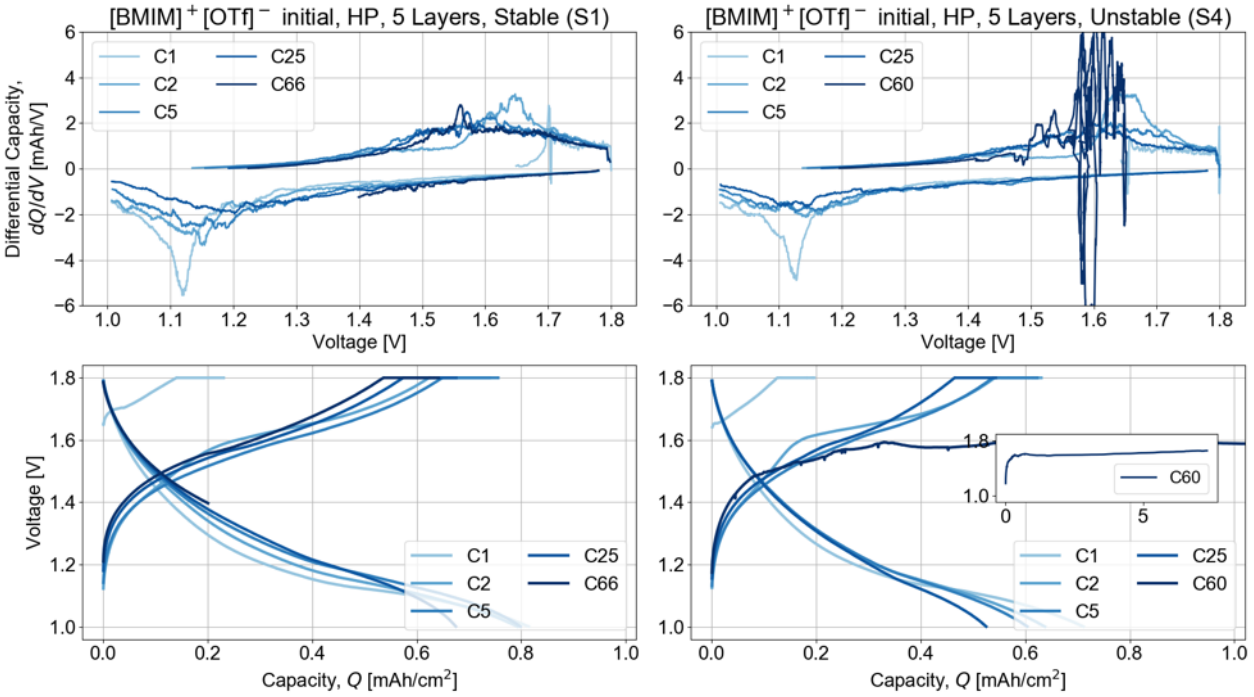

Figure 7.8: Differential capacity and voltage profile for stable and unstable initial half printed cells.

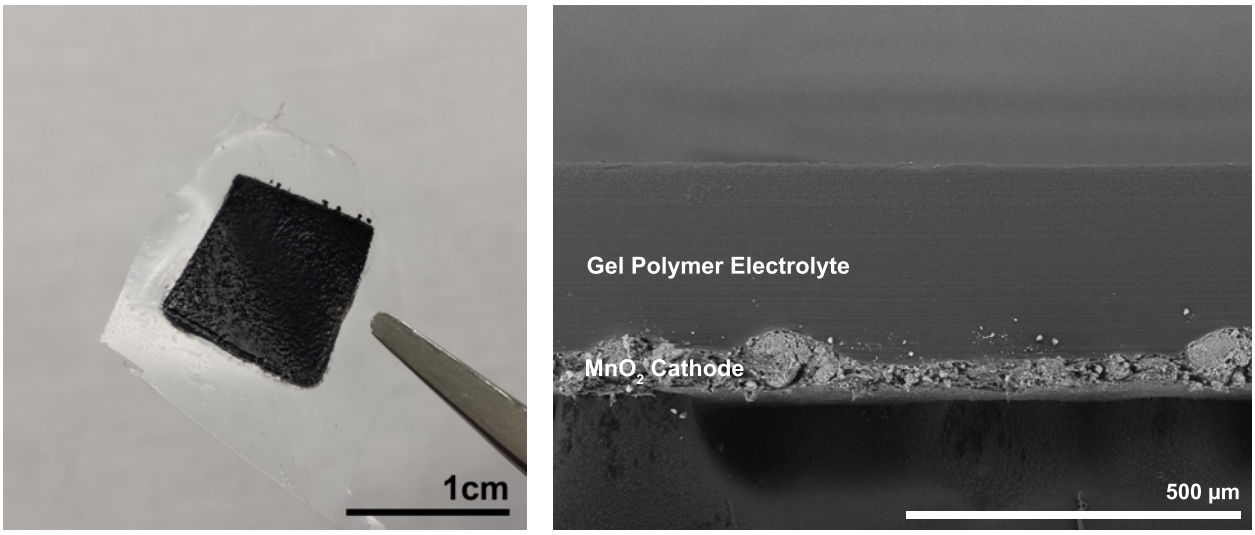

Figure 7.9: *Left*: half printed cell with printed MnO_2 cathode and GPE; *right*: SEM cross section of printed MnO_2 cathode and GPE. Tweezers are gripping excess overhanging GPE.

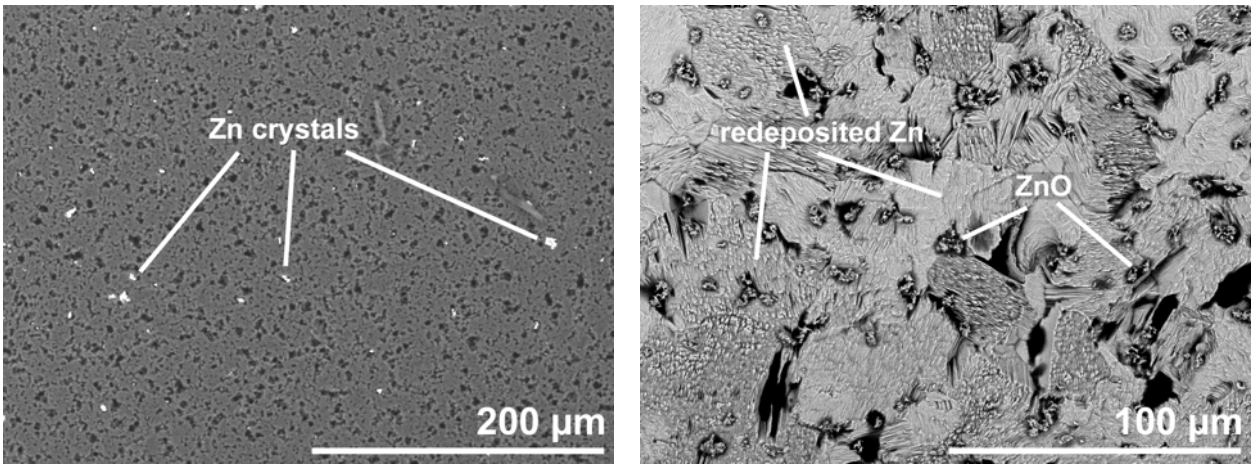

Figure 7.10: *Left*: SEM of GPE surface over cathode surface after cycling; *right*: SEM of Zn foil anode surface after cycling

end of testing remained close to btu still below unity, but internal resistance increased with cycling, starting around 250Ω and steadily increasing 100Ω every 50 cycles.

Higher cycle life for all cells suggests that the use of the directly cast GPE does mitigate electrode delamination by providing a structure upon which the cathode may be supported. Since the same polymer binder and solvent are used in both the cathode ink and the GPE, the binder in the cathode was partially dissolved during the drying process and combined with the polymer introduced by the GPE. In addition, higher discharge capacities compared to

mechanically assembled cells suggests that improved interfacial contact between the cathode and GPE improves utilization of Zn by allowing for higher MnO_2 accessibility.

As cycling behavior was similar for all half printed cells, differential capacity responses between cells with the highest and lowest discharge capacities (S1 and S4 respectively) were similar up until cell failure. The response from the highest capacity half printed cell closely matched the response of the highest capacity mechanically assembled cell, with the primary difference being an almost 6 times improvement in cycle life. A similar peak during the first discharge cycle at 1.12V as observed with mechanically assembled cells was also observed with both half printed cells. This indicates the same reaction is common to both mechanically assembled cells and half printed cells, though the exact identity of the reaction is unclear. However, more shifting of peaks is observed during discharge, suggesting a transition in Mn^{4+} reduction processes as cycling continues.

The unstable half printed cell again showed the same sign of failure as with mechanically assembled cells. However, this time the cell was unable to reach 1.8V at all and instead maintained a potential near 1.6V under the constant current regime of charging, though this potential did increase slightly through the remaining time allowed for charging. Internal resistance is likely not a factor as the cell's internal resistance decreased just prior to failure. This failure mechanism may again be due to Zn^{2+} deposition within the GPE contributing to loss of cycleable Zn.

7.4.1.3 Fully Printed Cells

Figures 7.11 and 7.12 respectively present discharge capacity, coulombic efficiency, and internal resistance from cycle life testing and differential capacity and voltage profiles from cycle life testing of initial fully printed cells with 5 layers of GPE. Figures 7.13 and 7.14 present the same data for initial fully printed cells with 3 layers of GPE. All cells were cycled for 200 cycles or until failure.

Figure 7.15 presents a fully printed cell prior to encapsulation in a coin cell. Figure 7.16 presents cross sections of initial fully printed cells with 5 layers and 3 layers of GPE respectively.

Similar to half printed cells, fully printed cells were free-standing and monolithic structures in which both electrodes were structurally supported by the GPE. Examination of the cross sections again shows good adhesion between both electrode-electrolyte interfaces, and cell layers were unable to be separated from each other. After cycling, no delamination or separation between layers was observed. Printed GPE thickness was about 160μm for cells with 5 layers of GPE and 65μm for cells with 3 layers of GPE. Interestingly, both cells showed similar overall thicknesses of about 275μm. Printed Zn anode thickness was about 85μm, and the corresponding mass for a 1cm^2 electrode is therefore roughly 0.035g, leading to an maximum capacity of 28.70mAh.

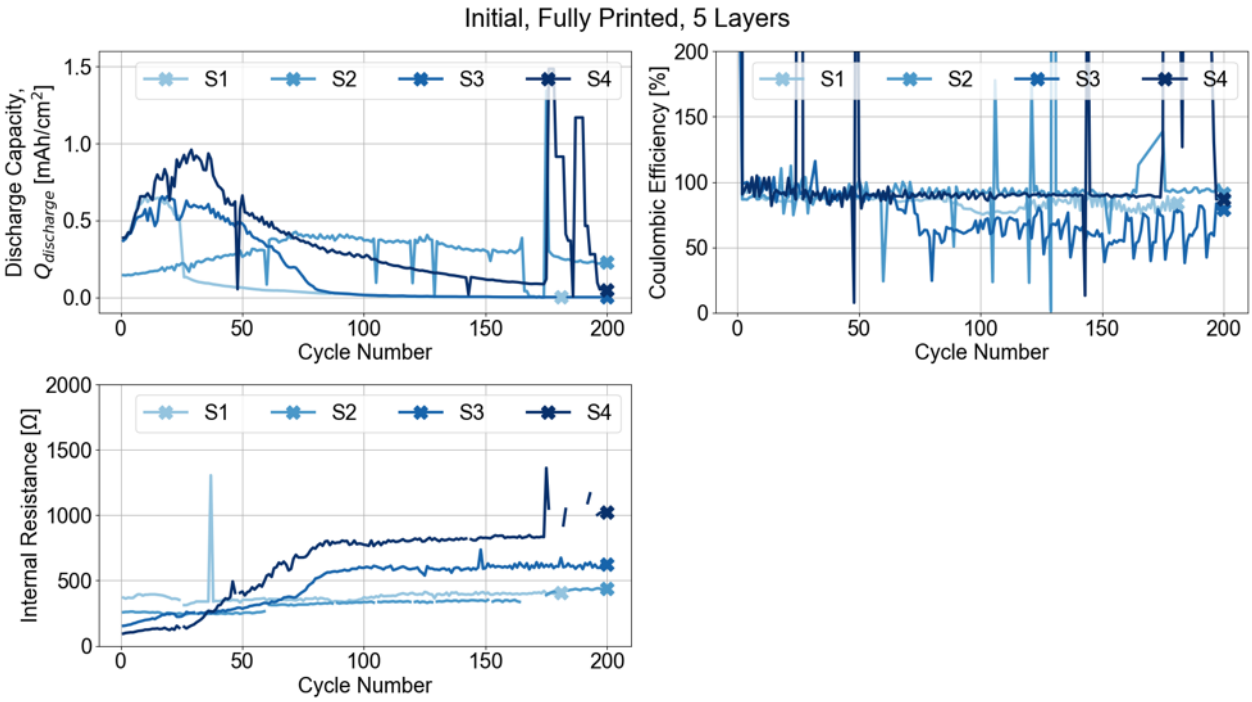

Figure 7.11: Discharge capacity, coulombic efficiency, and internal resistance of initial fully printed cells with 5 layers of GPE.

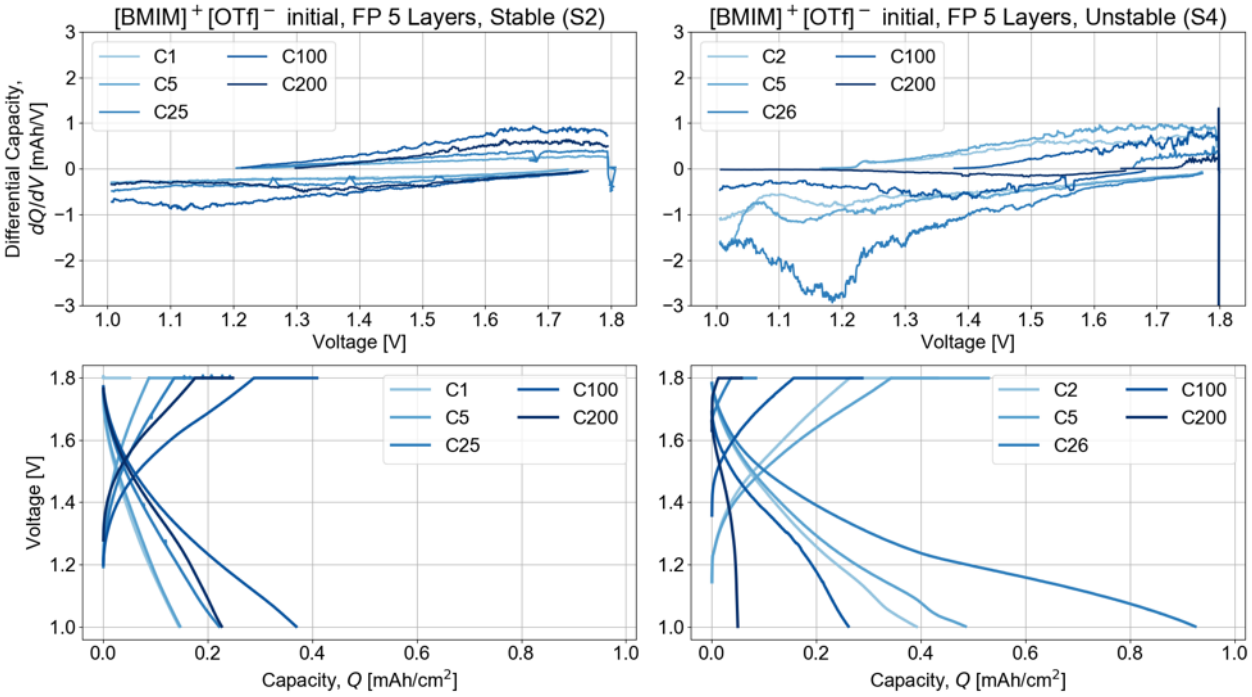

Figure 7.12: Differential capacity and voltage profile for stable and unstable initial fully printed cells with 5 layers of GPE. Note different scales and ranges for differential capacity.

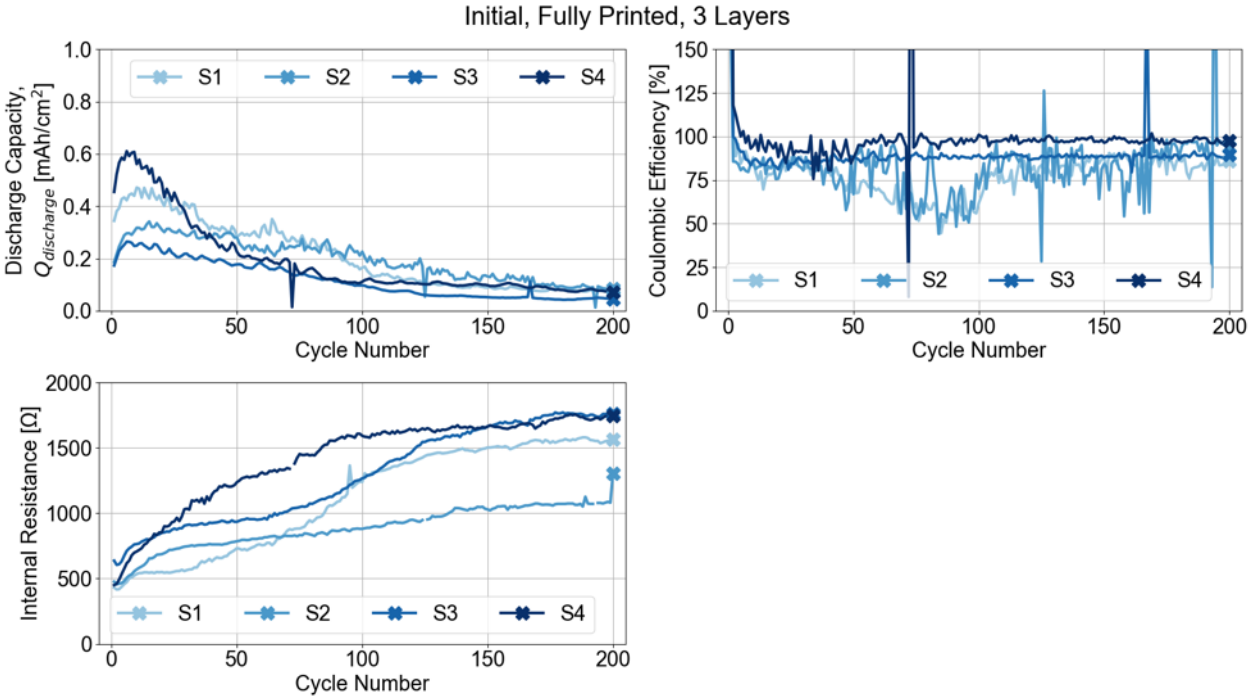

Figure 7.13: Discharge capacity, coulombic efficiency, and internal resistance of initial fully printed cells with 3 layers of GPE.

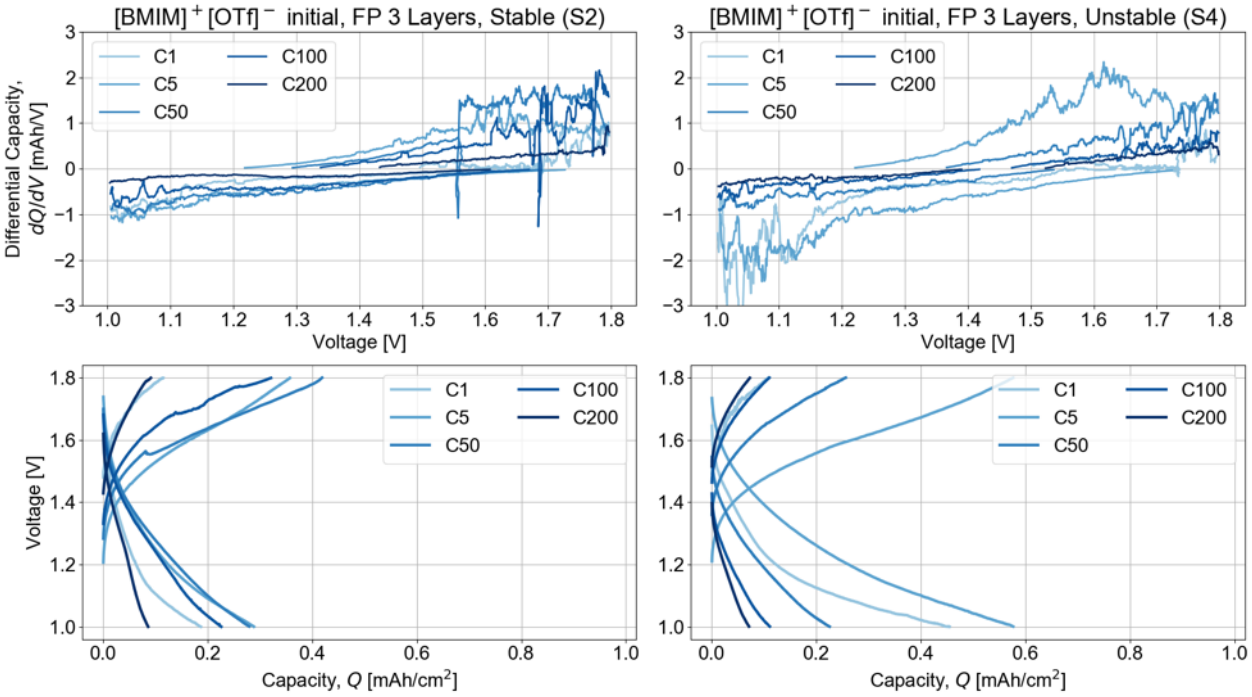

Figure 7.14: Differential capacity and voltage profile for stable and unstable initial fully printed cells with 3 layers of GPE.

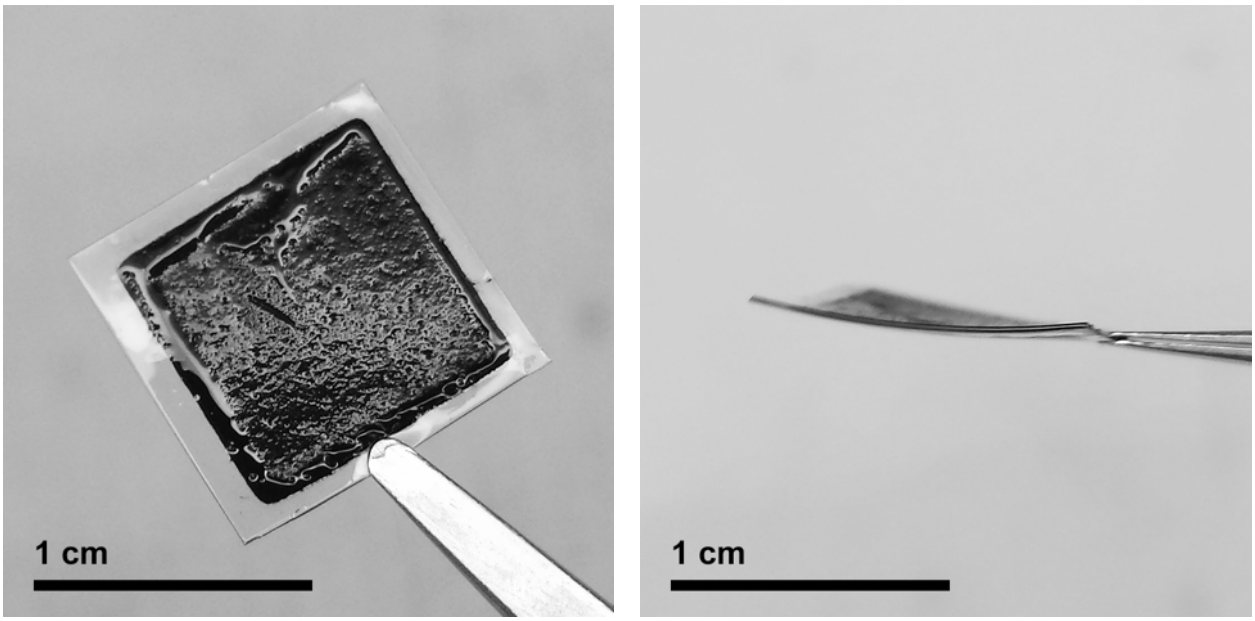

Figure 7.15: Front (*left*) and side (*right*) views of fully printed cell. From front to back, layers of the fully printed cell are MnO_2 cathode, GPE, Zn anode. Tweezers are holding the GPE.

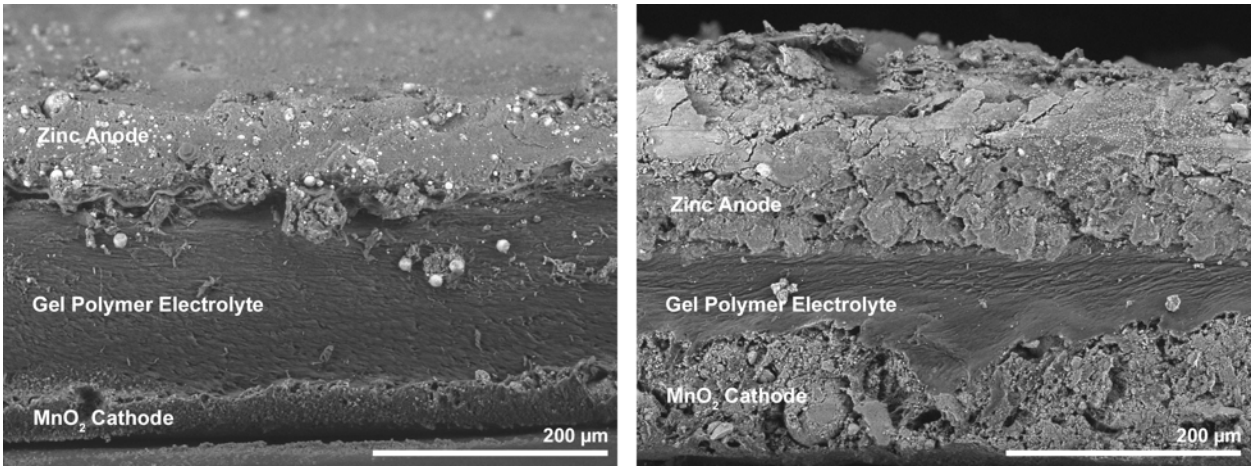

Figure 7.16: SEMs of initial fully printed cells with 5 layers (*left*) and 3 layers (*right*) of GPE.

A significant improvement in nominal cycle life is observed upon printing the anode with most cells cycling for 200 cycles, compared to an average cycle life of less than 20 cycles with mechanically assembled cells. However, discharge capacities are lower compared to mechanically assembled and half printed cells. Unlike with cells with Zn foil anodes, discharge capacity did not begin at its maximum and decline with further cycling. Instead,

discharge capacity increased for the first 10-20 cycles, after which a maximum was reached and capacity began to decrease. This maximum capacity was also achieved in fewer cycles for cells with 3 layers of GPE. While best performing cells with 5 layers and 3 layers showed maximum capacities of 0.95mAh/cm^2 (34.5mAh/cm^3) and 0.6mAh/cm^2 (21.8mAh/cm^3) respectively,capacities decreased throughout cycling to values close to 0.05-0.1mAh/cm^2 (1.8-3.6mAh/cm^3), corresponding to 0.17-0.35% of theoretical maximum. However, lower capacities are not unexpected even with comparable masses of Zn due to the addition of polymer binder and conductive additive hindering Zn accessibility.

This initial capacity increase is likely due to initially increasing availability of cycleable Zn due to the composite nature of the printed anode. As cycling initiates and Zn undergoes deposition and dissolution, conductive pathways likely form within the anode matrix that allow for accessibility of Zn particles further from the anode-electrolyte interface. However, loss of cycleable Zn likely persists throughout the entirety of cycling due to side reactions, loss of electrical connection, or other factors, and capacity eventually fades as observed with other cells.

More variation was observed in coulombic efficiency with some cells being significantly lower than unity and ranging from 50-80%. Internal resistances were also higher compared to cells with Zn foil anodes, likely due to the increased resistance added by the printed Zn anode. Cells with 5 layers of GPE exhibited initial internal resistances from 100-400Ω which then increased to 400-800Ω by Cycle 80. Cells with 3 layers of GPE showed higher internal resistances which started at 450-600Ω and increased to 1150-1800Ω by the end of cycling. The increased variability in internal resistance reflects the more complex manufacturing process involved with fully printed cells compared to mechanically assembled and half printed cells.

Catastrophic failure as observed with mechanically assembled cells and half printed cells was not observed with all tested fully printed cells, suggesting that use of the Zn foil anode contributes to the observed failure mechanism. The use of the composite printed Zn anode may decrease overall accessible Zn, thus reducing the amount of Zn deposited within the GPE, but the thinner GPEs for fully printed cells may play a more significant role in reducing tortuosity and the effective ion diffusion distance. Regardless, elimination of catastrophic failure allows for investigation of other degradation mechanisms that were overshadowed by earlier complete cell failure.

For cells with 5 layers of GPE, discharge capacities for two cells (S1 and S3) decreased to almost zero by cycle 80. This coincided with a decrease in coulombic efficiency and an increase in internal resistance for cell S1. The drop in discharge capacity is likely caused by a depletion of cycleable Zn, possibly due to deposition within the GPE. This is supported by the absence of precipitous drops in discharge capacity in cells with 3 layers of GPE, which would provide a shorter distance for Zn^{2+} diffusion between electrodes.

Differential capacity responses further support the loss of cycleable Zn. The magnitude of differential capacity follows capacity, with high discharge capacity cycles reflecting defined peaks and high plateaus in differential capacity. However, responses gradually declined to flat responses as cycling continued and capacity fades, particularly for cells with 3 layers of GPE. The absence of peaks and lower responses reflects a fewer number of redox reactions

with continued cycling until a minimum but stable amount of cycleable Zn remains. This likely coincides with progression from Mn^{4+} reduction from one oxidation state to another as irreversible phase changes progress and alter the crystal structure. This is supported by lower magnitude responses and the shift of the center of the broad peaks during charging to more positive potentials as cycling progresses.

From these initial results, fully printed cells eliminates catastrophic cell failure that prevents long cycle life testing, but at the expense of higher internal resistances and lower discharge capacities. Catastrophic failure is likely mitigated by use of the thinner printed GPE and printed anode, preventing delamination between layers and reducing Zn deposition within the GPE.

7.4.2 Final Cells

This section presents results obtained with final printed cells. The goal of these final cells was to print the thinnest possible layer of GPE in order to improve cell energy density and to improve overall cell performance as measured by discharge capacity, cycle life, and internal resistance. Cells utilized improvements and optimizations in electrode profilometry, rheology, and conductivity and in GPE composition as described in earlier chapters.

7.4.2.1 Half Printed Cells

Figures 7.17 and 7.18 present discharge capacity, coulombic efficiency, and internal resistance per cycle for half printed cells with $0.2m$ $[BMIM]^+[OTf]^-$ and $0.3m$ $[EMIM]^+[OTf]^-$ GPEs respectively. The cathode slurry was optimized for profilometry but had not yet been optimized for conductivity following the reduction in particle size. Cells were galvanostatically cycled from 1.0-1.8V at 125μm for both charge and discharge. A rest period was not included, so internal resistance was determined upon beginning discharge.

While cycling behavior itself is stable, this is due to extremely high internal resistances (on the order of MΩ) as a result of the printed cathode. In the process of optimizing for profilometry, the average particle size of nonconductive MnO_2 was decreased, increasing the number of contacts between MnO_2 particles and preventing the formation of long-range conductive pathways by added acetylene black. Therefore, resulting discharge capacities are 2 orders of magnitude lower than expected for $[BMIM]^+[OTf]^-$ GPEs and 3 orders of magnitude lower for $[EMIM]^+[OTf]^-$. The amount of charge measured per cycle is thus likely primarily a result of electric double layer capacitance rather than faradaic processes.

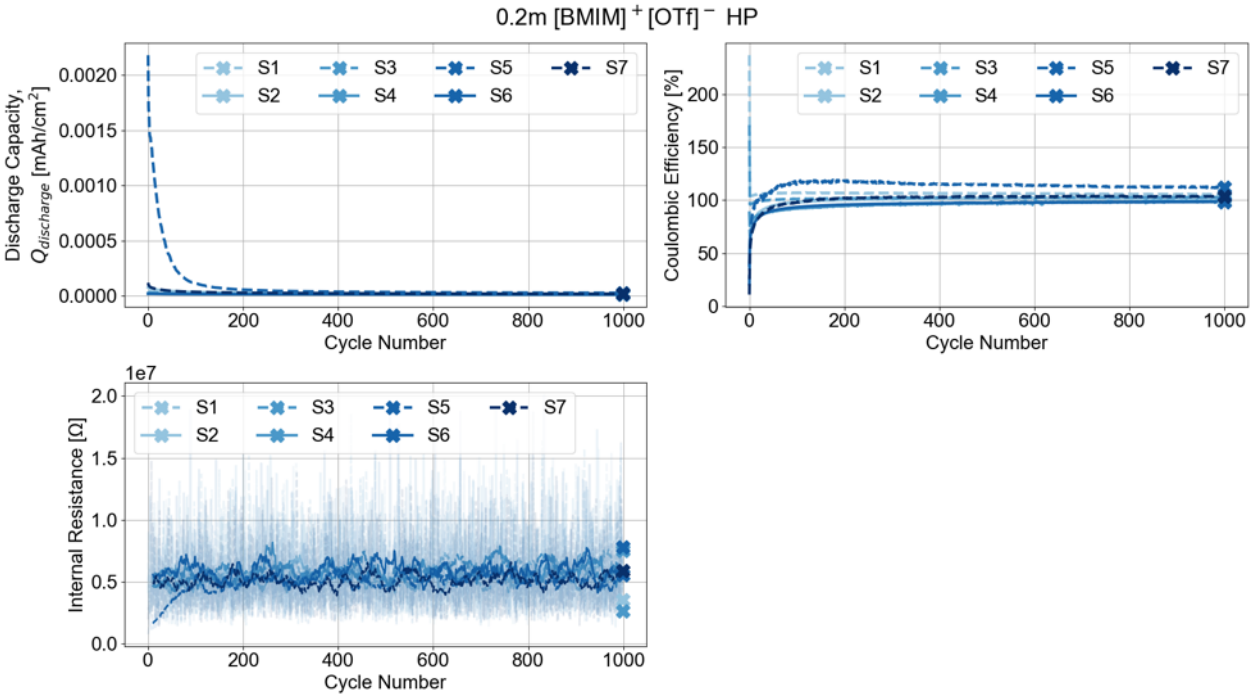

Figure 7.17: Discharge capacity, coulombic efficiency, and DC internal resistance per cycle for half printed cells with $0.2m$ $[BMIM]^+[OTf]^-$ GPEs, dried in ambient.

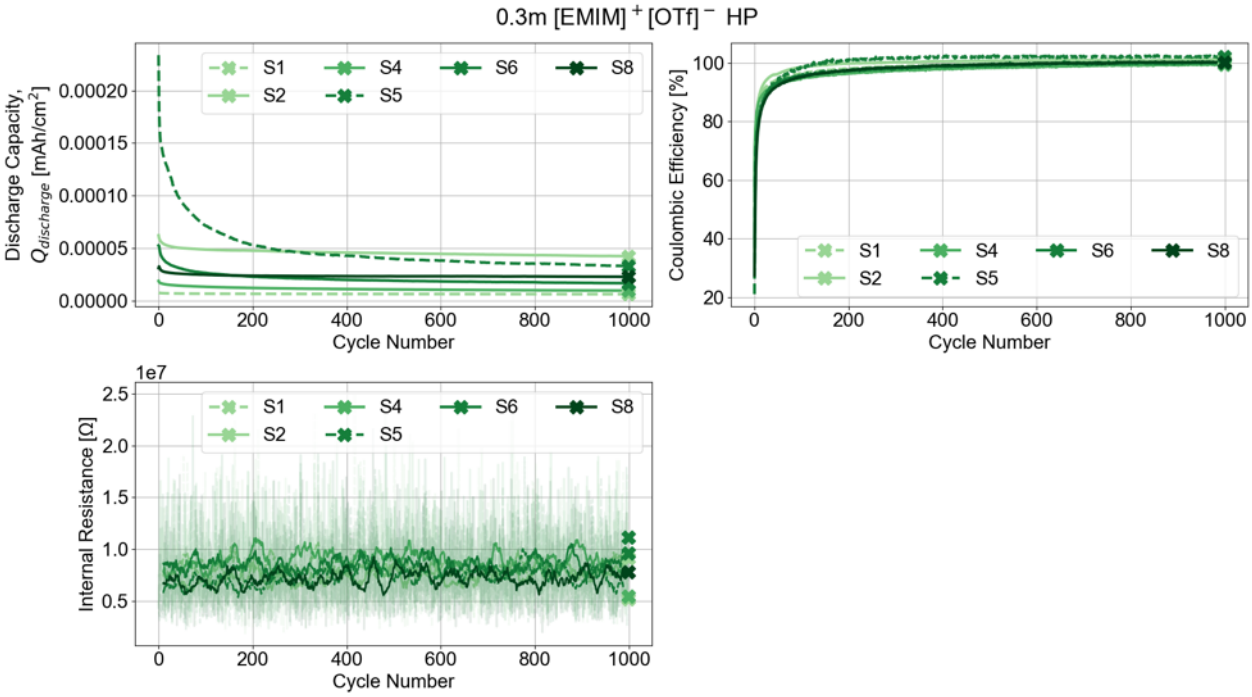

Figure 7.18: Discharge capacity, coulombic efficiency, and DC internal resistance per cycle for half printed cells with $0.3m$ $[EMIM]^+[OTf]^-$ GPEs, dried in ambient.

7.4.2.2 Fully Printed Cells, 2 Layers

Figure 7.19 presents discharge capacity, coulombic efficiency, and DC internal resistance for fully printed cells with 2 layers of $0.3m$ $[BMIM]^+[OTf]^-$ GPE. Figure 7.20 presents differential capacity for the same batch of cells. Figure 7.21 presents a cross section SEM of a representative cell. Cells were cycled for up to 200 cycles or until failure.

Cycling performance was poor for most cells. Of the cells that did successfully cycle, most failed by cycle 25, and only one cell cycled successfully for 200 cycles. For this cell, discharge capacity was inconsistent but settled towards $0.12mAh/cm^2$ ($4.4mAh/cm^3$). Internal resistances for cells during cycling ranged from 300-750Ω. For cells that failed early, coulombic efficiency remained close to zero, but the cell that successfully cycled generally returned to coulombic efficiency close to unity. From the SEM, GPE thickness was about 45μm and total cell thickness was 200μm.

While examination of the SEM cross section reveals a smooth and uniform cathode-electrolyte interface owing to the profile optimizing performed on the cathode ink, two discrete layers can be observed within the GPE. A denser layer can be observed immediately adjacent to the cathode layer. This layer is likely the result of rapid solvent evaporation of the first layer of electrolyte deposited and likely contributes significant impedance to ion transport to and from the cathode. In addition, the thinner GPE layer combined with the reduced amount of polymer in the cathode may result in volumetric expansion overcoming structural benefits afforded by the printed GPE. Because the printed GPE relies on excess solvent from subsequent layers partially dissolving already deposited layers, more strict process control is required when depositing only 2 layers.

Differential capacity shows responses similar to those seen for initial fully printed cells for cell S6 and mechanically assembled cells for S3. The stable cell (S6) again showed very flat differential capacity responses coinciding with steadily declining capacity before cycle 100. However, the unstable cell (S3) showed more catastrophic behavior than observed previously. The potential upon charging during the final cycle achieved a maximum of 1.65V, after which the potential periodically dropped to 0.1V. This behavior is very likely induced by the formation of conductive pathways bridging the two electrodes as Zn is redeposited through the GPE. The reduced thickness of the GPE compared to initial cells makes this a much more likely occurence, resulting in the observed voltage profile and differential capacity response. The periodic increase of the potential to 1.5-1.6V is due to the battery tester engaging and disabling current based on measured potentials exceeding cell safety limits.

In order to improve cell cycle life, subsequent cells were printed with additional layers of GPE.

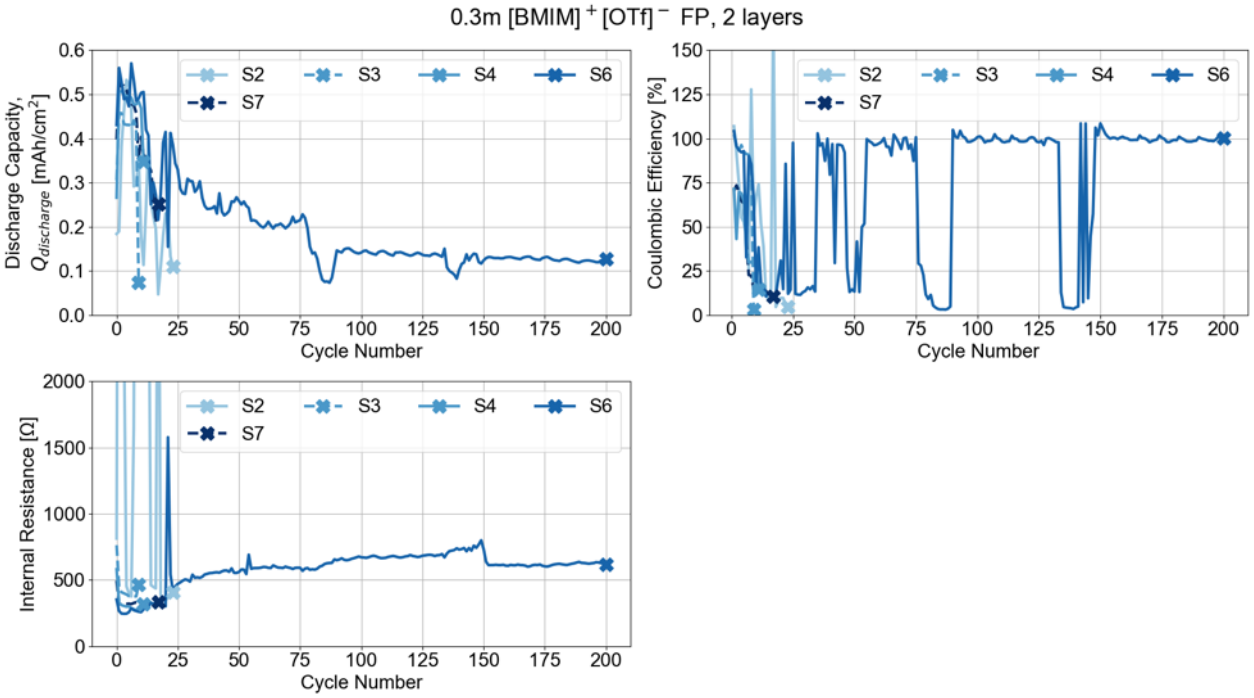

Figure 7.19: Discharge capacity, coulombic efficiency, and DC internal resistance per cycle for fully printed cells with 0.3m [BMIM]$^+$[OTf]$^-$ GPEs with 2 layers, dried in ambient.

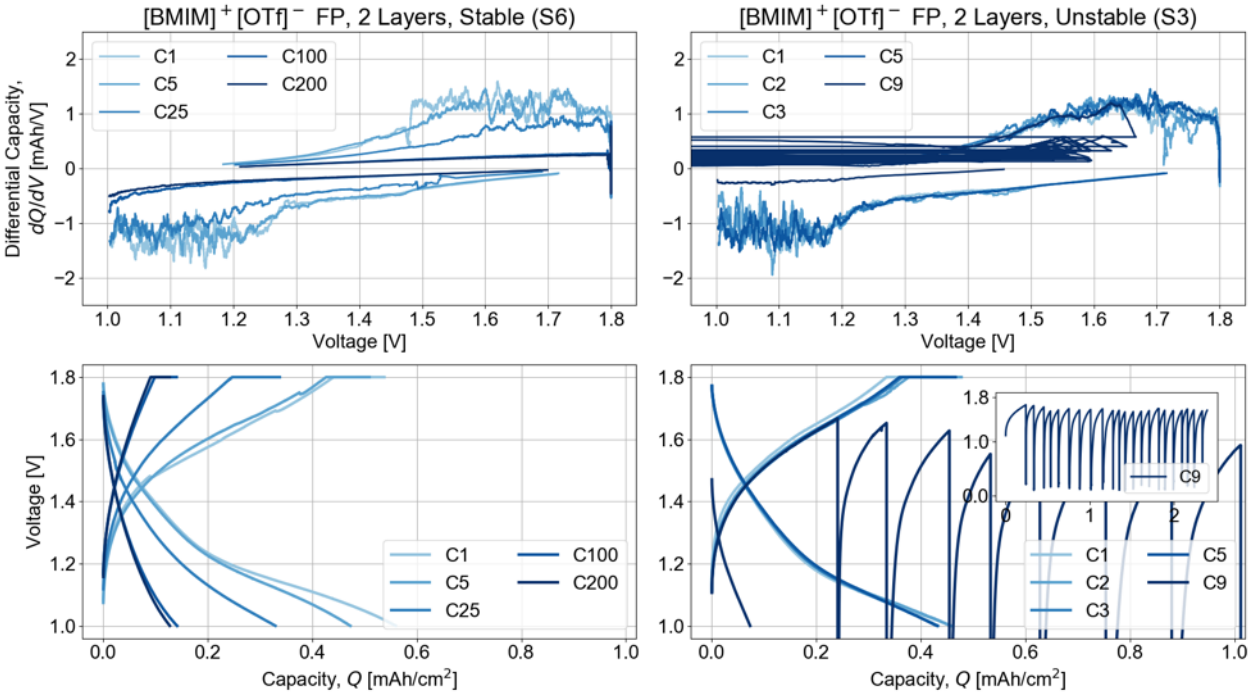

Figure 7.20: Differential capacity and charge/discharge voltages of most and least stable cells for fully printed cells with 0.3m [BMIM]$^+$[OTf]$^-$ GPEs with 2 layers, dried in ambient.

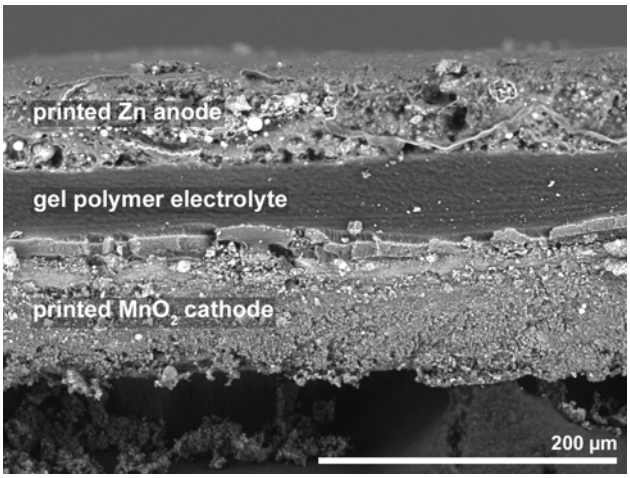

Figure 7.21: SEM cross section of fully printed cell with 2 layers of $0.3m$ $[BMIM]^+[OTf]^-$ GPE.

7.4.2.3 Fully Printed Cells, 3 and 4 Layers

GPEs were printed with 3 or 4 layers in order to determine the optimal thickness of GPE while preventing low cycle life. GPEs tested were $0.2m$ $[BMIM]^+[OTf]^-$, $0.3m$ $[BMIM]^+[OTf]^-$, and $0.3m$ $[EMIM]^+[OTf]^-$. These combinations of layers and electrolytes were chosen to try to identify the best combination for overall cell performance. For all batches of cells, discharge capacity, coulombic efficiency, and internal resistance per cycle and differential capacity and voltage profiles are plotted. The combinations of layers and GPEs tested and their corresponding figures are as follows:

1. $0.2m$ $[BMIM]^+[OTf]^-$, 3 layers, Figures 7.22 and 7.23,
2. $0.2m$ $[BMIM]^+[OTf]^-$, 4 layers, Figures 7.24 and 7.25,
3. $0.3m$ $[BMIM]^+[OTf]^-$, 4 layers, Figures 7.26 and 7.27,
4. $0.3m$ $[EMIM]^+[OTf]^-$, 4 layers, Figures 7.28 and 7.29,

Figure 7.30 presents cross section SEMs of representative cells for all combinations of layers and GPE. Measured GPE thickness for each cell is presented in Table 7.8. It was observed that the anode side of the cells were difficult to remove from its adjacent stainless steel spacer, so a razor was used to scrape off the cell while preserving as much of the anode as possible. However, partial loss of the anode layer was unavoidable for the cell with 4 layers of $0.3m$ $[BMIM]^+[OTf]^-$ (cell C in Figure 7.30).

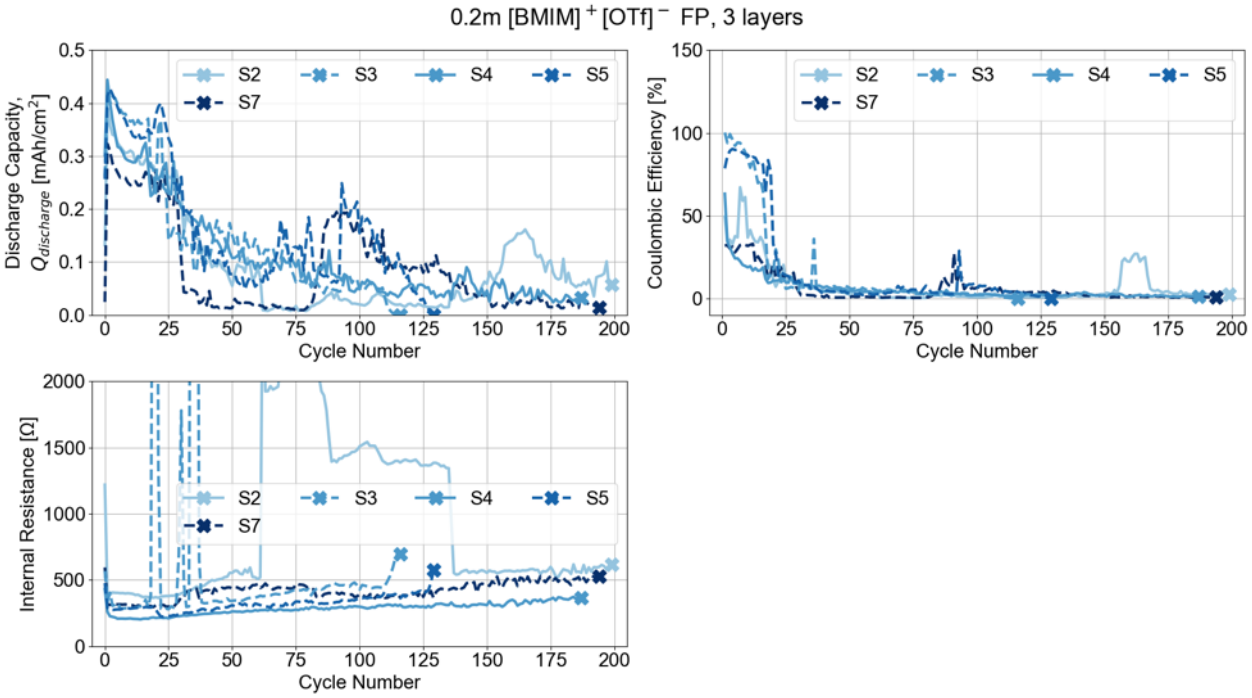

Figure 7.22: Discharge capacity, coulombic efficiency, and DC internal resistance per cycle for fully printed cells with 0.2m $[BMIM]^+[OTf]^-$ GPEs with 3 layers, dried in ambient.

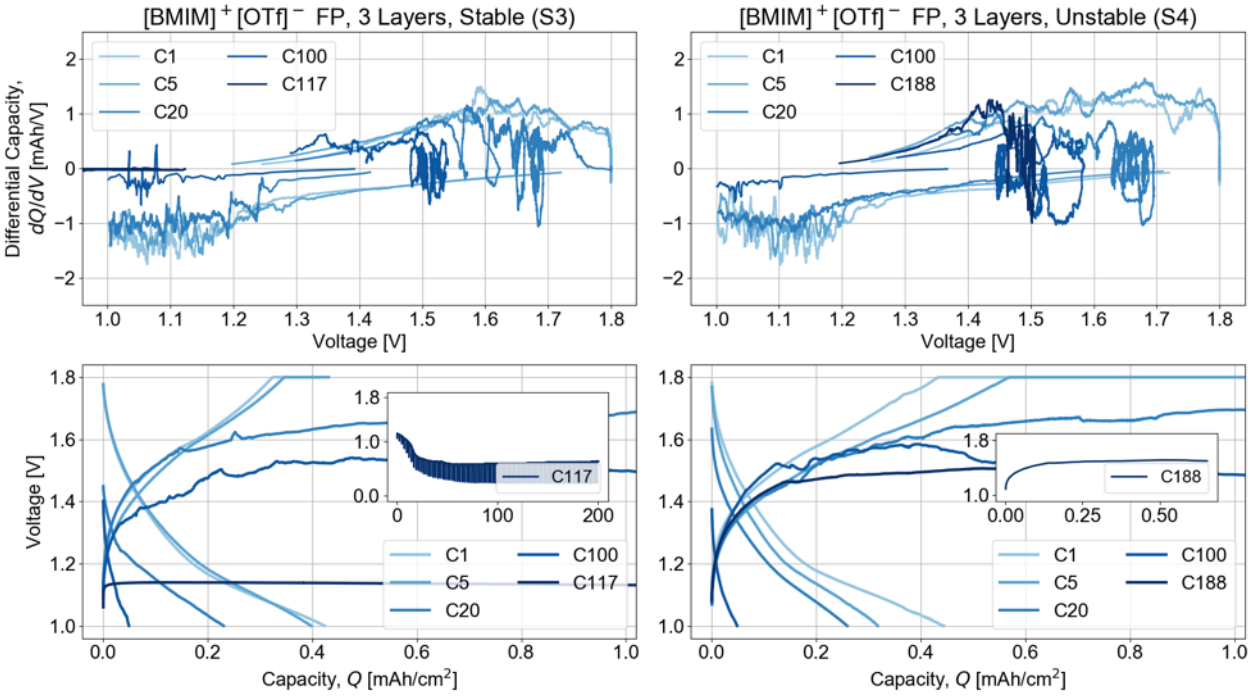

Figure 7.23: Differential capacity and charge/discharge voltages of most and least stable cells for fully printed cells with 0.2m $[BMIM]^+[OTf]^-$ GPEs with 3 layers, dried in ambient.

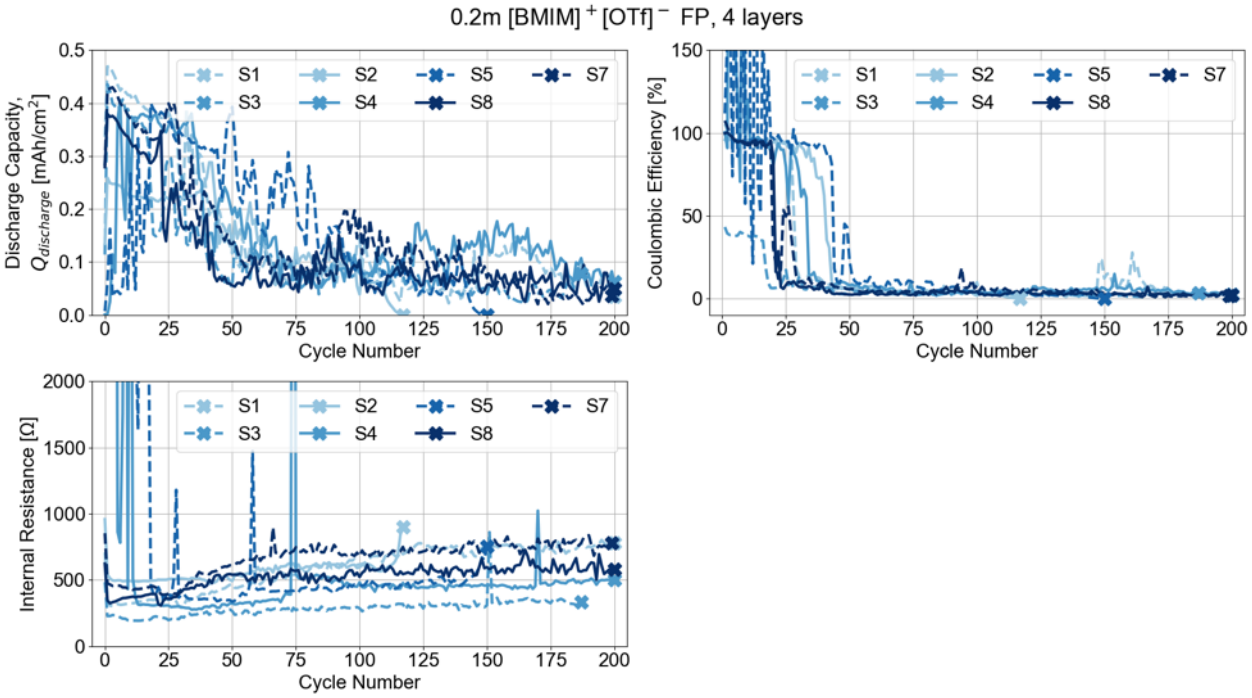

Figure 7.24: Discharge capacity, coulombic efficiency, and DC internal resistance per cycle for fully printed cells with 0.2 m $[BMIM]^+[OTf]^-$ GPEs with 4 layers, dried in ambient.

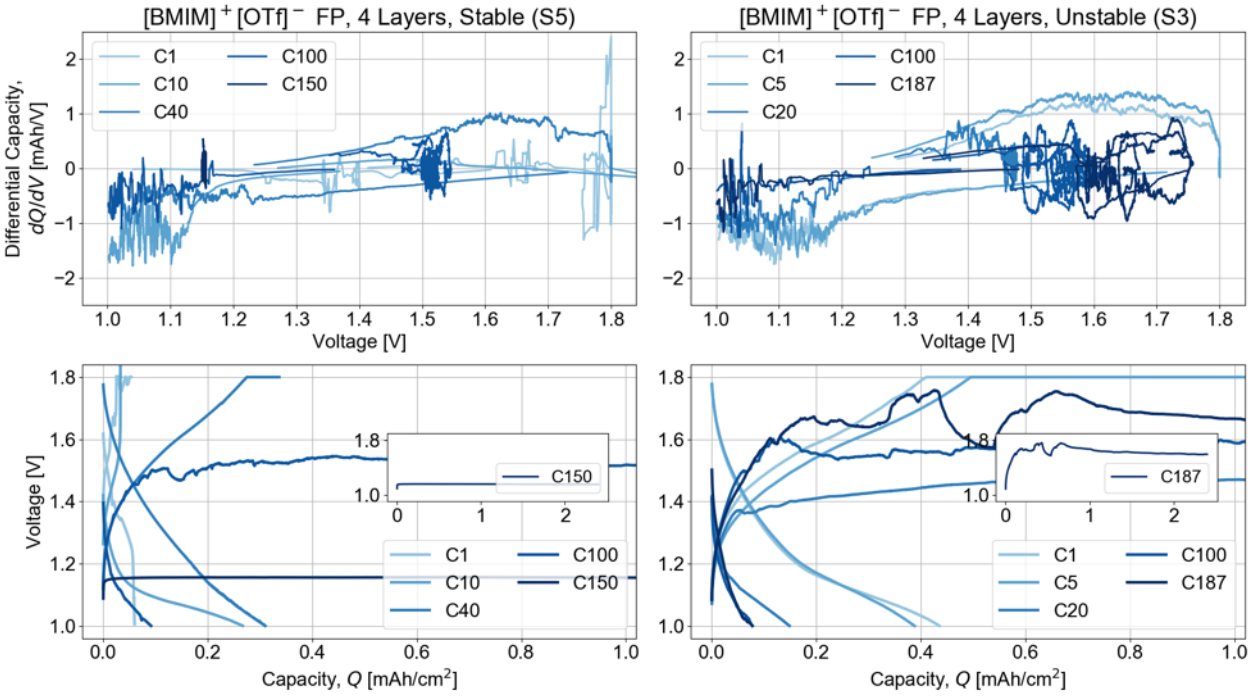

Figure 7.25: Differential capacity and charge/discharge voltages of most and least stable cells for fully printed cells with 0.2m $[BMIM]^+[OTf]^-$ GPEs with 4 layers, dried in ambient.

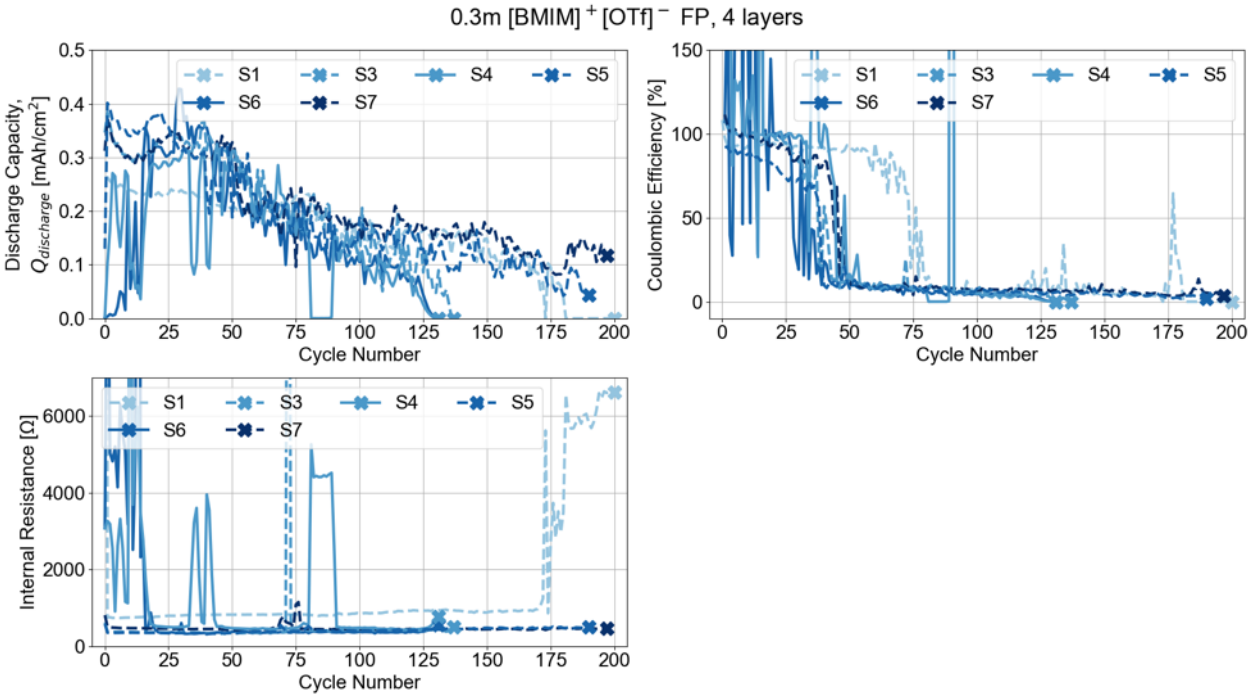

Figure 7.26: Discharge capacity, coulombic efficiency, and DC internal resistance per cycle for fully printed cells with 0.3m [BMIM]$^+$[OTf]$^-$ GPEs with 4 layers, dried in ambient.

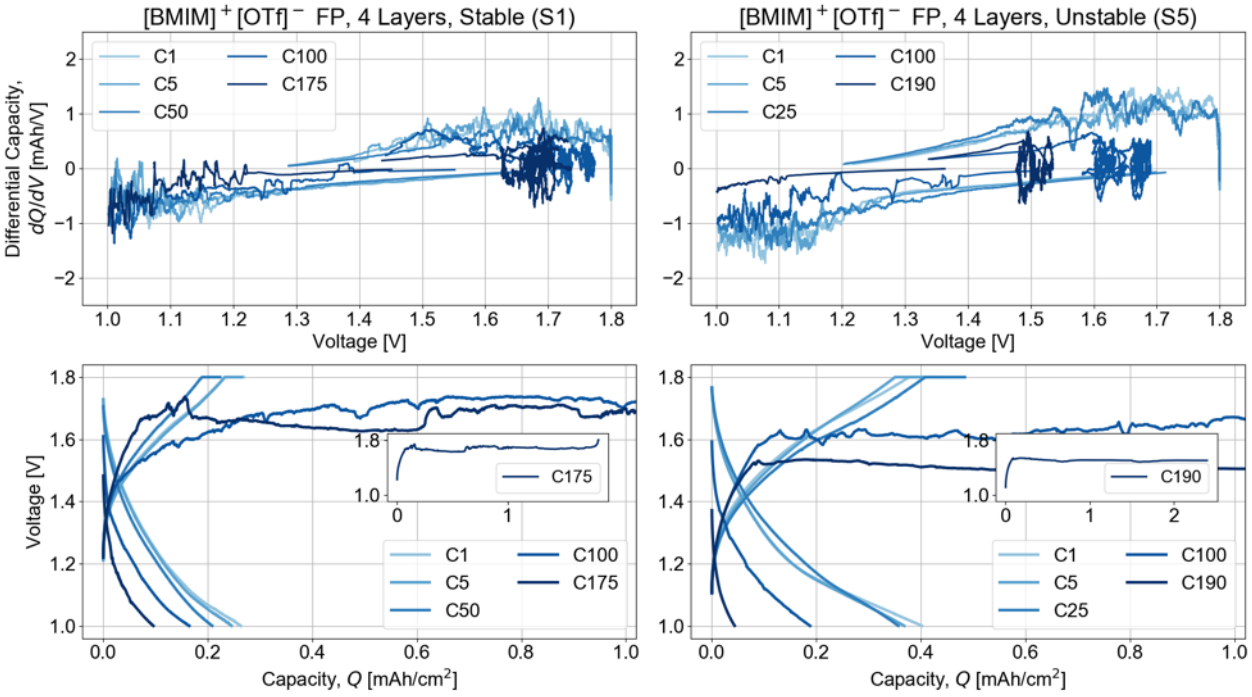

Figure 7.27: Differential capacity and charge/discharge voltages of most and least stable cells for fully printed cells with 0.3m [BMIM]$^+$[OTf]$^-$ GPEs with 4 layers, dried in ambient.

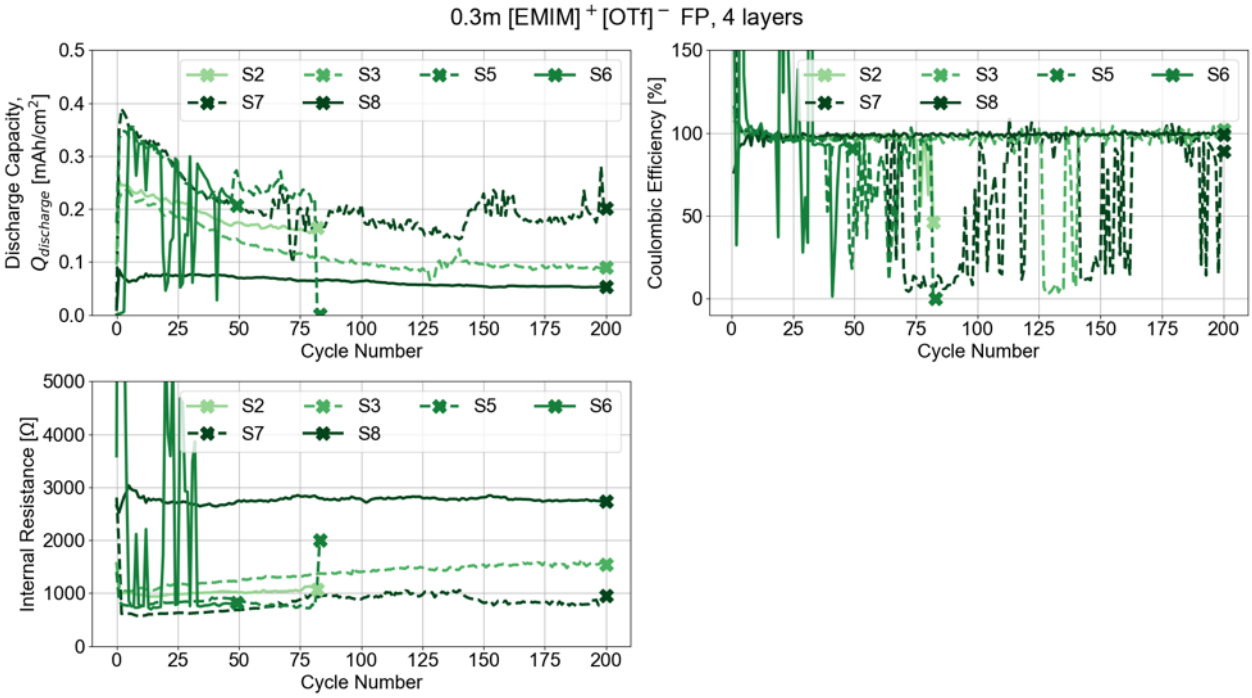

Figure 7.28: Discharge capacity, coulombic efficiency, and DC internal resistance per cycle for fully printed cells with 0.3m [EMIM]$^+$[OTf]$^-$ GPEs with 4 layers, dried in ambient.

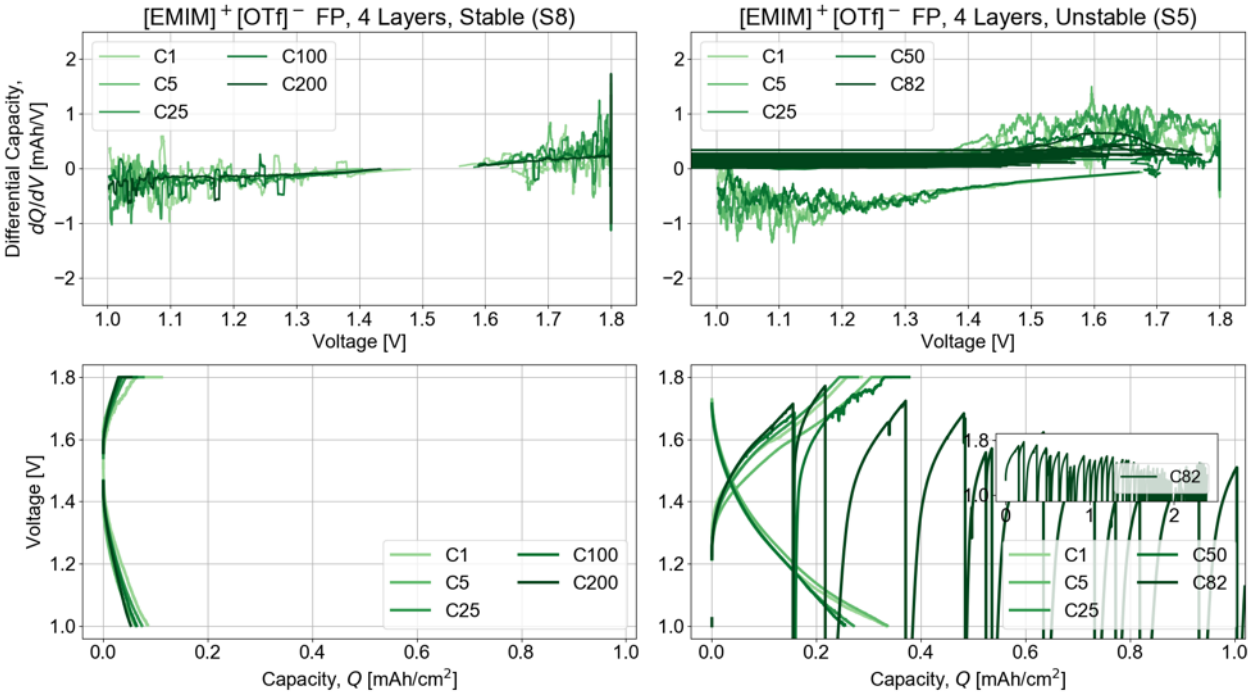

Figure 7.29: Differential capacity and charge/discharge voltages of most and least stable cells for fully printed cells with 0.3m [EMIM]$^+$[OTf]$^-$ GPEs with 4 layers, dried in ambient.

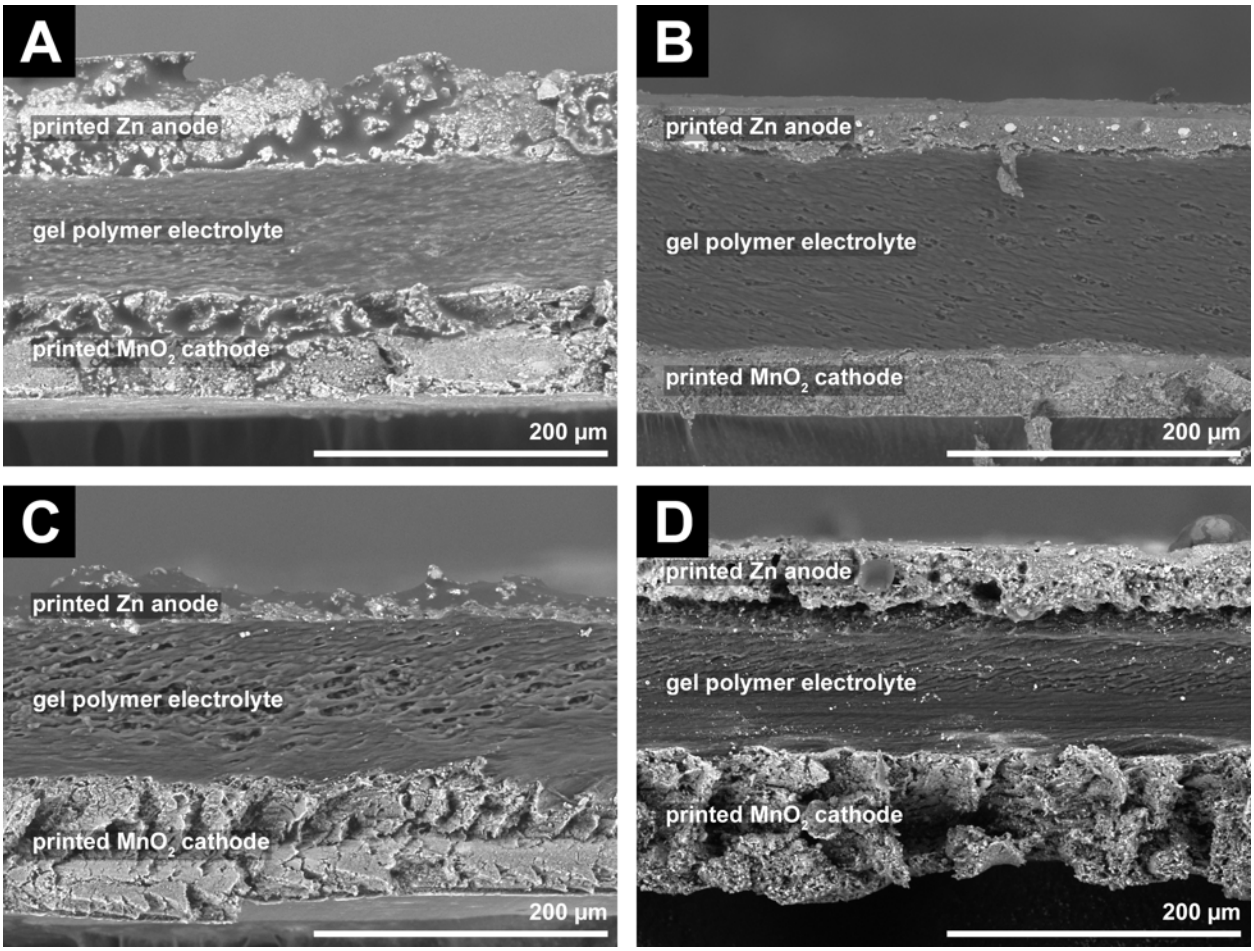

Figure 7.30: SEM cross sections of fully printed cell with 3 and 4 layers of GPE. *A*: 0.2m $[BMIM]^+[OTf]^-$, 3 layers; *B*: 0.2m $[BMIM]^+[OTf]^-$, 4 layers; *C*: 0.3m $[BMIM]^+[OTf]^-$, 4 layers; *D*: 0.3m $[EMIM]^+[OTf]^-$, 4 layers.

Despite careful control of manufacturing and automation of doctor blade coating, GPE thickness were not uniform between batches of cells where 4 layers were printed. GPE thickness for $[BMIM]^+[OTf]^-$ cells with 4 layers were actually 110μm and 130μm. GPE thickness for $[EMIM]^+[OTf]^-$ with 4 layers of GPE was equal to GPE thickness for $[BMIM]^+[OTf]^-$ with 3 layers (90μm). As discussed later, this actual GPE thickness significantly affects cell cycle life. However, adhesion between layers is excellent, and the cathode profile is significantly more uniform than with initial cells made without ink optimized for profilometry. Total cell thickness was about 225μm for all cells.

The SEM cross section for the cell with 0.3m $[EMIM]^+[OTf]^-$ shows bright particles within the GPE. While these may be Zn deposits resulting from cycling and deposition within the GPE, the possibility also exists that Zn particles were carried with the razor

Table 7.8: Final printed GPE thickness

Cell	**Thickness [μm]**
$0.2m$ $[BMIM]^+[OTf]^-$ 3 layers	90μm
$0.2m$ $[BMIM]^+[OTf]^-$ 4 layers	130μm
$0.3m$ $[BMIM]^+[OTf]^-$ 4 layers	110μm
$0.3m$ $[EMIM]^+[OTf]^-$ 4 layers	90μm

blade during the sample preparation process. However, the absence of similar particles with the other cross sections suggests this is unique to this cell alone, which would support the possibility of loss of cycleable Zin due to deposition within the GPE.

Due to the charging protocol used for combined galvanostatic and potentiostatic charging, cells were allowed to continue cycling longer than initial cells. If the specified potential and current limits were unable to be achieved, the testing protocol set a time limit of 24 hours before moving on to the next step. Thus, some cells failed earlier during cycling yet were allowed to continue.

In general, these final fully printed cells did not perform as well as prior batches of cells. While some cells per batch cycled for or close to 200 cycles, cells generally did not exhibit stable discharge capacities for the duration of cycling. Comparing discharge capacities, cells with $0.3m$ $[BMIM]^+[OTf]^-$ and $0.3m$ $[EMIM]^+[OTf]^-$ showed the best average performance with stable discharge capacities of 0.1-0.2mAh/cm^2 (4.4-8.9mAh/cm^3) and 0.08-0.2mAh/cm^2 (3.5-8.9mAh/cm^3) respectively. Cycle life improved with GPE thickness with cells lasting for up to 20, 40, and 75 cycles before failure for $[BMIM]^+[OTf]^-$ cells with 90, 130, and 110μm GPEs respectively. Of note is that $0.3m$ $[BMIM]^+[OTf]^-$ cells generally cycled for longer than $0.2m$ $[BMIM]^+[OTf]^-$ despite a thinner GPE, suggesting higher concentration electrolyte improves resistance to cell failure. This would be consistent with the possibility of insufficient Zn^{2+} contributing to cell failure as higher concentration electrolytes would contribute more Zn^{2+} ions.

Variation in internal resistance was observed to follow ionic liquid type, rather than salt concentration or GPE thickness. Cells with $[BMIM]^+[OTf]^-$ showed stable internal resistances ranging from 250-800Ω, with median resistances of 500Ω. Cells with $[EMIM]^+[OTf]^-$ showed a higher and wider range of internal resistance, ranging from 900-2800Ω. Like initial cells, most cells showed a sharp decrease in internal resistance during the first cycles, after which resistance generally increased and aligned with changes in discharge capacity.

Coulombic efficiency also followed ionic liquid type rather than other factors. Cells with $[BMIM]^+[OTf]^-$ started close to unity but quickly decreased until a precipitous decline to 10%, after which efficiency continued to decline. This precipitous drop in efficiency is caused

by similar failure mechanisms as observed with initial cells, specifically in cells unable to maintain voltages of 1.8V during charging.

Differential capacity responses provide more insight into cell failure and degradation. For cells with 90μm GPEs (0.2m $[BMIM]^+[OTf]^-$ with 3 layers and 0.3$m$$[EMIM]^+[OTf]^-$ with 4 layers), cells showed signs of electrical shorts forming through the GPE, as evidenced by potentials dropping close to zero at failure. Cells with both 0.2m $[BMIM]^+[OTf]^-$ with 4 layers and 0.3m $[BMIM]^+[OTf]^-$ with 4 layers showed similar voltage fluctuations during the potentiostatic portion of charging as seen previously. This is again likely due to loss of cycleable Zn. The formation of electrical shorts had not been previously observed and suggests there is a narrow window of GPE thicknesses that both prevents the formation of electrical shorts and miniminizes loss of cycleable Zn to deposition in the GPE. For all cells except some with $[EMIM]^+[OTf]^-$, a more stable discharging regime was not established, indicating MnO_2 phase changes resulted in catastrophic structural changes that prevented further ion insertion.

The only cell whose differential capacity was investigated that did not fail was S8 for cells with 0.3m $[EMIM]^+[OTf]^-$ GPE with 4 layers. The differential capacity response shows no significant peaks throughout the duration of cycling except for at the limits of the potential window, suggesting reduction of Mn^{4+} immediately occured within a stable phase change regime. Furthermore, there was no significant change in coulombic efficiency or internal resistance for this cell, though internal resistance was about 3 times higher than other cells within the same batch. The initially higher internal resistance may result in significant potential drops that result in more stable but shallower redox reactions.

A significant aspect of fully printed cells is their higher susceptibility to manufacturing variations. Mechanically assembled full cells made for GPE optimization in Chapter 6 showed significantly less variation within each batch, and a higher proportion of cells were able to cycle succesfully. This is likely exacerbated by manufacturing the cathode and the electrolyte separately as well as the use of a Zn foil anode. In addition, fully printed cells involved more individual processing steps, each of which increased the potential for contaminants or irregularities from sample to sample due to manual movement and alignment of the cells after printing each layer of GPE.

7.5 Conclusions

This chapter presented results from cycle life testing of Zn-MnO_2 cells. Initial cells demonstrated the viability of producing fully printed cells that showed at least 20x improvement in cycle life over mechanically assembled cells. However, average discharge capacities were lower with fully printed cells, dropping from 10.8mAh/cm^3 to 1.8-3.6mAh/cm^3, although a maximum of 34.5mAh/cm^3 was achieved for one cycle of the best performing. Final cells sought to incorporate individual component optimizations to electrode profilometry, rheology, and conductivity and GPE concentration and processing in order to decrease GPE thickness to

improve capacity density. However, cycle life performance of final cells was poorer with both lower cycle life and lower discharge capacity (4.4-8.9mAh/cm^3).

Results from this chapter confirmed that electrochemical cycle of secondary Zn-MnO_2 cells with $[BMIM]^+[OTf]^-$ or $[EMIM]^+[OTf]^-$ gel polymer electrolyte is possible. Furthermore, some reversible behavior was observed, though this typically followed a period of capacity loss and initial cell degradation.

A number of failure and degradation mechanisms are posited, for which strong evidence was identified. Structural and phase changes occur within the MnO_2 cathode as Mn^{4+} is reduced, resulting in local collapse of crystal structures or irreversible phase changes that limit or impede further Zn^{2+} intercalation. In addition, de-insertion of Zn^{2+} is likely not fully reversible, leading to loss of cycleable Zn to MnO_2 phase changes. Furthermore, stresses induced within the crystal structure during repeated cycling likely causes delamination of the printed cathode in traditionally mechanically assembled cells. Incorporation of a printed gel polymer electrolyte largely mitigates catastrophic failure modes due to electrode delamination, which leads to loss of electrical contact and loss of active material.

With the use of γ-MnO_2 as used in this work, the heterogenous tunnel structure likely leads to different phase change reactions which occur at different potentials. While the exact identity of these reactions is unclear, there is likely a more stable phase change regime that allows for significantly improved reversibility at the expense of lower discharge capacities.

Zn is likely able to deposit within the GPE separator and may form electrical shorts between the cathode and anode with insufficient GPE thickness. However, excessively thick GPE layers may also exacerbate loss of cycleable Zn as more tortuous pathways improve the likelihood of Zn deposition and loss of electrical connection. While thinner GPE layers had been posited to produce better performance, the GPE structure plays a significant role in the efficacy of the GPE layer itself in producing amenable Zn crystal structures during recharging.

One notable observation across all batches of cells is the extreme degree of variability, even between cells within the same batch. A number of factors may contribute, including ambient humidity, local asymmetries in printing speeds or pressures, thermal gradients during drying steps, and inhomogeneities within inks and slurries. However, care was taken to report a holistic view of results instead of only best performing cells per batch.

Future work should seek to further tighten process parameters affecting polymer structure as GPE morphology was observed to play a much more significant role in cell failure and degradation rates than anticipated, In addition, other charging and discharging rates and protocols should be explored as the limitations imposed on cells may have exacerbated cell degradation and failure. Finally, identification of MnO_2 phases during various depths of discharge, as well as exploration of other phases of MnO_2 with this system should be investigated.

Chapter 8

Battery Cycling for IoT Devices

This chapter presents results from pulsed current discharging of fully printed Zn-MnO_2 cells and megacycle testing via pulsed current discharge of commercial lithium-ion cells.

The goals of this work are

1. to determine typical load profile parameters for energy storage for Internet of Things (IoT) devices,
2. to characterize fully printed Zn-MnO_2 cells via pulsed current discharging, and
3. to characterize longevity and long-term cycling of commercial lithium-ion cells under conditions required for Internet of Things applictions.

Section 8.1 presents the motivation for investigating pulsed current discharging on fully printed and commercial lithium-ion cells. Section 8.2 presents information on radio power demands and battery performance consideratons for use in IoT devices. Section 8.3 presents the cycling parameters used for this work. Section 8.4 presents the findings from pulsed current discharge of fully printed cells and characterization and megacycle pulsed current discharge cycling of lithium-ion cells. Finally, Section 8.5 discusses conclusions and future work.

8.1 Motivation

As the applications for Internet of Things devices grow, the power consumption behaviors for these devices must also be considered. Small, low cost devices with bespoke geometries and applications may serve as a niche but important application for the fully printed Zn-MnO_2 cells presented in this work. In addition, for devices such as sensors, a low duty cycle but high power current pulse is typically required for data transmission while current demands are low otherwise. The long term effect of such a regime on onboard energy storage such as a battery has yet to be investigated over the time scale that such a sensor would be expected to operate without maintenance (2-3 years).

8.2 Background

This section discusses applications and power demands for devices for the Internet of Things. The effect pulsed current discharge loads on electrochemical energy storage systems and the resulting design considerations are also discussed.

8.2.1 Wireless Sensor Networks and the Internet of Things

Over the last twenty years, the concept of wireless sensor networks (WSN), also dubbed the Internet of Things (IoT) has been proposed and developed as a method to link communications and computation to the physical world with myriad applications. These include manufacturing, supply chain, medicine, agriculture, environmental monitoring, power systems, and defense [**Pottie:1998w**, 6, 35]. The value proposition of development of these systems is the ability to reduce waste, loss, and cost by economic and automous monitoring of real-world systems.

While a large portion of research directions for IoT focus on network infrastructure, device security, and communcations protocols, the energy demands of these devices must also be considered in order to realize this vision [91, 79]. Specifically, the peak power demands of devices during operation as well as their expected operating lifetimes must consider the lifetimes of any onboard energy storage devices as well as consideration of recharging via energy harvesting or energy scavenging devices [101].

8.2.2 Intermittent Duty Cycles for Radios

Devices for the Internet of Things largely rely on wireless communcation via radios in order transmit and receive data. The power demands of radios and other sensors are unique in that their duty cycles are characterized by periods of low current when inactive or in sleep mode and short pulses of high current when transmitting or receiving data [108, 42]. The magnitudes of these current pulses can vary between radios and thus play another design consideration in designing IoT devices. Table 8.1 presents transmission frequency, transmit and receive currents and powers, and voltage ranges for commercially available radios for use with wireless sensor and Internet of Things applications. Radio powers and sensitivities are presented in units of dBm (decibel-milliwatts). A value in dBm, x, can be converted to a value in mW, P, and vice versa via Equations 8.1 and 8.2.

$$x = 10 \log_{10} \frac{P}{1\text{mW}} \tag{8.1}$$

$$P = 1\text{mW} \cdot 10^{\frac{x}{10}} \tag{8.2}$$

Transmit and receive currents vary significantly from radio to radio but all fall within a range of 2.5-20mA. Sleep currents are not shown, but these typically range from 0.1-1mA depending on the device. Figure 8.1 presents an example of an expected load profile for a

Table 8.1: Transmission frequency, transmit and receive currents and powers, and voltage ranges for commercially available radios for wireless sensor applications (reproduced with permission from Bala Thoravi-Kumarel).

Name (Brand)	**Freq [MHz]**	**TX Current [mA]**	**TX Power [dBm]**	**RX Current [mA]**	**RX Sensitivity [dBm]**	**Voltage Range [V]**
ZL70550 (Microsemi)	779-965 *Sub-GHz*	2.75	-10	2.5	-95	1.71-3.6
ZL70251 (Microsemi)	779-965 *Sub-GHz*	2.4	-11	2.3	-94	1.2-1.9
Simblee (RFDigital)	2400 *BLE*	8	0	10	-93	1.8-3.6
nRF51822 (Nordic)	2400 *BLE*	8	0	9.7	-93	1.8-3.6
nRF8001 (Nordic)	2400 *BLE*	8.4	-18	14.6	-85	1.9-3.6
CC2640 (TI)	2400 *BLE*	6.1	0	5.9	-97	1.8-3.8
BC118 (BlueCreation)	2400 *BLE*	16	7.5	16	-92.5	3.3-4.7
PSoC4 (Cypress)	2400 *BLE*	16.5	0	18.7	-92	1.71-5.5
DA14580 (Dialog)	2400 *BLE*	4.9	0	4.9	-93	0.9-3.6
STM-300U (Enocean)	902 *Sub-GHz*	24	5.5	33	-98	2.6-4.5
SPSGRF (ST)	915 *Sub-GHz*	9	-7	10	-118	1.8-3.6
MKW01Z128 (NXP)	315-955 *Sub-GHz*	20	0	16	-120	1.8-3.6
nRF905 (Nordic)	433-915 *Sub-GHz*	9	-10	12.5	-100	1.9-3.6
CC1310 (TI)	315-920 *Sub-GHz*	12.9	-10	5.5	-124	1.8-3.6
CC430xx (TI)	315-915 *Sub-GHz*	15	0	15.4	-112	1.8-3.6
Si4455 (Silicon Labs)	284-960 *Sub-GHz*	18	10	10	-116	1.8-3.6

Nordic Semiconductor nrf51822 radio [19]. Multiple peaks corresponding to transmitting and receiving data are observed, with peak currents of 7mA and sleep currents of about 0.1mA. Thus, energy storage devices must be capable of providing both these longer duration, low current loads as well as the high current pulses necessary for device operation.

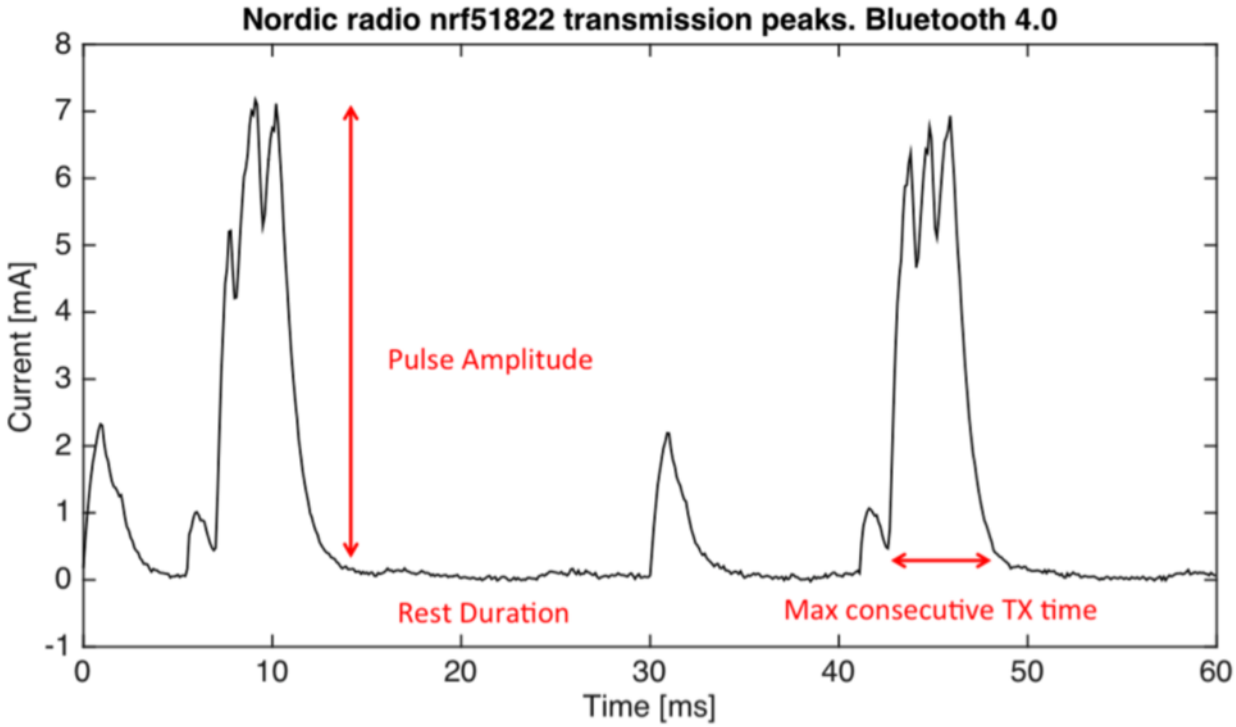

Figure 8.1: Pulse load demand profile of Nordic Semiconductor nrf51822 [19].

8.2.3 Pulsed Current Discharging for Energy Storage Devices

The load demands of wireless radios and Internet of Things devices poses a challenge for characterizing electrochemical energy storage device compatiblity with these systems. In particular, traditional characterization metrics for batteries focus primarily on the amount of charge remaining within the cell [26]. However, the rate which energy is discharged from the cell plays a significant role in battery degradation and thus overall device operation.

The cell internal resistance plays a significant role in battery operational lifetime, particularly at higher currents. Electronic devices require potential within a certain window in order to operate, as illustrated by Table 8.1. If the device voltage drops below a voltage minimum, the device experiences a brownout and is unable to properly function [29]. Cells must therefore be able to provide this minimum voltage in order to avoid brownouts and ensure proper device operation.

Figure 8.2 presents schematic discharge curves of a cell under constant current discharge and pulsed current discharge. While a given amount of capacity may be able to be discharged from the cell at a constant current, application of higher pulsed discharge currents momentarily cause a drop in cell potential. These drops are proportional to the cell's internal resistance and lead to the cell's potential prematurely crossing the device voltage limit, reducing the amount of accessible capacity compared to a cell discharged at constant current.

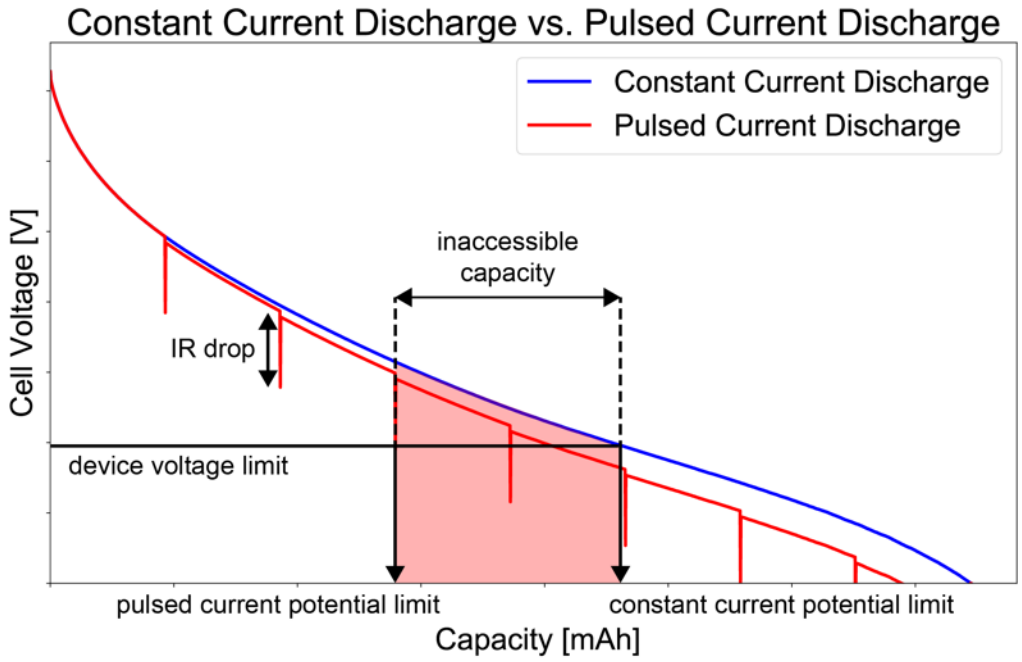

Figure 8.2: Discharge limit with constant current discharge vs. pulsed current discharge.

The factors that determine a cell's internal resistance vary by cell chemistry, manufacturing methods, as well as depths of discharge. For lithium-ion cells, internal resistance typically rises at higher depths of discharge due to changes in cell chemistry. The use of a capacitor in conjuction with a battery has been proposed in order to alleviate the load imposed on the battery in these systems [42], but in general, energy storage devices for wireless sensors must be appropriately considered depending on the specific application.

8.3 Experimental Methods

This section discusses the cycling parameters used for pulsed current discharge cycling of fully printed Zn-MnO_2 cells and characterization of commercial Panasonic ML2020 lithium-ion cells.

8.3.1 Pulsed Current Discharging for Zn-MnO_2 Cells

Fully printed Zn-MnO_2 cells were discharged under a pulsed current discharge regime in order to investigate cell compatibility with power demands for IoT devices. Cells were fully printed with 5 layers of $0.5M$ $[BMIM]^+[OTf]^-$ GPE and dried under vacuum, following the methods discussed in Chapter 6. These cells were chosen because they displayed the lowest internal resistance of all printed cells tested (300-500Ω).

Cells were cycled on a Bio-Logic BCS-805 battery tester. Cells were first charged with a constant current of 125μA until a potential of 1.8V was reached, then allowed to rest for 5 minutes, and then subjected to 5 1mA discharge current pulses of 4ms duration at 1 second intervals before repeating. Cells were cycled for 650 cycles. Figure 8.3 presents this pulsed current discharging protocol used for fully printed Zn-MnO_2 cells, and Table 8.2 presents the pulsed discharge cycling parameters used.

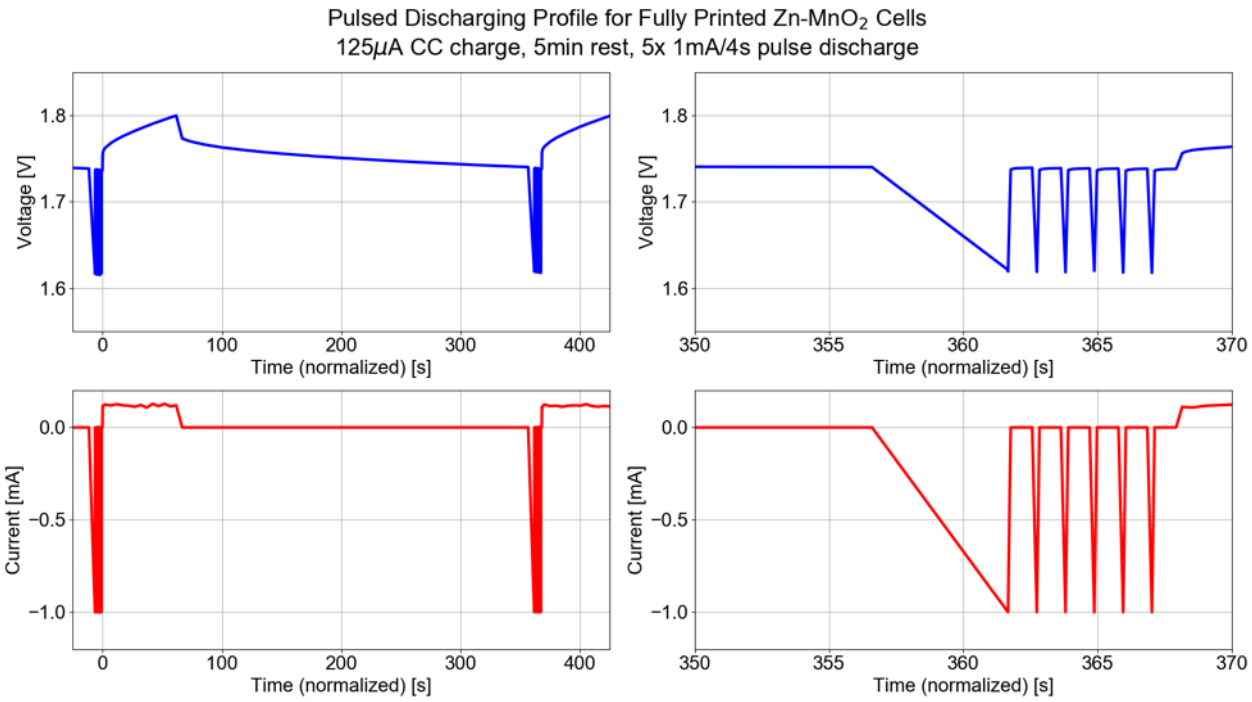

Figure 8.3: Pulsed discharge profile for fully printed Zn-MnO_2 cells. *Left*: example pulsed discharge profile for fully printed cells (with normalized time); *Right*: inset of pulsed discharging profile highlighting individual current pulses.

Table 8.2: Cycling parameters for pulsed discharging of printed Zn-MnO_2 cells.

Setting	**Value**		
	Sequence 0	**Sequence 1**	**Sequence 2**
Step 1			
Set I to I_s (vs. None) =	0mA	-1mA	0.125μA
for at most t_1 =	0h 0mn 0s	0.004s	24h
Limit $E_{cell} > E_M$ =	0V	1.0V	1.8V
Record up to t_{max} =	0	0.004s	2.0s
with geometric progression of time			
and then every dE_1 =	0mV	0mV	0V
or dt_1 =	0s	1s	5s
Hold E_M for t_M =	0h 0mn 0s	0h 0mn 0s	0h 0mn 0s
Limit |I| < I_m =	0mA	0mA	0mA
or |dI/dt| < dI/dt_f =	0mA/s	0mA/s	0mA/s
Record every dQ =	0A.h	0A.h	0A.h
or dt_q =	0s	0s	0s
Limit |ΔQ| > ΔQ_M =	0mA.h	0mA.h	0mA.h
<=> Δx_M =	0	0	0
Step 2			
Rest for t_R =	5mn	0h 0mn 0s	5mn
Limit |dE_{cell}/dt| < dE_R/dt =	0mV/h	0.0mV/h	0.0mV/h
Record every dE_R =	0mV	0mV	0mV
or dt_R =	10s	0s	10s
Step 3			
If $E_{cell} < E_L$ =	pass	pass	pass
Step 4			
Go back to seq. N'_s =	0	1	1
for n_c =	0	5	650

8.3.2 Cyclic Voltammetry for Commercial Lithium-Ion Cells

Cyclic voltammetry was performed on commercial lithium-ion cells to characterize their capacitive behavior. CV was performed from 3.2V to 2.0V at a scan rate of 100mV/s for 50 cycles. All other parameters were as presented in Chapter 6.

8.3.3 Pulsed Current Discharging for Commercial Lithium-Ion Cells

Pulsed discharge cycling was also performed on commercial lithium-ion cells. Panasonic ML2020 cells with a rated capacity of 45mAh were used for this work. All testing was performed on a Bio-Logic BCS-810 battery tester. New cells were used for all tests.

Cells were first tested via constant current discharging and constant current cycling in order to characterize discharge capacities at elevated currents. Cells were then discharged and cycled under a pulsed current discharge regime to investigate stability and long-term degradation.

For constant current discharging, cells were discharged with 200, 400, 600, 800, 1000, and 2000μA currents until a total capacity of 40mAh was discharged. No potential limitations were applied to these cells. Though the cells are rated for 45mAh capacity, dicharging was ceased at 40mAh to avoid potentially overdischarging cells. For constant current cycling, cells were cycled from 2.0-3.2V with a 10mA discharge current and a 1mA or 10mA charge current.

For pulsed current discharging, a pulsed discharge current was applied periodically, interrupting constant current discharge for potential limit characterization or constant current charge for megacycle testing. The frequency of the pulsed current discharge was maintained at 13.2s, and pulse widths of 0.132s, 0.660s, and 1.32s were used. These pulse widths and pulse frequency were chosen based on real-world wind speed sampling data [32].

For potential limit characterization, cells were discharged with a combined baseline current and pulsed discharge current until a potential limit of 2.0V was reached, with a baseline current of 1mA and a pulse discharge current of 10mA. For megacycle testing under pulsed discharge, cells were discharged with a 10mA current for 0.132, 0.660, or 1.32s. Cells were then recharged with a constant current of 10mA until 3.2V was reached or for 13.2s. Table 8.3 presents cycling parameters used for megacycle testing with pulsed current discharge.

Table 8.3: Cycling parameters for pulsed discharging of commercial li-ion cells.

Setting	**Value**		
	Sequence 0	**Sequence 1**	**Sequence 2**
Step 1			
Set I to I_s (vs. None) =	0mA	-10mA	10mA
for at most t_1 =	0h 0mn 0s	0.132s	13.2s
Limit $E_{cell} > E_M$ =	0V	2V	3.2V
Record up to t_{max} =	0	0.130s	2.0s
with geometric progression of time			
and then every dE_1 =	0mV	0mV	0V
or dt_1 =	0s	2s	2s
Hold E_M for t_M =	0h 0mn 0s	0h 0mn 0s	0h 0mn 0s
Limit $\|I\| < I_m$ =	0mA	0mA	0mA
or $\|dI/dt\| < dI/dt_f$ =	0mA/s	0mA/s	0mA/s
Record every dQ =	0A.h	0A.h	0A.h
or dt_q =	0s	0s	0s
Limit $\|\Delta Q\| > \Delta Q_M$ =	0mA.h	0mA.h	0mA.h
<=> Δx_M =	0	0	0
Step 2			
Rest for t_R =	0h 0mn 0s	0h 0mn 0s	0h 0mn 0s
Limit $\|dE_{cell}/dt\| < dE_R/dt$ =	0mV/h	0.0mV/h	0.0mV/h
Record every dE_R =	0mV	0mV	0mV
or dt_R =	10s	10s	10s
Step 3			
If $E_{cell} < E_L$ =	pass	pass	pass
Step 4			
Go back to seq. N'_s =	0	0	1
for n_c =	0	0	9999

8.4 Results and Discussion

This section presents results from pulsed current discharge of fully printed Zn-MnO_2 cells and from constant current and pulsed current discharge and cycling of commercial Panasonic ML2020 lithium-ion cells.

8.4.1 Pulsed Discharge of Printed Zn-MnO_2 Cells

Figure 8.4 presents internal resistance and average discharge potential by cycle. The average discharge potential was determined by taking the average potential upon discharge for each set of 5 pulses per cycle. Testing was interrupted due to equipment failure after about 150 cycles, resulting in an artificial drop in discharge potential.

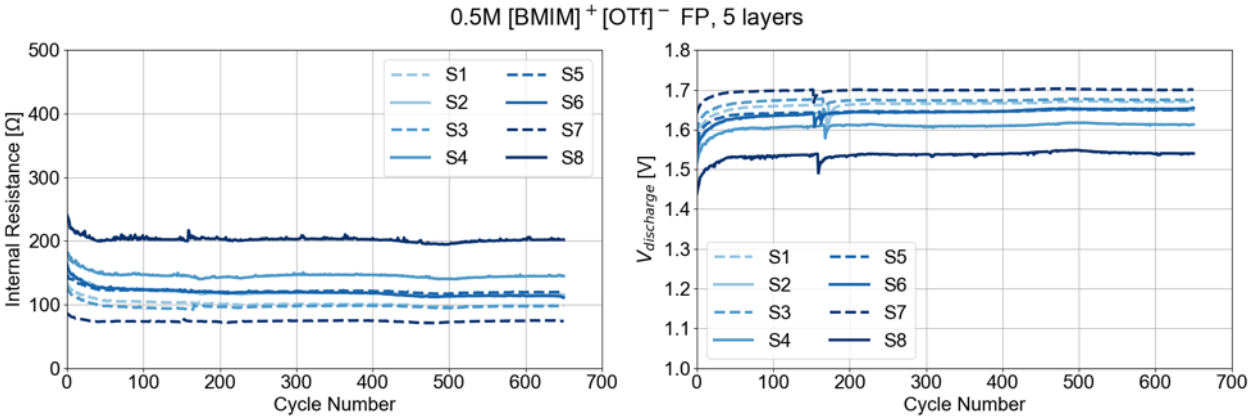

Figure 8.4: Pulsed discharge of 0.5M $[BMIM]^+[OTf]^-$ cell with GPE dried in vacuum, 5 layers. *Left*: internal resistance; *right*: average ending discharge voltage for each set of pulses.

After an initial increase decrease in internal resistance, which corresponded to an increase in discharge potential, cells showed no signs of degradation over the course of pulsed discharge cycling, unlike results from constant current cycling at 125μA as discussed in Chapter 6. After each pulsed discharge current, the potential drops slightly for each consecutive current pulse until the cell is recharged. Internal resistances as determined by pulsed discharge ranged from 90-220Ω with a median internal resistance of 115Ω, and average discharge potentials ranged from 1.54-1.7V with a median of 1.65V. For a 1mA discharge pulse with 4ms pulse width, this corresponds to 1.11e-6 mAh, significantly less than the typical discharge capacities observed with galvanostatic cycling.

With such short discharge times and consequently low amounts of charge required, electric double layer capacitance is likely responsible for providing the majority of these peak currents, rather than faradaic reactions. This capacitance likely originates from ion separation of the ionic liquid electrolyte. The lack of observable degradation shows promising

results for combined use of fully printed Zn-MnO_2 cells for wireless sensors as low current baseline loads under 125μA could be provided by charge transfer reactions while high current pulses could be provided mostly by electric double layer capacitance. However, further testing is required to probe the upper limits of both baseline and pulse currents with these cells due to kinetic and double layer formation limitations.

8.4.2 Characterization and Pulsed Discharge of Commercial Li-Ion Cells

This section presents results from cyclic voltammetry, constant current discharge, and pulsed current discharge and cycle life testing of Panasonic ML2020 cells.

8.4.2.1 Cyclic Voltammetry

Figure 8.5 presents the results of cyclic voltammetry on a Panasonic ML2020 cell at ν = 100mV/s. The current response is one order of magnitude higher than with Zn-MnO_2 cells presented in Chapter 6 with a minumum current of -45mA and a maximum current of 35mA during cycling. The shape of the voltammogram resembles those of mechanically assembled Zn-MnO_2 full cells in being similar to the response of a parallel resistor and capacitor. However, the scale of the response indicates a significantly lower resistance and higher capacitance compared to printed cells.

8.4.2.2 Constant Current Discharge and Cycling

Figure 8.6 presents voltage profiles of Panasonic ML2020 cells under constant current discharge. Cells were discharged until 40mAh of capacity was reached, and no potential limitation was applied. Figure 8.7 presents discharge capacity by cycle for cycle life testing of these cells under constant current charge and discharge. Cells were cycled from 2.0-3.2V, and two different charge currents were tested to investigate the effect of charge current on discharge capacity.

From Figure 8.6, there is a dependence of cell voltage upon discharging current. Though all cells begin at similar potentials (about 2.72V), their final potential decreases with increasing discharging current. While this may be partially due to increased contribution from internal resistance due to higher currents, it also indicates accelerated cell degradation with higher currents.

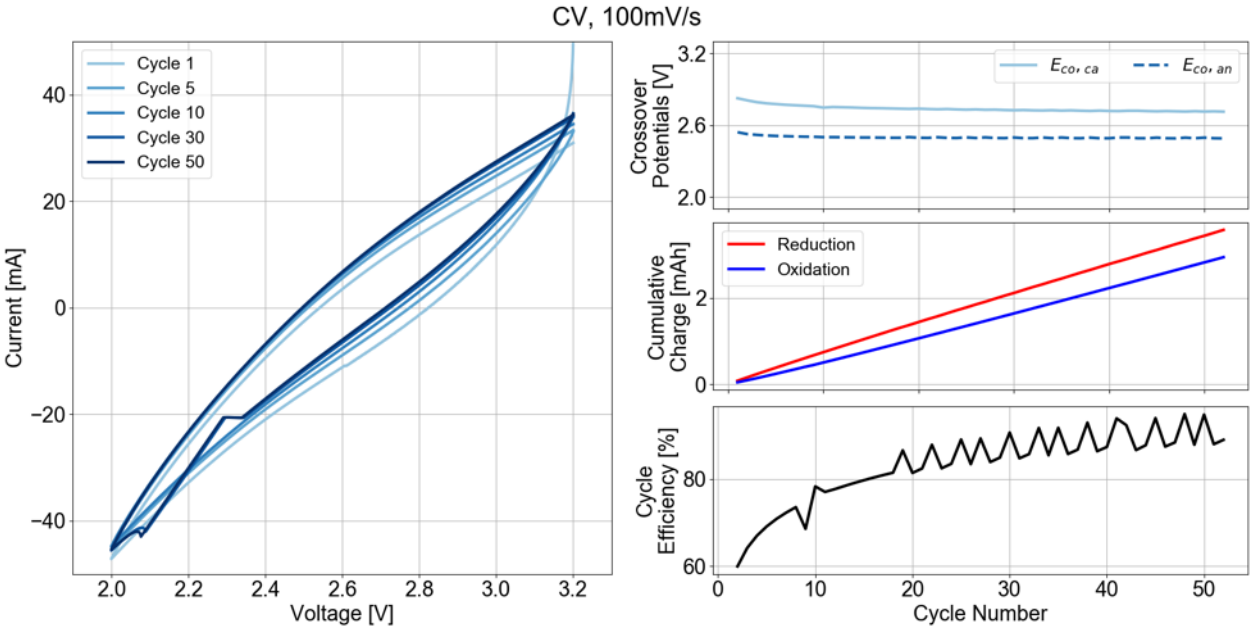

Figure 8.5: Cyclic voltammetry of Panasonic ML-2020 cell at 100mV/s scan rate. *Left*: CV for selected cycles; *right*: Crossover potentials, cumulative charge, and cycle efficiency per cycle.

From Figure 8.7, discharge capacities obtained from discharging at 10mA were significantly lower than the rated capacity of these cells. However, cell degradation rates were similar between cells regardless of charging current. The difference in capacities is likely due to shorter overall charging times for the higher charging current cell due to increased ohmic contributions. However, clear capacity loss is evidence after 100 cycles of constant current discharging, with cells dropping fom 12mAh to 8mAh and from 10mAh to 4.5mAh for cells with 1mA and 10mA charge currents respectively. This demonstrates significant degradation from deep discharge cycles at high currents.

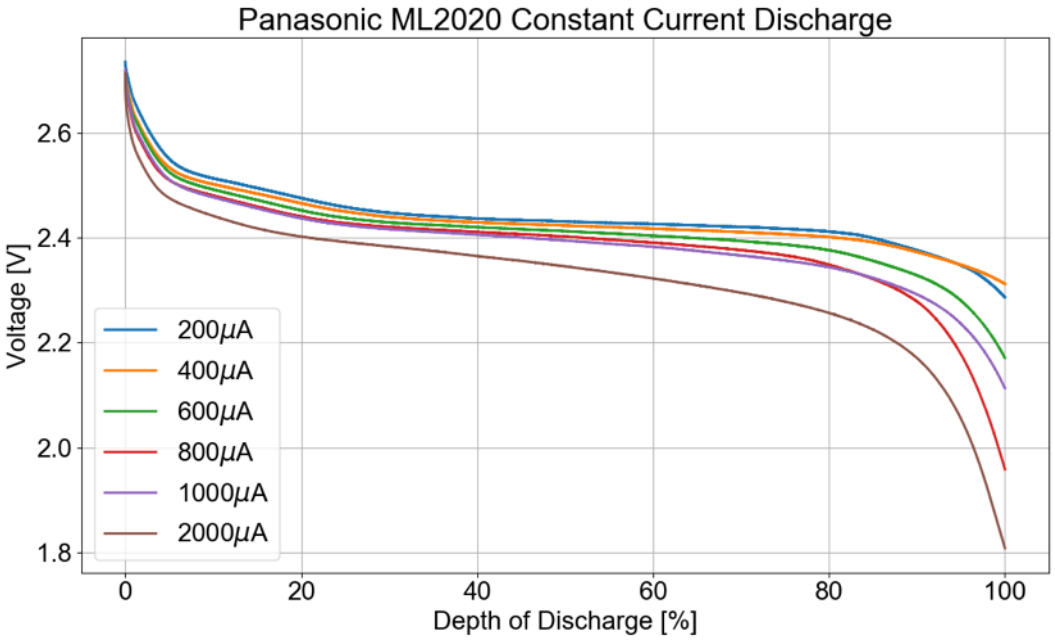

Figure 8.6: Voltage profiles of Panasonic ML-2020 cells during constant current discharge. Cells were discharged until 40mAh of capacity was discharged.

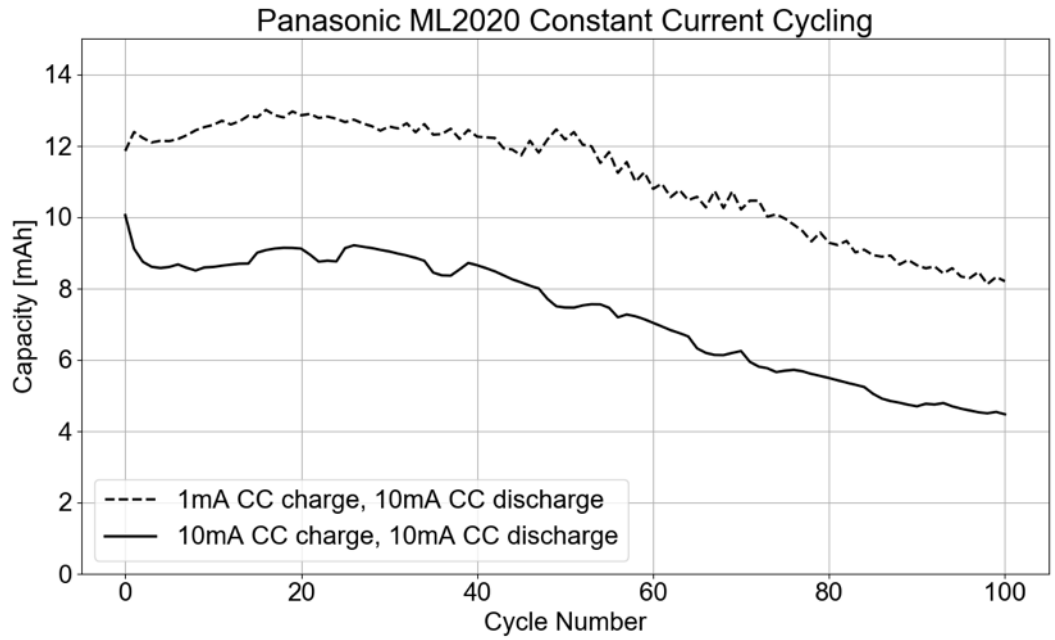

Figure 8.7: Discharge capacity during constant current (CC) cycling of Panasonic ML-2020 cells.

8.4.2.3 Pulsed Current Discharge and Cycling

Figure 8.8 presents voltage during pulsed current discharge with a pulse current of 10mA and a baseline current of 1mA. The solid line represents the cell voltage at the end of each baseline current discharge increment, and the dashed line represents the cell voltage at the end of each pulsed current discharge. These were separated in order to clarify the voltage drop due to pulsed current discharge. The plot inset shows the voltage of the cell during discharging with potential drops due to pulsed current discharging occurring every 13.2 seconds. Discharging was stopped once the cell voltage dropped below 2.0V.

Figure 8.9 presents discharge potential for cells subjected to megacycle testing by pulsed current discharge. All cells were still cycleable at the end of testing. The difference in the number of cycles tested between cells reflects the allowed length of time for testing and not cell failure. Two cells each were cycled with a pulse width of 0.132s and 0.660s and one cell for 1.32s pulse width. Due to excess noise present in calculated internal resistance, the discharge potential is presented as a measure of cell performance with cycling. Due to file size limitations, testing was divided into sets of cycles ranging from 100,000-1,000,000 cycles depending on memory and buffer size constraints. Table 8.4 presents the discharge capacity of each current pulse and the corresponding depth of discharge.

Table 8.4: Capacity and depth of discharge of pulsed current discharge.

Pulse Width [s]	**Capacity [mAh]**	**Depth of Discharge [%]**
0.132	0.000367	0.000815
0.660	0.00183	0.00407
1.32	0.00367	0.00815

The difference between the baseline voltage and the pulse discharge voltage increases as the cell discharges. This indicates higher ohmic losses, though it is unclear whether this is dependent on the depth of discharge or on cell aging. However, the lower potential limit of 2.0V is triggered by a discharge current pulse, demonstrating the shortened useable capacity of the cell before passing a device voltage threshold.

Megacycling of cells with varying degrees of current pulses shows that cells are able to provide at least 1 million discharge current pulses with no significant signs of degradation. The steps observed in discharge voltage for a single cell are due to varying amounts of time between cycling and are more related to calendar aging and temperature effects than degradation from cycling. Discharge voltages were about 3.02V for cells with 0.132s pulse width, 2.97V for cells with 0.660s pulse width, and 2.89V for cells with 1.32s pulse width. As the magnitude of the current pulse was kept constant (10mA), these lower voltages are due to longer pulse widths further discharging the cell.

Cells with 0.132s pulse width were tested for over 5 million pulse discharge cycles without clear indications of cell degradation, though a lower discharge potential was observed during the last set of cycling, likely due to calendar aging and fluctuating lab temperatures. The

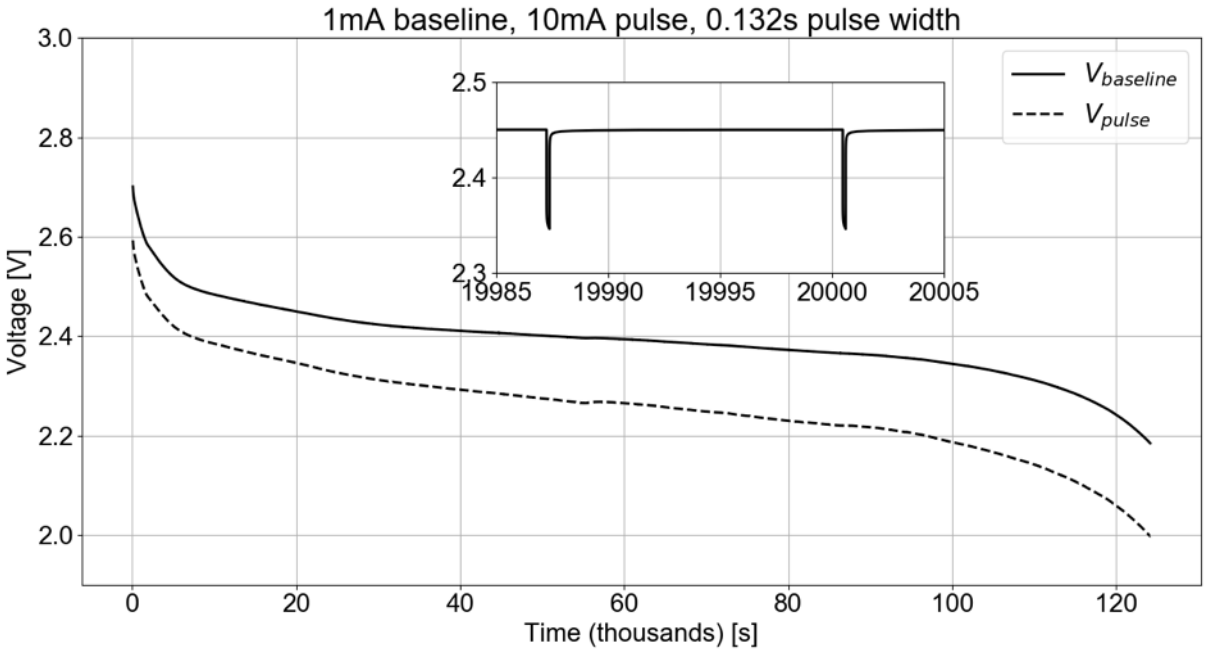

Figure 8.8: Cell voltage during 10mA pulsed current discharging with 1mA baseline discharge of Panasonic ML-2020 cell. *Inset*: voltage during pulsed current discharge.

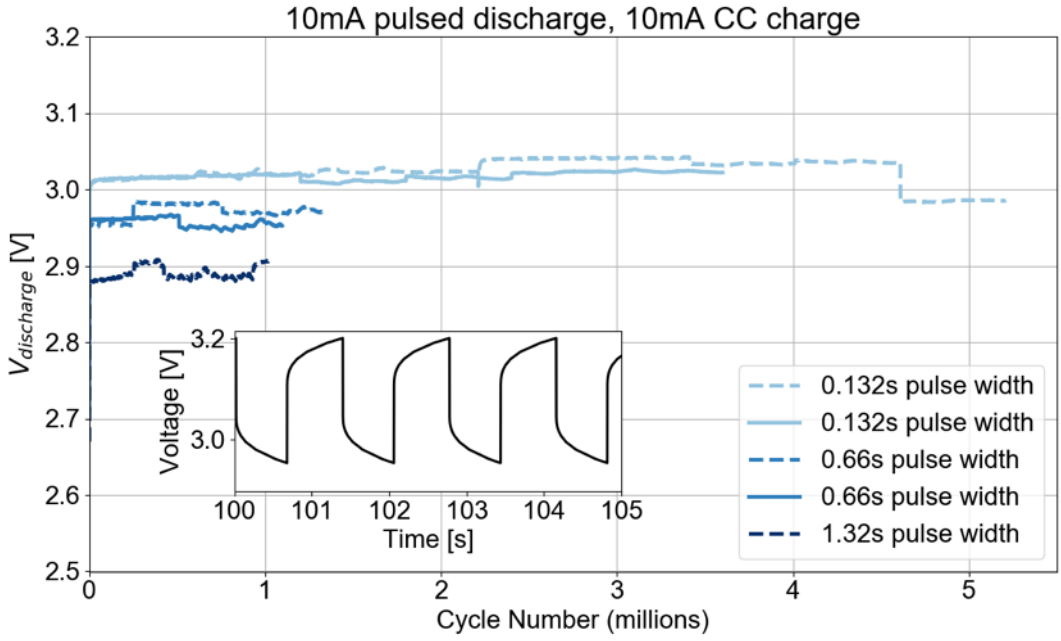

Figure 8.9: Megacycle testing by pulsed discharge of Panasonic ML-2020 cells with 10mA pulse and varying duty cycles. *Inset*: voltage of cell with 0.132s pulse width.

lack of observed degradation suggests that these cells are tolerant to the extremely shallow depths of discharge at currents expected for wireless radios.

With a rated capacity of 45mAh, a 10mA discharge current represents less than a C/4 discharge current, thus suggesting that these cells are capable of even higher pulse currents while providing enough usable capacity before crossing a voltage threshold. Design considerations for wireless sensors should consider sizing an appropriate cell based on device requirements, as these cells may be oversized for pulse current applications but may provide additional robustness in long term cycle life if lower baseline currents are also required.

8.5 Conclusion

This chapter presented results from pulsed current discharging of fully printed Zn-MnO_2 cells and commercial lithium-ion cells. Fully printed cells were able to cycle for 650 cycles under a 1mA pulsed current discharge with 4ms pulse width with no evident signs of degradation. This behavior is likely due to electric double layer contributions from the ionic liquid electrolyte and indicates these cells may be compatible for use with IoT devices.

Commercial lithium-ion cells (Panasonic ML2020) were characterized under constant current discharge, constant current cycling, pulsed current discharge, and megacycle testing via pulsed current discharge. With applied potential limits, lower capacities were observed with higher discharging currents, as expected, and capacities dropped significantly after 100 cycles of constant current cycling at 10mA from 10mAh to 4.5mAh at a constant charge and discharge current of 10mA. However, cells were also cycled with a pulsed discharge current of 10mA with pulse widths of 0.132s, 0.660s, and 1.32s and were cycled for each cell at least 1 million times with no signs of degradation. In addition, cells with 0.132s pulse width were cycled over 5 million times, again with no signs of degradation, indicating that the short duration of discharge offsets detrimental effects caused by sustained high currents.

Future work should seek to investigate the effects of more varied discharging protocols, changing the pulse magnitude, pulse width, and rest or charging times or currents, in order to determine the performance limits of fully printed cells and commercial cells. In addition, the longer cycle life testing should be conducted in order to investigate combined effects of discharge frequency and calendar aging on cells as may be demanded by practical IoT device considerations.

Chapter 9

Conclusions and Future Work

9.1 Conclusions

This research has determined the following conclusions.

9.1.1 Nickel Current Collector and Ball Milling

- The combination of ball milling parameters that yielded the most conductive printed nickel current collector was determined to be 30Hz, 10mm, 8 hours.
- Milling frequency and milling time is more significant in determining particle morphology than grinding ball size with the highest amount of particle deformation occurring for all ball sizes at 30Hz and 8 hours.

9.1.2 Optimization of Electrode Composition

- Cathode profilometry was significantly improved, reducing waviness and roughness by factors of about 10 and 5 respectively, by a combination of ball milling and sieving MnO_2 powder. However, optimizing for profilometry alone without simultaneously considering electrical conductivity resulted in extremely resistive cathodes.
- Cathode and anode inks were simultaneously optimized for profilometry, rheology, and electrical conductivity to yield acceptable values for all three metrics. Final cathode inks featured waviness and roughness values each 4 times lower than those for unoptimized inks.

9.1.3 Ionic Liquids and Electrochemical Analysis

- Zn^{2+} reduction in both ionic liquids was found to follow a two step mechanism in which Zn^{2+} is first adsorbed at nucleation sites and then further reduced. The initial adsorption and nucleation step is the rate determining step.

- Zn/Zn^{2+} redox is quasireversible in both ionic liquids.
- Redox kinetics were found to be faster in $[EMIM]^+[OTf]^-$ than in $[BMIM]^+[OTf]^-$, resulting in non-uniform surface morphologies. However, overall capacities are not significantly higher in $[EMIM]^+[OTf]^-$.
- The diffusivity of Zn^{2+} ranges from 1.42-3.38e-9 cm^2/s in $[BMIM]^+[OTf]^-$ and from 1.64-4.87e-9 cm^2/s in $[EMIM]^+[OTf]^-$ depending on salt concentration. As Zn^{2+} concentration increases, diffusivity decreases but higher currents are observed.
- Ionic conductivity ranges from 68.3-79.2 mS/cm in $[BMIM]^+[OTf]^-$ and from 223.8-237.6 mS/cm in $[EMIM]^+[OTf]^-$ and does not vary significantly with Zn^{2+} concentration.
- Charge transfer resistance decreased with increasing salt concentration and was generally lower for $[EMIM]^+[OTf]^-$ than for $[BMIM]^+[OTf]^-$, indicating faster kinetics in $[BMIM]^+[OTf]^-$.
- Generally, $[EMIM]^+[OTf]^-$ produced higher peak currents and coulombic efficiencies than $[BMIM]^+[OTf]^-$ but also led to more unstable and irregular deposition and dissolution.

9.1.4 Development of Gel Polymer Electrolyte

- PVDF-HFP microstructure was found to be more dependent on drying temperature than on drying environment and formed amorphous spherulites that were connected in semicrystalline domains when dried from NMP. Drying temperatures of 80°C were found to provide acceptable mechanical strength.
- GPEs dried in argon and thus in the absence of ambient moisture showed significantly lower electrochemical performance compared to GPEs dried in ambient and under vacuum. GPEs with $[BMIM]^+[OTf]^-$ showed more stable cycling behavior than GPEs with $[EMIM]^+[OTf]^-$, which quickly formed electrical shorts during cycling.
- GPEs dried under vacuum generally showed the highest ionic conductivities. $[BMIM]^+[OTf]^-$ GPEs showed higher ionic conductivities of 3.6mS/cm at slow scan rates, and $[EMIM]^+[OTf]^-$ showed higher ionic conductivities at fast scan rates of 6.8mS/cm. No significant changes were observed with cycling via CV, indicating no significant changes in bulk electrolyte composition. Charge transfer resistances were lower for $[BMIM]^+[OTf]^-$ GPEs and decreased significantly after cycling with CV. This is likely due to a change in electrode surface morphology.
- Mechanically assembled full cells with $[BMIM]^+[OTf]^-$ showed the highest stable discharge capacities of about 0.25-0.4mA/cm^2 when dried in vacuum and were cycled for 200 cycles. However, differential capacity analysis revealed the presence of phase change

or side reactions particularly during discharge, indicating phase changes within the MnO_2 crystal structure and the involvement of water in side reactions. $[BMIM]^+[OTf]^-$ GPEs are likely more sensitive to water than $[EMIM]^+[OTf]^-$ GPEs.

- Fully printed cells were successfully manufactured, but significant variation was observed within each batch during galvanostatic cycling. Cells with $[BMIM]^+[OTf]^-$ GPE dried in ambient displayed the highest discharge capacity of 0.1-0.4mAh/cm^2. Internal resistance was higher and charge transfer resistance was lower, likely due to the use of the printed Zn anode. However, ionic conductivity was lower with fully printed cells.
- Differential capacity analysis for fully printed cells compared to mechanically assembled cells reveals the presence of multiple potential-controlled discharge processes. Deeper depths of discharge that lead to irreversible phase changes in MnO_2 and thus capacity loss are prevented in the investigated fully printed cells due to their higher internal resistance.

9.1.5 Full Cell Manufacturing and Cycling

- Fully printed cells were manufactured that demonstrated at least a 20x improvement in cycle life over mechanically assembled cells with average discharge capacities of 1.8-3.6 mAh/cm^3. Cells were able to be cycled at least 200 times without catastrophic failure.
- Critical cell failure mechanisms were identified, including delamination of cathode material due to stresses from cycling, collapse of MnO_2 crystal structures, and deposition of Zn within poor GPE microstructures.
- Delamination of cathode material was mitigated by the use of fully printed GPEs.

9.1.6 Battery Cycling for IoT Devices

- Fully printed Zn-MnO_2 cells were discharged under a pulse current discharge regime for 650 cycles without signs of degradation.
- Commercial lithium-ion cells for use with Internet of Things devices were cycled for least 1 million cycles under pulsed current discharge without signs of degradation. One cell was cycled for over 5 million cycles.

9.2 Future Work

The results presented in this dissertation aim to optimize and develop a layer-by-layer fully printed secondary Zn-MnO_2 cell. While a number of optimizations were successfully performed on individual components, a number of critical degradation mechanisms have been identified that should be addressed for improved cell performance.

The phase transformations that occur in MnO_2 during discharge that limit cell reversibility and lead to capacity loss must be addressed and identified. XRD or EPS may be used to identify phases of MnO_2 present after discharge. Other phases of MnO_2 may be investigated, such as α-MnO_2 or layered γ-MnO_2, though synthesis of these phases may be necessary. These phases may allow for more reversible insertion and de-insertion of Zn^{2+} from their crystal structures. Another solution may be establishing stricter potential limits that restrict discharge to shallower depths of discharge. This is motivated by the lower but steady discharge capacities observed for some cells during galvanostatic cycle life testing which suggests the existence of a potential window in which irreversible phase changes do not occur. While this would allow for the continued use of γ-MnO_2, this would also lower discharge capacity per cycle.

There exists room for further optimization of electrode slurries. The combination of ball milling and sieving proved effective in improving surface profilometry but was extremely labor intensive. The use of high speed dispersion or more powerful sonication techniques may be adequate to achieve the same level of agglomerate separation with less manual effort. In addition, further optimization of electrode slurry composition may be necessary to further improve printed electrode conductivity while maintaining high levels of active material. Considering phase changes and strains that occur in γ-MnO_2 during Zn^{2+} insertion, the ratio of polymer to acetylene black may also need to be re-optimized to accomodate volume expansion and contraction during cycling to maintain electrical contact.

Further optimizations may also be made with the gel polymer electrolyte structure. While this work sought to minimize GPE thickness in order to improve capacity density, the formation of shorts with the thinnest printed layers prompts further investigation into GPE microstructure to control Zn deposition through the separator. This is especially applicable for $[EMIM]^+[OTf]^-$ electrolytes, which otherwise demonstrated superior mass transport and kinetic properties than $[BMIM]^+[OTf]^-$ electrolytes. Process controls should be further tightened to ensure optimal GPE morphology during the layer-by-layer printing process. This may involve printing in a separate chamber in which temperature and pressure can be controlled to influence solvent evaporation rates. In addition, other polymers or solvents should be explored to investigate other polymer structures aside from the spherulite-based structure observed in this work.

The layer-by-layer printing process may also be optimized to reduce the number of total drying steps involved. The multiple layers of GPE printed introduce multiple opportunities for variation within the polymer structure that may introduce undesired morphologies or inconsistencies within the GPE. The number of layers may be reduced by optimizing the amounts of ionic liquid electrolyte, polymer binder, and solvent while maintaining acceptable ink viscosity.

Finally, once degradation mechanisms have been addressed or mitigated, future work should seek to print larger cells or arrays of cells. This will necessitate extremely good environmental and manufacturing control as well as optimization of ink rheology for larger print areas to ensure uniform and repeatable ink deposition.

Appendix A

Python Code

This appendix presents select custom algorithms used in processing data for this work. Specifically, the code below presents the window-gradient algorithm used to isolate profilometry traces and the FFT algorithm used to calculate roughness and waviness in Chapter 4, the semicircle fitting algorithm used to calculate charge transfer resistance in Chapter 5, and the smoothing algorithm used to smooth cycle life data and differential capacity in Chapters 6 and 7. Selected code from the Python modules written is presented. All other custom Python code written for this work can be found at https://github.com/bernardkimj/battery.

Profilometry Module

```
''' Module for analyzing results retrieved from Dektak profilometer

Author: Bernard Kim
Principal Investigators: Prof. Paul Wright, Prof. James Evans
University: University of California, Berkeley

'''

from battery.utilities import utilities
from operator import itemgetter
import matplotlib
import matplotlib.pyplot as plt
import numpy as np
import csv
import re

font = {'family': 'Arial', 'size': 16}
matplotlib.rc('font', **font)

class profile:

    ''' Analyzes data from Dektak profilometer
        Pulls data from .csv file for plotting and analysis.
    '''

    def __init__(self, filename=None, isolate=True,
        showalg=False, savealg=False):
        ''' Opens file and retrieves data. '''

        # x    h
        # um   nm

        x, height = [], []

        rows = list(csv.reader(open(filename), delimiter=','))

        switch = None

        for index, row in enumerate(rows):
            try:
                if row:
                    # Find the part in the file where the actual data starts
                    if row[0][0:2] == 'um' and row[1] == 'A':
                        switch = index
                if switch is not None and index > switch:
                    if len(row) > 0:
                        x.append(float(row[0]))
                        # x.append(float(row[0]) * 0.001)
```

```
                    height.append(float(row[1]) * 0.001)

            except Exception:
                raise

        # Save data and convert measurements to mm and um for x and height
        # respectively
        self.line = {
            'x': np.array(x), # um (for now)
            'height': np.array(height), # um
        }

        self.title = filename[:-4]

        self.idxs = self.find_sample(isolate=isolate,
            showalg=showalg, savealg=savealg)
        self.get_roughness_waviness()

    def find_sample(self, isolate=True, showalg=False, savealg=False):
        '''
        Finds where the sample actually starts and ends
        Returns index ranges within self.line['x']
        Uses window-gradient with line fit
        '''

        location, height = self.line['x'], self.line['height']

        length = 0.30 # length of end of profile to check
        # window lower/upper bound half size for polyfit
        bounds = (0.025, 0.075)

        allvals = {}

        for edge in ['front', 'back']:
            x_edge, y_edge = self.get_edge(x=location, y=height,
                length=length, end=edge)

            if edge == 'front':
                slope_sign = 1
            elif edge == 'back':
                slope_sign = -1

            flat_coefs = self.window_gradient(x=x_edge, y=y_edge,
                bounds=bounds, slope=0)
            steep_coefs = self.window_gradient(x=x_edge, y=y_edge,
                bounds=bounds, slope=slope_sign)

            flat_line = np.polyval(flat_coefs, x_edge)
            steep_line = np.polyval(steep_coefs, x_edge)
```

```
            diff = 1
            for loc, flat, steep in zip(x_edge, flat_line, steep_line):
                if np.abs(flat-steep) < diff:
                    diff = np.abs(flat-steep)
                    xval = loc
            idx = np.where(location==xval)[0][0]

            allvals[edge] = {
                'idx': idx,
                'line_x': x_edge,
                'flat_line': flat_line,
                'steep_coefs': steep_coefs,
                'steep_line': steep_line,
            }

        if isolate:
            # center region of isolated sample to take mean
            meanregion = 0.80
            # length of overlap ends for inner intersection
            overlaplength = 0.30

            sub_idx = (allvals['front']['idx'], allvals['back']['idx'])
            sub_x = location[sub_idx[0]:sub_idx[1]]
            sub_y = height[sub_idx[0]:sub_idx[1]]

            x_mid, y_mid = self.get_edge(x=sub_x, y=sub_y,
                length=(1-meanregion)/2, end='middle')
            mean_coefs = np.polyfit(x_mid, y_mid, deg=1)

            for edge in ['front', 'back']:
                x_overlap, y_overlap = self.get_edge(x=location, y=height,
                    length=overlaplength, end=edge)

                mid_line = np.polyval(mean_coefs, x_overlap)
                steep_line = np.polyval(allvals[edge]['steep_coefs'],
                    x_overlap)

                diff = 1
                for loc, mid, steep in zip(x_overlap, mid_line, steep_line):
                    if np.abs(mid-steep) < diff:
                        diff = np.abs(mid-steep)
                        xval = loc
                mid_idx = np.where(location==xval)[0][0]

                allvals[edge]['mid_x'] = x_overlap
                allvals[edge]['mid_line'] = mid_line
                allvals[edge]['idx'] = mid_idx

        if showalg or savealg:
            font = {'family': 'Arial', 'size': 24}
```

```
        matplotlib.rc('font', **font)

        fig, ax = plt.subplots(figsize=(16,9), dpi=75)

        ax.plot(location*0.001, height,linewidth=2, color='k')
        ymin, ymax = ax.get_ylim()

        for edge in allvals:
            ax.plot(allvals[edge]['line_x']*0.001,
                allvals[edge]['steep_line'], linewidth=2, color='r')
            ax.plot(allvals[edge]['line_x']*0.001,
                allvals[edge]['flat_line'], linewidth=2, color='g')

            if isolate:
                ax.plot(allvals[edge]['mid_x']*0.001,
                    allvals[edge]['mid_line'],
                    linewidth=2, color='b')

        ax.set_ylim([ymin, ymax])

        ax.set_xlabel('Horizontal Position [mm]')
        ax.set_ylabel('Height [Âţm]')
        ax.set_title(self.title+'_edges')
        ax.grid()

        if savealg:
            plt.savefig(self.title + '_edges.png')
        if showalg:
            plt.show()

    return (allvals['front']['idx'], allvals['back']['idx'])


def get_edge(self, x, y, length, end):
    '''Isolates ends of raw profile data on which to run window gradient
        algorithm
        Returns x and y vectors corresponding to extracted ends
    '''

    if end == 'front':
        stop = int(length*len(x)) # right index of front range
        idxs = (0, stop) # beginning and ending indices of front range
    elif end == 'back':
        stop = int(len(x)*(1-length)) # left index of back range
        idxs = (stop, len(x)-1) # beginning and ending indices of back edge
    elif end == 'middle':
        leftstop = int(length*len(x)) # left index of middle range
        rightstop = int(len(x)*(1-length)) # right index of middle range
        idxs = (leftstop, rightstop)
```

```
        x_end = x[idxs[0]:idxs[1]]
        y_end = y[idxs[0]:idxs[1]]

        return x_end, y_end


    def window_gradient(self, x, y, bounds, slope):
        ''' Applies a window-gradient algorithm to find optimal linear fit
            Provide x, y data, window size boundaries, sign of slope to find
            Returns coefficients of optimal linear fit
        '''

        windownum = 50 # number of windows to iterate through
        positionnum = 50 # number of positions to iterate through

        lbound = np.round(min(bounds)*len(x)) # smallest window size
        ubound = np.round(max(bounds)*len(x)) # largest window size
        # array of window sizes
        windows = np.linspace(lbound, ubound, windownum)

        line_vals = []

        for window in windows:
            values = []

            # array of indices of center of window
            positions = np.linspace(window, len(x)-window, positionnum)

            for position in positions:
                win_x = x[int(position-window):int(position+window)]
                win_y = y[int(position-window):int(position+window)]

                # apply linear fit to section within window
                coefs = np.polyfit(win_x, win_y, deg=1)
                test_line = np.polyval(coefs, x)
                residuals = np.sum((test_line-y)**2)

                # store intermediate values
                values.append((residuals, coefs[0], coefs[1]))

            # depending on desired line slope, save best value for window
            if np.sign(slope) == 0:
                values.sort(key=lambda tup:np.abs(tup[1]))
                line_vals.append(values[0])
            elif np.sign(slope) == 1:
                line_vals.append(max(values, key=itemgetter(1)))
            elif np.sign(slope) == -1:
                line_vals.append(min(values, key=itemgetter(1)))

        # get set of coefficients for lines with lowest residual score
```

```
        line_coefs = min(line_vals, key=itemgetter(0))[1:3]

        return(line_coefs)

    def get_roughness_waviness(self):
        ''' Calculates roughness and waviness of 1-D profile
            Uses FFT
            Adapted from code by Rich Winslow
        '''

        cutoff = 80 # Âţm

        primary_x = self.line['x'][self.idxs[0]:self.idxs[1]]
        primary = self.line['height'][self.idxs[0]:self.idxs[1]]

        samplewidth = self.line['x'][self.idxs[1]] - \
            self.line['x'][self.idxs[0]]
        samplelength = len(primary)

        flipped = primary[::-1]

        extended = np.concatenate((flipped, primary, flipped))
        f = np.array(np.fft.fft(extended))
        f[1:-1] = f[1:-1]*2

        wavelengths = [
            2*samplewidth/N for N in range(1, samplelength)
        ]

        stop_index = 0
        while wavelengths[stop_index] > cutoff:
            stop_index += 1

        filtered = f
        filtered[stop_index:-1] = 0

        ifft_result = np.real(np.fft.ifft(filtered))
        waviness = ifft_result[samplelength:2*samplelength]

        roughness = primary - waviness

        self.primary = primary
        self.wavelengths = wavelengths
        self.waviness = waviness
        self.roughness = roughness

        self.zero_average_waviness()
        self.calculate_metrics()

    def zero_average_waviness(self):
```

```
        ''' Zero-averages the waviness so the center of the waviness
            profile is at zero

            Done by taking mean of waviness profile and subtracting mean
            at each point. '''

        waviness_avg = np.mean(self.waviness)
        self.waviness_zero_avg = self.waviness - waviness_avg
```

Smoothing Algorithm

```
''' Module containing common data processing scripts used across
    multiple modules

    Author: Bernard Kim
    Principal Investigators: Prof. Paul Wright, Prof. James Evans
    University: University of California, Berkeley
'''

import numpy as np
import matplotlib
import matplotlib.pyplot as plt
import re
import csv
from operator import itemgetter
import scipy.stats as stats
import json

class utilities:

    ''' Common functions and data processing scripts '''

    def __init__(self):
        pass

    def moving_average(interval, size, weight=None):
        ''' Calculates moving average to smooth noise from data
            Choose weighting option based on kwarg 'weight'
            Based on convolution, so weights must be centered on window
            'size' is desired fraction of interval to be considered for smoothing
            '''

        n = int(np.ceil(len(interval)*size))

        if weight == None or weight == 'unweighted':
            window = np.ones(n)/n
        # Weighting for linear and exp weights is not properly centered,
        # sample average is biased towards future numbers
        elif weight == 'linear':
            window = np.arange(1,n+1)/(n*(n+1)/2)
        elif weight == 'exp':
            alpha = 2/(n+1)
            coeffs = np.zeros(n)

            for idx, coeff in enumerate(coeffs):
                coeffs[idx] = (1 - alpha)**idx

            window = coeffs/np.sum(coeffs)
```

```
    smoothed = np.convolve(interval, window, 'valid')

    overhang = len(interval) - len(smoothed)
    frontpad = int(np.ceil(overhang/2))
    endpad = int(np.floor(overhang/2))
    idxs = (frontpad, len(interval)-endpad)

    return smoothed, idxs
```

EIS Module

```
''' Module for analyzing results retrieved from Gamry

Author: Bernard Kim
Principal Investigators: Prof. Paul Wright, Prof. James Evans
University: University of California, Berkeley

'''

import matplotlib
import matplotlib.pyplot as plt
from matplotlib.patches import Ellipse
import numpy as np
import csv
import re
import bisect
from scipy import optimize
from decimal import Decimal
from battery.utilities import utilities

class EIS:

    '''
        Analyzes data from Gamry EIS
        Pulls data from .dta file for plotting and analysis.
    '''

    def __init__(self, filename=None, thickness=None, area=1, zscale='k'):
        ''' Opens file and retrieves data.

        Retrieves time, frequency, real impedance, imaginary impedance,
        magnitude, and phase. Assumes that the first part of the file is an
        OCV test and that the header for the table consists of two lines.

        Unit requirements:
            R_solution [ohm]
            Thickness [cm]
            Area [cm^2]
        '''

        self.filename = filename
        self.thickness = thickness
        self.area = area

        self.zscalestr, self.zscaleval = self.get_zscale(zscale)

        titlesearch = re.search(r'EXDTA_.*_S\d{1,2}', self.filename)
        try:
            self.title = titlesearch.group(0)[6:]
```

```
        except AttributeError:
            self.title = self.filename[:-4]

        self.time = []
        self.freq = []
        self.realraw = []
        self.imagraw = []
        self.phase = []
        self.magnraw = []

        with open(filename, errors='replace') as f:
            rows = f.readlines()

            switch = False
            for index, row in enumerate(rows):
                row = row.split()
                try:
                    if row:
                        if row[0] == 'ZCURVE':
                            switch = index + 2

                        if (self.is_num(row[0]) and switch and index > switch):
                            self.time.append(float(row[1]))
                            self.freq.append(float(row[2]))
                            self.realraw.append(float(row[3]))
                            self.imagraw.append(float(row[4]))
                            self.magnraw.append(float(row[6]))
                            self.phase.append(float(row[7]))
                except Exception:
                    raise

        self.real = [realraw/self.zscaleval for realraw in self.realraw]
        self.imag = [-1*imagraw/self.zscaleval for imagraw in self.imagraw]
        self.magn = [magnraw/self.zscaleval for magnraw in self.magnraw]

        self.find_r_solution()

        if self.thickness:
            self.conductivity = (self.thickness*1000)/(self.area*self.r_solution)

    def get_nyquist_fit(self):
        ''' Calculates circular fit of Nyquist plot
            For determining r_sol and r_ct
        '''

        # Find where high frequency behavior ends as inclusion
        # messes up circular fit later
        hfend = False
        checklen = 10 # forward length of series to check for monotonicity
```

```
        # Check real and imaginary vectors until both are monotonically
        # increasing over checked length
        # Point where future points for both vectors are monotonically
        # increasing is where high frequency region ends
        for idx, real in enumerate(self.real[:-1]):
            if not hfend:
                realcheck = utilities.check_forward_monotonicity(
                    series=self.real[idx:],
                    type='increasing',
                    length=checklen
                )
                imagcheck = utilities.check_forward_monotonicity(
                    series=self.imag[idx:],
                    type='increasing',
                    length=checklen
                )

                if realcheck == True and imagcheck == True:
                    hfend = idx

        # Take derivative of remaining region
        d1 = []

        for idx in range(hfend, len(self.real[:-1])):
            delta_x = self.real[idx+1] - self.real[idx]
            delta_y = self.imag[idx+1] - self.imag[idx]
            d1.append(delta_y/delta_x)

        # plt.plot(list(range(len(d1))), d1)
        # plt.show()

        # Apply smoothing algorithm to derivative in order to smooth out
        # local minima
        smoothsize = 0.15
        d1s, idxs = utilities.moving_average(
            interval=d1, size=smoothsize, weight=None)
        pad = idxs[0] # front pad size after smoothing

        # Find point in smoothed derivative where derivative is maximum
        d1s_max = np.where(np.array(d1s) == np.max(d1s))[0][0]

        # Now find minimum of smoothed derivative to find where curvature
        # changes
        d1s_min = False

        # Forward length to check for monotonic decrease
        d1check = 15

        for idx, m in enumerate(d1s[d1s_max:-d1check-1],d1s_max):
            if not d1s_min:
```

```
            mincheck = utilities.check_forward_monotonicity(
                series=d1s[idx:],
                type='decreasing',
                length=d1check
            )

            # Find where next point after monotonic decrease increases
            # This is where curvature change is
            if mincheck == True and d1s[idx+d1check] < d1s[idx+d1check+1]:
                d1s_min = idx+d1check

    # If increase never happens, then minimum is just endpoint of vector
    if not d1s_min:
        d1s_min = len(d1s)+(len(d1)-idxs[1])

    # Add back missing lengths from high frequency identification and
    # smoothing
    bounds = (d1s_max+pad+hfend, d1s_min+pad+hfend)

    # plt.plot(list(range(pad+hfend, pad+hfend+len(d1s))), d1s)
    # plt.axvline(d1s_max+pad+hfend, color='k')
    # plt.axvline(d1s_min+pad+hfend, color='k')
    # plt.show()

    # plt.plot(self.real, self.imag)
    # plt.axvline(self.real[bounds[0]], color='k')
    # plt.axvline(self.real[bounds[1]], color='k')
    # plt.show()

    real = self.real[bounds[0]:bounds[1]]
    imag = self.imag[bounds[0]:bounds[1]]

    # Adopted from Scipy cookbook
    # https://scipy-cookbook.readthedocs.io/items/Least_Squares_Circle.html
    def calc_R(x, y, xc, yc):
        '''
        Calculate the distance of each point from the center (xc, yc)
        '''

        return np.sqrt((x-xc)**2 + (y-yc)**2)

    def f(c, x, y):
        '''
        Calcualte algebraic distance between the data points and
        the mean circle centered at c=(xc, yc)
        '''

        Ri = calc_R(x, y, *c)
        return Ri - Ri.mean()
```

```
real_m = np.mean(imag)
imag_m = 0
center_estimate = real_m, imag_m

center = optimize.least_squares(
    fun=f, x0=center_estimate, args=(real,imag),
    bounds=([-np.inf, 0], np.inf),
)

xc, yc = center.x
Ri = calc_R(real, imag, *center.x)
R = Ri.mean()
residual = np.sum((Ri - R)**2)

self.xc, self.yc = xc, yc
self.nyquist_R = R
```

Bibliography

[1] K M Abraham. "Directions in Secondary Lithium Battery Research and Development". In: *Electrochimica Acta* 38 (1993), pp. 1233–1248.

[2] Muhammad H Alfaruqi et al. "Electrochemically Induced Structural Transformation in a γ-MnO 2Cathode of a High Capacity Zinc-Ion Battery System". In: *Chemistry of Materials* 27.10 (May 2015), pp. 3609–3620.

[3] Arkema and Inc. "Kynar & Kynar Flex: Polyvinylidene Fluoride (PVDF) Resins for Batteries". In: (Oct. 2012), pp. 1–6.

[4] A Robert Armstrong et al. "Nonstoichiometric Layered Li xMn yO 2with a High Capacity for Lithium Intercalation/Deintercalation". In: *Chemistry of Materials* 14.2 (Feb. 2002), pp. 710–719.

[5] Jakob Asenbauer et al. "Solubilities and ionic conductivities of ionic liquids containing lithium salts". In: *Electrochimica Acta* 247 (Sept. 2017), pp. 1038–1043.

[6] Kevin Ashton. *That Internet of Things Thing*. June 2009. URL: `http://www.itrco.jp/libraries/RFIDjournal-That%20Internet%20of%20Things%20Thing.pdf`.

[7] Mark R Bailey and Scott W Donne. "Structural effects on the cyclability of the alkaline gamma-MnO2 electrode". In: *Electrochimica Acta* 56.14 (May 2011), pp. 5037–5045.

[8] Allen J Bard and Larry R Faulkner. *Electrochemical Methods: Fundamentals and Applications*. 2nd. John Wiley & Sons, Inc., 2001.

[9] Fritz Beck and Paul Rüetschi. "Rechargeable batteries with aqueous electrolytes". In: *Electrochimica Acta* 45 (2000), pp. 2467–2482.

[10] Kyle T Braam, Steven K Volkman, and Vivek Subramanian. "Characterization and optimization of a printed, primary silver–zinc battery". In: *Journal of Power Sources* 199 (Feb. 2012), pp. 367–372.

[11] E Oran Brigham. *The Fast Fourier Transform And Its Applications*. Englewood Cliffs, New Jersey 07632: Prentice Hall, 1988.

[12] F Bueche. "Electrical resistivity of conducting particles in an insulating matrix". In: *Journal of Applied Physics* 43.11 (Nov. 1972), pp. 4837–4838.

[13] J C Burns et al. "Evaluation of Effects of Additives in Wound Li-Ion Cells Through High Precision Coulometry". In: *Journal of The Electrochemical Society* 158.3 (2011), A255–7.

[14] A Calka and A P Radlinski. "Universal high performance ball-milling device and its application for mechanical alloying". In: *Materials Science and Engineering* A134 (1991), pp. 1350–1353.

[15] Pieremanuele Canepa et al. "Odyssey of Multivalent Cathode Materials: Open Questions and Future Challenges". In: *Chemical Reviews* 117.5 (Feb. 2017), pp. 4287–4341.

[16] J CAO, B ZHU, and Y XU. "Structure and ionic conductivity of porous polymer electrolytes based on PVDF-HFP copolymer membranes". In: *Journal of Membrane Science* 281.1-2 (Sept. 2006), pp. 446–453.

[17] Yuanyuan Cao et al. "Water sorption in ionic liquids: kinetics, mechanisms and hydrophilicity". In: *Physical Chemistry Chemical Physics* 14.35 (2012), pp. 12252–11.

[18] Ronald Chwang, B J Smith, and C R Crowell. "Contact size effects on the Van der Pauw method for resistivity and Hall coefficient measurement". In: *Solid-State Electronics* 17 (1974), pp. 1217–1227.

[19] Martin Andrew Cowell. "The role of energy reservoirs in distributed computing: Manufacturing, implementing, and optimizing energy storage in energy-autonomous sensor nodes". PhD thesis. University of California, Berkeley, July 2017.

[20] M Czerwicka et al. "Identification of ionic liquid breakdown products in an advanced oxidation system". In: *Journal of Hazardous Materials* 171.1-3 (Nov. 2009), pp. 478–483.

[21] John W Diggle, Robert J Fredericks, and Annemarie C Reimschuessel. "Crystallographic and morphological studies of electrolytic zinc dendrites grown from alkaline zincate solutions". In: *Journal of Materials Science* (1973), pp. 79–87.

[22] John L DiMeglio and Bart M Bartlett. "Interplay of Corrosion and Photocatalysis During Nonaqueous Benzylamine Oxidation on Cadmium Sulfide". In: *Chemistry of Materials* 29.17 (Aug. 2017), pp. 7579–7586.

[23] Nicholas E Dixon et al. "Trifluoromethanesulfonates and Trifluoromethanesulfonato-O Complexes". In: *Inorganic Syntheses*. Ed. by Robert J Anjelici. 1990, pp. 70–76.

[24] M A Dzieciuch, N Gupta, and H S Wroblowa. "Rechargeable Cells with Modified MnO2 Cathodes". In: *Journal of the Electrochemical Society Electrochemical Science and Technology* 135 (Oct. 1988), pp. 2415–2418.

[25] M Sherif El-Eskandarany. "Controlling the powder milling process". In: *Mechanical Alloying*. Elsevier, 2015, pp. 48–83.

[26] Laura Marie Feeney, Christian Rohner, and Anders Lindgren. "How do the dynamics of battery discharge affect sensor lifetime?" In: *IEEE* (Feb. 2014), pp. 1–8.

[27] S R Forrest and T A Witten Jr. "Long-range correlations in smoke-particle aggregates". In: *Journal of Physics A: Mathematical and General* 12.5 (Feb. 1979), pp. L109–L117.

[28] Stewart A Forsyth, Jennifer M Pringle, and Douglas R MacFarlane. "Ionic Liquids—An Overview". In: *Australian Journal of Chemistry* 57.2 (2004), pp. 113–7.

[29] Kjartan Furset, Peter Hoffman, and Nordic Semiconductor. *High pulse drain impact on CR2032 coin cell battery capacity*. Tech. rep. 2011.

[30] Maciej Galiński, Andrzej Lewandowski, and Izabela Stępniak. "Ionic liquids as electrolytes". In: *Electrochimica Acta* 51.26 (Aug. 2006), pp. 5567–5580.

[31] Guinevere A Giffin et al. "Complex Nature of Ionic Coordination in Magnesium Ionic Liquid-Based Electrolytes: Solvates with Mobile Mg 2+Cations". In: *The Journal of Physical Chemistry C* 118.19 (May 2014), pp. 9966–9973.

[32] google.org. *RE<C: Surface Level Wind Data Collection*. Tech. rep. Nov. 2011.

[33] Antoni S Gozdz et al. "LITHIUM SECONDARY BATTERY EXTRACTION METHOD". Pat. July 1996.

[34] Antoni S Gozdz et al. "POLYMERIC ELECTROLYTIC CELL SEPARATOR MEMBRANE". Pat. May 1995.

[35] Jayavardhana Gubbi et al. "Internet of Things (IoT): A vision, architectural elements, and future directions". In: *Future Generation Computer Systems* 29.7 (Sept. 2013), pp. 1645–1660.

[36] Sang-Don Han et al. "Mechanism of Zn Insertion into Nanostructured δ-MnO 2: A Nonaqueous Rechargeable Zn Metal Battery". In: *Chemistry of Materials* 29.11 (May 2017), pp. 4874–4884.

[37] Sang-Don Han et al. "Origin of Electrochemical, Structural, and Transport Properties in Nonaqueous Zinc Electrolytes". In: *ACS Applied Materials & Interfaces* 8.5 (Feb. 2016), pp. 3021–3031.

[38] Benjamin J Hertzberg et al. "Effect of Multiple Cation Electrolyte Mixtures on Rechargeable Zn–MnO2 Alkaline Battery". In: *Chemistry of Materials* 28.13 (July 2016), pp. 4536–4545.

[39] C C Ho, J W Evans, and P K Wright. "Direct write dispenser printing of a zinc microbattery with an ionic liquid gel electrolyte". In: *Journal of Micromechanics and Microengineering* 20.10 (Sept. 2010), pp. 104009–10.

[40] Gamry Instruments. *Basics of EIS: Electrochemical Research-Impedance*. https://www.gamry.com/application-notes/EIS/basics-of-electrochemical-impedance-spectroscopy/.

[41] Anna Jarosik et al. "Conductivity of ionic liquids in mixtures". In: *Journal of Molecular Liquids* 123.1 (Jan. 2006), pp. 43–50.

[42] Mathias Jensen and Texas Instruments, Incorporated. *Coin Cells And Peak Current Draw*. Tech. rep. Oct. 2010.

[43] M Johnsi and S Austin Suthanthiraraj. "Preparation, zinc ion transport properties, and battery application based on poly(vinilydene fluoride- co-hexa fluoro propylene) polymer electrolyte system containing titanium dioxide nanofiller". In: *High Performance Polymers* 27.7 (Dec. 2014), pp. 877–885.

[44] Jayme Scot Keist. "In-situ Analysis of Zinc Electrodeposition within an Ionic Liquid Electrolyte". In: (May 2013), pp. 1–158.

[45] Jayme Scot Keist et al. "An in situ AFM Study of the Evolution of Surface Roughness for Zinc Electrodeposition within an Imidazolium Based Ionic Liquid Electrolyte". In: *Electrochimica Acta* 152 (Jan. 2015), pp. 161–171.

[46] Saleem Khan, Leandro Lorenzelli, and Ravinder S Dahiya. "Technologies for Printing Sensors and Electronics Over Large Flexible Substrates: A Review". In: *IEEE Sensors Journal* 15.6 (Apr. 2015), pp. 3164–3185.

[47] B Kim et al. "Layer-by-layer fully printed Zn-MnO 2batteries with improved internal resistance and cycle life". In: *Journal of Physics: Conference Series* 660 (Dec. 2015), pp. 012009–6.

[48] B J Kim, J W Evans, and P K Wright. "Pulsed discharge of printed secondary Zn-MnO 2batteries for IoT and wearable devices". In: *Journal of Physics: Conference Series* 1052 (July 2018), pp. 012012–5.

[49] Kwang Man Kim et al. "Characteristics of PVdF-HFP/TiO2 composite membrane electrolytes prepared by phase inversion and conventional casting methods". In: *Electrochimica Acta* 51.26 (Aug. 2006), pp. 5636–5644.

[50] K Kordesch and M Weissenbacher. "Rechargeable alkaline manganese dioxide/zinc batteries". In: *Journal of Power Sources* 51 (1994), pp. 61–78.

[51] G Girish Kumar and S Sampath. "Electrochemical Characterization of a Zinc-Based Gel-Polymer Electrolyte and Its Application in Rechargeable Batteries". In: *Journal of The Electrochemical Society* 150.5 (2003), A608–8.

[52] G Girish Kumar and S Sampath. "Electrochemical characterization of poly(vinylidenefluoride)-zinc triflate gel polymer electrolyte and its application in solid-state zinc batteries". In: *Solid State Ionics* 160.3-4 (June 2003), pp. 289–300.

[53] C Lämmel et al. "Investigations of electrochemical double layer capacitor (EDLC) materials - a comparison of test methods". In: *Materialwissenschaft und Werkstofftechnik* 44.7 (July 2013), pp. 641–649.

[54] Boeun Lee et al. "Electrochemically-induced reversible transition from the tunneled to layered polymorphs of manganese dioxide". In: *Scientific Reports* 4.1 (Aug. 2014), pp. 3447–8.

[55] Boeun Lee et al. "Elucidating the intercalation mechanism of zinc ions into alpha-MnO2 for rechargeable zinc batteries". In: *Chemical Communications* 51.45 (May 2015), pp. 9265–9268.

[56] G Liu et al. "Effects of Various Conductive Additive and Polymeric Binder Contents on the Performance of a Lithium-Ion Composite Cathode". In: *Journal of The Electrochemical Society* 155.12 (2008), A887–6.

[57] G Liu et al. "Optimization of Acetylene Black Conductive Additive and PVDF Composition for High-Power Rechargeable Lithium-Ion Cells". In: *Journal of The Electrochemical Society* 154.12 (2007), A1129–6.

[58] Wenbao Liu et al. "Investigation of zinc ion storage of transition metal oxides, sulfides, and borides in zinc ion battery systems". In: *Chemical Communications* 53.51 (June 2017), pp. 6872–6874.

[59] Z Liu, S Zein El Abedin, and F Endres. "Electrodeposition of zinc films from ionic liquids and ionic liquid/water mixtures". In: *Electrochimica Acta* 89 (Feb. 2013), pp. 635–643.

[60] Zhen Liu, Sherif Zein El Abedin, and Frank Endres. "Electrochemical and spectroscopic study of Zn(ii) coordination and Zn electrodeposition in three ionic liquids with the trifluoromethylsulfonate anion, different imidazolium ions and their mixtures with water". In: *Physical Chemistry Chemical Physics* 17.24 (June 2015), pp. 15945–15952.

[61] Zhen Liu, Sherif Zein El Abedin, and Frank Endres. "Electrodeposition and stripping of zinc from an ionic liquid polymer gel electrolyte for rechargeable zinc-based batteries". In: *Journal of Solid State Electrochemistry* 18.10 (June 2014), pp. 2683–2691.

[62] Zhen Liu et al. "Dendrite-Free Nanocrystalline Zinc Electrodeposition from an Ionic Liquid Containing Nickel Triflate for Rechargeable Zn-Based Batteries". In: *Angewandte Chemie* 128.8 (Jan. 2016), pp. 2939–2943.

[63] Zhen Liu et al. "Suppressing the dendritic growth of zinc in an ionic liquid containing cationic and anionic zinc complexes for battery applications". In: *Dalton Trans.* 45.19 (2016), pp. 8089–8098.

[64] E Madej et al. "Optimization of primary printed batteries based on Zn/MnO2". In: *Journal of Power Sources* 261.C (Sept. 2014), pp. 356–362.

[65] A Manuel Stephan. "Review on gel polymer electrolytes for lithium batteries". In: *European Polymer Journal* 42.1 (Jan. 2006), pp. 21–42.

[66] *MatWeb: Material Property Data*. http://www.matweb.com/index.aspx. July 2019.

[67] P McCluskey et al. "Models of electrical conduction in nanoparticle filled polymers". In: *IEEE* (Mar. 2004). 0-7803-4934-2/98, pp. 84–89.

[68] A I Medalia and F A Heckman. "Morphology of Aggregates – II. Size and Shape Factors of Carbon Black Aggregates From Electron Microscopy". In: *Carbon* (Jan. 1969), pp. 567–582.

[69] Ruiying Miao et al. "PVDF-HFP-based porous polymer electrolyte membranes for lithium-ion batteries". In: *Journal of Power Sources* 184.2 (Oct. 2008), pp. 420–426.

[70] Manickam Minakshi et al. "The Zn–MnO2 Battery: The Influence of Aqueous LiOH and KOH Electrolytes on the Intercalation Mechanism". In: *Electrochemical and Solid-State Letters* 11.8 (2008), A145–5.

[71] Hiroshi Mio et al. "Optimum revolution and rotational directions and their speeds in planetary ball milling". In: *International Journal of Mineral Processing* 74 (Dec. 2004), S85–S92.

[72] Christian Mondoloni et al. "Rechargeable Alkaline Manganese Dioxide Batteries I. In Situ X-Ray Diffraction Investigation of the H+/gamma-MnO2 (EMD-Type) Insertion System". In: *Journal of The Electrochemical Society* 139 (Apr. 1992), pp. 1–6.

[73] Seung-Taek Myung, Yashiro Hitoshi, and Yang-Kook Sun. "Electrochemical behavior and passivation of current collectors in lithium-ion batteries". In: *Journal of Materials Chemistry* 21.27 (2011), pp. 9891–21.

[74] John Newman and Karen E Thomas-Alyea. *Electrochemical Systems*. John Wiley & Sons, Inc., 2004.

[75] Aminy E Ostfeld and Ana Claudia Arias. "Flexible photovoltaic power systems: integration opportunities, challenges and advances". In: *Flexible and Printed Electronics* 2.1 (Mar. 2017), pp. 013001–25.

[76] William R Pitner and Charles L Hussey. "Electrodeposition of Zinc from the Lewis Acidic Aluminum Chloride-1-Methyl-3-ethylimidazolium Chloride Room Temperature Molten Salt". In: *Journal of The Electrochemical Society* 144 (Sept. 1997), pp. 3095–3103.

[77] K Raeissi, A Saatchi, and M A Golozar. "Effect of nucleation mode on the morphology and texture of electrodeposited zinc". In: *Journal of Applied Electrochemistry* 33 (July 2003), pp. 635–642.

[78] V I Roldughin and V V Vysotskii. "Percolation properties of metal-filled polymer films, structure and mechanisms of conductivity". In: *Progress in Organic Coatings* 39 (Nov. 2000), pp. 81–100.

[79] K Romer, F Mattern, and ETH Zurich. "The Design Space of Wireless Sensor Networks". In: *IEEE Wireless Communications* 11.6 (July 2001), pp. 54–61.

[80] Ziqin Rong et al. "Materials Design Rules for Multivalent Ion Mobility in Intercalation Structures". In: *Chemistry of Materials* 27.17 (Sept. 2015), pp. 6016–6021.

[81] G R Ruschau, S Yoshikawa, and R E Newnham. "Resistivities of conductive composites". In: *Journal of Applied Physics* 72 (Aug. 1992), pp. 953–959.

[82] Benjamin Scharifker and Graham Hills. "Theoretical and Experimental Studies of Multiple Nucleation". In: *Electrochimica Acta* 28 (1983), pp. 879–889.

[83] G D Scott and D M Kilgour. "The density of random close packing of spheres". In: *Journal of Physics D: Applied Physics* 2 (Feb. 1969), pp. 863–866.

[84] Yuyan Shao et al. "Highly Reversible Mg Insertion in Nanostructured Bi for Mg Ion Batteries". In: *Nano Letters* 14.1 (Jan. 2014), pp. 255–260.

[85] Tristan J Simons et al. "Zn Electrochemistry in 1-Ethyl-3-Methylimidazolium and N-Butyl- N-Methylpyrrolidinium Dicyanamides: Promising New Rechargeable Zn Battery Electrolytes". In: *ChemElectroChem* 1.10 (Sept. 2014), pp. 1688–1697.

[86] A J Smith, J C Burns, and J R Dahn. "High-Precision Differential Capacity Analysis of LiMn2O4/graphite Cells". In: *Electrochemical and Solid-State Letters* 14.4 (2011), A39–3.

[87] A J Smith and J R Dahn. "Delta Differential Capacity Analysis". In: *Journal of The Electrochemical Society* 159.3 (Jan. 2012), A290–A293.

[88] J Y Song, Y Y Wang, and C C Wan. "Review of gel-type polymer electrolytes for lithium-ion batteries". In: *Journal of Power Sources* 77 (Feb. 1999), pp. 183–197.

[89] J Y Song et al. "Microstructure of Poly(vinylidene fluoride)-Based Polymer Electrolyte and Its Effect on Transport Properties". In: *Journal of The Electrochemical Society* 149.9 (2002), A1230–7.

[90] B E Springett. "Conductivity of a system of metallic particles dispersed in an insulating medium". In: *Journal of Applied Physics* 44.6 (June 1973), pp. 2925–2926.

[91] John A Stankovic. "Research Directions for the Internet of Things". In: *IEEE Internet of Things Journal* 1.1 (Apr. 2014), pp. 3–9.

[92] Piotr Stepnowski and Adriana Zaleska. "Comparison of different advanced oxidation processes for the degradation of room temperature ionic liquids". In: *Journal of Photochemistry and Photobiology A: Chemistry* 170.1 (Feb. 2005), pp. 45–50.

[93] Stefan Stolte et al. "Primary biodegradation of ionic liquid cations, identification of degradation products of 1-methyl-3-octylimidazolium chloride and electrochemical wastewater treatment of poorly biodegradable compounds". In: *Green Chemistry* 10.2 (2008), pp. 214–224.

[94] Jr T A Witten and L M Sander. "Diffusion-Limited Aggregation, a Kinetic Critical Phenomenon". In: *Physical Review Letters* 47 (Nov. 1981), pp. 1400–1403.

[95] Juan Tafur, Florencio Santos, and Antonio Romero. "Influence of the Ionic Liquid Type on the Gel Polymer Electrolytes Properties". In: *Membranes* 5.4 (Dec. 2015), pp. 752–771.

[96] Juan P Tafur et al. "Charge storage mechanism of MnO2 cathodes in Zn/MnO2 batteries using ionic liquid-based gel polymer electrolytes". In: *Electrochemistry Communications* 60.C (Nov. 2015), pp. 190–194.

[97] J M Tarascon et al. "Performance of Bellcore's plastic rechargeable Li-ion batteries". In: *Solid State Ionics* 86 (1996), pp. 49–54.

[98] Z Tehrani et al. "Ultra-thin flexible screen printed rechargeable polymer battery for wearable electronic applications". In: *Organic Electronics* 26.C (Nov. 2015), pp. 386–394.

[99] R Y Wang, D W Kirk, and G X Zhang. "Effects of Deposition Conditions on the Morphology of Zinc Deposits from Alkaline Zincate Solutions". In: *Journal of The Electrochemical Society* 153.5 (2006), pp. C357–8.

[100] Zuoqian Wang et al. "Development of MnO2 cathode inks for flexographically printed rechargeable zinc-based battery". In: *Journal of Power Sources* 268.C (Dec. 2014), pp. 246–254.

[101] Richard White et al. "Atmospheric Sensors and Energy Harvesters on Overhead Power Lines". In: *Sensors* 18.2 (Feb. 2018), pp. 114–7.

[102] Richard Lemuel Winslow IV. "Optimization of 3D-Printed, Flexible, Rechargeable, Zinc-baed Batteries via a Novel Gel Polymer Ionic Liquid Electrolyte". PhD thesis. University of California, Berkeley, 2014.

[103] W J Wruck et al. "Rechargeable Zn-Mn02 Alkaline Batteries". In: *Journal of The Electrochemical Society* 138 (Dec. 1991), pp. 3560–3567.

[104] Chengjun Xu et al. "Energetic Zinc Ion Chemistry: The Rechargeable Zinc Ion Battery". In: *Angewandte Chemie International Edition* 51.4 (Dec. 2011), pp. 933–935.

[105] Jun John Xu, Hui Ye, and Jian Huang. "Zinc Polymer Gel Electrolytes Based on Oligomeric Polyethers and Ionic Liquids". In: *ECS Meeting Abstracts* (Jan. 2005), pp. 1–1.

[106] M Xu et al. "Zn/Zn(II) Redox Kinetics and Zn Deposit Morphology in Water Added Ionic Liquids with Bis(trifluoromethanesulfonyl)imide Anions". In: *Journal of The Electrochemical Society* 161.1 (Oct. 2013), A128–A136.

[107] Pei Xu et al. "Enhanced dc conductivity and conductivity relaxation in PVDF/ionic liquid composites". In: *Materials Letters* 206 (Nov. 2017), pp. 60–63.

[108] Qiliang Richard Xu et al. "Miniature self-powered stick-on wireless sensor node for monitoring of overhead power lines". In: *2013 IEEE Energy Conversion Congress and Exposition* (July 2013), pp. 2672–2675.

[109] PeiXia Yang et al. "Gel polymer electrolyte based on polyvinylidenefluoride-co-hexafluoropropylene and ionic liquid for lithium ion battery". In: *Electrochimica Acta* 115 (Jan. 2014), pp. 454–460.

[110] Yun-Sheng Ye, John Rick, and Bing-Joe Hwang. "Ionic liquid polymer electrolytes". In: *J. Mater. Chem. A* 1.8 (2013), pp. 2719–2743.

[111] Chaosheng Yuan et al. "Effect of pressure on the structure and properties of polymeric gel based on polymer PVdF-HFP and ionic liquid [BMIM][BF4]". In: *Colloid and Polymer Science* 293.3 (Dec. 2014), pp. 925–932.

[112] Qibo Zhang and Yixin Hua. "Effects of [HMIM]HSO4 and [OMIM]HSO4 on the electrodeposition of zinc from sulfate electrolytes". In: *Journal of Applied Electrochemistry* 39.8 (Jan. 2009), pp. 1185–1192.

[113] Qibo Zhang and Yixin Hua. "Influence of [BMIM]HSO4 on electrodeposition and corrosion behavior of Zn coatings from acidic sulfate bath". In: *Surface and Interface Analysis* 44.9 (Mar. 2012), pp. 1254–1260.